Would you live in a wood skyscraper? *p. 1364*

Yeast genetic interactions revealed *p. 1381*

Remote sensing for induced seismic hazard *p. 1416*

Science

$15
23 SEPTEMBER 2016
sciencemag.org
AAAS

DRY FOREST

Diversity in the American tropics *p. 1383*

CONTENTS

1350
Neandertal handiwork

23 SEPTEMBER 2016 • VOLUME 353 • ISSUE 6306

1354 Concept for a wooden skyscraper

NEWS

IN BRIEF

1344 News at a glance

IN DEPTH

1347 THE SUBDUCTION ZONE OBSERVATORY TAKES SHAPE
Geoscientists want large project to study dynamic and dangerous plate boundaries *By J. Rosen*

1348 USING DNA, RADIATION THERAPY GETS PERSONAL
Gene-based tests aim to predict who will benefit from radiation, or suffer *By E. Dolgin*

1350 NEANDERTALS MADE JEWELRY, PROTEINS CONFIRM
"Landmark" study firmly links sophisticated artifacts from France to our extinct cousins *By L. Wade*

1351 PAIRED STARS SCULPT NEBULAE INTO FANCIFUL SHAPES
Survey suggests fast-orbiting binaries at work within many of the gas clouds shed by dying stars *By J. Sokol*

1352 ABORIGINES AND EURASIANS RODE ONE MIGRATION WAVE
Tide of genetic data refutes idea that an earlier expansion of modern humans populated the island continent *By E. Culotta and A. Gibbons*

1353 CHINA BETS BIG ON BIG FACILITIES
Anchored by a powerful synchrotron, first of a series of multidisciplinary national science centers will rise by 2023 *By J. Qiu*

FEATURES

1354 TALL TIMBER
High-tech wood is taking the place of steel in a new wave of green high-rises *By W. Cornwall*

1357 SOLVING AUSTRALIA'S LANGUAGE PUZZLE
Methods borrowed from evolutionary biology show how people spread across the continent, giving birth to new languages *By M. Erard*

INSIGHTS

PERSPECTIVES

1360 GATHERING LOTS OF DATA ON A SMALL BUDGET
Open-source hardware and software technology can redefine data collection *By A. C. Greenville and N. J. Emery*

1362 HOW CONIFERS ADAPT TO THE COLD
Highly diverged conifer species share many genetic signals of adaptation to local climate conditions *By A. M. Hancock*
▸ REPORT P. 1431

1363 COOL BY NEURONAL DECISION
An ion channel expressed in specific brain neurons is required for regulating core body temperature *By T. Bartfai*
▸ RESEARCH ARTICLE P. 1393

1365 HOW HYBRID PEROVSKITES GET THEIR GROOVE
Rotational motions of organic cations may screen charge carriers from defects *By M. E. Ziffer and D. S. Ginger*
▸ REPORT P. 1409

1366 FROM SCIENCE TO SERVICE
Climate services are crucial for successful adaptation to current and future climate conditions *By L. Goddard*

POLICY FORUM

1368 TOWARD STRATEGIC, COHERENT, POLICY-RELEVANT ARCTIC SCIENCE
A modified Arctic Council could play an expanded role *By C. Tesar* et al.

1368

BOOKS *ET AL.*

1371 MIND THE (HEALTH) GAP
A geographer turns a critical eye toward regional health disparities *By P. R. Reczek*

1372 STRANGE BEDFELLOWS
Scientific collaboration takes center stage in a participants' account of post–Cold War nuclear disarmament *By F. von Hippel*

Downloaded from http://science.sciencemag.org/ on September 30, 2016

PHOTO (TOP): ANDERS BERENSSON ARCHITECTS

Published by AAAS

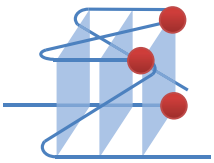

1382 The fate of RNA G-quadruplexes

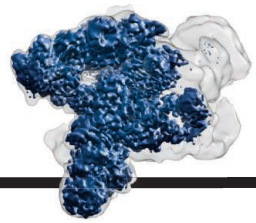

1399 The activated spliceosome

LETTERS

1374 COMPOUND HAZARDS YIELD LOUISIANA FLOOD
By F. Vahedifard et al.

1374 ADDRESSING OBESITY IN HOMELESS CHILDREN
By J. A. Levine et al.

1375 ZIKA VACCINE: CLINICAL TRIAL AND ERROR?
By D. P. Dittmer

RESEARCH

IN BRIEF

1377 From *Science* and other journals

REVIEW

1380 MATERIALS SCIENCE
Atomic electron tomography: 3D structures without crystals *J. Miao* et al.
REVIEW SUMMARY; FOR FULL TEXT:
dx.doi.org/10.1126/science.aaf2157

RESEARCH ARTICLES

1381 YEAST GENETICS
A global genetic interaction network maps a wiring diagram of cellular function *M. Costanzo* et al.
RESEARCH ARTICLE SUMMARY; FOR FULL TEXT:
dx.doi.org/10.1126/science.aaf1420

1382 RNA STRUCTURE
RNA G-quadruplexes are globally unfolded in eukaryotic cells and depleted in bacteria
J. U. Guo and D. P. Bartel
RESEARCH ARTICLE SUMMARY; FOR FULL TEXT:
dx.doi.org/10.1126/science.aaf5371

1383 FOREST ECOLOGY
Plant diversity patterns in neotropical dry forests and their conservation implications *DRYFLOR*

1387 INFECTIOUS DISEASE
Replication of human noroviruses in stem cell–derived human enteroids
K. Ettayebi et al.

1393 NEUROSCIENCE
The TRPM2 channel is a hypothalamic heat sensor that limits fever and can drive hypothermia
K. Song et al.
▸ PERSPECTIVE P. 1363

1399 STRUCTURAL BIOLOGY
Molecular architecture of the *Saccharomyces cerevisiae* activated spliceosome *R. Rauhut* et al.

REPORTS

1406 GEOPHYSICS
Tomography reveals buoyant asthenosphere accumulating beneath the Juan de Fuca plate
W. B. Hawley et al.

1409 SOLAR CELLS
Screening in crystalline liquids protects energetic carriers in hybrid perovskites *H. Zhu* et al.
▸ PERSPECTIVE P. 1365

1413 NANOMATERIALS
High-quality graphene via microwave reduction of solution-exfoliated graphene oxide *D. Voiry* et al.

1416 GEOPHYSICS
Surface uplift and time-dependent seismic hazard due to fluid injection in eastern Texas *M. Shirzaei* et al.

1419 CARBON CYCLE
Radiocarbon constraints imply reduced carbon uptake by soils during the 21st century *Y. He* et al.

1424 ATMOSPHERIC SCIENCE
An unexpected disruption of the atmospheric quasi-biennial oscillation
S. M. Osprey et al.
▸ PODCAST

1427 ATMOSPHERIC OXYGEN
A Pleistocene ice core record of atmospheric O_2 concentrations
D. A. Stolper et al.

1431 CONVERGENT EVOLUTION
Convergent local adaptation to climate in distantly related conifers
S. Yeaman et al.
▸ PERSPECTIVE P. 1362

1434 HOST TOLERANCE
A secreted bacterial peptidoglycan hydrolase enhances tolerance to enteric pathogens *K. J. Rangan* et al.
▸ *SCIENCE IMMUNOLOGY* RESEARCH ARTICLE BY L. A. K. PEDICORD *ET AL.*
10.1126/sciimmunol.aai7732

DEPARTMENTS

1343 EDITORIAL
Speaking of insects… *By May R. Berenbaum*

1458 WORKING LIFE
Managing my fear of missing out
By Shane M. Hanlon

ON THE COVER

A leafless tree (*Ceiba trischistandra*) in Machalilla National Park, Ecuador. This species is a characteristic element of Ecuadorean and northern Peruvian tropical dry forest, particularly during the dry season. The large differences in tree species composition found in dry forests across the American tropics indicate that many conservation areas will be required to protect the biodiversity of these threatened formations. See page 1383.
Photo: Pete Oxford/Minden Pictures

Science Staff 1340
Gordon Research Conferences 1438
New Products 1449
Science Careers 1450

SCIENCE (ISSN 0036-8075) is published weekly on Friday, except the last week in December, by the American Association for the Advancement of Science, 1200 New York Avenue, NW, Washington, DC 20005. Periodicals mail postage (publication No. 484460) paid at Washington, DC, and additional mailing offices. Copyright © 2016 by the American Association for the Advancement of Science. The title SCIENCE is a registered trademark of the AAAS. Domestic individual membership and subscription (51 issues): $165 ($74 allocated to subscription). Domestic institutional subscription (51 issues): $1522; Foreign postage extra: Mexico, Caribbean (surface mail) $55; other countries (air assist delivery) $89. First class, airmail, student, and emeritus rates on request. Canadian rates with GST available upon request, GST #1254 88122. Publications Mail Agreement Number 1069624. **Printed in the U.S.A.**
Change of address: Allow 4 weeks, giving old and new addresses and 8-digit account number. **Postmaster:** Send change of address to AAAS, P.O. Box 96178, Washington, DC 20090–6178. **Single-copy sales:** $15.00 current issue, $20.00 back issue prepaid includes surface postage; bulk rates on request. **Authorization to photocopy** material for internal or personal use under circumstances not falling within the fair use provisions of the Copyright Act is granted by AAAS to libraries and other users registered with the Copyright Clearance Center (CCC) Transactional Reporting Service, provided that $35.00 per article is paid directly to CCC, 222 Rosewood Drive, Danvers, MA 01923. The identification code for *Science* is 0036-8075. *Science* is indexed in the *Reader's Guide to Periodical Literature* and in several specialized indexes.

Downloaded from http://science.sciencemag.org/ on September 30, 2016

Published by AAAS

Science
AAAS
1200 New York Avenue, NW, Washington, DC 20005
Clarendon House, Clarendon Road, Cambridge, UK CB2 8FH

Editor-in-Chief Jeremy Berg
Executive Editor Monica M. Bradford **News Editor** Tim Appenzeller
Deputy Editors Lisa D. Chong, Andrew M. Sugden(UK), Valda J. Vinson, Jake S. Yeston

Research and Insights

DEPUTY EDITOR, EMERITUS Barbara R. Jasny **SR. EDITORS** Caroline Ash(UK), Gilbert J. Chin, Julia Fahrenkamp-Uppenbrink(UK), Pamela J. Hines, Stella M. Hurtley(UK), Paula A. Kiberstis, Marc S. Lavine(Canada), Kristen L. Mueller, Ian S. Osborne(UK), Beverly A. Purnell, L. Bryan Ray, Guy Riddihough, H. Jesse Smith, Jelena Stajic, Peter Stern(UK), Phillip D. Szuromi, Sacha Vignieri, Brad Wible, Nicholas S. Wigginton, Laura M. Zahn **ASSOCIATE EDITORS** Brent Grocholski, Keith T. Smith **ASSOCIATE BOOK REVIEW EDITOR** Valerie B. Thompson **LETTERS EDITOR** Jennifer Sills **LEAD CONTENT PRODUCTION EDITORS** Harry Jach, Lauren Kmec **CONTENT PRODUCTION EDITORS** Jeffrey E. Cook, Chris Filiatreau, Cynthia Howe, Barbara P. Ordway, Catherine Wolner **SR. EDITORIAL COORDINATORS** Carolyn Kyle, Beverly Shields **EDITORIAL COORDINATORS** Aneera Dobbins, Joi S. Granger, Jeffrey Hearn, Lisa Johnson, Maryrose Madrid, Anita Wynn **PUBLICATIONS ASSISTANTS** Nida Masiulis, Dona Mathieu, Le-Toya Mayne Flood, Shannon McMahon, Scott Miller, Jerry Richardson, Alice Whaley(UK), Brian White **EXECUTIVE ASSISTANT** Anna Bashkirova **ADMINISTRATIVE SUPPORT** Janet Clements(UK), Lizanne Newton(UK)

News

NEWS MANAGING EDITOR John Travis **INTERNATIONAL EDITOR** Richard Stone **DEPUTY NEWS EDITORS** Elizabeth Culotta, David Grimm, Eric Hand David Malakoff, Leslie Roberts **CONTRIBUING EDITOR** Martin Enserink(Europe) **SR. CORRESPONDENTS** Daniel Clery(UK), Jeffrey Mervis, Elizabeth Pennisi **NEWS WRITERS** Adrian Cho, Jon Cohen, Jennifer Couzin-Frankel, Carolyn Gramling, Jocelyn Kaiser, Catherine Matacic, Kelly Servick, Robert F. Service, Erik Stokstad(Cambridge, UK), Paul Voosen, Meredith Wadman **INTERNS** Jessica Boddy, Ben Panko **CONTRIBUTING CORRESPONDENTS** John Bohannon, Warren Cornwall, Ann Gibbons, Mara Hvistendahl, Sam Kean, Eli Kintisch, Kai Kupferschmidt(Berlin), Andrew Lawler, Mitch Leslie, Charles C. Mann, Eliot Marshall, Virginia Morell, Dennis Normile(Shanghai), Heather Pringle, Tania Rabesandratana(London), Emily Underwood, Gretchen Vogel(Berlin), Lizzie Wade(Mexico City) **CAREERS** Donisha Adams, Rachel Bernstein(Editor), Maggie Kuo **COPY EDITORS** Julia Cole, Dorie Chevlen, Jennifer Levin (Chief) **ADMINISTRATIVE SUPPORT** Jessica Adams

Executive Publisher Rush D. Holt
Publisher Bill Moran **Chief Digital Media Officer** Rob Covey

BUSINESS OPERATIONS AND PORTFOLIO MANAGEMENT DIRECTOR Sarah Whalen **PRODUCT DEVELOPMENT DIRECTOR** Will Schweitzer **PRODUCT DEVELOPMENT ASSOCIATE** Hannah Heckner **BUSINESS SYSTEMS AND FINANCIAL ANALYSIS DIRECTOR** Randy Yi **SENIOR SYSTEMS ANALYST** Nicole Mehmedovich **DIRECTOR, BUSINESS OPERATIONS & ANALYSIS** Eric Knott **MANAGER, BUSINESS OPERATIONS** Jessica Tierney **SENIOR BUSINESS ANALYST** Cory Lipman **BUSINESS ANALYSTS** David Garrison, Michael Hardesty Meron Kebede, Sandy Kim **FINANCIAL ANALYST** Drew Sher **DIRECTOR, COPYRIGHTS LICENSING SPECIAL PROJECTS** Emilie David **PERMISSIONS ASSOCIATE** Elizabeth Sandler **RIGHTS, CONTRACTS, AND LICENSING ASSOCIATE** Lili Kiser **RIGHTS & PERMISSIONS ASSISTANT** Alexander Lee

MARKETING DIRECTOR Elise Swinehart **ASSOCIATE MARKETING DIRECTOR** Stacey Burke Bowers **MARKETING ASSOCIATE** Steven Goodman **CREATIVE DIRECTOR** Scott Rodgerson **SENIOR ART ASSOCIATES** Paula Fry **ART ASSOCIATE** Kim Huynh

FULFILLMENT SYSTEMS AND OPERATIONS membership@aaas.org **MANAGER, MEMBER SERVICES** Pat Butler **SPECIALISTS** Terrance Morrison, Latasha Russell **MANAGER, DATA ENTRY** Mickie Napoleoni **DATA ENTRY SPECIALISTS** Brenden Aquilino, Fiona Giblin **MARKETING ASSOCIATE** Isa Sesay-Bah

PUBLISHER RELATIONS, EASTERN REGION Keith Layson **PUBLISHER RELATIONS, WESTERN REGION** Ryan Rexroth **SALES RESEARCH COORDINATOR** Aiesha Marshall **ASSOCIATE DIRECTOR, INSTITUTIONAL LICENSING OPERATIONS** Iquo Edim **SENIOR OPERATIONS ANALYST** Lana Guz **MANAGER, AGENT RELATIONS & CUSTOMER SUCCESS** Judy Lillibridge

WEB TECHNOLOGIES PORTFOLIO MANAGER Trista Smith **TECHNICAL MANAGER** Chris Coleman **PROJECT MANAGER** Nick Fletcher **DEVELOPERS** Ryan Jensen, Jimmy Marks, Brandon Morrison **BUSINESS ANALYST** Christina Wofford

DIGITAL MEDIA DIRECTOR OF ANALYTICS Enrique Gonzales **DIGITAL REPORTING ANALYST** Eric Hossinger **SR. MULTIMEDIA PRODUCER** Sarah Crespi **MANAGING DIGITAL PRODUCER** Alison Crawford **PRODUCER** Liana Birke **VIDEO PRODUCER** Chris Burns, Nguyên Khôi Nguyễn **DIGITAL SOCIAL MEDIA PRODUCER** Brice Russ

DIRECTOR OF OPERATIONS PRINT AND ONLINE Lizabeth Harman **DIGITAL/PRINT STRATEGY MANAGER** Jason Hillman **QUALITY TECHNICAL MANAGER** Marcus Spiegler **PROJECT ACCOUNT MANAGER** Tara Kelly **DIGITAL PRODUCTION MANAGER** Lisa Stanford **ASSISTANT MANAGER DIGITAL/PRINT** Rebecca Doshi **SENIOR CONTENT SPECIALISTS** Steve Forrester, Antoinette Hodal, Lori Murphy, Anthony Rosen **CONTENT SPECIALISTS** Jacob Hedrick, Kimberley Oster **ADVERTISING OPERATIONS SPECIALIST** Ashley Jeter

DESIGN DIRECTOR Beth Rakouskas **DESIGN EDITOR** Marcy Atarod **SENIOR DESIGNER** Chrystal Smith **GRAPHICS MANAGING EDITOR** Alberto Cuadra **GRAPHICS EDITOR** Garvin Grullón **SENIOR SCIENTIFIC ILLUSTRATORS** Chris Bickel, Katharine Sutliff **SCIENTIFIC ILLUSTRATOR** Valerie Altounian **INTERACTIVE GRAPHICS EDITOR** Jia You **SENIOR GRAPHICS SPECIALISTS** Holly Bishop, Nathalie Cary **PHOTOGRAPHY MANAGING EDITOR** William Douthitt **SENIOR PHOTO EDITOR** Christy Steele **PHOTO EDITOR** Emily Petersen

DIRECTOR, GLOBAL COLLABORATION, CUSTOM PUBLICATIONS, ADVERTISING Bill Moran **EDITOR, CUSTOM PUBLISHING** Sean Sanders: 202-326-6430 **ADVERTISING MARKETING MANAGER** Justin Sawyers: 202-326-7061 science_advertising@aaas.org **ADVERTISING SUPPORT MANAGER** Karen Foote: 202-326-6740 **ADVERTISING PRODUCTION OPERATIONS MANAGER** Deborah Tompkins **SR. PRODUCTION SPECIALIST/GRAPHIC DESIGNER** Amy Hardcastle **SR. TRAFFIC ASSOCIATE** Christine Hall **SALES COORDINATOR** Shirley Young **ASSOCIATE DIRECTOR, COLLABORATION, CUSTOM PUBLICATIONS/CHINA/TAIWAN/KOREA/SINGAPORE** Ruolei Wu: +86-186 0082 9345, rwu@aaas.org **COLLABORATION/CUSTOM PUBLICATIONS/JAPAN** Adarsh Sandhu + 81532-81-5142 asandhu@aaas.org **EAST COAST/E. CANADA** Laurie Faraday: 508-747-9395, FAX 617-507-8189 **WEST COAST/W. CANADA** Lynne Stickrod: 415-931-9782, FAX 415-520-6940 **MIDWEST** Jeffrey Dembksi: 847-498-4520 x3005, Steven Loerch: 847-498-4520 x3006 **UK EUROPE/ASIA** Roger Goncalves: TEL/FAX +41 43 243 1358 **JAPAN** Katsuyoshi Fukamizu(Tokyo): +81-3-3219-5777 kfukamizu@aaas.org **CHINA/TAIWAN** Ruolei Wu: +86-186 0082 9345, rwu@aaas.org

WORLDWIDE ASSOCIATE DIRECTOR OF SCIENCE CAREERS Tracy Holmes: +44 (0) 1223 326525, FAX +44 (0) 1223 326532 tholmes@science-int.co.uk **CLASSIFIED** advertise@sciencecareers.org **U.S. SALES** Tina Burks: 202-326-6577, Nancy Toema: 202-326-6578 **EUROPE/ROW SALES** Sarah Lelarge **SALES ASSISTANT** Kelly Grace **JAPAN** Hiroyuki Mashiki(Kyoto): +81-75-823-1109 hmashiki@aaas.org **CHINA/TAIWAN** Ruolei Wu: +86-186 0082 9345 rwu@aaas.org **MARKETING MANAGER** Allison Pritchard **MARKETING ASSOCIATE** Aimee Aponte

AAAS BOARD OF DIRECTORS, CHAIR Geraldine L. Richmond **PRESIDENT** Barbara A. Schaal **PRESIDENT-ELECT** Susan Hockfield **TREASURER** David Evans Shaw **CHIEF EXECUTIVE OFFICER** Rush D. Holt **BOARD** Cynthia M. Beall, May R. Berenbaum, Carlos J. Bustamante, Stephen P.A. Fodor, Claire M. Fraser, Michael S. Gazzaniga, Laura H. Greene, Elizabeth Loftus, Mercedes Pascual

SUBSCRIPTION SERVICES For change of address, missing issues, new orders and renewals, and payment questions: 866-434-AAAS (2227) or 202-326-6417, FAX 202-842-1065. Mailing addresses: AAAS, P.O. Box 96178, Washington, DC 20090-6178 or AAAS Member Services, 1200 New York Avenue, NW, Washington, DC 20005

INSTITUTIONAL SITE LICENSES 202-326-6730 **REPRINTS:** Author Inquiries 800-635-7181 **COMMERCIAL INQUIRIES** 803-359-4578 **PERMISSIONS** 202-326-6765, permissions@aaas.org **AAAS Member Services** 202-326-6417 or http://membercentral.aaas.org/discounts

Science serves as a forum for discussion of important issues related to the advancement of science by publishing material on which a consensus has been reached as well as including the presentation of minority of conflicting points of view. Accordingly, all articles published in *Science*—including editorials, news and comment, and book reviews—are signed and reflect the individual views of the authors and not official points of view adopted by AAAS or the institutions with which the authors are affiliated.

INFORMATION FOR AUTHORS See pages 624 and 625 of the 5 February 2016 issue or access www.sciencemag.org/authors/science-information-authors

SENIOR EDITORIAL BOARD
Gary King, *Harvard University,* **Susan M. Rosenberg,** *Baylor College of Medicine,*
Ali Shilatifard, *Northwestern University Feinberg School of Medicine*

BOARD OF REVIEWING EDITORS (Statistics board members indicated with **(S)**)

Adriano Aguzzi, *U. Hospital Zürich*
Takuzo Aida, *U. of Tokyo*
Leslie Aiello, *Wenner-Gren Foundation*
Judith Allen, *U. of Edinburgh*
Sonia Altizer, *U. of Georgia*
Sebastian Amigorena, *Institut Curie*
Kathryn Anderson, *Memorial Sloan-Kettering Cancer Center*
Meinrat O. Andreae, *Max-Planck Inst. Mainz*
Paola Arlotta, *Harvard U.*
Johan Auwerx, *EPFL*
David Awschalom, *U. of Chicago*
Clare Baker, *University of Cambridge*
Nenad Ban, *ETH Zurich*
Jordi Bascompte, *University of Zurich*
Franz Bauer, *Pontificia Universidad Católica de Chile*
Ray H. Baughman, *U. of Texas, Dallas*
David Baum, *U. of Wisconsin*
Carlo Beenakker, *Leiden U.*
Kamran Behnia, *ESPCI-ParisTech*
Yasmine Belkaid, *NIAID, NIH*
Philip Benfey, *Duke U.*
May Berenbaum, *U. of Illinois*
Gabriele Bergers, *U. of California, San Francisco*
Bradley Bernstein, *Massachusettes General Hospital*
Peer Bork, *EMBL*
Bernard Bourdon, *Ecole Normale Supérieure de Lyon*
Chris Bowler, *École Normale Supérieure*
Ian Boyd, *U. of St. Andrews*
Emily Brodsky, *U. of California, Santa Cruz*
Ron Brookmeyer, *U. of California Los Angeles* **(S)**
Christian Büchel, *U. Hamburg-Eppendorf*
Joseph A. Burns, *Cornell U.*
Carter Tribley Butts, *U. of California, Irvine*
Gyorgy Buzsaki, *New York U. School of Medicine*
Blanche Capel, *Duke U.*
Mats Carlsson, *U. of Oslo*
Ib Chorkendorff, *U. of Denmark*
David Clapham, *Children's Hospital Boston*
Joel Cohen, *Rockefeller U., Columbia U.*
James J. Collins, *MIT*
Robert Cook-Deegan, *Duke U.*
Lisa Coussens, *Oregon Health & Science U.*
Alan Cowman, *Walter & Eliza Hall Inst.*
Robert H. Crabtree, *Yale U.*
Roberta Croce, *Vrije Universiteit*
Janet Currie, *Princeton U.*
Jeff L. Dangl, *U. of North Carolina*
Tom Daniel, *U. of Washington*
Frans de Waal, *Emory U.*
Stanislas Dehaene, *Collège de France*
Robert Desimone, *MIT*
Claude Desplan, *New York U.*
Dennis Discher, *U. of Pennsylvania*
Gerald W. Dorn II, *Washington U. School of Medicine*
Jennifer A. Doudna, *U. of California, Berkeley*
Bruce Dunn, *U. of California, Los Angeles*
William Dunphy, *Caltech*
Christopher Dye, *WHO*
Todd Ehlers, *U. of Tuebingen*
David Ehrhardt, *Carnegie Inst. of Washington*
Tim Elston, *U. of North Carolina at Chapel Hill*
Jennifer Elisseeff, *U. of N*
Gerhard Ertl, *Fritz-Haber-Institut, Berlin*
Barry Everitt, *U. of Cambridge*
Ernst Fehr, *Johns Hopkins U.*
Anne C. Ferguson-Smith, *U. of Cambridge*
Michael Feuer, *The George Washington U.*
Toren Finkel, *NHLBI, NIH*
Kate Fitzgerald, *U. of Massachusetts*
Peter Fratzl, *Max-Planck Inst.*
Elaine Fuchs, *Rockefeller U.*
Daniel Geschwind, *UCLA*
Karl-Heinz Glassmeier, *TU Braunschweig*
Ramon Gonzalez, *Rice U.*
Julia R. Greer, *Caltech*
Elizabeth Grove, *U. of Chicago*
Nicolas Gruber, *ETH Zurich*
Kip Guy, *St. Jude's Children's Research Hospital*
Taekjip Ha, *U. of Illinois at Urbana-Champaign*
Wolf-Dietrich Hardt, *ETH Zurich*
Christian Haass, *Ludwig Maximilians U.*
Sharon Hammes-Schiffer, *U. of Illinois at Urbana–Champaign*
Michael Hasselmo, *Boston U.*
Martin Heimann, *Max-Planck Inst. Jena*
Yka Helariutta, *U. of Cambridge*
James A. Hendler, *Rensselaer Polytechnic Inst.*
Janet G. Hering, *Swiss Fed. Inst. of Aquatic Science & Technology*
Kai-Uwe Hinrichs, *U. of Bremen*
David Hodell, *U. of Cambridge*
Lora Hooper, *UT Southwestern Medical Ctr. at Dallas*
Tamas Horvath, *Yale University*
Raymond Huey, *U. of Washington*
Fred Hughson, *Princeton U.*
Auke Ijspeert, *EPFL Lausanne*
Stephen Jackson, *USGS and U. of Arizona*
Steven Jacobsen, *U. of California, Los Angeles*
Kai Johnsson, *EPFL Lausanne*
Peter Jonas, *Inst. of Science & Technology (IST) Austria*
Matt Kaeberlein, *U. of Washington*
William Kaelin Jr., *Dana-Farber Cancer Inst.*
Daniel Kahne, *Harvard U.*
Daniel Kammen, *U. of California, Berkeley*
Abby Kavner, *U. of California, Los Angeles*
Hitoshi Kawakatsu, *U. of Tokyo*
Masashi Kawasaki, *U. of Tokyo*
V. Narry Kim, *Seoul National U.*
Robert Kingston, *Harvard Medical School*
Etienne Koechlin, *Ecole Normale Suprieure*
Alexander Kolodkin, *Johns Hopkins U.*
Thomas Langer, *U. of Cologne*
Mitchell A. Lazar, *U. of Pennsylvania*
David Lazer, *Harvard U.*
Thomas Lecuit, *IBDM*
Virginia Lee, *U. of Pennsylvania*
Stanley Lemon, *U. of North Carolina at Chapel Hill*
Ottoline Leyser, *Cambridge U.*
Wendell Lim, *U.C. San Francisco*
Marcia C. Linn, *U. of California, Berkeley*
Jianguo Liu, *Michigan State U.*
Luis Liz-Marzan, *CIC biomaGUNE*
Jonathan Losos, *Harvard U.*
Ke Lu, *Chinese Acad. of Sciences*
Christian Lüscher, *U. of Geneva*
Laura Machesky, *CRUK Beatson Inst. for Cancer Research*
Anne Magurran, *U. of St. Andrews*
Oscar Marin, *CSIC & U. Miguel Hernández*
Charles Marshall, *U. of California, Berkeley*
C. Robertson McClung, *Dartmouth College*
Rodrigo Medellin, *U. of Mexico*
Graham Medley, *U. of Warwick*
Tom Misteli, *NCI*
Yasushi Miyashita, *U. of Tokyo*
Mary Ann Moran, *U. of Georgia*
Richard Morris, *U. of Edinburgh*
Alison Motsinger-Reif, *NC State U.* **(S)**
Thomas Murray, *The Hastings Center*
Daniel Neumark, *U. of California, Berkeley*
Kitty Nijmeijer, *U. of Twente*
Helga Nowotny, *European Research Advisory Board*
Ben Olken, *MIT*
Rachel O'Reilly, *Warwick U.*
Joe Orenstein, *U. of California Berkeley & Lawrence Berkeley National Lab*
Harry Orr, *U. of Minnesota*
Pilar Ossorio, *U. of Wisconsin*
Andrew Oswald, *U. of Warwick*
Isabella Pagano, *Istituto Nazionale di Astrofisica*
Margaret Palmer, *U. of Maryland*
Steve Palumbi, *Stanford U.*
Jane Parker, *Max-Planck Inst. of Plant Breeding Research*
Giovanni Parmigiani, *Dana-Farber Cancer Inst.* **(S)**
John H. J. Petrini, *Memorial Sloan-Kettering Cancer Center*
Samuel Pfaff, *Salk Institute for Biological Studies*
Joshua Plotkin, *U. of Pennsylvania*
Albert Polman, *FOM Institute AMOLF*
Philippe Poulin, *CNRS*
Jonathan Pritchard, *Stanford U.*
Wim van der Putten, *Netherlands Institute of Ecology*
David Randall, *Colorado State U.*
Felix Rey, *Institut Pasteur*
Trevor Robbins, *U. of Cambridge*
Jim Roberts, *Fred Hutchinson Cancer Research Ctr.*
Amy Rosenzweig, *Northwestern University*
Mike Ryan, *U. of Texas, Austin*
Mitinori Saitou, *Kyoto U.*
Shimon Sakaguchi, *Kyoto U.*
Miquel Salmeron, *Lawrence Berkeley National Lab*
Jürgen Sandkühler, *Medical U. of Vienna*
Alexander Schier, *Harvard U.*
Vladimir Shalaev, *Purdue U.*
Robert Siliciano, *Johns Hopkins School of Medicine*
Denis Simon, *Arizona State U.*
Uri Simonsohn, *U. of Pennsylvania*
Alison Smith, *John Innes Centre*
Richard Smith, *U. of North Carolina* **(S)**
John Speakman, *U. of Aberdeen*
Allan C. Spradling, *Carnegie Institution of Washington*
Jonathan Sprent, *Garvan Inst. of Medical Research*
Eric Steig, *U. of Washington*
Paula Stephan, *Georgia State U. and National Bureau of Economic Research*
Molly Stevens, *Imperial College London*
V. S. Subrahmanian, *U. of Maryland*
Ira Tabas, *Columbia U.*
Sarah Teichmann, *Cambridge U.*
John Thomas, *North Carolina State U.*
Shubha Tole, *Tata Institute of Fundamental Research*
Christopher Tyler-Smith, *The Wellcome Trust Sanger Inst.*
Herbert Virgin, *Washington U.*
Bert Vogelstein, *Johns Hopkins U.*
Cynthia Volkert, *U. of Göttingen*
David Wallach, *Weizmann Inst. of Science*
Ian Walmsley, *U. of Oxford*
Jane-Ling Wang, *U. of California, Davis* **(S)**
David Waxman, *Fudan U.*
Jonathan Weissman, *U. of California, San Francisco*
Chris Wikle, *U. of Missouri* **(S)**
Ian A. Wilson, *The Scripps Res. Inst.* **(S)**
Timothy D. Wilson, *U. of Virginia*
Rosemary Wyse, *Johns Hopkins U.*
Jan Zaanen, *Leiden U.*
Kenneth Zaret, *U. of Pennsylvania School of Medicine*
Jonathan Zehr, *U. of California, Santa Cruz*
Len Zon, *Children's Hospital Boston*
Maria Zuber, *MIT*

BOOK REVIEW BOARD
David Bloom, *Harvard U.*, **Samuel Bowring,** *MIT,* **Angela Creager,** *Princeton U.,*
Richard Shweder, *U. of Chicago,* **Ed Wasserman,** *DuPont*

Published by AAAS

EDITORIAL

Speaking of insects...

Given that *Aedes aegypti*, the main mosquito vector of Zika virus, has been an intense focus of public health attention in the Americas, most recently in Florida, it seems apt that next week, 7000 entomologists from around the world will converge on Orlando, Florida, for the 25th International Congress of Entomology (ICE), where, among other activities, 175 discipline thought-leaders will join policy-makers and other experts to address "Improving the Human Condition through Insect Science." The ICE summit's goals are to define the major global insect-related challenges—from arthropod-borne diseases to the protection of beneficial species—and plan collaborative efforts to meet these challenges through research and technology. These "grand challenges" aren't new. What's new, however, is an explicit effort to address one of the greatest challenges: effective engagement with the public about the value of insect science.

"...entomologists need to...talk about insect science with the rest of the world."

The public has long been generally unfamiliar and even unenamored with most insects. Notwithstanding, few entomologists communicate with the public about their work. This relationship is a major problem for two reasons. Finding new solutions to evolving insect-related challenges requires basic research, but fundamental insect science often appears arcane and irrelevant to the general public and policy-makers. Also, when basic knowledge produces new technology, that novelty can generate widespread public concern and even entrenched opposition to implementation.

One example, the sterile insect technique, is as mystifying to most people today as it was 80 years ago. In 1935, charged with controlling the screwworm fly, a devastating pest of livestock, entomologists Edward Knipling and Raymond Bushland commenced decades-long studies of its sexual behavior and population biology. Skepticism abounded when, in 1953, merging their findings with Hermann Muller's Nobel Prize–winning discovery that irradiation sterilizes male fruit flies, they released thousands of irradiated male screwworm flies on Curaçao, where livestock losses to the pest were unmanageable. In just 7 months, the breeding cycle was fatally disrupted, and screwworms were eradicated from the island with no adverse consequences. By 1966, the sterile insect technique had eradicated screwworms from the United States, saving the cattle industry millions of dollars in annual losses. Yet despite its demonstrable utility, funding for screwworm eradication in Central America by the U.S. Department of Agriculture (to prevent incursions northward into the United States) in 2005 was described as "getting 'screwed' by the government" in *The Pig Book: How Government Wastes Your Money*. Today, mosquito biologists have modernized sterile insect release, creating transgenic males that pass lethal genes to offspring, decimating populations harboring Zika and other viruses. Still, public distrust of genetically modified organisms is so pervasive that a survey in February revealed that 35% of Americans believe (mistakenly) that such mosquitoes ("Franken-flies") are responsible for Zika's spread. As the U.S. Food and Drug Administration considers the use of such insects for Zika control, there is public concern that they could have unintended effects on the environment. These two examples illustrate the continuing need for clearer communication with the public about how new science enhances pest management efforts.

Last March, the Entomological Society of America and the Sociedade Entomológica do Brasil held a summit in Brazil to discuss research and management strategies for *A. aegypti*, which transmits Zika, chikungunya, and dengue viruses. One outcome of this meeting was a consensus to improve communication with the public through strategies that are tailored for each country to best disseminate facts and dispel misinformation that hinders responses to disease outbreaks. The Leadership Summit at this year's ICE meeting will build on this message most opportunely, at the largest gathering of entomologists in the discipline's history. The world's entomologists need to talk among themselves about how best to talk about insect science with the rest of the world.

–May R. Berenbaum

May R. Berenbaum is the Swanlund Professor of Entomology at the University of Illinois, Urbana-Champaign, and is president of the Entomological Society of America. Email: maybe@illinois.edu

10.1126/science.aaj2166

PHOTOS: (INSET) MANODE/ISTOCKPHOTO.COM; (TOP RIGHT) RON SULLIVAN

Downloaded from http://science.sciencemag.org/ on September 30, 2016

Published by AAAS

> “Failing to approve a drug that actually works in devastating diseases—these consequences are extreme.”
>
> **Janet Woodcock of the U.S. Food and Drug Administration**, on the approval of a Duchenne muscular dystrophy drug this week despite FDA staff concerns of its efficacy.

IN BRIEF

First U.S. Atlantic marine monument

A feather star crinoid clings to the Mytilus Seamount, part of the new marine monument.

A 12,700-square-kilometer stretch of sea canyons and submerged mountains off the coast of Cape Cod, Massachusetts, is now the United States's first marine monument in the Atlantic Ocean. The designation of the Northeast Canyons and Seamounts Marine National Monument on 15 September, under the Antiquities Act, came 2 weeks after President Barack Obama expanded Hawaii's Papahānaumokuakea Marine National Monument to 1.5 million square kilometers, making it the largest protected area on the planet (*Science*, 2 September, p. 971). The new monument is in a region of rich biodiversity known as Georges Bank, home to an array of endangered whales and turtles that find shelter in the canyons and seamounts, as well as deep-sea corals, sponges, and other rare species, and valuable fish species including salmon, lobsters, and scallops. The designation bans oil and gas exploration and drilling as well as most commercial fishing within the monument, although “fixed-gear” lobster and red crab fisheries can continue operations for another 7 years. The monument's three canyons—considered productive fishing areas and reduced from a proposed region that would have encompassed eight canyons—remain an area of contention for the region's fisheries, some of which have decried the designation.

AROUND THE WORLD

Trial data sharing expanded

WASHINGTON, D.C. | Drug companies and academic researchers will have to step up their public reporting of clinical trial results under new federal policies released on 16 September. A final U.S. Department of Health and Human Services rule expands an existing requirement that sponsors of trials regulated by the U.S. Food and Drug Administration submit summary results no more than 1 year after a trial ends to the ClinicalTrials.gov database. Results must now be reported not only for approved products, but also for phase II and III trials of drugs and devices that haven't yet been approved. And the National Institutes of Health (NIH) in Bethesda, Maryland, will require submission of summary results for all clinical trials funded by the agency. NIH also laid out a new plan for bolstering the rigor of clinical studies. **http://scim.ag/trialsharing**

EU may loosen data mining limits

BRUSSELS | Researchers in the European Union may soon have more freedom to study text and data from copyright-protected papers. Under a proposal unveiled by the European Commission on 14 September, EU researchers would be able to mine content to which they have “lawful access” without prior authorization. Scientists can find it difficult to mine content from journals that their universities have subscribed to because they face a patchwork of complex rules that differ among publishers or countries. The exception would apply to public or private entities, as long as their research is in the “public interest.” The League of European Research Universities (LERU) said the proposal was welcome but questioned a provision that would let publishers “apply measures to ensure the security and integrity of the networks and databases” where content is hosted. “This provision will certainly be unfairly used (and abused) by publishers” to make data mining more difficult, LERU warned in a statement. The commission's proposal is part of a broader proposal to update and align copyright law across the bloc's 28 member states. It

PHOTO: NOAA OKEANOS EXPLORER PROGRAM, 2013 NORTHEAST U.S. CANYONS EXPEDITION

Downloaded from http://science.sciencemag.org/ on September 30, 2016

Published by AAAS

Some firefly populations grow and shrink in a 6-year cycle.

Fireflies in a changing climate

Fireflies are a perennial summertime favorite. But their fate is uncertain: Anecdotal data suggest that firefly populations are in decline in some locations, although they have not yet been systematically studied to determine when their numbers peak. Now, a new study examines numbers of fireflies caught in sticky traps over 12 years at 10 sites in Michigan, as well as precipitation and temperature data during that time. The findings suggest that firefly populations in Michigan seem to follow a 6-year cycle, increasing for 3 years and then decreasing for 3 years, the researchers reported last week on the preprint archive bioRxiv. But the conditions that determine fluctuations within that cycle are complex: Summer temperatures have to be warm enough, and for long enough, for fireflies to emerge—but too wet or too dry conditions can delay peak emergence for up to 2 weeks. Thus, the warmer springs predicted by climate change would mean an earlier firefly peak, but only if rainfall remains the same.

will now be debated with the European Parliament and member states.

First private weather satellites

WASHINGTON, D.C. | The U.S. National Oceanic and Atmospheric Administration (NOAA) made its first foray into supporting commercial weather satellites on 15 September, awarding $1.065 million in pilot contracts to two California-based startups, GeoOptics and Spire Global. The small deals—$695,000 to GeoOptics and $370,000 to Spire—are part of NOAA's Commercial Weather Data Pilot, which will allow the agency to evaluate the quality of the firms' data for forecasts and warnings, and could be the first step in a broader embrace of commercial satellites. Until now, NOAA has gathered data by building and launching its own weather satellites. However, with many satellites plagued by cost overruns, Congress has pressured NOAA to explore commercial weather satellites, including a mandate for the commercial weather pilot in its 2016 appropriations. The two companies must deliver their weather data by the end of April 2017, and NOAA will evaluate and report on their suitability for operations later that year. http://scim.ag/weathersats

NFL funds head trauma science

NEW YORK CITY | The National Football League (NFL) announced last week that it will fund $40 million in new medical research over the next 5 years, primarily to tackle the long-term effects of concussion and of the serious, degenerative brain disease chronic traumatic encephalopathy, which can result after repeated blows to the head. An additional $60 million will fund material scientists and engineers to work on projects like improving helmets. Roger Goodell, the NFL commissioner, said 14 September that an "independent, scientific advisory board" will "engage in a clear process to identify and support the most compelling proposals." He added: "We know there is skepticism about our work in this area." In May, Democrats in the House of Representatives issued a report accusing the league of trying to control the projects funded with an earlier, "unrestricted" $30 million gift to the National Institutes of Health (NIH). Last week, House Republicans called for a separate investigation of NIH's

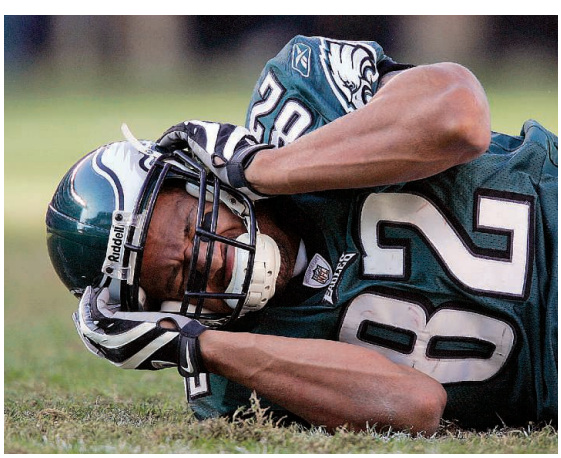

An NFL player reels after a hit during a 2009 game.

PHOTOS: (TOP TO BOTTOM) KIT_LEONG/ISTOCKPHOTO; AP PHOTO/MEL EVANS, FILE

Downloaded from http://science.sciencemag.org/ on September 30, 2016

Published by AAAS

actions by the inspector general of NIH's parent agency, the Department of Health and Human Services.

Billions planned for 'Biohub'

SAN FRANCISCO, CALIFORNIA | Facebook Co-Founder Mark Zuckerberg and his wife Priscilla Chan were expected to announce a major scientific philanthropy initiative this week as *Science* went to press; it would bring together engineering and basic research to combat human diseases. The couple pledged to their newborn daughter last December to donate 99% of their Facebook shares to improving the world during their lifetimes. They plan to pour billions of dollars over the coming decades into a science initiative to be led by neurobiologist Cori Bargmann of The Rockefeller University in New York City. The first investment will be a "Biohub" funded at $600 million over 10 years and located in San Francisco's Mission Bay. Led by technology expert Stephen Quake of Stanford University in Palo Alto, California, and University of California, San Francisco (UCSF), infectious disease expert Joseph DeRisi, the Chan Zuckerberg Biohub will bring together scientists and engineers from Stanford, UCSF, and UC Berkeley. Its first projects will be a cell atlas and an infectious disease initiative. **http://scim.ag/CZIscience**

NEWSMAKERS

Bad papers claim hits U. of Tokyo

The University of Tokyo announced it will investigate anonymous claims that 22 papers by six university research groups included fabricated and falsified data. The university did not name the researchers or the publications. But the anonymous individual or group, going by "Ordinary_researchers," detailed questions about data and graphs in more than 100 pages delivered to the university in two batches on 14 August and 29 August. The documents were also posted online and identify papers that appeared in *Nature*, *Cell*, and several other journals between 2003 and 2015. The corresponding author on seven of the papers was **Takashi Kadowaki**, a physician and diabetes specialist who is a former director of the university hospital and still on the faculty at the school of medicine. The university conducted a preliminary investigation that led to today's announcement of a full probe, though the announcement emphasized that the step does not confirm any misconduct. The school's internal regulations call for half the investigative panel members to come from outside the university. Kadowaki called the allegations "totally groundless and false." **http://scim.ag/Kadowaki**

Modern chickens are plump, year-round egg layers.

How a pope helped make chickens fatter

Chickens have been around for thousands of years—yet little is known about when the scrappy fowl of thousands of years ago became today's meaty morsels. Last week, researchers at the seventh International Symposium on Biomolecular Archaeology in Oxford, U.K., reported that a medieval religious edict likely set in motion changes to make them plumper. The number of chicken bones at European archaeological sites doubles abruptly around the mid–10th century—shortly after the Catholic Church required its followers to abstain from eating meat from four-legged animals for about 130 days a year. People began to selectively breed plump, year-round egg layers—birds that likely carried a gene variant known as the *thyroid stimulating hormone receptor* (*TSHR*), which regulates metabolism and reproduction. The researchers sequenced chicken DNA collected from 12 European archaeological sites dating from 280 B.C.E. to the 18th century—and found that few chickens carried this now dominant variant of the *TSHR* gene until about 1000 years ago. **http://scim.ag/popechick**

BY THE NUMBERS

1.1 billion

Stars in the Milky Way galaxy mapped by the European Space Agency's Gaia mission, including 400 million never seen before. **http://scim.ag/Gaiastars**

3.8 million

Age, in years, of the oldest proteins yet found on Earth, extracted from ancient ostrich eggshells in Tanzania. The previous acknowledged record holder were proteins from a 700,000-year-old horse (International Symposium on Biomolecular Archaeology).

$300 million

Amount given to the Johns Hopkins Bloomberg School of Public Health in Baltimore, Maryland, last week by former New York City Mayor Michael Bloomberg; his lifetime contribution to the institution is $1.5 billion.

PHOTO: VALERIJAP/ISTOCKPHOTO

Downloaded from http://science.sciencemag.org/ on September 30, 2016

Published by AAAS

Islands off Sumatra sank by a meter, drowning trees, after a 2005 earthquake lowered the sea floor.

PHOTO: JOHN STANMEYER/NATIONAL GEOGRAPHIC CREATIVE

EARTH SCIENCE

The Subduction Zone Observatory takes shape

Geoscientists want large project to study dynamic and dangerous plate boundaries

By **Julia Rosen**

In 2004, a magnitude-9.1 earthquake struck off the coast of Sumatra in Indonesia, triggering a monstrous tsunami that devastated coastlines around the Indian Ocean and killed 230,000 people. Almost 200 years before that, Mount Tambora erupted 2500 kilometers to the southeast, claiming 70,000 lives and plunging the planet into a "year without a summer." Although distant in time and location, these two events shared a common cause: the oceanic crust of the Indo-Australian Plate sliding grudgingly beneath Southeast Asia. The movement of this giant conveyor belt produces some of the largest earthquakes on Earth and a chain of restive volcanoes, fueled by magma stirred up by the sinking plate.

Depending on how you count, there are roughly a dozen of these subduction zones around the globe. They not only pose a threat to humans, but also act as critical gears in the rock cycle, recycling crust into Earth's interior and pumping up new volcanic rock. Scientists have spent decades studying how these systems work, but they still have many questions—which is why they are cooking up a plan for a major new research program: the Subduction Zone Observatory (SZO).

Just where the SZO will be located, what instruments it will include, and what it might cost will come into focus during a National Science Foundation (NSF)–sponsored workshop next week. Many hope the observatory could be NSF's next major investment in earth science research. "NSF has asked us to think big and be visionary," says Terry Plank, a geochemist at Columbia University's Lamont-Doherty Earth Observatory in Palisades, New York, and co-chair of the planning workshop, which will take place in Boise and will draw roughly 250 scientists from a range of disciplines and countries.

The first task will be setting scientific priorities for the SZO. One focus will be hazards like earthquakes, tsunamis, and volcanoes, which endanger the world's growing coastal populations. For instance, scientists still don't know why the locked interface between plates sometimes ruptures violently, producing earthquakes, whereas in other cases, it releases stress more gradually—through a recently recognized phenomenon known as slow slip. "We used to think it was earthquakes or nothing, and we now know there's a much bigger role for this slow but sort of jerky, episodic motion," says Joan Gomberg, a geophysicist at the U.S. Geological Survey (USGS) in Seattle, Washington.

There are environmental questions, too. Vast stores of methane gas can accumulate in the wedge of marine sediment that gets scraped off the downgoing plate at ocean trenches. The heat of the underlying crust accelerates the breakdown of organic matter, which produces the greenhouse gas. And as subduction compacts the sediments, methane is squeezed up toward the sea floor, where it cools and collects in frozen deposits. Researchers want to understand whether rising ocean temperatures might destabilize these deposits, releasing methane that would get gobbled up by microbes, driving down oxygen levels and producing carbon dioxide that could exacerbate acidification.

Next week's meeting aims to produce a white paper, which the organizers hope to deliver to NSF by early next year to begin the formal planning process. They are likely to cite a precedent: EarthScope, a program that in 2003 began deploying thousands of geophysical monitoring stations across the North American continent to probe its structure and evolution. It was the first earth science project funded through NSF's Major Research Equipment and Facilities Construction (MREFC) program, which was historically used to build telescopes and other single structures. Like EarthScope, the SZO would scatter instruments across wide areas, Plank says. "It's the whole suite of observations that we could make from outside of the trench all the way to the volcano."

The SZO could include seismometers and geodetic instruments for tracking crustal mo-

Downloaded from http://science.sciencemag.org/ on September 30, 2016

Published by AAAS

tions, sensors for gas seeping out of ocean sediments and volcanoes, and satellite-borne remote-sensing tools. Overlapping techniques are needed, says Diana Roman, a volcanologist at the Carnegie Institution for Science in Washington, D.C., who helped organize the workshop. For example, a burst of seismic unrest at a volcano could mean a fresh injection of magma—or not. The only way to tell is to compare seismic observations with simultaneous measurements of surface deformation and gas emissions.

Seafloor instrumentation will also play a key role in the SZO. GPS doesn't work underwater, but researchers can measure crustal motion using ship-based sonar to track the locations of acoustic transponders on the seabed. Another approach involves installing pressure gauges that can precisely measure water depth, a proxy for how the sea floor rises and falls during slow slip events. Some hope the SZO might enable the development of these and other novel instruments, like autonomous ocean "gliders" for acoustic surveys or seafloor cables for real-time data collection.

Basing the instrument network at least partly in the United States—for instance, along the Cascadia subduction zone in the Pacific Northwest—would provide an opportunity to collaborate with USGS, which is developing a parallel project, informally called the Ring of Fire, to monitor and forecast natural hazards in subduction zones.

On the other hand, many scientists—and NSF—recognize that studying subduction zones outside the United States would offer different lessons, and an incentive for international participation and funding. "Why not put it in three different places?" asks Kerry Sieh, a geologist and the director of the Earth Observatory of Singapore. For example, he suggests choosing one U.S. location, one along the Peru-Chile Trench in South America, and one along the Sunda Trench in Indonesia. Others, including Gomberg, say the SZO could be made up of much smaller pilot projects, or could even be an umbrella organization that merely facilitates collaboration and data sharing.

The different options imply wildly different price tags. At the upper end of the spectrum would be something like EarthScope, which cost roughly $200 million to build, was subject to a lengthy review process, and had to survive congressional budget negotiations.

In the next few years, pressure on the MREFC budget will ease up, with the completion of other major projects, such as the Large Synoptic Survey Telescope in Chile. It's too early to say whether the SZO will follow the same funding model as EarthScope, says Anne Meltzer, a seismologist at Lehigh University in Bethlehem, Pennsylvania, who helped spearhead the project. Although the MREFC could fund construction, a big project would need to find other ways to support ongoing science and operations. The payoff would be powerful, she says. "If we could marshal something on that scale we could really advance our understanding of subduction zone dynamics." ■

Julia Rosen is a writer in Portland, Oregon.

Earth's conveyor belts

Geoscientists are planning the Subduction Zone Observatory, which could place a diverse suite of sensors across the regions where ocean crust sinks below continents.

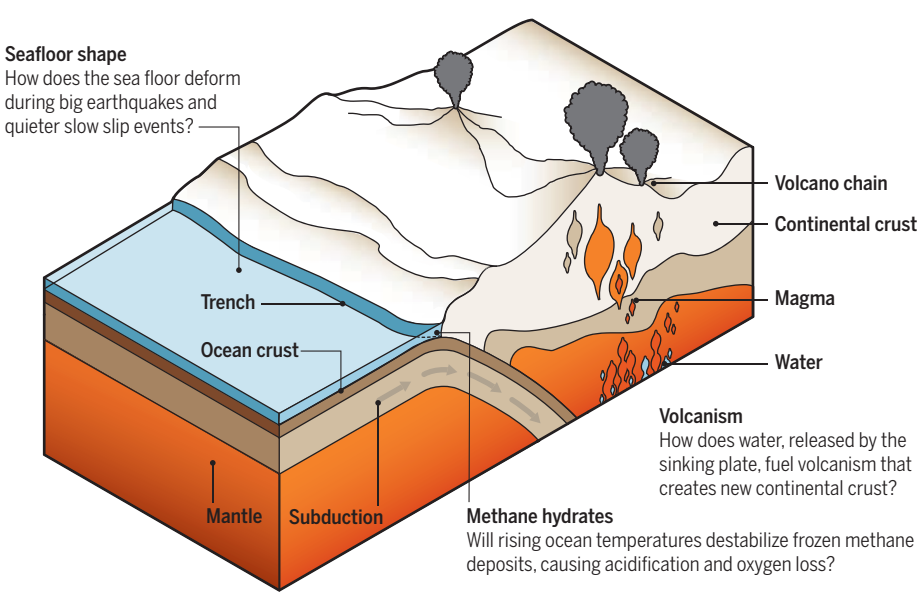

DIAGRAM: G. GRULLÓN/SCIENCE

CANCER

Using DNA, radiation therapy gets personal

Gene-based tests aim to predict who will benefit from radiation, or suffer

By **Elie Dolgin**

At most cancer hospitals today, medical oncologists routinely order genetic tests that help guide their treatment decisions. If the tumor has a certain DNA mutation, the patient may be a good candidate for a targeted drug therapy; if it overexpresses a series of genes, chemotherapy might work well. But down the hallway in the radiation ward, cancer patients typically get a one-size-fits-all course of radiotherapy, regardless of their genetics or those of their cancer.

A small but increasing number of radiation oncologists is hoping to change that. At the annual meeting of the American Society for Radiation Oncology (ASTRO) next week in Boston, researchers will describe their hunt for gene activity profiles in tumors that can help determine how susceptible the cancer will be to radiation. Others are looking for variations in patients' normal DNA that explain why some people tolerate radiation well, whereas others experience severe and lasting side effects ranging from trouble swallowing and memory loss to impotence and incontinence.

The work is still far from the cancer clinic, and some observers think it may be slow to realize its promise given the many false starts experienced by past gene signature tests for other conditions and the unique financial and logistical challenges of radiation oncology. "The process of advancing this might be like a wave lapping on the beach—a foothold here, a foothold there," says Siraj Ali, director of clinical development at Foundation Medicine, a cancer diagnostics company in Cambridge, Massachusetts.

But those looking for genetic predictors say there's an urgent need to personalize radiation therapy: Nearly two-thirds of people with cancer receive it, which means that anything that helps boost cure rates or mitigate

Downloaded from http://science.sciencemag.org/ on September 30, 2016

Published by AAAS

Unlike cancer drug therapy, radiation therapy for head and neck cancer is rarely guided by analyzing DNA.

toxicity problems could be a boon to patients. Most radiation oncologists, however, have focused almost exclusively on improving the machines and the targeting. "As a field, we've done very well on the technology side," says Judy Keen, director of scientific affairs at ASTRO in Arlington, Virginia. "Now is the time for the biology to really explode more."

One approach now under investigation is to look at gene activity in the tumor itself. That's the strategy of a University of Michigan (UM) spinoff company called PFS Genomics in Vancouver, Canada, which used breast cancer cell lines to identify a 51-gene expression signature of radiation sensitivity. Validation of the signature in patient tumor samples suggests it could help determine which women undergoing lumpectomies will benefit from radiation, which would do fine without it, and which patients won't respond and might thus need additional interventions.

Nearly all women get radiation after this kind of breast-conserving surgery, yet close to three-quarters of them may not need it, notes UM Ann Arbor physician-scientist Corey Speers, a PFS co-founder. "We're overtreating patients," says Speers, who will discuss the firm's risk-stratifying strategy at the ASTRO meeting. Felix Feng, another PFS co-founder, will also describe a 24-gene test for men with prostate cancer, designed to predict who will benefit from radiation after surgery.

Also at ASTRO, Javier Torres-Roca of the Moffitt Cancer Center in Tampa, Florida, will present a new concept he has dubbed the "genomic-adjusted radiation dose," which takes advantage of gene expression data from the tumor to indicate how much radiation each patient should receive. In recent years, Torres-Roca has published papers showing that a 10-gene test—which includes genes involved in DNA damage response, cell-cycle control, and epigenetic regulation—could retrospectively predict survival rates in patients undergoing radiation for a variety of cancers, including those of the brain, pancreas, and breast. Torres-Roca has founded a company called Cvergenx, which aims to market a system to help oncologists fine-tune radiation dosing to account for a person's genomic features. He argues that those whose gene expression test predicts low survival should get greater than average radiation doses. Some of his peers, however, express concern that the test doesn't account for radiation effects such as toxicity.

> ***"Now is the time for the biology to really explode more."***
>
> **Judy Keen**, American Society for Radiation Oncology

Many researchers are also hunting for gene variants that predict adverse reactions to radiation. Members of the international Radiogenomics Consortium, an effort backed by the National Cancer Institute in Bethesda, Maryland, are searching across the genomes of thousands of cancer patients for common polymorphisms linked to problems after radiotherapy. In July, they reported two new gene variants tied to urinary troubles such as incontinence in men whose prostate cancer had been bombarded with radiation. So far, half a dozen variants linked to radiation toxicity have been tallied—typically in "genes that control some aspect of the tissue or organ impacted by the complication," says consortium co-leader Barry Rosenstein from the Icahn School of Medicine at Mount Sinai in New York City—but the group may need at least twice as many to create a useful test.

Tim Ward in Manchester, U.K., a patient advocate with the consortium who suffers from rectal bleeding as a consequence of his own radiation treatment for prostate cancer 4 years ago, says that such a test could help people with cancer make more informed decisions. "Certainly, a lot of patients who have severe [gastrointestinal] problems say to me, 'If I'd known this was going to happen I may not have had the radiotherapy, because my life is completely blighted,'" he says.

But bringing a genetic test for radiation response to market will not be easy. "The number of hurdles we need to jump through to achieve that are not trivial," says Feng, who moved from UM Ann Arbor to the University of California (UC), San Francisco, earlier this year. Other DNA-based predictive tests—for drug responses, for example—often don't survive replication attempts by independent groups or in large populations. And evidence that tests to guide radiation therapy actually work could be slow in coming.

For starters, radiation is often given to cancer patients in the earliest stages of the disease, which means that it could take years to know whether genomic data can boost long-term survival or limit toxicity. In contrast, most new cancer drugs are tested in people with metastatic disease who often have just months to live. The centers that conduct radiotherapy (and the companies that manufacture the equipment) also have little financial incentive to weed out potential clients with such tests, so it's hard to attract the investment needed to validate any of these products.

Joanne Weidhaas, a radiation oncologist at UC Los Angeles, hopes to drum up commercial interest for the DNA test she's developing through a startup called Mira Dx by considering genetic biomarkers that can predict responses both to radiation and to certain drug treatments, including the cancer immunotherapies that have taken the pharmaceutical industry by storm. "For me, I need to make what's best for patients, and for the business people they need to make money," Weidhaas says. "And if you can do both, that's a path forward." ■

Elie Dolgin is a writer based in Somerville, Massachusetts.

PHOTO: RGB VENTURES/SUPERSTOCK/ALAMY STOCK PHOTO

Downloaded from http://science.sciencemag.org/ on September 30, 2016

Published by AAAS

ARCHAEOLOGY

Neandertals made jewelry, proteins confirm

"Landmark" study firmly links sophisticated artifacts from France to our extinct cousins

By **Lizzie Wade**

The "necklaces" are tiny: beads of animal teeth, shells, and ivory no more than a centimeter long. But they provoked an outsized debate that has raged for decades. Found in the Grotte du Renne cave at Arcy-sur-Cure in central France, they accompanied delicate bone tools and were reportedly found in the same layers as fossils from Neandertals. Some archaeologists credited the artifacts, described as part of the so-called Châtelperronian culture, to our archaic cousins. But others argued that Neandertals were incapable of the kind of symbolic expression reflected in jewelry and insisted that modern humans must have been the creators (*Science*, 20 November 1998, p. 1451).

Now, a pioneering study uses ancient proteins to identify Neandertal bone fragments from Grotte du Renne for direct radiocarbon dating. The team finds that the link between the archaic humans and the artifacts is real. It's "a landmark study" in the burgeoning field of paleoproteomics, says paleontologist Ross MacPhee of the American Museum of Natural History in New York City. Others say it shores up the picture of Neandertals as smart, symbolic humans.

Unearthed between 1949 and 1963, the controversial artifacts were crafted during a transitional time more than 40,000 years ago, when modern humans were sweeping across Europe and the Neandertals who had lived there for hundreds of thousands of years were dying out. Although the artifacts were reportedly from the same layer as Neandertal fossils, researchers such as Thomas Higham of the University of Oxford in the United Kingdom suspected that artifacts and bones from different layers got mixed up during the decades-old excavation (see http://scim.ag/NeandertalSmarts).

One way to solve the debate would be to radiocarbon date the Neandertal fossils to be sure they came from the Châtelperronian rather than older, lower layers in the cave. But that would require destroying the valuable specimens, which are mostly teeth. Hoping to find other material to date, bioarchaeologist Matthew Collins of the University of York in the United Kingdom and grad student Frido Welker of the Max Planck Institute for Evolutionary Anthropology in Leipzig, Germany, turned to the trove of unidentified bone fragments found in the Châtelperronian layer. They applied a new method for extracting and analyzing ancient proteins (*Science*, 24 July 2015, p. 372) to nearly 200 nondescript bone scraps.

The results, published online in the *Proceedings of the National Academy of Sciences* last week, showed that at least three of the scraps were human. But was it an archaic human, like a Neandertal, or a modern human?

To answer that question, the researchers compared the chemical composition of the collagen in the fragments with the collagen produced by modern and archaic humans. Modern human collagen contains high amounts of an amino acid called aspartic acid. But the team found that the Neandertal genome, first sequenced in 2010 from other fossils, includes a gene that likely produced collagen rich in a different amino acid, asparagine. The Châtelperronian collagen was asparagine-rich, indicating that it came from a Neandertal. To be certain, the researchers sequenced the bones' mitochondrial DNA as well, finding that it also indicated Neandertal ancestry. The bone scraps have turned out to be "a great molecular record," Collins says.

In addition to being asparagine-rich, the collagen was a form found only in growing bone. The fragment also had a high proportion of certain nitrogen isotopes associated with children who are breastfeeding. So the researchers infer that at least some of the bone fragments likely came from the skull of a Neandertal infant. Direct radiocarbon dating of the infant bone showed that it's about 42,000 years old—just when the Châtelperronian culture was in full swing in France and northern Spain.

"You can invent all sorts of stories. But the simplest explanation is that this assemblage was made at least in part by Neandertals," says co-author Jean-Jacques Hublin, a paleoanthropologist at the Max Planck Institute in Leipzig. He believes that Neandertals made the artifacts themselves but likely picked up the idea from their new modern human neighbors. But João Zilhão at the University of Barcelona in Spain, who has long argued that Neandertals had sophisticated cognitive abilities, says there's no evidence that they had any help from the new arrivals. He contends that Neandertals in the Iberian Peninsula made body ornaments from shells as early as 50,000 years ago—thousands of years before modern humans showed up in the region.

Higham himself is now convinced. "This paper is the first time that a Neandertal bone has been dated from this key site, and it … provides additional data to support a Châtelperronian-Neandertal link," he says. "I think it is quite possible that Neandertals were capable of making and using personal ornaments." ■

Analysis of ancient proteins shores up the idea that Neandertals fashioned these beads as jewelry more than 40,000 years ago.

PHOTO: DR. MARIAN VANHEREN

Downloaded from http://science.sciencemag.org/ on September 30, 2016

Published by AAAS

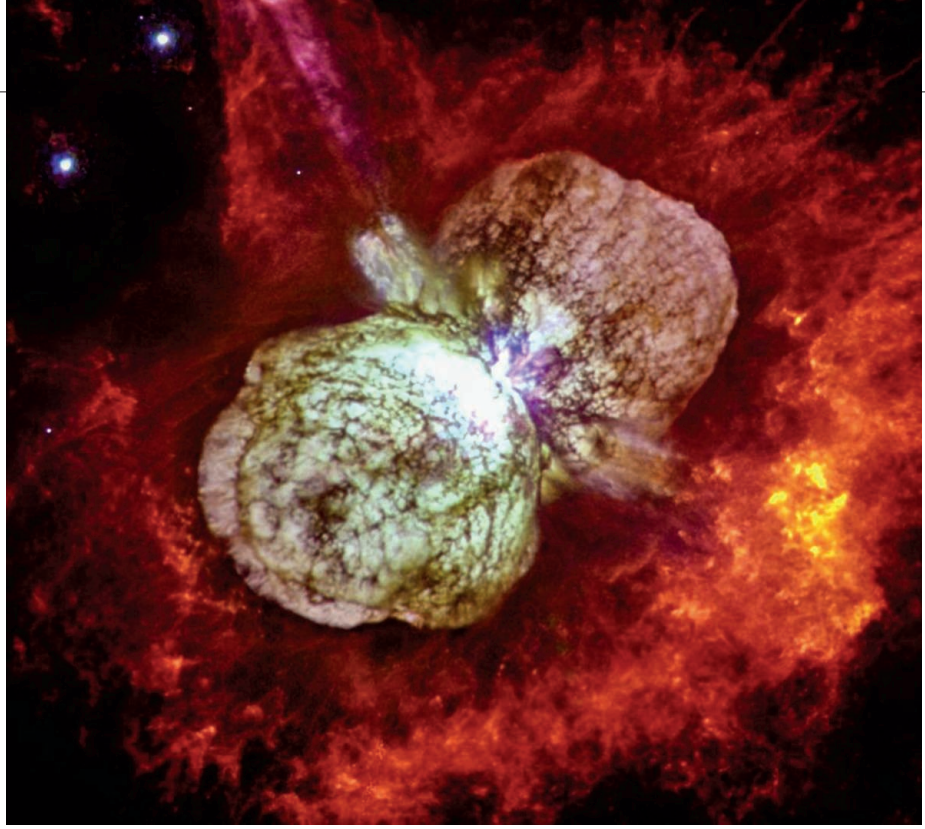

The Eta Carinae star system erupted in 1841 with a near supernova that led to the Homunculus Nebula.

PHOTO: NATHAN SMITH (UNIVERSITY OF CALIFORNIA, BERKELEY) AND NASA

ASTRONOMY

Paired stars sculpt nebulae into fanciful shapes

Survey suggests fast-orbiting binaries at work within many of the gas clouds shed by dying stars

By **Joshua Sokol**

For decades, astronomers have suspected that planetary nebulae—dazzlingly colorful shrouds of gas cast off by dying stars—owe their weird, often symmetrical shapes to the sculpting magnetic forces of two stars orbiting each other at the nebula's center. Now, a new study has helped confirm theorists' picture that many nebulae are the handiwork of binary stars in which the companions orbit each other so closely that they share the same atmosphere.

There are more than a thousand known planetary nebulae, and few have the simple, spherical shape that would be expected from a solitary star expelling its outer layers in dying gasps. Instead, they often look like hourglasses or butterflies. For a binary pair to produce that shape, the nebula's long axis of symmetry should point in the same direction as the axis around which the stars orbit.

So Todd Hillwig, an astronomer at Valparaiso University in Indiana, and his colleagues set out to find planetary nebulae with binary stars at their center where both axes could be measured. Doing so requires plenty of telescope time and a decent view through the nebula to track the stars' orbits, plus a good understanding of the nebula's shape. As a result, the team could only identify eight systems. But in each, allowing for uncertainties, the axes point the same way.

"Eight doesn't seem like a lot," Hillwig says. "But once we get to the kind of statistics we have here it becomes very convincing that there's a real connection." There's only about a one-in-a-million chance that all the systems just happen to be aligned, according to the paper, which has been accepted for publication at *The Astrophysical Journal*.

"The conclusions of this work are on quite solid grounds," says Henri Boffin, an astronomer at the European Southern Observatory in Garching, Germany, who was not involved in the work. Another outsider, Noam Soker, a theorist at the Technion-Israel Institute of Technology in Haifa, says the result is a big development. "It tells us, look: What shapes the planetary nebula is a binary system."

That conclusion has been 4 decades coming. In 1975, astronomer Howard Bond, a co-author on Hillwig's paper, spent a cloudy night at Kitt Peak National Observatory near Tucson, Arizona, browsing through the library. In reference materials, he noticed two objects suspiciously close to each other in the sky: UU Sagittae, a binary pair discovered in 1932, and Abell 63, a planetary nebula found in 1966.

Bond soon confirmed that the nebula and stars were in one and the same place, making them the first example of a binary pair surrounded by a symmetrical nebula. But the two stars of UU Sagittae—a small dwarf star and the hot, shrunken remnant of a red giant that had recently shed its outer layers—were locked in an improbably close orbit, Bond says. "You have the core of a red giant, orbited by another star so close together that the star would have been inside the red giant."

In 1976, Bohdan Paczynski, an astrophysicist at the Polish Academy of Sciences in Warsaw who was unaware of Bond's discovery, predicted how such a binary pair could end up inside a nebula. His starting point was a red giant with a companion star. When the giant swells up, it engulfs the other star. The companion spirals in until it closely orbits the giant's core, gathering gas to itself in a disk in the same plane of the orbit.

Later, theorists would sketch out how these pairs might sculpt the gas. In their scenarios, magnetic fields in the disk send jets of material spurting from its poles, which then blow the outer atmosphere of the red giant into an elongated nebula, perhaps cinched around the waist by rings. That nebula glows, blasted by ultraviolet radiation from the exposed red giant core.

The details of how such "common envelope" systems work are still fuzzy, according to Soker. "Actually, it's embarrassing how little we know about the common envelope evolution," he says. But Hillwig's work makes it clear that these turbulent binaries are at work in many planetary nebulae.

For Bond, the finding is bittersweet. On the one hand, he's pleased to have observations that help confirm his predictions from 40 years ago. On the other hand, the link suggests that a single-star solar system like our own may end with a disappointing fizzle, contrary to the spectacular nebula many textbooks forecast, he says.

"We have this disappointment that maybe our own sun won't participate in making a spectacular butterfly, or a cigar-shaped nebula." ■

Joshua Sokol is a writer based in Boston.

Downloaded from http://science.sciencemag.org/ on September 30, 2016

Published by AAAS

Eske Willerslev (left) meets Aboriginal elders during the genetic sampling project he led.

HUMAN ORIGINS

Aborigines and Eurasians rode one migration wave

Tide of genetic data refutes idea that an earlier expansion of modern humans populated the island continent

By **Elizabeth Culotta** *and* **Ann Gibbons**

Australian Aborigines have long been cast as a people apart. Although Australia is halfway around the world from our species's accepted birthplace in Africa, the continent is nevertheless home to some of the earliest undisputed signs of modern humans outside Africa, and Aborigines have unique languages and cultural adaptations. Some researchers have posited that the ancestors of the Aborigines were the first modern humans to surge out of Africa, spreading swiftly eastward along the coasts of southern Asia thousands of years before a second wave of migrants populated Eurasia.

Not so, according to a trio of genomic studies, the first to analyze many full genomes from Australia and New Guinea. They conclude that, like most other living Eurasians, Aborigines descend from a single group of modern humans who swept out of Africa 50,000 to 60,000 years ago and then spread in different directions. The papers "are really important," says population geneticist Joshua Akey of the University of Washington, Seattle, offering powerful testimony that "the vast majority of non-Africans [alive today] trace their ancestry back to a single out-of-Africa event."

Yet the case isn't closed. One study argues that an earlier wave of modern humans contributed traces to the genomes of living people from Papua New Guinea. And perhaps both sides are right, says archaeologist Michael Petraglia of the Max Planck Institute for the Science of Human History in Jena, Germany, a co-author on that paper who has long argued for an early expansion out of Africa. "We're converging on a model where later dispersals swamped the earlier ones," he says.

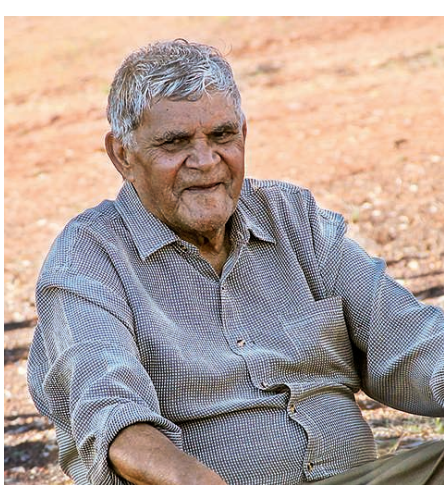

Aubrey Lynch, an Aboriginal elder, agreed to participate in a project to study his people's roots.

A decade ago, some researchers proposed the controversial idea that an early wave of modern humans left Africa more than 60,000 years ago via a so-called coastal or southern route. These people would have launched their migration from Ethiopia, crossing the Red Sea at its narrowest point to the Arabian Peninsula, then rapidly pushing east along the south Asian coastline all the way to Australia. Some genetic studies, many on mitochondrial DNA of living people, supported this picture by indicating a relatively early split between Aborigines and other non-Africans. But analysis of whole genomes—the gold standard for population studies—was scanty for many key parts of the world.

Three large groups of geneticists independently set out to fill the gaps, adding hundreds of fully sequenced genomes from Africa, Australia, and Papua New Guinea to existing databases. Each team used complex computer models and statistical analyses to interpret the population history behind the patterns of similarity and difference in the genomes.

A team led by evolutionary geneticist Eske Willerslev of the University of Copenhagen zeroed in on Australia and New Guinea in what Akey calls a "landmark" paper detailing the colonization of Australia (see Feature, p. 1357). By comparing Aboriginal genomes to other groups, they conclude that Aborigines diverged from Eurasians between 50,000 and 70,000 years ago, after the whole group had already split from Africans. That means Aborigines and all other non-African people descend from the same out-of-Africa sweep, and that Australia was initially settled only once, rather than twice as some earlier evidence had suggested. Patterns in the Aboriginal DNA also point to a genetic bottleneck about 50,000 years ago: the lasting legacy of the small group that first colonized the ancient continent.

In another paper, a team led by population geneticist David Reich of Harvard University comes to a similar conclusion after examining 300 genomes from 142 populations. "The take-home message is that modern human people today outside of Africa are descended from a single founding population almost completely," Reich says. "You can exclude and rule out

PHOTOS: PREBEN HJORT, MAYDAY FILM

Downloaded from http://science.sciencemag.org/ on September 30, 2016

Published by AAAS

an earlier migration; the southern route."

But the third paper, by a team led by Mait Metspalu of the Estonian Biocentre in Tartu, makes a different claim. Analyzing 379 new genomes from 125 populations worldwide, the group concludes that at least 2% of the genomes of people from Papua New Guinea comes from an early dispersal of modern humans, who left Africa perhaps 120,000 years ago. Their paper proposes that *Homo sapiens* left Africa in at least two waves.

Reich questions that result, but says that his and Willerslev's studies can't rule out a contribution of only 1% or 2% from an earlier *H. sapiens* migration. Akey says: "As population geneticists, we could spend the next decade arguing about that 2%, but in practical terms it doesn't matter." The most recent migration "explains more than 90% of the ancestry of living people."

Still, changes in climate and sea level would have favored earlier migrations, according to a fourth *Nature* paper. Axel Timmermann and Tobias Friedrich of the University of Hawaii, Manoa, in Honolulu reconstructed conditions in northeastern Africa and the Middle East, based on the astronomical cycles that drove the ice ages. They find that a wetter climate and lower sea levels could have enticed humans to cross from Africa into the Arabian Peninsula and the Middle East during four periods, roughly around 100,000, 80,000, 55,000, and 37,000 years ago. "I'm very happy," Petraglia says. His and others' discoveries of early stone tools in India and Arabia suggest that moderns did expand out of Africa during the early migration windows (*Science*, 29 August 2014, p. 994).

But those lineages mostly died out. The major migration, with more people and reaching all the way to Australia, came later. "Demographically, after 60,000 years ago something happens, with larger waves of moderns across Eurasia," Petraglia says. "All three papers agree with that."

The studies show Aborigines' ties to other Eurasians but also reinforce Australia's relatively early settlement and long isolation. As such, they reaffirm its unique place in the human story. The continent holds "deep, deep divisions and roots that we don't see anywhere else except Africa," Willerslev says. That echoes the views of Aborigines themselves. "The majority of Aboriginal people here in Australia believe that we have been here in this land for many thousands of years," Colleen Wall, a co-author on the Willerslev paper and elder of the Aboriginal Dauwa Kau'bvai Nation in Wynnum, Australia, wrote in an email to *Science*. "I am 'over the moon' with the findings." ■

SCIENCE POLICY

China bets big on big facilities

Anchored by a powerful synchrotron, first of a series of multidisciplinary national science centers will rise by 2023

By **Jane Qiu**, *in Beijing*

The Chinese Academy of Sciences (CAS) this month unveiled plans for a national science center that will carry out mission-driven research along the lines of the U.S. Department of Energy's (DOE's) national laboratories. Forming the backbone of the first center, slated for completion in 2023, will be a synchrotron, a supercomputer, and two other big-ticket facilities that will together cost $1.4 billion to build. More such laboratories are on the drawing board.

Last November, Chinese President Xi Jinping called for the creation of multidisciplinary labs that would concentrate money and manpower on the country's development while taking marching orders from the central government. Such labs would have "a real impact on society, especially for a big country like China where the scale of challenges is immense," says Antonio Masiero, vice president of the National Institute of Nuclear Physics in Rome. CAS took up the challenge in its new 13th 5-year plan, which cites the multipurpose labs as vital to helping China create 150,000 jobs over the next 5 years and to generating $720 billion from new technology, more than tripling the figure of the previous 5 years.

> ***"The idea is not to undermine basic research, but to ... solve tough problems in a concerted way."***
>
> **Bai Chunli**, Chinese Academy of Sciences

The first multipurpose lab will rise in Huairou Science Park, a technology park planned for Beijing's northern outskirts. Its crown jewel will be the $750 million Beijing Advanced Photon Source. The synchrotron's beams will be brighter, narrower, and more uniform than those of other top synchrotrons, resulting in images with nanometer resolution—10 times higher than the best resolutions achieved today. The machine "will be able to observe single atoms inside bulk materials," says Peter Littlewood, director of DOE's Argonne National Laboratory in Lemont, Illinois, which manages the U.S. Advanced Photon Source. Such capabilities will, for instance, allow researchers to image atoms as they make and break chemical bonds. "This is unprecedented," Littlewood says.

Huairou will also be home to the Synergetic Extreme Condition User Facility (SECUF), a set of 17 labs that will expose materials to extremes of temperature, pressure, and magnetic fields. These torture chambers, of sorts, will help develop novel superconductors and materials for quantum computing and nuclear fusion, says project leader Ding Hong, a physicist at CAS's Institute of Physics here. "Having the capacity to create all the combinations SECUF can create is unique." Meanwhile, a supercomputer called the Earth System Simulator will model geology, climate, pollution, and other complex processes, and a suite of state-of-the-art imaging instruments will help push the frontiers of biomedical research in areas like protein structure and brain mapping. The center is expected to have a staff of 3000 scientists and will be paid for by China's powerful National Development and Reform Commission; groundbreaking is slated to begin by the end of the year.

Some worry that the Huairou center may put too much emphasis on short-term gains, such as new products and jobs. "The pressure [on CAS] to be economically relevant has been overwhelming," says Mu-ming Poo, director of CAS's Institute of Neuroscience in Shanghai. "It's a balancing act," says Thom Mason, director of DOE's Oak Ridge National Laboratory in Tennessee. "If you are exclusively focusing on doing things that are relevant to industry next year, it's not going to be that transformational."

"The idea is not to undermine basic research, but to promote technology transfer and solve tough problems in a concerted way," responds CAS President Bai Chunli here in Beijing. "A sense of urgency can help focus our efforts." More such ventures are in the works. CAS intends to build a second national center in Shanghai, and similar research hubs are planned for regions that are lagging in technological prowess. "Ultimately," Ding says, "there will be a network of multipurpose laboratories that are catered towards regional characteristics and regional needs." ■

Jane Qiu is a writer in Beijing.

Downloaded from http://science.sciencemag.org/ on September 30, 2016

Published by AAAS

FEATURES

TALL TIMBER

High-tech wood is taking the place of steel in a new wave of green high-rises

By **Warren Cornwall**

An 80-story tower envisioned for central London would require new wood-building technologies.

GRAPHIC: PLP ARCHITECTURE

A Douglas fir tree is a marvel of natural engineering. The trunk, made mostly of slender dead cells each a few millimeters long, can reach heights of 100 meters. It's supple enough to sway in windstorms without snapping, yet strong enough to support its weight—up to 160 metric tons. Kilogram for kilogram, a wooden beam made from this fir is 3.5 times stronger than steel. A single tree can store half its weight in carbon and can replace itself, given enough time. Its luminous, patterned wood can be sculpted into virtually any shape.

Not far from Canadian forests thick with Douglas firs, the most ambitious effort yet to harness these remarkable qualities in a human structure is rising. A few kilometers from downtown Vancouver, on the University of British Columbia campus, workers are putting the finishing touches on an 18-story dormitory set to be the world's tallest wooden building. As skyscrapers go, the boxy structure is modest. Yet it represents a leap forward for a material long regarded as too weak, variable, and flammable to support high-rise buildings.

Scientists and architects across the globe are trying to adapt this ancient building material for the demands of the modern city. Spurred by new ways to work with wood and concerns about the environmental toll of urban construction, they are trying to push the limits of height for wood construction and win wider acceptance for its use.

"We're in sort of the early, early days of this," says Michael Green, a Vancouver architect who has gained international attention for evangelizing about the potential for tall wooden buildings. "Right now I liken it to kind of the beginning of the steel revolution 120 years ago."

The Vancouver building, assembled from composite wooden components engineered to be stronger and more fire-resistant than ordinary wood, is unlikely to remain the tallest wooden structure for long. Engineers have conceived designs for soaring wooden skyscrapers that, at up to 80 stories, would rival their steel-framed cousins. But wood's true potential for 21st century cities is likely to emerge in the lab, where scientists are conducting myriad torture tests on new designs for wooden walls, beams, ceilings, and floors. Their goal: to see whether wood can overcome the safety concerns that, in the past, helped relegate it to the little leagues.

In 2013, Green's 29-meter-tall Wood Innovation and Design Centre in Prince George,

Downloaded from http://science.sciencemag.org/ on September 30, 2016

Published by AAAS

Canada, earned bragging rights as what was then the tallest wooden building in North America. But it came with this qualifier: the tallest modern one. A 111-year-old building not far from his office in Vancouver rises 34 meters, supported by massive beams carved from old-growth Douglas firs. "It's hard to feel like you're some hero of science or innovation when you're trying to keep up with what we used to do," Green says ruefully.

When true skyscrapers started rising in the late 19th century, wood's drawbacks began to loom. Its cells act like little sponges, swelling and shrinking by as much as 10% as they absorb and release moisture. Knots and twists in the grain make wood behave in unpredictable ways. It's more brittle than steel and more bendable than concrete. It rots, and, of course, it burns.

This final quality played a pivotal role in its decline as a structural material for large buildings, says David Barber, a Washington, D.C.–based fire engineer and expert in wooden buildings at the engineering firm Arup. As fire storms swept through cities built chiefly of wood—San Francisco, California, in 1851 and 1906; Chicago, Illinois, in 1871; Boston in 1872—insurers and officials discouraged tall wooden buildings in favor of less combustible material. Wood was consigned to low-rises and single-family houses.

The beams and panels in today's tall wooden buildings, however, are a far cry from natural wood. Instead of being hewn from a single tree, they're made of myriad bits of wood, glued together in a range of patterns. For tall buildings, a key innovation is known as cross-laminated timber, or CLT. Imagine plywood on a huge scale. Long pieces of lumber much like standard two-by-fours are glued together edge to edge, forming sheets. Those sheets are then pressed together in three or more layers, the wood in each layer running perpendicular to the adjacent sheets.

Developed in Europe in the 1990s, CLT has several advantages over conventional wood. The perpendicular layers counter wood's tendency to warp and twist and add strength. Individual wood pieces can be selected to create a more uniform final product. Sheets of CLT can span gaps of 18 meters—wide enough to serve as the floor for a multistory building. For going tall with wood, "CLT was kind of the trigger," says Erol Karacabeyli, a veteran engineer at a Vancouver lab of FPInnovations, a nonprofit created by the Canadian government and the timber industry to find new ways to use wood.

At FPInnovations, Karacabeyli leads the way into a cavernous room, where CLT panels 17 centimeters thick and 8 meters long, like those making up the floors in the new wooden dorm nearby, lie in a stack. They were being tested to see how much weight they could handle. Or, as Karacabeyli puts it, "So what happens if you have a really big party?"

ALTHOUGH CLT HAS BEEN AROUND for a quarter-century, tall wooden buildings are only now taking off. Credit growing concerns about climate and computer advances that make it easier to fashion custom-shaped panels, says Sam Zelinka, head of building and fire sciences research at the Forest Products Laboratory, an arm of the U.S. Department of Agriculture, in Madison. "The carbon thing has got people thinking about—I don't know what kind of word you want to use—sustainability and greenness," he says.

Besides being renewable, wood proponents argue, timber offers a double helping of carbon benefits. It's less energy intensive to produce than steel and concrete. And the wood in a building effectively sequesters carbon, while trees regrowing in logged areas can absorb additional carbon dioxide (CO_2). A report from the University of Canterbury in Christchurch, New Zealand, estimated that throughout its entire life, a large building made mostly from wood would have a carbon footprint a third smaller than a comparable one made from steel or concrete.

On a global scale, replacing the steel used in construction with timber such as CLT could cut CO_2 emissions by 15% to 20%, according to a 2014 study in the *Journal of Sustainable Forestry*. "It's amazing what can be done," says Chad Oliver, the study's lead author and head of the Global Institute of Sustainable Forestry at Yale University.

But others question those projections. William Keeton, a forest ecologist at the University of Vermont in Burlington, found in a 2010 study that a New England forest left alone or lightly logged for more than a century would store approximately a third more carbon than a more heavily logged forest plus the wood products coming from it. He also cautions that it's hard to predict whether swapping wood for steel would lead to a perfect one-to-one exchange. For example, building designs could change in response to the shift in materials. "We just have to be a little careful to recognize that wood products are not the panacea," he says.

A mass switch to wood could also have major implications for forests. Oliver estimates that replacing the world's structural steel with wood could require 40% of global annual forest growth—almost a tripling of today's logging levels. That's still less than the new wood grown in forests each year, Oliver says. But given today's logging techniques, he says, "we would have a lot of highly degraded forests."

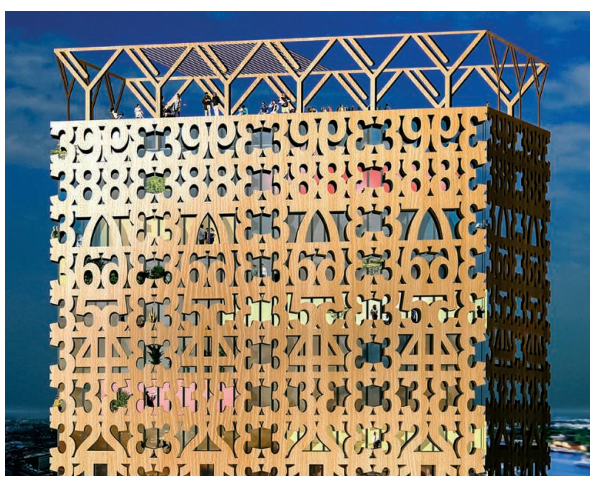

Numbers count the floors in a concept for Trätoppen (Treetop), a wooden high-rise that would be Stockholm's tallest.

GRAPHIC: ANDERS BERENSSON ARCHITECTS

THE PUSH TO DEMONSTRATE the potential of wood has touched off a skyscraper race. The new Vancouver dormitory risks being surpassed by a 21-story residential tower in Amsterdam, scheduled to start construction in 2017. In April, Michael Ramage, an architect and structural engineer at the University of Cambridge in the United Kingdom, unveiled a plan for a needle-thin, 80-story skyscraper in London, one of four designs he's creating with architects in three different cities. There's no imminent plan to build any of them. But Ramage predicts that wooden towers this tall could go up within a decade, and he and his colleagues are now testing the kinds of beams and steel connectors that could support a supertall wooden structure.

Others, meanwhile, are campaigning to change building codes that, in most of North America, cap wooden buildings at six stories. The Vancouver dormitory is a case in point: Its designers had to apply for a special exemption from the building code. To assuage fire safety concerns, they sheathed its interior wooden columns in three layers of sheetrock. They also used reinforced concrete for the first floor and two major rectangular cores housing the elevator and stairs. The cores could have been built of wood, but doing so could have made it even harder to win government permits. "Until these kinds of innovative products or design methods or construction methods are in the code, they're not likely to be widespread," says Eric Karsh, a principal engineer at Equilibrium Consult-

Downloaded from http://science.sciencemag.org/ on September 30, 2016

Published by AAAS

New heights

Brock Commons, an 18-story student dormitory under construction in Vancouver, Canada, will be the world's tallest wooden building. Prefabricated pieces go together quickly, at a rate of two floors a week (above).

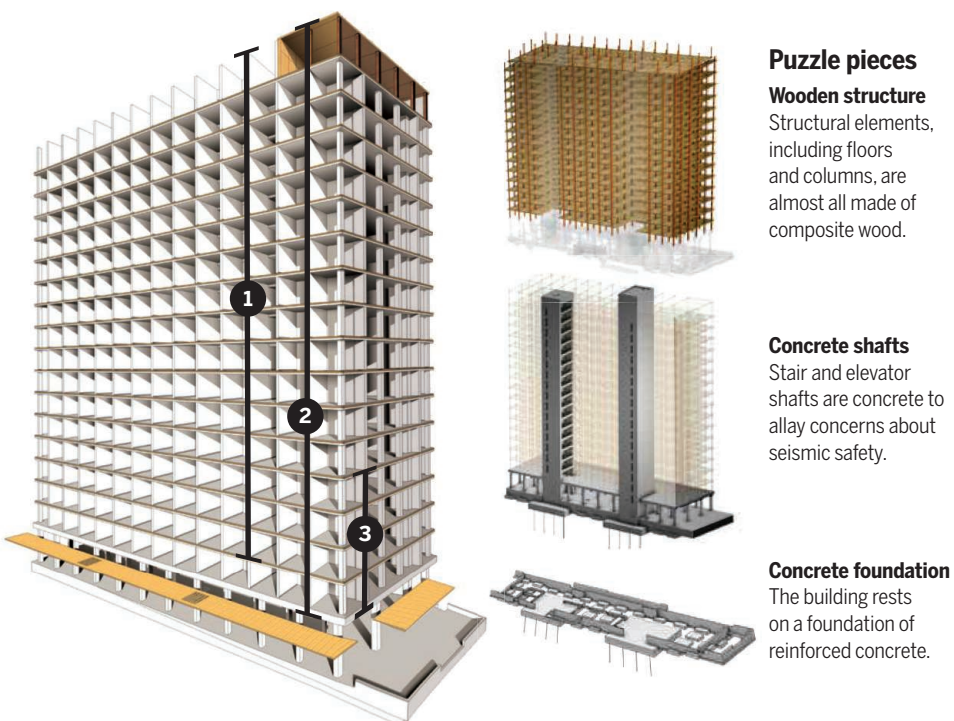

Puzzle pieces

Wooden structure
Structural elements, including floors and columns, are almost all made of composite wood.

Concrete shafts
Stair and elevator shafts are concrete to allay concerns about seismic safety.

Concrete foundation
The building rests on a foundation of reinforced concrete.

Three kinds of wood

1 Cross-laminated timber
Crossed-grain panels for load-bearing floors, walls, and roofs.

2 Glue-laminated timber
Composite material for beams, girders, and columns.

3 Parallel-strand lumber
Used in heavily loaded columns, beams, and headers.

ing in Vancouver, who has worked on other tall wooden buildings.

Government, university, and private scientists are now doing the meticulous tests that could make future building codes friendlier to wood. The Vancouver dorm will be outfitted with motion sensors and moisture detectors as scientists gauge how the building endures perhaps its most brutal trial—housing 400 college students. In the United States, scientists plan to erect a 10-story wooden building on a massive earthquake simulator at the University of California, San Diego, in 2020, to see how well a seismic protection system performs. Another group is setting off explosives near CLT-built walls to test how they would withstand a blast. Others are igniting a model apartment lined with CLT to see how the interior burns.

Barber, the fire engineer, says that much of the rap against wood reflects confusion between familiar wood-framed buildings, built of small, combustible lumber, and tall ones with massive timbers. Those huge pieces of wood actually withstand fire well, burning slowly and predictably, he says. An exterior layer of charred wood insulates the center of the timber, helping preserve its strength. "The science is somewhat already proven," Barber says. "It's more the case of the construction industry getting more familiar with how these buildings can be constructed and that they can be constructed safely."

The results so far have won over officials in Quebec in Canada, which last year raised the height limit to 12 stories for buildings using so-called mass timber. In the United States, the International Code Council, whose rulebook guides local building codes, announced in January that it was forming a committee to evaluate tall wooden buildings.

Meanwhile, a handful of U.S. architects and developers are already moving forward. Alan Organschi, a Connecticut architect who teaches at Yale, wants to turn four blocks of downtown New Haven into a thicket of wooden mid-rise buildings ranging from six to eight stories. The project, called Timber City, envisions as many as 12 buildings in a former industrial neighborhood near the Yale campus. He's now working with a developer to build the first—a six-story mix of apartments and shops.

For Organschi, like many in the field, the measure of success will be when a new 10-story wooden building is considered as unremarkable as the antique sitting in downtown Vancouver once was. "If we could get up to eight to 10 stories and really build it well and efficiently, I think we'd start to see real gains," he says. "I think we'd have a more renewable way of thinking about city building." ■

IMAGES: (TOP TO BOTTOM) KK LAW/NATURALLYWOOD.COM; RENDERINGS COURTESY OF THE UNIVERSITY OF BRITISH COLUMBIA AND ACTON OSTRY ARCHITECTS INC.

Downloaded from http://science.sciencemag.org/ on September 30, 2016

Published by AAAS

An Aboriginal elder, speaking one of the remaining Pama-Nyungan languages, explains ancient customs to boys at Mudjawakalal in Australia.

PHOTO: PENNY TWEEDIE/ALAMY

Downloaded from http://science.sciencemag.org/ on September 30, 2016

SOLVING AUSTRALIA'S LANGUAGE PUZZLE

Methods borrowed from evolutionary biology show how people spread across the continent, giving birth to new languages

By **Michael Erard**

The first person to set foot on the continent of Australia was a woman named Warramurrungunji. She emerged from the sea onto an island off northern Australia, and then headed inland, creating children and putting each one in a specific place. As she moved across the landscape, Warramurrungunji told each child, "I am putting you here. This is the language you should talk! This is your language!"

This myth, from the Iwaidja people of northwestern Australia, has more than a grain of truth, for the peopling and language origins of Australia are closely entwined, says linguist Nicholas Evans of Australian National University (ANU) in Canberra. But researchers have long puzzled over both. When Europeans colonized Australia 250 years ago, the continent was home to an estimated half-million to 2 million people who were organized into about 700 different groups and spoke at least 300 languages.

Linguists have struggled to work out how these languages were related and when they

Published by AAAS

emerged. Each was spoken by relatively few people, and as cultures were wiped out by disease and violence, many languages vanished before they could be studied. Researchers prioritized gathering information from the few remaining speakers over deciphering ancient language relationships. But in recent years, researchers borrowing methods used in biology to derive evolutionary trees have begun to unravel the Australian linguistic puzzle. And this week, the approach takes a major step forward, with a combined genetic and linguistic study of the largest Australian language family.

The paper, published in this week's issue of *Nature* along with two other genomic studies of the peopling of Australia (see p. 1352), offers a modern version of Warramurrungunji's story. It paints a picture of how people entered and spread across the continent, giving birth to new languages as they went. It's "a major advance," says Peter Hiscock, an archaeologist at the University of Sydney in Australia. "It presents evidence for an elaborate population history in Australia, spanning 50 millennia." The study, led by evolutionary geneticist Eske Willerslev of the University of Copenhagen, also marks a milestone in collaboration between geneticists and linguists, who for years stayed in their separate camps.

Warramurrungunji came out of the ocean and walked across the land of Australia, planting languages as she went, as depicted in this illustration of an Aboriginal myth.

The 25 Aboriginal languages still being passed to new generations make up one of the last and most diverse great hunter-gatherer linguistic groups left. So understanding how they and their extinct relatives diversified could open a window on how language itself emerged among small social groups in the distant human past. "We need to look at places like Australia, which offer models of language diversification closest to the earliest state that shaped humankind," Evans says.

BACK IN 1963, linguist Ken Hale of the Massachusetts Institute of Technology in Cambridge identified what he considered to be a new Australian language family. He named it Pama-Nyungan ("pama-nahyoongan") for two distinct words for "person," drawn from the geographical extremes of the family's range, which extends across most of Australia (see map, p. 1359). If Hale was right, then Pama-Nyungan, with more than 200 identified languages, would be one of the world's largest language families—larger than Indo-European and almost as large as Sino-Tibetan.

Not everyone agrees that Pama-Nyungan is one family, however, for, like other Australian language families, it presents a puzzling pattern of similarities and differences. Linguists had long noted that most languages across Australia draw from the same set of sounds, and that their verbs and pronouns share similar patterns of construction.

Given these similarities, linguists would expect the languages to share many cognates, or words derived from a common ancestor. (The English word "knee," ancient Greek "gónu," and Sanskrit "jānu" are all cognates, descended from the Proto-Indo-European word "génu.")

But Australian languages have few cognates. For example, the sentence "you eat fish" in the Aboriginal languages Iwaidja and Gundjeihmi shares only one cognate element, a grammatical particle that marks the tense of verbs. In Russian ("ty esh rybku") and Elizabethan English ("thou eatest fish"), the sentence shares three—"ty" and "thou," "e-" with "eat," and "-sh" with "est." Yet Moscow and London are much farther apart than the areas where the two Aboriginal languages are spoken.

Perhaps because of these puzzling patterns, linguists have diverged sharply over basic questions such as whether and how Australian languages are related to each other and to languages in nearby New Guinea, likely the source of the first settlers. Some suggested that the Pama-Nyungan family, if it exists, entered the continent in a separate migration, whereas others argued that it split off from other Aboriginal languages only a few thousand years ago.

Now, a new generation of researchers is attacking the problem, and a small but growing group is taking its cue from evolutionary biology, which relies on genetic clues to decipher relationships between organisms. They are using computers to sort giant databases of cognates and generate millions of possible family trees based on assumptions about, say, how quickly languages split. The method, called computational Bayesian phylogenetics, forces researchers to explicitly quantify the uncertainty in the models, says linguist Claire Bowern of Yale University, a pioneer of the approach and co-author of the new study. "That's useful in Pama-Nyungan," she explains, "because you don't have good data, and you have to rely on single authors who may not be that familiar with the languages." Based on a set of parameters, researchers can winnow millions of trees into groups of the most plausible ones.

The first such computational efforts, done by biologists borrowing linguistic data, drew harsh responses from many linguists (*Science*, 19 September 2014, p. 1443). "Most look exclusively at words, seen as something like the equivalent of the gene as a unit of analysis in genetics," says Lyle Campbell, a historical linguist at the University of Hawaii, Manoa. But linguists traditionally determined historical relationships through sounds and grammar, which are more stable parts of language.

Bowern counters that the "instability" of words can actually be a boon, serving as a tracer for how languages change over time. In 2012, she and Quentin Atkinson, a biologist at the University of Auckland in New Zealand, constructed a family tree for the

ILLUSTRATION: DAVID GRUBIN PRODUCTIONS, FROM THE FILM *LANGUAGE MATTERS WITH BOB HOLMAN*

Downloaded from http://science.sciencemag.org/ on September 30, 2016

Published by AAAS

elusive Pama-Nyungan, using a massive database of 600,000 words to compensate for the low number of cognates. They analyzed 36,000 words from 195 Pama-Nyungan languages and compared the loss and gain of cognate words in 189 meanings through time.

This initial work found that Pama-Nyungan has a deep family tree with four major divisions tied to the southeastern, northern, central, and western regions of the continent. For the study published in *Nature*, Bowern drew from an expanded database of 800,000 words, which contains 80% of all Australian language data ever published, and looked at cognates from 28 languages across 200 meanings. Then she compared her tree with genomic data from Willerslev's new survey.

Willerslev's team sequenced complete genomes from 83 Aboriginal Australians as well as 25 Highland Papuans, and combined those data with published genomes. Using genetic changes as a molecular clock, they conclude that Papuan and Aboriginal Australian ancestors diverged perhaps 37,000 years ago, long before Australia and New Guinea were separated by rising seas. That suggests that people separated into distinct groups while still living on the ancient continent of Sahul, which included modern Australia, New Guinea, and Tasmania. The genetic analysis also found no evidence of multiple migrations into Australia, suggesting that Pama-Nyungan languages must have diversified on the continent.

To the researchers' amazement, the genetic pattern mirrored the linguistic one. "It's incredible that those two trees match. None of us expected that," says paleoanthropologist Michael Westaway of Griffith University, Nathan, in Australia, a co-author on the Willerslev paper. "But it's confusing: The [genetic splits] date to 30,000 years ago or more but the linguistic divisions are only maybe 6000 years old."

Willerslev says he first thought the languages must be much older than thought. "But the linguists told me, 'no way.'"

Both types of data also show that the population expanded from the northeast to the southwest. This migration occurred within the last 10,000 years and likely came in successive waves, Bowern says, in which existing languages were overlaid by new ones. This expansion also seems to correspond with a stone tool innovation called a backed edge blade. But the accompanying gene flow was just a trickle, suggesting that only a few people had an outsize cultural impact, Willerslev says. "It's like you had two men entering a village, convincing everyone to speak a new language and adopt new tools, having a little sexual interaction, then disappearing," he says. Then the new languages continued to develop, following the older patterns of population separation. "It's really strange but it's the best way we can interpret the data at this stage."

When it comes to languages, the Pama-Nyungan tree "gives us the first and only hypothesis of the higher-level branching of the Pama-Nyungan family," says Harold Koch, a historical linguist at ANU who was not involved in the *Nature* study, although he was Bowern's undergraduate adviser. "No one else has tried to answer this question, not because we don't believe there was such a grouping, but because the task seemed too hard. This makes the contribution of huge significance." With his field's usual care, Koch says he'd like to see the model tested with other types of linguistic evidence.

Bowern hopes to also mine the cognate database for insights into pronouns, color terms, and changes of meaning that may give clues to ancient ways of life when climate conditions changed or trading intensified. Last fall in a paper in the *Proceedings of the Royal Society B*, for example, she used the database to analyze how languages gain and lose numbers. One finding was that acquiring a word for "five" often tipped a language into accumulating words for even higher numbers, a change that may have reflected new trade relations that required the ability to count higher (see http://scim.ag/CountLang).

Not all linguists embrace Bowern's method or results. Linguist R.M.W. Dixon of James Cook University, Cairns, in Australia, who made his name in the 1960s and 1970s doing fieldwork on Aboriginal languages, says these languages are so unique that new theories of linguistic change must be invented to explain them. In his view the best model of Pama-Nyungan family relations is the parallel tines of a rake, not a tree, and the many similarities in these languages can mainly be accounted for by diffusion—in which language A gets word X from language B because the speakers interact or many people speak both languages. (That's why the word "taco" diffused from Spanish into English, for example.)

Other linguists argue that the computational models, built for genes that can only be inherited, deal poorly with languages that spread by diffusion. "Borrowings don't really tell us anything about language relatedness," says Asya Pereltsvaig, an independent linguist in Santa Clara, California. "They only obscure it."

Bowern counters that the phylogenetic methods are actually ideal for investigating borrowing, because you can test models with different rates of borrowing and see how well the resulting trees match known facts. Worldwide, about 5% to 10% of languages' vocabularies are borrowed from other languages; Bowern estimates the Pama-Nyungan rate to be 9%. That suggests that Pama-Nyungan languages developed much as other world languages did, rather than being a rarefied case, she argues.

The Aboriginal stories suggest as much, describing the birth of languages much the way Bowern thinks it happened. In 2004, Evans recorded an Iwaidja speaker, Brian Yambikbik, explaining how his language might be related to the one spoken on distant islands. "We used to speak the same language as them, but then the sea came up and we drifted apart, and now our languages are different." ■

Michael Erard is the author of Babel No More: The Search for the World's Most Extraordinary Language Learners.

Tracking a linguistic expansion

Pama-Nyungan is spoken across 90% of Australia. Linguists conclude that the family originated in northeastern Australia and spread to the southwest over millennia.

MAP: A. CUADRA/*SCIENCE*

Downloaded from http://science.sciencemag.org/ on September 30, 2016

Published by AAAS

INSIGHTS

Fever control *p. 1363*

Explaining perovskite performance *p. 1365* ▸

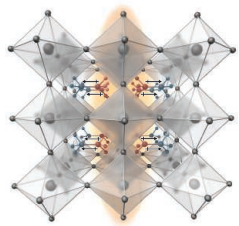

PERSPECTIVES

A remote tracking device can operate for longer periods of time if its system is designed to minimize power use.

INSTRUMENTATION

Gathering lots of data on a small budget

Open-source hardware and software technology can redefine data collection

By **Aaron C. Greenville**[1,2] *and* **Nathan J. Emery**[3]

Many science research projects rely on specialized electronic devices and software to gather data that often come with a high price tag. Advances in open-source hardware and software are occurring at an astounding rate, but scientists are often slow to take advantage of these for purposes beyond their original scope. Here, we advocate that open-source technology can be easily applied in science research to collect large data sets, at the same time reducing costs and increasing the repeatability of experiments.

Open-source technology requires both computational resources and devices that can control and receive data from equipment. Two families of commercial products have spurred this development: Arduino microcontrollers and Raspberry Pi microcomputers.

The Arduino microcontroller electronics and software platform was introduced in 2005 and is now available from third-party manufacturers for as little as US$5. The Raspberry Pi, developed in 2012, is a credit card–sized microcomputer that includes important components for connectivity, such as an Ethernet port, and Wi-Fi and Bluetooth modules. It also enables

PHOTO: DREW RUSH/NATIONAL GEOGRAPHIC CREATIVE

Downloaded from http://science.sciencemag.org/ on September 30, 2016

Published by AAAS

multipurpose usage with USB ports, general purpose input/output (GPIO) pins, and operating system (OS) compatibility. Customizable storage with the micro-SD card slot allows users to run Linux, Windows 10 Internet of Things (IoT) Core, or Android OS, so it can serve as a central hub to interface with different devices and peripherals such as Arduinos, camera modules, and third-party wireless modules (*1*, *2*). The Arduino and Raspberry Pi platforms can be easily adopted by researchers who are familiar with the R software for statistical analysis and graphics, and Python software environments. Python code can be run on the Raspberry Pi, and the availability of prewritten software libraries (or code), like that for R, makes it easy to set up and run sensors and other components quickly.

The Arduino and Raspberry Pi can be used with open-source software for both field and laboratory-based research and can return cost savings up to a factor of 100 relative to commercial suppliers (*3*). Arduinos are frequently used for weather-monitoring stations [see, for example, (*4*)], but other applications include Global Positioning System (GPS) tracking (*5*), controlling wireless sensor networks (*6*), robotic pollination systems (*7*), soil-moisture probes and crop-water use (*6*), vision research (*8*), underwater imaging systems (*9*), and in quantitative polymerase chain reaction analyses (*10*). Similarly, the Raspberry Pi has been used for projects involving image capture and recognition (*1*), automated controllers for weather protection (*2*), and cardiac monitoring (*11*). Further uses for both devices could include laboratory and field automation (e.g., telescope dome opening and rotation, automatic feeding or watering systems, and photo-recognition controllers), a wide range of environmental sensors (e.g., gas, light, and cloud sensors), and spectroscopy. With the rise of the IoT environment, connecting and powering multiple devices are no longer limiting factors (*12*).

Several research groups have recently demonstrated the potential of the new open-source hardware environment, thereby illustrating the feasibility and practicality of developing custom devices. Fisher and Kebede (*13*) developed a microcontroller-based unit to monitor temperature and water status in cropped fields. The unit consisted of air, soil, and canopy temperature sensors and a soil moisture sensor, and required about 4 hours to build and test. Each unit was produced at a cost of US$84. Furthermore, all sensors were tested in controlled conditions before deployment in the field, and the accuracy of all sensors was within the manufacturer's specifications. Sreejith *et al.* (*14*) designed and built a microcomputer-based altimeter for high-altitude, lightweight balloon flights in astronomy. Using a Raspberry Pi equipped with an accelerometer, a magnetometer, and a gyroscope, the researchers could keep the total weight under a critical 6 kg. The cost savings of their custom altimeter were estimated to be 5 to 10 times that of commercially available products.

By combining open-source hardware and software, researchers can increase the repeatability and reproducibility of their studies. Researchers can share and publish the exact component list and wiring instructions to make their hardware, along with the code to run the device. Open-source device code can be published and made citable (*15*). The openness of these platforms allows researchers to harness global electronics design knowledge and increase multidisciplinary collaborations. The potential to roll out inexpensive data collection devices across global research networks provides an exciting opportunity to test ideas and explore general patterns across many scientific disciplines. The greatest strength of open-source technology is that any modifications to designs or codes are freely shared, which helps boost accessibility of the technology and repeatability of results. ■

Customizing environmental monitoring

The new open-source hardware environment can be used to build a range of cost-effective devices, as shown in an example of a multidisciplinary research station. A range of wirelessly connected sensors or remote data loggers can be deployed.

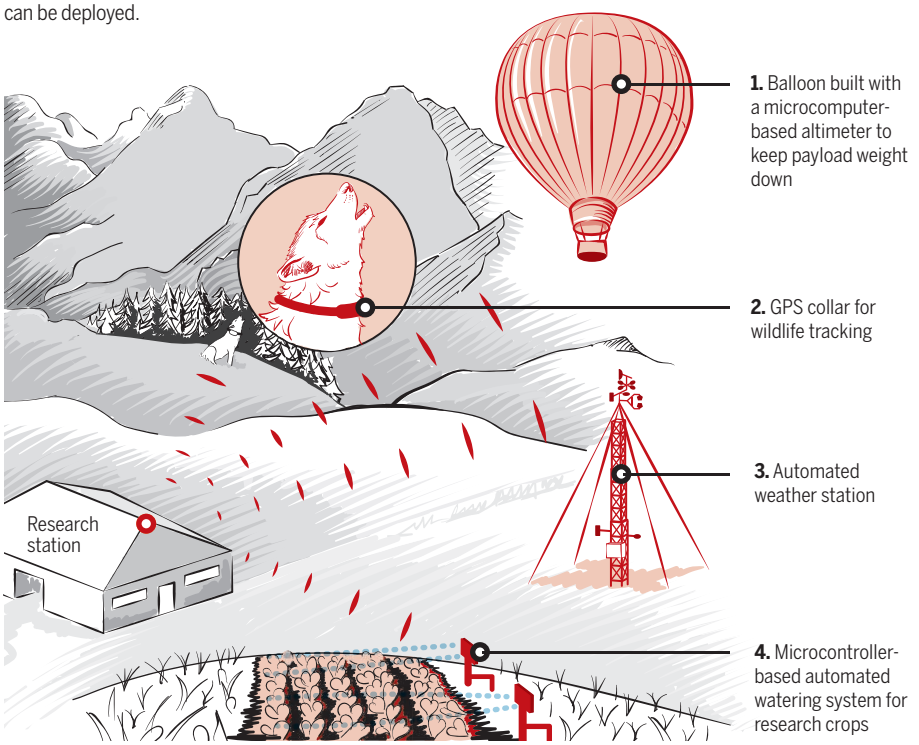

GRAPHIC: K. SUTLIFF/*SCIENCE*

[1]*Desert Ecology Research Group, School of Life and Environmental Sciences, University of Sydney, New South Wales 2006, Australia.* [2]*Long Term Ecological Research Network, Terrestrial Ecosystem Research Network, Australia.* [3]*The Australian PlantBank, Royal Botanic Gardens and Domain Trust, Australian Botanic Garden Mount Annan, New South Wales 2567, Australia. Email: aaron.greenville@sydney.edu.au*

REFERENCES AND NOTES

1. G. Senthilkumar, K. Gopalakrishnan, V. S. Kumar, *Int. J. Emerging Trends Technol. Comput. Sci.* **3**, 213 (2014).
2. M. Cagnetti, F. Leccese, D. Trinca, *J. Agric. Sci. Technol. B* **3**, 853 (2013).
3. J. M. Pearce, *Open-Source Lab: How to Build Your Own Hardware and Reduce Research Costs* (Newnes, 2013).
4. K. A. Noordin, C. C. Onn, M. F. Ismail, *CMU J.* **5**, 33 (2006).
5. W. Lyon, P. De Joux, *Marine Technol. Soc. J.* **48**, 14 (2014).
6. G. Vellidis, M. Tucker, C. Perry, C. Kvien, C. Bednarz, *Comput. Electron. Agric.* **61**, 44 (2008).
7. E. Kuusela, J. Lämsä, *Ecol. Evol.* **6**, 2594 (2016).
8. P. Teikari *et al.*, *J. Neurosci. Methods* **211**, 227 (2012).
9. F. Cazenave, C. Kecy, M. Risi, S. H. D. Haddock, in *2014 Oceans—St. John's* (IEEE, 2014), pp. 1–7.
10. D. K. Harshman, B. M. Rao, J. E. McLain, G. S. Watts, J.-Y. Yoon, *Sci. Adv.* **1**, e1400061 (2015).
11. T. Nagy, Z. Gingl, in *14th International Symposium on Computational Intelligence and Informatics (CINTI)* (IEEE, 2013), pp. 163–167.
12. R. Haight, W. Haensch, D. Friedman, *Science* **353**, 124 (2016).
13. D. K. Fisher, H. Kebede, *Comput. Electron. Agric.* **74**, 168 (2010).
14. A. G. Sreejith *et al.*, *J. Astron. Instrum.* **03**, 1440006 (2014).
15. GitHub, *Making Your Code Citable* (2014); https://guides.github.com/activities/citable-code/.

ACKNOWLEDGMENTS

We thank C. Dickman and T. Newsome for discussions on earlier drafts of this article.

10.1126/science.aag3057

Downloaded from http://science.sciencemag.org/ on September 30, 2016

Published by AAAS

Lodgepole pine (left) and interior spruce (right) occupy overlapping ranges in western Canada, where they are exposed to a range of environments.

EVOLUTION

How conifers adapt to the cold

Highly diverged conifer species share many genetic signals of adaptation to local climate conditions

By **Angela M. Hancock**

In convergent evolution, different species independently acquire similar traits. Knowing whether divergent species use the same or different genetic solutions to adapt to similar selection pressures can illuminate innate constraints on underlying molecular networks. Most cases of convergence that are understood at the genetic level are relatively simple, involving one or a few genes. On page 1431 of this issue, Yeaman *et al.* (*1*) report mapping of locally adaptive genes in lodgepole pine (*Pinus contorta*) and interior spruce (the species complex that includes *Picea engelmannii* and *Picea glauca*) (see the photo). The authors show that many genes implicated in local adaptation are shared among the two species.

Many examples of convergent evolution at the morphological level have been documented, and in some cases the genetic basis for convergence is known. Examples include loss of pigmentation in mice, lizards, and humans via mutations in *melanocortin-1 receptor* (*MC1R*) (*2*), adjustment of reproductive timing in plants via *flowering locus C* (*FLC*) and its homologs (*3, 4*), loss of trichomes in *Drosophila* via *shavenbaby* (*5*), and resistance to toxic cardenalides in insects (*6, 7*).

However, these well-studied cases tend to involve genetically simple traits, in which one or two genes are credited with the repeated phenotypic changes (*8*). In these cases, pathway constraints have been invoked to explain cases where different species have adapted via changes in the same genes (*9*). The idea is that a pathway can only be perturbed in a limited number of ways; thus, the possible genetic modifications that can occur to enable adaptation are also limited. However, many adaptive traits are likely to be genetically complex, involving many small-effect variants (*10*). In these cases, adaptation could act in more varied ways, making extensive overlap in the genes underlying adaptive responses across diverged species improbable.

Plant species are particularly powerful models for examining local adaptation, because they cannot hide from environmental insults and must face them head-on. Yeaman *et al.* sequenced the protein-coding genome regions of more than 250 populations from two diverged conifer species, lodgepole pine and interior spruce. For each individual, they collected climatic data from the site of origin as well as phenotypic data, which were measured under simulated natural conditions. They then identified regions of the genome that were correlated with variation in phenotypes or climate to pinpoint loci implicated in local adaptation. In both species, the majority of traits and climatic factors with the strongest signals underlie the ability to deal with cold stress.

Given the observed convergence in cold tolerance adaptation, the authors next explored whether the associated loci were shared or different between the two conifer species. They expected the traits and the adaptive signals examined to involve many genes and overlap of the loci identified in the two species to be limited.

Yet they found extensive overlap, with 47 genes showing signals in both species (see the figure). Moreover, many shared signals were in genes that were duplicated in one or both species. This is consistent with the proposition that duplicated genes may be more likely than nonduplicated genes to be used in adaptive bouts because of reduced constraint on function. The reasoning is

Department of Plant Developmental Biology, Max Planck Institute of Plant Breeding Research, Cologne, Germany. Email: hancock@mpipz.mpg.de

Local adaptation

Although lodgepole pine and interior spruce diverged about 140 million years ago, they share genetic signals of adaptations to environmental conditions, particularly cold tolerance.

250
Number of pine and spruce populations studied

1 million
Number of SNPs in 23,000 genes identified in these populations

47
Number of genes that are locally adapted in both pine and spruce

65%
Enrichment of duplicated genes among those locally adapted in both species

PHOTO: YEAMAN *ET AL.*

Downloaded from http://science.sciencemag.org/ on September 30, 2016

Published by AAAS

that when a gene is duplicated, one copy can take responsibility for some or all core functions, leaving the other copy free to evolve new or modified functions (*11, 12*).

The study by Yeaman *et al.* provides solid evidence that independent and parallel changes at the molecular level can underlie phenotypic convergence even for traits with complex genetic architectures. But many open questions remain. The genomes interrogated here are large (around 20 billion base pairs) and derived from non–model organisms; the genome assemblies are therefore incomplete, and functional annotation is not available for many loci. Given the interesting finding that duplicated genes show an enrichment of signals of convergent evolution, more complete assemblies will be useful. Improved genome assemblies will allow for finer-scale resolution of the relative adaptive importance of orthologs (genes derived directly from the same ancestral loci) and paralogs (genes derived from ancestral duplications within the genome).

In addition, knowing more about the functional consequences of the signals detected will provide a deeper understanding of the types of changes responsible for the observed adaptive evolution in conifers. For example, it will be interesting to know whether the observed convergent patterns are due to repeated losses of gene function across lineages, or to more subtle changes. Losses of function, which are common in single-gene convergences (*2, 8*), may occur readily when selection is strong because they have large effects and can be achieved in a variety of ways.

Yeaman *et al.*'s study is likely to become an important model for future research that examines convergence in local adaptation among species with overlapping ranges. Extending the approach to more diverse species will be important for determining whether the observed patterns are widespread in nature. ■

REFERENCES

1. S. Yeaman *et al.*, *Science* **353**, 1431 (2016).
2. M. Manceau, V. S. Domingues, C. R. Linnen, E. B. Rosenblum, H. E. Hoekstra, *Philos. Trans. R. Soc. London B Biol. Sci.* **365**, 2439 (2010).
3. M. J. Kobayashi *et al.*, *Mol. Ecol.* **22**, 4767 (2013).
4. R. Wang *et al.*, *Nature* **459**, 423 (2009).
5. N. Frankel, S. Wang, D. L. Stern, *Proc. Natl. Acad. Sci. U.S.A.* **109**, 20975 (2012).
6. S. Dobler, S. Dalla, V. Wagschal, A. A. Agrawal, *Proc. Natl. Acad. Sci. U.S.A.* **109**, 13040 (2012).
7. Y. Zhen, M. L. Aardema, E. M. Medina, M. Schumer, P. Andolfatto, *Science* **337**, 1634 (2012).
8. A. Martin, V. Orgogozo, *Evolution* **67**, 1235 (2013).
9. D. L. Stern, *Nat. Rev. Genet.* **14**, 751 (2013).
10. R. A. Fisher, *The Genetical Theory of Natural Selection* (Clarendon, UK, 1930).
11. A. L. Hughes, *Proc. Biol. Sci.* **256**, 119 (1994).
12. S. Ohno, *Evolution by Gene Duplication* (Springer, Berlin, 1970).

10.1126/science.aai8284

NEUROSCIENCE

Cool by neuronal decision

An ion channel expressed in specific brain neurons is required for regulating core body temperature

By **Tamas Bartfai**

Inside the well-protected and well-ventilated human skull, the temperature of a few hundred thousand neurons can deviate by several degrees centigrade from that of the surrounding 100 billion or so cells. These cells constitute around 15% of the neurons in the brain's preoptic area (POA) and can change their firing rate dramatically upon a 1° to 3°C change in local temperature (*1*). Astoundingly, this change in activity can alter the body's core temperature. Cellular and molecular details of the warm and cold sensitivity of these neurons are not well understood. Although the induction of fever has been well studied, the mechanisms that terminate fever are not yet clear. On page 1393 of this issue, Song *et al.* (*2*) report that a transient receptor potential (TRP) cation channel (*3*, *4*) is key to the function of these neurons in thermoregulation, particularly in response to fever.

"...TRPM2 presents a potential drug target for inducing therapeutic hypothermia..."

Human core body temperature is kept within the most narrow range of all the human physiological parameters (compared with blood pressure and blood glucose concentration). Measuring body temperature remains the most widely used, noninvasive method of monitoring the presence of infection or inflammation. The state of having a fever—a coordinated stress response that, through increased thermogenesis and reduced heat loss, is achieved by vasoconstriction—was shown to be regulated by the POA (*5*, *6*). But how does change in the firing rate of temperature-sensitive POA neurons bring about a change in body temperature? A proposed signaling pathway involves the relay of information from POA neurons to brown adipose tissue, via the dorsomedial hypothalamic nucleus, the nucleus raphe pallidus in the brain stem, and postganglionic fibers (see the figure) (*7*). In this scheme, a fever-inducing substance (pyrogen), such as the hormone prostaglandin E_2 (PGE_2) or the cytokine interleukin-1 (IL-1), can inhibit the activity of warm-sensitive POA neurons and ultimately change the uncoupling mechanism in the mitochondria of brown adipose tissue, causing heat production (instead of generating energy in the form of adenosine triphosphate).

When transcripts from single, warm-sensitive neurons were eventually characterized, it was clear that the majority release the neurotransmitter γ-aminobutyric acid (GABA), with a smaller population releasing the neurotransmitter glutamate (*8*). Moreover, it was also established that receptors for various pyrogens—including PGE_2, IL-1, and metabolic hormones such as insulin and adiponectin—are present in some warm-sensitive neurons (*8*). Thus, heat production and concomitant vasoconstriction, which jointly increase core body temperature during fever, could be explained (*5*–*7*), but the mechanism(s) responsible for terminating the fever response remained an enigma.

TRP channels expressed in the peripheral nervous system and the skin (TRPV1–8) have been well studied (*3*, *4*). Those expressed in skin keratinocytes are thought to play an important role in nociception, including sensing heat. Although transcripts encoding some TRP channels had been identified in warm-sensitive neurons of the hypothalamus, their functional importance was not understood because the temperature range in which peripheral TRP channels are activated is outside the range that activates POA neurons.

Song *et al.* show, with in situ hybridization and immunohistochemistry, that many mouse POA neurons express TRPM2, which is a thermosensitive and redox-sensitive channel. The authors observed that the sensitivity of these neurons to warm temperature is affected by TRPM2 sensitizers, including the reactive oxygen species H_2O_2. They also noted the sensitivity of warm-sensitive POA neurons expressing TRPM2 in vitro to either an intracellular agonist of the adenosine diphosphate receptor or an exogenous inhibitor of TRP channels called 2-aminoethoxydiphenyl borate (2-APB). Moreover, Song *et al.* show that these TRPM2-expressing neurons

Department of Neurochemistry, Stockholm University, 106 91 Stockholm, Sweden. Email: tamas.bartfai@neurochem.su.se

Downloaded from http://science.sciencemag.org/ on September 30, 2016

Published by AAAS

Controlling body temperature

Proposed signaling pathways from the brain's preoptic area to brown adipose tissue promote an increase in core body temperature (fever) (*7*) and limit the fever response (*2*). Glu, glutamate; Ach, acetylcholine; NE, norepinephrine; CRH, corticotropin-releasing hormone; ACTH, adrenocorticotropic hormone.

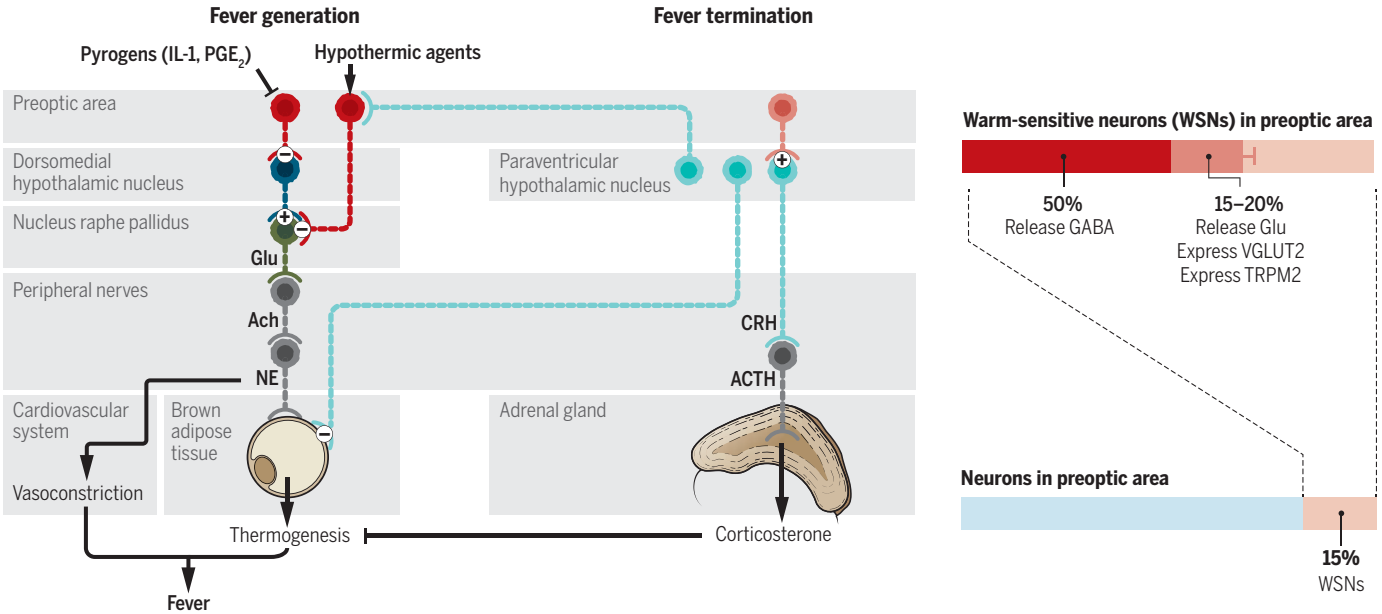

increase their intracellular Ca^{2+} concentration in response to heat. TRPM2 of warm-sensitive POA neurons became activated above 38°C, and thus within the higher fever temperature range. Notably, H_2O_2, which sensitizes TRPM2-expressing POA neurons to warmth, actually reduces the temperature at which TRPM2 is activated and brings it into a range that corresponds to reversible high fever (and not irreversible brain damage). Furthermore, when TRPM2 was inhibited with 2-APB, or when the POA neuronal cell cultures were prepared from TRPM2-null mice, the intracellular Ca^{2+} response to increased temperature was abolished.

Song *et al.* further examined the in vivo fever response of POA neurons in TRPM2-null mice. In the absence of TRPM2, neither injection of the pyrogen PGE_2 nor the TRP inhibitor 2-APB affected the inability of the mice to terminate the fever response (or to bring about hypothermia when starting from normal temperature). Because no selective agonist of TRPM2 is currently known, Song *et al.* used transgenic mice that express a form of TRPM2 that is sensitive to clozapine-*N*-oxide (*9*). The authors demonstrated that selective activation of TRPM2 in the POA with this chemical agent induces hypothermia, even in nonfeverish animals. Thus, Song *et al.* have defined a key role for TRPM2 in fever response and in generating hypothermia. They also have created a useful paradigm for developing selective TRPM2 agonists for use as hypothermic agents to treat trauma.

Surprisingly, Song *et al.* noted that although 57% of TRPM2 in the mouse POA are expressed in GABAergic neurons, those channels that function in thermoregulation are localized to glutamatergic neurons of the POA that express vesicular glutamate transporter 2 (VGLUT2). The authors propose that these excitatory glutamatergic neurons activate downstream neurons in the paraventricular hypothalamic nucleus—and thus the hypothalamic-pituitary-adrenal axis—and therefore assume that the hypothermic effect arises from the glandular release of corticosterone. This steroid hormone functions in energy regulation. The role of POA glutamatergic neurons that express VGLUT2 in energy homeostasis has been recently described (*10*), and it is likely that they also express TRPM2.

The molecular events that lead from an increase in circulating corticosterone to mitochondrial uncoupling in brown fat and, ultimately, the termination of thermogenesis need further investigation. As well, the association of thermogenesis with the duration and amplitude of hypothalamic-pituitary-adrenal axis activation is unclear. Activation of this axis has more often been correlated to stress and hyperthermia; corticotropin-releasing factor, a hormone released by the hypothalamus in response to stress and hyperthermia, acts as a pyrogen when injected into the POA (*8*, *11*). That hypothermia is an instantaneous effect of TRPM2 activation suggests that it does not arise through the control of transcription of pyrogenic cytokines (IL-1 and IL-6 expression are suppressed by corticosterone). It is more likely that paraventricular neurons in the hypothalamus act on GABAergic neurons in the POA to reduce sympathetic activation of thermogenesis in brown fat. Thus, additional studies into the mechanisms activated by TRPM2 in POA neurons are also needed. Identity of the natural agonist of TRPM2 in the POA is also of great interest.

A recent study identified TRPM2 expression in peripheral autonomic neurons (in the mouse spinal cord), which function in sensing warm temperature and promoting cool-seeking behavior (*12*). This finding dovetails with that of Song *et al.*, that POA neurons expressing TRPM2 limit fever and induce hypothermia. Thus, TRPM2 presents a potential drug target for inducing therapeutic hypothermia for conditions such as stroke. Details of the regulatory mechanisms in the TRPM2-expressing neurons will be of great interdisciplinary interest. ■

REFERENCES

1. J. A. Boulant, *Yale J. Biol. Med.* **59**, 179 (1986).
2. K. Song *et al.*, *Science* **353**, 1393 (2016).
3. R. Latorre *et al.*, *Cell Calcium* **42**, 427 (2007).
4. D. E. Clapham *et al.*, *Pharmacol. Rev.* **55**, 591 (2003).
5. H. T. Hammel *et al.*, *Am. J. Physiol.* **198**, 481 (1960).
6. T. Bartfai, B. Conti, *Sci. World J.* **10**, 490 (2010).
7. S. F. Morrison, *Auton. Neurosci.* **196**, 14 (2016).
8. J. Eberwine, T. Bartfai, *Pharmacol. Ther.* **129**, 241 (2011).
9. W. D. Dietrich, H. M. Bramlett, *Brain Res.* **1640**, 94 (2016).
10. S. Yu *et al.*, *J. Neurosci.* **36**, 5034 (2016).
11. C. J. Madden, S. F. Morrison, *Am. J. Physiol. Regul. Integr. Comp. Physiol.* **296**, R831 (2009).
12. C-H. Tan, P. A. McNaughton, *Nature* **536**, 460 (2016).

10.1126/science.aai8465

GRAPHIC: V. ALTOUNIAN/*SCIENCE*

Downloaded from http://science.sciencemag.org/ on September 30, 2016

Published by AAAS

How hybrid perovskites get their groove

Rotational motions of organic cations may screen charge carriers from defects

By **Mark E. Ziffer** *and* **David S. Ginger**

Polycrystalline thin films of hybrid organic-inorganic lead halide perovskites (HOIPs) show remarkable performance in semiconductor devices from light-emitting diodes to solar cells (*1*, *2*). Despite modest charge carrier mobilities (*3*) and a known presence of defect sites (*4*), polycrystalline HOIP films prepared under comparatively crude conditions exhibit minority carrier lifetimes and diffusion lengths comparable with those of high-purity single-crystal GaAs (*3*). What makes HOIPs so special? On page 1409 of this issue, Zhu *et al.* (*5*) argue that the answer may lie in the rotational motion of the dipolar organic cations in the perovskite lattice. These motions seem to screen charge carriers from defects and other scattering potentials, much like ions screen electric fields in solution.

Lead halide HOIPs are polar semiconductors with the perovskite crystal structure ABX_3, where B is Pb^{2+}; X is I^-, B^-, Cl^-, or a combination thereof; and A is an organic cation, typically methylammonium (MA) or formamidinium (FA) in photovoltaics. Single-crystal HOIPs behave like a textbook semiconductor suited for solar cells (*1*), but it remains unclear how HOIPs can maintain exceptional optoelectronic performance even in defective polycrystalline thin films.

Proposals for explaining this unusual behavior include the effects of the lattice's ionicity on the energetics of defect sites (*6*); peculiarities of the band structure that may enhance charge carrier lifetimes (*7*); and the effects of lattice polarization on charge carrier dynamics (*3*, *5*). Zhu *et al.* now make a strong case that dynamic polarization of the organic cations in HOIPs screens charge carriers from interactions that would otherwise sap their performance (see the figure).

The authors studied how long it takes photoexcited hot carriers to relax to the semiconductor band edge in single crystals of two HOIPs ($MAPbBr_3$ and $FAPbBr_3$) and one all-inorganic lead halide perovskite, $CsPbBr_3$, with cesium in the A site. Using time-resolved photoluminescence spectroscopy, they found that hot carrier cooling is much slower in $MAPbBr_3$ and $FAPbBr_3$ than in the all-inorganic $CsPbBr_3$. Thus, the lattice vibrations responsible for cooling the hot carriers via scattering appear to be less effective in HOIPs with A-site polar organic cations that can rotate freely at room temperature (*8*). In $MAPbBr_3$, the carrier cooling rate increases at low temperatures, when changes in its crystal structure restrict the rotational motions of the organic cations, suggesting that rotation of the polar cations plays a key role.

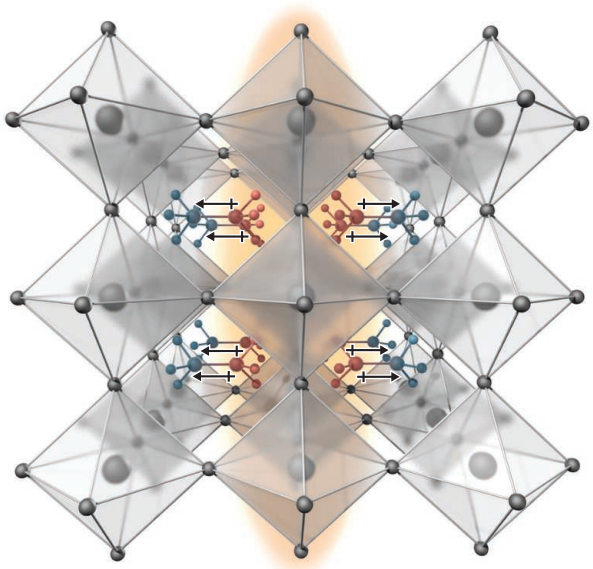

In the ground-state $APbBr_3$ lattice, dipolar organic cations occupying the A site are randomly oriented. Zhu *et al.* propose that in the excited state of the same lattice, a free electron cloud (shown as an orange haze) induces reorientation of the dipolar organic cations, thereby screening the charge carrier from scattering by defects or LO phonons.

Zhu *et al.* also performed time-resolved optical Kerr effect measurements, which reveal signatures of liquid-like molecular reorientations in $MAPbBr_3$ and $FAPbBr_3$. These signatures are absent in the all-inorganic $CsPbBr_3$. The authors maintain that the liquid-like signatures are also consistent with carrier-induced polarization of the organic cations, which show orientational disorder on ultrafast time scales (*8*). The interaction between a charge carrier and the polarization that it induces in the crystal lattice forms a quasi-particle known as a polaron (*9*). Zhu *et al.* argue that a polaron made possible by the rotation of the organic cations creates a "cloaking field" that screens the carriers from scattering events by defects and optically active vibrational lattice modes (LO phonons).

In the classic case of a large polaron formed in polar inorganic semiconductors such as AgCl and AgBr, charge screening by the polar lattice modes does not necessarily protect polarons from scattering by LO phonons, especially at elevated temperatures (*9*–*11*). In contrast, the polarons in HOIPs are formed by interactions between electrons and lattice vibrational modes that are associated with orientationally disordered organic cations (*12*). These polarons may be more effective for screening charge carriers from scattering by LO-phonon modes—possibly those of the PbX_3^- sublattice (*13*). These observations will likely spark a search to gain a clearer picture of the electronic structure and transport dynamics of these unusual polarons.

It remains unclear whether other theories proposed to explain the performance of HOIPs are mutually exclusive with that of Zhu *et al.* or act in concert. Regardless, if charge carrier dynamics in semiconductors can indeed benefit from crystal structures with freely rotating polar cations, this materials design motif could be used to design low-cost, high-performance semiconductors for optoelectronics and energy conversion. ■

Department of Chemistry, University of Washington, Seattle, WA 98195, USA. Email: ginger@chem.washington.edu

ILLUSTRATION: C. BICKEL/*SCIENCE*

REFERENCES

1. W. Zhang *et al.*, *Nat. Energy* **1**, 16048 (2016).
2. NREL Best Research-Cell Efficiencies; www.nrel.gov/ncpv/images/efficiency_chart.jpg.
3. Y. Chen *et al.*, *Nat. Commun.* **7**, 12253 (2016).
4. D. W. de Quilettes *et al.*, *Science* **348**, 683 (2015).
5. H. Zhu *et al.*, *Science* **353**, 1409 (2016).
6. E. Yablonovitch, *Science* **351**, 1401 (2016).
7. P. Azarhoosh *et al.*, *APL Mater.* **4**, 091501 (2016).
8. J. M. Frost, A. Walsh, *Acc. Chem. Res.* **49**, 528 (2016).
9. J. Appel, in *Solid State Physics*, F. Seiz *et al.*, Eds. (Academic Press, 1968), vol. 21, pp. 193–391.
10. R. Van Heyningen, *Phys. Rev.* **128**, 2112 (1962).
11. D. C. Burnham *et al.*, *Phys. Rev.* **119**, 1560 (1960).
12. J. Even *et al.*, *Nanoscale* **8**, 6222 (2016).
13. M. Sendner *et al.*, *arXiv:1607.08541* (July 2016).

10.1126/science.aai7682

Downloaded from http://science.sciencemag.org/ on September 30, 2016

Published by AAAS

CLIMATE CHANGE

From science to service

Climate services are crucial for successful adaptation to current and future climate conditions

By **Lisa Goddard**

People rely on daily weather services to decide what to wear, make transport choices, prepare for rain, and more. Many societal decisions, however, need information not on time scales of days, but on climate time scales of months, years, or decades. New initiatives such as that of Copernicus in Europe provide a wealth of climate data, which are integral to climate services. However, data are only one aspect of climate services, which also involve translation and use of relevant information with the aim to help society manage the risks and opportunities of climate variability and change (*1*–*5*). To be successful, any climate service must have a clear problem focus, build on good-quality observations, and consider climate across different time scales.

WHAT'S YOUR PROBLEM?

Climate is rarely the only factor guiding decisions and actions. Even for sectors where climate is clearly a factor, such as in agriculture, climate considerations on their own may not be important enough to shape a particular decision. For example, in southeastern South America, rainfed soybean farming has expanded into less climatically suitable areas. This decision may be justified by rising global prices for soybeans in recent decades that make the industry less susceptible to drought occurrence. In other situations, climate information may not be certain enough to motivate its use. For example, the risk of extreme events is inherently uncertain even if the predicted odds of their occurrence may have doubled or tripled in next season's forecast. Projections for rainfall under climate change are also highly uncertain in regions where observed trends have been relatively weak and climate models disagree or have little skill.

Mounting evidence shows, however, that climate information can improve behaviors and outcomes when appropriately incorporated within the decision context. Rahman *et al*. recently conducted an independent evaluation of a newly developed seasonal drought information service in Jamaica. The service included drought monitoring, forecasting, agricultural extension, farmer forums, and regular SMS messaging and was developed cooperatively across several disciplines, ministries, international donors, and nongovernmental organizations. On average, those farmers who recognized climate as an important factor in their yields (and were thus more likely to use the drought outlooks in planning and practice) experienced 50% lower losses in the recent 2014 drought than did other farmers (*6*).

In another application of climate services, this time to the health sector, a comprehensive surveillance and early warning system for dengue was set up in Ecuador over several years. Climate scientists working with health experts, including the Ministry of Health, found that periods of high rainfall and high temperatures were associated with dengue outbreaks in many parts of the tropics, in addition to nonclimate triggers. As Borbor-Cordova *et al*. describe, the early warning system in Ecuador led to more targeted seasonal vector control interventions, risk maps, knowledge-translation through climate-health forums, as well as social media and bulletins for the health sector (*7*).

> ***"...any climate service must have a clear problem focus, build on good-quality observations, and consider climate across different time scales."***

Thus, to develop effective climate services, it is important to clearly define the role of climate within the broader decision-making context.

KNOW YOUR DATA

Good observational data are critical to climate services. Climate observations allow us to understand the past, monitor the present, and judge how well climate models perform for a particular region or application. Observations are thus necessary to help predict the future through model validation and calibration. However, not all observational data sets are created equal.

Many global data sets appear to provide amazingly high-resolution observations over a country or region. But peek under the hood and you start to see potential problems or limitations. For example, compared to Germany, the entire continent of Africa has less than 10% the number of rain gauges reporting to global data centers. And the number of these gauges worldwide is decreasing, especially in African countries. Such gaps in observational records severely limit their value.

Observational data sets with greater integrity are being created, however. For example, historical data may be available from written logs of temperature, rainfall, humidity, and other observations. Data rescue projects, such as the International Environmental Data Rescue Organization, rely on volunteers to recover and digitize these data and bring it online. These efforts contribute directly to a country's data wealth and facilitate a more informed use of models and forecasts. Other efforts merge station data with satellite data to increase the coverage of in situ observations (*8*) worldwide while helping to validate satellite-derived products. Even higher resolution and improved data quality can be achieved by working at the national level, because many countries hold more data than they make available to the global data community (*9*).

TIME SCALES MATTER

The climate varies continuously on time scales from months to centuries, with and without humanity's influence. Rarely is a region, sector, or company impacted by only a single time scale. For example, managers of municipal water systems consider a time horizon of 5 to 30 years when deciding on how much to expand. However, they must also address weekly, seasonal, and annual targets for water supply, hydropower production, and flood control. Dynamic risk assessment requires climate information that addresses time scales from weeks to decades (*10*).

The relative importance of the climate on different time scales varies with variable, location, and even time of year (see the figure). Understanding the magnitudes of climate variations and trends can help guide what information is most needed for planning and resilience. Such analyses also provide a focus to the study of historical social and economic impacts from past climate variations, which may guide future adaptation efforts.

Warming trends have dominated the annual mean temperatures records for some parts of the world over the past 100 years; in other areas, the long-term trends are

International Research Institute for Climate and Society, Columbia University, Monell Building, 61 Route 9W, Palisades, NY 10964-8000, USA. Email: goddard@iri.columbia.edu

Downloaded from http://science.sciencemag.org/ on September 30, 2016

Published by AAAS

Two regions, two climate stories

In the outlined area of the U.S., year-to-year variability has been the primary driver of rainfall, accounting for 75% of the variance we see in the historical record. The long-term climate trend accounts for only 1% of the variance. The story is different in the Sahel, where fluctuations on a decadal scale were more dominant, accounting for about 40% of the variance (*11*).

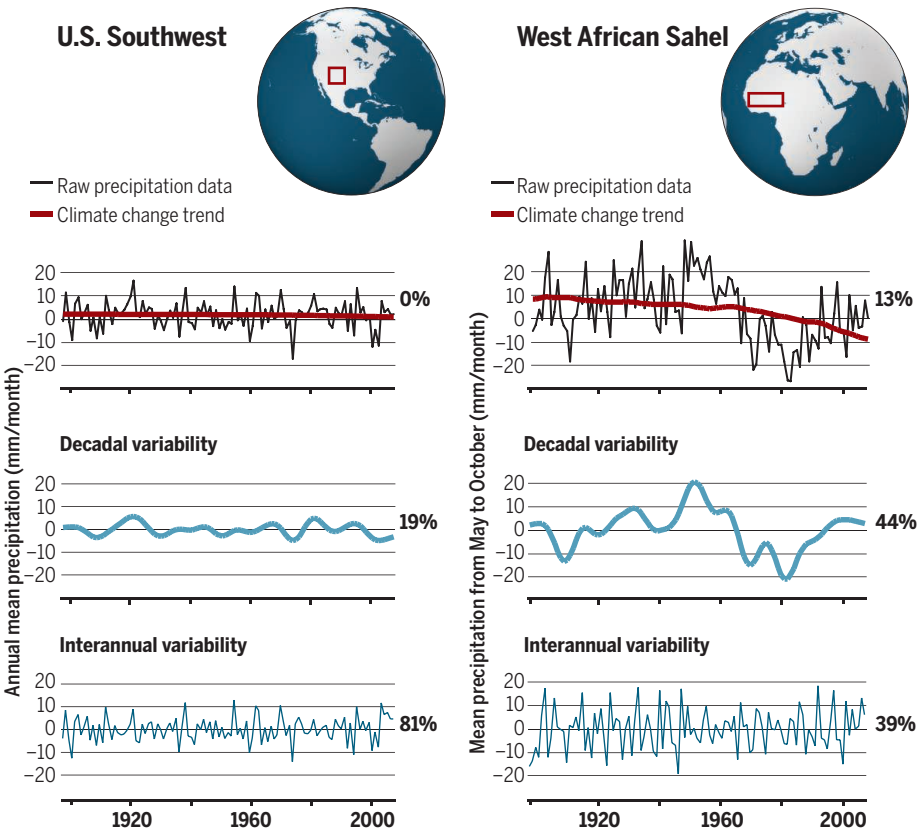

GRAPHIC: N. CARY/*SCIENCE*

secondary to interannual or decadal variability. For precipitation, the story is totally different. Most observations indicate that long-term trends accounted for only a few percent of the variance over the 20th century. The relative importance of decadal-scale variability on precipitation is typically 20 to 30%. Year-to-year variations account for most of the rainfall variations that communities experience locally.

For example, over much of the western United States, decadal rainfall variability accounts for only about 20% of what people living there experienced (see the figure). Yet such variability can have significant social impacts, such as the Dust Bowl of the 1930s, the Great Basin Drought of the 1950s, and recent dry conditions. Most of the variability by far is at the interannual time scale, causing either severe drought years or years of extreme flooding. Much of the interannual-to-decadal variability derives from slow changes in ocean temperatures and may be potentially predicted for preparedness measures, or at least characterized to help build resilience. Any predictive capacity adds to the value of climate services beyond the mere characterization for resilience.

Contrast the western U.S. with the western Sahel (see the figure). Here, decadal variability, tied to both natural and aerosol-forced changes in Atlantic Ocean temperatures, has a relatively much larger influence on the historical climate record. Additionally, climate-change scale trends have been large compared to other parts of the world. The compounding effect of year-to-year variability is to worsen or ameliorate the dry and wet periods. This can result in shifts that are as large as the decadal ones, and larger than the century-long trend. The confluence of factors here points to the need for climate information across scales for national adaptation and resilience planning, and that decisions across time scales would benefit from information focused at that time scale, from monitoring to seasonal forecasts to climate change projections.

OUTLOOK

The field of climate services is relatively new. Despite the WMO's Global Framework for Climate Services (*1*) and the growing body of literature, considerable confusion remains about what climate services are or what they should provide. What is clear is that climate services require more than just climate science. To work, they depend on a solid understanding of how climate fits into the broader decision context, as well as the political will to foster multidisciplinary research and practice.

The humanitarian community—including the International Federation of Red Cross/Red Crescent and the World Food Programme—has recently embraced preparedness and resilience more actively. Climate information was used much more effectively to guide the response to the large El Niño event of 2015–2016 than to the comparable sized El Niño event in 1997–1998. Such applications of climate services are important steps toward helping vulnerable populations and sectors to adapt to the climate of today and of the future. The success of climate services will depend on their ability to address risks and opportunities at relevant time scales with appropriate solutions informed by high-quality data. ■

REFERENCES AND NOTES

1. C. Hewitt, S. Mason, D. Walland, *Nat. Clim. Change* **2**, 831 (2012).
2. P. Adams *et al.*, *WMO Bull.* **64**, 51 (2015).
3. J. Brugger, A. Meadow, A. Horangic, *Bull. Am. Meteorol. Soc.* **97**, 355 (2016).
4. C. Vaughan, S. Dessai, *Wiley Interdiscip. Rev.: Clim. Change* **5**, 587 (2014).
5. R. Moss, *Clim. Change* **135**, 143 (2015).
6. T. Rahman, J. Buizer, Z. Guido, *The Economic Impact of Seasonal Drought Forecast Information Service in Jamaica, 2014-2015.* Paper prepared for USAID (2016); see www.climatelinks.org/sites/default/files/asset/document/Economic-Impact-of-Drought_Information_Service_FINAL.pdf.
7. M. Borbor-Cordova *et al.*, in *WHO/WMO, Climate Services for Health: Improving Public Health Decision-Making in a New Climate*, J. Shumake-Guillemot, L. Fernandez-Montoya, Eds. (WHO/WMO, Geneva, 2016), pp. 108–109.
8. C. Funk *et al.*, *U. S. Geological Survey Data Series 832* (USGS, Washington, DC, 2014).
9. T. Dinku *et al.*, *The ENACTS Approach: Transforming Climate Services in Africa One Country at a Time*, New York: World Policy Institute, New York, 2016); www.worldpolicy.org/policy-paper/2016/03/16/enacts-approach.
10. G. Pizarro, U. Lall, M. Atallah, *Environ. Fin.* **10**, 26 (2009).
11. The figure shows a time series decomposition of annual rainfall (mm/month) from CRU-TS3.1 (*12*) over the 20th century for the demarked regions of the western United States (37°N to 42°N; 110°W to 102°W) and of the African Sahel (12.5°N to 17°N; 17.5°W to 10°E) [see (*13*) for details of the methodology]. The top graphs show the full time series with the time mean average removed. The red lines are an estimate of the climate change trend in the data. Once this trend signal is removed, the data are low-pass filtered at decadal and longer time scales (center graphs). The remaining variabilities represent the year-to-year variabilities (bottom graphs). The percentages to the right represent the total variance contained in each time scale. Covariance between decadal and interannual variability may reduce the total.
12. I. Harris, P. Jones, T. Osborn, D. Lister, *Int. J. Climatol.* **34**, 623 (2014).
13. A. Greene, L. Goddard, R. Cousin, *Eos Trans.* **92**, 397 (2011).

10.1126/science.aag3087

Downloaded from http://science.sciencemag.org/ on September 30, 2016

Published by AAAS

PHOTO: PAUL NICKLEN/NATIONAL GEOGRAPHIC CREATIVE

Downloaded from http://science.sciencemag.org/ on September 30, 2016

ARCTIC SCIENCE POLICY

Toward strategic, coherent, policy-relevant arctic science

A modified Arctic Council could play an expanded role

By **Clive Tesar, Marc-Andre Dubois, Alexander Shestakov**

Later this month, government science officials from the Arctic and other nations will be in Washington, D.C., invited by the White House to the first ever Arctic Science Ministerial meeting (*1*). The event is framed as a response to rapid climate-driven change in the Arctic and impacts of that change on the rest of the world. Although the White House has grasped the urgency of scientific responses to the unprecedented change gripping the Arctic, we think the ministerial delegates could aspire to address "What science needs to be done?" and "How is it done?" There are opportunities to better shape aspects of the science that should be focused on the needs of Arctic policy and management, in addition to fundamental curiosity-driven science. Also critical is the question of how decisions the ministers make should be actualized, whether through the Arctic Council (AC), the most formalized body for Arctic cooperation, or through other existing or new mechanisms.

There are many avenues where arctic science agendas are developed, coordinated and implemented, such as national science programs (both in Arctic and non-Arctic states); the AC; global conventions (e.g., Convention on Biological Diversity); the United Nations bodies (e.g., World Meteorological Organization); regional initiatives and platforms (e.g., International Polar Year); and scientific associations [e.g., International Arctic Science Committee (IASC)]. There is a need to align and further coordinate across these efforts to improve efficiency, to effectively use scarce financial resources and research capacities, and to better address urgent needs. The AC is well-positioned to provide a platform to achieve this. Although we respect and promote the role of knowledge systems of the Arctic's indigenous peoples, often called "traditional knowledge," in informing Arctic policy, we focus in this article on scientific research.

PRINCIPLES TO DRIVE ARCTIC SCIENCE

Some of the principles below are being implemented by various institutions; others require further recognition and work.

Policy and management driven. Among many urgent policy and management questions for arctic science are these: "How can conservation respond to systems in which times and places identified as important to arctic species are changing rapidly?" or "What science is necessary to implement the Arctic Marine Strategic Plan?" In response to issues discovered by fundamental research, the AC's approach is to collect and collate existing science through different Working Groups (WGs). Although some AC assessments are collaborations between WGs (e.g., report on Identification of Arctic Marine Areas of Heightened Ecological and Cultural Significance), many are the result of a specific WG (e.g., Arctic Biodiversity Assessment) operating in a silo. When approved by senior Arctic officials and ministers, these WG policy recommendations require implementation. This is when new science could be crucial. For example, implementation of the Arctic Biodiversity Assessment recommendations requires new research on ecosystem services.

The AC should commission new research, through enhanced collaboration at the national level between its members, observers, and other stakeholders, that may be necessary to answer implementation questions raised from AC assessments and reports. There are good examples when AC managed to do so (e.g., the Snow, Water, Ice, and Permafrost in the Arctic assessment), but there is a need to strengthen the process to bring together science and policy agendas. Arctic countries should establish a cooperative research program, supported by joint earmarked funding, to build knowledge and practice communities and to carry out implementation research (see the first photo).

WWF Arctic Programme, Ottawa, Ontario, K1P 5H9, Canada. Email: ctesar@WWFCanada.org

Published by AAAS

Researchers in survival suits ride to sea ice with blue pond melts in the Canada basin, Arctic Ocean.

Coherent and strategic. Arctic science (and all who require its outputs) would benefit from a coherent agenda to avoid duplication and focus attention on the most urgent management and policy challenges. At present, there are a variety of agendas, mostly nationally oriented, as in an increasing number of national Arctic strategies in both Arctic and non-Arctic states. There are efforts to design a coherent approach outside the AC. The IASC, which brings together 23 countries with arctic science programs, has coordinated a "Roadmap for the Future" (*2*) to identify science priorities and coordinate research agendas. This roadmap involved some AC WGs. IASC is an observer at AC, and there are some informal and ad hoc attempts to promote research synergies between AC WGs. But these are based on a "soft approach," with no institutionalized process to integrate and coordinate the research needs of the AC WGs in a coherent and strategic fashion with systemic engagement of non-Arctic players. AC has taken recent steps in this direction through hosting cross-WG meetings and talking more proactively with observers. A strategic approach to needed science can be achieved only when governments know their long-term vision for the Arctic with clear goals, targets, and time frame. This requires the AC to be clear about its long-term strategic objectives and targets. The first step was to agree on a high-level vision for the Arctic (*3*).

Inclusive. Arctic science should be contributed to by all with an interest, including non-Arctic states and commercial interests. For research by non-Arctic states to be coherent and strategic, interested parties would need to be invited to help shape the arctic science agenda. A draft Agreement on Enhancing International Arctic Scientific Cooperation recently negotiated under the AC takes steps in this direction. In the case of commercial interests, scientific data (e.g., project background research, environmental impact assessments, and monitoring activities) are rarely publicly shared (*4*). Such information gathered by commercial companies, for example, at a research station by Russian oil and gas giant Rosneft in the Kara Sea (*5*), should become public record as a condition of operating and license agreements.

Accessible and organized. It is important to build on existing efforts to make arctic research available widely. Open-access journals sometimes have credibility problems (*6*), so they do not hold the complete answer. The draft Agreement on Arctic Scientific Cooperation promotes access to arctic research, and there are platforms to organize and communicate scientific findings such as the Polar Data Catalogue. Agreeing to find ways to make research more accessible, e.g., in a searchable database, would be a worthy outcome of the ministerial meeting. Even better would be to make it understandable for the public and policy-makers, e.g., via plain-language summaries of important research and translating research results (e.g., making Russian science accessible).

Social science. Natural science gets the bulk of money and effort spent on science in the Arctic (*7*). It is important to understand natural systems but also to understand how they interact with human systems. Two coming AC products on resilience (*8*) and adaptation (*9*) have been designed to integrate natural science, social science, and traditional knowledge. These are expected to help policy-makers respond to climate- and development-driven change in the Arctic. The AC is compiling valuable information on economics and human development in the Arctic, often created by the AC Sustainable Development WG, but not systematically used by other WGs to enhance understanding of arctic social-ecological systems (see the second photo).

RESEARCH PRIORITIES

The process of organizing Arctic research is fragmented. A strong mechanism is needed to steer some of the science agenda toward policy and management. The AC Task Force on enhancing Scientific Cooperation in the Arctic promises to facilitate movements of scientists and access to research sites, as well as data exchange and young scientist engagement. But it does not do enough to set a coherent set of arctic science priorities overall or to overcome challenges of coordinating research activities of AC WGs. The following areas for focused research reflect primarily conservation priorities informed by urgency and lack of knowledge. We do not imply that they should be the only priorities.

Climate. Arctic change permeates almost every aspect of science in the region and beyond, including in mid-latitudes. Developing and implementing adaptation strategies appropriate to the scale and nature of anticipated changes will require reducing uncertainty in predicting change (*10*) and increasing the capacity to model and downscale climate impacts across the region. There is a need to enhance understanding of water-ice-atmosphere processes, dynamics, and interactions (*11*). Climate science must better grasp the implications of exchanges between arctic change and adjacent and distant systems (*12*), as well as more solid knowledge of ecosystem, species, and human response to environmental changes.

Baseline knowledge. Knowledge of population size, structure, status, and life history of many arctic species and the status of arctic ecosystems (including pollution levels and habitat conditions) should be a priority emerging from the science ministerial meeting. Such baseline knowledge is essential to understand the effects of climate change on species—including shifting food web structures, increased competition and predation as more temperate species, such as orcas, shift their range into arctic waters—and fragmentation and loss of sea ice habitat. Many aspects of arctic social science face the lack of even basic information; production should be a priority.

Trends and indicators. Large-scale efforts are being made to integrate arctic observation data through the Sustaining Arctic Observing Networks (SAON), a network of observation networks that range from human health to meteorology to biodiversity (*13*). For example, there are no trend data available for subpopulations of narwhal in the Arctic (*14*), making their response to climate change impossible to track and manage at a meaningful scale. More support is needed to establish and maintain collaborative monitoring and observations networks (*15*). These include new observation stations, coordination and data sharing between national and regional observation systems, expanding the set of objects and phenomena to be observed, and better access to observation data. There are multiple initiatives to develop indicators that rely on monitoring information, e.g., the AC Circumpolar Biodiversity Monitoring Program. These efforts should further focus to evaluate trends, provide early warnings, and identify tipping points.

Identifying resilience. World Wildlife Fund (WWF) believes that identifying arctic resilience should be central in the scientific agenda, providing knowledge that informs

Downloaded from http://science.sciencemag.org/ on September 30, 2016

Published by AAAS

hope, rather than despair. Recognizing that approaches to managing often vulnerable arctic habitats and species are not keeping pace with accelerating climate change, new research should instead locate sources of ecological strength and durability—ecosystem resilience—and look ahead to whether these wellsprings of resilience will persist in a climate-altered future. WWF developed a methodology—Rapid Assessment of Circum-Arctic Ecosystem Resilience (RACER)—for identifying and mapping resilient features throughout the Arctic. For instance, the Beaufort Sea ecoregion's major river, the Mackenzie River in Canada, delivers ecologically important nutrients, sediments, and freshwater to the shelf and, thus, is a source of ecoregion-wide strength. Whether through RACER or a similar tool, identification of resilient features across the Arctic is a key for policy and management.

Hydrocarbons and the environment. Long-term oil and gas development plans, on and offshore, are under way in the Arctic. Oil spills from shipping and oil and gas activities represent a threat to ecosystem health. The Arctic scientific community and key stakeholders should direct research toward understanding the effects of development and use of hydrocarbons in the Arctic. Unknown effectiveness and impacts of oil spill–response tactics, such as in situ burning or use of dispersants are major barriers to sound response decisions and regulatory developments in cold waters. Science that will help develop arctic-specific prevention measures should be prioritized.

Food security. Inuit Circumpolar Council—Alaska lays out a process to assess food security (*16*), an important area of impact of change on arctic peoples. Priority should be given to the study of ecosystems and biodiversity provisioning services, as well as resultant health, social, cultural, and economic impacts of dietary change on arctic indigenous peoples.

Natural capital and ecosystem services. Understanding ecosystem services and valuing them to inform decision-making in the Arctic requires a global and coordinated scientific agenda. The Economics of Ecosystems and Biodiversity (TEEB) scoping study for the Arctic (*17*) provides a foundation for work on delineating ecosystem services as a resource for policy-making at a range of jurisdictional and spatial scales.

Arctic conservation measures. New management tools that can respond to foreseen and unforeseen regime shifts in ecosystems will be essential. Some such tools have been proposed, for example, seasonal spatial regulation of areas used by caribou during different life stages (*18*). These tools would vary according to species, downscaled climate projections, and other pressures on populations. As the patterns of sea ice formation and break up and related pulses of life are changing in both time and space, a research agenda for conservation science is needed to inform adaptive management.

Sergue Chorolya, a Nenet herder, selecting draft reindeer (*Rangifer tarandus*) to pull sleds during spring migration in Yamal, northwest Siberia, Russia, April 2016.

PHOTO: ERIC BACCEGA/MINDEN PICTURES

ORGANIZING TO DELIVER

This coming ministerial meeting is different from others, as it is focused only on the science. The ministers, their advisers, and the indigenous peoples' representatives will face questions of science principles and priorities but also must consider how best to organize to deliver on what is decided. It seems unlikely that the ministers will decide to make new treaties or memoranda governing all of these things and then arrange to meet every year and set up a structure to monitor their progress. Instead, key existing institutions should strive to align their arctic research agendas. The AC, as a body that brings together most of the players among the ministers, and that already has regular meetings and a capable secretariat, may lead such an integrative initiative.

We believe this science-focused ministerial group can appreciate the need to fuse new scientific research in the Arctic with a strategic approach that will support immediate and long-term policy and management needs. WWF's preferred solution for achieving this is to strengthen the AC, so that it becomes more capable of setting a policy-relevant science agenda and bridging it with implementation at national and international levels. This would be achieved by cutting through existing sectoral divisions within the AC, and creating instead three cross-cutting bodies, one responsible for science, one for policy formulation, and another for implementation (*19*). The scientific body should incorporate current WGs and allow for cross-WG dialogue for setting research priorities focused on supporting AC recommendations and decisions. This committee should engage observers and others to discuss and coordinate research agendas. Results will be brought to the policy committee for deciding on policy recommendations, and the implementation committee will be responsible for translating them into actions.

Whatever the ministers decide, they should respond collectively in a coordinated manner to the urgent need for informing policy and management in a changing arctic, mapping out a sustainable future that rests on a solid foundation of knowledge. ■

REFERENCES AND NOTES

1. J. P. Holdren, White House Arctic Science Ministerial: September 28, 2016 [blog]; http://bit.ly/2cjcEI5.
2. IASC, Integrating Arctic Research—A Roadmap for the Future, Third International Conference on Arctic Research Planning (ICARP III), Toyama, Japan, 23 to 30 April 2015 (IASC, Geneva, 2015); http://bit.ly/2bXtY6H.
3. Arctic Council, *Kiruna Vision for the Arctic 2015* (Arctic Council, Kiruna, Sweden, 2013).
4. P. M. Pedroni *et al.*, *J. Appl. Ecol.* **50**, 539 (2013).
5. Arctic, Natural Resources or Rosneft to establish first Arctic scientific outpost (Arctic, 2016); http://bit.ly/2cG6vUA.
6. J. Bohannon, *Science* **342**, 60 (2013).
7. B. Parlee, C. Furgal, *Clim. Change* **115**, 13 (2012).
8. Arctic Council, Arctic Resilience Report [in process] (2016); http://arctic-council.org/arr/.
9. Arctic Monitoring and Assessment Programme, Adaptation Actions for a Changing Arctic, Part C (AMAP, Oslo, Norway, 2016); http://bit.ly/2cG9axE.
10. AMAP, *Snow, Water, Ice and Permafrost in the Arctic: Executive Summary* (AMAP, Oslo, Norway, 2011).
11. N. Morata *et al.*, paper presented at Arctic Science Summit Week, Toyama, Japan, 23 April 2015 to 30 April 2015 (Alfred Wegener Institute, Bremerhaven, Germany, 2015).
12. J. Overland *et al.*, *J. Clim.* **28**, 7917 (2015).
13. K. L. Laidre *et al.*, *Ecol. Appl.* **18** (suppl.), S97 (2008).
14. Sustaining Arctic Observing Networks (SAON 2016); www.arcticobserving.org/assets.
15. SAON, To the organizers and participants of the 2016 Arctic Science Ministerial [letter] (SAON, 2016); http://bit.ly/2cdxeZI.
16. Inuit Circumpolar Council—Alaska, *Alaskan Inuit Food Security Conceptual Framework: How to Assess the Arctic from An Inuit Perspective: Summary and Recommendations Report* (Inuit Circumpolar Council—Alaska, Anchorage, AK, 2015).
17. TEEB, *Valuing the Arctic: A Scoping Study* (Conservation of Arctic Flora and Fauna Assessment Series, Akureyri, Iceland, 2015); http://arcticteeb.net/.
18. K. Poole, A. Gunn, *Mobile Caribou Conservation Measures for the Kivalliq Region, Nunavut* (for the Kivalliq Inuit Association, Nunavat, Canada, 2015).
19. WWF Arctic Programme, Options for Arctic Marine Cooperation [blog] (WWF Arctic Programme, Ottawa, 2016); http://arctic.blogs.panda.org/default/marine-cooperation-wwf-vision/.

10.1126/science.aai8198

Downloaded from http://science.sciencemag.org/ on September 30, 2016

Published by AAAS

Scotland's high mortality rates and poor health outcomes may have roots in socioeconomic factors.

PHOTO: 2CROWS/ISTOCK PHOTO.COM

PUBLIC HEALTH

Mind the (health) gap

A geographer turns a critical eye toward regional health disparities

By **Peter R. Reczek**

Health care workers, public health officials, and governments have long sought ways to improve the health of those in their charge. But identifying those factors most relevant to local and regional differences in health has been a formidable task.

In her new book, *Health Divides*, Clare Bambra uses systematic investigation to uncover the underlying factors responsible for health disparities. Her journey begins with the observation that health disparities vary in clear geographic demarcations that she terms "health divides."

Bambra focuses her discussion on three areas in high-income countries that are characterized by stark regional differences in health outcomes. These include poor health outcomes in the United States, referred to as the "US health disadvantage"; a North-South divide in the United Kingdom (the so-called "Scottish health effect"); and a local example of health disparity in the town of Stockton-on-Tees in the northeast of England.

The author is a freelance writer and former AAAS Science and Technology Policy Fellow. Email: peter.reczek@gmail.com

Health Divides
Where You Live Can Kill You
Clare Bambra
Policy Press, 2016.
256 pp.

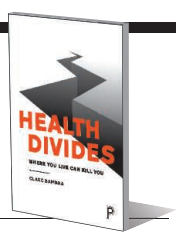

Despite the highest expenditures on health in the world, the United States falls woefully short on a range of health outcomes. Using the obesity epidemic as an example, Bambra shows that this particular health disadvantage, seen throughout the country today, was not always so uniform. She traces a clear geographic distinction, with higher obesity rates in the South and lower rates in the Northeast in the 1990s, a phenomenon that became more uniform at the turn of the century. A similar, if opposite, picture arises in the United Kingdom, where health outcomes improve and average life expectancy increases the farther south one travels.

Bambra notes that health divides can even exist at the local level. In the small East Anglian town of Stockton-on-Tees, the incidence of health conditions, including cardiovascular disease and cancer, is greater in northern, more impoverished neighborhoods, then in the southern, more affluent, neighborhoods.

Not all regions show a north-south divide. For example, health outcomes from cancer and cardiovascular disease, once much worse for residents of East Germany, improved along with life expectancy in the years immediately after the fall of the Berlin Wall.

Geography per se seems to play a limited role in health disparities. The importance of a "health divide" is that it provides a starting point for the identification of causative factors of these disparities.

Bambra examines a number of factors that may contribute to geographic differences in health outcomes, including a region's basic sanitation or a resident's access to health care, as well as factors such as an overreliance on market forces, which can lead to lower income and poor working conditions that preserve inequalities over time. Health inequalities are complicated and multifaceted, she concludes, occurring as a result of the people involved, the context or environment, and ultimately the political and economic factors that perpetuate the status quo.

In the final section of the book, Bambra turns her attention to how geography relates to the politics of health and how policies have, and can be, changed to reduce health divides. As she writes, "place matters for health, but politics matters for place."

Bambra goes into detail in her analysis of the health disparities that changed as the United Kingdom moved from a Labour government to a Conservative one in 1979. For example, life expectancy among individuals in lower socioeconomic groups were stagnant or decreased during Margaret Thatcher's tenure as Prime Minister, a time when it continued an historic rise in the upper classes. Bambra attributes these changes to diminished support for access to health care and programs such as food vouchers. These trends were later reversed when funding for social welfare programs was increased.

Bambra makes it clear that she believes that the evidence supports poverty as the key factor in health care disparities and sketches a plan to overcome the political and economic factors that enable economic disparities in the United States and the United Kingdom. Her analysis is forthright and nonpartisan. However, she does not address one of the key considerations that governments will need to address to find the political will to reverse health trends: What will it cost?

Bambra's well-referenced book and case study approach make it a welcome supplemental text for courses in health policy and introductory epidemiology, as well as a valuable primer for policy-makers. But her systematic analysis and clear exposition will also allow the general reader to appreciate the value of health disparities research.

10.1126/science.aah6065

Downloaded from http://science.sciencemag.org/ on September 30, 2016

Published by AAAS

PHOTO: JOHN VAN HASSELT, CORBIS/CONTRIBUTOR

NUCLEAR HISTORY

Strange bedfellows

Scientific collaboration takes center stage in a participants' account of post–Cold War nuclear disarmament

By **Frank von Hippel**

In the late 1980s, Soviet General Secretary Mikhail Gorbachev ushered in a new era of government transparency in the Soviet Union, a move that enabled the country's nuclear scientists to interact with their counterparts in the United States for the first time. Driven at first by curiosity, these interactions took on greater meaning when the Soviet Union fell apart and Russia's economy collapsed in 1991. When this happened, the United States became concerned that Russian nuclear scientists and materials might be snapped up by volatile states with nuclear ambitions, such as Iran. To mitigate this possibility, U.S. scientists were encouraged to reach out to their Russian colleagues with proposals for joint scientific projects with civilian applications and were charged with helping Russia adapt its nuclear security system as the country transitioned to a more open society.

The reviewer is at the Program on Science and Global Security, Princeton University, Princeton, NJ 08542, USA. Email: fvhippel@princeton.edu

This two-volume work, published by the Los Alamos Historical Society, is a comprehensive participants' account of the cooperation between U.S. and Russian nuclear-weapons laboratories that began during the Gorbachev period and ended in 2014 after Russia's annexation of Crimea. Siegfried Hecker, who was director of Los Alamos National Laboratory at the beginning of the period of cooperation, edited the work and provides lucid introductory and overview sections. The volumes contain essays by, and interviews with, key leaders who coordinated the efforts on both sides. A parallel work is to appear in Russian, edited and with overviews by two former Russian lab directors.

The U.S. Cooperative Threat Reduction program was established within the Department of Defense (DOD) in 1991 with the goal of working with Russia's Ministry of Defense to eliminate the country's excess Cold War bombers, missiles, and submarines. The program's creation was spearheaded by the senior Democratic and Republican members of the Senate Armed Services Committee: former Senators Sam Nunn and Richard Lugar.

Doomed to Cooperate
How American and Russian Scientists Joined Forces to Avert Some of the Greatest Post–Cold War Nuclear Dangers
Siegfried S. Hecker, Ed.
Bathtub Row Press, 2016. 976 pp.

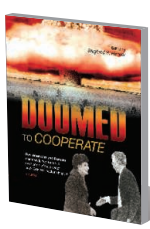

Despite Russia's huge stocks of nuclear weapons materials, the DOD was reluctant to fund work with the country's Ministry of Atomic Energy. In 1995, Senator Pete Domenici, chair of the Senate Appropriations subcommittee responsible for the Department of Energy's (DOE's) defense activities, arranged for that agency to receive funds directly from Congress to work on the security of nuclear-weapons materials in Russia. The DOE would serve as the primary overseer of this unprecedented cooperation moving forward.

While the era of cooperation lasted, its achievements were remarkable. In 1988, the weapons laboratories calibrated the seismic signals from each other's nuclear test sites and found that, contrary to the claims of the Reagan Administration, the Soviets had not violated the 150-kiloton limit of the bilateral Threshold Test Ban Treaty.

In 1992, the United States provided equipment to strengthen the security and safety of warheads being evacuated to Russia from Belarus, Kazakhstan, and Ukraine. During this period, U.S. and

Downloaded from http://science.sciencemag.org/ on September 30, 2016

Published by AAAS

The USSR detonated hundreds of nuclear bombs at Semipalatinsk (shown) before the site was decommissioned.

Russian laboratories worked together to upgrade nuclear-materials security throughout Russia's nuclear complex. Cumulatively, the U.S. government spent $4 billion on these efforts. Finally, starting in 2000, the labs embarked on a secret 15-year-long project to secure approximately 200 kilograms (25 weapon equivalents) of plutonium residues in tunnels and boreholes at the Soviet nuclear test site near Semipalatinsk, Kazakhstan.

These projects were implemented via contracts with Russia's laboratories and equipment suppliers. Where equipment was not available, contracts were let for their development. This gave Russian organizations much-needed financial support while minimizing the government's concerns that the United States was using its access and equipment to collect intelligence. At sensitive sites, the Russian labs also helped devise nonintrusive means for the United States to verify that its funding was being used as intended.

The most surprising breakthrough of this effort was in 1996, when Russia's Navy decided to accept U.S. assistance for security upgrades at its storage sites for nuclear fuel. In the following years, the Navy, the Strategic Rocket Forces, and finally the Ministry of Defense all agreed to work with the U.S. labs on security upgrades to their warhead storage sites.

The U.S. and Russian heroes of this story all appear in *Doomed to Cooperate*. They include Thomas Cochran and Christopher Paine of the Natural Resources Defense Council and Russia's Minister of Atomic Energy, Viktor Mikhailov, who worked with key congressional leaders to procure support and funding for the program.

When the Cooperative Threat Reduction program was established, the two countries were at approximately the same level with regard to technical accomplishments, and scientists on both sides treated each other as respected colleagues. The economic status of the two countries was definitely unequal, however. In 1999, at the bottom of its economic collapse, Russia's gross domestic product per capita was only 4% that of America's. (Today, it is about 16%.)

The second volume begins with a chapter on the U.S.-led billion-dollar attempt to support some of Russia's nuclear weapon scientists with nonweapon R&D projects during the period of the Russian economic collapse. Those involved in this effort acknowledge that few of these scientists were permanently converted to nonweapons work but argue that the programs helped stabilize the Russian nuclear laboratories and reduce nuclear brain drain.

In 1993, the U.S. lab directors agreed not to oppose the Comprehensive Nuclear-Test-Ban Treaty if a science-based "stockpile stewardship" program was established. Based on computer simulations of nuclear explosions, the program is focused on safely maintaining existing warheads. Russia's government established a similar program around 2000.

Scientific delegates from the United States visit the Russian VNIIEF laser lab in 1992.

PHOTO: LOS ALAMOS HISTORICAL SOCIETY

I supported the "lab-to-lab" program in 1993 and 1994 while working on issues related to national security in the White House Office of Science and Technology Policy. At the time, I hoped that the new focus on cooperative security would become permanent on both sides and would become eligible for funding comparable to that dedicated to nuclear weapons research. Unfortunately, this would not come to pass.

In fiscal year 2016, the DOE's nuclear weapons budget of $8.8 billion exceeded its 1985 Cold War peak in constant dollars. Each of the three U.S. nuclear weapons laboratories received an average of $1.4 billion per year for weapons activities, eight times the average dedicated to nonproliferation and disarmament activities. A primary justification for the high nuclear-weapons budgets was the need for a deeper theoretical understanding of nuclear explosion physics to maintain weapons' reliability in the absence of nuclear testing.

When Vladimir Putin, a former officer in Russia's intelligence service, became president in 2000 and the rise in the price of oil facilitated Russia's economic recovery, concerns about U.S. access to Russia's most sensitive nuclear facilities came to the fore. Cooperative programs were cut back and, after the Russian annexation of Crimea in 2014, terminated altogether.

Hecker ends volume 2 with an essay arguing that, despite its smaller funding, Russia's nuclear-weapons program is now in much better shape than that of the United States. Since the end of the Cold War, Russia has made nuclear deterrence the core of its strategy for dealing with potential threats from NATO and China, he maintains. For the United States, with its powerful high-tech conventional military, maintaining an effective nuclear-weapons program has been a much lower priority.

During the Cold War, the U.S. nuclear-weapons design laboratories at Los Alamos, New Mexico, and Livermore, California, were relatively autonomous. In response to a series of security infractions, however, Congress decided that management was too loose.

In 2003, DOE contracted with business consortia to remedy safety and environmental hazards that had been created by Cold War shortcuts. Unfortunately, the contractors hired to manage these projects had little nuclear weapons experience. The result has been a dramatic escalation in costs and missed deadlines to refurbish U.S. nuclear weapons and replace unsafe and aging facilities.

In a better world, this problem could be swept away by nuclear disarmament. The precedent described in these volumes provides important evidence that such a world might be achievable.

10.1126/science.aah6011

Downloaded from http://science.sciencemag.org/ on September 30, 2016

Published by AAAS

LETTERS

Edited by **Jennifer Sills**

Compound hazards yield Louisiana flood

ON 11 AUGUST 2016, a severe weather system dropped 433 mm of rain in about 72 hours, triggering widespread flooding in southern Louisiana. This flood damaged at least 60,000 homes, required evacuation of more than 20,000 people, and led to 13 deaths (*1*). At one point, the Amite river crest rose to 1.5 m above the 1983 record (*2*). The record flood stage was the result of compounding effects of multiple local floods. Several creeks and rivers across a large area in southern Louisiana flooded simultaneously, which led to overtopping of levees and floodwalls (*3*).

Resilience of flood protection infrastructure, such as levees, is critical to avoiding community-wide disasters. However, the majority of the 160,000 km earthen levees across the United States are in marginal condition (*4*). We must make the inspection and maintenance of levees a priority, given evidence that events such as the Louisiana flood are becoming more frequent and severe (*5*). Increased global temperatures in the past decades have likely contributed to nine unprecedented floods since 2010, including costly and deadly events in West Virginia, southern Louisiana, Maryland, and Texas (*6*).

In Louisiana, anomalously high temperatures in the past two months—especially July, which was the warmest month in the past 136 years of modern observations (*7*)—may have contributed to record-high moisture in the atmosphere (*8*), increasing the flood's severity. In a warming climate, the water-holding capacity of the atmosphere is expected to increase by about 7% for every 1°C increase (*9*). Additional moisture in the atmosphere could potentially lead to longer and more severe storms, thereby increasing the likelihood of floods (*9*).

Anthropogenic activities, such as land-use and land-cover changes and urbanization, can intensify the impact of natural hazards on infrastructure (*10*). This makes an extreme rainfall event, combined with other natural hazards, such as sea level rise, land subsidence, drought, hurricanes, or earthquakes, even more likely to cause substantial damage. Such compounded extreme events are likely inevitable and have been reported on several occasions (*11*).

To prepare for future climatic events, we need to understand the interactions between extreme events such as floods and other natural hazards, as well as anthropogenic activities. Advancements in these areas will allow us to prevent compound hazards from turning into a disaster.

Extreme weather events like the Louisiana flood are more likely to occur as the climate grows warmer.

Farshid Vahedifard,[1]* Amir AghaKouchak,[2] Navid H. Jafari[3]

[1]Department of Civil and Environmental Engineering, Mississippi State University, Mississippi State, MS 39762, USA. [2]Department of Civil and Environmental Engineering, University of California, Irvine, CA 92697, USA. [3]Department of Civil and Environmental Engineering, Louisiana State University, Baton Rouge, LA 70803, USA.

*Corresponding author. Email: farshid@cee.msstate.edu

REFERENCES

1. R. Santana, "Flood-wary Louisiana cleans house while search continues," *ABC News* (2016).
2. NOAA National Weather Service, Amite River at Denham Springs Hydrograph (http://water.weather.gov/ahps2/hydrograph.php?wfo=LIX&gage=DENL1).
3. D. Mitchell, S. Hardy, "Ascension officials: 15,000 homes, businesses flooded so far; levee overtopped," *The Advocate* (2016).
4. N. Keegan *et al.*, "Locally operated levees: Issues and federal programs" (Congressional Research Service, 2011).
5. National Research Council, "Dam and levee safety and community resilience: A vision for future practice" (National Academies Press, 2012).
6. A. Freedman, "How the deadly Louisiana floods happened, and why you should worry," *Mashable* (2016).
7. J. Stevens, "July 2016 temperature anomaly" (2016); http://earthobservatory.nasa.gov/IOTD/view.php?id=88607
8. G. Vaidyanathan, "Why the deadly Louisiana flood occurred," *Scientific American* (2016).
9. E. K. Trenberth, *Clim. Res.* **47**, 123 (2011).
10. M. V. Bilskie *et al.*, *Geophys. Res. Lett.* **41**, 927 (2014).
11. J. C. Gill, B. D. Malamud, *Rev. Geophys.* **52**, 680 (2014).

10.1126/science.aai8579

Addressing obesity in homeless children

A HOMELESS CHILD "lacks a fixed, regular, and adequate nighttime residence" (*1*). On any given night, more than 125,000 children are homeless in the United States (*2*). Surprisingly, obesity is more common in homeless children than in other populations. In one homeless shelter in the Midwest, one-fifth of 6- to 12-year-olds had weight-for-height greater than the 95th percentile (*2*). In Minneapolis, 45% of homeless children were overweight or had obesity (*3*). Anthropometric data from homeless children in Baltimore showed that none were underweight and that 42% were either overweight or at risk of becoming overweight (*4*). In New York, obesity rates were a third higher in homeless children, aged 6 to 11, than in locally domiciled children (*5*). In homeless children in Kansas City, 33% of 4- to 6-year-olds and 26% of 7- to 10-year-olds had weights above the 95th percentile (*6*).

Homeless children develop obesity in part because of food insecurity; food provision is unpredictable, diets lack fresh components, and fat intakes are 47 to 52% of energy intake (*6*). Also, physical activity spaces are scarce and exercise participation is low (*7*). However, although poor diet and low physical activity are important for understanding high obesity rates in homeless children, social determinants of health such the physical environment, poverty, violence, health illiteracy, and inadequate physical and mental health care are likely to be more important (*8*).

Policy-based intervention can help these children. The Family Options Study followed 2282 families for 36 months. It showed that providing homeless families with time-limited or permanent rent assistance not only reversed homelessness but also improved food security (*9*). Research suggests that tackling social determinants can also lead to policies that improve health (*10*). Federal and local policies should prioritize homeless families for rent assistance and link those programs with others supporting food security and physical health for children.

James A. Levine,[1,2]* Shelly K. McCrady-Spitzer,[1] Samantha M. Batko[3]

[1]Department of Endocrinology, Mayo Clinic, Rochester, MN 55905, USA. [2]Obesity Solutions, Mayo Clinic Arizona, Scottsdale, AZ 85259, USA and Arizona State University, Tempe, AZ 85281, USA. [3]Homelessness Research Institute, National Alliance to End Homelessness, Washington, DC 20005, USA.

*Corresponding author. Email: levine.james@mayo.edu

REFERENCES

1. The McKinney-Vento Homeless Assistance Act (www.hudexchange.info/resources/documents/HomelessAssistanceActAmendedbyHEARTH.pdf).
2. S. H. Chiu *et al.*, *J. Pediatric Health Care* **27**, 278 (2013).
3. R. Richards *et al.*, *Childhood Obesity* **9**, 240 (2013).
4. K. B. Schwarz *et al.*, *MedGenMed* **9**, 48 (2007).
5. K. E. Thorpe *et al.*, *Health Aff (Millwood) Suppl Web Exclusives*, W4-480-486 (2004).
6. M. A. Drake, *Public Health Rep.* **107**, 312 (1992).

PHOTO: REUTERS/DAN ANDERSON

Downloaded from http://science.sciencemag.org/ on September 30, 2016

Published by AAAS

7. I. Darnton-Hill, E. T. Coyne, *Public Health Nutrition* **1**, 23 (1998).
8. L. M. Rossen, *J. Epidemiol. Commun. Health* **68**, 123 (2014).
9. U.S. Department of Housing and Urban Development, "Family options study: Short-term impacts of housing and services interventions for homeless families" (2015).
10. D. R. Williams et al., *J. Public Health Manag. Pract.* **14**, S8 (2008).

10.1126/science.aaj1468

Zika vaccine: Clinical trial and error?

RESEARCHERS ARE RACING to develop a vaccine for the Zika virus and move it to clinical trials ("Protective efficacy of multiple vaccine platforms against Zika virus challenge in rhesus monkeys," P. Abbink *et al.*, Research Article, 4 August, aah6157), but they are not considering whether the current candidates will be too expensive to make it to market. It remains unclear which of the current approaches is the most effective, whether the more sophisticated approaches are truly needed, and whether these vaccines will be affordable where they are needed most.

Zika is a flavivirus, and its effect is similar to West Nile virus and yellow fever virus. Relative to human immunodeficiency virus (HIV) and other viruses with more complex life cycles, it is easy to make a flavivirus vaccine. As in the cases of West Nile virus and yellow fever virus, a one-time exposure to Zika confers immunity in mouse models and nonhuman primates [Abbink *et al.* and (*1*)], and this appears to be the case in humans as well. Immunity developed after one exposure explains the pattern of short-term episodic Zika outbreaks on the Pacific Islands (*2*). The virus may cause a similarly short-lived epidemic in Puerto Rico.

For West Nile virus, a simple virus vaccine that does not contain live, attenuated virus has been in veterinary use for years and is as protective as the live virus infection (*3*). Inactivated virus vaccines are extremely inexpensive to make [e.g., (*4*)]. Yet, given the relatively low number of West Nile virus cases reported in the United States each year, clinical trials to develop a human vaccine have been deemed too expensive (*5*). The Salk Polio vaccine, another inactivated virus vaccine, costs about $2.04 per dose (*6*), but it is only widely used thanks to funding from supporters such as Gavi (*7*).

There are two cost-benefit trade-offs to consider before moving forward. First, we must weigh the cost of the Zika virus vaccine against the cost of disease treatment with no vaccine. Second, we must prioritize the Zika virus in the context of development of life-saving vaccines for other epidemics. It would be prudent to determine which of the current Zika vaccine candidates has the best cost-to-benefit ratio before diverting vast public health resources to vaccine production and large-scale clinical trials.

Dirk P. Dittmer

Department of Microbiology and Immunology, School of Medicine, University of North Carolina at Chapel Hill, Chapel Hill, NC 27516, USA. Email: ddittmer@med.unc.edu

REFERENCES

1. D. M. Dudley *et al.*, *Nat. Commun.* **7**, 12204 (2016).
2. V. M. Cao-Lormeau *et al.*, *Lancet* **387**, 1531 (2016).
3. D. Champ *et al.*, *Dev. Biol.* **114**, 221 (2003).
4. P. Chong *et al.*, *Hum. Vaccin. Immunother.* **8**, 1775 (2012).
5. A. Zohrabian *et al.*, *Emerg. Infect. Dis.* **12**, 375 (2006).
6. Polio Global Eradication Initiative, "Availability and price of inactivated polio vaccine" (2014); www.polioeradication.org/tabid/488/iid/354/Default.aspx .
7. Gavi, he Vaccine Alliance (www.gavi.org).

10.1126/science.aai8117

Downloaded from http://science.sciencemag.org/ on September 30, 2016

RESEARCH

Seeing the disorder in ordered materials

Miao et al., *p. 1380*

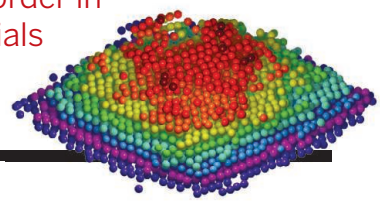

IN *SCIENCE* JOURNALS

Edited by **Nick Wigginton**

CARBON CYCLE

Less storage sinks soil models

Soils may be a smaller carbon sink than previously assumed and might provide less relief from future global warming than expected. Soils contain more carbon than any other terrestrial reservoir and thus can have large impacts on climate, depending how much atmospheric carbon dioxide they sequester. He *et al*. use soil radiocarbon measurements to show that models tend to overestimate how much carbon soils will store by the year 2100, mostly because they underestimate the turnover time of soil carbon. Consequently, model projections of carbon storage by the end of the century may be too high by a factor of 2. —HJS

Science, this issue p. 1419

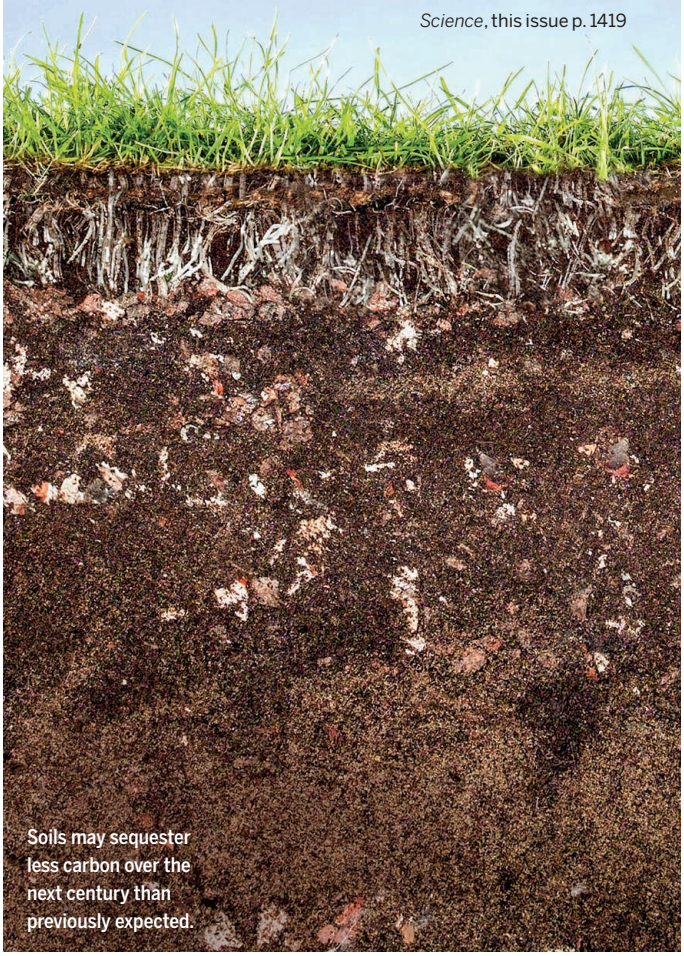

Soils may sequester less carbon over the next century than previously expected.

PHOTOS (FROM LEFT): GLENN MILLINGTON/ALAMY STOCK PHOTO; CITIZEN OF THE PLANET/ALAMY STOCK PHOTO

STRUCTURAL BIOLOGY

Keeping the spliceosome in check

In eukaryotes, RNA is transcribed as precursor mRNA. Noncoding sequences must be spliced out before proteins are made. Mechanistic insight into the splicing process has come from determining the structures of distinct spliceosome complexes at different steps of the reaction. Rauhut *et al*. describe the structure of the activated spliceosome (B^{act}) in *Saccharomyces cerivisiae* at 5.8 Å resolution. The complex is held in a state that is inactive but ready to be remodeled into a catalytically active machine. —VV

Science, this issue p. 1399

FOREST ECOLOGY

Diversity in neotropical dry forests

Dry forests in the American tropics are not as extensive as rain forests and are more severely threatened by human activity. The DRYFLOR network compiled a floristic inventory of the entire neotropical dry forest biome and used this database of nearly 5000 woody species to analyze the geographical distribution of plant diversity that it hosts. Large variation in floristic composition between different sites and regions implies that effective conservation of dry forest plant diversity will require the protection of numerous priority areas across neotropical nations. —AMS

Science, this issue p. 1383

EVOLUTION

G proteins diverge and conquer

In plants, signaling through G (heterotrimeric GTP-binding) proteins involves either canonical Gα proteins, which are structurally and functionally similar to animal Gα proteins, or extra-large Gα (XLG) proteins. Urano *et al*. found that plant canonical Gα proteins evolved slowly, like their animal counterparts, and were involved in developmental processes. In contrast, XLG proteins rapidly diversified early in the land plant lineage and mediated stress responses. Thus, diversification of plant XLG proteins coincided with the colonization of land and may have helped plants to withstand the new stresses encountered in this environment. —AV

Sci. Signal. **9**, ra93 (2016).

GEOPHYSICS

Catching earthquakes from the sky

Wastewater injection appears to be driving the sharp increase in earthquakes in the central United States. Shirzaei *et al*. use

Deep injection well used for disposal of wastewater

Published by AAAS

satellites to show that wastewater injection caused surface deformation before the 2012 magnitude-4.8 Timpson earthquake in eastern Texas. Changes in subsurface pore pressure link injection to the surface deformation. Using satellites to track the impact of wastewater injection may improve earthquake forecasting in regions that are prone to induced seismicity. —BG

Science, this issue p. 1416

HOST TOLERANCE

Microbes teach tolerance in the gut

The trillions of microbes inhabiting and interacting in our gut can greatly influence how we respond to infection. Rangan *et al*. find that worms and mice harboring *Enterococcus faecium* in their guts can better tolerate *Salmonella* infections. Tolerance requires *E. faecium* to express the enzyme SagA, which can also exert a probiotic effect when expressed by other bacteria. SagA protects worms by cleaving bacterial peptide fragments so that they stimulate the tol-1 protein. In contrast, Pedicord *et al.* find that SagA protects mice against *Salmonella* and *Clostridium difficile* infections in a manner dependent on antimicrobial peptides and multiple innate immune receptors. —KLM

Science, this issue p. 1434; *Sci. Immunol.* **1**, eaai7732 (2016).

INFECTIOUS DISEASE

Cultured guts combat gastroenteritis

Human noroviruses are highly contagious. They cause explosive outbreaks of gastrointestinal disease, which can be dangerous to the very young, the elderly, and the immunocompromised. Ettayebi *et al*. succeeded in growing several strains of noroviruses in human gut stem cell cultures and found that the addition of bile substantially increased viral infectivity. This culture system will allow evaluation of new methods to inactivate human noroviruses for vaccine development and to determine the effectiveness of disinfectants and novel control measures. —CA

Science, this issue p. 1387

Cultures of human gut stem cells enable the growth of norovirus strains in the laboratory.

NANOMATERIALS

Rapidly reducing graphene oxide

The reduction of exfoliated graphene oxide platelets can produce graphene for applications in materials, energy storage, and catalysis. However, reduction methods often leave a substantial fraction of oxygenated functional groups in graphene, lowering its electrical conductivity. Voiry *et al.* report that brief microwave pulses (1 to 2 s) resulted in the near-complete reduction of graphene oxide. The resultant high-quality graphene, with high carrier mobility, served as a catalyst support with low overpotential for the oxygen reduction reaction. —PDS

Science, this issue p. 1413

CONVERGENT EVOLUTION

Genetic convergence to the extreme

Species in the same habitat may be only distantly related but yet share the need to adapt to environmental extremes. Yeaman *et al*. examined the underlying genetics of local environmental adaptation in lodgepole pine and interior spruce, which diverged over 140 million years ago (see the Perspective by Hancock). A suite of duplicated genes, which exhibited the hallmark of selection, were associated with cold tolerance in both species. Adaptations to climate may therefore be genetically constrained, even among distantly related species. —LMZ

Science, this issue p. 1431; see also p. 1362

IN OTHER JOURNALS

Edited by **Sacha Vignieri** *and* **Jesse Smith**

DISEASE ECOLOGY

No touching, please

European badgers have been blamed for the transmission of bovine tuberculosis in the United Kingdom and, despite much evidence to the contrary, have endured regular and repeated culling efforts based on the assumption that their lethal removal decreases the spread of the disease. Woodroffe *et al.* used GPS and contact collars to record the degree to which badgers and cattle actually come into contact. Despite finding that badgers prefer to spend their time in pastures, they recorded no direct contact between the two species, with badgers tending to say at least 50 m from cattle. Thus, any transmission between these two species seems to be environmentally mediated, a result that could be instrumental in targeting nonlethal ways to prevent the spread of the disease. —SNV

Ecol. Lett. 10.1111/ele.12654 (2016).

European badgers avoid cattle in pastures, reducing bovine tuberculosis transmission routes.

PHOTOS (FROM LEFT): SCIEPRO/SCIENCE SOURCE; ROBERTHARDING/ALAMY STOCK PHOTO

HOST RESPONSES

An appetite for tolerance

The proverb "feed a cold, starve a fever" may contain a kernel of truth after all. Animals from insects to humans display certain types of behaviors when they are sick, including reduced appetite and social withdrawal. To better understand the importance of these behaviors, Wang *et al.* studied the effects of sickness-induced anorexia in bacterially or virally

Published by AAAS

ALSO IN *SCIENCE* JOURNALS

Edited by **Nick Wigginton**

MATERIALS SCIENCE

Seeing the disorder in the ordered

The ordered nature of crystalline materials makes it relatively straightforward to calculate their bulk structures from partial information. In contrast, it can be much harder to describe the local structure of defects in a crystal, such as grain boundaries, vacancies, or stacking faults. Miao *et al*. review the advances in atomic electron tomography that make it possible, at least in some materials, to determine the three-dimensional coordinates for partially disordered systems. —MSL

Science, this issue p. 1380

YEAST GENETICS

A global genetic interaction network

Studies of genetic interactions help identify networks and pathways that may not be easily apparent through observations of single mutations. Constanzo *et al*. mapped the global network of genetic interactions, both positive and negative, for essential and nonessential genes in yeast. From this, they were able to map a hierarchy of gene and cellular function, as well as connectivity between networks, and identify the function of previously uncharacterized genes. The interactions identified in this study may even be extended to generate predictions for human genetic interactions. —LMZ

Science, this issue p. 1381

RNA STRUCTURE

Unfolded in vivo

RNA can form a diverse array of folded structures. The four-stranded RNA G-quadraplex is a potentially very stable structure that has been implicated in both gene regulation and disease. Guo and Bartel show that many eukaryotic RNA sequences have the potential to form G-quadraplexes, yet most of them are unfolded in eukaryotic cells. Because there are very few RNA G-quadraplex structures in prokaryotic RNA, despite also being stable in vivo, G-quadraplexes may have been actively eliminated from the genome. —GR

Science, this issue p. 1382

SOLAR CELLS

Protective liquid motions

Hybrid organic-inorganic perovskites used in solar cells exhibit long carrier lifetimes compared with all-inorganic perovskites. This is in spite of the higher amount of disorder in the former that would normally increase unproductive carrier recombination. Zhu *et al*. used time-resolved photoluminescence and optical Kerr effect spectroscopies to compare the hybrid organic-inorganic perovskites $CH_3NH_3PbBr_3$ and $CH(NH_2)_2PbBr_3$ and the all-inorganic perovskite $CsPbBr_3$ (see the Perspective by Ziffer and Ginger). The hybrid materials exhibited hot fluorescence indicative of liquid-like organic cation motion, which may protect charge carriers through solvation or formation of large polarons. —PDS

Science, this issue p. 1409; see also p. 1365

ATMOSPHERIC OXYGEN

Oxygen deficit

The partial pressure of atmospheric O_2 has declined by 0.7% over the past 800,000 years, according to data from air trapped in polar ice cores. Stolper *et al*. compiled existing records of O_2/N_2 to determine this loss. O_2 sinks must have been about 2% larger than sources over that time interval, possibly because of increasing rates of global erosion or decreasing rates of marine organic carbon burial. Declining O_2 requires a CO_2-dependent feedback such as silicate weathering to help stabilize atmospheric CO_2 concentrations on geological time scales. —HJS

Science, this issue p. 1427

NEUROSCIENCE

How brain neurons turn down the heat

The preoptic area of the hypothalamus serves as the brain's thermostat. Song *et al*. found that a particular set of neurons mediate this function and identified the molecular heat sensor that they use (see the Perspective by Bartfai). Neurons in cultures of mouse brain that were activated in response to warming expressed temperature-sensitive TRPM2 ion channels. In mice lacking these channels, body temperature increased more in response to an induced fever than it did in control animals. In mice engineered to allow specific control of the TRPM2-containing neurons, the activity of the neurons was shown to modulate core body temperature. —LBR

Science, this issue p. 1393; see also p. 1363

CLIMATE CHANGE

Services for successful adaptation

Nations around the world are seeking the help of climate services to adapt to climate change. In a Perspective, Goddard explains that for climate services to be successful, they must be based on a clear understanding of the place of climate considerations in the decision-making process. Also, climate services must be built on the best-available observational data sets and must consider climatic patterns at time scales from seasonal to decadal. Because each region will experience climate change in different ways, successful adaptation will depend on close cooperation between climate services and national agencies. —JFU

Science, this issue p. 1366

INFECTIOUS DISEASE

Stemming MRSA-induced pneumonia

Controversies persist about the use of human intravenous immunoglobulin (IVIG) as an adjunct treatment for severe pneumonia caused by *Staphylococcus aureus* infections. Diep *et al*. show that in rabbits, only two specific antibodies contained in IVIG are necessary and sufficient to confer protection against necrotizing pneumonia caused by methicillin-resistant *S. aureus* (MRSA) strains. These antibodies neutralize the toxic effects of α-toxin and Panton-Valentine leukocidin. Preexposure prophylaxis with IVIG, or postexposure treatment with IVIG in combination with either vancomycin or linezolid, improved survival outcomes. —OMS

Sci. Transl. Med. **8**, 357ra124 (2016).

GEOPHYSICS

Finding the weak spots of subduction

The asthenosphere is a weak layer in the Earth that allows the rigid plates of Earth's crust to move over geologic time. Hawley *et al*. found an unexpectedly large accumulation of a weak material just beneath the rigid Juan de Fuca slab in the Cascadia subduction zone, located along the northwestern coast of the United States. Seismically imaging this "roll" of weak material required the use of both onshore and offshore seismometers. The roll appears to be positioned underneath where the Juan de Fuca plate bends and plunges into the mantle, providing potential explanations for several puzzling features of this and other subduction zones. —BG

Science, this issue p. 1406

Published by AAAS

ATMOSPHERIC SCIENCE

A change in the wind

The quasi-biennial oscillation (QBO), one of the most dependable features of atmospheric circulation, was unexpectedly disrupted in 2016. Normally, the winds in the equatorial stratosphere between the altitudes of ~16 and 50 km alternate between eastward and westward motion at intervals between 22 and 36 months. In February 2016, however, Osprey *et al*. show that an easterly jet formed within the westerly phase that occupied the lower stratosphere—an occurrence that existing models of the QBO did not predict. Some climate projections suggest that this behavior may become more frequent in the future as climate warms, which could affect winter storminess and rainfall over northern Europe in particular. —HJS

Science, this issue p. 1424

Published by AAAS

REVIEW SUMMARY

MATERIALS SCIENCE

Atomic electron tomography: 3D structures without crystals

Jianwei Miao,* Peter Ercius, Simon J. L. Billinge

BACKGROUND: To understand material properties and functionality at the most fundamental level, one must know the three-dimensional (3D) positions of atoms with high precision. For crystalline materials, x-ray crystallography has provided this information since the pioneering work of Max von Laue, William Henry Bragg, and William Lawrence Bragg around 100 years ago. But perfect crystals are rare in nature. Real materials often contain defects, surface reconstructions, nanoscale heterogeneities, and disorders, which strongly influence material properties and performance. Completely different approaches from crystallography are needed to determine the 3D atomic arrangement of crystal defects and noncrystalline systems. Although single-particle cryo–electron microscopy (cryo-EM) has been under rapid development for 3D structure determination of macromolecules with identical or similar conformations at near-atomic resolution, this method cannot be generally applied to the physical sciences for the following three reasons. First, most materials do not have identical copies and cannot be averaged to achieve atomic resolution. Second, a priori knowledge of the peptide sequence and stereochemistry in protein molecules greatly facilitates their 3D atomic structure determination, but this knowledge is not applicable to physical science samples. Third, unlike in biological specimens, the presence of diffraction and phase contrast in the transmission electron microscopy images of most materials poses a challenge for tomographic reconstruction. These difficulties have made the objective of solving the 3D atomic structure of crystal defects and noncrystalline systems a major challenge for structural characterization in the physical sciences.

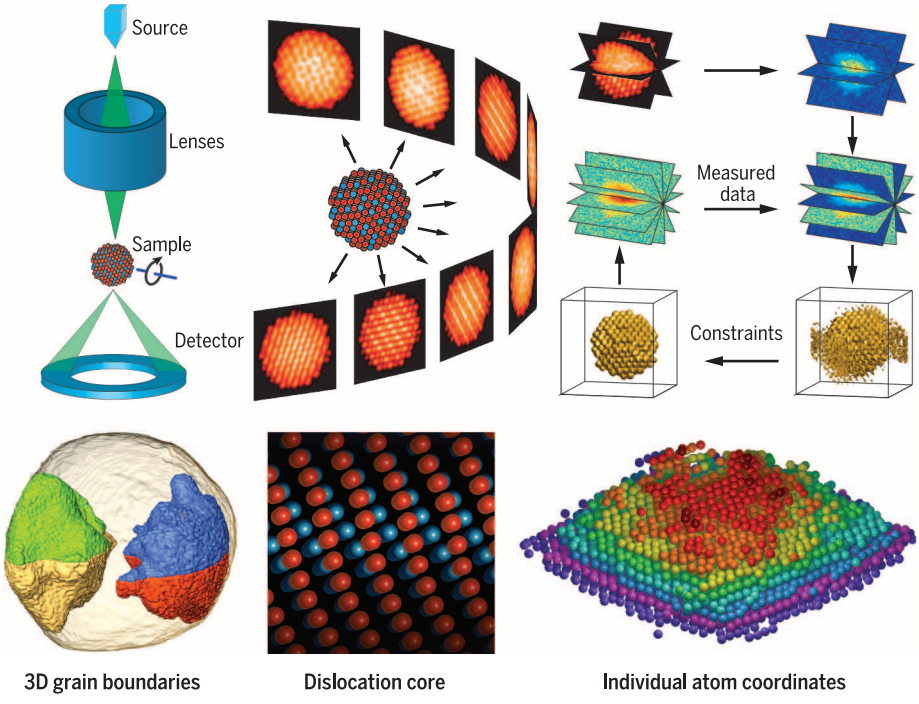

Atomic electron tomography (AET) and its transformative impact on the physical sciences. (**Top**) Schematic diagram of AET, in which 2D images are measured with an advanced electron microscope by tilting a sample to many different orientations. The 3D structure of the sample is iteratively reconstructed from the images, and the coordinates of individual atoms are localized. (**Bottom**) AET enables 3D imaging of crystal defects—such as grain boundaries, stacking faults, dislocations, and point defects—at atomic resolution. The ability to precisely determine the 3D coordinates of individual atoms allows direct measurements of atomic displacements and the full strain tensor in materials.

ADVANCES: Major developments in aberration-corrected electron microscopes, advanced detectors, data acquisition methods, powerful 3D image reconstruction, and atom-tracing algorithms have placed one method—atomic electron tomography (AET)—on the cusp of this breakthrough. In recent years, AET has been used to image the 3D structure of grain boundaries and stacking faults and the 3D core structure of edge and screw dislocations at atomic resolution. This technique has also revealed the existence of atomic steps at 3D twin boundaries that are hidden in conventional 2D projections. Furthermore, the combination of AET and atom-tracing algorithms has enabled the determination of the coordinates of individual atoms and point defects in materials with a 3D precision of ~19 pm, allowing direct measurements of 3D atomic displacements and the full strain tensor. Finally, the single-particle reconstruction method developed in cryo-EM has been applied for 3D structure determination of small (≤2-nm) gold nanoparticles and heterogeneous platinum nanocrystals at atomic-scale resolution.

ON OUR WEBSITE

Read the full article at http://dx.doi.org/10.1126/science.aaf2157

OUTLOOK: The future research frontiers of AET involve increasing the sample complexity (including real materials with different atomic species and disordered systems), image contrast (determining the 3D atomic positions of both heavy and light elements), detection sensitivity (revealing individual atoms at surfaces and interfaces), and data acquisition speed (probing the dynamics of individual atoms and defects). The ability to precisely determine all atomic coordinates and species in real materials without assuming crystallinity will transform our understanding of structure-property relationships at the most fundamental level. For instance, using atomic coordinates as inputs to first-principles calculations, it is possible to compute the effect on the material properties of each defect and atomic reorganization, giving precious clues about how to modify and engineer materials at the atomic level to yield better performance in a device. Catalysis involves atoms interacting on nanoparticle surfaces in poorly understood ways, and the mechanisms of particle growth in synthesis reactors or in devices under load are largely unknown. Breakthroughs in our ability to reliably measure this information in 3D will have effects across disciplines from electronics and catalysis to energy conversion. ■

The list of author affiliations is available in the full article online.
*Corresponding author. Email: miao@physics.ucla.edu
Cite this article as J. Miao *et al.*, *Science* **353**, aaf2157 (2016).
DOI: 10.1126/science.aaf2157

Downloaded from http://science.sciencemag.org/ on September 30, 2016

REVIEW

MATERIALS SCIENCE

Atomic electron tomography: 3D structures without crystals

Jianwei Miao,[1]* Peter Ercius,[2] Simon J. L. Billinge[3,4]

Crystallography has been fundamental to the development of many fields of science over the last century. However, much of our modern science and technology relies on materials with defects and disorders, and their three-dimensional (3D) atomic structures are not accessible to crystallography. One method capable of addressing this major challenge is atomic electron tomography. By combining advanced electron microscopes and detectors with powerful data analysis and tomographic reconstruction algorithms, it is now possible to determine the 3D atomic structure of crystal defects such as grain boundaries, stacking faults, dislocations, and point defects, as well as to precisely localize the 3D coordinates of individual atoms in materials without assuming crystallinity. Here we review the recent advances and the interdisciplinary science enabled by this methodology. We also outline further research needed for atomic electron tomography to address long-standing unresolved problems in the physical sciences.

Perfect crystals are rare in nature, and much of our modern science and technology depends on crystals with defects and noncrystalline systems (*1*–*7*). In fact, these systems are the rule rather than the exception; they include high-strength structural materials (dislocations and grain boundaries) (*1*, *2*), information processing (defects and dopants in semiconductors) (*3*), heterogeneous catalysis (reactions on nanoparticle surfaces) (*7*), renewable energy (amorphous silicon) (*8*), energy storage (solid electrolyte glasses and oxides) (*9*), telecommunication and computer networking (optical fibers) (*10*), high-efficiency transformers (metallic glasses) (*6*), and nonvolatile memory (amorphous-crystalline transitions) (*11*). In these applications, it is not just the average structure but also the defects and crystalline imperfections that need to be engineered to obtain the desired properties. Presently, several methods can be used to image crystal defects and noncrystalline specimens, but each has its limitations. Transmission electron microscopy (TEM) has long been used to produce images of crystal defects and dislocations at atomic resolution (*12*), but these are two-dimensional (2D) projection images and are not fully representative of the underlying 3D structures (*13*, *14*). Scanning probe microscopy can provide subatomic resolution only for surface structure (*15*). Although coherent diffractive imaging can determine the 3D structure of noncrystalline specimens and nanocrystals at the nanoscale resolution (*16*–*18*), it requires the further development of coherent x-ray and electron sources, detectors, and advanced image reconstruction algorithms to achieve 3D atomic resolution (*19*–*22*). Atom probe tomography enables the 3D reconstruction of billions of atoms from a tip specimen but cannot offer true atomic resolution because of imperfect spatial resolution and limited detection efficiency (*23*, *24*).

One powerful method to address this major challenge that is under rapid development in both the physical and biological sciences is electron tomography. Electron tomography was developed in 1968 (*25*–*27*) and has been primarily applied to image the 3D structure of biological specimens by rapidly freezing them at cryogenic temperatures (*28*). For cells and cellular organelles, cryo–electron tomography can achieve a 3D resolution of 2 to 5 nm (*29*–*31*), which is mainly limited by radiation damage to the sample (*32*). For large protein molecules with identical or similar conformations, single-particle cryo–electron microscopy (cryo-EM) has been used to image the average 3D structure at near-atomic resolution without the need for crystallization (*33*–*37*), driven by the recent advances in direct electron detectors (*38*), image processing, and reconstruction methods (*39*, *40*). However, these methods cannot be generally applied to solve the 3D atomic structure of physical science samples for the following three reasons. First, most materials do not have identical copies and therefore cannot be averaged to achieve atomic resolution. For example, from one crystallite to another, the structure of a dislocation will be similar (there is a well-defined structural solution) (*1*, *2*), but the location of the dislocation at the atomic scale will differ. Averaging over different crystallites will eliminate the signal of the defect. Thus, we need a method sensitive enough to detect the 3D positions of individual atoms buried in a single object. Second, for protein molecules, a priori knowledge such as the atomic structure of amino acid residues and the peptide sequence of the molecules provides important constraints that greatly reduce the experimental information required for their 3D structure determination (*41*). This knowledge is not applicable to physical science samples. Third, unlike biological specimens, diffraction and phase contrast in the TEM images of most physical science samples prevent the direct application of tomographic reconstruction (*13*, *14*) and require greater ingenuity to solve the reconstruction problem. Despite these challenges, the past few years have seen breakthroughs in the development of atomic electron tomography (AET), which enables 3D structure determination of crystal defects and potentially disordered systems at atomic resolution (*42*–*51*). Here we review the recent advances of AET and the interdisciplinary science enabled by this methodology.

Aberration-corrected electron microscopy

The first TEM to surpass the resolution of the optical microscope was built by Ernst Ruska in the 1930s (*52*). During early research to further improve this instrument, Otto Scherzer realized that a TEM's resolution would always substantially underperform relative to the expected wavelength of the accelerated electrons because of geometrical aberrations inherent to the round electron lenses themselves (known as the Scherzer theorem) (*53*). The most limiting of these aberrations is the well-known third-order spherical aberration, which cannot be corrected with a round lens. In 1947, the use of optical elements with nonrotational symmetry was proposed to compensate for this inherent limitation (*54*). In effect, a set of lenses could be devised that created the exact opposite effect of the aberrations induced by a conventional round lens, and the two effects would cancel out.

Decades of research and development in this area have led to the current generation of aberration-corrected electron microscopes (*55*–*58*), which reach ~0.5 Å resolution with much-improved contrast (*59*). Such high-resolution and high-contrast images benefit the AET reconstruction, allowing precise determination of the 3D coordinates of individual atoms in materials (*49*). Increases in signal-to-noise ratio and image quality also reduce the required beam dose delivered to the sample. On the other hand, aberration-corrected electron lenses reduce the depth of field and limit the sample thickness (*60*). This problem can be overcome by acquiring a through-focal series at each tilt angle. Furthermore, the limited depth of field can also be used as an advantage for observing depth-dependent atomic structures in crystals (*61*). Collectively, the combination of aberration-corrected electron microscopes and AET will greatly facilitate the

[1]Department of Physics and Astronomy and California NanoSystems Institute, University of California, Los Angeles, CA 90095, USA. [2]National Center for Electron Microscopy, Molecular Foundry, Lawrence Berkeley National Laboratory, Berkeley, CA 94720, USA. [3]Department of Applied Physics and Applied Mathematics, Columbia University, 200 Mudd Building, 500 West 120th Street, New York, NY 10027, USA. [4]Department of Condensed Matter Physics and Materials Science, Brookhaven National Laboratory, Upton, NY 11973, USA.
*Corresponding author. Email: miao@physics.ucla.edu

Downloaded from http://science.sciencemag.org/ on September 30, 2016

3D characterization of materials at the single-atom level.

Atomic STEM tomography

Acquisition of tomographic tilt series

Although TEM-based tomography has been widely applied in the biological sciences (*29*–*31*, *33*–*37*), a major limitation for the physical science application is the presence of diffraction and phase contrast (*13*, *14*, *62*, *63*). This limitation can be overcome by using the scanning transmission electron microscopy (STEM) mode and an annular dark-field (ADF) detector (*64*–*70*). In ADF-STEM, an electron beam is focused to a small spot and scanned over a sample to form a 2D image (Fig. 1A). The scattered signal at each scanning position is recorded by the ADF detector, which consists of a sensitive annular region with inner and outer angles ranging from a few tens to several hundreds of milliradians, respectively (*71*–*73*). By measuring the signal only at high angles, ADF-STEM satisfies the incoherent imaging approximation in which diffraction and phase contrast are substantially suppressed and the image intensity is approximately proportional to the sample thickness and the atomic number as $Z^{1.8}$ (*71*–*73*). To acquire a tomographic tilt series, the sample is rotated around a tilt axis and a series of 2D images is measured at different tilt angles (Fig. 1B). Due to geometric constraints, most samples cannot be tilted beyond ±79°, which is known as the missing wedge problem. One solution to this problem is to use needle-shaped specimens (*49*), allowing a full rotation around the axis of the needle. Another problem in STEM tomography is the electron beam damage to the specimen. This can be mitigated through a combination of approaches, including (i) choosing low operating voltages (such as 80 and 120 keV) to reduce the knock-on damage (*74*); (ii) using a dose-efficient STEM method (*75*), coupled with a direct electron detector (*37*); (iii) depositing a very thin layer of carbon film on the surface of the specimen (*44*); and (iv) implementing a low-exposure acquisition scheme—when acquiring an image at a tilt angle, a nearby sample is used to align and focus the image, thus reducing the unnecessary electron dose to the sample under study (*42*, *44*).

After the acquisition of an experimental tilt series, sample drift and scan distortion are corrected to minimize the experimental error (*49*). Advanced denoising techniques can also be applied to improve the image quality (*76*). The alignment of the tilt series is achieved by the center-of-mass method (*42*), which is based on the fact that the center of mass of a 3D object coincides with that of its projection images. By aligning all of the 2D images to the center of mass, a coarse alignment of the tilt series is accomplished. To achieve subangstrom precision, a fine alignment must be implemented by computing a 3D reconstruction from the coarse-aligned tilt series. The 3D reconstruction is back-projected to calculate a sequence of images at the corresponding experimental tilt angles. Quantitative comparison of the calculated and measured images allows fine-tuning of the alignment. This process is iterated until the alignment procedure converges.

Iterative algorithms for atomic tomographic reconstruction

To achieve atomic tomographic reconstruction, three issues associated with experimental tilt series must be addressed. First, the data are incomplete due to the missing wedge problem and because radiation damage limits the number of images. Second, there are experimental errors in the tilt series, such as small structure changes of the specimen during data acquisition, the mechanical tilt error of a sample stage, sample drift, and scanning distortion. Third, noise is present in every image. Although careful sample preparation, data acquisition, and denoising techniques can alleviate the experimental errors and reduce noise (*44*, *49*, *76*), iterative tomographic reconstruction algorithms are more suited to tackle the incomplete data issue than noniterative methods. Presently, there are two types of iterative algorithms for tomographic reconstruction. The first are real-space iterative algorithms, such as the algebraic reconstruction technique (ART), the simultaneous ART (SART), and the simultaneous iterative reconstruction technique (SIRT) (*77*–*79*). These algorithms compute a 3D reconstruction by iteratively solving a system of linear equations, in which positivity and mathematical regularization can be incorporated as constraints to reduce artifacts. Recently, SIRT has been applied to determine the 3D structure of a decahedral gold nanoparticle and a silver-gold nanocluster at atomic resolution (*50*, *51*).

The second type of algorithms iterates between real and Fourier space, an example being equal slope tomography (EST) (*80*–*84*), where the angles of a tomographic tilt series are spaced by equal slope instead of equal angle increments. The equal slope acquisition scheme allows the use of a variant of the fast Fourier transform (FFT), the pseudopolar FFT (PPFFT) (*85*). The PPFFT and its inverse are mathematically faithful and have a computing time comparable to that of the FFT. From an aligned tilt series, each image is inverted to a Fourier slice by a generalized Fourier transform called the fractional Fourier transform (Fig. 1C) (*86*). Using the inverse PPFFT, a 3D reconstruction is computed from this set of Fourier slices. Two general physical constraints are then applied to the reconstruction. First, a loose support (i.e., a 3D boundary larger than the shape of a specimen) is defined, and the intensity outside the support is set to zero. Next, any negative intensity inside the support is set to zero (positivity constraint), which produces a revised 3D reconstruction. The forward PPFFT is applied to the revised reconstruction, generating a full set of Fourier slices. The Fourier slices corresponding to the measured tilt angles are replaced with the experimental data, and the remaining slices are kept unchanged (Fig. 1C). This step produces a new full set of Fourier slices as an input for the next iteration. Progress is monitored by an error metric defined as the difference between the computed and measured slices at each iteration step, and the algorithm is terminated when no further improvement can be made (*80*–*84*). This entire process is then repeated using a tighter support, closer to the real shape of the object. After fine-tuning of the alignment with more iterations, a final 3D reconstruction is obtained. Through iterating between real and Fourier space, EST is gradually guided toward a best-possible solution that is concurrently consistent with the measured data and the general physical constraints. Quantitative comparison with experimental data indicates that EST produces 3D reconstructions with higher resolution, better contrast, and less distortion than real-space iterative algorithms such as ART and SART for a limited number of 2D images and a missing wedge (*81*). Furthermore, if needed, EST can also incorporate mathematical regularization

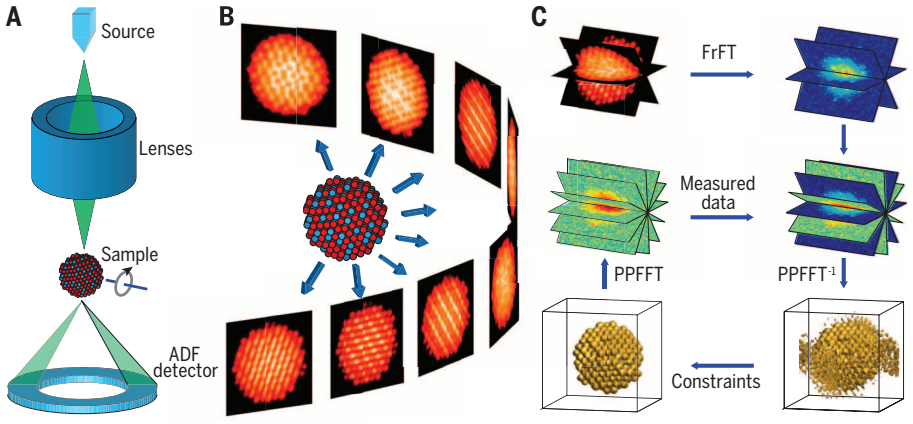

Fig. 1. Schematic layout of AET. (**A**) An electron beam is focused on a small spot and scanned over a sample to form a 2D image. The integrated signal at each scanning position is recorded by an ADF detector. (**B**) By rotating the sample around a tilt axis, a series of 2D images is measured at different tilt angles. (**C**) After preprocessing and alignment, the tilt series is inverted to Fourier slices by the fractional Fourier transform (FrFT). A 3D reconstruction is computed by using a Fourier-based iterative algorithm. From the 3D reconstruction, the coordinates of individual atoms are traced and refined to produce the 3D atomic model of the sample.

Downloaded from http://science.sciencemag.org/ on September 30, 2016

identical to real-space iterative algorithms (82–84). The drawback of EST is the requirement that the experimental tilt angles must be consistent with equal slope increments (80).

Two other methods have also been applied to AET through the incorporation of additional a priori constraints. By fitting atoms rigidly onto a crystal lattice, discrete tomography has been implemented to image the 3D atomic structure of a silver nanoparticle embedded in an aluminum matrix using only two high-angle ADF (HAADF)–STEM images (70). However, the crystallinity requirement limits the applicability of this approach, and the small number of images make this method sensitive to experimental errors and noise. A second approach is to reduce the input information needed through the use of compressed sensing electron tomography (87–89), which is based on the principle that a physically meaningful structure is usually sparse in some domain. If the sparse domain can be found, then the 3D structure can be reconstructed from a very small number of images (89). Compressed sensing electron tomography has been applied to image localized surface plasmon resonances of a silver nanocube (90) and to reach the atomic scale. By using only four or five HAADF-STEM images, the 3D structures of a gold nanorod and a core-shell Au@Ag nanorod have been imaged at atomic resolution (43, 45). However, it remains a challenge to find an appropriate sparse domain for each tomographic reconstruction. Furthermore, there are adjustable parameters in compressed sensing tomography, which vary for different samples. It is not straightforward to choose these parameters, especially with the presence of noise and experimental errors (89).

3D determination of the coordinates of individual atoms in materials

To probe material properties and functionality at the most fundamental scale, the 3D coordinates of individual atoms need to be determined from the 3D reconstruction, which can be accomplished using the following procedure (49). First, all local intensity maxima are identified from the 3D reconstruction and sorted from highest to lowest. Starting from the highest intensity, a 3D Gaussian function is fit to each peak. If a minimum distance between two neighboring atoms is satisfied, the peak of the Gaussian function is labeled as a candidate atom position, and the Gaussian function is subtracted from the 3D reconstruction. This step is repeated for all local maximum peaks. Second, a 3D atom profile is calculated by averaging the Gaussian functions of the most plausible atoms, excluding peaks with extremely high or low intensity. The Gaussian function of each candidate atom is quantitatively compared with the average atom profile. If the candidate atom matches more with the average atomic than the background, it is identified as an atom. This step produces a 3D atomic model. Third, a refinement procedure is implemented to improve the precision of the atom model using the measured images. Each measured image is Fourier transformed to produce a Fourier slice, and a corresponding Fourier slice is also calculated from a linear projection of the atomic coordinates. The positions of all atoms are iteratively refined by minimizing the difference between the measured and calculated Fourier slices. The refined atomic model is then compared with the 3D reconstruction, and a very small percentage of atoms are manually adjusted to ensure that they are consistent with the reconstructed intensity and the local stereochemistry of the material (41). An updated atomic model is obtained and refined once again with the measured data. This step is repeated until no further improvements can be made. Fourth, to verify the final atomic model, 2D images are calculated from the atomic coordinates using multislice simulations with the same experimental parameters (91). After adding noise, the calculated images should agree well with the measured ones. Furthermore, by using the same reconstruction, atomic tracing, and refinement procedures, a new 3D atomic model can be computed from the noisy multislice images. This model must be consistent with the final model; otherwise, the whole atom tracing and refinement process must be redone to obtain a final model. Although the procedures described here focus on samples with a single atomic species, they can, in principle, be extended to determine the coordinates of multiple atomic species in materials based on the Z-contrast of STEM images (46).

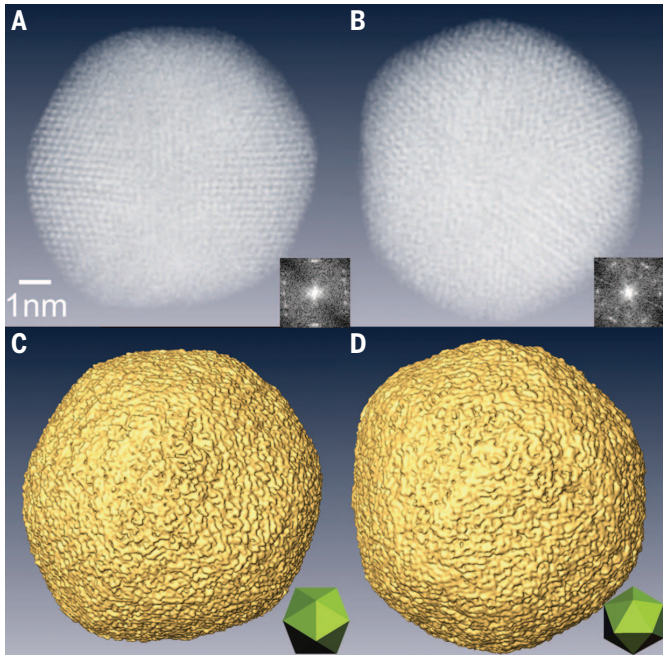

Fig. 2. Experimental demonstration of AET without assuming crystallinity or using averaging. (**A** and **B**) Volume renderings of the 3D reconstruction of a gold nanoparticle and their Fourier transforms (insets) along the two- and threefold symmetry directions, respectively. Individual atoms are visible in the reconstruction, and several major 3D grains are identified at atomic-scale resolution. (**C** and **D**) Surface renderings of the 3D reconstruction along the two- and threefold symmetry directions, respectively, indicating that this is a multiply twinned icosahedral nanoparticle. The insets show an icosahedron model along the same symmetry directions. [From (42)]

Single-particle reconstruction: From 3D structure determination of macromolecules to small metal nanoparticles at atomic-scale resolution

Single-particle cryo-EM has become a very important method for 3D structure determination of macromolecules at near-atomic resolution (33–37). High-resolution imaging of biological materials at room temperature is difficult in the transmission electron microscope due to electron beam damage and the low scattering contrast of light atoms such as carbon (32). Plunge freezing of buffered aqueous solutions to produce vitreous ice containing purified biological molecules was developed to prepare the structure for imaging in their native hydrated state (28). Noisy projection images of individual molecules with identical or similar conformations can be acquired at very low doses (20 to 40 electrons per Å^2). Traditionally, hundreds of thousands to millions of such images are first classified, averaged, and then oriented in 3D space to produce a tomographic reconstruction of the molecule (33). Until recently, the resolution of this technique was generally limited to >4 Å because the extremely low doses resulted in noisy images with poor contrast (33). High-resolution structures have only become achievable with the development of the direct electron detector, resulting in a revolution in cryo-EM with near atomic (<4 Å) resolution (34–37). The direct electron detector provides substantially better quantum efficiency, point spread function, and acquisition speed than a traditional scintillator paired with a charge-coupled device, allowing the accurate determination of the position of individual electron strikes (38). Rapidly acquired images can also be aligned and averaged to high accuracy to remove sample drift and beam-induced motion during acquisition (92). Furthermore, through a combination of statistical approach and prior knowledge, advanced 3D reconstruction algorithms have been developed to extract as much structure information as possible from very noisy cryo-EM data (39, 40).

Single-particle 3D reconstruction developed for cryo-EM has also been applied to image small (≤2 nm) metal clusters at atomic-scale resolution.

Downloaded from http://science.sciencemag.org/ on September 30, 2016

Homogeneous gold clusters consisting of 68 atoms were imaged at random orientations with an aberration-corrected TEM. These 2D images were then combined to determine the 3D atomic structure of the gold cluster (*47*). In situ TEM was also coupled with a fast-acquisition direct electron detector to image platinum nanocrystals freely rotating in a graphene liquid cell. By acquiring many images at different orientations, the 3D structure of individual heterogeneous nanocrystals was determined at near-atomic resolution (*48*). In addition to single-particle 3D reconstruction, TEM-based methods have also been demonstrated to determine the 3D atomic positions of two-layer graphene (*93*) utilizing the curvature of the scattered electron wave (*94*) and the 3D atomic morphology of a thin MgO crystal (*95*), each of which was achieved from a single sample orientation.

Interdisciplinary science enabled by AET

3D imaging of crystal defects in materials at atomic resolution

Crystal defects such as point defects, dislocations, grain boundaries, and stacking faults strongly influence material properties and are crucial to materials engineering (*1*–*3*). Although a number of experimental methods have been used to image crystal defects since the 1950s (*12*, *96*–*99*), 3D imaging of the atomic arrangements in the cores of dislocations, grain boundaries, and stacking faults has only recently become possible through the use of AET. By combining ADF-STEM with EST, AET was first demonstrated to image a gold nanoparticle at 2.4 Å resolution without assuming crystallinity or using averaging (*42*). Figure 2, A to D, shows volume and iso-surface renderings of the 3D reconstruction, indicating that this is a multiply-twinned icosahedral nanoparticle. Individual atoms are visible in the reconstruction, and several major 3D grains are identified at atomic-scale resolution.

To probe crystal defects at higher resolution and contrast, AET was applied to image the 3D structure of a platinum nanoparticle from a large number of STEM images (*44*). Due to the weak signal from individual atoms, 3D Fourier filtering was used to enhance the signal-to-noise ratio of the reconstruction. As this may potentially introduce artifacts (*100*, *101*), two independent approaches were implemented to verify the results of using the Fourier filtering. First, multislice STEM calculations were combined with EST to examine and optimize the filtering parameters while avoiding artifacts. Second, well-established Wiener filtering was used to corroborate the experimental results (*102*). Figure 3, A and B, shows the grain boundaries of the platinum nanoparticle after independent filtering verification. A measured 2D image suggests that this is a multiply twinned decahedral nanoparticle with flat twin boundaries (Fig. 3A).

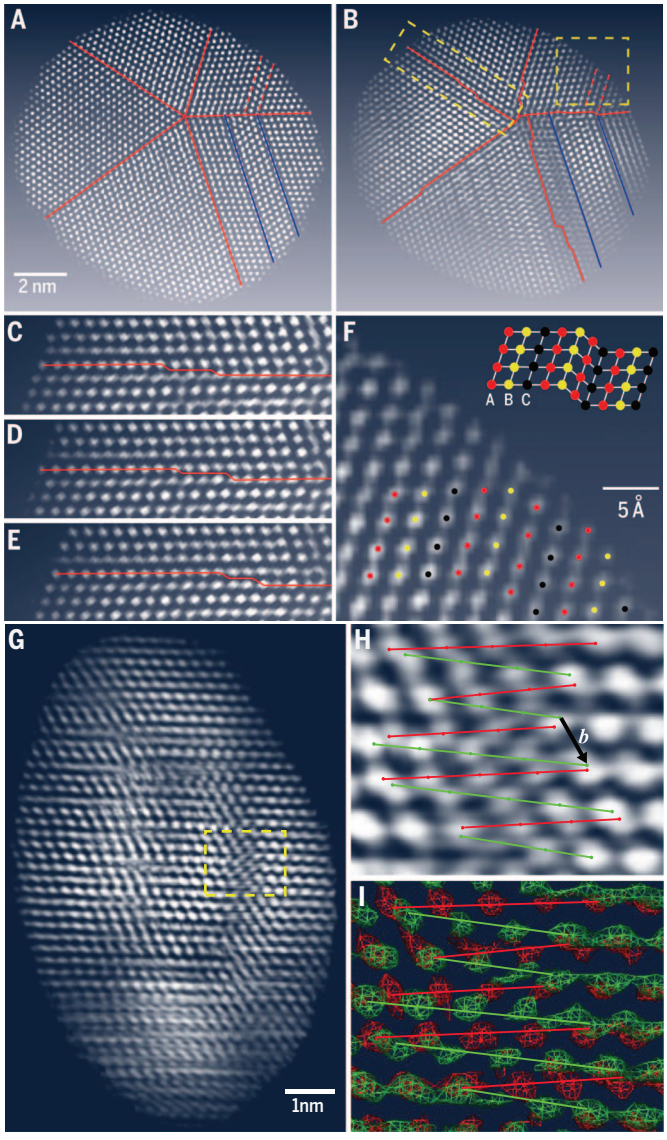

Fig. 3. 3D imaging of crystal defects in materials at atomic resolution. (**A**) STEM image of a decahedral platinum nanoparticle, showing flat twin boundaries. (**B**) A 2.6 Å thick internal atomic layer of the nanoparticle reconstructed by AET, revealing that the twin boundaries are not flat but instead form atomic steps. Boxed areas indicate a grain boundary and a stacking fault. (**C**) Enlarged view of the grain boundary in (B). (**D** and **E**) A 2.6 Å thick atomic layer above and below the layer shown in (C). The three consecutive internal atomic layers further confirm that the atomic steps continuously vary along the consecutive layers. (**F**) Enlarged view of the 2.6 Å thick stacking fault in (B), which ends at a twin boundary. The inset shows a classical model of an fcc extrinsic stacking fault. (**G**) A 5.3 Å thick internal slice (two atomic layers) of the nanoparticle reconstructed by AET. (**H** and **I**) 3D volume and surface renderings of an enlarged view of the core of a screw dislocation in (G) with the Burgers vector (**b**) of $\frac{1}{2}[01\bar{1}]$. [From (*44*)].

However, an internal atomic layer reveals that the twin boundaries are not flat but instead form atomic steps (Fig. 3B). Three consecutive internal atomic layers further confirm that the atomic steps continuously vary along the consecutive atomic layers (Fig. 3, C to E). Figure 3B also shows that the subgrain boundaries in an internal atomic layer are slightly widened relative to those in the 2D image (Fig. 3A). In relation to the grain boundary, a stacking fault is also observed at the single-atom level (Fig. 3F), which ends at a twin boundary (Fig. 3B). Furthermore, from the 3D reconstruction of the platinum nanoparticle, the 3D core structure of both edge and screw dislocations are imaged at atomic resolution (*44*). Figure 3G shows a 5.3 Å thick internal slice of the nanoparticle, and a zigzag pattern, a characteristic feature of a screw dislocation core, is visible in the enlarged views (Fig. 3, H and I). The Burgers vector of the screw dislocation was measured to be $\frac{1}{2}[01\bar{1}]$. Careful examination of the locations of the screw dislocation and the atomic steps at the twin boundary indicates that they are associated with a strain relaxation mechanism for the multiply twinned decahedral nanoparticle (*44*). These results indicate that AET is crucial to probing crystal defects in materials as 2D projection images may sometimes provide deceptive structural information.

3D measurements of the atomic displacements and the full strain tensor in materials

The structural, mechanical, electronic, and optical properties of many materials are directly related to the strain in the materials (*1*, *2*, *103*). However, conventional methods to measure local strain at the nanoscale, using TEM, electron diffraction, and holography, are limited to 2D (*103*–*105*). Although coherent diffractive imaging, x-ray diffraction microscopy, and through-focal ADF imaging can measure the strain tensor in 3D (*17*, *19*, *106*, *107*), they offer limited spatial resolution. Recently, the 3D strain field in a gold nanorod was imaged at high resolution using compressed sensing electron tomography (*43*). However, because this method used four STEM images, only one of the six components of the strain tensor (ε_{zzz}) was measured. In order to determine the full strain tensor in materials with high precision and spatial resolution, a method must be able to precisely localize the coordinates of individual atoms without assuming crystallinity.

Downloaded from http://science.sciencemag.org/ on September 30, 2016

AET was recently used to determine the 3D positions of individual atoms in a tungsten needle sample (*49*). A tilt series of 62 images was measured with an aberration-corrected ADF-STEM. By combining EST with 3D atom tracing and refinement procedures, the coordinates of 3769 individual atoms of the needle apex were determined with a precision of about 10.5, 15, and 5.5 pm along the *x*, *y*, and *z* axes, respectively (i.e., ~19 pm in three dimensions) (Fig. 4A) (*49*). The ability to precisely localize the individual atom positions with AET is attributed to minimizing the dynamical scattering effect by avoiding the exact zone axes and measuring many images at different sample orientations (i.e., a rotational average), which is analogous to the reduction of dynamical effects in precession electron diffraction (*108*). Furthermore, a point defect is identified in the 3D reconstruction with high precision (*49*). Figure 4, B and C, shows the reconstructed intensity and its surface rendering surrounding a point defect in layer six, indicating that there is no tungsten atom in the defect site. Although field ion microscopy has been applied to obtain 3D information of atoms and vacancies in needle-shaped specimens with a priori assumptions and low precision (*109*, *110*), 3D identification and localization of point defects in materials at high precision without any prior knowledge has been considered to be one of the ultimate goals in materials characterization.

By comparing the coordinates of individual atoms (Fig. 4D) with an ideal tungsten crystal lattice, the atomic displacement field and the strain tensor were determined in three dimensions (*49*). As the strain measurements require differentiation of the displacement field and are sensitive to noise, a 5.5 Å wide 3D Gaussian kernel was convolved with the displacement field to enhance the signal-to-noise ratio and precision. Figure 4, E to G, shows the 3D atomic displacements of the tungsten needle sample, exhibiting expansion in the $[0\bar{1}1]$ direction (*x* axis) and compression in the [100] direction (*y* axis). The atomic displacements along the [001] direction (*z* axis) are much smaller than those in the *x* and *y* axes. The six components of the strain tensor (ε_{xx}, ε_{yy}, ε_{zz}, ε_{xy}, ε_{xz}, and ε_{yz}) were obtained from the convolved displacement field with a 3D resolution of 1 nm and a precision of 10^{-3} (Fig. 4, H to M). The ε_{xx} and ε_{yy} maps show features related to the lattice expansion and compression along the *x* and *y* axes, respectively, while the ε_{zz} component is smaller and smoother. Shear in the *xy*, *xz*, and *yz* planes is observed in the ε_{xy}, ε_{xz}, and ε_{yz} maps. The principal strains were determined to be 0.81%, −0.87%, and −0.15% along the [0.074 0.775 −0.628], [0.997 −0.083 0.015], and [0.041 0.627 0.778] directions, respectively. Further experimental, density functional theory (DFT), and molecular dynamics results have confirmed that the strain was induced by surface tungsten carbide and the diffusion of carbon atoms below the tungsten surface (*49*). As conventional methods for strain measurements are primarily based on geometric-phase analysis of crystalline samples in Fourier space (*103*, *104*), the ability to precisely determine the 3D positions of individual atoms opens the door toward directly measuring the strain tensor in materials at the atomic scale (*49*–*51*).

3D structure determination of ligand-protected gold nanoparticles at atomic resolution

Ligand-protected gold nanoparticles on the order of 1 to 2 nm in diameter exhibit different electronic and optical properties from bulk materials and are expected to find broad applications in several disciplines (*111*). However, these water-soluble nanoparticles are difficult to crystallize, and only a small number of structures have been solved by x-ray crystallography (*112*). Single-particle 3D reconstruction was recently applied to determine the structure of ligand-protected Au nanoparticles at atomic resolution (*47*). In this experiment, 939 aberration-corrected TEM images of homogeneous 68-gold-atom nanoparticles (Au_{68}NPs) were used to reconstruct the 3D structure. Figure 5A shows the reconstructed intensity and the positions of all 68 gold atoms. The 3D atomic model of the Au_{68}NP reveals that a gold atom at the center is surrounded by a cagelike cuboctahedron of 12 atoms. Twenty-four additional atoms form a face-centered cubic (fcc)–like shell around the cuboctahedron, whereas the remaining 31 atoms deviate from fcc packing (Fig. 5B). Because the surface ligand molecules and sulfur atoms cannot be measured by this method, 32 sulfur atoms were manually added to

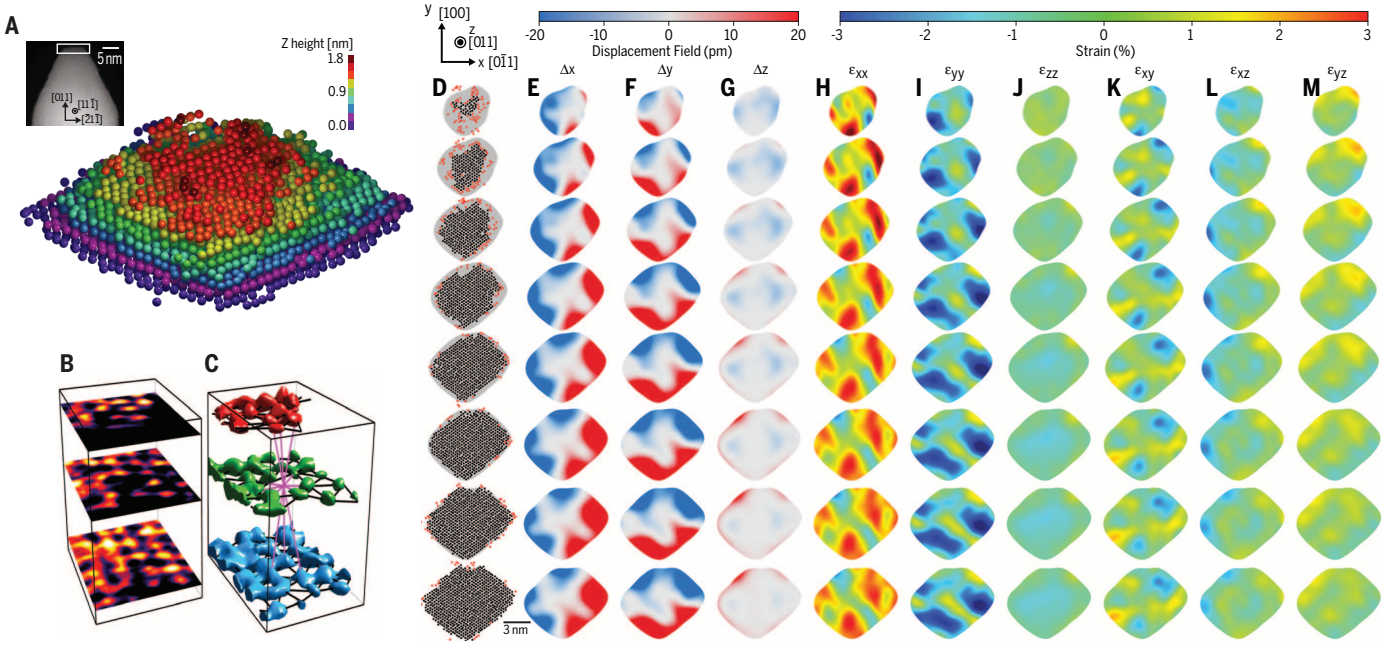

Fig. 4. 3D measurements of individual atom coordinates, atomic displacements, and the strain tensor in materials. (**A**) Coordinates of 3769 individual atoms determined from the top nine layers of a tungsten needle sample (inset) with a 3D precision of ~19 pm. Layers one to nine are shown in dark red, red, orange, yellow, green, cyan, blue, magenta, and purple, respectively. (**B** and **C**) 3D reconstructed intensity and its surface rendering surrounding a point defect in layer six of the needle sample. (**D**) Individual atoms in layers two to nine of the tungsten needle sample used to determine the atomic displacements and the strain tensor. Layer one and some surface atoms in red were excluded due to their large deviation from an ideal body-centered cubic lattice. (**E** to **G**) 3D atomic displacements of the needle sample, exhibiting expansion in the $[0\bar{1}1]$ direction (*x* axis) and compression in the [100] direction (*y* axis). (**H** to **M**) The ε_{xx}, ε_{yy}, ε_{zz}, ε_{xy}, ε_{xz}, and ε_{yz} components of the strain tensor. The ε_{xx} and ε_{yy} components exhibit features directly related to the lattice expansion and compression along the *x* and *y* axes, respectively. Shear in the *xy*, *xz*, and *yz* planes is visible in the ε_{xy}, ε_{xz}, and ε_{yz} maps, respectively. [From (*49*)]

Downloaded from http://science.sciencemag.org/ on September 30, 2016

the final model based on the positions of the gold atoms and the local stereochemistry (Fig. 5C). DFT calculations were used to relax the final atomic model to a local minimum energy, confirming that the positions of most gold atoms remain the same (Fig. 5D) (*47*, *113*). Several surface atoms deviate from measured positions, probably because of hydrogen bonding between surface ligands. The 3D atomic model of Au_{68}NP determined from this experiment exhibits lower symmetry than that of Au_{102}NP and is also different from the theoretical prediction of the highly symmetrical atomic structure of a similar nanoparticle, $Au_{67}(SR)_{35}$. This work shows that single-particle 3D reconstruction can be used to determine the atomic structure of small (≤2 nm) and homogeneous metal nanoparticles that are difficult to crystallize. To achieve a full 3D reconstruction of both the highly scattering and lightly scattering atoms (such as ligand molecules), further improvements could involve the use of direct electron detectors to improve the signal-to-noise ratio and reduce the radiation dose (*38*). Also, imaging of frozen hydrated samples in vitreous ice could provide the structure of the nanoparticles in their native solvated state (*33*).

3D structure of individual heterogeneous nanoparticles in solution at near-atomic resolution

In situ liquid cell using graphene offers the opportunity to image single objects at atomic resolution under dynamic conditions (*114*). It was noticed that the objects are randomly rotating in solution, providing many different views that could be used in electron tomography. This led to the development of 3D structure determination of heterogeneous nanoparticles at near-atomic resolution using the single-nanoparticle reconstruction method (*48*). In this first experiment, platinum nanoparticles were chosen for their high scattering signals and scientific importance in catalysis applications. Two sheets of graphene were used to contain a solution of the nanocrystals within the vacuum of an aberration-corrected TEM. A fast acquisition direct electron detector was used to rapidly acquire many images of the nanoparticles freely rotating in solution (*38*). An ab initio single-particle reconstruction approach was used to determine projection orientations stochastically without fitting to an a priori model (*115*), thus avoiding model bias. The final reconstructions of two individual ~2-nm diameter platinum nanoparticles reach near-atomic resolution (Fig. 6).

Figure 6, A and B, shows the 3D reconstruction of two nanoparticles and the cross-sectional views along the vertical plane, respectively. The overall nonsymmetric structures of the two nanoparticles are similar and described as a central disc of {111} atomic planes with two conical crystalline protrusions attached by screw dislocations on either end of the disc (Fig. 6C) (*48*). The observation of screw dislocations in platinum nanoparticles independently confirms the earlier AET results (*44*), suggesting that the 3D atomic structure of nanoparticles is more complex than previously thought. Figure 6D shows the 3D structure of the nanoparticles viewed along the conical protrusion direction. The crystalline lattices of the protrusion (Fig. 6D) and the core (Fig. 6E) form a tilt angle of 14° for particle one and 7° for particle two (Fig. 6F). Additional differences between the two structures of the nanoparticles include surface morphology and the degree of crystallinity in each domain. Calculations of the exposed-surface free energy and grain-boundary free energy indicate a strong driving force for coalescence and support that the orientation of the side protrusions with respect to the central section are the minimum energy of the system.

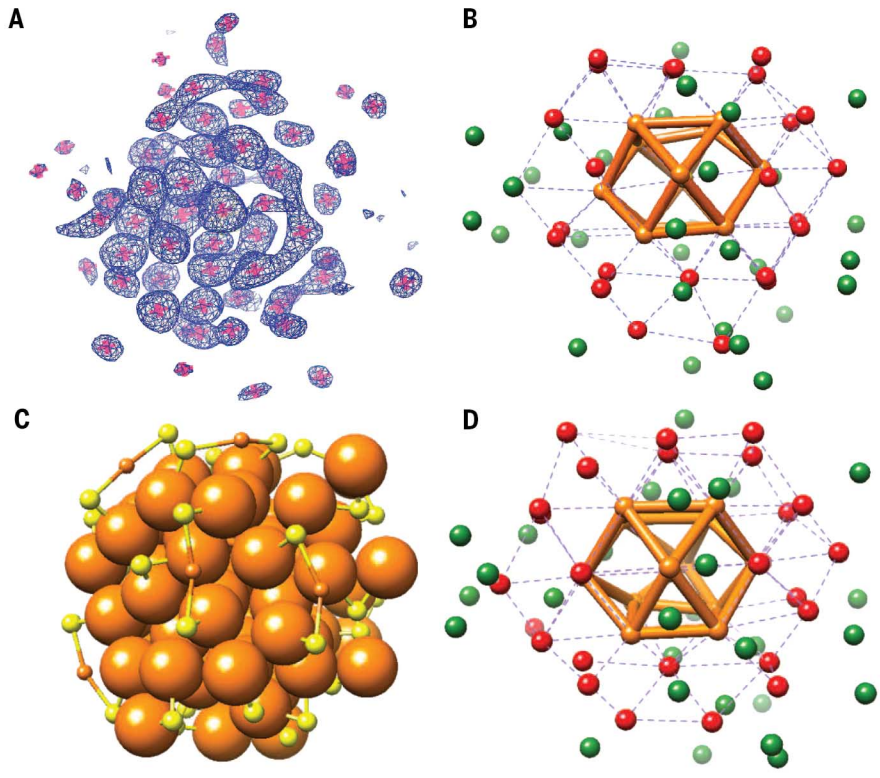

Fig. 5. 3D structure determination of ligand-protected gold nanoparticles at atomic resolution. (**A**) 3D intensity and positions of 68 gold atoms reconstructed from 939 Au_{68}NPs using the single-particle method. (**B**) 3D atomic model of Au_{68}NP. A gold atom at the center is surrounded by a cagelike cuboctahedron of 12 atoms (orange). Twenty-four additional atoms (red) form a fcc-like shell around the cuboctahedron, whereas the remaining 31 atoms (green) deviate from fcc packing. (**C**) 3D atomic model of $Au_{68}(SH)_{32}$. Thirty-two sulfur atoms (yellow) were manually added to the final model based on the positions of the gold atoms (orange) and the local stereochemistry. Gold atoms outside the Au_{15} fcc core are labeled with smaller spheres to better show Au-S motifs. (**D**) The Au_{68} atomic model from DFT calculations, confirming that the positions of most gold atoms are consistent with those of the measured model shown in (B). Several surface atoms deviate from measured positions, probably due to hydrogen bonding between surface ligands. [From (*47*)]

Looking forward

Although x-ray crystallography has been the primary method of solving the 3D atomic structure of crystals over the last century, the ability to determine the 3D structure of crystal defects and noncrystalline systems at atomic resolution will transform our understanding of materials properties and functionality at the most fundamental level. Here we identify five future research frontiers enabled by AET. First, 3D localization and identification of all atomic species in complex systems (including dopants, interstitials, light elements, and vacancies) require the further developments of AET. New STEM imaging methods such as matched illumination and detector interferometry can be implemented to image simultaneously heavy and light elements (*75*). Advanced image reconstruction and atom-tracing algorithms must be further improved to precisely localize the 3D atomic positions of individual light elements such as C and O, based on the intensity of reconstructed peaks. The measured atomic positions can then be used by DFT to obtain the 3D electronic properties of these complex systems at the single-atom level (*116*). Furthermore, AET may be combined with electron energy loss spectroscopy to directly measure the electronic states of these systems and verify the DFT results (*117*). Second, surfaces and interfaces strongly influence the catalytic, electronic, magnetic, and optical properties of many materials (*118*). Although x-ray, electron, and neutron diffraction and scanning probe microscopes have been successfully applied to investigate the atomic and electronic structure of surfaces and interfaces (*118*), AET is specifically suited

Downloaded from http://science.sciencemag.org/ on September 30, 2016

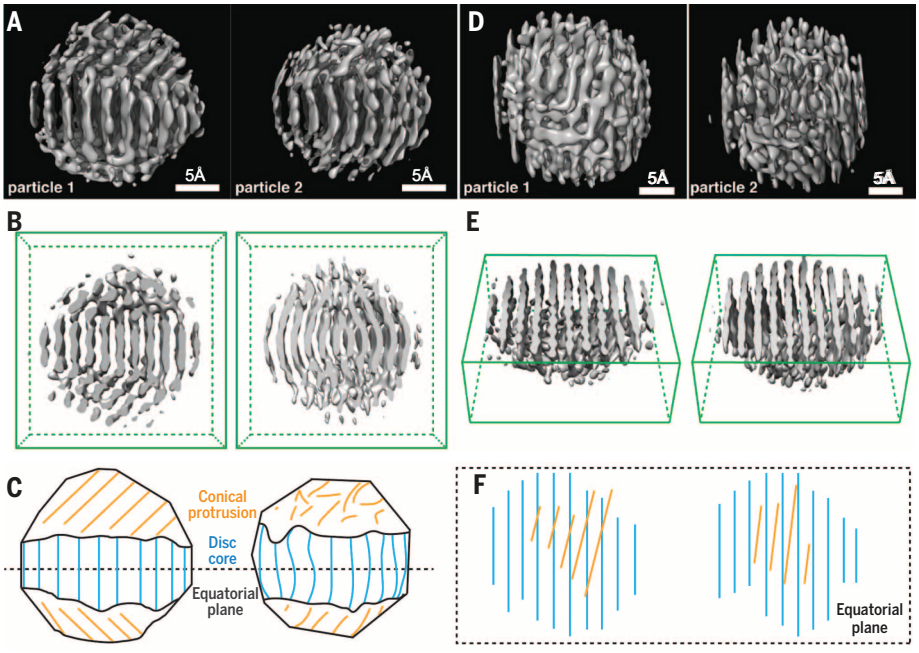

Fig. 6. 3D imaging of individual heterogeneous nanoparticles in solution at near-atomic resolution. (**A**) 3D structure of two platinum nanoparticles in liquid reconstructed by the single-particle method. (**B**) Cross-sectional views of the two 3D structures along the vertical plane of (A). (**C**) Schematic illustration of the atomic planes in the nanoparticles viewed at the same orientation as in (A). The overall structure of each nanoparticle consists of a central disc of {111} planes (blue) with two attached conical protrusions (yellow). (**D**) 3D structure of the two nanoparticles viewed along the conical protrusion direction. (**E**) Cross-sectional views of the two 3D structures along the equatorial plane shown in (C). (**F**) Schematic illustration of the nanoparticles viewed along the conical protrusion direction, showing that the lattice of the core (blue lines) and protrusions (yellow lines) form a tilt angle of 14° for particle one and 7° for particle two. [From (*48*)]

to precise probing of the 3D positions of individual atoms of many important systems, including the surface and subsurface atomic structure of heterogeneous catalysts, as well as metal-semiconductor, metal-oxide, and crystal-amorphous interfaces. Achieving these challenging goals will require sophisticated sample preparation, state-of-the-art electron microscopes equipped with advanced detectors, new STEM imaging methods with reduced electron doses, advanced tomographic reconstruction, and atom-tracing algorithms. In addition, many interfaces are extended in two dimensions, and determining the 3D arrangement of extended objects requires the further improvement of the reconstruction algorithm. Third, amorphous materials such as glasses are ubiquitous in our daily life, but the 3D atomic structure of glasses and other amorphous materials has thus far defied any direct experimental determination due to its lack of long-range translational and orientational order (*4*, *119*). Through a combination of multislice simulations of an aberration-corrected STEM and EST, the 3D atomic structure of a simulated glass particle was reconstructed from a tilt series of 55 noisy images, from which the 3D positions of individual Si and O atoms were identified (*46*). These numerical results indicate the feasibility of applying AET to determine the 3D atomic structure of amorphous materials. Likewise, AET can, in principle, be used to resolve the 3D atomic positions and species in quasicrystals (*120*, *121*). Fourth, an ultimate challenge is to develop AET for probing the dynamics of individual atoms and defects in materials (*122*). For example, understanding the 3D motion and interaction of point defects, dislocations, and grain boundaries at atomic resolution remains a long-standing unresolved problem in materials science. Likewise, monitoring the motion of individual atoms in complex systems during phase transitions or under external mechanical stress is beyond the capability of any existing experimental techniques (*5*). Addressing these challenging problems demands far more advanced electron microscopes and tomographic reconstruction methods than currently exist.

Finally, we note that small particles are rarely used individually in applications. Real devices consist of multiscale heterogeneous assemblies of materials that work together to yield the desired functionality. To study materials in action, we desire experimental methods that can carry out in situ or operando studies of local structure from actual devices (*123*–*126*). Enormous progress has been made in this endeavor through the use of so-called total scattering methods, such as the atomic pair distribution function method that scatters x-rays, neutrons, or electrons from ensembles of fine-grained and nanosized materials (*127*). Total scattering allows movies to be made showing how functional materials change under load (for example, by following structural changes in a battery electrode during discharge, or in an operating fuel cell). But averaging, as the measurements do, over many particles and particle orientations, results in considerable information loss in the signal and a fuzzy, nonunique picture of what is occurring in the material (*128*, *129*). Combining detailed structures from AET with total scattering approaches holds the transformational promise of giving us truly robust models of complex, heterogeneous materials in action; helping us to understand why high-performance materials work so well; and providing insights into how to design better ones (*130*, *131*).

REFERENCES AND NOTES

1. A. A. Kelly, K. M. Knowles, *Crystallography and Crystal Defects* (Wiley, ed. 2, 2012).
2. D. J. Bacon, D. Hull, Eds., *Introduction to Dislocations* (Butterworth-Heinemann, ed. 5, 2011).
3. M. D. McCluskey, E. E. Haller, *Dopants and Defects in Semiconductors* (CRC Press, 2012).
4. R. Zallen, *The Physics of Amorphous Solids* (Wiley, 1998).
5. P. G. Debenedetti, F. H. Stillinger, Supercooled liquids and the glass transition. *Nature* **410**, 259–267 (2001). doi: 10.1038/35065704; pmid: 11258381
6. H. W. Sheng, W. K. Luo, F. M. Alamgir, J. M. Bai, E. Ma, Atomic packing and short-to-medium-range order in metallic glasses. *Nature* **439**, 419–425 (2006). doi: 10.1038/nature04421; pmid: 16437105
7. J. M. Thomas, W. J. Thomas, *Principles and Practice of Heterogeneous Catalysis* (Wiley, ed. 2, 2014).
8. M. A. Green, K. Emery, Y. Hishikawa, W. Warta, E. D. Dunlop, Solar cell efficiency tables (version 45). *Prog. Photovolt. Res. Appl.* **23**, 1–9 (2015). doi: 10.1002/pip.2573
9. A. S. Aricò, P. Bruce, B. Scrosati, J.-M. Tarascon, W. van Schalkwijk, Nanostructured materials for advanced energy conversion and storage devices. *Nat. Mater.* **4**, 366–377 (2005). doi: 10.1038/nmat1368; pmid: 15867920
10. J. Senior, *Optical Fiber Communications: Principles and Practice* (Pearson, ed. 3, 2008).
11. M. Wuttig, N. Yamada, Phase-change materials for rewriteable data storage. *Nat. Mater.* **6**, 824–832 (2007). doi: 10.1038/nmat2009; pmid: 17972937
12. P. Hirsch, D. Cockayne, J. Spence, M. Whelan, 50 Years of TEM of dislocations: Past, present and future. *Philos. Mag.* **86**, 4519–4528 (2006). doi: 10.1080/14786430600768634
13. D. B. Williams, C. B. Carter, *Transmission Electron Microscopy: A Textbook for Materials Science* (Springer, ed. 2, 2009).
14. J. C. H. Spence, *Experimental High-Resolution Electron Microscopy* (Oxford Univ. Press, ed. 3, 2003).
15. B. Bhushan, O. Marti, in *Springer Handbook of Nanotechnology*, P. B. Bhushan, Ed. (Springer, 2010), pp. 573–617.
16. J. Miao, P. Charalambous, J. Kirz, D. Sayre, Extending the methodology of x-ray crystallography to allow imaging of micrometre-sized non-crystalline specimens. *Nature* **400**, 342–344 (1999). doi: 10.1038/22498
17. I. Robinson, R. Harder, Coherent x-ray diffraction imaging of strain at the nanoscale. *Nat. Mater.* **8**, 291–298 (2009). doi: 10.1038/nmat2400; pmid: 19308088
18. J. Miao, T. Ishikawa, I. K. Robinson, M. M. Murnane, Beyond crystallography: Diffractive imaging using coherent x-ray light sources. *Science* **348**, 530–535 (2015). doi: 10.1126/science.aaa1394; pmid: 25931551
19. J. Miao, T. Ohsuna, O. Terasaki, K. O. Hodgson, M. A. O'Keefe, Atomic resolution three-dimensional electron diffraction microscopy. *Phys. Rev. Lett.* **89**, 155502 (2002). doi: 10.1103/PhysRevLett.89.155502; pmid: 12365999
20. J. M. Zuo, I. Vartanyants, M. Gao, R. Zhang, L. A. Nagahara, Atomic resolution imaging of a carbon nanotube from diffraction intensities. *Science* **300**, 1419–1421 (2003). doi: 10.1126/science.1083887; pmid: 12775837
21. W. J. Huang *et al.*, Coordination-dependent surface atomic contraction in nanocrystals revealed by coherent diffraction. *Nat. Mater.* **7**, 308–313 (2008). doi: 10.1038/nmat2132; pmid: 18327263

Downloaded from http://science.sciencemag.org/ on September 30, 2016

22. K. Ayyer *et al.*, Macromolecular diffractive imaging using imperfect crystals. *Nature* **530**, 202–206 (2016). doi: 10.1038/nature16949; pmid: 26863980
23. T. F. Kelly, M. K. Miller, Atom probe tomography. *Rev. Sci. Instrum.* **78**, 031101 (2007). doi: 10.1063/1.2709758; pmid: 17411171
24. M. P. Moody *et al.*, Atomically resolved tomography to directly inform simulations for structure-property relationships. *Nat. Commun.* **5**, 5501 (2014). doi: 10.1038/ncomms6501; pmid: 25407499
25. D. J. De Rosier, A. Klug, Reconstruction of three dimensional structures from electron micrographs. *Nature* **217**, 130–134 (1968). doi: 10.1038/217130a0; pmid: 23610788
26. W. Hoppe, R. Langer, G. Knesch, C. Poppe, Protein-Kristallstrukturanalyse mit Elektronenstrahlen. *Naturwissenschaften* **55**, 333 (1968). doi: 10.1007/BF00600449; pmid: 5700719
27. R. G. Hart, Electron microscopy of unstained biological material: The polytropic montage. *Science* **159**, 1464–1467 (1968). doi: 10.1126/science.159.3822.1464; pmid: 4183952
28. J. Dubochet *et al.*, Cryo-electron microscopy of vitrified specimens. *Q. Rev. Biophys.* **21**, 129–228 (1988). doi: 10.1017/S0033583500004297; pmid: 3043536
29. J. Frank, *Electron Tomography: Methods for Three-Dimensional Visualization of Structures in the Cell* (Springer, 2010).
30. V. Lučić, F. Förster, W. Baumeister, Structural studies by electron tomography: From cells to molecules. *Annu. Rev. Biochem.* **74**, 833–865 (2005). doi: 10.1146/annurev.biochem.73.011303.074112; pmid: 15952904
31. C. M. Oikonomou, G. J. Jensen, A new view into prokaryotic cell biology from electron cryotomography. *Nat. Rev. Microbiol.* **14**, 205–220 (2016). doi: 10.1038/nrmicro.2016.7; pmid: 26923112
32. R. Henderson, The potential and limitations of neutrons, electrons and x-rays for atomic resolution microscopy of unstained biological molecules. *Q. Rev. Biophys.* **28**, 171–193 (1995). doi: 10.1017/S003358350000305X; pmid: 7568675
33. J. Frank, *Three-Dimensional Electron Microscopy of Macromolecular Assemblies: Visualization of Biological Molecules in Their Native State* (Oxford Univ. Press, 2006).
34. E. Callaway, The revolution will not be crystallized: A new method sweeps through structural biology. *Nature* **525**, 172–174 (2015). doi: 10.1038/525172a; pmid: 26354465
35. Y. Cheng, Single-particle cryo-EM at crystallographic resolution. *Cell* **161**, 450–457 (2015). doi: 10.1016/j.cell.2015.03.049; pmid: 25910205
36. E. Nogales, The development of cryo-EM into a mainstream structural biology technique. *Nat. Methods* **13**, 24–27 (2016). doi: 10.1038/nmeth.3694; pmid: 27110629
37. A. Bartesaghi *et al.*, 2.2 Å resolution cryo-EM structure of β-galactosidase in complex with a cell-permeant inhibitor. *Science* **348**, 1147–1151 (2015). doi: 10.1126/science.aab1576; pmid: 25953817
38. M. Battaglia, D. Contarato, P. Denes, P. Giubilato, Cluster imaging with a direct detection CMOS pixel sensor in transmission electron microscopy. *Nucl. Instrum. Methods* **608**, 363–365 (2009). doi: 10.1016/j.nima.2009.07.017
39. S. H. W. Scheres, RELION: Implementation of a Bayesian approach to cryo-EM structure determination. *J. Struct. Biol.* **180**, 519–530 (2012). doi: 10.1016/j.jsb.2012.09.006; pmid: 23000701
40. D. Lyumkis, A. F. Brilot, D. L. Theobald, N. Grigorieff, Likelihood-based classification of cryo-EM images using FREALIGN. *J. Struct. Biol.* **183**, 377–388 (2013). doi: 10.1016/j.jsb.2013.07.005; pmid: 23872434
41. A. T. Brünger *et al.*, Crystallography & NMR system: A new software suite for macromolecular structure determination. *Acta Crystallogr. D* **54**, 905–921 (1998). doi: 10.1107/S0907444998003254; pmid: 9757107
42. M. C. Scott *et al.*, Electron tomography at 2.4-ångström resolution. *Nature* **483**, 444–447 (2012). doi: 10.1038/nature10934; pmid: 22437612
43. B. Goris *et al.*, Atomic-scale determination of surface facets in gold nanorods. *Nat. Mater.* **11**, 930–935 (2012). doi: 10.1038/nmat3462; pmid: 23085569
44. C.-C. Chen *et al.*, Three-dimensional imaging of dislocations in a nanoparticle at atomic resolution. *Nature* **496**, 74–77 (2013). doi: 10.1038/nature12009; pmid: 23535594
45. B. Goris *et al.*, Three-dimensional elemental mapping at the atomic scale in bimetallic nanocrystals. *Nano Lett.* **13**, 4236–4241 (2013). doi: 10.1021/nl401945b; pmid: 23952010
46. C. Zhu *et al.*, Towards three-dimensional structural determination of amorphous materials at atomic resolution. *Phys. Rev. B* **88**, 100201 (2013). doi: 10.1103/PhysRevB.88.100201
47. M. Azubel *et al.*, Electron microscopy of gold nanoparticles at atomic resolution. *Science* **345**, 909–912 (2014). doi: 10.1126/science.1251959; pmid: 25146285
48. J. Park *et al.*, 3D structure of individual nanocrystals in solution by electron microscopy. *Science* **349**, 290–295 (2015). doi: 10.1126/science.aab1343; pmid: 26185247
49. R. Xu *et al.*, Three-dimensional coordinates of individual atoms in materials revealed by electron tomography. *Nat. Mater.* **14**, 1099–1103 (2015). doi: 10.1038/nmat4426; pmid: 26390325
50. B. Goris *et al.*, Measuring lattice strain in three dimensions through electron microscopy. *Nano Lett.* **15**, 6996–7001 (2015). doi: 10.1021/acs.nanolett.5b03008; pmid: 26340328
51. G. Haberfehlner *et al.*, Formation of bimetallic clusters in superfluid helium nanodroplets analysed by atomic resolution electron tomography. *Nat. Commun.* **6**, 8779 (2015). doi: 10.1038/ncomms9779; pmid: 26508471
52. E. Ruska, The development of the electron microscope and of electron microscopy. *Rev. Mod. Phys.* **59**, 627–638 (1987). doi: 10.1103/RevModPhys.59.627
53. O. Scherzer, Über einige Fehler von Elektronenlinsen. *Z. Phys.* **101**, 593–603 (1936). doi: 10.1007/BF01349606
54. O. Scherzer, Spharische und Chromatische Korrektur von Elektronen-Linsen. *Optik* **2**, 114–132 (1947).
55. H. H. Rose, Historical aspects of aberration correction. *J. Electron Microsc.* **58**, 77–85 (2009). doi: 10.1093/jmicro/dfp012; pmid: 19254915
56. D. J. Smith, Development of aberration-corrected electron microscopy. *Microsc. Microanal.* **14**, 2–15 (2008). doi: 10.1017/S1431927608080124; pmid: 18171498
57. M. Haider *et al.*, Electron microscopy image enhanced. *Nature* **392**, 768–769 (1998). doi: 10.1038/33823
58. P. E. Batson, N. Dellby, O. L. Krivanek, Sub-ångstrom resolution using aberration corrected electron optics. *Nature* **418**, 617–620 (2002). doi: 10.1038/nature00972; pmid: 12167855
59. R. Erni, M. D. Rossell, C. Kisielowski, U. Dahmen, Atomic-resolution imaging with a sub-50-pm electron probe. *Phys. Rev. Lett.* **102**, 096101 (2009). doi: 10.1103/PhysRevLett.102.096101; pmid: 19392535
60. R. Hovden *et al.*, Breaking the Crowther limit: Combining depth-sectioning and tilt tomography for high-resolution, wide-field 3D reconstructions. *Ultramicroscopy* **140**, 26–31 (2014). doi: 10.1016/j.ultramic.2014.01.013; pmid: 24636875
61. J. G. Lozano *et al.*, Direct observation of depth-dependent atomic displacements associated with dislocations in gallium nitride. *Phys. Rev. Lett.* **113**, 135503 (2014). doi: 10.1103/PhysRevLett.113.135503; pmid: 25302902
62. G. Möbus, B. J. Inkson, Nanoscale tomography in materials science. *Mater. Today* **10**, 18–25 (2007). doi: 10.1016/S1369-7021(07)70304-8
63. M. Bar Sadan *et al.*, Toward atomic-scale bright-field electron tomography for the study of fullerene-like nanostructures. *Nano Lett.* **8**, 891–896 (2008). doi: 10.1021/nl073149i; pmid: 18237147
64. M. Koguchi *et al.*, Three-dimensional STEM for observing nanostructures. *J. Electron Microsc.* **50**, 235–241 (2001). doi: 10.1093/jmicro/50.3.235; pmid: 11469412
65. P. A. Midgley, M. Weyland, J. M. Thomas, B. F. G. Johnson, Z-contrast tomography: A technique in three-dimensional nanostructural analysis based on Rutherfordscattering. *Chem. Commun.* **2001**, 907–908 (2001). doi: 10.1039/b101819c
66. P. A. Midgley, M. Weyland, 3D electron microscopy in the physical sciences: The development of Z-contrast and EFTEM tomography. *Ultramicroscopy* **96**, 413–431 (2003). doi: 10.1016/S0304-3991(03)00105-0; pmid: 12871805
67. P. A. Midgley, R. E. Dunin-Borkowski, Electron tomography and holography in materials science. *Nat. Mater.* **8**, 271–280 (2009). doi: 10.1038/nmat2406; pmid: 19308086
68. I. Arslan, T. J. V. Yates, N. D. Browning, P. A. Midgley, Embedded nanostructures revealed in three dimensions. *Science* **309**, 2195–2198 (2005). doi: 10.1126/science.1116745; pmid: 16195455
69. H. L. Xin, P. Ercius, K. J. Hughes, J. R. Engstrom, D. A. Muller, Three-dimensional imaging of pore structures inside low-κ dielectrics. *Appl. Phys. Lett.* **96**, 223108 (2010). doi: 10.1063/1.3442496
70. S. Van Aert, K. J. Batenburg, M. D. Rossell, R. Erni, G. Van Tendeloo, Three-dimensional atomic imaging of crystalline nanoparticles. *Nature* **470**, 374–377 (2011). doi: 10.1038/nature09741; pmid: 21289625
71. S. J. Pennycook, P. D. Nellist, *Scanning Transmission Electron Microscopy: Imaging and Analysis* (Springer, 2011).
72. J. M. LeBeau, S. D. Findlay, L. J. Allen, S. Stemmer, Quantitative atomic resolution scanning transmission electron microscopy. *Phys. Rev. Lett.* **100**, 206101 (2008). doi: 10.1103/PhysRevLett.100.206101; pmid: 18518557
73. D. A. Muller, Structure and bonding at the atomic scale by scanning transmission electron microscopy. *Nat. Mater.* **8**, 263–270 (2009). doi: 10.1038/nmat2380; pmid: 19308085
74. R. F. Egerton, R. McLeod, F. Wang, M. Malac, Basic questions related to electron-induced sputtering in the TEM. *Ultramicroscopy* **110**, 991–997 (2010). doi: 10.1016/j.ultramic.2009.11.003
75. C. Ophus *et al.*, Efficient linear phase contrast in scanning transmission electron microscopy with matched illumination and detector interferometry. *Nat. Commun.* **7**, 10719 (2016). doi: 10.1038/ncomms10719; pmid: 26923483
76. K. Dabov, A. Foi, V. Katkovnik, K. Egiazarian, Image denoising by sparse 3-D transform-domain collaborative filtering. *IEEE Trans. Image Process.* **16**, 2080–2095 (2007). doi: 10.1109/TIP.2007.901238; pmid: 17688213
77. R. Gordon, R. Bender, G. T. Herman, Algebraic reconstruction techniques (ART) for three-dimensional electron microscopy and x-ray photography. *J. Theor. Biol.* **29**, 471–481 (1970). doi: 10.1016/0022-5193(70)90109-8; pmid: 5492997
78. A. H. Andersen, A. C. Kak, Simultaneous algebraic reconstruction technique (SART): A superior implementation of the art algorithm. *Ultrason. Imaging* **6**, 81–94 (1984). doi: 10.1177/016173468400600107; pmid: 6548059
79. P. Gilbert, Iterative methods for the three-dimensional reconstruction of an object from projections. *J. Theor. Biol.* **36**, 105–117 (1972). doi: 10.1016/0022-5193(72)90180-4; pmid: 5070894
80. J. Miao, F. Förster, O. Levi, Equally sloped tomography with oversampling reconstruction. *Phys. Rev. B* **72**, 052103 (2005). doi: 10.1103/PhysRevB.72.052103
81. E. Lee *et al.*, Radiation dose reduction and image enhancement in biological imaging through equally-sloped tomography. *J. Struct. Biol.* **164**, 221–227 (2008). doi: 10.1016/j.jsb.2008.07.011; pmid: 18771735
82. Y. Mao, B. P. Fahimian, S. J. Osher, J. Miao, Development and optimization of regularized tomographic reconstruction algorithms utilizing equally-sloped tomography. *IEEE Trans. Image Process.* **19**, 1259–1268 (2010). doi: 10.1109/TIP.2009.2039660; pmid: 20051344
83. Y. Zhao *et al.*, High-resolution, low-dose phase contrast x-ray tomography for 3D diagnosis of human breast cancers. *Proc. Natl. Acad. Sci. U.S.A.* **109**, 18290–18294 (2012). doi: 10.1073/pnas.1204460109; pmid: 23091003
84. B. P. Fahimian *et al.*, Radiation dose reduction in medical x-ray CT via Fourier-based iterative reconstruction. *Med. Phys.* **40**, 031914 (2013). doi: 10.1118/1.4791644; pmid: 23464329
85. A. Averbuch, R. Coifman, D. Donoho, M. Israeli, Y. Shkolnisky, A Framework for discrete integral transformations I—The pseudopolar Fourier transform. *SIAM J. Sci. Comput.* **30**, 764–784 (2008). doi: 10.1137/060650283
86. D. H. Bailey, P. N. Swarztrauber, The fractional Fourier transform and applications. *SIAM Rev.* **33**, 389–404 (1991). doi: 10.1137/1033097
87. Z. Saghi *et al.*, Three-dimensional morphology of iron oxide nanoparticles with reactive concave surfaces. A compressed sensing-electron tomography (CS-ET) approach. *Nano Lett.* **11**, 4666–4673 (2011). doi: 10.1021/nl202253a; pmid: 21950497
88. B. Goris, W. Van den Broek, K. J. Batenburg, H. Heidari Mezerji, S. Bals, Electron tomography based on a total variation minimization reconstruction technique. *Ultramicroscopy* **113**, 120–130 (2012). doi: 10.1016/j.ultramic.2011.11.004
89. R. Leary, Z. Saghi, P. A. Midgley, D. J. Holland, Compressed sensing electron tomography. *Ultramicroscopy* **131**, 70–91 (2013). doi: 10.1016/j.ultramic.2013.03.019; pmid: 23834932
90. O. Nicoletti *et al.*, Three-dimensional imaging of localized surface plasmon resonances of metal nanoparticles. *Nature* **502**, 80–84 (2013). doi: 10.1038/nature12469; pmid: 24091976
91. E. J. Kirkland, *Advanced Computing in Electron Microscopy* (Springer, ed. 2, 2010).

Downloaded from http://science.sciencemag.org/ on September 30, 2016

92. A. F. Brilot *et al*., Beam-induced motion of vitrified specimen on holey carbon film. *J. Struct. Biol.* **177**, 630–637 (2012). doi: 10.1016/j.jsb.2012.02.003; pmid: 22366277
93. D. Van Dyck, J. R. Jinschek, F.-R. Chen, 'Big Bang' tomography as a new route to atomic-resolution electron tomography. *Nature* **486**, 243–246 (2012). doi: 10.1038/nature11074; pmid: 22699616
94. K. S. Raines *et al*., Three-dimensional structure determination from a single view. *Nature* **463**, 214–217 (2010). doi: 10.1038/nature08705; pmid: 20016484
95. C. L. Jia *et al*., Determination of the 3D shape of a nanoscale crystal with atomic resolution from a single image. *Nat. Mater.* **13**, 1044–1049 (2014). doi: 10.1038/nmat4087; pmid: 25242534
96. P. B. Hirsch, R. W. Horne, M. J. Whelan, LXVIII. Direct observations of the arrangement and motion of dislocations in aluminium. *Philos. Mag.* **1**, 677–684 (1956). doi: 10.1080/14786435608244003
97. W. Bollmann, Interference effects in the electron microscopy of thin crystal foils. *Phys. Rev.* **103**, 1588–1589 (1956). doi: 10.1103/PhysRev.103.1588
98. J. W. Menter, The direct study by electron microscopy of crystal lattices and their imperfections. *Proc. R. Soc. London Ser. A* **236**, 119–135 (1956). doi: 10.1098/rspa.1956.0117
99. A. Howie, M. J. Whelan, Diffraction contrast of electron microscope images of crystal lattice defects. III. Results and experimental confirmation of the dynamical theory of dislocation image contrast. *Proc. R. Soc. London Ser. A* **267**, 206–230 (1962). doi: 10.1098/rspa.1962.0093
100. P. Rez, M. M. J. Treacy, Three-dimensional imaging of dislocations. *Nature* **503**, E1 (2013). doi: 10.1038/nature12660; pmid: 24256805
101. J. Miao *et al*., Reply to 'Three-dimensional imaging of dislocations'. *Nature* **503**, E2 (2013).
102. L. D. Marks, Wiener-filter enhancement of noisy HREM images. *Ultramicroscopy* **62**, 43–52 (1996). doi: 10.1016/0304-3991(95)00085-2; pmid: 22666916
103. M. J. Hÿtch, A. M. Minor, Observing and measuring strain in nanostructures and devices with transmission electron microscopy. *MRS Bull.* **39**, 138–146 (2014). doi: 10.1557/mrs.2014.4
104. M. Hÿtch, F. Houdellier, F. Hüe, E. Snoeck, Nanoscale holographic interferometry for strain measurements in electronic devices. *Nature* **453**, 1086–1089 (2008). doi: 10.1038/nature07049; pmid: 18563161
105. J. H. Warner, N. P. Young, A. I. Kirkland, G. A. D. Briggs, Resolving strain in carbon nanotubes at the atomic level. *Nat. Mater.* **10**, 958–962 (2011). doi: 10.1038/nmat3125; pmid: 21963574
106. B. C. Larson, W. Yang, G. E. Ice, J. D. Budai, J. Z. Tischler, Three-dimensional x-ray structural microscopy with submicrometre resolution. *Nature* **415**, 887–890 (2002). doi: 10.1038/415887a; pmid: 11859363
107. S. Kim *et al*., 3D strain measurement in electronic devices using through-focal annular dark-field imaging. *Ultramicroscopy* **146**, 1–5 (2014). doi: 10.1016/j.ultramic.2014.04.010; pmid: 24859824
108. R. Vincent, P. A. Midgley, Double conical beam-rocking system for measurement of integrated electron diffraction intensities. *Ultramicroscopy* **53**, 271–282 (1994). doi: 10.1016/0304-3991(94)90039-6
109. L. A. Beavan, R. M. Scanlan, D. N. Seidman, The defect structure of depleted zones in irradiated tungsten. *Acta Metall.* **19**, 1339–1350 (1971). doi: 10.1016/0001-6160(71)90071-X
110. B. Gault, M. P. Moody, J. M. Cairney, S. P. Ringer, in *Atom Probe Microscopy* (Springer Series in Materials Science, Springer, 2012), pp. 9–28.
111. M.-C. Daniel, D. Astruc, Gold nanoparticles: Assembly, supramolecular chemistry, quantum-size-related properties, and applications toward biology, catalysis, and nanotechnology. *Chem. Rev.* **104**, 293–346 (2004). doi: 10.1021/cr030698+; pmid: 14719978
112. P. D. Jadzinsky, G. Calero, C. J. Ackerson, D. A. Bushnell, R. D. Kornberg, Structure of a thiol monolayer-protected gold nanoparticle at 1.1 Å resolution. *Science* **318**, 430–433 (2007). doi: 10.1126/science.1148624; pmid: 17947577
113. W. W. Xu, Y. Gao, X. C. Zeng, Unraveling structures of protection ligands on gold nanoparticle $Au_{68}(SH)_{32}$. *Sci. Adv.* **1**, e1400211 (2015). doi: 10.1126/sciadv.1400211; pmid: 26601162
114. J. M. Yuk *et al*., High-resolution EM of colloidal nanocrystal growth using graphene liquid cells. *Science* **336**, 61–64 (2012). doi: 10.1126/science.1217654; pmid: 22491849
115. H. Elmlund, D. Elmlund, S. Bengio, PRIME: Probabilistic initial 3D model generation for single-particle cryo-electron microscopy. *Structure* **21**, 1299–1306 (2013). doi: 10.1016/j.str.2013.07.002; pmid: 23931142
116. R. G. Parr, W. Yang, *Density-Functional Theory of Atoms and Molecules* (Oxford Univ. Press, 1994).
117. Q. M. Ramasse *et al*., Probing the bonding and electronic structure of single atom dopants in graphene with electron energy loss spectroscopy. *Nano Lett.* **13**, 4989–4995 (2013). doi: 10.1021/nl304187e; pmid: 23259533
118. H. Lüth, *Solid Surfaces, Interfaces and Thin Films* (Springer, ed. 6, 2015).
119. W. H. Zachariasen, The atomic arrangement in glass. *J. Am. Chem. Soc.* **54**, 3841–3851 (1932). doi: 10.1021/ja01349a006
120. P. Bak, Icosahedral crystals: Where are the atoms? *Phys. Rev. Lett.* **56**, 861–864 (1986). doi: 10.1103/PhysRevLett.56.861; pmid: 10033305
121. H. Takakura, C. P. Gómez, A. Yamamoto, M. De Boissieu, A. P. Tsai, Atomic structure of the binary icosahedral Yb-Cd quasicrystal. *Nat. Mater.* **6**, 58–63 (2007). doi: 10.1038/nmat1799; pmid: 17160006
122. Y. Zhu, H. Dürr, The future of electron microscopy. *Phys. Today* **68**, 32–38 (2015). doi: 10.1063/PT.3.2747
123. K. W. Chapman, P. J. Chupas, C. J. Kepert, Selective recovery of dynamic guest structure in a nanoporous prussian blue through in situ x-ray diffraction: A differential pair distribution function analysis. *J. Am. Chem. Soc.* **127**, 11232–11233 (2005). doi: 10.1021/ja053266k; pmid: 16089438
124. E. L. Redmond, B. P. Setzler, P. Juhas, S. J. L. Billinge, T. F. Fuller, In-situ monitoring of particle growth at PEMFC cathode under accelerated cycling conditions. *Electrochem. Solid-State Lett.* **15**, B72–B74 (2012). doi: 10.1149/2.004206esl
125. H. Liu *et al*., Capturing metastable structures during high-rate cycling of $LiFePO_4$ nanoparticle electrodes. *Science* **344**, 1252817 (2014). doi: 10.1126/science.1252817; pmid: 24970091
126. Z. Huang *et al*., Grain rotation and lattice deformation during photoinduced chemical reactions revealed by in situ x-ray nanodiffraction. *Nat. Mater.* **14**, 691–695 (2015). doi: 10.1038/nmat4311; pmid: 26053760
127. T. Egami, S. J. L. Billinge, *Underneath the Bragg Peaks: Structural Analysis of Complex Materials* (Elsevier, ed. 2, 2012).
128. S. J. L. Billinge, I. Levin, The problem with determining atomic structure at the nanoscale. *Science* **316**, 561–565 (2007). doi: 10.1126/science.1135080; pmid: 17463280
129. D. A. Keen, A. L. Goodwin, The crystallography of correlated disorder. *Nature* **521**, 303–309 (2015). doi: 10.1038/nature14453; pmid: 25993960
130. V. Krayzman *et al*., A combined fit of total scattering and extended x-ray absorption fine structure data for local-structure determination in crystalline materials. *J. Appl. Cryst.* **42**, 867–877 (2009). doi: 10.1107/S0021889809023541
131. C. L. Farrow, C. Shi, P. Juhás, X. Peng, S. J. L. Billinge, Robust structure and morphology parameters for CdS nanoparticles by combining small-angle x-ray scattering and atomic pair distribution function data in a complex modeling framework. *J. Appl. Cryst.* **47**, 561–565 (2014). doi: 10.1107/S1600576713034055

ACKNOWLEDGMENTS

We thank U. Dahmen and M. C. Scott for stimulating discussions and Y. Yang, G. Melinte, C.-C. Chen, and I.-S. Chou for help with the figures and references. This work was primarily supported by the Office of Basic Energy Sciences of the U.S. Department of Energy (DOE) (grant DE-SC0010378). J.M. acknowledges the partial support by NSF (grant DMR-1437263), Office of Naval Research Multidisciplinary University Research Initiative (grant N00014-14-1-0675), and the Defense Advanced Research Projects Agency Program in Ultrafast Laser Science and Engineering through a grant from the Aviation and Missile Research, Development, and Engineering Center. P.E. acknowledges support for the Molecular Foundry, Lawrence Berkeley National Laboratory, which is supported by the DOE under contract no. DE-AC02-05CH11231. S.J.L.B. acknowledges support from NSF through grant DMR-1534910.

10.1126/science.aaf2157

Downloaded from http://science.sciencemag.org/ on September 30, 2016

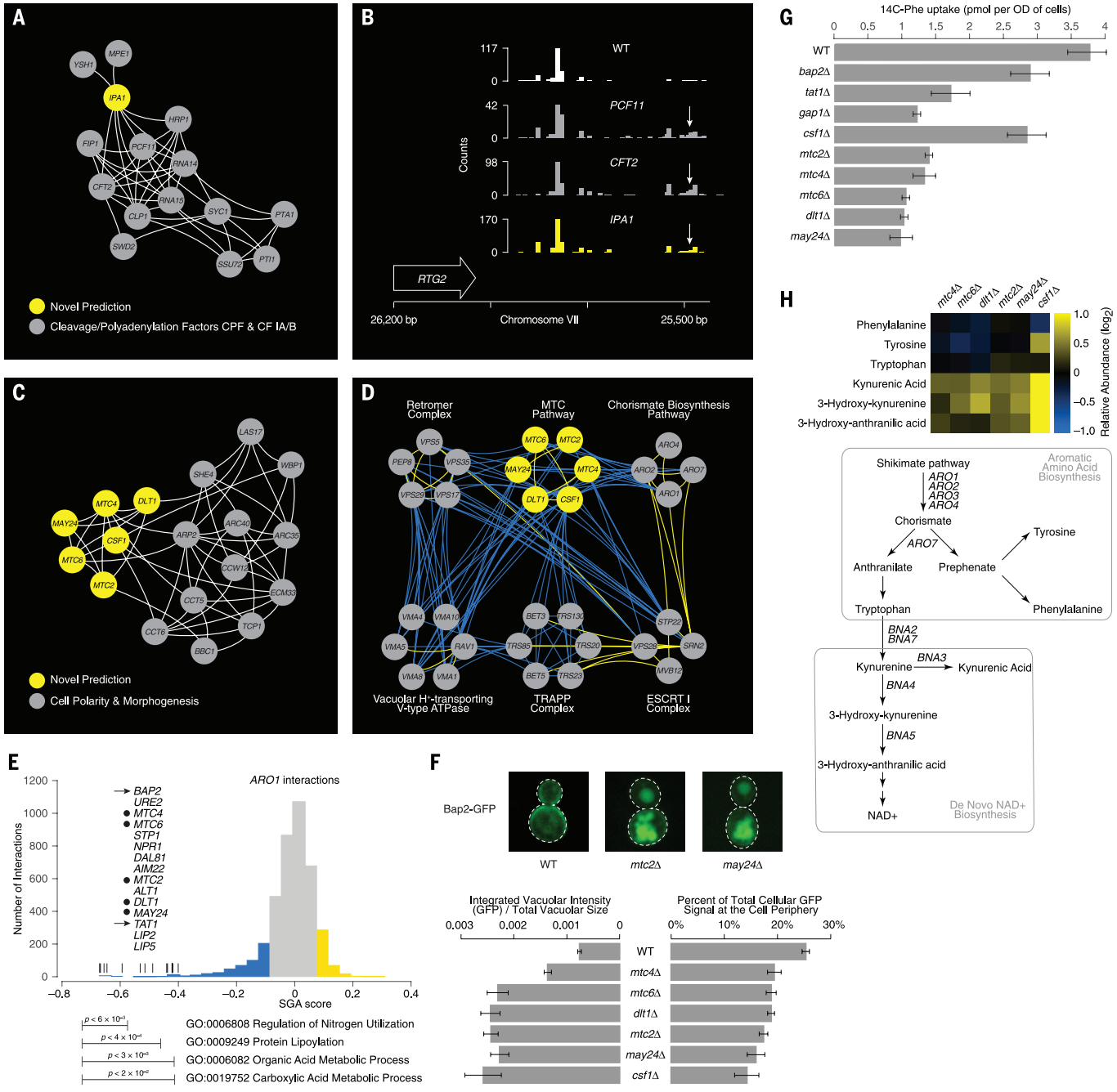

Fig. 5. Validating functional predictions for IPA1 and the MTC pathway. (**A**) A genetic interaction profile similarity subnetwork for the uncharacterized essential gene, *IPA1* (yellow node), extracted from the transcription and chromatin organization enriched biological process cluster. (**B**) Polyadenylation profiles for a representative gene, *RTG2*, generated from genome-wide sequencing of mRNA purified from a wild-type (WT) strain and strains carrying TS mutations of *PCF11*, *CFT2*, or *IPA1*. The horizontal arrow indicates the orientation of the *RTG2* open reading frame; the vertical arrows indicate the mutant, increased aberrant, 3′ mRNA cleavage and polyadenylation. (**C**) A genetic interaction profile similarity subnetwork for *MTC2*, *MTC4*, *MTC6*, *CSF1*, *DLT1*, and *MAY24* genes (yellow nodes) extracted from the network region in the vicinity of the cell polarity and morphogenesis biological process cluster. (**D**) The MTC pathway genetic interaction network. Nodes are grouped according to genetic interaction profile similarity and edges represent negative (blue) and positive (yellow) interactions (genetic interaction score, $|\varepsilon| > 0.08$, $P < 0.05$). (**E**) Distribution of *ARO1* negative (blue) and positive (yellow) genetic interactions ($|\varepsilon| > 0.08$, $P < 0.05$) (gene pairs that failed to meet the threshold for interactions are colored gray). Functions enriched among genes that displayed an extreme negative interaction with *ARO1* are indicated, and a subset of these genes and where they are located within the SGA score distribution is shown. Closed circles indicate members of the MTC pathway, and arrows indicate amino acid permease encoding genes. (**F**) (Top) Representative cell images illustrating Bap2-GFP (green fluorescent protein) localization in WT, *mtc2*Δ, and *may24*Δ deletion mutant strains. (Bottom) Vacuolar intensity (total GFP signal in the vacuole/vacuolar area) and percentage of total cellular GFP present at the cell periphery (cell periphery GFP/total cellular GFP signal) were quantified for WT cells and MTC pathway mutants. Error bars indicate standard deviation from three replicate experiments. (**J**) Cellular uptake of ^{14}C-labeled phenylalanine in WT and deletion mutant strains. Error bars indicate standard deviation from three replicate experiments. (**H**) (Top) Metabolite levels for the indicated mutants were analyzed by full-scan liquid chromatography–mass spectrometry. The levels of selected metabolites are presented as $\log_2$ ratios relative to wild type cells. (Bottom) Schematic diagram illustrating aromatic amino acid and de novo NAD$^+$ biosynthesis pathways.

Downloaded from http://science.sciencemag.org/ on September 30, 2016

functionally enriched regions of the genetic profile similarity network, allows us to predict functions for these genes (Fig. 4B) (*8*). Notably, while most essential genes are relatively well studied, our network uncovered a role for a previously uncharacterized essential gene, *YJR141W*, which we named *IPA1* (important for cleavage and polyadenylation), in the highly conserved process of mRNA 3′-end processing and polyadenylation. *IPA1* shares many genetic interactions in common with genes encoding members of the cleavage/polyadenylation factor (CPF) and cleavage factor IA (CF IA) protein complexes (Figs. 4B and 5A), which, along with *HRP1*, are essential for mRNA 3′ end processing (*19*). We also found that Ipa1 physically interacted with CPF complex members Mpe1 and Ysh1 (data file S8) (*8*), further supporting a role for *IPA1* in this process. Indeed, as shown previously for TS mutants in components of CF IA and CPF complexes (*20*), such as *pcf11* and *cft2* TS mutants, an *ipa1* TS mutant was impaired for in vitro mRNA cleavage and polyadenylation (fig. S8) and showed widespread defects in mRNA processing accuracy and efficiency, with a significant bias toward the use of downstream polyadenylation sites ($P < 2 \times 10^{-16}$; Wilcoxon rank sum) (Fig. 5B and fig. S8) (*8*).

Six poorly characterized genes—*MTC2*, *MTC4*, *MTC6*, *CSF1*, *DLT1*, and *YPR153W*—localized in the vicinity of the cell polarity and morphogenesis cluster on the global network (Fig. 4B) and displayed highly similar genetic interaction profiles, suggesting that they work together as a novel functional module (Fig. 5C). Interestingly, all of these genes were identified as important for growth in high-pressure and cold environments (*21*). Thus, we called this module the MTC pathway and named *YPR153W* as *MAY24* (genetic interaction profile similarity to MTC annotated yeast genes *MTC2* and *MTC4*). *MTC2*, *MTC4*, and *MTC6* mutants were previously shown to enhance the mutant phenotype associated with perturbation of *CDC13*, which controls the maintenance of telomere capping (*22*). We found that the MTC pathway genes showed strong negative interactions with protein-trafficking genes, as well as aromatic amino acid biosynthesis genes *ARO1* and *ARO2* (Fig. 5D and fig. S9). Because pathway components often share phenotypes with their target genes, a genetic interaction profile that contains members of a particular pathway may also identify potential targets of the same pathway. For example, the *ARO1* genetic interaction profile revealed strong negative interactions with genes involved in amino acid metabolism, the entire MTC pathway, and the aromatic amino acid transporters *BAP2* and *TAT1* (Fig. 5E and fig. S9), suggesting that the MTC pathway may control amino acid metabolism or affect trafficking of Bap2 and Tat1 permeases. Indeed, mutations of MTC pathway genes resulted in Bap2 mislocalization (Fig. 5F and fig. S9) and a defect in phenylalanine uptake, resembling that of strains deleted for genes encoding amino acid transporters, including *BAP2*, *TAT1*, and *GAP1* (Fig. 5G) (*8*). Furthermore, unbiased metabolomics analysis revealed that the MTC pathway mutants exhibited elevated levels of kynurenine biosynthetic pathway metabolites, precursors of nicotinamide adenine dinucleotide (oxidized form) (NAD^+) (Fig. 5H) (*8*). Previous studies showed that defects in kynurenine biosynthesis suppressed *cdc13-1* TS mutants, suggesting that elevated NAD^+ levels inhibit telomere capping (*23*). Thus, the global genetic interaction network traced functional connections whereby defects in MTC pathway-dependent protein trafficking alter aromatic amino acid homeostasis, which appears to modulate steady-state levels of kynurenine biosynthetic pathway metabolites, linking cell polarity to telomere capping through altered NAD^+ levels.

Genetic interaction network connectivity

Genetic interaction profiles connect a particular gene to other genes through both negative and positive interactions. Although the average gene participated in ~100 negative interactions (2% of genes tested) and ~65 positive interactions (1% of genes tested), when assessed at an intermediate confidence threshold (*8*), a wide range of connectivity exists in the genetic interaction network (fig. S10 and data file S9). For example, the 10% most connected genes (i.e., high interaction degree genes or hub genes) in the genetic interaction network participated in 3.5-fold more genetic interactions than the average gene. More specifically, negative interaction hubs had an average degree of 340 negative interactions, and the average positive interaction hub displayed 200 positive interactions. In general, essential genes participated in ~5-fold more negative and positive interactions than nonessential genes, confirming previous estimates (Fig. 6A) (*24*).

As observed previously (*1*), fitness defects associated with both deletion alleles of nonessential genes and TS alleles of essential genes were highly correlated with the degree of genetic interaction (figs. S11 and S12, table S1, and data file S10). In the global network, genetic interaction hubs tended to encode conserved, multifunctional, highly expressed, and abundant proteins that exhibit many physical interactions and also participated in numerous chemical-genetic interactions (data file S9 and table S1). Genes encoding proteins involved in specific biochemical functions, or those that contain specific functional domains, such as an SH3 (SRC homology 3) protein-protein interaction domain, were also associated with a higher number of genetic interactions (figs. S13 and S14). In the nonessential genetic interaction network (NxN), negative and positive interaction hubs were enriched for biological processes including chromatin organization, transcription, and vesicle trafficking (data file S11). In the essential genetic network (ExE), negative interaction hubs were relatively uniformly distributed across all bioprocesses, whereas positive interaction hubs were specifically enriched for proteostasis-related bioprocesses (data file S11).

Genes that exhibited relatively few genetic interactions were also associated with specific features (figs. S11 to S14, table S2, and data file S10). For example, ATP-binding cassette transporters, which belong to functionally redundant gene families and thus are extensively buffered, exhibited fewer genetic interactions (figs. S11 to S14 and table S2). Interestingly, genes with the lowest interaction degree (lowest 20%) (data file S9) were often associated with more deleterious single-nucleotide polymorphisms (SNPs), exhibited a higher ratio of nonsynonymous to synonymous nucleotide substitutions (dN/dS), and displayed high expression variance across different genetic backgrounds and environments. This suggests that these genes are under reduced evolutionary constraints and subject to condition-specific regulation (table S2 and figs. S11 and S12). About 1000 genes (~20%), the majority of which are nonessential genes, displayed few genetic interactions and had profiles that generally displayed a relatively low level of functional information, suggesting that the connectivity for some genes will only be revealed under different environmental or genetic conditions. The functional, physiological, and evolutionary properties associated with genetic interaction frequency should predict genetic network connectivity and candidate genes that may serve as important genetic modifiers in other organisms, including humans (*25*).

Negative and positive genetic interactions of essential and nonessential genes

The global genetic interaction network, encompassing the majority of both nonessential and essential genes, enabled a comprehensive comparative analysis with other functional information (*8*). Both nonessential and essential genetic interactions were predictive of functionally related gene pairs (Fig. 6, B and C, and fig. S15). In particular, negative interactions among essential genes showed a striking overlap with protein-protein interactions (Fig. 6C and fig. S15). For example, 50% of essential gene pairs whose products physically interact also share a negative interaction, representing a ~10-fold enrichment for protein-protein interactions among essential genes displaying negative genetic interactions. Similarly, 63% of gene pairs annotated to the same essential protein complex were connected by a negative genetic interaction, representing a ~15-fold enrichment for cocomplexed pairs among essential genes connected by negative interactions. In fact, individual negative interactions were as informative as genetic interaction profile similarity for predicting membership to the same essential pathway or complex, a property that does not hold for nonessential genes (fig. S16). This observation highlights the reduced ability of a cell to tolerate multiple partial loss-of-function mutations in the same essential pathway or complex (Fig. 6C and fig. S15).

Consistent with previous observations (*1*), positive genetic interactions between nonessential genes also overlapped with protein-protein interactions, albeit to a lesser extent (0.5%, 3.7-fold enrichment) (Fig. 6C and fig. S15). This reflects that simultaneous perturbation of two genes encoding members of the same nonessential protein complex often shows a fitness defect resembling the corresponding single mutants.

Downloaded from http://science.sciencemag.org/ on September 30, 2016

In contrast, we did not detect significant overlap between the positive interactions of essential genes and other molecular or functional relationships, including physical interactions (Fig. 6, B and C, and fig. S15). The lack of a functional signal could not be explained by differences in data quality because replicate analysis confirmed that SGA-derived positive and negative interactions showed similar levels of reproducibility (fig. S2). Furthermore, members of the same essential protein complex or different alleles of the same essential gene often showed similar positive interaction profiles (fig. S17). Thus, while negative interactions identified clear functional relationships between genes, positive interactions among partial loss-of function alleles of essential genes represent a different type of relationship that is not captured by other large-scale data sets or functional standards.

Functional distribution of genetic interactions within and between bioprocesses

We further examined the functional distribution of genetic interactions through the enrichment for negative and positive interactions within and between biological processes (Fig. 1F and data file S6) (*8*). Negative genetic interactions were significantly enriched ($P < 0.05$, hypergeometric) among genes belonging to the same biological process in both the nonessential (NxN) and essential (ExE) genetic interaction networks (Fig. 6D, on-diagonal). Negative interactions were also enriched between deletion alleles of nonessential genes in different biological processes (Fig. 6D, off-diagonal). In contrast, negative interactions between TS alleles of essential genes,

Fig. 6. Negative and positive genetic interactions connecting nonessential and essential genes. (**A**) The network density (observed interactions/total gene pairs screened) of negative (blue) and positive (yellow) genetic interactions, expressed as a fraction of all tested gene pairs, associated with nonessential and essential genes, at a defined threshold (genetic interaction score, $|\varepsilon| > 0.08$, $P < 0.05$). Error bars indicate the standard deviation across multiple samplings of the alleles for essential genes, where each gene is represented by a single, randomly selected allele in each sampling. (**B**) Plots of precision versus recall [number of true positives (TPs)] for negative (blue) and positive (yellow) interactions for nonessential and essential genes, as determined by our genetic interaction score ($|\varepsilon| > 0.08$, $P < 0.05$). TP interactions were defined as those involving gene pairs coannotated to a gold standard set of GO terms. The precision and recall values were calculated as described (*8*). (**C**) Fold enrichment for colocalized, coexpressed, or physically interacting genes among negative (blue) and positive (yellow) genetic interactions connecting pairs of nonessential or essential genes. (**D**) Network density (observed interactions/total gene pairs screened) of genetic interactions within and across biological processes. The fraction of screened nonessential and essential gene pairs exhibiting negative or positive interactions, as determined by our genetic interaction score ($|\varepsilon| > 0.08$, $P < 0.05$), was measured for the 15 gene sets enriched for specific biological processes, as defined in Fig. 1F. Node size reflects the fraction of interacting gene pairs observed for a given pair of biological processes. Dark blue and dark yellow nodes indicate the frequency of interaction that is significantly above random expectation. Light blue and light yellow nodes represent a frequency of interaction that is not significantly higher than random expectation. Nodes on the diagonal represent the frequency of interactions among genes belonging to the same biological process. Nodes off the diagonal represent the frequency of interactions between different biological processes.

Downloaded from http://science.sciencemag.org/ on September 30, 2016

despite higher abundance (Fig. 6A), were biased toward gene pairs in the same biological processes (Fig. 6D, on-diagonal) and were rarely enriched between genes involved in different biological processes (Fig. 6D, off-diagonal). Although these trends could reflect the different genetic perturbations used to interrogate nonessential and essential genes, negative interactions among essential genes highlight a core set of cellular bioprocesses, and nonessential genes appear to mediate connections between these bioprocesses.

While nonessential genes involved in the same biological process were modestly enriched for positive interactions, we failed to observe a similar enrichment for positive interactions among functionally related essential genes (Fig. 6D, on-diagonal). Instead, positive interactions tended to connect essential genes with roles in highly distinct biological processes. In particular, we observed significant enrichment for positive interactions that connected essential genes with nuclear-related functions to essential genes required for vesicle traffic–dependent functions (Fig. 6D and fig. S17).

The architecture of negative interactions within the genetic network hierarchy

To explore the functional distribution of genetic interactions in more detail, we examined where genetic interactions occurred within the genetic network hierarchy of gene function derived from profile similarities. Specifically, we assessed how frequently negative interactions connected a pair of genes belonging to the same cluster within the hierarchy of genetic interaction profiles (Fig. 2A), and we examined clusters corresponding to either a cellular compartment, biological process, or pathway/complex (Fig. 7A) (*8*). The density (i.e. the number of observed genetic interactions relative to the total number of gene pairs screened) of negative interactions, among genes in both the nonessential (NxN) and essential (ExE) genetic interaction networks, increased with the functional specificity of a given cluster. Accordingly, genes within a cluster enriched for specific pathways or complexes were connected by negative interactions more often than genes in the same biological process–enriched cluster, which, in turn, were more frequently connected by negative interactions than genes belonging to a cluster enriched for a particular cell compartment (Fig. 7B). For example, essential genes that fall into a cluster within the set that was enriched for complexes/pathways (PCC 0.4 to 0.8) were connected by a negative interaction with a relatively high density (60 to 90%), but they were rarely connected by a

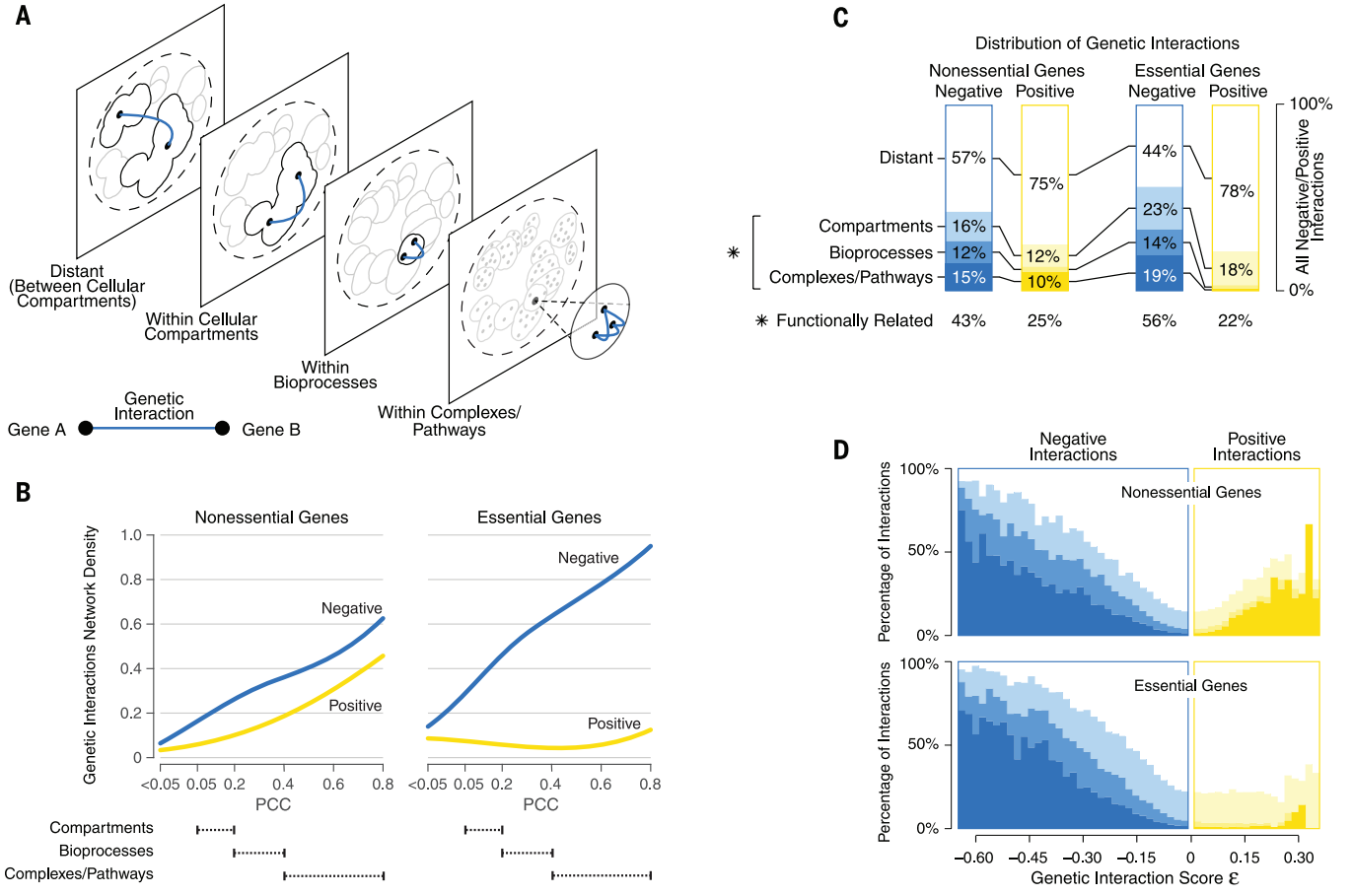

Fig. 7. Mapping negative and positive interactions across the genetic network–based functional hierarchy. (**A**) Schematic representation of the genetic network–based functional hierarchy illustrating interactions between genes within the same complex, biological process, or cellular compartment, as well as distant interactions that span different cellular compartments. (**B**) The network density of genetic interactions between of genes in the same cluster, at a given level of profile similarity (PCC) in the genetic network hierarchy for negative (blue) or positive (yellow) genetic interactions (genetic interaction score, $|\varepsilon| > 0.08$, $P < 0.05$). Dashed lines indicate the PCC range within which clusters in the genetic network hierarchy were enriched for cell compartments, bioprocesses, and protein complexes. (**C**) The functional distribution of all negative (blue) and all positive (yellow) interactions ($|\varepsilon| > 0.08$, $P < 0.05$) among genes in the genetic network hierarchy. The percentage of all interactions connecting nonessential gene pairs and essential gene pairs in the same clusters corresponding to a cell compartment, bioprocess, or complex/pathway is shown. The combined fraction of functionally related interactions (i.e., interactions connecting genes in the same compartment, bioprocess, complex or pathway) is also indicated (*). (**D**) The percentage of negative (blue) and positive (yellow) interactions within a specified genetic interaction score (ε) range that connects genes belonging to the same cluster at the indicated level of the genetic network–based hierarchy. Different shades of blue and yellow correspond to levels of functional relatedness shown in (C). The white area corresponds to the fraction of interactions that connect genes in different cellular compartments (i.e., distant).

Downloaded from http://science.sciencemag.org/ on September 30, 2016

positive interaction (Fig. 7B). In total, 43% of nonessential and 56% of essential gene pairs connected by negative interactions shared some degree of functional relatedness (Fig. 7C).

The magnitude of a given negative interaction was also associated with the extent of functional similarity shared between genes (Fig. 7D). For both nonessential and essential genetic interactions, stronger interactions tended to connect genes with closer functional relationships (Fig. 7D). Thus, on the basis of the strength of negative genetic interaction, we can predict whether two genes share an intimate relationship and possibly function in the same pathway or complex. For example, members of the conserved endoplasmic reticulum (ER) membrane protein complex—including *EMC1*, *EMC2*, and *EMC6*, which play a role in phospholipid transfer from the ER to mitochondria to facilitate phosphatidylethanolamine biosynthesis (*26*)—showed strong negative genetic interactions (genetic interaction score < −0.65) with a previously uncharacterized essential gene, *YNL181W*, suggesting a role for this gene in lipid metabolism. Indeed, *YNL181W* encodes a putative oxidoreductase that localizes to the ER (*27*) and, consistent with defective membrane function, *ynl181w* hypomorphic mutants showed altered sensitivities to numerous bioactive compounds (fig. S18) (*8*). We named this gene *PBR1* (potentiates bioactive compound response) to highlight its role in xenobiotic sensitivity.

The architecture of positive interactions within the genetic network hierarchy

Positive interactions among nonessential genes exhibited similar, albeit weaker, trends, where the density of interactions increased gradually with the functional specificity of hierarchy-derived clusters (Fig. 7B) and the magnitude of nonessential positive interactions was predictive of nonessential pathway or complex membership (Fig. 7D). In contrast, the density of positive interactions detected in the essential network was not related to functional specificity. In fact, the most distantly related essential gene pairs were more frequently connected by positive interactions than gene pairs mapping to the same biological process-level clusters (Fig. 7B). The majority of positive interacting gene pairs in both the essential (ExE, 78%) and nonessential (NxN, 75%) genetic interaction networks occurred between distantly connected genes whose products appeared to function in different cell compartments (Fig. 7C). Moreover, we did not observe a relationship between functional similarity and the magnitude of positive interactions between essential gene pairs (Fig. 7D). Thus, positive interactions between essential genes generally appear to reflect more functionally distant relationships.

Genetic interactions within and between protein complexes

Consistent with previous findings (*1*, *5*, *28*, *29*), we found that protein complexes exhibited highly organized patterns of genetic interactions. For example, many protein complexes tested (60 of 141, 43%) were enriched ($P < 0.01$, hypergeometric) for genetic interactions within the set of protein complex–encoding genes and were biased for a single type of interaction, either negative or positive, highlighting the coherent nature of genetic interactions shared among genes encoding members of the same complex. The type of interaction observed within protein complexes depended on essentiality. For example, complexes composed primarily of nonessential genes (>75% nonessential genes) (data file S12) were more often enriched for positive (21%; 20 of 97 complexes) compared with negative (5%; 5 of 97 complexes) interactions among their members (Fig. 8A and data file S13). In contrast, most essential protein complexes (>75% essential genes; data file S12) were enriched for negative interactions among their members (82%; 35 of 44 complexes). Notably, none of the essential complexes in our data set were enriched for positive interactions (Fig. 8A and data file S13).

The genetic interactions occurring within protein complexes can even resolve the structural organization of large, multisubunit complexes. For example, although proteasome genes tend to be connected by negative genetic interactions, genes encoding components of the same subunit (e.g., within 19*S* or within 20*S*) interact more frequently with one another than genes belonging to different subunits (between 19*S* and 20*S*) (fig. S19). Phenotypic differences between proteasome subunits were also supported by chemical-genetic interactions observed in yeast (fig. S19) (*30*), as well as in *Drosophila melanogaster* cultured cells (fig. S20 and data file S14) (*8*), suggesting that the topology of genetic networks connecting genes within protein complexes by uniform sets of genetic interactions is conserved in higher eukaryotes.

We also examined the topology of genetic interactions occurring between protein complexes and found a large number of complex-complex pairs that were both enriched for genetic interactions ($P < 0.001$, hypergeometric) and strongly biased toward either negative or positive interactions (*8*). More complex-complex pairs were connected by coherent sets of negative than positive interactions (Fig. 8B and data file S13). For example, 4% of all nonessential pairs of protein complexes tested (293 of 6899) were connected by negative interactions, whereas positive interactions connected less than 2% of nonessential complexes (130 of 6899). Similarly, 5% (74 of 1597) of all essential complex pairs in our data set were connected by negative interactions, whereas less than 2% (29 of 1597) of essential protein complex pairs shared positive interactions (Fig. 8B and data file S13). Nonetheless, we observed hundreds of instances of both coherent negative (470) and positive (192) interactions connecting pairs of essential and nonessential complexes, emphasizing the highly organized topology of genetic interaction networks (Fig. 8B and data file S13).

Functional wiring diagrams of protein complexes

Extracting all genetic interactions for specific protein complexes generated functional wiring diagrams that revealed the set of genes, pathways, and bioprocesses, modulated by mutation of a particular complex (Fig. 9, A and B). For example, coherent sets of negative interactions involving the ORC, which specifies sites of initiation of DNA replication throughout the genome (*31*), linked functionally related complexes, including the MCM (mini-chromosome maintenance) and the GINS (Go, Ichi, Ni, San) complexes (Fig. 9A), both of which participate in the initiation of DNA replication (*32*, *33*). In another example, negative interactions associated with the 19*S* proteasome highlighted diverse functions that are particularly important when proteasome activity is compromised (Fig. 9B),

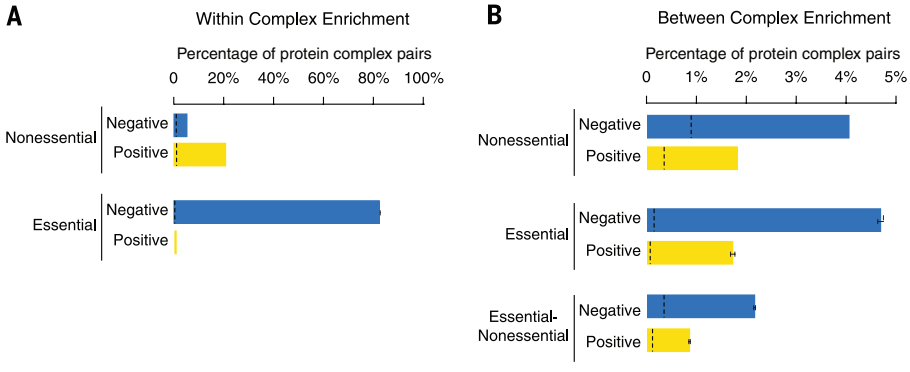

Fig. 8. Genetic interactions within and between protein complexes. (**A**) The percentage of nonessential and essential complexes whose members were enriched for genetic interactions with each other and biased (i.e., coherent) for either mostly negative (blue) or mostly positive (yellow) interactions. (**B**) The percentage of nonessential-nonessential, essential-essential, or essential-nonessential complex-complex pairs found to be enriched for genetic interactions and biased (i.e., coherent) for either mostly negative (blue) or mostly positive (yellow) interactions. Black dashed lines indicate the background rate of coherent genetic interaction enrichment within individual complexes or between pairs of protein complexes. Error bars indicate the standard deviation across multiple samplings of different alleles for the same essential genes, where each gene is represented by a single, randomly selected allele in each sampling.

Downloaded from http://science.sciencemag.org/ on September 30, 2016

including interactions with genes encoding the APC (anaphase-promoting complex), which targets cell cycle proteins for degradation to promote exit from mitosis (*34*). Interestingly, essential genes that showed negative interactions with the proteasome were enriched for multidomain proteins, suggesting that TS alleles may perturb folding of more complex proteins, resulting in a greater dependence on proteasome activity in mutants (fig. S21).

Positive interactions among essential genes reflect general regulatory mechanisms

Protein complexes involved in proteostasis, including several chaperones and the proteasome, exhibited among the strongest enrichment for positive genetic interactions, especially in the essential gene network (Fig. 9C, fig. S22, and data file S15). Positive genetic interactions connected the proteasome and other proteostasis-related complexes to genes involved in various functions, including vesicle trafficking and transcription (Figs. 6D and 9B and fig. S23). Because the proteasome plays a direct role in controlling protein turnover, we hypothesized that a subset of its positive interactions may reflect genetic suppression through the stabilization of a mutant protein (*35*). Indeed, we further tested a subset of these positive interactions (*8*) and, based on this analysis, we estimated that ~30% of proteasome-positive interactions represent genetic suppression, where a fitness defect associated with a hypomorphic TS allele of an essential gene is suppressed by a second mutation in a proteasome-encoding gene (table S3, fig. S24, and data file S16). In total, 16% of positive interactions with essential genes appear to be associated with proteostasis. In a similar regulatory relationship, positive interactions were also enriched between genes involved in mRNA decay and essential gene DAmP alleles (*13*), which often affect mRNA stability via disruption of their 3′ untranslated region (fig. S24).

Interestingly, a subset of protein complexes, in addition to being enriched for positive interactions (Fig. 9C), also exhibited more positive interactions compared with negative interactions with essential genes (Fig. 9D and data file S15). The positive interactions of these biased complexes were also more functionally diverse compared with their negative interactions. For example, ORC subunits were connected by coherent sets of positive interactions to genes with roles in several different functions, including members of the ER-associated translocon complex (Fig. 9A). The ORC-translocon connection reflects enrichment for cross-compartment positive interactions observed between genes encoding essential, nuclear, and vesicle traffic-dependent functions (Fig. 6D).

Protein complexes with a positive interaction bias tend to be involved in cell cycle progression, and their disruption often leads to a cell cycle delay or arrest phenotype (Fig. 9D and fig. S22). A cell cycle delay may result when a mutation activates a checkpoint pathway that slows cell cycle progression, allowing the cell to correct an otherwise rate-limiting defect and mask the phenotypic effect normally associated with a second mutation (*36*). Thus, an ORC-dependent S-phase cell cycle delay may mask growth defects associated with perturbation of genes required for polarized secretion during budding, thereby resulting in positive interactions. Protein complexes biased for positive interactions with essential genes also exhibited many negative interactions with checkpoint genes ($P < 4 \times 10^{-56}$; Fisher's exact test) (fig. S22), suggesting that cell viability depends on an active checkpoint response in the absence of these complexes. Genes with cell cycle progression–related roles accounted for 30% of essential gene-positive interactions, which, combined with genes involved in proteostasis, explain 46% of the positive interactions among essential genes.

Discussion

A global network based on genetic interaction profile similarity resolves a hierarchy of modules, enriched for sets of genes within specific pathways and protein complexes, biological processes, or subcellular compartments. In the context of this functional organization, coherent sets of negative and positive genetic interactions connect both within and between the highly resolved complex and pathway modules to map a functional wiring diagram of the cell.

Our comprehensive analysis of genetic interactions among essential genes revealed several illuminating principles. First, consistent with the results of our previous smaller-scale surveys (*1*, *24*), essential genes are major hubs and form the basic scaffold of the global genetic interaction network. Second, the extreme negative or synthetic lethal interactions among essential genes often occur between genes within the same protein complex, or between genes in different protein complexes but within the same biological process or subcellular compartment, properties that may prove useful for predicting genetic interactions in other systems. Third, positive genetic interactions between two essential genes typically do not reflect shared function, but rather often occur between genes in distant cellular compartments and reflect more general regulatory connections associated with a cell cycle delay or proteostasis.

An important property associated with the global network is the potential for digenic interactions to compound the phenotypes associated with single gene mutations. Whereas only ~1000 genes in the yeast genome are individually essential in standard growth conditions and cause lethality when mutated (*9*, *10*), we showed that hundreds of thousands of mutant gene pair combinations result in a negative interaction in the global genetic interaction network, including an extreme set of ~10,000 synthetic lethal interactions between nonessential gene pairs (*8*). In other words, we discovered a genetic background in which an additional ~3300 genes are essential for viability (*8*). Despite the power of this approach for uncovering growth dependencies, ~1000 of the 5400 yeast genes we examined showed relatively few genetic interactions and remain sparsely connected. Our global genetic network was mapped under a particular condition in a specific genetic background, and we anticipate that changing these two key factors may reveal new interactions for many of the sparsely connected genes (*37*). Ultimately, broad mapping of both core and condition-specific genetic interactions promises to accelerate the field of synthetic biology, providing a rational understanding of the requirements for the design of minimal genomes (*38*).

It is also important to consider other types of genetic interactions, beyond those associated with loss-of-function mutations in haploid cells. Our analysis revealed that relatively severe deletion alleles of nonessential genes or TS alleles of essential genes often show extensive digenic interaction profiles. However, it is possible that the more subtle mutations associated with natural genetic variation may require higher-order combinations, involving more than two genes, to modulate phenotype and influence heritability extensively (*39*). One interesting case involves duplicated genes with overlapping function, which often are buffered more extensively, such that more complex triple-mutant analysis will be required to reveal their genetic interaction profiles (*1*, *40*). We must also understand the general principles associated with genetic networks involving gain-of-function alleles and more complex genetic interactions that can occur in diploid and polyploid organisms (*41*), across a variety of different cell types, within whole animals (*42*–*44*), or between hosts and their symbiotic organisms (*45*).

Because negative genetic interactions are highly ordered and often occur as coherent sets, (e.g., predominantly negative genetic interactions connecting genes within a protein complex or between two different protein complexes), many different pairs of mutations may lead to the same terminal synthetic lethal/sick phenotype. We suspect that this network topology is important when considering the genotype-to-phenotype problem in human genetics. Because biological systems are built upon sets of conserved genes whose products participate in functional modules, it is reasonable to expect that the general topology of genetic networks will also be conserved (*25*). As observed for the complex-complex connections on the global yeast genetic network, mutations in many different pairs of genes may lead to the same phenotype, such as a disease state, in humans. This property of genetic networks means that scanning disease cohorts for genetic variation that corresponds to coherent sets of mutations that connect genes within or between protein complexes and pathways (e.g., see functional wiring diagrams for the ORC the 19*S* proteasome in Fig. 9) may reveal genetic networks underlying diseases.

The regulatory mechanisms associated with positive genetic interactions among essential genes, which include genetic suppression interactions, are also potentially relevant to human

Downloaded from http://science.sciencemag.org/ on September 30, 2016

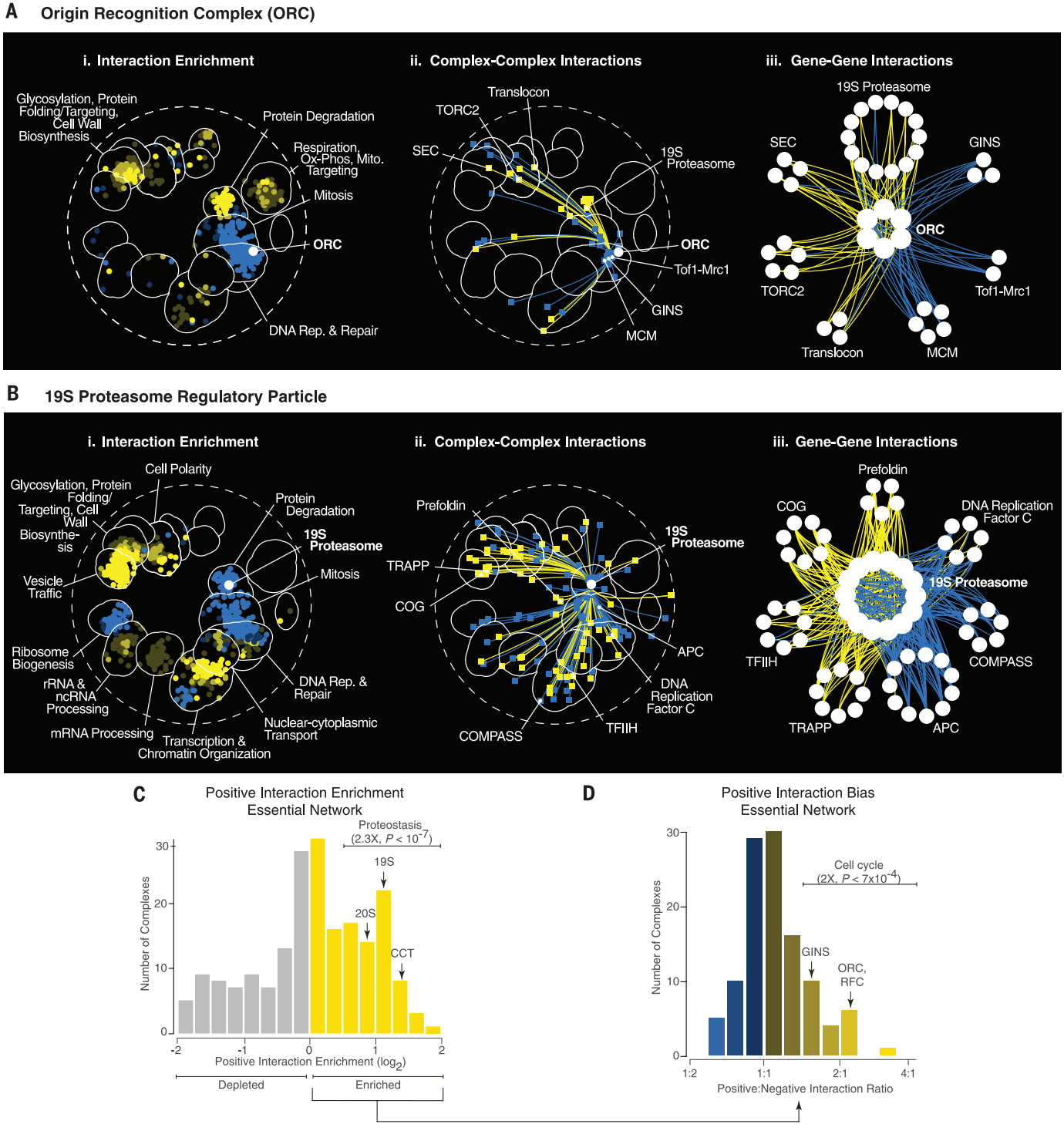

Fig. 9. Functional wiring diagrams for specific protein complexes. (**A**) Genetic interaction map for the ORC. (i) Regions of the global similarity network significantly enriched for genes exhibiting negative (blue) or positive (yellow) genetic interactions with ORC members were mapped using SAFE. (ii) Protein complexes that showed coherent negative or positive genetic interactions with ORC were placed on a schematic representation of the global similarity network based on the average genetic interaction profile similarity of the complex and connected with blue or yellow edges, respectively. (iii) A subset of protein complexes from (ii) that showed coherent negative (blue) or positive (yellow) genetic interactions with genes encoding the ORC are shown. (**B**) Genetic interaction map for the 19S proteasome. The 19S proteasome networks shown in (i) to (iii) were constructed as described in (A). (**C**) Distribution of positive genetic interaction enrichment for protein complexes screened against the essential gene array (TSA). Protein complexes enriched for positive interactions with essential genes (yellow bars) tend to be associated with proteostasis-related functions (2.3X, $P < 10^{-7}$; Fisher's exact test), including the 19S and 20S proteasome subunits as well as the chaperonin-containing T complex (CCT) and prefoldin chaperone complexes (indicated on the graph). (**D**) Distribution of positive versus negative genetic interactions for protein complexes enriched for positive interactions shown in (C). Essential protein complexes that show a bias toward positive interactions, such as the ORC, RFC, and GINS, are often required for normal cell cycle progression (2X, $P < 7 \times 10^{-4}$; Fisher's exact test).

Downloaded from http://science.sciencemag.org/ on September 30, 2016

genetics because they may inspire therapeutic approaches and elucidate mechanisms of heritability (*46*, *47*). Notably, mutations that compromise the cellular proteostasis network often suppressed TS alleles of essential genes (table S3 and data file S16). It is possible that, similar to yeast, certain variants of the human proteasome also suppress the detrimental effects of genetic variation associated with numerous other genes, and their corresponding complexes and pathways, within the human genome. Although the genes encoding the proteasome are essential in human cells, and severe mutations in these genes may cause disease (*48*), genetic variation that modulates proteasome function subtly may have the potential to be disease protective.

It is clear that the digenic interactions we have mapped in yeast can be conserved in different yeast species over hundreds of millions of years of evolution (*49*, *50*). Likewise, conservation of genetic interactions from yeast to human cells has been observed (*51*, *52*), particularly within fundamental bioprocesses like DNA synthesis and repair and chromosome segregation, which is particularly relevant for the identification of targets for novel synthetic lethal cancer therapies (*53*, *54*). However, the general extent and breadth of network conservation remain largely unexplored. Importantly, genome-scale application of CRISPR (clustered regularly interspaced short palindromic repeats)–Cas9 genome editing approaches offer the potential to map global genetic interaction networks in human cells (*55*–*57*). We suspect that the general principles of the global yeast genetic network described here will be highly relevant for both the efficient mapping and the interpretation of analogous networks in a variety of different cells and organisms.

Methods summary

Methods for construction of yeast double-mutant strains, identification, and measurement of genetic interactions—as well as all analyses pertaining to genetic interaction profiles and negative and positive interactions—are described in detail in the supplementary materials. General information about our methods, accompanied by specific references to the supplementary materials, is included throughout the text.

REFERENCES AND NOTES

1. M. Costanzo *et al*., The genetic landscape of a cell. *Science* **327**, 425–431 (2010). doi: 10.1126/science.1180823; pmid: 20093466
2. J. L. Hartman 4th, B. Garvik, L. Hartwell, Principles for the buffering of genetic variation. *Science* **291**, 1001–1004 (2001). doi: 10.1126/science.291.5506.1001; pmid: 11232561
3. O. Zuk, E. Hechter, S. R. Sunyaev, E. S. Lander, The mystery of missing heritability: Genetic interactions create phantom heritability. *Proc. Natl. Acad. Sci. U.S.A.* **109**, 1193–1198 (2012). doi: 10.1073/pnas.1119675109; pmid: 22223662
4. J. S. Bloom *et al*., Genetic interactions contribute less than additive effects to quantitative trait variation in yeast. *Nat. Commun.* **6**, 8712 (2015). doi: 10.1038/ncomms9712; pmid: 26537231
5. A. Baryshnikova *et al*., Quantitative analysis of fitness and genetic interactions in yeast on a genome scale. *Nat. Methods* **7**, 1017–1024 (2010). doi: 10.1038/nmeth.1534; pmid: 21076421
6. T. Roemer, C. Boone, Systems-level antimicrobial drug and drug synergy discovery. *Nat. Chem. Biol.* **9**, 222–231 (2013). doi: 10.1038/nchembio.1205; pmid: 23508188
7. H. E. Bryant *et al*., Specific killing of BRCA2-deficient tumours with inhibitors of poly(ADP-ribose) polymerase. *Nature* **434**, 913–917 (2005). doi: 10.1038/nature03443; pmid: 15829966
8. Materials and methods are available as supporting materials on *Science* Online.
9. E. A. Winzeler *et al*., Functional characterization of the *S. cerevisiae* genome by gene deletion and parallel analysis. *Science* **285**, 901–906 (1999). doi: 10.1126/science.285.5429.901; pmid: 10436161
10. G. Giaever *et al*., Functional profiling of the *Saccharomyces cerevisiae* genome. *Nature* **418**, 387–391 (2002). doi: 10.1038/nature00935; pmid: 12140549
11. M. Kofoed *et al*., An updated collection of sequence barcoded temperature-sensitive alleles of yeast essential genes. *Genes Genomes Genetics* **5**, 1879–1887 (2015). doi: 10.1534/g3.115.019174; pmid: 26175450
12. Z. Li *et al*., Systematic exploration of essential yeast gene function with temperature-sensitive mutants. *Nat. Biotechnol.* **29**, 361–367 (2011). doi: 10.1038/nbt.1832; pmid: 21441928
13. M. Schuldiner *et al*., Exploration of the function and organization of the yeast early secretory pathway through an epistatic miniarray profile. *Cell* **123**, 507–519 (2005). doi: 10.1016/j.cell.2005.08.031; pmid: 16269340
14. M. Ashburner *et al*., Gene ontology: Tool for the unification of biology. *Nat. Genet.* **25**, 25–29 (2000). doi: 10.1038/75556; pmid: 10802651
15. A. Baryshnikova, Systematic functional annotation and visualization of biological networks. *Cell Syst.* **2**, 412–421 (2016).
16. J. Dutkowski *et al*., A gene ontology inferred from molecular networks. *Nat. Biotechnol.* **31**, 38–45 (2013). doi: 10.1038/nbt.2463; pmid: 23242164
17. J. L. Koh *et al*., CYCLoPs: A comprehensive database constructed from automated analysis of protein abundance and subcellular localization patterns in *Saccharomyces cerevisiae*. *Genes Genomes Genetics* **5**, 1223–1232 (2015). doi: 10.1534/g3.115.017830; pmid: 26048563
18. T. A. Sangster, S. Lindquist, C. Queitsch, Under cover: Causes, effects and implications of Hsp90-mediated genetic capacitance. *BioEssays* **26**, 348–362 (2004). doi: 10.1002/bies.20020; pmid: 15057933
19. S. Chan, E. A. Choi, Y. Shi, Pre-mRNA 3′-end processing complex assembly and function. *RNA* **2**, 321–335 (2011). doi: 10.1002/wrna.54; pmid: 21957020
20. J. M. Gordon *et al*., Reconstitution of CF IA from overexpressed subunits reveals stoichiometry and provides insights into molecular topology. *Biochemistry* **50**, 10203–10214 (2011). doi: 10.1021/bi200964p; pmid: 22026644
21. F. Abe, H. Minegishi, Global screening of genes essential for growth in high-pressure and cold environments: Searching for basic adaptive strategies using a yeast deletion library. *Genetics* **178**, 851–872 (2008). doi: 10.1534/genetics.107.083063; pmid: 18245339
22. S. G. Addinall *et al*., A genomewide suppressor and enhancer analysis of cdc13-1 reveals varied cellular processes influencing telomere capping in *Saccharomyces cerevisiae*. *Genetics* **180**, 2251–2266 (2008). doi: 10.1534/genetics.108.092577; pmid: 18845848
23. A. Greenall *et al*., A genome wide analysis of the response to uncapped telomeres in budding yeast reveals a novel role for the NAD^+ biosynthetic gene BNA2 in chromosome end protection. *Genome Biol.* **9**, R146 (2008). doi: 10.1186/gb-2008-9-10-r146; pmid: 18828915
24. S. Mnaimneh *et al*., Exploration of essential gene functions via titratable promoter alleles. *Cell* **118**, 31–44 (2004). doi: 10.1016/j.cell.2004.06.013; pmid: 15242642
25. E. N. Koch *et al*., Conserved rules govern genetic interaction degree across species. *Genome Biol.* **13**, R57 (2012). doi: 10.1186/gb-2012-13-7-r57; pmid: 22747640
26. S. Lahiri *et al*., A conserved endoplasmic reticulum membrane protein complex (EMC) facilitates phospholipid transfer from the ER to mitochondria. *PLOS Biol.* **12**, e1001969 (2014). doi: 10.1371/journal.pbio.1001969; pmid: 25313861
27. R. Sánchez, A. Sali, Large-scale protein structure modeling of the *Saccharomyces cerevisiae* genome. *Proc. Natl. Acad. Sci. U.S.A.* **95**, 13597–13602 (1998). doi: 10.1073/pnas.95.23.13597; pmid: 9811845
28. D. Segrè, A. Deluna, G. M. Church, R. Kishony, Modular epistasis in yeast metabolism. *Nat. Genet.* **37**, 77–83 (2005). pmid: 15592468
29. S. Bandyopadhyay, R. Kelley, N. J. Krogan, T. Ideker, Functional maps of protein complexes from quantitative genetic interaction data. *PLOS Comput. Biol.* **4**, e1000065 (2008). doi: 10.1371/journal.pcbi.1000065; pmid: 18421374
30. D. Hoepfner *et al*., High-resolution chemical dissection of a model eukaryote reveals targets, pathways and gene functions. *Microbiol. Res.* **169**, 107–120 (2014). doi: 10.1016/j.micres.2013.11.004; pmid: 24360837
31. S. P. Bell, The origin recognition complex: From simple origins to complex functions. *Genes Dev.* **16**, 659–672 (2002). doi: 10.1101/gad.969602; pmid: 11914271
32. M. Lei, B. K. Tye, Initiating DNA synthesis: From recruiting to activating the MCM complex. *J. Cell Sci.* **114**, 1447–1454 (2001). pmid: 11282021
33. S. A. MacNeill, Structure and function of the GINS complex, a key component of the eukaryotic replisome. *Biochem. J.* **425**, 489–500 (2010). doi: 10.1042/BJ20091531; pmid: 20070258
34. J. M. Peters, The anaphase promoting complex/cyclosome: A machine designed to destroy. *Nat. Rev. Mol. Cell Biol.* **7**, 644–656 (2006). doi: 10.1038/nrm1988; pmid: 16896351
35. F. Khosrow-Khavar *et al*., The yeast ubr1 ubiquitin ligase participates in a prominent pathway that targets cytosolic thermosensitive mutants for degradation. *Genes Genomes Genetics* **2**, 619–628 (2012). doi: 10.1534/g3.111.001933; pmid: 22670231
36. R. Li, A. W. Murray, Feedback control of mitosis in budding yeast. *Cell* **66**, 519–531 (1991). doi: 10.1016/0092-8674(81)90015-5; pmid: 1651172
37. S. Bandyopadhyay *et al*., Rewiring of genetic networks in response to DNA damage. *Science* **330**, 1385–1389 (2010). doi: 10.1126/science.1195618; pmid: 21127252
38. C. A. Hutchison 3rd *et al*., Design and synthesis of a minimal bacterial genome. *Science* **351**, aad6253 (2016). doi: 10.1126/science.aad6253; pmid: 27013737
39. R. D. Dowell *et al*., Genotype to phenotype: A complex problem. *Science* **328**, 469 (2010). doi: 10.1126/science.1189015; pmid: 20413493
40. B. VanderSluis *et al*., Genetic interactions reveal the evolutionary trajectories of duplicate genes. *Mol. Syst. Biol.* **6**, 429 (2010). doi: 10.1038/msb.2010.82; pmid: 21081923
41. D. Altshuler, M. J. Daly, E. S. Lander, Genetic mapping in human disease. *Science* **322**, 881–888 (2008). doi: 10.1126/science.1156409; pmid: 18988837
42. B. Lehner, C. Crombie, J. Tischler, A. Fortunato, A. G. Fraser, Systematic mapping of genetic interactions in *Caenorhabditis elegans* identifies common modifiers of diverse signaling pathways. *Nat. Genet.* **38**, 896–903 (2006). doi: 10.1038/ng1844; pmid: 16845399
43. A. B. Byrne *et al*., A global analysis of genetic interactions in *Caenorhabditis elegans*. *J. Biol.* **6**, 8 (2007). doi: 10.1186/jbiol58; pmid: 17897480
44. B. Fischer *et al*., A map of directional genetic interactions in a metazoan cell. *eLife* **4**, e05464 (2015). doi: 10.7554/eLife.05464; pmid: 25748138
45. R. Blekhman *et al*., Host genetic variation impacts microbiome composition across human body sites. *Genome Biol.* **16**, 191 (2015). doi: 10.1186/s13059-015-0759-1; pmid: 26374288
46. C. M. Buchovecky *et al*., A suppressor screen in Mecp2 mutant mice implicates cholesterol metabolism in Rett syndrome. *Nat. Genet.* **45**, 1013–1020 (2013). doi: 10.1038/ng.2714; pmid: 23892605
47. K. M. Keeling, X. Xue, G. Gunn, D. M. Bedwell, Therapeutics based on stop codon readthrough. *Annu. Rev. Genomics Hum. Genet.* **15**, 371–394 (2014). doi: 10.1146/annurev-genom-091212-153527; pmid: 24773318
48. P. Tsvetkov *et al*., Compromising the 19S proteasome complex protects cells from reduced flux through the proteasome. *eLife* **4**, e08467 (2015). doi: 10.7554/eLife.08467; pmid: 26327695
49. S. J. Dixon *et al*., Significant conservation of synthetic lethal genetic interaction networks between distantly related eukaryotes. *Proc. Natl. Acad. Sci. U.S.A.* **105**, 16653–16658 (2008). doi: 10.1073/pnas.0806261105; pmid: 18931302
50. A. Roguev *et al*., Conservation and rewiring of functional modules revealed by an epistasis map in fission yeast. *Science* **322**, 405–410 (2008). doi: 10.1126/science.1162609; pmid: 18818364
51. R. Deshpande *et al*., A comparative genomic approach for identifying synthetic lethal interactions in human cancer. *Cancer Res.* **73**, 6128–6136 (2013). doi: 10.1158/0008-5472.CAN-12-3956; pmid: 23980094
52. K. J. McManus, I. J. Barrett, Y. Nouhi, P. Hieter, Specific synthetic lethal killing of RAD54B-deficient human colorectal cancer cells by FEN1 silencing. *Proc. Natl. Acad. Sci. U.S.A.* **106**, 3276–3281 (2009). doi: 10.1073/pnas.0813414106; pmid: 19218431
53. D. M. van Pel *et al*., An evolutionarily conserved synthetic lethal interaction network identifies FEN1 as a broad-spectrum

Downloaded from http://science.sciencemag.org/ on September 30, 2016

target for anticancer therapeutic development. *PLOS Genet.* **9**, e1003254 (2013). doi: 10.1371/journal.pgen.1003254; pmid: 23382697
54. L. H. Hartwell, P. Szankasi, C. J. Roberts, A. W. Murray, S. H. Friend, Integrating genetic approaches into the discovery of anticancer drugs. *Science* **278**, 1064–1068 (1997). doi: 10.1126/science.278.5340.1064; pmid: 9353181
55. T. Hart *et al.*, High-resolution CRISPR screens reveal fitness genes and genotype-specific cancer liabilities. *Cell* **163**, 1515–1526 (2015). doi: 10.1016/j.cell.2015.11.015; pmid: 26627737
56. T. Wang *et al.*, Identification and characterization of essential genes in the human genome. *Science* **350**, 1096–1101 (2015). doi: 10.1126/science.aac7041; pmid: 26472758
57. V. A. Blomen *et al.*, Gene essentiality and synthetic lethality in haploid human cells. *Science* **350**, 1092–1096 (2015). doi: 10.1126/science.aac7557; pmid: 26472760

ACKNOWLEDGMENTS

We thank D. Botstein, H. Bussey, A. Fraser, H. Friesen, M. Meneghini, and M. Tyers for critical comments. This work was primarily supported by the National Institutes of Health (R01HG005853) (C.B., B.A., and C.L.M.), Canadian Institutes of Health Research (FDN-143264 and FDN-143265) (C.B. and B.A.), RIKEN Strategic Programs for R&D (C.B.), JSPS Kakenhi (15H04483) (C.B.), National Institutes of Health (R01HG005084 and R01GM104975) (C.L.M), and the National Science Foundation (DBI\0953881) (C.L.M.). Computing resources and data storage services were partially provided by the Minnesota Supercomputing Institute and the UMN Office of Information Technology, respectively. Additional support was provided by the Canadian Institutes of Health Research (A.A.C.), National Science Foundation (MCB\1244043) (C.M.), European Research Council (ERC) Advanced Investigator Grant (AdG-294542) (L.M.S), ERC Advanced Grant (European Commission) (M.B.), Ministry of Education, Culture, Sports, Sciences and Technology, MEXT (15H04402) (Y.O.), Canadian Institutes of Health Research (FDN143301), Genome Canada Genome Innovation network (through the Ontario Genomics Institute) (A.-C.G), the Ontario Genomics Institute, Canadian Cystic Fibrosis Foundation, Canadian Cancer Society, Pancreatic Cancer Canada, University Health Network (I.S.), National Science Foundation, Cyber-Enabled Discover and Innovation (CDI) (OIA-1028394), ERC Starting Independent Researcher Grant (278212), ARRS project (J1-5424), Serbian Ministry of Education and Science Project 11144006 (N.P.), National Natural Science Foundation of China (T.X), RIKEN Foreign Postdoctoral Researcher Program (J.S.P., S.C.L.), National Science Foundation Graduate Research Fellowship (NSF 00039202) (E.N.K. and S.W.S), U. of Minnesota Doctoral Dissertation Fellowship (B.V. and E.N.K.). O.G.T, C.L.M, B.A., and C.B are fellows of the Canadian Institute for Advanced Research (CIFAR). All data files (Data Files S1 to 17) associated with this study are described in detail in the supplementary materials and can be downloaded from http://boonelab.ccbr.utoronto.ca/supplement/costanzo2016. Data Files S1 to S17 were also deposited in the DRYAD Digital Repository (doi:10.5061/dryad.4291s). Raw mass spectrometry data and downloadable identification and SAINTexpress results tables were deposited in the MassIVE repository housed at the Center for Computational Mass Spectrometry at UCSD (http://proteomics.ucsd.edu/ProteoSAFe/datasets.jsp). The endogenously tagged GFP and Gal-inducible hemagglutinin data sets have been assigned the MassIVE IDs MSV000079157 and MSV000079368 and are available for FTP download at ftp://MSV000079157@massive.ucsd.edu and ftp://MSV000079368@massive.ucsd.edu, respectively. The data sets were assigned the ProteomeXchange Consortium (http://proteomecentral.proteomexchange.org) identifiers PXD002368 and PXD003147 (data set password: SGA).

SUPPLEMENTARY MATERIALS

www.sciencemag.org/content/353/6306/aaf1420/suppl/DC1
Materials and Methods
Figs. S1 to S24
Tables S1 to S3
Data File Descriptions
References (*58*–*120*)

10.1126/science.aaf1420

Downloaded from http://science.sciencemag.org/ on September 30, 2016

RESEARCH ARTICLE SUMMARY

RNA STRUCTURE

RNA G-quadruplexes are globally unfolded in eukaryotic cells and depleted in bacteria

Junjie U. Guo and David P. Bartel*

INTRODUCTION: Many cellular RNAs contain regions that fold into stable structures required for function. Both Watson-Crick and noncanonical interactions can play important roles in forming these structures. An intriguing noncanonical structure is the RNA G-quadruplex (RG4), a four-stranded structure containing two or more layers of G-quartets, in which the Watson-Crick face of each of four G residues pairs to the Hoogsteen face of the neighboring G residues. RG4 regions can be very stable in vitro, particularly in the presence of K^+, and thus they are generally assumed to be predominantly folded within cells, which have ample K^+. Indeed, these structures have been implicated in mRNA processing and translation, with recently proposed roles in cancer and other human diseases. However, the number of cellular RNAs that can fold into RG4 structures has been unclear, as has been the extent to which these RG4 regions are folded in cells.

RATIONALE: Enzymes and chemicals that act on RNA with structure-dependent preferences provide valuable tools for detecting and monitoring RNA folding. For example, dimethyl sulfate (DMS) treatment of RNA, either in vitro or in cells, coupled with high-throughput sequencing of abortive primer-extension products can monitor the folding states of many RNAs in one experiment. Analogous high-throughput methods use cell-permeable variants of SHAPE (selective 2′-hydroxyl acylation analyzed by primer extension) reagents. These methods reveal important differences between RNA structures formed in vivo and those formed in vitro. However, they are designed to detect Watson-Crick pairing and thus do not identify RG4 structures or provide information on their folding states. After recognizing that RG4 regions can block reverse transcriptase, we reasoned that this property, together with the known ability of RG4s to protect the N7 of participating G nucleotides from DMS modification, could be used to develop a suite of high-throughput methods to both identify endogenous RNAs that can fold into RG4s in vitro and determine whether these regions also fold in cells.

RESULTS: We first developed a high-throughput method that identifies RG4 regions on the basis of their propensity to stall reverse transcriptase in a K^+-dependent manner. Applying this method to RNA from mammalian cell lines and yeast, we identified >10,000 endogenous regions that form RG4s in vitro, thereby expanding by a factor of >100 the catalog of endogenous regions with experimentally supported propensity to fold into RG4 structures. To infer the folding state of these RG4 regions in vitro and in cells, DMS treatment was performed before profiling of reverse-transcriptase stops. These analyses showed that, in contrast to previous assumptions, regions that folded into RG4 structures in vitro were overwhelmingly unfolded in vivo, as indicated by their accessibility to DMS modification in cells. A complementary probing strategy using a SHAPE reagent confirmed the unfolded state of most RG4 regions in eukaryotic cells. Moreover, RG4 regions remained unfolded both in cells depleted of adenosine 5′-triphosphate and in cells lacking a helicase known to unfold RG4 regions in vitro. Applying our probing methods to bacteria revealed a different behavior, in that model RG4 regions that were unfolded in eukaryotic cells were folded when expressed in *Escherichia coli*. However, these ectopically expressed quadruplexes impaired mRNA translation and cell growth, which helps explain why very few endogenous sequences that could fold into RG4s were detected in the transcriptomes of *E. coli* and the two other eubacteria analyzed.

ON OUR WEBSITE

Read the full article at http://dx.doi.org/10.1126/science.aaf5371

CONCLUSION: In mammals, thousands of endogenous RNA sequences have regions that can fold into RG4s in vitro, but these regions are globally unfolded in eukaryotic cells, presumably by robust and effective machinery that remains to be fully characterized. In contrast, RG4 regions are permitted to fold in *E. coli* cells, but *E. coli* and other bacteria have undergone evolutionary depletion of endogenous RG4-forming sequences. ■

The list of author affiliations is available in the full article online.
*Corresponding author. Email: dbartel@wi.mit.edu
Cite this article as J. U. Guo, D. P. Bartel, *Science* 353, aaf5371 (2016). DOI: 10.1126/science.aaf5371

The different mechanisms that eukaryotic and eubacterial cells use to avoid RG4 structures. RG4 regions are abundant but overwhelmingly unfolded in mammalian and yeast cells, implying robust and efficient molecular machinery, presumably involving helicases and RNA-binding proteins, which specifically unfolds RG4 regions and maintains them in an unfolded state (left). In contrast, regions that can fold into RG4 structures are depleted in bacteria, implying fewer progeny of cells that acquire these regions (right).

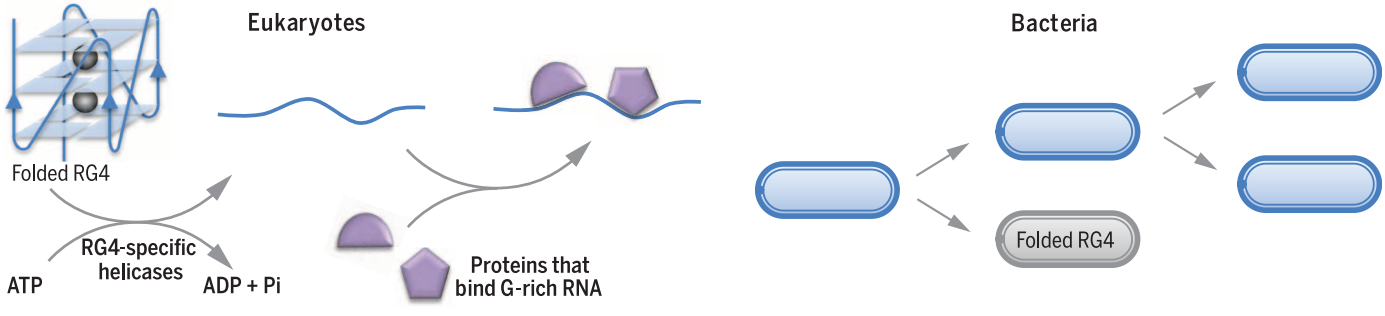

Downloaded from http://science.sciencemag.org/ on September 30, 2016

RESEARCH ARTICLE

RNA STRUCTURE

RNA G-quadruplexes are globally unfolded in eukaryotic cells and depleted in bacteria

Junjie U. Guo[1,2] and David P. Bartel[1,2]*

In vitro, some RNAs can form stable four-stranded structures known as G-quadruplexes. Although RNA G-quadruplexes have been implicated in posttranscriptional gene regulation and diseases, direct evidence for their formation in cells has been lacking. Here, we identified thousands of mammalian RNA regions that can fold into G-quadruplexes in vitro, but in contrast to previous assumptions, these regions were overwhelmingly unfolded in cells. Model RNA G-quadruplexes that were unfolded in eukaryotic cells were folded when ectopically expressed in *Escherichia coli*; however, they impaired translation and growth, which helps explain why we detected few G-quadruplex–forming regions in bacterial transcriptomes. Our results suggest that eukaryotes have a robust machinery that globally unfolds RNA G-quadruplexes, whereas some bacteria have instead undergone evolutionary depletion of G-quadruplex–forming sequences.

Many cellular RNAs contain regions that fold into stable structures required for function (*1*, *2*). These structures can be studied with chemical probes that modify accessible or flexible nucleotides (*3*–*5*). For example, dimethyl sulfate (DMS) methylates A and C residues that are not protected by Watson-Crick pairing or other interactions, and because these modifications stall reverse transcriptase, primer-extension reactions can detect modification and thereby report on the folding state of these nucleotides. DMS also penetrates living cells and modifies RNAs within these cells, and with high-throughput sequencing of global primer-extension products, the intracellular folding of numerous RNAs can be simultaneously monitored in a procedure called DMS-seq (*6*, *7*). Analogous high-throughput methods have also been developed with cell-permeable SHAPE (selective 2′-hydroxyl acylation analyzed by primer extension) reagents (*8*, *9*). These methods reveal important differences between RNA structures formed in vivo and those formed in vitro (*7*, *9*). However, these high-throughput methods are designed to detect Watson-Crick pairing, which leaves the folding states of noncanonical structures difficult to assess.

One such noncanonical structure is the RNA G-quadruplex (RG4), in which four strands of RNA interact, either intramolecularly or intermolecularly, through the formation of two or more layers of G-quartets, in which each of four G residues pairs to two neighboring G residues (Fig. 1A) (*10*, *11*). Owing to the extensive hydrogen-bonding and base-stacking interactions, RG4 structures can be very stable, with in vitro melting temperatures well exceeding physiological temperatures. This stability typically depends on the presence of K^+, which is the optimal size to bind at the center of two stacked G-quartets and thereby counter the otherwise repulsive partial negative charges that converge at the quadruplex core (Fig. 1A).

Because of the high stability of RG4 structures in vitro and the high concentration of K^+ in cells (typically >100 mM, well above that required for quadruplex formation), regions that fold into RG4 structures in vitro are generally assumed to fold into these structures in cells. Indeed, RG4s are implicated in control of mRNA processing and translation, with recently proposed roles in human diseases, such as cancer (*12*) and neurodegeneration (*13*). Supporting the idea that RG4s are folded in cells, immunostaining with G4-specific antibodies yields a detectable, albeit

[1]Howard Hughes Medical Institute, Whitehead Institute for Biomedical Research, Cambridge, MA 02142, USA. [2]Department of Biology, Massachusetts Institute of Technology, Cambridge, MA 02139, USA.
*Corresponding author. Email: dbartel@wi.mit.edu

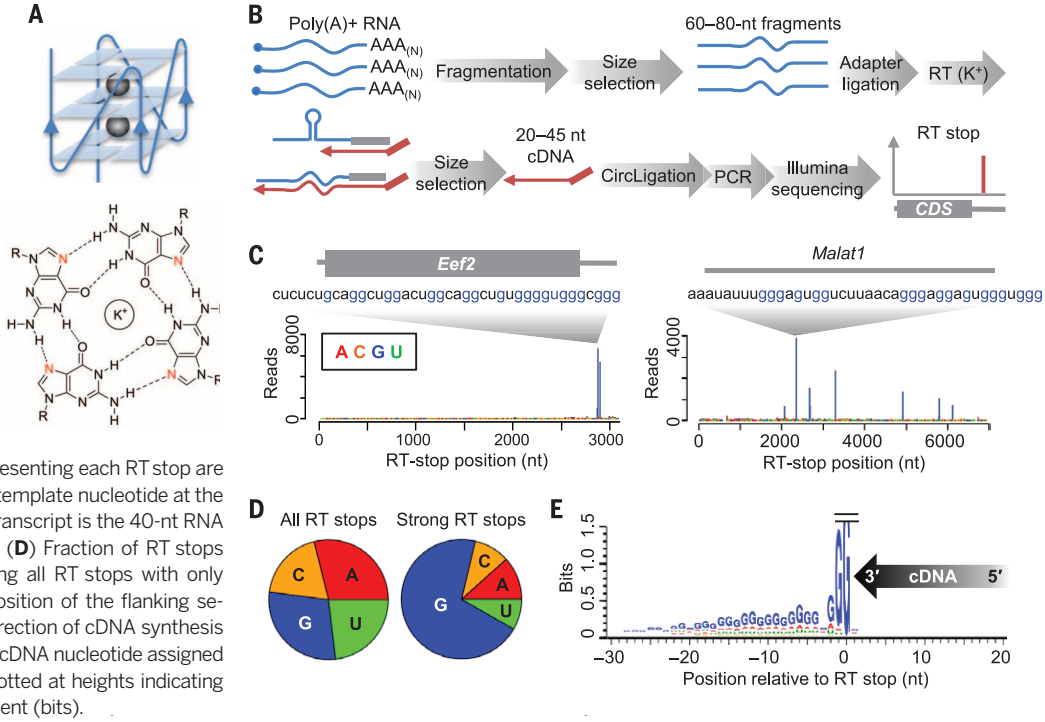

Fig. 1. Strong RT stops at G-rich regions in the mESC transcriptome. (**A**) The RNA G-quadruplex. The schematic (top) depicts a three-tiered RG4, with a parallel RNA-backbone orientation (solid line) and three G-quartets stabilized by two K^+ ions (spheres). The chemical structure of a G-quartet (bottom) highlights hydrogen bonding (dashed lines) to the N7 positions (red) and K^+-facilitated convergence of the exocyclic oxygens of the four G residues (R, ribose). (**B**) Schematic of RT-stop profiling. See text for explanation. (**C**) RT-stop profiles for *Eef2* mRNA (box, coding sequence) and *Malat1*. Bars representing each RT stop are colored according to the identity of the template nucleotide at the stall (position 0). Also shown for each transcript is the 40-nt RNA segment ending at the strongest stop. (**D**) Fraction of RT stops observed at each nucleotide, comparing all RT stops with only strong RT stops. (**E**) Nucleotide composition of the flanking sequences of strong RT stops at G. The direction of cDNA synthesis is indicated (arrow), with the 3′-terminal cDNA nucleotide assigned position +1. Template nucleotides are plotted at heights indicating the information content of their enrichment (bits).

Downloaded from http://science.sciencemag.org/ on September 30, 2016

weak, ribonuclease-sensitive signal in the cytoplasm (*14*). However, these immunostaining results leave open the possibility of folding during the processes of fixing, permeabilizing, or staining cells, and even if this signal represented quadruplex formation in cells, it could not provide information regarding either the sequence identities or the overall fraction of RG4 regions that fold in vivo.

Many RNAs with quadruplex-forming capacity

To systematically search for structure-forming potential in mammalian cellular RNAs, we exploited the ability of stable structures to stall reverse trancription. Polyadenylate [poly(A)]–selected mRNAs from mouse embryonic stem cells (mESCs) were randomly fragmented, and 60- to 80-nucleotide (nt) fragments were ligated to a common 3′ adapter used for global primer extension. Complementary DNAs (cDNAs) resulting from reverse transcription (RT) that stalled after only 20 to 45 nt of extension were purified and sequenced to identify the RT stops (Fig. 1B), by means of a procedure resembling that developed for DMS-seq (*7*). As illustrated for the *Eef2* (*Eukaryotic elongation factor 2*) mRNA and the *Malat1* (*Metastasis-associated lung-adenocarcinoma transcript 1*) noncoding RNA, most of the strong RT stops (65%) were at G nucleotides (Fig. 1, C and D, and fig. S1; $P < 10^{-15}$, χ^2 test). Analysis of the flanking sequences of these strong RT stops at G nucleotides showed that the 30 nucleotides upstream of the RT stops were also enriched in G (and depleted in C), particularly at positions −1 and −2 (92 and 66% G, respectively; Fig. 1E). In contrast, no enrichment was detected downstream, except for weak G enrichment at position +1 (38% G; Fig. 1E).

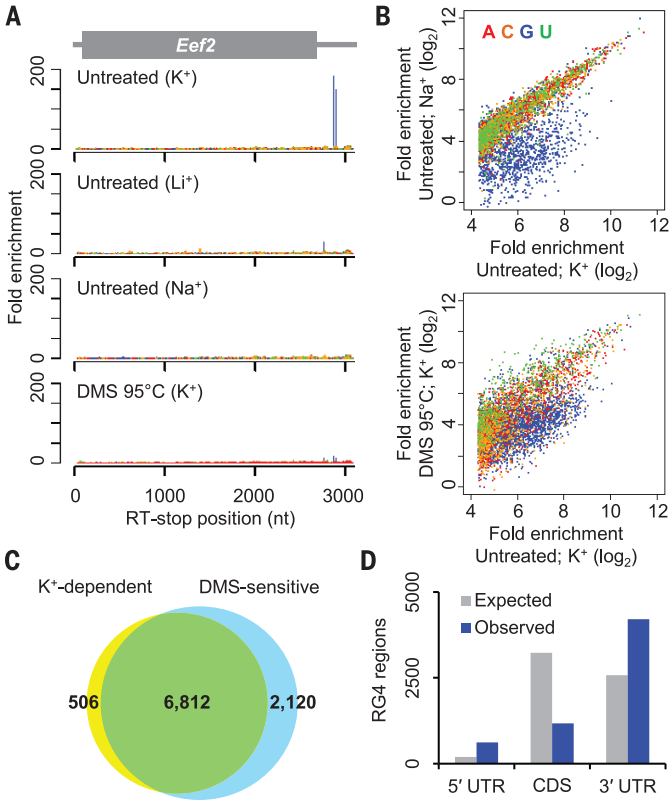

Fig. 2. Folded RG4 structures cause strong RT stops. (**A**) RT-stop profiles of *Eef2*, showing enrichment observed in the original conditions (K^+) and that observed when either substituting the monovalent cation used during RT (Li^+ or Na^+) or treating the RNA with DMS under denaturing conditions before RT (DMS 95°C). At each position within the mRNA, the fold enrichment was calculated as the number of RT-stop reads observed at that position, divided by the average number of RT-stop reads observed for all the mRNA positions with the same nucleotide identity. (**B**) Global analyses of strong RT stops, comparing the enrichment of stops observed in the original conditions (untreated; K^+) to those observed when either substituting K^+ with Na^+ (top) or pretreating RNA with DMS at 95°C (bottom). RT-stop values are colored according to the template nucleotide at position 0. The distributions are truncated at the left because stops with enrichment by less than a factor of 20 in the untreated K^+ sample were not classified as strong stops. (**C**) Overlap between K^+-dependent and DMS-sensitive strong RT stops (yellow and blue, respectively). (**D**) Abundance of RG4 regions within mRNA translated and untranslated regions. The expected abundances were estimated on the basis of the relative number of G nucleotides within these three regions of detected mRNAs.

The upstream G enrichment, together with recent studies of individual transcripts (*15*), suggested that formation of intramolecular RG4 structures caused these strong RT stops. To test this possibility, we examined whether these RT stops were sensitive to the identity of the monovalent counterion and found that substituting K^+ in the RT reaction with either Na^+ or Li^+ greatly diminished the RT stops at G residues (Fig. 2, A and B, and fig. S2A). Another diagnostic feature of RG4s is their sensitivity to modification of the N7 position of G (Fig. 1A). Methylating this position by using DMS (*16*) under denaturing conditions (95°C, 0 mM K^+) also substantially diminished the RT stops at G residues, despite the presence of K^+ during RT (Fig. 2, A and B, and fig. S2B). Most strong RT stops that were K^+-dependent were also DMS-sensitive (Fig. 2C and table S1; $P < 10^{-15}$, χ^2 test), and vice versa. Moreover, 6140 (90%) of the 6812 RT stops that exhibited factor of ≥2 decrease in Na^+/Li^+ reactions and factor of ≥2 decrease after 95°C DMS treatment were at G nucleotides (fig. S2C and table S1). In contrast, the 2120 DMS-sensitive but K^+-independent RT stops did not exhibit strong nucleotide enrichment at position 0 (fig. S2C), as would be expected for RT stops caused by other types of stable structures. Analysis of the remaining 672 RT stops that were K^+-dependent and DMS-sensitive but not at G nucleotides showed that their upstream sequences were also somewhat enriched in G (fig. S2D), suggesting that at least some of these RT stops also involved RG4 structures that caused RT to stall before reaching the 3′-terminal G nucleotides. Collectively, these results indicated that most G-rich regions that caused strong RT stops did so by forming RG4 structures in vitro.

The four strands of RG4 structures typically assume a parallel orientation (*17*) (Fig. 1A). The circular dichroism spectra of the 60-nt regions upstream of K^+-dependent strong RT stops in *Eef2* and *Malat1*, as well as that of a canonical RG4 sequence $G_3A_2G_3A_2G_3A_2G_3$ (hereafter referred to as the G3A2 quadruplex), exhibited a K^+-dependent increase at 263 nm, diagnostic of parallel RG4 structures (*17*) (fig. S3).

Features of mammalian RG4 regions

Of the many endogenous RNA sequences with predicted RG4-forming potential (*18*), only ~100 have been experimentally tested (*11*, *19*). Therefore, the 6140 RG4 regions in the mESC transcriptome, 4034 of which were nonoverlapping, considerably expanded the repertoire of endogenous RNA sequences with experimentally supported RG4-forming capacity. Nonetheless, cellular transcripts presumably contain additional regions with intrinsic RG4-forming potential not detected in our experiment. For example, our strategy would miss (i) structures with stabilities insufficient to block RT; (ii) structures spanning more than ~60 nt, which would be too large to reside within the RNA fragments assayed for RT stops; or (iii) regions within transcripts that were not expressed in mESCs at levels sufficient to be detected in our sequencing.

To benchmark our method with previously supported examples, nearly all of which are in human transcripts (*19*), we performed RT-stop profiling on mRNA from human cell lines. We identified 12,009 and 12,035 RG4 regions (6506 and 6281 nonoverlapping regions) in the human embryonic kidney 293T (HEK293T) and HeLa transcriptome, respectively; of these, 7852 nonoverlapping regions were identified in at least one of the two cell lines, and 4935 were identified in both cell lines (table S2). Of the known RG4 regions within detected mRNAs, about half were detected as K^+-dependent strong RT stops (fig. S4A and table S2).

Recently, a high-throughput method has been developed to identify genomic sequences that can fold into DNA G-quadruplexes in vitro (*20*). Because DNA and RNA of the same sequence often have distinct three-dimensional structures and some

Downloaded from http://science.sciencemag.org/ on September 30, 2016

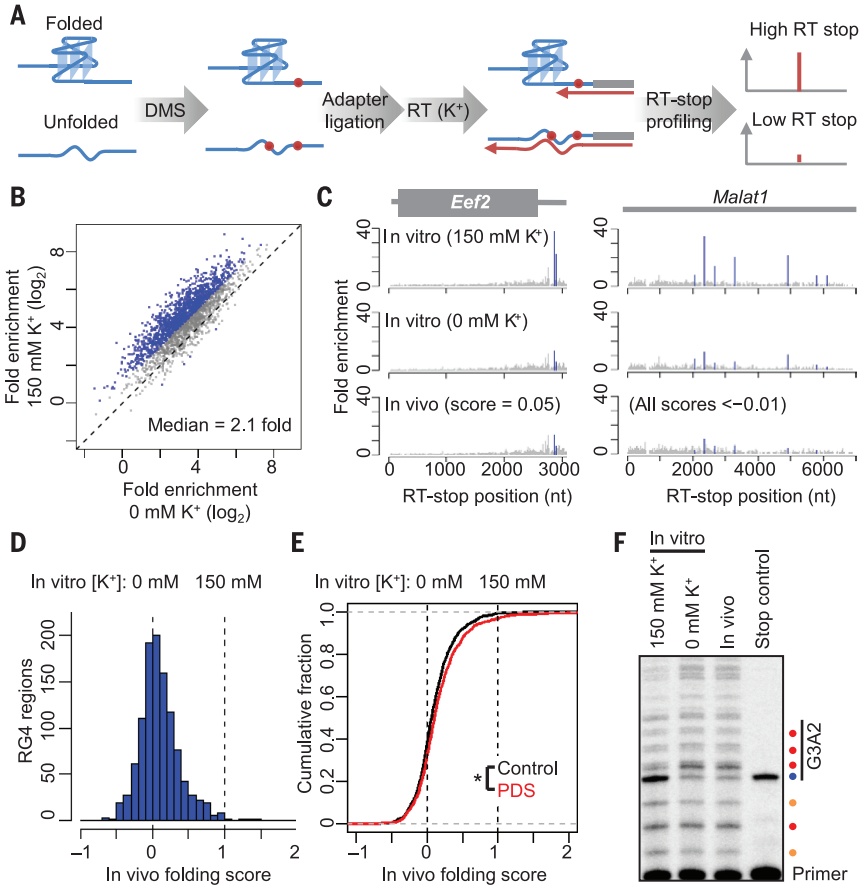

Fig. 3. RG4 regions are unfolded in mESCs. (**A**) Schematic of transcriptome-wide probing of RG4 folding. (**B**) Probing RG4 folding in vitro. The RT-stop enrichment observed after DMS treatment of RNA folded in K^+ (150 mM K^+) was compared to that observed after DMS treatment of RNA folded without K^+ (0 mM K^+). Values for regions with differences equal to or greater than a factor of 2 are indicated (blue). (**C**) RT-stop profiles of *Eef2* and *Malat1*, showing results observed after DMS treatment in vitro, either with or without K^+, and those observed after DMS treatment in vivo. RT-stop enrichment values corresponding to RG4 regions are in blue; values for other RT stops at G nucleotides are in gray. In vivo folding scores for the RG4 regions are shown. (**D**) The distribution of in vivo folding scores of the 1141 mESC RG4 regions that were examined. The 0 and 1 reference values, which represent the signal observed when treating with DMS in vitro after folding with or without K^+ (B), are marked (dashed lines). (**E**) Distribution of in vivo folding scores observed for RG4 regions after either treating the cells with 2 μM PDS for 24 hours (PDS, red) or mock treatment (control, black). *$P < 10^{-8}$, paired *t* test. (**F**) Gene-specific primer extension of the ectopically expressed G3A2 quadruplex probed in vitro (after folding in either 0 or 150 mM K^+) or in vivo. Shown is a phosphorimage of a denaturing gel that resolved the extension products of a P^{33}-radiolabeled primer. In the stop control, the β-mercaptoethanol quench was added to cells before DMS. The stronger RT stops are colored according to the nucleotide at the stall (A, red; C, orange; G, blue). The RG4 region is indicated (vertical line). For additional controls and sequencing ladders, see fig. S6E.

regions of DNA are either not expressed as RNA or are expressed as spliced transcripts that do not match the DNA, we expected that many DNA- or RNA-specific G4 regions would exist. Indeed, only 0.16% of the recently identified DNA G4 regions corresponded to RG4 regions found in HeLa and HEK293T cells, and of the nonoverlapping HeLa and HEK293T RG4 regions that uniquely mapped to the human genome, only 19% mapped to identified DNA G4 regions (fig. S4B).

Compared to control regions with matched nucleotide composition, the identified RG4 regions were more likely to have the four G-triplets needed to match the canonical RG4 motif (fig. S3C), $G_{\geq 3}N_xG_{\geq 3}N_xG_{\geq 3}N_xG_{\geq 3}$, in which each N_x represents a linker of any sequence ranging from 1 to ~7 nt in length (*18*). However, 37% of these regions had fewer than four G-triplets within 60 nt upstream of the RT stop (fig. S4C) and thus would be missed by most G4-searching algorithms (*18*). The 6140 RG4 regions from mESCs were found in 2792 transcripts (table S1), which included both mRNAs and noncoding RNAs, such as *Malat1*, which was sufficiently abundant to be analyzed despite its lack of a poly(A) tail. As previously predicted (*18*), RG4 regions were enriched within untranslated regions (UTRs) relative to mRNA coding sequences (CDSs) (Fig. 2D; $P < 10^{-15}$, χ^2 test), as might be expected if some of these regions have regulatory functions. However, G nucleotides within the 60-nt regions upstream of RT stops were not more conserved than G nucleotides within flanking regions (fig. S5), suggesting that the RG4 structure–forming capacity of most RG4 regions was not evolutionarily conserved.

In sum, RT-stop profiling identified thousands of RG4 regions in the mammalian transcriptomes, thereby expanding the catalog of experimentally supported endogenous RG4 regions by a factor of >100. As predicted computationally (*18*), regions that form RG4 structures in vitro are not an esoteric feature of dozens of mRNAs but rather are ubiquitous within mammalian transcriptomes, bringing to the fore the question of their in vivo folding status.

Globally unfolded RG4 regions in mESCs

To identify RG4 regions that are folded in cells, we combined RT-stop profiling with elements of DMS-seq (*7*) to develop a method that measures, transcriptome-wide, the in vivo folding states of endogenous sequences with RG4-forming potential (Fig. 3A). In this method, cells are first treated with DMS, which rapidly enters and randomly methylates accessible N7 positions of G residues (*4*). RNA isolated from these cells is then subjected to RT-stop profiling. Although DMS modifies the N7 position of G more efficiently than it modifies the N1 and N3 positions of A and C residues, respectively (*21*), modification at N7 does not prevent Watson-Crick pairing and thus does not cause an RT stop. Nonetheless, RT-stop profiling can distinguish between RG4 regions that are folded in cells from those that are not because those that are folded in vivo are protected from modification at positions participating in the RG4 structure, enabling them to later refold during RT to generate RT stops, whereas those that are unfolded in cells can be irreversibly modified at residues that would otherwise participate in quadruplex formation in vitro, resulting in RT read-through and correspondingly attenuated RT stops (Fig. 3A).

Reasoning that the RT-stop signals of different RG4 regions might have different sensitivities to DMS treatment, we first determined, for each RG4 region, the difference in RT-stop signal observed when mRNAs were modified in vitro either with or without K^+. On average, the mESC RG4 regions that were refolded and DMS-treated in the presence of K^+ had RT stops that were stronger by a factor of 2.5 than those observed when refolding and treating in the absence of K^+ (median, factor of 2.1), and 1342 regions had a difference of a factor of 2 or greater (Fig. 3B and table S3). These in vitro results confirmed that DMS accessibility with readout from RT-stop profiling could indeed report on the folding states of many RG4 regions.

To probe the intracellular folding state of these regions, we treated mESCs with DMS and extracted poly(A)-selected RNAs for RT-stop profiling. As a positive control, results within the 5.8*S* ribosomal RNA (rRNA) were analyzed as a DMS-seq experiment (monitoring RT stops at A and C

Downloaded from http://science.sciencemag.org/ on September 30, 2016

nucleotides), which showed that, as expected (7), DMS probing in vivo captured known Watson-Crick pairing within the 5.8*S* rRNA, as well as the intermolecular pairing between the 5.8*S* and 28S rRNAs (fig. S6A). Moreover, the RT-stop signals for RG4s were highly correlated between biological replicates (fig. S6B, Pearson's r = 0.88). Inspection of the RG4 regions in both *Eef2* mRNA and *Malat1* indicated that these RG4 regions were accessible to DMS modification in vivo, as revealed by greatly reduced RT-stop signals (Fig. 3C). The signals observed for the in vivo–modified sample resembled those observed when omitting K^+ from the in vitro folding and modification reaction, which indicated that these RG4 regions were unfolded in mESCs (Fig. 3C).

To infer the folding state, DMS-probing assays must be performed within their dynamic range; beyond this range, a transiently unfolded region might instead appear to be mostly unfolded, as most of the molecules eventually become modified. The RT-stop signal at RG4 regions diminished in the unfolded reference (0 mM K^+) but did not reach baseline (Fig. 3, B and C), which indicated that our in vitro treatment left a fraction of these molecules unmodified and thus showed that our in vitro modification was within its dynamic range. Moreover, DMS modification of A's and C's in vivo resembled that observed for our in vitro references (fig. S6C), which indicated that our in vivo probing was also within the dynamic range of the assay.

We next expanded the analysis to 1141 regions that retained a strong RT-stop signal (a factor of 10 above background) when treated with DMS in the presence of K^+ in vitro and had at least a 50% reduction in that signal when K^+ was excluded. For each of these regions, an in vivo folding score was calculated in which the RT-stop signal observed in vivo was expressed relative to the range of signal observed in vitro, assigning scores of 1 and 0 to the signals observed in vitro with and without K^+, respectively. In vivo folding scores for the 1141 RG4 regions centered near 0 (median = 0.06) (Fig. 3D and table S3), which indicated that in mESCs, the folding of most RG4 regions resembled the unfolded state observed in vitro without K^+. RG4 regions in 5′ UTRs, CDSs, and 3′ UTRs, as well as those in noncoding RNAs, were similarly unfolded (fig. S6D). Treating mESCs with pyridostatin (PDS), a G4-stabilizing reagent (*14*, *15*), induced a detectable but modest increase in global RG4 folding (0.04 increase in median folding score) (Fig. 3E; $P < 10^{-8}$, paired t test).

Although most RG4 regions are unfolded in mESCs, we cannot rule out the possibility that a few RG4 structures form in cells but could not be distinguished from experimental variability, or escaped our detection for other reasons, such as stable folding even in the absence of K^+. An inability of DMS to penetrate the cell and modify the regions cannot be a source of false-negatives, as the decrease in the RG4-specific RT stops observed for RNA isolated from DMS-treated cells confirmed that DMS was indeed able to access and efficiently modify these regions in vivo. To confirm the unfolded state of RG4 regions with strong canonical motifs, we inserted the G3A2 quadruplex into an mRNA 3′ UTR, ectopically expressed the mRNA in HEK293T cells, and performed DMS modification followed by gene-specific primer extension. Again, the RT-stop pattern observed after DMS modification in vivo strongly resembled that observed after modifying in vitro without K^+ (Fig. 3F and fig. S6E), further supporting the conclusion that RG4 regions are mostly unfolded in mammalian cells.

Globally unfolded RG4 regions in yeast cells

To determine whether the globally unfolded state of RG4 regions extends beyond mammalian cells, we applied our methods to the budding yeast *Saccharomyces cerevisiae*. We identified 744 strong RT stops within RNA isolated from exponentially growing yeast (table S4A), 133 of which were K^+-dependent stops at G nucleotides. Among them, 47 showed a difference of a factor of 2 or more in RT-stop signal when comparing samples probed after folding with and without K^+ (Fig. 4A and table S4B). The folding scores of endogenous RG4 regions centered near 0 (median = −0.15) (Fig. 4, B and C), again indicating a globally unfolded state. As observed in HEK293T cells, the ectopically expressed G3A2 quadruplex was also highly accessible to DMS, as indicated by an RT stop matching that observed for RNA modified in vitro without K^+ (Fig. 4D). These results indicate that the globally unfolded state of RG4 regions is a broadly conserved feature of eukaryotic cells.

SHAPE probing of RG4 regions

In addition to the chemical probes that modify the bases, such as DMS, probes that modify ribose 2′-hydroxyl groups with efficiency depending on the local chemical environment, known as SHAPE reagents, can provide useful tools for studying RNA structures (*3*, *5*). Among these reagents, 2-methylnicotinic acid imidazolide (NAI) has been used to probe Watson-Crick RNA structures in cells (*9*, *22*). To test whether NAI can also distinguish the folding states of RG4 regions, we used it to treat the G3A2 quadruplex folded in vitro with or without K^+ and quantified its reactivity at each nucleotide using gene-specific primer extension, substituting Na^+ for K^+ in the RT reaction, so that modifications within RG4 regions could be detected (Fig. 5A). Whereas the formation of Watson-Crick structure typically decreases SHAPE reactivity, formation of the G3A2 quadruplex in the presence of K^+ increased NAI reactivity (Fig. 5A). Furthermore, the enhanced reactivity occurred at the last G residue of each of the first three G tracts of the G3A2 quadruplex (Fig. 5A), consistent with a recent report describing in vitro NAI probing of two other quadruplexes (*23*). Perhaps the transition between a G tract and a short loop in a parallel RG4 structure bends the RNA backbone to expose the 2′-hydroxyl of the last residue of the G tract (fig. S7A). In vivo NAI treatment of the G3A2 quadruplex ectopically expressed in *S. cerevisiae* generated a modification pattern resembling that observed for this region folded in vitro without K^+ (Fig. 5A), supporting the conclusion that this quadruplex is unfolded in yeast cells. Analogous results were observed for another model RG4, which had single-nucleotide U loops linking the G tracts (the G3U quadruplex) (fig. S7B).

To probe endogenous RG4 regions, we treated mESC RNA with NAI either in vitro (refolded with or without K^+) or in vivo and used RT-stop profiling with Na^+ to determine the modification patterns (Fig. 5B). As with the G3A2 quadruplex, when folding endogenous RG4 regions in the presence of K^+ in vitro, we observed preferential modification of the last G residue in G tracts followed by short loops (Fig. 5C and fig. S7C). This pattern generated greater unevenness of modifications among G nucleotides within the RG4 region, which we quantified by calculating the Gini coefficient (*7*) for each of the 310 nonoverlapping

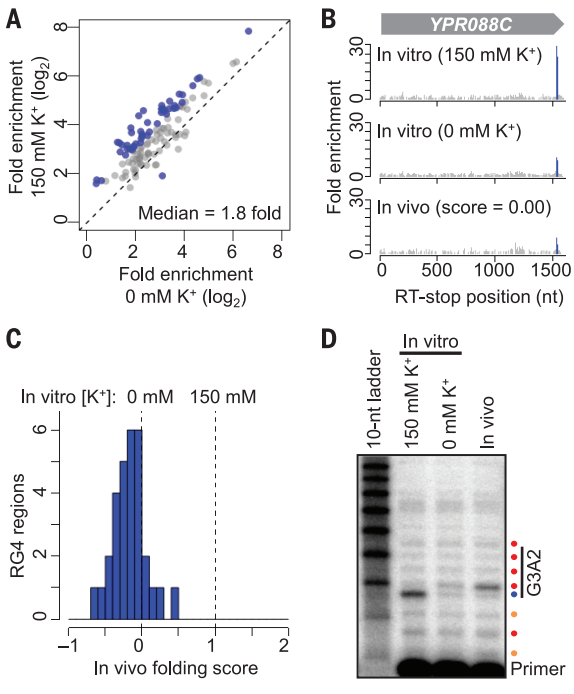

Fig. 4. RG4 regions are unfolded in *S. cerevisiae*. (**A**) Probing in vitro folding of yeast RG4s. Otherwise, as in Fig. 3B. (**B**) RT-stop profiles of *YPR088C*. Otherwise, as in Fig. 3C. (**C**) The distribution of in vivo folding scores of the 31 RG4 regions that were examined in yeast. Otherwise, as in Fig. 3D. (**D**) Gene-specific primer extension of the ectopically expressed G3A2 quadruplex probed in vitro (after folding in either 0 or 150 mM K^+) or in vivo. The primer was labeled with P^{32}; otherwise, as in Fig. 3F.

Downloaded from http://science.sciencemag.org/ on September 30, 2016

endogenous RG4 regions that had sufficient read coverage (≥100 RT-stop reads at G nucleotides in each sample). Among these, 49 had a ≥0.1 increase in Gini coefficient when comparing the modification observed in vitro after folding with K^+ compared to that observed after folding without K^+ (Fig. 5D). For these 49 regions, we calculated in vivo folding scores calibrated on the Gini-coefficient differences observed in vitro (table S5). As observed with the DMS probing, the distribution of in vivo folding scores centered near 0 (median = −0.02) (Fig. 5E), indicating that the in vivo NAI modification patterns of most RG4 regions resembled those of the unfolded state.

NAI probing complements DMS probing in three respects. First, NAI preferentially modifies specific residues of folded RG4s, whereas DMS modifies residues of unfolded RG4s. Second, NAI modification generates RT stops without requiring RG4 refolding, whereas DMS probing requires the refolding of RG4 structures in the presence of K^+ to generate an RT stop. Third, NAI probing might detect less stable RG4 structures that do not stall RT in vitro and thereby escape identification by RT-stop profiling. However, unlike DMS probing of RG4 regions, NAI probing does not focus the signal onto a single RT-stop nucleotide, and it requires specific RG4 configurations, such as G tracts followed by short loops, which also reduced the number of quantifiable RG4 regions. Nevertheless, the results from these two complementary chemical-probing methods both indicated that, despite the high intracellular K^+ concentration, RG4 regions are overwhelmingly unfolded in eukaryotic cells.

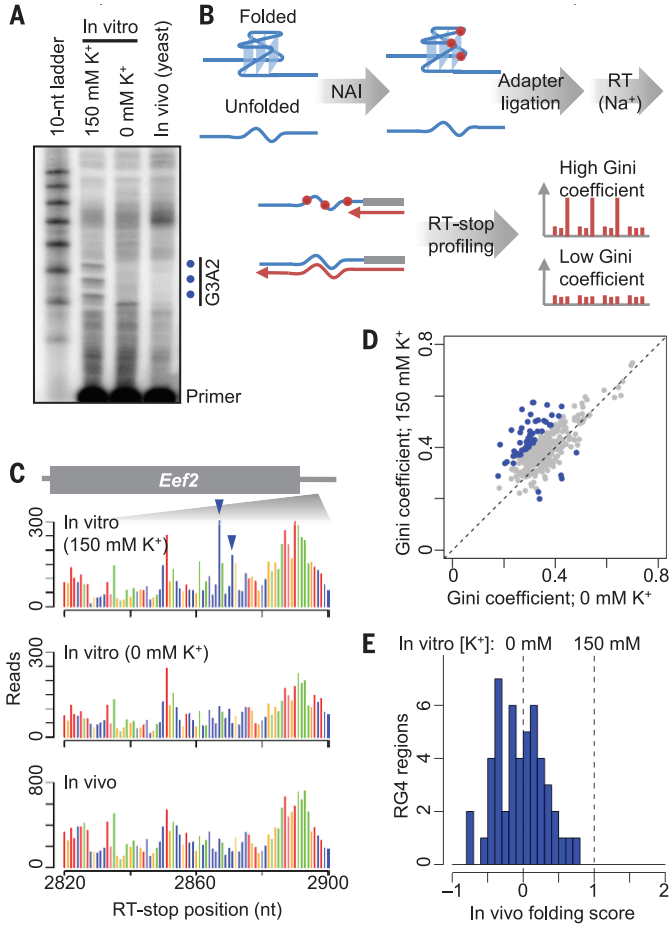

Fig. 5. Probing RG4 folding with NAI. (**A**) Gene-specific primer extension of the ectopically expressed G3A2 quadruplex probed with NAI in vitro (after folding in either 0 or 150 mM K^+) or in yeast. Shown is a phosphorimage of a denaturing gel that resolved the extension products of a P^{32}-radiolabeled primer. RT stops corresponding to the preferential modifications of NAI within the G3A2 quadruplex are indicated (blue dots). (**B**) Schematic of transcriptome-wide probing of RG4 folding with NAI. (**C**) RT-stop profiles of an RG4 and its flanking regions within the *Eef2* 3′ UTR, showing raw read counts colored according to the identity of the template nucleotide at the stall (position 0). G residues preferentially modified after folding in K^+ are indicated (blue arrowheads). (**D**) Comparison of Gini coefficients of the 310 RG4 regions with ≥100 RT stop reads in each of the two samples probed with NAI in vitro after folding in either 0 or 150 mM K^+. Values for regions with differences of ≥0.1 between the two samples are indicated (blue). (**E**) Distribution of in vivo folding scores of the 49 RG4 regions that were examined by NAI probing. Otherwise, as in Fig. 3D.

Robust RG4 unfolding in eukaryotic cells

Our results in eukaryotic cells resembled those of recent high-throughput studies showing that Watson-Crick secondary structures that form in vitro are frequently unfolded in cells (*7*, *9*), except that the intracellular unfolding of RG4 regions was more pervasive. Whereas the previous studies identified many instances in which Watson-Crick structures do form in vivo, as expected from the known Watson-Crick pairing within ribosomal RNAs, tRNAs, pri-microRNAs, mRNAs, and other RNAs, we found no compelling evidence for the folding of an RG4 region in eukaryotic cells, which implies that these cells have a very effective molecular machinery that specifically remodels RG4s and maintains them in their unfolded state.

This remodeling presumably involves adenosine 5′-triphosphate (ATP)–dependent processes. ATP depletion in yeast causes a global increase in Watson-Crick structures, suggesting that ATP-dependent processes, in particular ATP-dependent RNA helicases, play a major role in the cellular remodeling of these structures (*7*). Among the characterized ATP-dependent RNA helicases, DEAH box–containing helicase 36 (DHX36) accounts for most RG4-unfolding activity in HeLa cell extracts (*24*). To test whether DHX36 contributes to the globally unfolded state of RG4 regions in vivo, we applied DMS probing to mouse embryonic fibroblasts (MEFs) in which DHX36 was inducibly deleted through Cre-mediated recombination (*25*). The global distribution of folding scores was largely unchanged after DHX36 deletion, and values for individual RG4 regions were highly correlated before and after DHX36 deletion (fig. S8, A to C), indicating that DHX36 was dispensable for the global unfolding of endogenous RG4 regions. We also tested whether ATP depletion affected RG4 folding and found that the ectopically expressed G3A2 quadruplex remained largely unfolded (fig. S8D). Although redundant functions with other helicases and the inability to completely deplete ATP might explain the negative results of these experiments, our results show that the mechanism responsible for remodeling RG4s and maintaining their unfolded state is robust to either the deletion of a key helicase known to unfold RG4 structures or the substantial depletion of ATP.

Folding of RG4 structures in bacteria

We next applied our methods to bacterial transcriptomes. Compared to the mammalian transcriptome, the *Escherichia coli* transcriptome was substantially depleted in regions with K^+-dependent strong RT stops (Fig. 6A and table S6). Only 35 K^+-dependent strong RT stops were identified in *E. coli*, of which only 14 (40%) were at G nucleotides. Among these 14, none had differential DMS accessibility when comparing the results of in vitro modification with and without K^+ (table S6). Similar depletion was observed within the transcriptomes of the other two bacteria that we examined, *Pseudomonas putida* and *Synechococcus* sp. WH8102 (Fig. 6A and table S6), even though their genomes are more G-rich than mammalian genomes. Only one region within the transcriptomes of these two species passed our cutoffs for calculating an in vivo folding score (a *P. putida* region with a folding score of 0.5; table S6).

Having acquired evidence for only a single, weak RG4 region in endogenously expressed bacterial RNA, we ectopically expressed the G3A2 quadruplex within the 3′ UTR of an *mCherry* transcript and probed its folding state in *E. coli*. In contrast to our results in eukaryotic cells, the strong RT stop corresponding to the G3A2 quadruplex was resistant to in vivo DMS modification, indicating that this region was folded in *E. coli* cells (Fig. 6, B and C). Likewise, the G3U quadruplex, was also folded in *E. coli* (Fig. 6C). Although intracellular NAI probing of the G3A2 quadruplex was

Downloaded from http://science.sciencemag.org/ on September 30, 2016

inconclusive, intracellular NAI probing of the G3U quadruplex generated the modification pattern specific to that of the folded G3U quadruplex (fig. S9), confirming that RG4 folding rather than protein binding protected the region from DMS modification in vivo. Thus, RG4 regions are permitted to fold in *E. coli* but are strongly depleted among endogenous *E. coli* RNAs.

To understand this depletion, we compared the growth of strains that expressed G3A2 or G3U quadruplexes to those of strains that expressed the corresponding quadruplex mutants in which point substitutions abolished RG4-forming capacity and found that the RG4-expressing strains grew more slowly than the corresponding mutant-expressing strains (Fig. 6D). Moreover, these growth defects were exacerbated after introducing stop-codon mutations that caused the *mCherry* coding sequence to extend through the RG4 regions (Fig. 6D). Although effects from the RG4 regions in UTRs might be attributable to either RNA or DNA quadruplex formation, the enhanced growth defects observed after introducing stop-codon mutations were attributable to only RG4 structures.

To determine the influence of folded RG4 structures on translation, we examined the translation products from each of the strains. Consistent with a previous study (*26*), RG4 regions downstream of the stop codon did not substantially influence mCherry production. In contrast, the G3A2 quadruplex upstream of the stop codon caused read-through of the stop codon and/or frame-shifting, generating polypeptides that were longer than expected (Fig. 6E). The G3U quadruplex also perturbed translation, causing the production of both longer and shorter polypeptides (Fig. 6E). The products of the expected size dominated when mutant RG4 regions were placed upstream of the stop codon, which indicated that the aberrant translation products were primarily the consequence of stable RG4 structures.

Discussion

The mammalian, yeast, and bacterial cells that we studied all strongly avoid the presence of folded RG4 structures in their transcriptomes but do so through different mechanisms. Based on our in vivo probing, the eukaryotic cells appear to have a robust and effective molecular machinery that specifically unfolds and maintains the thousands of RG4 regions in an unfolded state, whereas bacteria lack this machinery and have instead eliminated sequences with RG4-forming potential over the course of evolution. When considering the impaired growth rates observed for strains ectopically expressing RG4 regions, the bacterial mechanism is easy to understand, but how might the eukaryotic mechanism act? Although the critical factors remain to be identified, this mechanism differs from that which unfolds Watson-Crick structure in two key aspects. First, it is less sensitive to ATP depletion, and second, it is more pervasive, unfolding essentially every RG4 that could be monitored in mESCs, MEFs, and yeast, whereas the activities that unfold Watson-Crick structure allow many RNAs to remain folded.

We suspect that single-stranded RNA-binding proteins lie at the center of the mechanism that unfolds most eukaryotic RG4 regions. A wide variety of abundant RNA-binding proteins bind to G-rich RNA, including the heterogeneous nuclear ribonucleoprotein (hnRNP) F/H family (*27*, *28*), hnRNP D0 (*29*), hnRNP M (*30*), hnRNP A/B (*31*), hnRNP A1 (*32*, *33*), hnRNP A2 (*34*), CBF-A (*34*), and SRSF1/2 (*35*). The solution structures of the three quasi-RNA recognition motifs (qRRMs) of hnRNP F in complex with G-tract RNA show how qRRMs could maintain G tracts in a single-stranded conformation without blocking solvent accessibility to the N7 positions (*36*), which is consistent with our DMS probing results. Regardless of the identity of the machinery that operates in eukaryotic cells, it must be acting broadly throughout the transcriptome, including on untranslated RNAs and nuclear RNAs, as illustrated by the unfolding of RG4 regions within *Malat1* (Fig. 3C), a nuclear noncoding RNA.

The evolutionary depletion of RG4 regions might be more tenable for bacteria than for eukaryotes for two reasons. First, maintaining machinery dedicated to the remodeling of RG4s would be more costly for species under greater selective pressure to minimize their genomes. Second, species with smaller genomes would face less frequent de novo emergence of new RG4 regions. By contrast, the eukaryotic mechanism provides opportunities for regulation. Indeed, the relative enrichment of RG4-forming regions in untranslated regions hints at the possibility that RG4 regions might be allowed to fold and impart regulatory functions in certain cell types and states or subcellular compartments (*37*). Alternatively,

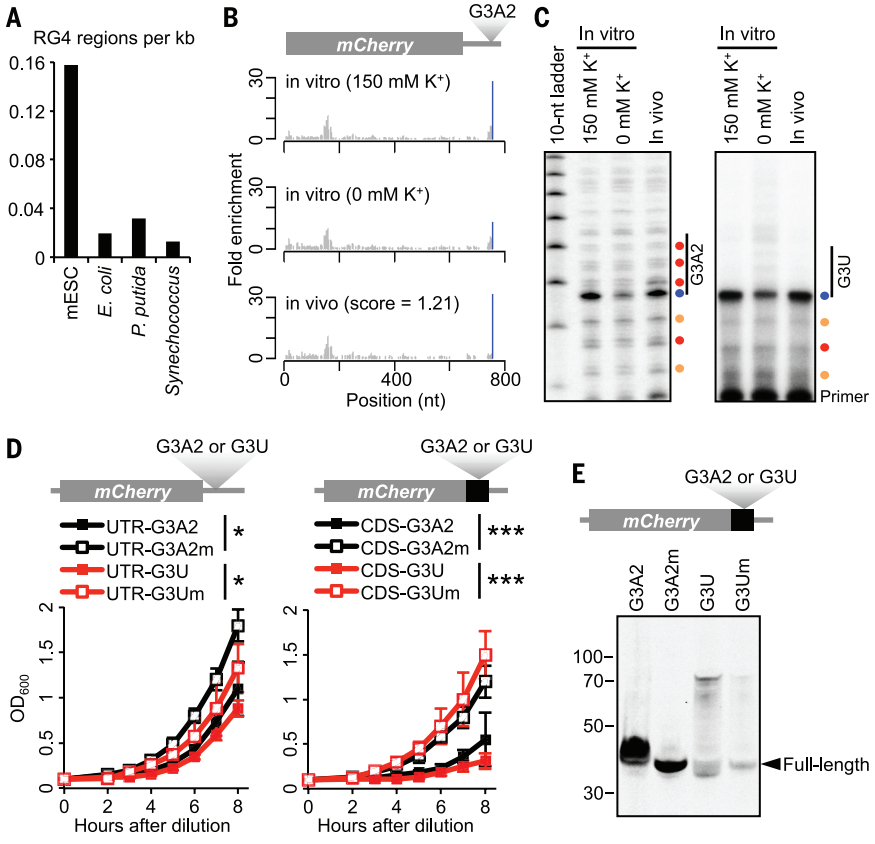

Fig. 6. RG4 folding and interference with growth and translation in *E. coli*. (**A**) Density of RG4 regions in bacterial and mESC transcriptomes. For each species, the number of RG4 regions, as identified from K^+-dependent strong RT stops at G nucleotides, was normalized to the total length of all detected transcripts. (**B**) RT-stop profiles of an ectopically expressed *mCherry* mRNA with a G3A2 quadruplex inserted into its 3′ UTR, showing results observed after DMS treatment in vitro, either with or without K^+, and in vivo. Otherwise, as in Fig. 3C. (**C**) Gene-specific primer extension of ectopically expressed G3A2 (left, P^{33}-labeled primer) and G3U (right, P^{32}-labeled primer) quadruplexes probed with DMS. Otherwise, as in Fig. 3F. (**D**) Growth curves of strains expressing *mCherry* transcripts with the indicated RG4 (G3A2 or G3U) or RG4 mutant (G3A2m or G3Um) in either the 3′ UTR (left) or the CDS (right). Growth was monitored by optical density at a wavelength of 600 nm (OD_{600}). Plotted are mean values ± SD ($n = 6$). *$P < 0.05$; ***$P < 0.001$; Student's t tests using measurements at the last time point. (**E**) Immunoblot probed for the translation products of the *mCherry* constructs with either the indicated RG4 or its respective mutant inserted between the *mCherry* sequence and the stop codon. Mobilities of molecular-weight markers and the full-length products are shown.

Downloaded from http://science.sciencemag.org/ on September 30, 2016

these regions might impart function through transient folding that cannot be detected in our steady-state measurements. Another possibility is that the previously reported regulatory roles of RG4 regions, such as translational repression by RG4 regions within 5′ UTRs (*10*), might result from the stable association of the RNA-binding proteins that maintain the RG4 regions in the unfolded state. In this scenario, the bound proteins rather than a folded RG4 would inhibit translation initiation. Clearly, more needs to be learned about this RNA structure in its native cellular contexts, and our results and methods provide the framework for doing so.

Materials and methods

In vivo DMS modification

DMS (Sigma-Aldrich; 50% diluted with ethanol) was added to mESCs or HEK293T cells cultured in 15 cm dishes to a final concentration of 8%, and evenly distributed by slow swirling. After incubating at 37°C for 5 min, the media and excess DMS were decanted, and cells were washed twice with 25% β-mercaptoethanol (Sigma-Aldrich) in PBS to quench any residual DMS. After washing, cells were lysed in 10 mL TRIzol reagent (Invitrogen) supplemented with 5% β-mercaptoethanol, and lysates were stored at −80°C. DMS was added to 10 ml of yeast culture to a final concentration of 8%. After incubating at 30°C with continuous shaking for 5 min, two volumes of 25% β-mercaptoethanol were added to the culture to stop the modification. Cells were harvested by centrifugation at 4,000 rpm for 5 min and washed with 25% β-mercaptoethanol until no residual DMS was observed at the bottom of tubes. After the final centrifugation, cells were resuspended in RNAlater solution (Invitrogen) and stored at −80°C. DMS treatment of the *E. coli* culture was similar to that of the yeast culture, except it was performed at 37°C. For additional details on culture of and transfection of mammalian cells, culture and induction of yeast cells, culture and induction of bacteria, and construction of RG4 expression constructs, see the supplementary materials.

In vitro folding and DMS modification

Poly(A)-selected RNA in 1 mM Mg^{2+} and 50 mM Tris-Cl (pH 7.0), either with or without 150 mM K^+, was heated to 80°C for 2 min and then rapidly cooled to 0°C for 1 min. DMS was added to a final concentration of 8% and the mixture was incubated at either 37°C (mammalian and *E. coli* RNA) or 30°C (yeast RNA) for 5 min with constant mixing. Two volumes of 25% β-mercaptoethanol were added to stop the reaction before RNA was phenol-chloroform extracted and precipitated. For details on RNA purification, see the supplementary materials.

RT-stop profiling

The DMS-seq protocol (*7*) was adapted to detect RT stops in unmodified RNA. Poly(A)-selected RNA (1 μg) in 10 mM Tris-Cl (pH 7.5) was denatured at 95°C for 2 min, supplemented with RNA-fragmentation reagent (Ambion) and incubated at 95°C for additional 1 min before adding EDTA stop solution (Ambion). After ethanol precipitation, RNA fragments were dephosphorylated at their 3′ ends with T4 polynucleotide kinase (New England BioLabs). 60–80-nt RNA fragments were gel-purified and ligated to a pre-adenylated 3′ DNA adapter (AppTCGTATGCCGTCTTCTGCTTGddC) with T4 RNA ligase 1 (New England BioLabs) without ATP. Products of the expected size (82–102 nt) were gel-purified and resuspended in 6 μl water. For reverse transcription, 1 μl 0.2 M Tris-Cl (pH 7.5), 1 μl 1.5 M KCl (or NaCl or LiCl), 0.5 μl 60 mM $MgCl_2$, 0.5 μl 10 mM dNTP mix and 0.5 μl 1 μM 5′-radiolabeled primer (^{32}p-NNNNNNGATCGTCGGACTGTAGAACTCTGAACCTGTCG/iSp18/CAAGCAGAAGACGGCATACG, in which N is any nucleotide, and iSp18 is an 18-atom hexa-ethyleneglycol spacer, IDT) were added to the RNA template. The mixture was incubated at 80°C for 2 min then cooled down to 42°C and incubated for additional 2 min before adding 100 units of SuperScript III reverse transcriptase (Invitrogen). After incubation at 42°C for 10 min, the reaction was stopped with addition of 1 μl of 1 M NaOH, and the mixture was heated at 98°C for 15 min to hydrolyze the RNA. cDNAs from extension that stalled after addition of 20 to 45 nt were separated from primers and full-length cDNAs on a 10% urea gel, eluted and precipitated. Purified cDNA fragments were circularized with 50 units of CircLigase (Epicentre) at 60°C for 4 hours before inactivation at 80°C for 10 min. Circularized cDNAs were amplified with a 5′ indexed primer (AATGATACGGCGACCACCGACAGGTTGGAATTCTCGGGTGCCAAGGAACTCCAGTCACxxxxxxATCCGACAGGTTCAGAGTTCTACAGTCCGA, in which xxxxxx is the multiplexing index), a common 3′ primer (CAAGCAGAAGACGGCATACGA), and Platinum Taq DNA Polymerase High Fidelity (Invitrogen) for 10 to 13 cycles of PCR. Libraries were purified on an 8% formamide gel and sequenced on a HiSeq 2000 sequencing machine (Illumina; 40 cycles, single-end mode). For details on transcript-specific analyses of model RG4 regions using primer-extension assays, see the supplementary materials.

Analysis of sequencing reads

For each read that uniquely mapped to the cognate transcriptome, the nucleotide immediately upstream of the first aligned position was annotated as an RT stop. At each position of the transcriptome with ≥3 RT-stop reads, a fold-enrichment value (f) for RT stops was calculated as the ratio between the number of reads stalled at that position and the background read density, which was the average number of reads over all positions of the same nucleotide within the same transcript (e.g., all G nucleotides). RT stops with ≥10 reads and fold enrichment values ≥20 were designated strong stops (fig. S1). When calculating the fold enrichment values for negative-control samples (Li^+, Na^+, and 95°C DMS), the position under consideration was assigned a pseudo read count of 1 if it had no RT-stop reads (with no change to the background read density). Strong RT stops for which enrichment decreased by more than 50% in 150 mM Na^+ compared to 150 mM K^+ were designated K^+-dependent. For details on read mapping, see the supplementary materials.

NAI probing

NAI was synthesized as described (*22*) and stored as a 1M solution in DMSO at −80°C. For treatment in vivo, mESCs and yeast cells were treated with 80 mM NAI for 15 min at 37°C and 30°C, respectively, and washed three times with PBS before RNA extraction and poly(A) selection. For treatment in vitro, poly(A)-selected RNA in 1 mM Mg^{2+} and 50 mM Tris-Cl (pH 7.0), either with or without 150 mM K^+, and was heated to 80°C for 2 min and then rapidly cooled to 0°C for 1 min. This refolded RNA was treated with 80 mM NAI for 5 min at either 37°C (mammalian RNA) or 30°C (yeast RNA). After treatment, RNA was phenol-chloroform extracted and precipitated. NAI-treated RNA was subjected to RT-stop profiling, with 150 mM Na^+ instead of 150 mM K^+ during primer extension. Gini coefficients were calculated for each nonoverlapping RG4-containing region (identified as 60-nt regions upstream of K^+-dependent strong RT stops) as

$$Gini = \frac{\sum_{i=1}^{n}\sum_{j=1}^{n}|r_i - r_j|}{2n^2\,\bar{r}}$$

where n denotes the number of G residues in the RG4 region, and r_i denotes the RT-stop read number at position i.

Calculation of in vivo folding scores

For each RG4 region that retained a strong RT-stop signal (10 fold above background) when treated with DMS in the presence of K^+ in vitro and had at least a 50% reduction in that signal when K^+ was excluded, an in vivo folding score (s) was calculated as

$$s = \frac{f(\text{in vivo}) - f(\text{in vitro; 0 mM K}^+)}{f(\text{in vitro; 150 mM K}^+) - f(\text{in vitro; 0 mM K}^+)}$$

For the regions that had ≥100 RT-stop reads at G nucleotides after NAI probing and a difference of ≥0.1 in Gini coefficients when comparing results of RNA folded in vitro with K^+ to those of RNA folded in vitro without K^+, an in vivo folding score (s) was calculated as

$$s = \frac{Gini(\text{in vivo}) - Gini(\text{in vitro; 0 mM K}^+)}{Gini(\text{in vitro; 150 mM K}^+) - Gini(\text{in vitro; 0 mM K}^+)}$$

Although folding scores were calculated using linear functions, the conclusions of this study were not dependent on a linear relationship between the fraction of folded molecules and the extent of DMS or NAI modification.

REFERENCES AND NOTES

1. S. A. Mortimer, M. A. Kidwell, J. A. Doudna, Insights into RNA structure and function from genome-wide studies. *Nat. Rev. Genet.* **15**, 469–479 (2014). doi: 10.1038/nrg3681; pmid: 24821474
2. Y. Wan, M. Kertesz, R. C. Spitale, E. Segal, H. Y. Chang, Understanding the transcriptome through RNA structure. *Nat. Rev. Genet.* **12**, 641–655 (2011). doi: 10.1038/nrg3049; pmid: 21850044
3. K. M. Weeks, Advances in RNA structure analysis by chemical probing. *Curr. Opin. Struct. Biol.* **20**, 295–304 (2010). doi: 10.1016/j.sbi.2010.04.001; pmid: 20447823

Downloaded from http://science.sciencemag.org/ on September 30, 2016

4. S. E. Wells, J. M. Hughes, A. Haller Igel, M. Ares Jr., Use of dimethyl sulfate to probe RNA structure in vivo. *Methods Enzymol.* **318**, 479–493 (2000). doi: 10.1016/S0076-6879(00)18071-1; pmid: 10890007
5. M. Kubota, C. Tran, R. C. Spitale, Progress and challenges for chemical probing of RNA structure inside living cells. *Nat. Chem. Biol.* **11**, 933–941 (2015). doi: 10.1038/nchembio.1958; pmid: 26575240
6. Y. Ding *et al*., In vivo genome-wide profiling of RNA secondary structure reveals novel regulatory features. *Nature* **505**, 696–700 (2014). doi: 10.1038/nature12756; pmid: 24270811
7. S. Rouskin, M. Zubradt, S. Washietl, M. Kellis, J. S. Weissman, Genome-wide probing of RNA structure reveals active unfolding of mRNA structures in vivo. *Nature* **505**, 701–705 (2014). doi: 10.1038/nature12894; pmid: 24336214
8. D. Loughrey, K. E. Watters, A. H. Settle, J. B. Lucks, SHAPE-Seq 2.0: Systematic optimization and extension of high-throughput chemical probing of RNA secondary structure with next generation sequencing. *Nucleic Acids Res.* **42**, 42 (2014). pmid: 25303992
9. R. C. Spitale *et al*., Structural imprints in vivo decode RNA regulatory mechanisms. *Nature* **519**, 486–490 (2015). doi: 10.1038/nature14263; pmid: 25799993
10. A. Bugaut, S. Balasubramanian, 5′-UTR RNA G-quadruplexes: Translation regulation and targeting. *Nucleic Acids Res.* **40**, 4727–4741 (2012). doi: 10.1093/nar/gks068; pmid: 22351747
11. S. Millevoi, H. Moine, S. Vagner, G-quadruplexes in RNA biology. *Wiley Interdiscip. Rev. RNA* **3**, 495–507 (2012). doi: 10.1002/wrna.1113; pmid: 22488917
12. A. L. Wolfe *et al*., RNA G-quadruplexes cause eIF4A-dependent oncogene translation in cancer. *Nature* **513**, 65–70 (2014). doi: 10.1038/nature13485; pmid: 25079319
13. A. R. Haeusler *et al*., C9orf72 nucleotide repeat structures initiate molecular cascades of disease. *Nature* **507**, 195–200 (2014). doi: 10.1038/nature13124; pmid: 24598541
14. G. Biffi, M. Di Antonio, D. Tannahill, S. Balasubramanian, Visualization and selective chemical targeting of RNA G-quadruplex structures in the cytoplasm of human cells. *Nat. Chem.* **6**, 75–80 (2014). doi: 10.1038/nchem.1805; pmid: 24345950
15. C. K. Kwok, S. Balasubramanian, Targeted detection of G-quadruplexes in cellular RNAs. *Angew. Chem. Int. Ed. Engl.* **54**, 6751–6754 (2015). doi: 10.1002/anie.201500891; pmid: 25907625
16. D. A. Peattie, Direct chemical method for sequencing RNA. *Proc. Natl. Acad. Sci. U.S.A.* **76**, 1760–1764 (1979). doi: 10.1073/pnas.76.4.1760; pmid: 377283
17. M. Vorlíčková *et al*., Circular dichroism and guanine quadruplexes. *Methods* **57**, 64–75 (2012). doi: 10.1016/j.ymeth.2012.03.011; pmid: 22450044
18. J. L. Huppert, A. Bugaut, S. Kumari, S. Balasubramanian, G-quadruplexes: The beginning and end of UTRs. *Nucleic Acids Res.* **36**, 6260–6268 (2008). doi: 10.1093/nar/gkn511; pmid: 18832370
19. J. M. Garant, M. J. Luce, M. S. Scott, J. P. Perreault, G4RNA: An RNA G-quadruplex database. *Database (Oxford)* **2015**, bav059 (2015). pmid: 26200754
20. V. S. Chambers *et al*., High-throughput sequencing of DNA G-quadruplex structures in the human genome. *Nat. Biotechnol.* **33**, 877–881 (2015). doi: 10.1038/nbt.3295; pmid: 26192317
21. P. D. Lawley, P. Brookes, Further studies on the alkylation of nucleic acids and their constituent nucleotides. *Biochem. J.* **89**, 127–138 (1963). doi: 10.1042/bj0890127; pmid: 14097355
22. R. C. Spitale *et al*., RNA SHAPE analysis in living cells. *Nat. Chem. Biol.* **9**, 18–20 (2013). doi: 10.1038/nchembio.1131; pmid: 23178934
23. C. K. Kwok, A. B. Sahakyan, S. Balasubramanian, Structural analysis using SHALiPE to reveal RNA G-quadruplex formation in human precursor microRNA. *Angew. Chem. Int. Ed.* **55**, 8958–8961 (2016). doi: 10.1002/anie.201603562; pmid: 27355429
24. S. D. Creacy *et al*., G4 resolvase 1 binds both DNA and RNA tetramolecular quadruplex with high affinity and is the major source of tetramolecular quadruplex G4-DNA and G4-RNA resolving activity in HeLa cell lysates. *J. Biol. Chem.* **283**, 34626–34634 (2008). doi: 10.1074/jbc.M806277200; pmid: 18842585
25. J. S. Yoo *et al*., DHX36 enhances RIG-I signaling by facilitating PKR-mediated antiviral stress granule formation. *PLOS Pathog.* **10**, e1004012 (2014). doi: 10.1371/journal.ppat.1004012; pmid: 24651521
26. I. T. Holder, J. S. Hartig, A matter of location: Influence of G-quadruplexes on Escherichia coli gene expression. *Chem. Biol.* **21**, 1511–1521 (2014). doi: 10.1016/j.chembiol.2014.09.014; pmid: 25459072
27. M. J. Matunis, J. Xing, G. Dreyfuss, The hnRNP F protein: Unique primary structure, nucleic acid-binding properties, and subcellular localization. *Nucleic Acids Res.* **22**, 1059–1067 (1994). doi: 10.1093/nar/22.6.1059; pmid: 7512260
28. M. Caputi, A. M. Zahler, Determination of the RNA binding specificity of the heterogeneous nuclear ribonucleoprotein (hnRNP) H/H′/F/2H9 family. *J. Biol. Chem.* **276**, 43850–43859 (2001). doi: 10.1074/jbc.M102861200; pmid: 11571276
29. T. Nagata *et al*., Structure and interactions with RNA of the N-terminal UUAG-specific RNA-binding domain of hnRNP D0. *J. Mol. Biol.* **287**, 221–237 (1999). doi: 10.1006/jmbi.1999.2616; pmid: 10080887
30. K. V. Datar, G. Dreyfuss, M. S. Swanson, The human hnRNP M proteins: Identification of a methionine/arginine-rich repeat motif in ribonucleoproteins. *Nucleic Acids Res.* **21**, 439–446 (1993). doi: 10.1093/nar/21.3.439; pmid: 8441656
31. A. Kumar, H. Sierakowska, W. Szer, Purification and RNA binding properties of a C-type hnRNP protein from HeLa cells. *J. Biol. Chem.* **262**, 17126–17137 (1987). pmid: 2445755
32. Q. S. Zhang, L. Manche, R. M. Xu, A. R. Krainer, hnRNP A1 associates with telomere ends and stimulates telomerase activity. *RNA* **12**, 1116–1128 (2006). doi: 10.1261/rna.58806; pmid: 16603717
33. C. G. Burd, G. Dreyfuss, RNA binding specificity of hnRNP A1: Significance of hnRNP A1 high-affinity binding sites in pre-mRNA splicing. *EMBO J.* **13**, 1197–1204 (1994). pmid: 7510636
34. S. Khateb, P. Weisman-Shomer, I. Hershco-Shani, A. L. Ludwig, M. Fry, The tetraplex (CGG)n destabilizing proteins hnRNP A2 and CBF-A enhance the in vivo translation of fragile X premutation mRNA. *Nucleic Acids Res.* **35**, 5775–5788 (2007). doi: 10.1093/nar/gkm636; pmid: 17716999
35. A. Expert-Bezançon *et al*., hnRNP A1 and the SR proteins ASF/SF2 and SC35 have antagonistic functions in splicing of beta-tropomyosin exon 6B. *J. Biol. Chem.* **279**, 38249–38259 (2004). doi: 10.1074/jbc.M405377200; pmid: 15208309
36. C. Dominguez, J. F. Fisette, B. Chabot, F. H. Allain, Structural basis of G-tract recognition and encaging by hnRNP F quasi-RRMs. *Nat. Struct. Mol. Biol.* **17**, 853–861 (2010). doi: 10.1038/nsmb.1814; pmid: 20526337
37. M. Subramanian *et al*., G-quadruplex RNA structure as a signal for neurite mRNA targeting. *EMBO Rep.* **12**, 697–704 (2011). doi: 10.1038/embor.2011.76; pmid: 21566646

ACKNOWLEDGMENTS

We thank S. Rouskin and members of the Bartel lab for helpful discussions; C. Kayatekin, G. Johnson, and K. Heindl for experimental assistance; J. S. Yoo, T. Fujita, and Y. Nagamine for the *Dhx36* cell lines; and S. Chisholm, S. Biller, and K. Dooley for the *Synechococcus* culture. This work was supported by NIH grant GM118135 (D.P.B.). J.U.G. is a Damon Runyon Fellow supported by the Damon Runyon Cancer Research Foundation (DRG-2152-13). D.P.B. is an investigator of the Howard Hughes Medical Institute. Sequencing data were deposited in Gene Expression Omnibus (accession number GSE83617).

SUPPLEMENTARY MATERIALS

www.sciencemag.org/content/353/6306/aaf5371/suppl/DC1
Materials and Methods
Figs. S1 to S9
References (*38*–*40*)
Tables S1 to S6

25 February 2016; accepted 15 August 2016
10.1126/science.aaf5371

Downloaded from http://science.sciencemag.org/ on September 30, 2016

RESEARCH ARTICLES

FOREST ECOLOGY

Plant diversity patterns in neotropical dry forests and their conservation implications

DRYFLOR*†

Seasonally dry tropical forests are distributed across Latin America and the Caribbean and are highly threatened, with less than 10% of their original extent remaining in many countries. Using 835 inventories covering 4660 species of woody plants, we show marked floristic turnover among inventories and regions, which may be higher than in other neotropical biomes, such as savanna. Such high floristic turnover indicates that numerous conservation areas across many countries will be needed to protect the full diversity of tropical dry forests. Our results provide a scientific framework within which national decision-makers can contextualize the floristic significance of their dry forest at a regional and continental scale.

Neotropical seasonally dry forest (dry forest) is a biome with a wide and fragmented distribution, found from Mexico to Argentina and throughout the Caribbean (*1*, *2*) (Fig. 1). It is one of the most threatened tropical forests in the world (*3*), with less than 10% of its original extent remaining in many countries (*4*).

Following other authors (*5*, *6*), we define dry forest as having a closed canopy, distinguishing it from more open, grass-rich savanna. It occurs on fertile soils where the rainfall is less than ~1800 mm per year, with a period of 3 to 6 months receiving less than 100 mm per month (*5*–*7*), during which the vegetation is mostly deciduous. Seasonally dry areas, especially in Peru and Mexico, were home to pre-Columbian civilizations, so human interaction with dry forest has a long history (*8*). The climates and fertile soils of dry forest regions have led to higher human population densities and an increasing demand for energy and land, enhancing degradation (*9*). More recently, destruction of dry forest has been accelerated by intensive cultivation of crops, such as sugar cane, rice and soy, or by conversion to pasture for cattle.

Dry forest is in a critical state because so little of it is intact, and of the remnant areas, little is protected (*3*). For example, only 1.2% of the total Caatinga region of dry forest in Brazil is fully protected compared with 9.9% of the Brazilian Amazon (*10*). Conservation actions are urgently needed to protect dry forest's unique biodiversity—many plant species and even genera are restricted to it and reflect an evolutionary history confined to this biome (*1*).

We evaluate the floristic relationships of the disjunct areas of neotropical dry forest and highlight those that contain the highest diversity and endemism of woody plant species. We also explore woody plant species turnover across geographic space among dry forests. Our results provide a framework to allow the conservation significance of each separate major region of dry forest to be assessed at a continental scale. Our analyses are based on a subset of a data set of 1602 inventories made in dry forest and related semi-deciduous forests from Mexico and the Caribbean to Argentina and Paraguay that covers 6958 woody species, which has been compiled by the Latin American and Caribbean Seasonally Dry Tropical Forest Floristic Network [DRYFLOR, www.dryflor.info; (*11*)].

We present analyses that focus principally on DRYFLOR sites in deciduous dry forest vegetation growing under the precipitation regime outlined above (*5*–*7*), as measured using climate data from Hijmans *et al.* (*12*). We excluded most Brazilian sites in the DRYFLOR database with vegetation classified as "semi-deciduous" because these have a less severe dry season and a massive contribution of both the Amazonian and Atlantic rain forest floras (*11*). The only semi-deciduous sites retained from southeast Brazil were from the Misiones region, which has been included in numerous studies of dry forest biogeography [e.g., (*13*, *14*)] (fig. S1), and we therefore wished to understand its relationships. We also excluded sites from the chaco woodland of central South America because it is considered a distinct biome with temperate affinities characterized by frequent winter frost (*13*, *15*). Sites occurring in the central Brazilian region are small patches of deciduous forest that are scattered on areas of fertile soil within savanna vegetation known as "cerrado." We performed clustering and ordination analyses on inventories made at 835 DRYFLOR sites that covered 147 families, 983 genera, and 4660 species (*11*).

Floristic relationships, diversity, endemism, and turnover

Our clustering analyses, based on the unweighted pair-group method with arithmetic mean (UPGMA) and using the Simpson dissimilarity index as a distance measure (*16*), identified 12 floristic groups: (i) Mexico, (ii) Antilles, (iii) Central America–northern South America, (iv) northern inter-Andean valleys, (v) central inter-Andean valleys, (vi) central Andes coast, (vii) Tarapoto-Quillabamba, (viii) Apurimac-Mantaro, (ix) Piedmont, (x) Misiones, (xi). central Brazil, and (xii) Caatinga (Fig. 2 and table S1).

The relationships among the floristic groups were similar in both the analysis of 835 sites (Fig. 2) and another that pooled all species lists from all sites in each of the 12 floristic groups in order to explore the support for relationships among them (fig. S2). The placement of the geographically small Peruvian inter-Andean groups of Apurimac-Mantaro and Tarapoto-Quillabamba is uncertain as previously reported by Linares-Palomino *et al.* (*2*), and differs in the two cluster analyses (Fig. 2 and fig. S2), which is reflected in low AU (approximately unbiased probability support) values (0.71) (fig. S2). More detailed floristic inventory is required in these poorly surveyed forests, which is also suggested by species accumulation curves that have not leveled in these geographic areas (fig. S3).

The analysis pooling all species lists in each floristic group (fig. S2) and a nonmetric multidimensional scaling (NMDS) ordination (fig. S4A for all sites and fig. S4B pooling all species in each floristic group) recognizes a higher-level northern

Fig. 1. Schematic dry forest distribution in the Neotropics. [Based on Pennington *et al.* (*13*), Linares-Palomino *et al.* (*2*), Olson *et al.* (*45*), and the location of DRYFLOR inventory sites (see Fig. 2)]

Latin American and Caribbean Seasonally Dry Tropical Forest Floristic Network, Royal Botanic Garden Edinburgh, 20a Inverleith Row, Edinburgh, EH3 5LR, UK.
*All authors with their affiliations appear at the end of this paper. †Corresponding author. Email: t.pennington@rbge.ac.uk

Downloaded from http://science.sciencemag.org/ on September 30, 2016

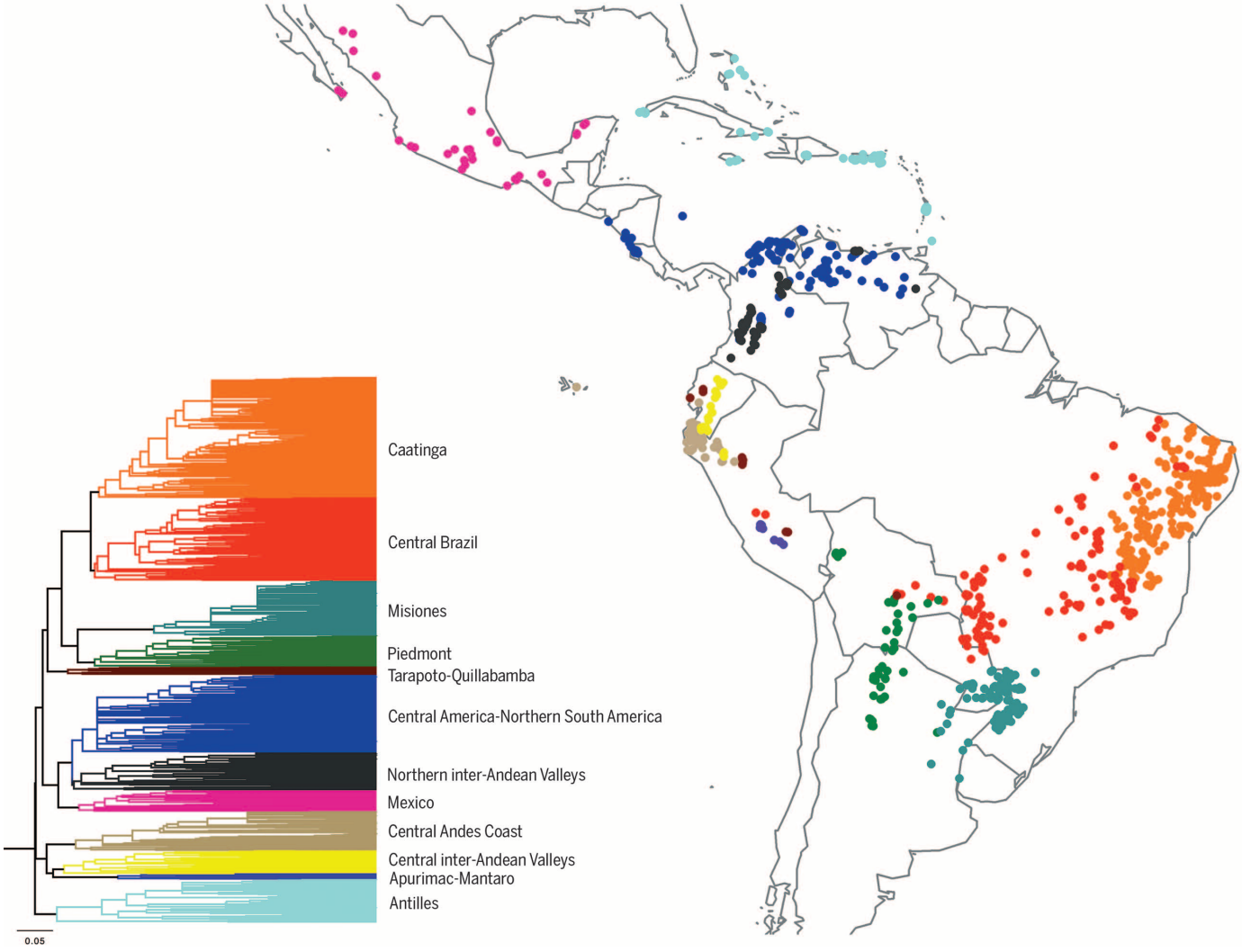

Fig. 2. Neotropical dry forest floristic groups based on woody plants. Geographical representation of UPGMA clustering of 835 dry forest sites using the Simpson dissimilarity index as a measure of distance.

cluster (Mexico, Antilles, Central America–northern South America, and northern inter-Andean valleys). The distinctiveness of Mexican dry forests has been widely recognized (*6*), and the well-supported Antillean floristic group reflects that the Caribbean is also a distinctive neotropical phytogeographic region with high endemism (*17*, *18*). The support for a higher-level northern cluster confirms a north-south division in neotropical dry forest that was suggested by Linares-Palomino *et al.* (*2*) based on a data set that was more sparse in the northern Neotropics (57 sites compared with 276 here). The separation of a northern cluster of neotropical dry forests, which includes all areas in Colombia and Venezuela, from all other dry forest areas further south in South America may reflect the effectiveness of the rain forests of Amazonia and the Chocó as a barrier for migration of dry forest species, as suggested by Gentry (*19*).

A higher-level southern cluster comprises eastern and southern South American areas that divide into two subclusters, the first formed by Piedmont and Misiones and the second by central Brazil and the Caatinga (Fig. 2). In the analysis of pooled species lists, the Misiones group clusters with the central Brazil and Caatinga floristic groups with strong support (1.0 AU) (fig. S2), which is due to the large number of species shared among them as a whole (Misiones shares 409 spp. with central Brazil and 264 spp. with Caatinga) (Fig. 3 and table S2).

There are six Andean dry forest floristic groups (northern inter-Andean valleys, central inter-Andean valleys, central Andes coast, Apurimac-Mantaro, Piedmont, and Tarapoto-Quillabamba), which are scattered across our UPGMA clusterings (Fig. 2 and fig. S2) and ordinations (fig. S4); this scattering reflects the great floristic heterogeneity of dry Andean regions first highlighted by Sarmiento (*20*). For example, the northern inter-Andean valleys of the Rio Magdalena and Cauca are placed within the higher-level northern South American cluster, whereas the Piedmont, Tarapoto-Quillabamba, and Apurimac-Mantaro floristic groups are placed in the higher-level southern cluster in our pooled analysis (fig. S2).

The central Brazil, Caatinga, and Mexico floristic groups contain the most species (1344, 1112, and 1072 species, respectively) (table S1), and the central inter-Andean valleys and Apurimac-Mantaro inter-Andean valleys contain the least (165 and 78 species, respectively). Overall regional species richness may reflect an integrated time-area effect (*21*). The age of the dry forest biome is not known throughout the Neotropics, but the fossil record and dated phylogenies suggest a Miocene origin in Mexico (*22*) and the Andes (*23*). Our data suggest that larger areas of dry forest, such as in the Caatinga and Mexico, have accumulated more species. The small number of species in inter-Andean dry forests reflects their tiny area; the dry forests of the Marañón, Apurimac, and Mantaro inter-Andean valleys in Peru are estimated to occupy 4411 km^2 in total (*24*) compared with ~850,000 km^2 estimated for the Caatinga (*25*). What is notable is the lack of an equatorial peak in regional species diversity (fig. S5). The northerly Mexican dry forests, which reach the Tropic of Cancer, have high species

Downloaded from http://science.sciencemag.org/ on September 30, 2016

numbers similar to the more equatorial Caatinga (1072 compared with 1112), despite being covered by far fewer surveys (33 compared with 184) (fig. S6) and in one-third of the land area [280,000 km^2 (*26*)]. It is intriguing that there may be a peak in regional dry forest species richness around 20 degrees latitude (fig. S5), which may reflect a "reverse latitudinal gradient" of regional species richness in neotropical dry forest, which was suggested by Gentry (*6*). Our inventories used heterogeneous methodologies (e.g., plots and transects of varying sizes or general floristic surveys), which precludes any definitive discussion of alpha diversity at individual sites, but the high regional diversity of Mexican forests, which are distant from the equator, is remarkable. The high species richness of Mexican dry forests merits further investigation and may reflect their Miocene age combined with rates of species diversification that are potentially higher than in other dry forest regions.

Species restricted to one of the 12 floristic groups ("exclusive" species in table S1) may not be strictly endemic to them, because they may be found elsewhere in areas not covered by our surveys. However, we believe that they do serve as a proxy for species endemism, which is supported by independent evidence from floristic checklists. For example, Linares-Palomino (*27*) reported 43% endemism of woody plants for the Marañón valley, Peru, which forms a major part of our central Andean group and has 41% exclusive species. Mexican and Antillean dry forests have the highest percentages of exclusive species (73% and 65%, respectively). The lowest percentage of exclusive species is found in central Brazil dry forests, which reflects the larger numbers of species shared with neighboring floristic groups. Despite their close geographical proximity, Andean floristic groups each have about 30 to 40% of exclusive species, reflecting high floristic turnover at relatively small spatial scales, which may be caused by dispersal limitation among the geographic groups and in situ speciation within them (*1*, *28*).

Pairwise dissimilarity values for the whole data set have a mean of 0.90 for Simpson dissimilarity (median of 0.94) and 0.94 for Sørensen dissimilarity (median of 0.97). The dissimilarity values among the 12 floristic groups (using the entire combined lists for each) (table S3, A and B) ranged from 0.38 to 0.94 (mean, 0.79; median, 0.82) for Simpson dissimilarity and 0.43 to 0.98 (mean, 0.87; median, 0.90) for Sørensen dissimilarity. High floristic turnover in dry forest has been shown in Mexico (*29*), but our data set allows a thorough assessment at a continental scale. In general, few species are shared among the floristic groups (Fig. 3), and this underlines the high levels of species turnover. It is also notable that dissimilarity values are high within all the deciduous dry forest floristic groups as well, with median Sørensen values ranging from 0.74 within the Caatinga to 0.90 within the Tarapoto-Quillabamba group (table S4) (the median value is slightly lower at 0.70 within the semi-deciduous Misiones group). These dissimilarity values are higher than those reported for the cerrado biome. Bridgewater *et al.* (*30*) showed Sørensen dissimilarities with a lower mean value of 0.58 among cerrado floristic provinces separated by ~1000 km, based on floristic lists similar to those in the DRYFLOR data set. The probable higher species turnover in dry forests at continental, regional, and local scales is a result with considerable implications for conservation.

The strongest floristic affinities are found among (i) central Brazil, Caatinga, Piedmont, and Misiones and (ii) Central America and northern South America, Mexico and the northern inter-Andean valleys (Fig. 3). The relationship of the Caatinga and central Brazil dry forests, which share almost 700 species, has been highlighted previously (*2*, *14*, *31*), but what is striking elsewhere is the low levels of floristic similarity, even among geographically proximal floristic groups (e.g., northern and central inter-Andean valleys).

The high floristic turnover reflects that few species are widespread and shared across many areas of neotropical dry forest. No species is reported for all 12 floristic groups; there are only three species shared among 11 groups and nine species among 10 groups (table S5). Some of the species recorded across most sites are widespread ecological generalists like *Maclura tinctoria* (Moraceae), *Guazuma ulmifolia* (Malvaceae), and *Celtis iguanaea* (Cannabaceae), which are common in other biomes, such as rain forest. These species tend to grow in disturbed areas, so their presence in many dry forest sites could be a consequence of their high level of degradation and fragmentation. In other cases, highly recorded species are dry forest specialists, such as *Anadenanthera colubrina* (Leguminosae)—which occurs in eight of the floristic groups and in more than 74% of the sites in the Caatinga, central Brazil, and Piedmont—and *Cynophalla flexuosa* (Capparaceae), which occurs in 11 groups and is commonly recorded (~40% of the sites) in the Antilles, Caatinga, and central Andes coast.

However, most frequently recorded species, defined as those registered in many sites, are seldom shared among any of our 12 floristic groups. For example, 85% of the top 20 most frequently recorded species in each floristic group (table S6) are restricted to a single group, with a few exceptions where the same species was frequent across several groups (e.g., *Anadenanthera colubrina* and *Guazuma ulmifolia*, in five groups each). In other cases, there is a particular set of species characteristic for pairs of geographically proximal floristic groups such as the central inter-Andean valleys and central Andes coast, where the dry forest specialist species, *Loxopterygium huasango* (Anacardiaceae), *Ceiba trichistandra* (Malvaceae), *Coccoloba ruiziana* (Polygonaceae), and *Pithecellobium excelsum* (Leguminosae), are recorded in >15% of the sites.

Our presence-absence database cannot assess abundance in terms of numbers of stems or basal area. However, the extensive field experience of the DRYFLOR network team suggests that when frequently recorded species are dry forest specialists, they tend to be locally abundant and often dominant. Our observations are reinforced by quantitative inventory data that indicate that the most dominant species in dry forest plots represent 8.5 to 62.1% of stems per plot, with a median relative abundance of 17.9% (*32*). In contrast to dry forest specialist species, widespread and frequently recorded ecological generalist species are often not locally abundant.

Although frequently recorded dry forest specialist species in our data set may be locally abundant and dominant, they generally have geographically restricted total distributions. Widespread species that are common in more than one dry forest floristic group (Fig. 2), such as *Anadenanthera colubrina*, which was emphasized in early discussions of neotropical dry forest biogeography [e.g., (*13*, *14*)], are the exception. In summary, there is little evidence for any oligarchy of species that dominates across neotropical dry forest as a whole. These patterns contrast strongly with the rain forests of Amazonia (*33*, *34*) and the savannas of central Brazil (*30*), which are often dominated by a suite of oligarchic species over large geographic areas. The lack of an oligarchy of widespread, dominant dry forest species reflects the limited opportunities for dispersal and successful establishment among dry forest areas (*1*, *28*).

Conservation

Our data show that variation in floristic composition at a continental scale defines 12 dry forest floristic groups across the Neotropics. The floristic differentiation of these main dry forest groups is marked; 23 to 73% of the species found in each are exclusive to it. These figures are likely to indicate high levels of species endemism, which is illustrative of the high floristic turnover (beta diversity) that our data reveal. This high endemism and floristic turnover across the dry forest floristic groups indicate that failure to protect the forest in every one would result in major losses of unique species diversity.

The example of the Andean dry forest is illustrative in this context of the need for multiple protected areas. Andean dry forests fall into six floristic groups in our analysis (Fig. 2). Of these, two geographically small but highly distinct groups in Peru, Apurimac-Mantaro and Tarapoto-Quillabamba, have no formal protection at all. Only 1.4% (3846 ha) of the total remaining dry forest in the northern inter-Andean valleys—one of the most transformed land areas in Colombia (*35*)—are protected (*4*), well short of Aichi biodiversity target 11 that calls for conservation of 17% of terrestrial areas of importance for biodiversity (*36*). In other Andean areas, accurate maps of all remaining areas of dry forest are unavailable, but given that DRYFLOR sites were chosen because they represent well-preserved areas of dry forest, we can ask the question of how well protected these survey sites are. For example, only 14% of the central inter-Andean valleys, 18% of the central Andes coast, and 32% of Piedmont DRYFLOR sites occur within a protected area. If we are to conserve the full floristic diversity of Andean dry forest from north to south, future conservation planning must prioritize

Downloaded from http://science.sciencemag.org/ on September 30, 2016

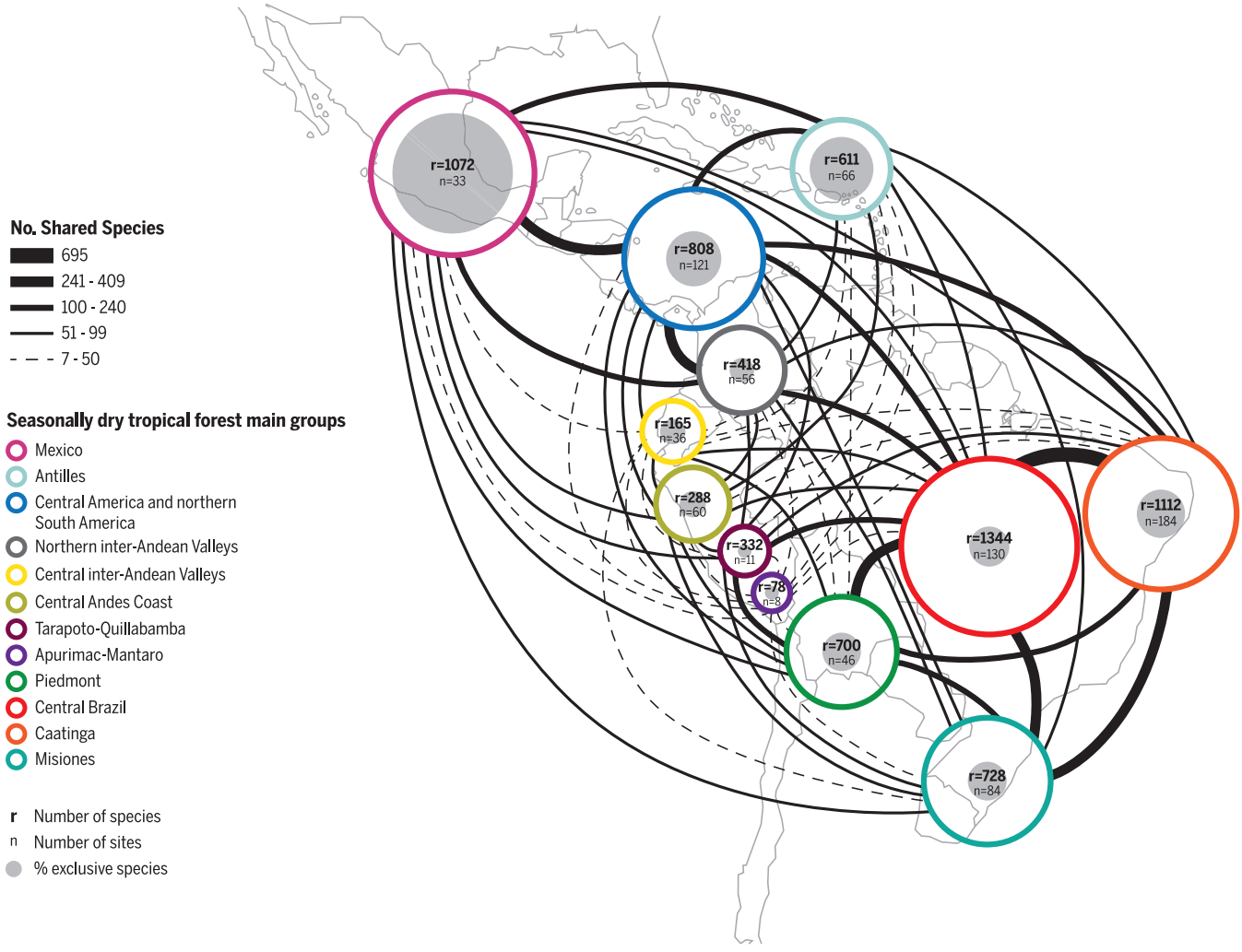

Fig. 3. Geographical patterns of species turnover among 12 dry forest floristic groups. (Fig. 2). Size of the circles is proportional to the number of species per group; size of colored circles is proportional to the total number of species and of gray circles to the number of exclusive species. The species turnover among areas is described by line widths proportional to the number of species shared (values from table S2).

areas in Peru and elsewhere in the Andes that are globally unique but entirely unprotected. These Andean forests, like virtually all neotropical dry forests, have high local human populations and are exploited for agriculture and fuelwood. Conservation solutions therefore require a social dimension, including opportunities and incentives for human communities and private landowners (*9*).

Median pairwise floristic dissimilarity values within the floristic groups of 0.73 for Simpson dissimilarity and 0.85 for Sørensen dissimilarity show that floristic turnover is also high at regional scales, a result only previously shown for Mexico (*29*). Major dry forest regions, such as the Caatinga and Mexico, are each home to more than a thousand woody species, and the high floristic turnover within them means that to protect this diversity fully will require multiple, geographically dispersed protected areas. Conservation of some of these areas could be promoted by classifying their endemic species using International Union for the Conservation of Nature (IUCN) Red List criteria, for which the distribution data in the DRYFLOR database can provide a valuable basis.

Overall, only 14% of sites in the DRYFLOR database, which were chosen to cover the maximum remaining area of neotropical dry forest, fall within protected areas. Placed in the context of our data set, which shows high diversity, high endemism, and high floristic turnover, it is clear that current levels of protection for neotropical dry forest are woefully inadequate. It is our hope that our data set for Latin American and Caribbean dry forests and the results shown here can become a basis for future conservation decisions that take into account continental-level floristic patterns and thereby conserve the maximum diversity of these threatened but forgotten forests.

REFERENCES AND NOTES

1. R. T. Pennington, M. Lavin, A. Oliveira-Filho, *Annu. Rev. Ecol. Evol. Syst.* **40**, 437–457 (2009).
2. R. Linares-Palomino, A. T. Oliveira-Filho, R. T. Pennington, in *Seasonally Dry Tropical Forest: Ecology and Conservation*, R. Dirzo, H. S. Young, H. A. Mooney, G. Ceballos, Eds. (Island Press, 2011), pp. 3–21.
3. L. Miles *et al.*, *J. Biogeogr.* **33**, 491–505 (2006).
4. H. García, G. Corzo, P. Isaacs, A. Etter, in *El Bosque seco Tropical en Colombia*, C. Pizano and H. García, Eds. (Instituto de Investigación de Recursos Biológicos Alexander von Humboldt (IAvH), Bogotá D.C., Colombia, 2014), pp. 228–251.
5. G. Murphy, A. E. Lugo, *Annu. Rev. Ecol. Syst.* **17**, 67–88 (1986).
6. A. H. Gentry, in *Seasonally Dry Tropical Forests*, S. Bullock, H. Mooney, E. Medina, Eds. (Cambridge Univ. Press, Cambridge, 1995), pp. 146–194.
7. G. A. Sanchez-Azofeifa *et al.*, *Biotropica* **37**, 477–485 (2005).
8. A. M. Hocquenghem, *Para Vencer la Muerte: Piura y Tumbes. Raíces en el Bosque Seco y en la Selva Alta—Horizontes en el Pacífico y en la Amazonia* [CNRS-IFEA (l'Institut Français d'Études Andines), Lima, Peru, 1998].
9. R. Blackie *et al.*, "Tropical dry forests: The state of global knowledge and recommendations for future research" (2014 CIFOR Discussion paper 2; Center for International Forestry Research, Jawa Barat, Indonesia, 2014); http://dx.doi.org/10.17528/cifor/004408.
10. Ministério do Meio Ambiente [Ministry of the Environment], Unidades de Conservação por Bioma (CNUC/MMA, Brasília-DF, Brasil, 2016); www.mma.gov.br/images/arquivo/80112/CNUC_PorBiomaFev16.pdf.
11. Materials and methods are available as supplementary materials on *Science* Online.
12. R. J. Hijmans, S. E. Cameron, J. L. Parra, P. G. Jones, A. Jarvis, *Int. J. Climatol.* **25**, 1965–1978 (2005).
13. R. T. Pennington, D. E. Prado, C. A. Pendry, *J. Biogeogr.* **27**, 261–273 (2000).
14. D. E. Prado, P. E. Gibbs, *Ann. Mo. Bot. Gard.* **80**, 902–927 (1993).
15. D. E. Prado, *Candollea* **48**, 145–172 (1993).
16. H. Kreft, W. Jetz, *J. Biogeogr.* **37**, 2029–2053 (2010).
17. M. Maunder *et al.*, *Bot. Rev.* **74**, 197–207 (2008).
18. P. Acevedo-Rodríguez, M. T. Strong, *Smithsonian Contrib. Bot.* **98**, 1–1192 (2012).
19. A. H. Gentry, *Ann. Mo. Bot. Gard.* **69**, 557–593 (1982).
20. G. Sarmiento, *J. Biogeogr.* **2**, 233–251 (1975).

Downloaded from http://science.sciencemag.org/ on September 30, 2016

21. P. V. A. Fine, R. H. Ree, *Am. Nat.* **168**, 796–804 (2006).
22. J. X. Becerra, *Proc. Natl. Acad. Sci. U.S.A.* **102**, 10919–10923 (2005).
23. R. J. Burnham, N. L. Carranco, *Am. J. Bot.* **91**, 1767–1773 (2004).
24. Ministry of the Environment, Peru, *Mapa Nacional de Cobertura Vegetal: Memoria Descriptiva* (Ministerio del Ambiente, Lima, Perú, 2015).
25. L. P. de Queiroz, in *Neotropical Savannas and Seasonally Dry Forests: Plant Diversity, Biogeography, and Conservation*, R. T. Pennington, G. P. Lewis, J. A. Ratter, Eds. (CRC Press, Boca Raton, FL 2006) pp. 121–157.
26. J. Rzedowski, G. C. de Rzedowski, *Acta Bot. Mex.* **102**, 1–23 (2013).
27. R. Linares-Palomino, in *Neotropical Savannas and Seasonally Dry Forest: Plant Diversity, Biogeography and Conservation*, R. T. Pennington, G. P. Lewis, J. A. Ratter, Eds. (CRC Press, Boca Raton, 2006) pp. 227–280.
28. C. E. Hughes, R. T. Pennington, A. Antonelli, *Bot. J. Linn. Soc.* **171**, 1–18 (2013).
29. I. Trejo, R. Dirzo, *Biodivers. Conserv.* **11**, 2063–2084 (2002).
30. S. Bridgewater, J. A. Ratter, J. F. Ribeiro, *Biodivers. Conserv.* **13**, 2295–2317 (2004).
31. D. M. Neves, K. G. Dexter, R. T. Pennington, M. L. Bueno, A. T. Oliveira-Filho, *J. Biogeogr.* **42**, 1566–1576 (2015).
32. K. G. Dexter *et al.*, *Int. For. Rev.* **17**, 10–32 (2015).
33. N. C. A. Pitman *et al.*, *Ecology* **82**, 2101–2117 (2001).
34. H. ter Steege *et al.*, *Science* **342**, 1243092 (2013).
35. G. Forero-Medina, L. Joppa, *PLOS ONE* **5**, e13210 (2010).
36. Convention on Biological Diversity, Quick guide to the Aichi Biodiversity Targets: Protected areas increased and improved, TARGET 11—Technical Rationale extended (COP/10/INF/12/Rev, Convention on Biological Diversity, 2011); https://www.cbd.int/doc/strategic-plan/targets/T11-quick-guide-en.pdf.

ACKNOWLEDGMENTS

This paper is the result of the Latin American and Caribbean Seasonally Dry Tropical Forest Floristic Network (DRYFLOR), which has been supported at the Royal Botanic Garden Edinburgh by a Leverhulme Trust International Network Grant (IN-074). This work was also supported by the U.K. Natural Environment Research Council grant NE/I028122/1; Colciencias Ph.D. scholarship 529; Synthesys Programme GBTAF-2824; the NSF (NSF 1118340 and 1118369); the Instituto Humboldt (IAvH)–Red colombiana de investigación y monitoreo en bosque seco; the Inter-American Institute for Global Change Research (IAI; Tropi-Dry, CRN2-021, funded by NSF GEO 0452325); Universidad Nacional de Rosario (UNR); and Consejo Nacional de Investigaciones Científicas y Técnicas (CONICET). The data reported in this paper are available at www.dryflor.info. R.T.P. conceived the study. M.P., A.O.-F., K.B.-R., R.T.P., and J.W. designed the DRYFLOR database system. K.B.-R. and K.G.D. carried out most analyses. K.B.-R. R.T.P., and K.G.D. wrote the manuscript with substantial input from A.D.-S., R.L.-P., A.O.-F., D.P., C.Q., and R.R. All the authors contributed data, discussed further analyses, and commented on various versions of the manuscript. K.B.-R. thanks G. Galeano who introduced her to dry forest research. We thank J. L. Marcelo, I. Huamantupa, C. Reynel, S. Palacios, and A. Daza for help with fieldwork and data entry in Peru.

DRYFLOR authors

Karina Banda-R,[1,9] Alfonso Delgado-Salinas,[2] Kyle G. Dexter,[1,3] Reynaldo Linares-Palomino,[4,10] Ary Oliveira-Filho,[5] Darién Prado,[6] Martin Pullan,[1] Catalina Quintana,[7] Ricarda Riina,[8] Gina M. Rodríguez M.,[9] Julia Weintritt,[1] Pedro Acevedo-Rodríguez,[11] Juan Adarve,[12] Esteban Álvarez,[13] Anairamiz Aranguren B.,[14] Julián Camilo Arteaga,[15] Gerardo Aymard,[16] Alejandro Castaño,[17] Natalia Ceballos-Mago,[18] Álvaro Cogollo,[13] Hermes Cuadros,[19] Freddy Delgado,[20] Wilson Devia,[21] Hilda Dueñas,[15] Laurie Fajardo,[22] Ángel Fernández,[23] Miller Ángel Fernández,[24] Janet Franklin,[25] Ethan H.Freid,[26] Luciano A. Galetti,[6] Reina Gonto,[23] Roy González-M.,[27,44] Roger Graveson,[28] Eileen H. Helmer,[29] Álvaro Idárraga,[30] René López,[31] Humfredo Marcano-Vega,[29] Olga G. Martínez,[32] Hernán M. Maturo,[6] Morag McDonald,[33] Kurt McLaren,[34] Omar Melo,[35] Francisco Mijares,[36] Virginia Mogni,[6] Diego Molina,[30] Natalia del Pilar Moreno,[37] Jafet M. Nassar,[22] Danilo M. Neves,[1,45] Luis J. Oakley,[6] Michael Oatham,[38] Alma Rosa Olvera-Luna,[2] Flávia F. Pezzini,[1] Orlando Joel Reyes Dominguez,[39] María Elvira Ríos,[40] Orlando Rivera,[37] Nelly Rodríguez,[41] Alicia Rojas,[42] Tiina Särkinen,[1] Roberto Sánchez,[40] Melvin Smith,[28] Carlos Vargas,[43,44] Boris Villanueva,[35] R. Toby Pennington[1]

[1]Royal Botanic Garden Edinburgh, 20a Inverleith Row, EH3 5LR, Edinburgh, UK. [2]Departamento de Botánica, Universidad Nacional Autónoma de México, México D.F., México. [3]School of GeoSciences, University of Edinburgh, Edinburgh, UK. [4]Universidad Nacional Agraria La Molina, Avenida La Molina, Lima, Perú. [5]Universidade Federal de Minas Gerais (UFMG), Instituto de Ciências Biológicas (ICB), Departamento de Botânica, Avenida Antônio. Carlos, 6627-Pampulha, Belo Horizonte, Minas Gerais, Brazil. [6]Cátedra de Botánica, IICAR-CONICET, Facultad de Ciencias Agrarias, Universidad Nacional de Rosario, C.C. Nº 14, S2125ZAA Zavalla, Argentina. [7]Pontificia Universidad Católica del Ecuador, Facultad de Ciencias Exactas, Escuela de Biología, Avenida 12 de Octubre 1076 y Roca, Quito, Ecuador. [8]Real Jardín Botánico, RJB-CSIC, Plaza de Murillo 2, 28014 Madrid, Spain. [9]Fundación Ecosistemas Secos de Colombia, Calle 5 A No. 70 C-31, Bogotá, Colombia. [10]Smithsonian Conservation Biology Institute, Los Libertadores 215, San Isidro, Lima, Perú. [11]Smithsonian National Museum of Natural History, West Loading Dock, 10th and Constitution Avenue, NW, Washington, DC 20560-0166, USA. [12]Parque Regional "El Vínculo"–INCIVA, El Vínculo–Kilometro 3 al sur de Buga sobre la Carretera Panamericana, Valle del Cauca, Colombia. [13]Jardín Botánico de Medellín "Joaquín Antonio Uribe," Calle 73 No. 51D-14, Medellín, Colombia. [14]Instituto de Ciencias Ambientales y Ecológicas, Facultad de Ciencias, Núcleo Pedro Rincón, La Hechicera, 3er Piso, Universidad de los Andes (ULA), Mérida, Venezuela. [15]Herbario SURCO, Universidad Surcolombiana, Neiva, Colombia. [16]Programa de Ciencias del Agro y el Mar, Herbario Universitario (PORT), UNELLEZ-Guanare, Mesa de Cavacas, Estado Portuguesa 3350, Venezuela. [17]Jardín Botánico "Juan María Céspedes" INCIVA, Mateguadua, Tuluá, Valle del Cauca, Colombia. [18]Proyecto Mono de Margarita and Fundación Vuelta Larga, Isla de Margarita, Estado Nueva Esparta, Venezuela. [19]Universidad del Atlántico, Kilometro 7 Vía Puerto, Barranquilla, Atlántico, Colombia. [20]Centro de Investigaciones y Servicios Ambientales (ECOVIDA), Delegación Territorial del Ministerio de Ciencia, Tecnología, y Medio Ambiente, Pinar del Río, Cuba. [21]Unidad Central del Valle del Cauca (UCEVA), Carrera 25 B No. 44-28, Tulúa, Valle del Cauca, Colombia. [22]Centro de Ecología, Instituto Venezolano de Investigaciones Científicas, Apartado 20632, Caracas 1020-A, Venezuela. [23]Centro de Biofísica y Bioquímica (Herbarium), Instituto Venezolano de Investigaciones Científicas, Apartado 20632, Caracas 1020-A, Venezuela. [24]Consultant Botanist, Yopal, Casanare, Colombia. [25]School of Geographical Sciences and Urban Planning, Arizona State University, Post Office Box 875302, Tempe, AZ 85287-5302, USA. [26]Bahamas National Trust, Leon Levy Native Plant Preserve, Eleuthera, Bahamas. [27]Instituto de Investigación de Recursos Biológicos Alexander von Humboldt, Avenida Paseo Bolívar 16-20, Bogotá, D.C., Colombia. [28]Consultant Botanist, Cas en Bas Road, Gros Islet, St. Lucia. [29]Forest Service, Southern Research Station, International Institute of Tropical Forestry, Jardín Botánico Sur, 1201 Calle Ceiba, San Juan, PR00926, Puerto Rico. [30]Grupo de Estudios Botánicos, Universidad de Antioquia, AA 1226 Medellín, Colombia. [31]Universidad Distrital Francisco José de Caldas, Carrera 5 Este No. 15-82, Bogotá, Colombia. [32]Facultad de Ciencias Naturales, Universidad Nacional de Salta, Avenida Bolivia 5150, 4400 Salta, Argentina. [33]School of Environment, Natural Resources, and Geography, Thoday Building, Room G21, Bangor University, Bangor LL57 2DG, UK. [34]Department of Life Sciences, University of West Indies, Mona, Jamaica. [35]Universidad del Tolima, Barrio Santa Helena Parte Alta, Código Postal 730006299, Ibagué, Tolima, Colombia. [36]Fundación Orinoquia Biodiversa, Calle 15 No. 12-15, Tame, Arauca, Colombia. [37]Instituto de Ciencias Naturales, Universidad Nacional de Colombia, Sede Bogotá, Código Postal 111321, Avenida Carrera 30 No. 45-03, Edificio 425, Bogotá, Colombia. [38]Department of Life Sciences, The University of The West Indies St. Augustine, Natural Sciences Building, Old Wing, Room 222, St. Augustine, Trinidad and Tobago. [39]Centro Oriental de Ecosistemas y Biodiversidad BIOECO, Cuba. [40]Universidad de Pamplona, Ciudad Universitaria, Pamplona, Norte de Santander, Colombia. [41]Departamento de Biología, Universidad Nacional de Colombia, Sede Bogotá, Código Postal 111321, Avenida Carrera 30 No. 45-03, Edificio 476, Bogotá, Colombia. [42]Jardín Botánico Eloy Valenzuela, Avenida Bucarica, Floridablanca, Santander, Colombia. [43]Jardín Botánico de Bogotá "José Celestino Mutis," Avenida Calle 63 No. 68-95, Bogotá, Colombia. [44]Facultad de Ciencias Naturales y Matemática, Universidad del Rosario, Carrera 26 No. 63B-48, Bogotá, Colombia. [45]Royal Botanic Gardens, Kew, Richmond, Surrey, UK.

SUPPLEMENTARY MATERIALS

www.sciencemag.org/content/353/6306/1383/suppl/DC1
Materials and Methods
Figs. S1 to S6
Tables S1 to S6
References (*37*–*45*)

26 February 2016; accepted 11 August 2016
10.1126/science.aaf5080

INFECTIOUS DISEASE

Replication of human noroviruses in stem cell–derived human enteroids

Khalil Ettayebi,[1]* Sue E. Crawford,[1]* Kosuke Murakami,[1]* James R. Broughman,[1] Umesh Karandikar,[1] Victoria R. Tenge,[1] Frederick H. Neill,[1] Sarah E. Blutt,[1] Xi-Lei Zeng,[1] Lin Qu,[1] Baijun Kou,[1] Antone R. Opekun,[2,3,4] Douglas Burrin,[3,4] David Y. Graham,[1,2,5] Sasirekha Ramani,[1] Robert L. Atmar,[1,2] Mary K. Estes[1,2]†

The major barrier to research and development of effective interventions for human noroviruses (HuNoVs) has been the lack of a robust and reproducible in vitro cultivation system. HuNoVs are the leading cause of gastroenteritis worldwide. We report the successful cultivation of multiple HuNoV strains in enterocytes in stem cell–derived, nontransformed human intestinal enteroid monolayer cultures. Bile, a critical factor of the intestinal milieu, is required for strain-dependent HuNoV replication. Lack of appropriate histoblood group antigen expression in intestinal cells restricts virus replication, and infectivity is abrogated by inactivation (e.g., irradiation, heating) and serum neutralization. This culture system recapitulates the human intestinal epithelium, permits human host-pathogen studies of previously noncultivatable pathogens, and allows the assessment of methods to prevent and treat HuNoV infections.

Human noroviruses (HuNoVs) are the most common cause of epidemic and sporadic cases of acute gastroenteritis worldwide, and are the leading cause of food-borne gastroenteritis (*1*–*3*). Since the introduction of rotavirus vaccines, HuNoVs have become the predominant gastrointestinal pathogen within pediatric populations in developed countries (*4*). HuNoVs are highly contagious, with rapid person-to-person transmission directly through the fecal-oral route

Downloaded from http://science.sciencemag.org/ on September 30, 2016

and indirectly from contact with contaminated fomites or by consumption of contaminated food or water. In addition to causing morbidity and mortality in young children, immunocompromised patients, and the elderly, norovirus disease causes substantial economic burden as a result of health care costs and loss of productivity (*5*, *6*). HuNoVs have resisted efforts to establish in vitro cultivation methods for more than 40 years. Previous reports of possible cultivation systems have not been reproduced or support limited replication of a single strain (*7*–*10*). Insight into the pathophysiology of HuNoV infections has been elucidated primarily from studies using healthy adult volunteers. The lack of a reproducible culture system for HuNoVs has remained the major barrier to achieving a full mechanistic understanding of their replication, stability, antigenic complexity, and evolution. An in vitro cultivation system is critical to define HuNoV-host interactions that underlie the high virus infectivity and explosive illness they cause, to determine how to prevent transmission, and to treat infections and illness.

[1]Department of Molecular Virology and Microbiology, Baylor College of Medicine, Houston, TX, USA. [2]Department of Medicine, Baylor College of Medicine, Houston, TX, USA. [3]Section of Gastroenterology, Hepatology and Nutrition, Department of Pediatrics, Baylor College of Medicine, Houston, TX, USA. [4]USDA/ARS Children's Nutrition Research Center, Houston, TX, USA. [5]Department of Medicine, Michael E. DeBakey VA Medical Center, Houston, TX, USA.
*These authors contributed equally to this work. †Corresponding author. Email: mestes@bcm.edu

Ex vivo human intestinal enteroid cultures support HuNoV replication

Attempts to culture HuNoVs in transformed intestinal epithelial cells and in primary human immune cells have been unsuccessful (*8*, *11*, *12*). We hypothesized that a novel culture system pioneered by the Clevers group in the Netherlands, which generates human intestinal enteroids (HIEs) from stem cells isolated from intestinal crypts in human intestinal tissues (*13*, *14*) and recapitulates the natural intestinal epithelium, should support HuNoV growth. These multicellular, differentiated HIEs are nontransformed, physiologically active cultures that respond to agonists and contain multiple intestinal epithelial cell types (enterocytes, goblet, enteroendocrine, and Paneth cells), whether grown as three-dimensional or monolayer cultures (fig. S1) (*13*–*16*).

To evaluate whether these novel cultures support replication of the previously noncultivatable HuNoVs, we inoculated monolayers of HIEs with GII.4 HuNoVs, which cause the majority of pandemic and outbreak infections worldwide (*1*). Jejunal monolayer cultures were readily infected by stool filtrates of multiple GII.4 variants (GII.4/2006a, GII.4/2006b-1 to -3, GII.4/2009, and GII.4/2012-1 and -2; table S1). At 96 hours post-infection

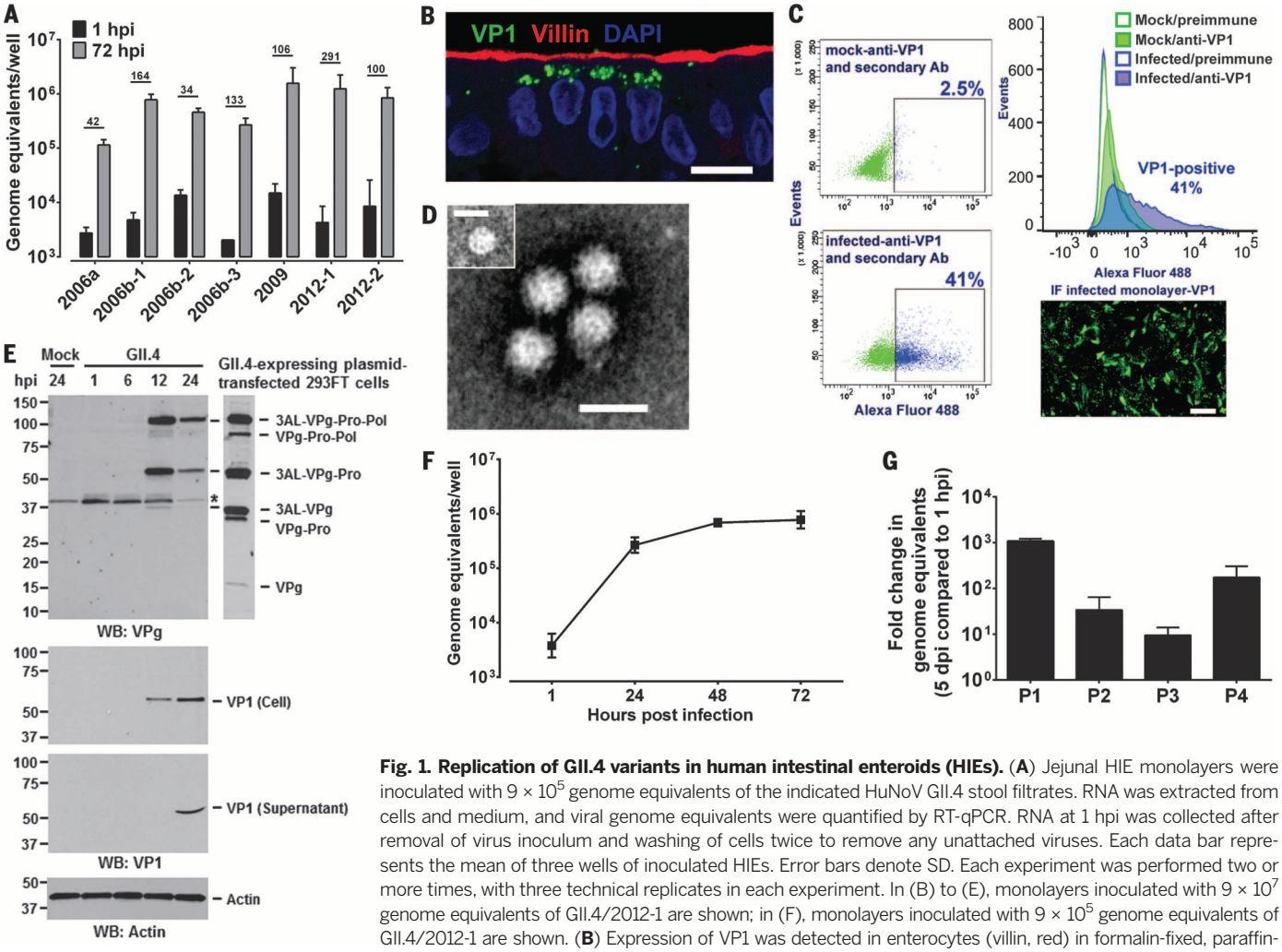

Fig. 1. Replication of GII.4 variants in human intestinal enteroids (HIEs). (**A**) Jejunal HIE monolayers were inoculated with 9×10^5 genome equivalents of the indicated HuNoV GII.4 stool filtrates. RNA was extracted from cells and medium, and viral genome equivalents were quantified by RT-qPCR. RNA at 1 hpi was collected after removal of virus inoculum and washing of cells twice to remove any unattached viruses. Each data bar represents the mean of three wells of inoculated HIEs. Error bars denote SD. Each experiment was performed two or more times, with three technical replicates in each experiment. In (B) to (E), monolayers inoculated with 9×10^7 genome equivalents of GII.4/2012-1 are shown; in (F), monolayers inoculated with 9×10^5 genome equivalents of GII.4/2012-1 are shown. (**B**) Expression of VP1 was detected in enterocytes (villin, red) in formalin-fixed, paraffin-embedded enteroid monolayer sections using antibody against GII.4/2012 VLPs (green). DAPI (4′,6-diamidino-2-phenylindole) detects nuclei (blue). Scale bar, 25 μm. (**C**) Flow cytometry quantitation and immunofluorescent detection of infected cells. Scale bar, 100 μm. (**D**) Electron micrograph of HuNoV particles from the supernatant of infected HIEs. Scale bar, 50 nm. Inset: small particle. Scale bar, 25 nm. (**E**) Western blot detecting polyprotein processing and VP1 expression. Asterisk marks a nonspecific band. (**F**) Kinetics of HuNoV yield at the indicated time points. (**G**) Passaging of GII.4/2009 HuNoV in jejunal HIEs. In (F) and (G), viral genome equivalents were quantified by RT-qPCR as in (A).

Downloaded from http://science.sciencemag.org/ on September 30, 2016

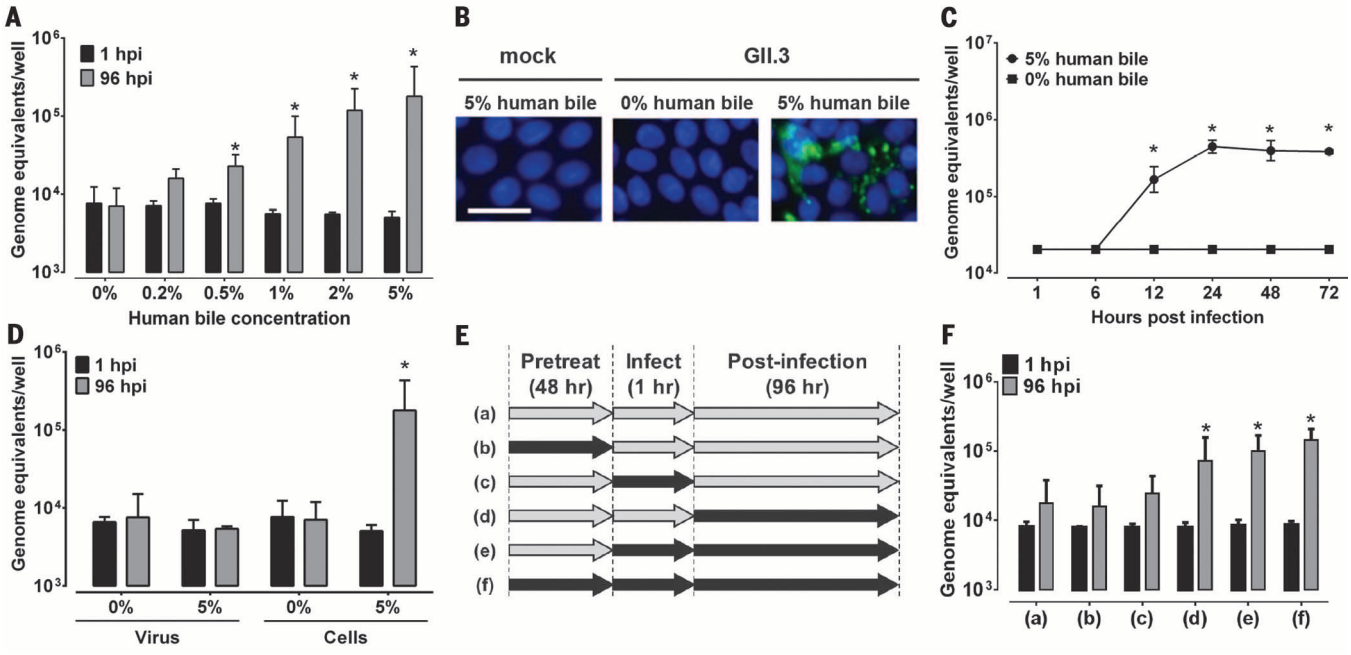

Fig. 2. Bile is required for GII.3 HuNoV replication and affects the cells. (**A** to **C**) Jejunal HIE monolayers were pretreated with the indicated concentrations of human bile for 2 days and then inoculated with GII.3 stool filtrate [(A) and (C), 4.3×10^5 genome equivalents; (B), 4.3×10^7 genome equivalents] and incubated with the same bile concentrations as used for pretreatment (see supplementary materials). (B) VP1 was detected in methanol-fixed monolayers at 24 hpi using guinea pig anti-GII.3 VLP antiserum (green) and DAPI to detect nuclei (blue). Scale bar, 25 μm. (**D**) Determination of effect of bile treatment on virus or cells. Virus was either not treated or treated with 5% human bile for 1 hour at 37°C, and then diluted to decrease the bile concentration to 0.025% before infection of HIE monolayers not pretreated with bile; cells were either not treated or treated with 5% human bile for 2 days before and during infection. Inoculations were performed with 4.3×10^5 genome equivalents. (**E**) Schematic showing with black arrows when bile was added to HIEs for the experiment shown in (F). (**F**) HIE monolayers treated with bile as indicated in (E) were infected with 4.3×10^5 genome equivalents of GII.3 stool filtrate. For (A), (C), (D), and (F), genome equivalents were determined as indicated in Fig. 1. Error bars denote SD. *$P < 0.05$ comparing genome equivalents to 1 hpi.

(hpi), 1.5 to 2.5 $\log_{10}$ increases in genome equivalents of viral progeny were identified by reverse transcription–quantitative polymerase chain reaction (RT-qPCR) in comparison to the amount of genomic RNA detected at 1 hpi after removal of the virus inoculum and two washes of the monolayers to remove unattached virus (Fig. 1A, relative changes indicated above the bars for each variant). All inocula used to infect enteroid cultures were fecal filtrates, which suggests that bacteria were not required as cofactors for infection, in contrast to previous reports of HuNoV cultivation in BJAB and Raji B cell lines (*9*, *10*). Lipopolysaccharide (LPS) in stool filtrates did not promote replication, as there was no reduction in HuNoV replication in samples treated with polymyxin B that reduced LPS levels from 4.84 to 0.63 endotoxin units (*12*) (fig. S2A).

We next evaluated the growth characteristics of HuNoV infection by assessing cytopathic effect (CPE), antigen detection, and the kinetics of infection. Cytopathic changes such as cell rounding, destruction of the monolayer, and an increase in the number of dead cells as assessed by trypan blue staining were observed in GII.4-inoculated cultures. CPE was observed for the tested GII.4 variants GII.4/2012-1, GII.4/2012-2, and GII.4/2006b-3 (see table S1 for strain details; GII.4/2012-1 results shown in fig. S2B, left panel). CPE was not reduced by inoculation with polymyxin B–treated samples (fig. S2B), and CPE was not observed in cultures inoculated with γ-irradiated stool filtrate (fig. S2B, right panels), which abrogated viral replication. Viral replication was demonstrated by detecting the major viral capsid protein (VP1) with nonstructural proteins [RNA-dependent RNA polymerase (Pol) and nucleotide triphosphatase (NTPase)] or double-stranded RNA (dsRNA, an intermediate in HuNoV RNA replication) in infected cells by confocal microscopy (Fig. 1B and fig. S3, A to C). Immunofluorescent analysis for VP1 revealed that 35 to 45% of cells in the HIE monolayer were infected, which was confirmed by flow cytometry where 41% of cells were VP1-positive (Fig. 1C). HIE cultures contain multiple cell types (stem cells, Paneth cells, and goblet, enteroendocrine, and enterocyte cells), and only the enterocytes were infected. Detection of villin, an enterocyte marker, in VP1-positive cells showed that HuNoVs infected and replicated in enterocytes (Fig. 1B).

Productive infection was confirmed by transmission electron microscopy, which yielded images of virus particles with typical morphology (*17*) in the supernatant of infected HIEs (Fig. 1D). Two particle sizes were detected (Fig. 1D), with particles of the expected size (31.6 ± 3.3 nm) and some smaller particles (18.5 ± 3.7 nm; Fig. 1D, inset). Both particle sizes have been observed previously in stools of children infected with HuNoVs and in preparations of recombinant virus-like particles (VLPs) (*18*). By Western blot analysis, nonstructural polyprotein synthesis and processing [as evidenced by the detection of several viral protein genome-linked (VPg)–containing polyprotein processing intermediates] and capsid protein (VP1) production were first detected at 12 hpi in infected cells but not at 1 or 6 hpi or in mock-infected cells (Fig. 1E). Consistent with the production of virus particles (Fig. 1D), VP1 was detected in the culture supernatant by 24 hpi (Fig. 1E). Replication was confirmed by the growth kinetics of GII.4/2012-1 in jejunal HIE monolayer cultures, which showed a time-dependent increase in genome equivalents between 1 and 24 hpi, after which a plateau was reached (Fig. 1F). Because polyprotein processing, RNA replication, and synthesis of subgenomic RNA are required for VP1 and particle production (*19*), these findings demonstrate that an entire HuNoV replication cycle occurs in infected HIEs by 24 hpi. GII.4/2009 and GII.4/2012-1 HuNoV could also be passaged in jejunal HIEs with optimized conditions (Fig. 1G, GII.4/2009 shown; see below for conditions). Cells expressing VP1 and VPg were observed during infection with passaged virus (fig. S4A), and particles of both sizes (fig. S4B) were seen. Together, these results indicate that GII.4 HuNoV infection of HIEs results in a productive and complete virus replication cycle,

Downloaded from http://science.sciencemag.org/ on September 30, 2016

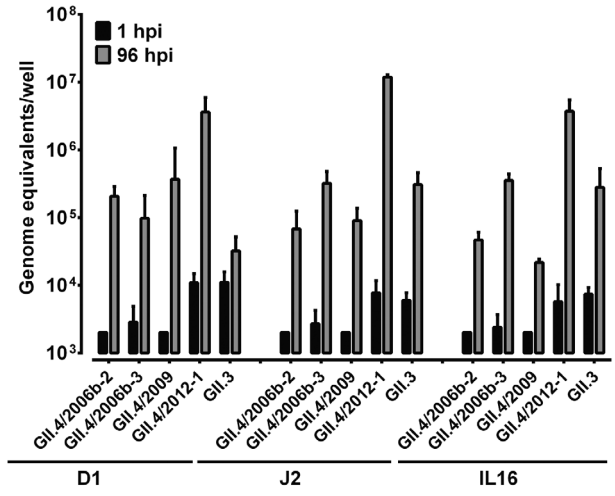

Fig. 3. GII.4 variants and GII.3 HuNoVs replicate in HIEs generated from different intestinal segments. Duodenal (D1), jejunal (J2), and ileal (IL16) HIEs were treated with 1% sow bile for the GII.4 variants or 5% human bile for GII.3 for 48 hours, and then inoculated with the indicated HuNoVs (GII.4/2006b-2, GII.4/2009, and GII.4/2012-1, 9×10^5 genome equivalents; GII.4/2006b-3, 5.5×10^5 genome equivalents; GII.3, 4.3×10^5 genome equivalents) and cultured in the presence of bile. Genome equivalents were determined as indicated in Fig. 1. Error bars denote SD.

and that this system can be used to define cellular processes that HuNoVs co-opt to replicate and induce pathogenesis.

Replication of some HuNoV strains requires the presence of bile

Noroviruses are genetically diverse. Most HuNoVs are classified into two genogroups (GI and GII), which are further subdivided into nine GI genotypes and 20 GII genotypes. We next tested whether monolayer cultures of jejunal HIEs could support replication of other HuNoV strains (GI.1, GII.3, GII.17). Initially, no replication of these viruses was observed. Consequently, several components of the intestinal milieu were assessed for their ability to promote replication of these HuNoVs in HIE monolayers. Addition of proteases (trypsin, pancreatin) required for the replication of another gastrointestinal virus, human rotavirus, failed to enhance HuNoV replication. In contrast, viral replication, as demonstrated by RT-qPCR and immunofluorescence analyses, was observed in HIEs pretreated with nontoxic levels of human bile and inoculated with stool filtrates of GII.3, GII.17, and GI.1 HuNoVs (Fig. 2, A and B, and fig. S5). Replication occurred in a bile dose–dependent manner, with concentrations of human bile greater than or equal to 0.5% being required for GII.3 replication (Fig. 2A). Bile from different sources, such as human, sow, and commercially available bovine and porcine, all promoted GII.3 replication without CPE (fig. S6). Assessment of the kinetics of GII.3 infection demonstrated that, similar to GII.4 strains, virus yields increased between 1 and 24 hpi (Fig. 2C). The addition of bile to GII.4 HuNoV-inoculated cultures was not required, but it enhanced virus replication (fig. S7). Enhancement was observed when human (fig. S7A), piglet (fig. S7B), porcine (fig. S7C), and sow (fig. S7D) bile were evaluated.

These results indicate that there are strain-specific differences in the requirement for factors in the intestinal milieu such as bile to support or enhance HuNoV replication. Of note, even with the addition of bile, the increases in yields for GII.3 as well as for GII.17 and GI.1 virus strains were lower than that observed for the GII.4 variants. In 12 independent experiments performed in triplicate on jejunal HIEs, the mean relative increase of GII.3 genome equivalents from 1 hpi to a later time point ranged from a factor of 10 to a factor of 173 (average increase, factor of 48); for GII.4 HuNoVs, the mean relative increase ranged from a factor of 34 to a factor of 6730 (average increase, factor of 670). Evaluation of additional intestinal components or further optimization of conditions may be required to achieve higher levels of replication for GII.3 and other HuNoVs. To date, we have successfully obtained replication of two HuNoV genogroups comprising four genotypes of virus (including four GII.4 variants and GII.3, GII.17, and GI.1 strains) in human jejunal enteroid monolayers (table S1).

Table 1. Comparison of BT50 and 50% neutralization titers. BT50 denotes a serum titer that blocks the interaction of HuNoV VLPs with H type 1 and H type 3 and porcine gastric mucin glycans by 50%; 50% neutralization denotes a serum titer that reduces the infectivity of indicated HuNoV strains by 50%.

Serum	GII.3		GII.4	
	BT50	50% neutralization	BT50	50% neutralization
1	187	990	671	105,000
2	70	835	53	214

We next evaluated whether the requirement of bile for GII.3 HuNoV infection and replication was due to a bile effect on the HIE cells or on the virus. Stool filtrate was pretreated with 5% bile or phosphate-buffered saline (PBS) for 1 hour and then diluted in PBS (final concentration of 0.025% in the bile-treated sample) prior to inoculating HIE cultures not treated with bile. HIEs also were either not treated or treated with 5% bile for 48 hours prior to and during infection. The pretreatment of cells with bile was carried out for a longer duration as compared to pretreatment of the virus with bile because bile has multiple known effects on cellular functions, including acting as a detergent, increasing digestion and absorption of fat, and regulating metabolic and inflammatory processes by activating various signaling pathways (*20*). An increase in genome equivalents was observed only when HIE cells were treated with bile (Fig. 2D), indicating that the bile effect is on the cells and not on the virus.

Further assessment of bile treatment revealed that addition of bile to cultures during or after virus adsorption, but not prior to adsorption, is required for GII.3 replication (Fig. 2, E and F). Testing of heat- or trypsin-treated bile for GII.3 infections in HIEs found no effect on replication (fig. S8), indicating that the active factor is not proteinaceous. The successful cultivation of GII.3 HuNoV required both novel HIE cultures and supplementary bile, because the addition of bile to transformed epithelial cell lines including Huh7, Vero, HEK293FT, and undifferentiated or differentiated Caco-2 BBe cells did not promote HuNoV replication (fig. S9). These results indicate that HIEs and bile together mimic the human replication niche of HuNoVs.

The sensitivity of the HIE culture system to support HuNoV replication was evaluated by determining the lower limit of virus required for successful infection. For this, the dose required to produce infection in 50% of the inoculated cultures (ID_{50}) for GII.4 and GII.3 HuNoVs was calculated by the Reed-Muench method (*21*). The ID_{50} values for GII.4/2012-1 and GII.3 HuNoVs were ~1200 and ~2.0×10^4 genome equivalents per well, respectively, assessed at 7 days post-infection (dpi; geometric mean of two experiments, representative experiments shown in fig. S10, A and B). These results indicate that this replication system is amenable to determining the infectivity of low levels of virus, as has been observed in emesis, contaminated food, and fecal samples after recovery from illness (*8*, *22*, *23*). This replication system also will allow evaluation of whether a given virus, currently detected in a variety of samples by molecular methods, is infectious and poses a potential risk to human health.

HuNoVs replicate in enterocytes in cultures from different segments of the small intestine

The site of replication of HuNoVs in immunocompetent individuals is unknown, although histologic alterations have been observed in small

Downloaded from http://science.sciencemag.org/ on September 30, 2016

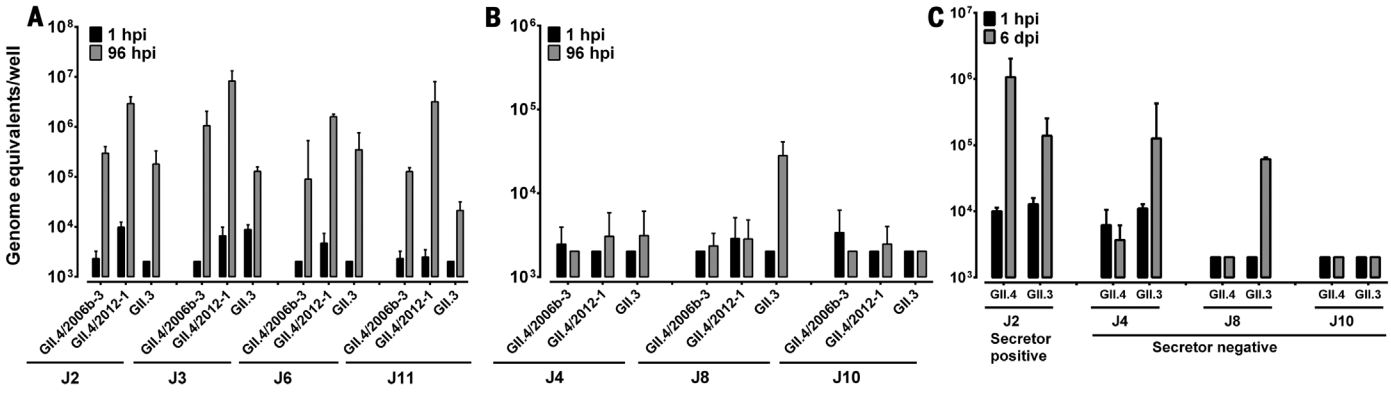

Fig. 4. Replication of GII.4 strains but not GII.3 depends on HIE secretor status. (**A**) Secretor-positive jejunal (J2, J3, J6, and J11) or (**B**) secretor-negative jejunal (J4, J8, and J10) HIEs were inoculated with the indicated GII.4 or GII.3 HuNoVs (with the same amounts of genome equivalents as indicated in Fig. 3) in the presence of bile (1% sow bile for GII.4 variants or 5% human bile for GII.3) for 96 hours. At 96 hpi, GII.4 strains replicate in secretor-positive HIEs but not secretor-negative lines, while GII.3 replicates in all secretor HIEs and one secretor-negative line (J8). (**C**) At 6 dpi, the GII.3 virus shows replication in an additional secretor-negative HIE (J4) while no growth of GII.4/2012-1 virus is seen. A secretor J2 HIE is included as control to show replication of GII.4 at 6 dpi. In (A) to (C), genome equivalents were determined as indicated in Fig. 1. Error bars denote SD.

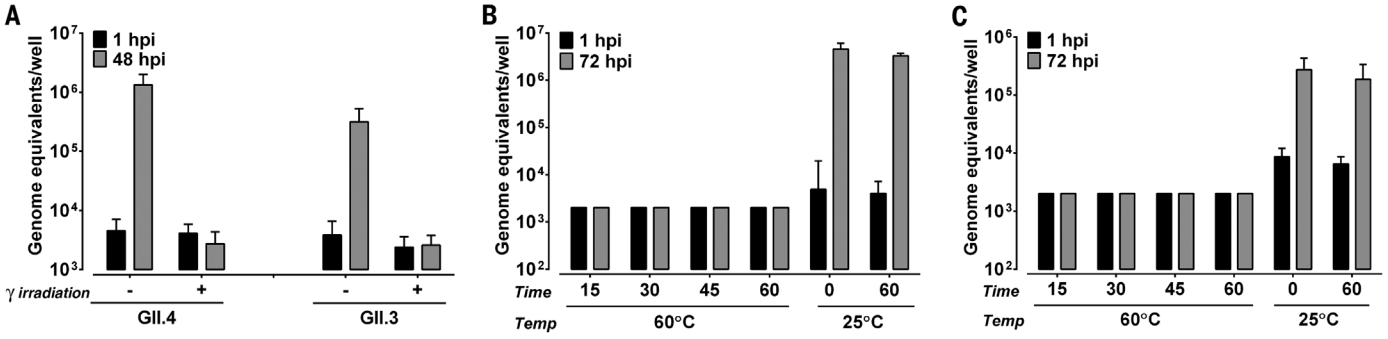

Fig. 5. Inactivation of GII.4 and GII.3 HuNoV infectivity by γ irradiation and heat treatment. (**A**) GII.4/2012-1 and GII.3 HuNoVs were γ-irradiated or incubated at room temperature overnight. (**B** and **C**) GII.4/2012-1 (9×10^5 genome equivalents) (B) or GII.3 (4.3×10^5 genome equivalents) (C) were heat-inactivated at 60°C for the indicated time points or incubated at room temperature for 0 and 60 min. Jejunal HIEs were inoculated with each sample. Genome equivalents were determined as shown in Fig. 1. Error bars denote SD.

intestinal biopsies from volunteers infected with Norwalk virus (*24*) and antigen has been detected in duodenal, jejunal, and (to a lesser extent) ileal enterocytes from gnotobiotic pigs infected with a GII.4 HuNoV (*25*). We therefore evaluated whether HuNoVs infect cells derived from different regions of the small intestine by inoculating HIE cultures made from biopsies obtained from different intestinal segments that retain segment-specific properties (*26*). GII.4 and GII.3 HuNoVs replicated in enteroids derived from duodenal, jejunal, and ileal intestinal segments (Fig. 3). Replication varied by strain and intestinal segment, with GII.4 variants showing increases by factors of 11 to 1535 between 1 and 96 hpi in the three segments and GII.3 virus showing increases by factors of 3 to 51.

We investigated whether HuNoVs replicated in cell types other than enterocytes. HuNoV antigen was not detected in goblet cells (n = 200) or enteroendocrine cells (n = 50) assessed in duodenal, jejunal, and ileal HIEs. Together, the growth of HuNoVs in HIEs from all segments of the small intestine detected by RNA replication and confocal staining indicates that enterocytes (Fig. 1B) are the primary target for infection and replication.

Secretor status of HIEs affects strain-specific HuNoV replication

HuNoV infection is dependent on expression of genetically determined histoblood group antigens (HBGAs), and genetic resistance to some HuNoV genotypes has been documented in challenge and outbreak studies (*27*). The presence of a functional fucosyltransferase 2 (FUT2, secretor-positive genotype) enzyme, which transfers fucose to HBGA precursors in gastrointestinal cells in secretor-positive persons, correlates with susceptibility to infection with most GII.4 HuNoVs. We generated HIEs from secretor-positive and -negative persons to determine whether these cultures recapitulate genotype-specific patterns of HuNoV susceptibility (*14*). All secretor-positive jejunal HIEs supported productive replication of GII.4 variants (by factors of 44 to 1270) and GII.3 HuNoVs (by factors of 10 to 173), as assessed by increases in genome equivalents between 1 and 96 hpi (Fig. 4A). In contrast, GII.4 strains did not infect HIEs generated from secretor-negative individuals when assayed at 96 hpi or 6 dpi (Fig. 4, B and C, respectively). However, GII.3 virus infected two of three secretor-negative HIEs, one of which was positive only after 6 days in culture (Fig. 4, B and C, respectively). These results mirror epidemiologic data showing that GII.3 HuNoVs, but not GII.4 HuNoVs, can infect some individuals (*27*) and indicate that HuNoV infection of HIEs is a biologically relevant system that mimics infections in genetically defined individuals. Further analysis of genetically defined HIEs will aid in determining additional host susceptibility factors to infection.

HuNoV cultivation in HIEs allows evaluation of virus neutralization and inactivation

Functional antibodies in serum that block the binding of HuNoV VLPs to HBGAs correlate with protection against clinical gastroenteritis in volunteer challenge and vaccination studies (*28*–*30*). HBGA-blocking assays examine the ability of human serum to block the interaction

Downloaded from http://science.sciencemag.org/ on September 30, 2016

of HuNoV VLPs with H type 1 and H type 3 glycans and porcine gastric mucin (*31*, *32*), and the antibody titer that results in 50% blocking (BT50) has been used as a surrogate for virus neutralization (*28*). We used the HIE cultivation system to directly measure virus neutralization. Neutralizing antibody titers (the reciprocal antibody dilution present in serum able to reduce virus yields by 50% relative to virus incubated in media alone) were compared to HBGA-blocking titers. Serum samples from two individuals, one with a high BT50 and another with a low BT50 against GII.4 VLPs, were tested (Table 1). Both samples had low BT50s against GII.3 VLPs. The neutralization titers were higher than the BT50 values (Table 1 and fig. S11, A to D) and virus-induced CPE was neutralized (fig. S11E); these findings suggest that virus neutralization is a more sensitive assay than the HBGA blocking assay, and that neutralization epitopes other than HBGA-blocking epitopes may exist on norovirus particles.

The previous inability to cultivate HuNoVs has hampered the development of strategies to control and prevent HuNoV infection, and has limited the ability to determine the effectiveness of existing methods to inactivate virus to prevent transmission in various settings, including in food or on contaminated surfaces. The persistence of HuNoVs in the environment, their high transmissibility, and the problem of chronic infection of immunocompromised individuals document a need for antiviral treatment and prophylaxis of norovirus infections. To determine whether the HIE infection model is suitable for testing virus inactivation, we evaluated GII.3 and GII.4 HuNoV inactivation by γ irradiation and heat treatment. No growth was observed after γ irradiation of either GII.4 or GII.3 HuNoVs (Fig. 5A). Compared to incubation of GII.4 or GII.3 viruses at room temperature for 60 min, heating at 60°C for as little as 15 min inactivated both viruses; no increase in yield was detected from 1 to 72 hpi (Fig. 5, B and C). These studies indicate that HuNoV infection of HIEs will allow evaluation of new methods to inactivate HuNoVs and to measure the effectiveness of disinfectants and sanitizers, including characterization of the efficacy of both traditional and novel control measures.

Implications of in vitro replication of HuNoV for understanding its biology

HuNoV was visualized by Albert Kapikian in 1972 (*17*), but conditions to grow these viruses in vitro have remained an unsolved mystery for more than 40 years. Our results show that HuNoV replication in HIEs is robust, based on achieving several $\log_{10}$ increases in replication of multiple variants of the epidemiologically predominant GII.4 HuNoVs in HIE lines from different small intestinal segments from multiple immunocompetent individuals; replication was documented by expression of structural and nonstructural proteins, production and release of virus particles into culture supernatants, and successful passaging of virus. The cultivation system described in this study has biologic relevance, with replication of different strains being consistent with known host restriction based on HBGA expression. Variability in replication between different HIE cultures is observed; specific cultures (secretor-positive) are highly susceptible to HuNoV strains, and other cultures (secretor-negative) show variable resistance to infection with specific HuNoV strains. These results mirror infectivity patterns seen in epidemiological studies. Future work with additional strains is needed to understand the basis for this variability, particularly for infection of different secretor-negative lines with GII.3 viruses.

HuNoVs replicate in enterocytes from different intestinal segments in HIEs. In addition, factors present in the intestinal milieu, such as bile, enhance or are required for replication to occur. Bile obtained from various mammalian sources (human, sow, piglet, porcine, and bovine) mediates this effect, although there is variability between bile sources and virus strains. These results are consistent with previous data from intestinal biopsies from HuNoV-infected immunocompromised transplant patients and studies in large animals (gnotobiotic pigs and newborn calves) infected orally with HuNoV GII.4 or bovine norovirus GIII.1 strains, respectively, where enterocytes in different segments of the small intestine are clearly infected and express viral antigen (*25*, *33*, *34*). Filtered stool was used as inoculum in the present study, and bacterial LPS was not required for infectivity. These results differ from reports of cultivation of a single strain of HuNoV in B cells where unfiltered inocula and commensal bacteria are required as cofactors (*9*, *10*), and of HuNoV replication in other animal models following nonoral routes of inoculation, including intraperitoneal injection of immunodeficient mice (*35*) or intravenous injection of chimpanzees (*36*); in those models, virus was not detected in the intestinal epithelium but was detected in cells in the lamina propria, with some expressing DC-SIGN (chimpanzees) or with a macrophage-like morphology (mice).

Replication of HuNoVs in enterocytes in HIEs supports the observation that another site(s) of primary replication besides B cells must exist, because HuNoVs can infect B cell–deficient patients (*37*, *38*). Our results are reminiscent of initial conditions that required the addition of intestinal contents from gnotobiotic piglets to successfully culture a porcine enteric calicivirus (PEC), a member of the *Sapovirus* genus of the Caliciviridae family, using primary porcine kidney cells (*39*). Species-specific bile enhanced primary replication in that system, and subsequent studies showed that bile acids and a continuous porcine kidney cell line can support PEC replication (*40*). Additional studies are needed to determine the active components of bile needed to support HuNoV replication in HIEs. The active component(s) in bile and mechanism(s) of action required for HuNoV cultivation in HIEs remain to be fully characterized, but initial characterization demonstrates that it is not a protein. The establishment of this cultivation system will facilitate applications in many different realms of public health importance—such as food safety and the development of new diagnostics, vaccines, and therapeutics—and will advance research on HuNoV evolution, immunity, and pathogenesis.

REFERENCES AND NOTES

1. S. Ramani, R. L. Atmar, M. K. Estes, *Curr. Opin. Gastroenterol.* **30**, 25–33 (2014).
2. S. M. Ahmed *et al.*, *Lancet Infect. Dis.* **14**, 725–730 (2014).
3. A. J. Hall *et al.*, *Emerg. Infect. Dis.* **19**, 1198–1205 (2013).
4. D. C. Payne *et al.*, *N. Engl. J. Med.* **368**, 1121–1130 (2013).
5. K. Y. Green, *Clin. Microbiol. Infect.* **20**, 717–723 (2014).
6. G. Belliot, B. A. Lopman, K. Ambert-Balay, P. Pothier, *Clin. Microbiol. Infect.* **20**, 724–730 (2014).
7. T. M. Straub *et al.*, *Emerg. Infect. Dis.* **13**, 396–403 (2007).
8. M. D. Moore, R. M. Goulter, L. A. Jaykus, *Annu. Rev. Food Sci. Technol.* **6**, 411–433 (2015).
9. M. K. Jones *et al.*, *Nat. Protoc.* **10**, 1939–1947 (2015).
10. M. K. Jones *et al.*, *Science* **346**, 755–759 (2014).
11. E. Duizer *et al.*, *J. Gen. Virol.* **85**, 79–87 (2004).
12. M. K. Lay *et al.*, *Virology* **406**, 1–11 (2010).
13. T. Sato *et al.*, *Gastroenterology* **141**, 1762–1772 (2011).
14. K. Saxena *et al.*, *J. Virol.* **90**, 43–56 (2016).
15. K. L. VanDussen *et al.*, *Gut* **64**, 911–920 (2015).
16. N. C. Zachos *et al.*, *J. Biol. Chem.* **291**, 3759–3766 (2016).
17. A. Z. Kapikian *et al.*, *J. Virol.* **10**, 1075–1081 (1972).
18. L. J. White, M. E. Hardy, M. K. Estes, *J. Virol.* **71**, 8066–8072 (1997).
19. K. Y. Green, in *Fields Virology*, D. M. Knipe, P. M. Howley, Eds. (Lippincott Williams and Wilkins, 2013), pp. 582–608.
20. A. F. Hofmann, in *Physiology of the Gastrointestinal Tract*, L. R. Johnson, Ed. (Raven, New York, 1994), pp. 1555–1576.
21. L. J. Reed, H. Muench, *Am. J. Hyg.* **27**, 493 (1938).
22. R. L. Atmar *et al.*, *Emerg. Infect. Dis.* **14**, 1553–1557 (2008).
23. F. Le Guyader *et al.*, *Appl. Environ. Microbiol.* **62**, 4268–4272 (1996).
24. S. G. Agus, R. Dolin, R. G. Wyatt, A. J. Tousimis, R. S. Northrup, *Ann. Intern. Med.* **79**, 18–25 (1973).
25. S. Cheetham *et al.*, *J. Virol.* **80**, 10372–10381 (2006).
26. S. Middendorp *et al.*, *Stem Cells* **32**, 1083–1091 (2014).
27. N. Ruvoën-Clouet, G. Belliot, J. Le Pendu, *Rev. Med. Virol.* **23**, 355–366 (2013).
28. A. Reeck *et al.*, *J. Infect. Dis.* **202**, 1212–1218 (2010).
29. C. Richardson, R. F. Bargatze, R. Goodwin, P. M. Mendelman, *Expert Rev. Vaccines* **12**, 155–167 (2013).
30. R. L. Atmar *et al.*, *N. Engl. J. Med.* **365**, 2178–2187 (2011).
31. R. L. Atmar, M. K. Estes, *Gastroenterol. Clin. North Am.* **35**, 275–290 (2006).
32. M. Tan, X. Jiang, *Trends Microbiol.* **13**, 285–293 (2005).
33. P. H. Otto *et al.*, *J. Virol.* **85**, 12013–12021 (2011).
34. U. C. Karandikar *et al.*, *J. Gen. Virol.* 10.1099/jgv.0.000545 (2016).
35. S. Taube *et al.*, *MBio* **4**, e00450-13 (2013).
36. K. Bok *et al.*, *Proc. Natl. Acad. Sci. U.S.A.* **108**, 325–330 (2011).
37. K. Y. Green, *Clin. Infect. Dis.* **62**, 1139–1140 (2016).
38. J. R. Brown, K. Gilmour, J. Breuer, *Clin. Infect. Dis.* **62**, 1136–1138 (2016).
39. W. T. Flynn, L. J. Saif, *J. Clin. Microbiol.* **26**, 206–212 (1988).
40. K. O. Chang *et al.*, *Proc. Natl. Acad. Sci. U.S.A.* **101**, 8733–8738 (2004).

ACKNOWLEDGMENTS

Supported in part by Public Health Service grant PO1 AI 057788 (M.K.E.) and Agriculture and Food Research Initiative competitive grant 2011-68003-30395 from the USDA National Institute of Food and Agriculture. We acknowledge the assistance of the Study Design and Clinical Research Core and Cellular and Molecular Morphology Core of the Texas Medical Center Digestive Diseases Center and the Cytometry and Cell Sorting Core, which are supported in part by Public Health Service grants P30 DK-56338, P30 CA-125123 (to C. K. Osborne), National Institute of Allergy and Infectious Diseases grant AI036211, and the Dan L. Duncan Cancer Center at Baylor College of Medicine. We thank B. V. V. Prasad, T. Palzkill, S. Marriott, and M. Donowitz for critical reading of the manuscript. Author contributions: S.E.C., R.L.A., and M.K.E. supervised the project; K.E., K.M., J.R.B., U.K., V.R.T., L.Q., B.K., X.-L.Z., and F.H.N. designed and performed experiments and analyzed data; S.E.C., R.L.A., S.R., S.E.B., and M.K.E. designed experiments and analyzed data; A.R.O.,

Downloaded from http://science.sciencemag.org/ on September 30, 2016

D.B., and D.Y.G. provided reagents and conceptual advice; M.K.E., S.E.C., and K.E. wrote the initial draft of the manuscript; and all authors provided critical review and final approval of the manuscript. All relevant data are within this paper and the supplementary materials. Enteroids are available via a materials transfer agreement from Baylor College of Medicine. Baylor College of Medicine has filed a patent application related to this work: Cultivation of human noroviruses; provisional patent application no. 62/236,294.

SUPPLEMENTARY MATERIALS
www.sciencemag.org/content/353/6306/1387/suppl/DC1
Materials and Methods
Figs. S1 to S11
Table S1
References (*41*–*47*)

25 February 2016; accepted 18 August 2016
Published online 25 August 2016
10.1126/science.aaf5211

NEUROSCIENCE

The TRPM2 channel is a hypothalamic heat sensor that limits fever and can drive hypothermia

Kun Song,[1]*† Hong Wang,[1]† Gretel B. Kamm,[1]† Jörg Pohle,[1] Fernanda de Castro Reis,[2] Paul Heppenstall,[2,3] Hagen Wende,[1] Jan Siemens[1,3]‡

Body temperature homeostasis is critical for survival and requires precise regulation by the nervous system. The hypothalamus serves as the principal thermostat that detects and regulates internal temperature. We demonstrate that the ion channel TRPM2 [of the transient receptor potential (TRP) channel family] is a temperature sensor in a subpopulation of hypothalamic neurons. TRPM2 limits the fever response and may detect increased temperatures to prevent overheating. Furthermore, chemogenetic activation and inhibition of hypothalamic TRPM2-expressing neurons in vivo decreased and increased body temperature, respectively. Such manipulation may allow analysis of the beneficial effects of altered body temperature on diverse disease states. Identification of a functional role for TRP channels in monitoring internal body temperature should promote further analysis of molecular mechanisms governing thermoregulation and foster the genetic dissection of hypothalamic circuits involved with temperature homeostasis.

Core body temperature (T_{core}) is normally maintained very accurately in mammals within a narrow range around 37°C and serves as an important vital sign that is routinely monitored in hospitalized patients. Pathological conditions such as infections and systemic inflammation cause fever (*1*, *2*), an increase in the body's temperature that is thought to be mediated by prostaglandin E_2 (PGE_2)–induced inhibition of warm-sensitive neurons (WSNs) in the hypothalamic thermoregulatory center (*3*). Adverse drug-induced fluctuations in T_{core} can have severe and even fatal consequences (*4*). Conversely, clinically controlled modulation of T_{core} has beneficial effects and can prevent tissue damage, promote trauma recovery (*5*, *6*), or help decrease obesity (*7*).

The preoptic area (POA) of the hypothalamus serves as a thermostat, integrating temperature information to orchestrate the autonomous and behavioral adaptations needed to achieve thermal homeostasis (*3*, *8*). POA neurons receive and integrate information from peripheral temperature sensors located in the skin, spinal cord, and viscera. Local POA warming and cooling experiments (*9*–*13*) and genetic manipulations (*14*) have shown that this region of the central nervous system also detects local brain temperature changes, which have a strong impact on T_{core}. In fact, temperature changes in the POA can exert a dominant effect on T_{core} and can override lower-priority temperature inputs from peripheral temperature sensors, such as those located in the skin (*15*, *16*). Warming of the POA induces heat dissipation mechanisms such as cutaneous vasodilation, evaporative heat loss mechanisms, and behavioral adaptations, whereas cooling of the POA triggers heat conservation and thermogenesis.

POA neurons exhibiting pronounced temperature sensitivity have been described in in vivo models and in vitro preparations (*17*–*19*). WSNs enhance their firing rate upon warming, a process that is thought to relay temperature information to peripheral organs to promote heat loss (*3*). Conversely, a drop in deep brain temperature inhibits WSNs, a process that correlates with induction of thermogenesis and heat gain.

However, the genetic identity of WSNs and the molecular basis of their temperature sensitivity have remained elusive. Our work defined a population of WSNs that controls temperature homeostasis and identified a transient receptor potential (TRP) ion channel that subserves thermodetection in hypothalamic neurons.

TRPM2 is a heat sensor in a subset of POA neurons

To identify thermosensory molecules in the thermoregulatory center of the hypothalamus, we established calcium imaging as a means to monitor warming-induced responses of primary POA neuronal cultures (fig. S1, A to F). We applied a stringent criterion to identify WSNs by fura-2–mediated calcium imaging. We only counted neurons as WSNs if their relative increase in signal on receiving a thermal stimulus (up to 45°C) was larger than the mean fura-2 signal plus 5 times the standard deviation (5SD) of thermally unresponsive human embryonic kidney–293 cells subjected to the same temperature stimulus (fig. S1, E and F). This procedure allowed us to account and correct for the small unspecific temperature effect on the fluorescent fura-2 signal (*20*) (see fig. S1F and table S1 for details). We found that 16.3 ± 4.7% (mean ± SEM; n = 6 mice) of cultured POA neurons responded to warming, a fraction that is in the same range (10 to 16%) observed in electrophysiological studies of rodent POA cultures (*21*, *22*) and slightly lower than WSN percentages (20 to 40%) observed in POA slice preparations (*17*, *23*). Extracellular calcium appeared to be the source of the temperature-triggered increase in intracellular concentrations of free calcium, because chelation of external calcium abolished the response, whereas depletion of intracellular calcium stores did not have any effect on warm sensitivity (fig. S1, D and G).

Several ion channels are thermosensitive, exemplified by a steep temperature dependence (Q_{10} coefficient) of their opening probabilities. In particular, cationic TRP ion channels have been identified as thermosensors in the peripheral nervous system and function in the detection of ambient temperature changes (*24*–*27*).

To identify candidate channels mediating the observed warm sensitivity in neuronal POA cultures, we tested various inhibitors and agonists of TRPs and other thermosensitive ion channels (fig. S1, H to L). The calcium response appeared to be mediated by direct Ca^{2+} flux through a thermosensitive ion channel and not an indirect readout of voltage-gated channels, because nifedipine and tetrodotoxin, which are blockers of voltage-gated calcium and sodium channels, respectively, had only a small effect on the responses to increased temperature (fig. S1, H, J, K, and L). 2-aminoethoxydiphenyl borate (2-APB), a potent inhibitor of several ion channels and activator of TRPV-type channels (*28*–*30*), abolished the temperature response of POA neurons in a reversible manner (Fig. 1A).

[1]Department of Pharmacology, University of Heidelberg, Im Neuenheimer Feld 366, 69120 Heidelberg, Germany. [2]European Molecular Biology Laboratory (EMBL), Adriano Buzzati-Traverso Campus, Via Ramarini 32, 00016 Monterotondo, Italy. [3]Molecular Medicine Partnership Unit, EMBL, Meyerhofstraße 1, 69117 Heidelberg, Germany. *Present Address: Max Delbrück Center for Molecular Medicine, Robert Rössle Straße 10, 13125 Berlin, Germany. †These authors contributed equally to this work. **‡Corresponding author. Email: jan.siemens@pharma.uni-heidelberg.de**

Downloaded from http://science.sciencemag.org/ on September 30, 2016

Among known temperature-responsive ion channels, TRPC5, TRPM2, TRPM3, TRPM8, TRPV1, TRPV2, TRPV3, and STIM1-ORAI1 are sensitive to 2-APB (fig. S1M) (*24*–*26*). Because TRPC5 and TRPM8 are cold-sensitive channels (*31*–*33*), we eliminated them from our list of candidates. The STIM1-ORAI1 channel complex responds to cooling subsequent to a heat stimulus (*34*), a characteristic that differs from the POA responses described here.

The TRPV1 to -3 channels are activated rather than inhibited by 2-APB (*28*, *35*), and capsaicin, the cognate agonist of heat-sensitive TRPV1, did not have any effect on POA neurons (fig. S1N), suggesting that TRPV1 to -3 do not serve as temperature sensors in POA neurons. Moreover, these channels are sensitive to the pore blocker ruthenium red (*36*), a substance that had only a subtle effect on the temperature sensitivity of POA neurons (fig. S1, I and L).

TRPM3, one of the two remaining candidates, appeared to be expressed in the POA, albeit in low amounts, as assessed by in situ hybridization (fig. S1O). However, the TRPM3 agonist pregnenolone sulfate did not produce calcium responses in neuronal POA cultures (fig. S1N). It did so in dorsal root ganglia sensory neurons that express the receptor (*37*), which we used as a positive control.

Immunohistochemistry and in situ hybridization for TRPM2 showed prominent labeling within the mouse POA (Fig. 1, B and C, and fig. S3, B and C). H_2O_2, a sensitizer of TRPM2 channel activity (*38*), shifted the warm sensitivity of POA cultures to a lower activation temperature (Fig. 1D). Moreover, adenosine diphosphate ribose (ADPR), an intracellular agonist of TRPM2 (*39*, *40*), induced large currents in POA neurons that were identified by calcium imaging to be warm-sensitive (Fig. 1, E and F, and fig. S1, P to S). The ADPR-induced current showed a TRPM2-characteristic linear current-voltage relationship (*39*, *40*). Additionally, a similar current was induced in these neurons by increased temperatures (Fig. 1F).

Thus, TRPM2 may mediate responses to temperature increases in the POA. To test this, we used cultures obtained from *Trpm2*$^{-/-}$ mice (*41*) and compared their thermal responses with those from wild-type (*Trpm2*$^{+/+}$) littermate controls. The magnitude of the response of POA neurons to increased temperature was decreased in the absence of TRPM2, and these neurons were indistinguishable from warm-insensitive (non-WSN) *Trpm2*$^{+/+}$ POA neurons (Fig. 1, G and H). Using our stringent definition of warm sensitivity (fig. S1F), no responses to increased temperatures were detected in cultures obtained from *Trpm2*$^{-/-}$ mice (Fig. 1I).

The activation temperature of cultured WSNs—in the absence of a sensitizer such as H_2O_2 or any other reactive oxygen species—was in the range of 45°C (fig. S2A). Although this temperature is similar to that previously reported for TRPM2 activation (*38*), it exceeds any physiologically relevant deep brain temperature, even when compared with extreme forms of fever and hyperthermia (*42*). However, similar to other thermosensitive TRP channels, the activation temperature for TRPM2 appears not to be a fixed threshold temperature. Rather, it ranges from 33° to 47°C, depending on the cellular context (*38*, *43*). We therefore tested whether the activation temperature of POA neurons shifted to lower, more physiological temperatures when calcium imaging was performed on acutely obtained brain slices from 7- to 8-week-old mice. In this experimental setting, the neurons largely retained their native cellular environment and had attained maturity.

To this end, we injected virus particles into the mouse POA for Cre-dependent expression of the virally encoded intracellular calcium indicator GCaMP6, which shows increased fluorescence

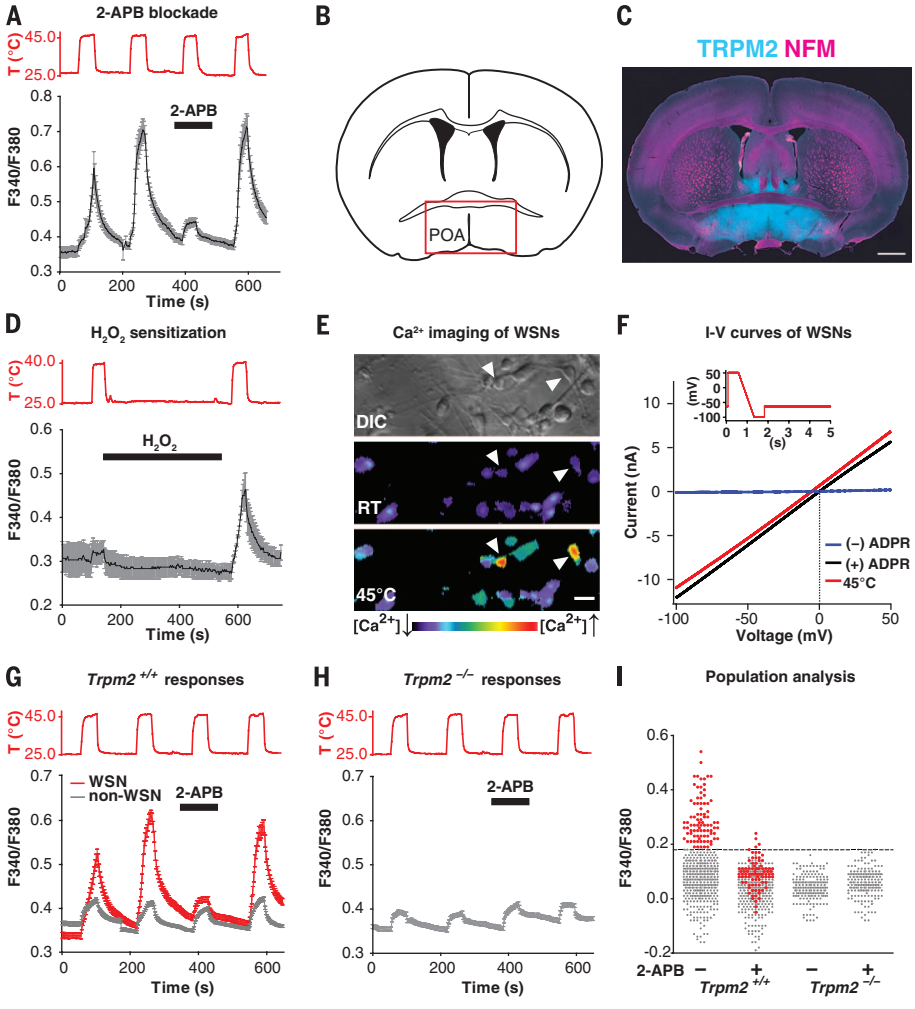

Fig. 1. TRPM2 mediates heat responses in a subset of POA neurons. (**A**) Cultured mouse POA neurons were examined for calcium responses [black trace; plotted are non-normalized fura-2 fluorescence intensity ratios after excitation at 340 and 380 nm (F340/F380)] to repetitive increases in temperature (red trace). 2-APB (30 μM, black bar) reversibly blocked thermal responses in POA neurons. (**B**) Cartoon depicting a coronal section of a mouse brain (Bregma level anterior-posterior, 0.14 mm). (**C**) Immunostaining of a representative mouse brain section corresponding to the cartoon in (B), using antibodies against TRPM2 (cyan) and neurofilament medium (NFM, magenta). Scale bar, 1 mm. (**D**) H_2O_2 (1 mM, black bar) sensitized POA neurons to respond to lower activation temperatures (40°C), as assessed by fura-2–based calcium imaging (black trace). (**E**) Differential interference contrast (DIC) image (top) and fura-2 ratio images before (middle; RT, room temperature) and during (bottom) a temperature stimulus of cultured POA neurons. Arrowheads indicate WSNs. (**F**) Current-voltage (*I-V*) relationships of voltage-clamped WSNs shown in (E) in response to a voltage ramp shown at the top, in the absence (blue) or presence (black) of ADPR (100 μM) or at a temperature stimulus of 45°C (red). (**G** and **H**) POA cultures from *Trpm2*$^{+/+}$ (G) and *Trpm2*$^{-/-}$ (H) mice were examined by calcium imaging for responses to repetitive thermal stimuli (upper red traces) in the presence or absence of 2-APB (30 μM, black bar). In *Trpm2*$^{+/+}$ cultures, both WSNs (red) and non-WSNs (light gray) could be detected, whereas WSNs were absent in cultures of *Trpm2*$^{-/-}$ mice. (**I**) Population analysis of thermal responses of POA neurons from *Trpm2*$^{+/+}$ and *Trpm2*$^{-/-}$ mice as shown in (G) and (H). Plotted are the peak responses of individual neurons at the second (without 2-APB) and third (with 2-APB) temperature stimulus. POA neurons of both genotypes had similar responses to a high-potassium solution (100 mM KCl, not shown). WSNs are colored in red and non-WSNs in gray. The dashed line demarcates the cutoff for warm sensitivity as defined in fig. S1F and table S1. Throughout, error bars indicate SEM.

Downloaded from http://science.sciencemag.org/ on September 30, 2016

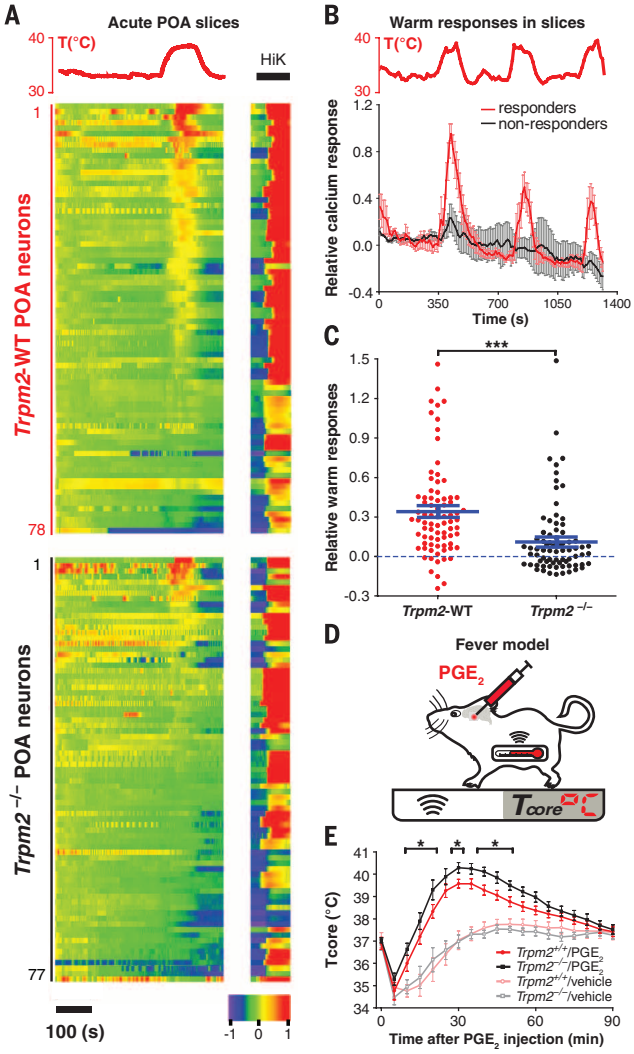

Fig. 2. TRPM2 mediates heat responses in POA brain slices and modulates fever temperature in vivo. (**A**) Acute POA slice preparations from *Nestin-Cre* mice with (*Trpm2*-WT; upper panel) or without (*Trpm2*$^{-/-}$; lower panel) functional TRPM2 were consecutively subjected to a temperature stimulus of 38 ± 1°C (red) and a high-potassium stimulus (HiK, black). Neuronal activity was recorded by means of a Cre-induced, virally encoded GCaMP6 calcium sensor that was stereotactically introduced into the POA 2 weeks before slice preparation. A nonlinear pseudocolor scale (bottom) indicates relative calcium responses in individual neurons. Numbering on the left refers to individual neurons. The black bar indicates the time scale. (**B**) Average relative calcium responses of exemplary GCaMP6^{+} WSNs (red; n = 5) and non-WSNs (black; n = 3) from *Nestin-Cre* mice to repetitive temperature stimuli of up to 40°C (top, red trace). (**C**) Population analysis of cellular responses shown in (A), demonstrating that relative heat-induced calcium signals are reduced in POA slices from mice lacking functional TRPM2 (***P < 0.0001, two-tailed Mann-Whitney test). Blue bars show the mean and SEM. (**D**) Cartoon depicting the experimental paradigm used to examine the fever response by thermotelemetrical measurements of T_{core} upon preoptic injection of PGE_2 into the POA. (**E**) Enhanced PGE_2-induced fever in *Trpm2*$^{-/-}$ mice (black trace; n = 9) compared with littermate *Trpm2*$^{+/+}$ controls (red trace; n = 10). Mice were briefly anesthetized to allow stereotactic injection of PGE_2 (or vehicle control), resulting in a transient drop of T_{core} for all conditions and genotypes. *P < 0.05, two-way analysis of variance (ANOVA) ($F_{1,318}$ = 40.78) followed by post hoc Fisher's least significant difference (LSD) test.

at 500 to 530 nm upon an increase in cytosolic calcium levels (*44*). To test temperature sensitivity in POA neurons, we used the neuron-specific *Nestin-Cre* mice (*45*) that express Cre recombinase, and thus GCaMP6, in POA neurons. Subsequent temperature stimulation of brain slices prepared from these animals revealed calcium responses in POA neurons at 38 ± 1°C (Fig. 2, A and B). Moreover, POA neurons in slices derived from mice lacking TRPM2 (*Nestin-Cre Trpm2*$^{-/-}$) had attenuated responses to the same temperature stimulus [mean relative heat responses ± SEM: *Nestin-Cre Trpm2*$^{-/-}$, 0.111 ± 0.033 (n = 78); *Nestin-Cre Trpm2*-WT, 0.341 ± 0.040 (n = 79); P < 0.0001, two-tailed Mann-Whitney test; *Trpm2*-WT signifies *Trpm2*$^{+/+}$ and *Trpm2*$^{+/-}$ mice] (Fig. 2, A and C, and fig. S2B). General excitability, as assessed by high potassium stimulation, was indistinguishable in the presence or absence of TRPM2 (fig. S2C). These results demonstrate that preoptic TRPM2 mediates responses to heat stress at temperatures of (or exceeding) 38°C.

Preoptic TRPM2 receptors modulate the magnitude of fever temperature

Fever is a cardinal response to infection and systemic inflammation. The POA, as part of its thermoregulatory function, is the key brain structure in controlling the increased body temperature in fever (*2*, *3*). The TRPM2-mediated activation of POA neurons at stimulation temperatures slightly above the physiological set point of 37°C (sometimes referred to as the balance point), might allow hypothalamic TRPM2 to detect and modulate inflammatory fever temperature.

As a consequence of infection and downstream of the resulting immune response, PGE_2 is the final mediator that triggers fever by acting directly on POA neurons (*2*, *46*). To address a putative fever-modulatory role for TRPM2 directly in the POA, we microinjected PGE_2 into this brain area in mice (Fig. 2D and fig. S2D), an established fever model (*46*–*48*). Telemetrically measured T_{core} revealed similar diurnal temperatures in the presence and absence of TRPM2 at normothermic (nonfever) conditions (fig. S2E). We found that injection of a low dose of PGE_2 (0.4 nmol per mouse) produced a mild fever response that was similar in both genotypes (fig. S2, F and I). However, a high dose of PGE_2 (4 nmol per mouse) caused an increased fever temperature in *Trpm2*$^{-/-}$ mice compared with that of *Trpm2*$^{+/+}$ littermate controls (Fig. 2E and fig. S2I). In the absence of functional TRPM2 protein, the maximal fever temperature reached 40.4 ± 0.2°C, compared with 39.6 ± 0.2°C in the presence of the receptor (n = 9 *Trpm2*$^{-/-}$ and 10 *Trpm2*$^{+/+}$ mice; P < 0.001, two-tailed unpaired t test).

We also tested the effects of the interleukins IL-1β and IL-6, which have been shown to synergistically induce fever at central sites (*49*). Again, significantly higher fever was detected in *Trpm2*$^{-/-}$ mice only for the stronger of the two stimuli, when both interleukins were co-injected into the POA, but not when IL-1β was injected alone (fig. S2, G to I). Together, these results indicate that preoptic TRPM2 limits the magnitude of the temperature increase in strong fever responses, presumably to prevent excessive temperature increases and tissue damage.

Trpm2-expressing POA neurons are part of a circuit controlling body temperature homeostasis

Our results indicated that *Trpm2*-expressing (*Trpm2*$^{+}$) neurons might be part of a thermoregulatory circuit and that TRPM2-driven activity might counteract body heating and perhaps promote peripheral heat loss at normothermic conditions as well. In the absence of specific agents to modulate TRPM2 function in vivo, we generated *Trpm2-2A-Cre* knock-in mice (referred to hereafter as *Trpm2-Cre* mice) that express Cre recombinase exclusively in *Trpm2*$^{+}$ cells (fig. S3A). We thereby gained genetic access to *Trpm2*$^{+}$ POA neurons and ascertained the potential thermoregulatory role of this specific cell population in unrestrained, conscious mice. We first assessed proper *Cre* expression in *Trpm2*$^{+}$ neurons, using in situ hybridization and *Cre* reporter mice. *Cre* was expressed in the POA of *Trpm2-Cre* mice, and its expression pattern recapitulated that of native *Trpm2* transcripts (fig. S3, B to F). Two-color in situ hybridization analysis of the POA revealed essentially complete cellular overlap of *Trpm2* and *Cre* (fig. S3F), with 97% of *Trpm2*$^{+}$ neurons (335 out of 344 cells) expressing the Cre-induced reporter.

We then tested whether modulating the activity of *Trpm2*$^{+}$ POA neurons influenced body temperature in freely moving mice. We chose a chemogenetic, DREADD (designer receptors exclusively activated by designer drugs) receptor–assisted approach that enabled us to remotely turn the activity of *Trpm2*$^{+}$ neurons on and off.

Downloaded from http://science.sciencemag.org/ on September 30, 2016

DREADDs are engineered heteromeric guanine nucleotide–binding protein (G protein)–coupled receptors that are activated by the otherwise inert drug clozapine-*N*-oxide (CNO) and couple to different G protein signaling cascades that either activate (Gq-DREADD) or inhibit (Gi-DREADD) neuronal activity (*50*). We injected viral constructs encoding Cre-dependent ("flexed") DREADD receptor expression cassettes (*51*) into the POA of *Trpm2-Cre* mice (Fig. 3A). This allowed the specific activation or inhibition of *Trpm2-Cre*$^+$ POA neurons through systemic application of CNO. No expression of DREADDs occurred in the absence of Cre recombinase.

To verify the capacity of CNO to exert control over *Trpm2*$^+$ neurons in vitro, we co-infected POA neurons by stereotactic injection of Cre-inducible DREADD receptors and GCaMP6 viral constructs into *Trpm2-Cre* mice. In brain slices derived from these mice, the respective DREADD receptor and GCaMP6 are coexpressed in *Trpm2*$^+$ neurons. Calcium imaging of POA neurons expressing Gq-DREADD or Gi-DREADD together with GCaMP6 confirmed that CNO application activated or inhibited *Trpm2*$^+$ neurons, respectively (fig. S3G).

We implanted telemetric temperature probes in the peritoneal cavity of DREADD-virus–injected *Trpm2-Cre* mice to permit recording of T_{core} in conscious, unrestrained animals (Fig. 3B). Diurnal body temperature regulation of DREADD-infected *Trpm2-Cre* mice in the absence of CNO was similar to that of control animals (fig. S3H). In contrast, CNO-mediated activation of *Trpm2*$^+$ POA neurons resulted in a sustained decrease in body temperature (Fig. 3, C to E, and fig. S3I). T_{core} dropped to 27.4 ± 0.6°C when *Trpm2*$^+$ neurons were activated in Gq-DREADD–infected mice but not in control-infected or saline-injected mice.

The temperature decrease correlated with a reduction in activity of the animals and was also reflected by a temperature drop of the body shell, as visualized by infrared (IR) imaging (Fig. 3F and movie S1). The hypothermic state lasted several hours (0.3 mg/kg of CNO induced hypothermia for 12.5 ± 2.4 hours) and could be induced repetitively without causing any apparent long-term adverse effects (Fig. 3E).

The animal's tail, an important thermal effector organ controlling heat dissipation (*3*, *52*), showed an increase in surface temperature of 3.7 ± 0.5°C that coincided with the overall heat loss (Fig. 3, F and G; fig. S3J; and movie S1), demonstrating that *Trpm2*$^+$ POA neurons drive hypothermia by triggering cutaneous vasodilation. Additionally, stimulation of *Trpm2*$^+$ neurons prevented activation of interscapular brown adipose tissue (BAT; fig. S3K), which normally mediates thermogenesis when the body cools.

Conversely, Gi-DREADD receptor–mediated inhibition of *Trpm2*$^+$ POA neurons resulted in a significant temperature increase, reaching a T_{core} of up to 39.1 ± 0.1°C (Fig. 3H and fig. S3I), suggesting that under normothermic conditions, *Trpm2*$^+$ neurons in the POA are tonically active. This is in agreement with previous electrophysiological recordings that show tonic ongoing activity of WSNs (*17*–*19*). Gi-DREADD–mediated neuronal inhibition had no significant effect on tail vasomotor tone at ambient temperature (~20°C), likely because the prominent vasoconstriction that prevails under these conditions (*53*) precludes detection of any further reduction of the IR signal (Fig. 3G). These results demonstrate that *Trpm2*$^+$ neurons in the POA are part of a circuit that orchestrates thermal effector processes to modulate T_{core} homeostasis.

Excitatory *Trpm2*$^+$ neurons drive hypothermia

WSNs in the POA have been proposed to be γ-aminobutyric acid (GABA)–releasing neurons that exert their effect largely by inhibiting downstream components of the thermoregulatory circuit (*3*). We therefore used two-color in situ hybridization on *Trpm2-Cre* reporter mice to ascertain whether *Trpm2*$^+$ neurons are of inhibitory or excitatory origin. We used in situ probes for transcripts encoding the vesicular glutamate transporter 2 (VGLUT2) and glutamate decarboxylase 1 (GAD1), which are excitatory and inhibitory markers, respectively (*54*) (Fig. 4A).

By this analysis, 30 ± 1% of *Trpm2*$^+$ POA neurons were excitatory (*Vglut2*$^+$) neurons, whereas 57 ± 7% coexpressed the inhibitory marker *Gad1* (mean ± SEM; n = 3 mice) (Fig. 4A and fig. S4A). We therefore tested whether activation of the excitatory or inhibitory neuronal population within the POA recapitulated the strong thermoregulatory phenotype observed on activation of *Trpm2*$^+$ neurons (Fig. 3, C to G). *Vgat-Cre* (*54*) and

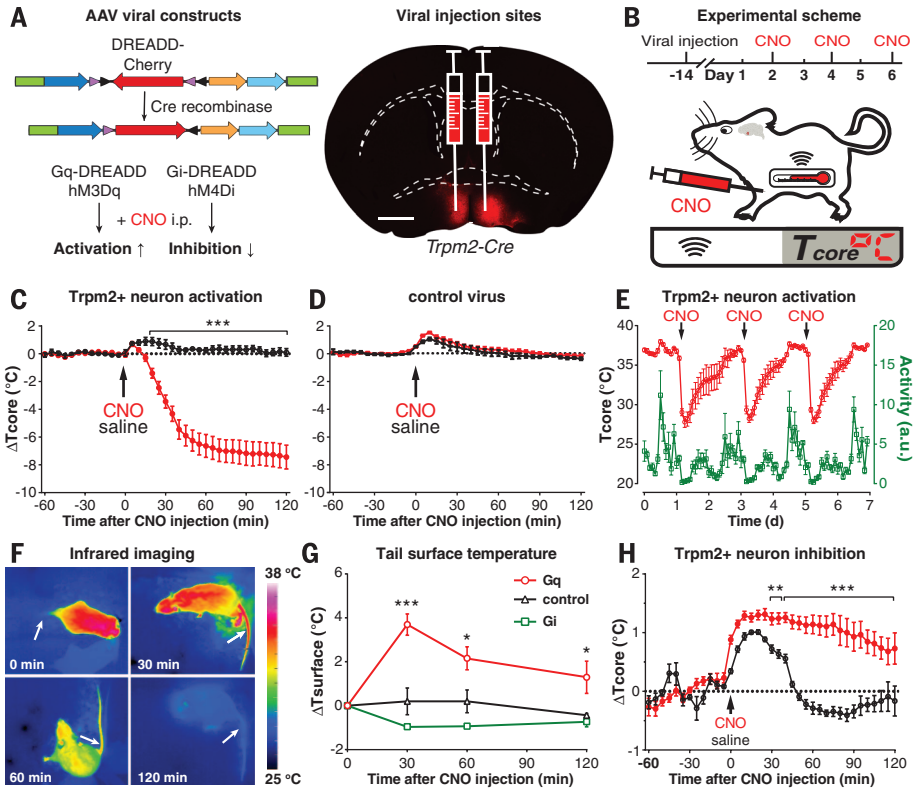

Fig. 3. Control of core body temperature by *Trpm2*$^+$ POA neuron activity. (**A**) Virally encoded, Cre-inducible DREADD-receptor–cherry fusion proteins (left panel) were bilaterally injected into the POA of *Trpm2-Cre* mice and visualized by fluorescent microscopy (right panel). The red arrows indicate the orientation of the DREADD–cherry cDNA reading frame; i.p., (injected) intraperitoneally. (**B**) Illustration detailing the experimental paradigm for examining the impact of *Trpm2*$^+$ neuronal activity on T_{core}. (**C** to **E**) CNO (0.3 mg/kg; red) or vehicle (saline; black) was intraperitoneally injected into mice infected with Gq-DREADD [(C) and (E)] or control virus (D), and T_{core} and activity [green trace in (E)] were measured telemetrically. Arrows indicate the time of injection. a.u., arbitrary units. (**F**) IR thermal imaging of *Trpm2-Cre* mice preoptically expressing Gq-DREADD in *Trpm2*$^+$ neurons, before (0 min) or at indicated time points after CNO injection, revealed pronounced cutaneous heat dissipation through tail vasodilation (arrows). (**G**) Change in tail temperature over time [(arrows in (F)] in *Trpm2-Cre* mice infected with Gq-DREADD (red), saline control (black), or Gi-DREADD (green) upon CNO treatment. (**H**) CNO-mediated inhibition of *Trpm2*$^+$ neurons in Gi-DREADD–infected *Trpm2-Cre* mice showed an oppositely directed effect compared with that in Gq-DREADD–infected animals (C) and resulted in a significant increase in T_{core}. The arrow indicates the time of injection. Telemetry data [(C), (D), and (H)]: Gq-DREADD $F_{1,6} = 75.6$, ***$P < 0.0001$; control virus $F_{1,6} = 1.55$; Gi-DREADD $F_{1,6} = 38.5$, **$P < 0.01$, ***$P < 0.0001$. IR imaging (G): Gq-DREADD $F_{1,5} = 9.3$, *$P < 0.05$, ***$P < 0.001$; Gi-DREADD $F_{1,4} = 5.2$; two-way ANOVA followed by post hoc Fisher's LSD test (n = 4 mice per group). P values indicate significance of the post hoc test.

Downloaded from http://science.sciencemag.org/ on September 30, 2016

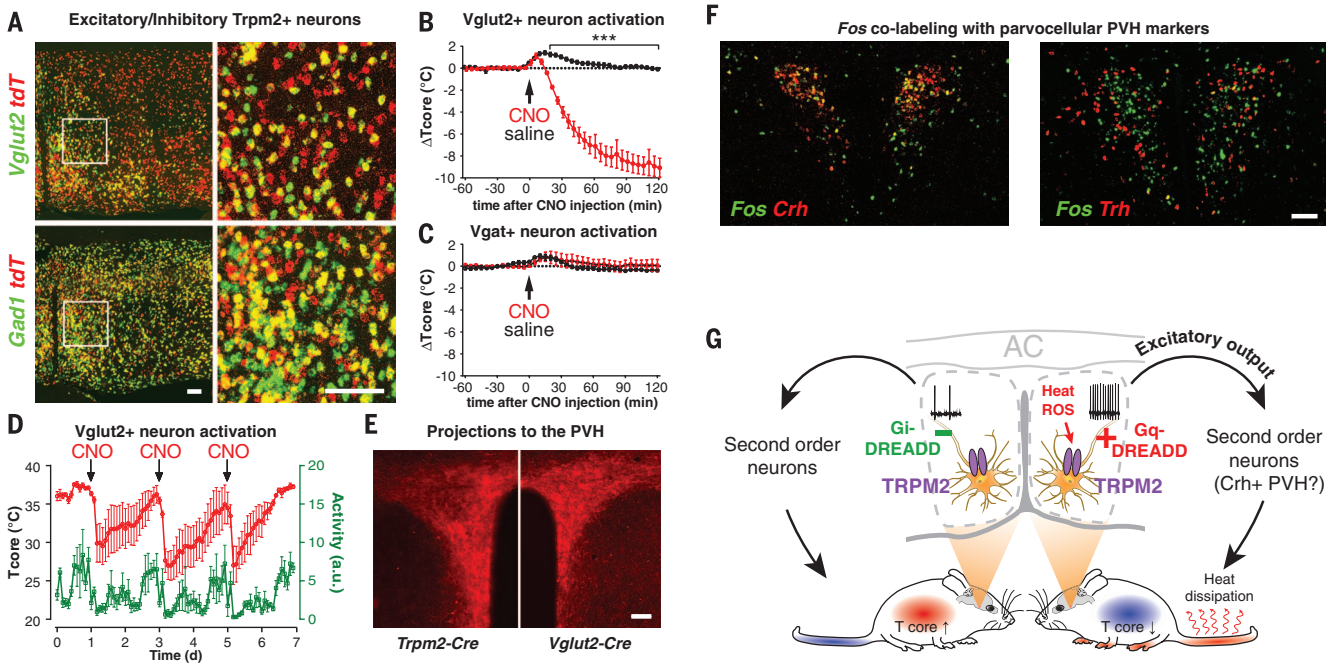

Fig. 4. Stimulation of preoptic *Vglut2*$^+$ neurons recapitulates *Trpm2*$^+$ neuron–driven hypothermia and activates *Crh*$^+$ neurons in the PVH. (**A**) Representative two-color in situ hybridizations of coronal brain sections from *Trpm2-Cre* mice crossed with a *Cre* reporter expressing *tdTomato* (*tdT*) with probes detecting *tdT* (red) and *Gad1* or *Vglut2* (green). The right panels show close-up views indicated by the boxes in the left panels. (**B** to **D**) *Vglut2-Cre* mice and *Vgat-Cre* mice were bilaterally injected with Gq-DREADD virus and subjected to the same experimental paradigm as shown in Fig. 3B. Arrows indicate the time of injection. CNO-mediated activation of *Vglut2-Cre* mice [(B) and (D)], but not *Vgat-Cre* mice (C), recapitulated *Trpm2*$^+$ neuron–driven hypothermia both in magnitude (B) and kinetics (D). *Vglut2-Cre* $F_{1,6} = 86.08$, $^{***}P < 0.0001$; *Vgat-Cre* $F_{1,4} = 0.44$; two-way ANOVA followed by post hoc Fisher's LSD test ($n = 4$ *Vglut2-Cre* and 3 *Vgat-Cre* mice). (**E**) Representative fluorescent images of brain sections from *Vglut2-Cre* and *Trpm2-Cre* mice preoptically expressing Gq-DREADD–cherry fusion protein (Fig. 3A), showing cherry$^+$ fibers projecting to the PVH. (**F**) Two-color fluorescent in situ hybridizations of brain sections from *Vglut2-Cre* mice preoptically expressing Gq-DREADD, using probes to detect *Fos* (green) and *Crh* or *Trh* (red). The animals were injected with CNO 30 minutes before preparation of the tissue sections. Neuronal activation of *Crh*$^+$ neurons but not *Trh*$^+$ neurons in the PVH was detected. (**G**) Model depicting *Trpm2*$^+$ POA neurons and their bidirectional effect on T_{core}. Heat (and reactive oxygen species, ROS) activate TRPM2 to depolarize WSNs, a process that can be mimicked by exogenous Gq-DREADD activation. Increased WSN activity (black traces) triggers an excitatory pathway that promotes heat loss and hypothermia, possibly through a circuit involving *Crh*$^+$ neurons in the PVH. Conversely, inhibiting *Trpm2*$^+$ neurons results in an elevation of T_{core}. AC, anterior commissure. *P* values indicate significance of the post hoc test. All scale bars, 100 μm.

Vglut2-Cre (*55*) mice have been used previously to label inhibitory and excitatory hypothalamic neurons, respectively. Thus, T_{core} recordings of Gq-DREADD–injected *Vgat-Cre* and *Vglut2-Cre* mice were acquired, and viral expression in the respective POA neurons was later verified (fig. S4, B and C). CNO activation of *Vglut2*$^+$ neurons but not *Vgat*$^+$ neurons reproduced the prolonged drop in T_{core} (Fig. 4, B to D), indicating that excitatory, *Trpm2*$^+$ neurons mediate the strong thermoregulatory effect. *Vglut2*$^+$ neuron–driven hypothermia could be induced repetitively and was well tolerated by the animals (Fig. 4D), similar to observations for in vivo chemogenetic activation of preoptic *Trpm2*$^+$ neurons (Fig. 3E). In situ hybridization revealed that Cre recombinase in the *Vglut2-Cre* line was expressed only in ~20% of all *Vglut2*$^+$ POA neurons (fig. S4D). This indicates that activation of a subpopulation of *Vglut2*$^+$ POA neurons, making up only ~6% of all preoptic *Trpm2*$^+$ neurons (fig. S4A), is sufficient to mediate the strong hypothermic effect (Fig. 4, B and D).

Thermoregulatory signals arising from the POA are channeled to different peripheral effector organs through discrete hypothalamic and extrahypothalamic output nuclei (*3*). Given the overlapping expression pattern of *Vglut2* and *Trpm2* in the POA and a similar capacity of both neuron groups to trigger hypothermia on activation, we reasoned that axons of both neuron cohorts might converge on the same downstream output nucleus. Projections of *Cre*-expressing POA neurons were labeled with fluorescent reporters that were introduced together with the DREADD expression cassette by viral infection of the POA area (Fig. 3A). POA infections of *Trpm2-Cre* and *Vglut2-Cre* mice resulted in prominent labeling of fibers terminating in the paraventricular nucleus of the hypothalamus (PVH) (Fig. 4E), a region not previously identified as a major thermoregulatory outlet (*3*). Moreover, CNO administration in *Trpm2-Cre* and *Vglut2-Cre* mice harboring Gq-DREADD–infected POA neurons resulted in DREADD-specific expression of *Fos* in the PVH, demonstrating that *Trpm2*$^+$ *Vglut2*$^+$ POA neurons can excite PVH neurons (fig. S4E). Corticotropin-releasing hormone–positive (*Crh*$^+$) neurons in the PVH are part of the hypothalamic-pituitary-adrenal (HPA) stress response system, which is also activated in response to fever (*56*). We found that DREADD-mediated activation of *Vglut2*$^+$ POA neurons specifically excites parvocellular *Crh*$^+$ neurons but not neighboring thyrotropin-releasing hormone–positive (*Trh*$^+$) neurons or magnocellular vasopressin$^+$ and oxytocin$^+$ PVH neurons (Fig. 4F and fig. S4F). Of all *Fos*$^+$ neurons, we found that 88.4 ± 1.5% (mean ± SEM; $n = 3$ mice) are *Crh*$^+$.

Collectively, these results indicate that *Trpm2*$^+$ *Vglut2*$^+$ POA neurons detect increased body temperature and initiate thermoregulatory defense mechanisms, putatively through activation of stress-responsive *Crh*$^+$ neurons in the PVH (Fig. 4G).

Discussion

Explanations of the molecular mechanisms mediating thermal detection in preoptic WSNs have remained speculative (*57*, *58*). We identified TRPM2 as a thermal sensor in a subset of POA neurons that are part of a circuit controlling T_{core}.

Preoptic TRPM2 was activated at temperatures above the physiological set point of 37°C, arguing for a function of this receptor at conditions of elevated core temperatures and heat stress. Our results demonstrate a role for preoptic TRPM2 in regulating the magnitude of the fever response, suggesting that heightened temperatures, potentially

Downloaded from http://science.sciencemag.org/ on September 30, 2016

together with reactive oxygen species that are produced under these conditions (*59*), activate the channel to promote heat loss and prevent overheating.

Fever temperatures activate the immune system to modulate inflammatory responses (*60*). TRPM2 is expressed in the immune system (*61*), suggesting that fever-activated TRPM2 might modulate immune cell function. TRPM2 activity has been shown to inhibit and counteract inflammatory (pyrogenic) signaling in phagocytes (*62*), paralleling our results and emphasizing a convergent TRPM2-based mechanism used by both the immune and nervous systems to limit the extent of an inflammatory response and the mediation of antipyresis.

We observed a TRPM2-mediated reduction in T_{core} only when strong fever responses were induced, suggesting that TRPM2 limits the upper fever range and acts as an "emergency break" to prevent overheating and tissue damage. Alternatively, it is possible that TRPM2 plays a more prominent role in fever regulation, but that this function is masked by compensatory mechanisms triggered in *Trpm2*$^{-/-}$ mice that ubiquitously lack this ion channel throughout development.

The current model of thermoregulation predicts that the action potential firing rate of WSNs in the POA underlies T_{core} homeostasis and controls peripheral autonomous thermal responses (*3*). We found that chemogenetic activation and inhibition of *Trpm2*$^{+}$ WSNs in mice results in hypo- and hyperthermia, respectively, providing direct in vivo evidence for the validity of this hypothesis.

Twenty to 40% of POA neurons are sensitive to temperature and respond to stimuli around 37°C in electrophysiological experiments (*17*). Using calcium imaging, we found that only around 16% of neurons responded to a temperature increase. It is possible that our approach only allowed the detection of neurons that robustly responded to a thermal stimulus. Buffering of intracellular free calcium by the calcium indicators used in our experiments is one possible explanation for the reduced sensitivity and might explain the lower percentage of responsive neurons. Our data indicate that the TRPM2 receptor is unlikely to account for temperature sensitivity at normothermia but rather detects heat stress above 37°C. Accordingly, in POA brain slices, some thermal responses were still detectable in the absence of TRPM2, implying that additional mechanisms mediate preoptic responses to warming. Given the relatively broad expression of TRPM2 in the POA, it is plausible that the receptor covers detection of the upper, pathological temperature range in many or even all WSNs.

Previous single-cell transcriptome analysis has shown that preoptic WSNs are unexpectedly heterogeneous (*63*). Nevertheless, WSNs have been found to largely be inhibitory (GABAergic) neurons, which is in agreement with our histochemical analysis (summarized in fig. S4A). However, because the hypothermic phenotype that we observed in *Trpm2-Cre* mice was recapitulated by activating the smaller subpopulation of excitatory *Vglut2*$^{+}$ neurons but not by activating inhibitory (*Vgat*$^{+}$) neurons, we focused on the excitatory branch of the *Trpm2*$^{+}$ population. We found that preoptic *Vglut2*$^{+}$ neurons project to and excite *Crh*$^{+}$ neurons in the PVH, a hypothalamic cell population that is not primarily associated with thermoregulation (*3*), but rather controls stress reactions including fever responses by activation of the HPA axis. Excitation of PVH neurons inhibits PGE_2-induced fever (*47*). Moreover, corticosterone release by HPA axis activation has been found to counteract and reduce fever responses (*64*, *65*). These findings are in agreement with our data. The TRPM2 receptor may curtail PGE_2-triggered fever and induce hypothermia by mediating monosynaptic excitation of *Crh*$^{+}$ neurons in the PVH through an excitatory thermoregulatory pathway that connects the POA with the HPA axis.

Our study delineates a genetic framework for dissecting the central pathways controlling temperature homeostasis and provides a way to remotely control core body temperature in conscious, unrestrained mice by chemogenetic manipulation of the hypothalamic thermostat. These hypo- and hyperthermic model systems may help in exploring the effects of altered core body temperature on diverse processes such as trauma recovery, immune modulation, energy expenditure, obesity, and longevity.

REFERENCES AND NOTES

1. T. Bartfai, B. Conti, *Sci. World J.* **10**, 490–503 (2010).
2. C. B. Saper, A. A. Romanovsky, T. E. Scammell, *Nat. Neurosci.* **15**, 1088–1095 (2012).
3. S. F. Morrison, *Auton. Neurosci.* **196**, 14–24 (2016).
4. M. E. Musselman, S. Saely, *Am. J. Health Syst. Pharm.* **70**, 34–42 (2013).
5. W. D. Dietrich, H. M. Bramlett, *Brain Res.* **1640**, 94–103 (2016).
6. T. C. Wu, J. C. Grotta, *Lancet Neurol.* **12**, 275–284 (2013).
7. T. L. Horvath, N. S. Stachenfeld, S. Diano, *Yale J. Biol. Med.* **87**, 149–158 (2014).
8. H. C. Heller, L. I. Crawshaw, H. T. Hammel, *Sci. Am.* **239**, 102–110, 112–113 (1978).
9. B. A. Baldwin, D. L. Ingram, *J. Physiol.* **191**, 375–392 (1967).
10. H. T. Hammel, J. D. Hardy, M. M. Fusco, *Am. J. Physiol.* **198**, 481–486 (1960).
11. H. W. Magoun, F. Harrison, J. R. Brobeck, S. W. Ranson, *J. Neurophysiol.* **1**, 101–114 (1938).
12. E. Satinoff, *Am. J. Physiol.* **206**, 1389–1394 (1964).
13. B. Folkow, G. Strom, B. Uvnas, *Acta Physiol. Scand.* **17**, 317–326 (1949).
14. B. Conti *et al.*, *Science* **314**, 825–828 (2006).
15. M. M. Fusco, J. D. Hardy, H. T. Hammel, *Am. J. Physiol.* **200**, 572–580 (1961).
16. H. C. Heller, *Experientia Suppl.* **32**, 267–276 (1978).
17. J. A. Boulant, *J. Appl. Physiol.* **100**, 1347–1354 (2006).
18. T. Nakayama, J. S. Eisenman, J. D. Hardy, *Science* **134**, 560–561 (1961).
19. T. Nakayama, H. T. Hammel, J. D. Hardy, J. S. Eisenman, *Am. J. Physiol.* **204**, 1122–1126 (1963).
20. A. E. Oliver, G. A. Baker, R. D. Fugate, F. Tablin, J. H. Crowe, *Biophys. J.* **78**, 2116–2126 (2000).
21. C. Cai, X. Meng, J. He, H. Wu, F. Zou, *Neurosci. Lett.* **506**, 336–341 (2012).
22. I. V. Tabarean, B. Conti, M. Behrens, H. Korn, T. Bartfai, *Neuroscience* **135**, 433–449 (2005).
23. J. A. Boulant, J. B. Dean, *Annu. Rev. Physiol.* **48**, 639–654 (1986).
24. R. Palkar, E. K. Lippoldt, D. D. McKemy, *Curr. Opin. Neurobiol.* **34**, 14–19 (2015).
25. J. Vriens, B. Nilius, T. Voets, *Nat. Rev. Neurosci.* **15**, 573–589 (2014).
26. H. Wang, J. Siemens, *Temperature* **2**, 178–187 (2015).
27. L. Vay, C. Gu, P. A. McNaughton, *Br. J. Pharmacol.* **165**, 787–801 (2012).
28. H. Z. Hu *et al.*, *J. Biol. Chem.* **279**, 35741–35748 (2004).
29. K. Togashi, H. Inada, M. Tominaga, *Br. J. Pharmacol.* **153**, 1324–1330 (2008).
30. S. Z. Xu *et al.*, *Br. J. Pharmacol.* **145**, 405–414 (2005).
31. D. M. Bautista *et al.*, *Nature* **448**, 204–208 (2007).
32. A. Dhaka *et al.*, *Neuron* **54**, 371–378 (2007).
33. K. Zimmermann *et al.*, *Proc. Natl. Acad. Sci. U.S.A.* **108**, 18114–18119 (2011).
34. B. Xiao, B. Coste, J. Mathur, A. Patapoutian, *Nat. Chem. Biol.* **7**, 351–358 (2011).
35. J. Siemens *et al.*, *Nature* **444**, 208–212 (2006).
36. D. E. Clapham, C. Montell, G. Schultz, D. Julius, *Pharmacol. Rev.* **55**, 591–596 (2003).
37. J. Vriens *et al.*, *Neuron* **70**, 482–494 (2011).
38. M. Kashio *et al.*, *Proc. Natl. Acad. Sci. U.S.A.* **109**, 6745–6750 (2012).
39. A. L. Perraud *et al.*, *Nature* **411**, 595–599 (2001).
40. Y. Sano *et al.*, *Science* **293**, 1327–1330 (2001).
41. S. Yamamoto *et al.*, *Nat. Med.* **14**, 738–747 (2008).
42. W. P. Cheshire Jr., *Auton. Neurosci.* **196**, 91–104 (2016).
43. K. Togashi *et al.*, *EMBO J.* **25**, 1804–1815 (2006).
44. T. W. Chen *et al.*, *Nature* **499**, 295–300 (2013).
45. F. Tronche *et al.*, *Nat. Genet.* **23**, 99–103 (1999).
46. M. Lazarus *et al.*, *Nat. Neurosci.* **10**, 1131–1133 (2007).
47. C. J. Madden, S. F. Morrison, *Am. J. Physiol. Regul. Integr. Comp. Physiol.* **296**, R831–R843 (2009).
48. T. E. Scammell, J. K. Elmquist, J. D. Griffin, C. B. Saper, *J. Neurosci.* **16**, 6246–6254 (1996).
49. L. M. Harden, I. du Plessis, S. Poole, H. P. Laburn, *Brain Behav. Immun.* **22**, 838–849 (2008).
50. B. L. Roth, *Neuron* **89**, 683–694 (2016).
51. M. Koch *et al.*, *Nature* **519**, 45–50 (2015).
52. R. M. McAllen, M. Tanaka, Y. Ootsuka, M. J. McKinley, *Eur. J. Appl. Physiol.* **109**, 27–33 (2010).
53. C. J. Gordon, *Temperature Regulation in Laboratory Rodents* (Cambridge Univ. Press, 1993).
54. L. Vong *et al.*, *Neuron* **71**, 142–154 (2011).
55. L. Borgius, C. E. Restrepo, R. N. Leao, N. Saleh, O. Kiehn, *Mol. Cell. Neurosci.* **45**, 245–257 (2010).
56. Y. Matsuoka *et al.*, *Proc. Natl. Acad. Sci. U.S.A.* **100**, 4132–4137 (2003).
57. J. A. Boulant, *Am. J. Physiol. Regul. Integr. Comp. Physiol.* **290**, R1481–R1484, discussion R1484 (2006).
58. S. Kobayashi, A. Hori, K. Matsumura, H. Hosokawa, *Am. J. Physiol. Regul. Integr. Comp. Physiol.* **290**, R1479–R1480, discussion R1484 (2006).
59. W. Riedel, G. Maulik, *Mol. Cell. Biochem.* **196**, 125–132 (1999).
60. S. S. Evans, E. A. Repasky, D. T. Fisher, *Nat. Rev. Immunol.* **15**, 335–349 (2015).
61. H. Knowles, Y. Li, A. L. Perraud, *Immunol. Res.* **55**, 241–248 (2013).
62. A. Di *et al.*, *Nat. Immunol.* **13**, 29–34 (2012).
63. J. Eberwine, T. Bartfai, *Pharmacol. Ther.* **129**, 241–259 (2011).
64. I. Chowers, N. Conforti, S. Feldman, *Am. J. Physiol.* **214**, 538–542 (1968).
65. J. L. McClellan, J. J. Klir, L. E. Morrow, M. J. Kluger, *Am. J. Physiol.* **267**, R705–R711 (1994).

ACKNOWLEDGMENTS

We thank Y. Mori for *Trpm2*$^{-/-}$ mice and TRPM2 antisera; B. Lowell for *Vgat-Cre* mice; members of R. Kuner's laboratory, the Nikon Imaging Center, and V. Grinevich for sharing reagents, equipment, and expertise; A. von Seggern and C. Steinmeyer-Stannek for technical support; K. Schrenk-Siemens, W. de Lima, and P. Bengtson for help with calcium imaging; and C. Bohlen and A. Littlewood-Evans for criticism and reading of the manuscript. All data necessary to understand the study and its conclusions are in the body of the manuscript and in the supplementary materials. All primary data are archived on secure servers at the University Hospital Heidelberg. All data will be made available upon request. This work was supported by the European Research Council (grant ERC-2011-StG-280565 to J.S.), the Alexander von Humboldt Foundation (German Federal Ministry for Education and Research, BMBF; fellowship to G.B.K. and grant to J.S.), and the German Research Foundation (grants as part of the Collaborative Research Center SFB-1158 to P.H. and J.S.). Additional support came from the CellNetworks Cluster of Excellence. J.S., together with K.S., H.Wa., and G.B.K., conceived the project and designed the experiments. K.S. designed and conducted the cellular screen and analysis; J.P. designed and performed electrophysiological experiments; G.B.K. conceived the slice physiology and fever experiments; and H.Wa. conceived and conducted the chemogenetic experiments and, together with H.We., P.H., and F.d.C.R., generated *Trpm2-Cre* mice. H.We. and H.Wa. conducted histochemical analysis. J.S. wrote the paper. All authors commented on and approved the paper.

SUPPLEMENTARY MATERIALS

www.sciencemag.org/content/353/6306/1393/suppl/DC1
Materials and Methods
Figs. S1 to S4
Table S1
References (*66*–*76*)
Movie S1

24 March 2016; accepted 27 July 2016
Published online 25 August 2016
10.1126/science.aaf7537

Downloaded from http://science.sciencemag.org/ on September 30, 2016

STRUCTURAL BIOLOGY

Molecular architecture of the *Saccharomyces cerevisiae* activated spliceosome

Reinhard Rauhut,[1]* Patrizia Fabrizio,[1]* Olexandr Dybkov,[1]* Klaus Hartmuth,[1] Vladimir Pena,[2] Ashwin Chari,[3] Vinay Kumar,[1] Chung-Tien Lee,[4,5] Henning Urlaub,[4,5] Berthold Kastner,[1]† Holger Stark,[3,6]† Reinhard Lührmann[1]†

The activated spliceosome (B^{act}) is in a catalytically inactive state and is remodeled into a catalytically active machine by the RNA helicase Prp2, but the mechanism is unclear. Here, we describe a 3D electron cryomicroscopy structure of the *Saccharomyces cerevisiae* B^{act} complex at 5.8-angstrom resolution. Our model reveals that in B^{act}, the catalytic U2/U6 RNA-Prp8 ribonucleoprotein core is already established, and the 5′ splice site (ss) is oriented for step 1 catalysis but occluded by protein. The first-step nucleophile—the branchsite adenosine—is sequestered within the Hsh155 HEAT domain and is held 50 angstroms away from the 5′ss. Our structure suggests that Prp2 adenosine triphosphatase–mediated remodeling leads to conformational changes in Hsh155's HEAT domain that liberate the first-step reactants for catalysis.

The spliceosome is a highly dynamic molecular machine that assembles de novo for each round of splicing by the ordered interaction of the U1, U2, U4/U6, and U5 small nuclear ribonucleoprotein (snRNPs) with a pre-mRNA intron (*1*). A key step toward a catalytically active spliceosome is the transformation of the spliceosomal B complex, which lacks an active site, into an activated B^{act} complex (fig. S1). This entails extensive structural rearrangements, including release of the U4 small nuclear RNA (snRNA) (catalyzed by the RNA helicase Brr2), and all U4/U6 and several U5 snRNP proteins (fig. S1). At the same time, the Prp19 complex (NTC), retention and splicing (RES) proteins, and about 10 so-called B^{act} proteins are recruited or stably integrated (*2*). B^{act} is transformed into the catalytically active B* complex by the Prp2 RNA helicase and its cofactor Spp2, which facilitate RNP remodeling, including destabilization of the U2 snRNP SF3a and SF3b proteins (*3*–*6*). B* catalyzes step 1 of the splicing reaction, namely 5′ splice site (ss) cleavage and formation of a lariat-intron-3′exon intermediate. The subsequently formed C complex then catalyzes step 2, which entails 3′ss cleavage and the ligation of the 5′ and 3′ exons.

During activation, a catalytic RNA-RNA network, very similar to the catalytic core of group II self-splicing introns (*7*), is established (*8*, *9*), as documented with high-resolution cryogenic electron microscopy (cryo-EM) of endogenous, post–step 2, intron lariat spliceosomes (ILSs) from *Schizosaccharomyces pombe* (*10*). Unlike group II introns, formation of the catalytic RNA network requires spliceosomal proteins (*1*), foremost the U5 Prp8 protein (*10*–*12*). Although the cryo-EM model of the *S. pombe* ILS provides molecular insight into the architecture of the spliceosome's catalytic RNP core, it does not reveal (i) how and when the latter is generated during the spliceosome's stepwise catalytic activation process; (ii) the architecture of the BS/U2 snRNA helix, and the U2 SF3a and SF3b proteins that stabilize the BS/U2 interaction; or (iii) the mechanisms by which the BS adenosine (BS-A, the step 1 nucleophile) is positioned for step 1 catalysis during Prp2-mediated remodeling of the B^{act} complex. High- to medium-resolution cryo-EM structures of the *Saccharomyces cerevisiae* and human U4/U6.U5 tri-snRNPs have been published (*13*–*16*); however, no high-resolution structures of spliceosomes during their catalytic activation phase are available. A comparison of two-dimensional (2D) EM images of purified yeast B, B^{act}, and B* complexes indicates substantial structural changes during the transitions from one complex to the next (*2*, *17*). Here, we report a 3D cryo-EM structure of the *S. cerevisiae* spliceosomal B^{act} complex at an overall resolution of 5.8 Å, which allowed us to resolve the spatial organization of most of its protein and RNA components.

Structure determination and model-building

S. cerevisiae B^{act} spliceosomal complexes assembled in vitro were affinity purified (fig. S1), and an initial 3D model was determined by means of random-conical-tilt 3D reconstruction followed by 3D maximum-likelihood alignment and 3D classification (*18*). The calculated low-resolution structure was used as a starting model to determine the final 5.8 Å reconstruction from an initial data set of 1 million particle images after several steps of image-sorting and classification (fig. S2). The 3D structure of B^{act} encloses a total volume corresponding to a molecular mass of ~3.8 MDa (Fig. 1A). The major parts of the B^{act} spliceosome (~70% of the total mass) are well-defined in the high-resolution structure. However, some areas that are either more dynamic or contain components with less than stoichiometric occupancies are not visible in the final structure. The pseudo-atomic model was built for the stabler part of B^{act}, in which the resolution sufficed for clear identification of structured protein domains and double-strand RNA elements, allowing us to fit known x-ray structures or homology models of structured regions of B^{act} complex components into the EM density map (table S1). Additionally, we performed chemical protein cross-linking coupled to mass spectrometry (CX-MS) (table S2) to validate the locations of large proteins and facilitate the docking of smaller ones.

The conformation of Prp8 and Brr2 differs substantially in the tri-snRNP and B^{act} complex

Tri-snRNP components still present in the spliceosome at the B^{act} stage include the guanosine triphosphatase (GTPase) Snu114, the major scaffolding protein Prp8 found at the spliceosome's catalytic core, and the spliceosome-activating RNA helicase Brr2, in addition to the U5 Sm core and U5 and U6 snRNAs (figs. S1 and S3). Snu114 is located as a compact structure at the lower end of the main body of the B^{act} structure (Fig. 1B and fig. S4A). Prp8, which has an open conformation in the tri-snRNP (*13*–*16*), has adopted a closed conformation in the B^{act} structure (Figs. 1B and 2), similar—but not identical—to its conformation in the *S. pombe* ILS complex (*10*). That is, the middle part of the RT/En domain contacts the NTD1 domain but not the tip of the En domain (Fig. 2A). The reason for this may be that the En domain has moved ~12 Å upward in B^{act} compared with the ILS (Fig. 2, B and C). In the *S. cerevisiae* and human tri-snRNPs, and in the *S. pombe* ILS, there is a major β-hairpin-loop (henceforth termed the switch loop) from the Prp8 linker region that runs along the long axis of the RT/En domain and touches the En domain. In the B^{act} complex, the EM density and protein cross-links (table S2) indicate that this switch loop (comprising Prp8 amino acids H1404 to L1436 in *S. cerevisiae*) has been rearranged into a loop that protrudes from the interface between Prp8's thumb/X and linker domains and is situated close to exon 1 (Figs. 2 and 4C). Last, Prp8's RH domain is closely associated with the En domain in B^{act}, in a region where in the ILS and tri-snRNPs the tip of the switch loop is instead located (Fig. 2 and fig. S4C). Thus, the Prp8 RH domain is located in different places in each of the spliceosomal cryo-EM structures analyzed so far (fig. S4, B and C).

[1]Department of Cellular Biochemistry, Max Planck Institute (MPI) for Biophysical Chemistry, Am Fassberg 11, D-37077 Göttingen, Germany. [2]Research Group Macromolecular Crystallography, MPI for Biophysical Chemistry, Am Fassberg 11, 37077 Göttingen, Germany. [3]3D Electron Cryomicroscopy Group, MPI for Biophysical Chemistry, Am Fassberg 11, D-37077 Göttingen, Germany. [4]Bioanalytical Mass Spectrometry, MPI for Biophysical Chemistry, Am Fassberg 11, D-37077 Göttingen, Germany. [5]Bioanalytics Group, Institute for Clinical Chemistry, University Medical Center, Göttingen, Robert-Koch-Straße 40, D-37075 Göttingen, Germany. [6]Department of 3D Electron Cryomicroscopy, Georg-August Universität, Göttingen, Justus von-Liebig-Weg 11, D-37077 Germany.
*These authors contributed equally to this work. †**Corresponding author. Email: b.kastner@mpi-bpc.mpg.de (B.K.); hstark1@gwdg.de (H.S.); reinhard.luehrmann@mpi-bpc.mpg.de (R.L.)**

Downloaded from http://science.sciencemag.org/ on September 30, 2016

The RNA helicase Brr2 contains two tandemly organized helicase cassettes (fig. S3A) that we could localize in B^{act} in complex with the Prp8 Jab1 domain (*19*, *20*) close to the tip of the Prp8 En domain (Fig. 1B and fig. S5A). Brr2's general location is similar in the yeast B^{act} complex and yeast tri-snRNP, but in B^{act}, Brr2 is rotated by ~45° toward the long axis of the RT/En domain (fig. S5B) and shares an interface with Prp8's En domain through the helix-loop-helix domain of its N-terminal helicase cassette (NC) (fig. S5A). In the human tri-snRNP, Brr2 is located in a substantially different position (compared with the yeast tri-snRNP), close to Prp8's RT domain (fig. S5C) (*16*). Because the human and yeast B^{act} complexes are structurally similar, at least at the level of 2D EM class averages (*2*, *21*), hBrr2 must thus be dramatically repositioned after tri-snRNP integration into the human spliceosome (*16*).

The locations of all high-density RNA helical elements within the B^{act} structure are shown in Fig. 1C. The major stem-loop (SL) of U5 fits into the long RNA helical density element, so that the 3′ terminal U5 snRNA Sm site (and thus Sm RNP core) is located at the foot of the 5.8 Å B^{act} EM density map, whereas U5 loop 1 is found in the upper region of the elongated main body (Fig. 1C and fig. S6). U5 snRNA has essentially the same structure in the yeast tri-snRNP (*13*) and B^{act} complex and tightly interacts with Prp8's NTD1 domain.

The catalytic U2/U6 RNA network is established in the B^{act} structure

In the *S. pombe* ILS, a group II–intron-like catalytic RNA center is found. That is, the U2 and U6 snRNAs are extensively base-paired and form a triple helix that brings the U6 ISL and the catalytic U6 AGC triad close together, allowing U6 to bind two Mg^{2+} ions for catalysis (*7*, *22*–*25*). In the precatalytic spliceosomal B complex, the U6 snRNA is based-paired with the U4 snRNA, preventing formation of the U6 ISL, U2/U6 helix I, and thus triple helix formation (fig. S1B). Biochemical and genetic evidence (*7*, *24*), together with the closed conformation of Prp8 that we observed in the B^{act} complex, suggests that the U2 and U6 snRNAs are rearranged in B^{act} to form the catalytic U2/U6 triplex structure observed in the ILS. Indeed, there is a high-density, RNA-shaped element in the B^{act} model, close to U5 snRNA loop 1, into which the rearranged catalytic U2/U6 RNA structure of the *S. pombe* ILS can be fit (Fig. 1C and fig. S6). The well-defined density allows the placement of the U6 ISL loop (close to U5 loop 1), the kinked stem of the U6 ISL, the U2/U6 helices Ia and Ib, and the sharp U6 snRNA turn between the U6 ACAGA box helix and U2/U6 helix Ia (Fig. 3, A and B). The density of the

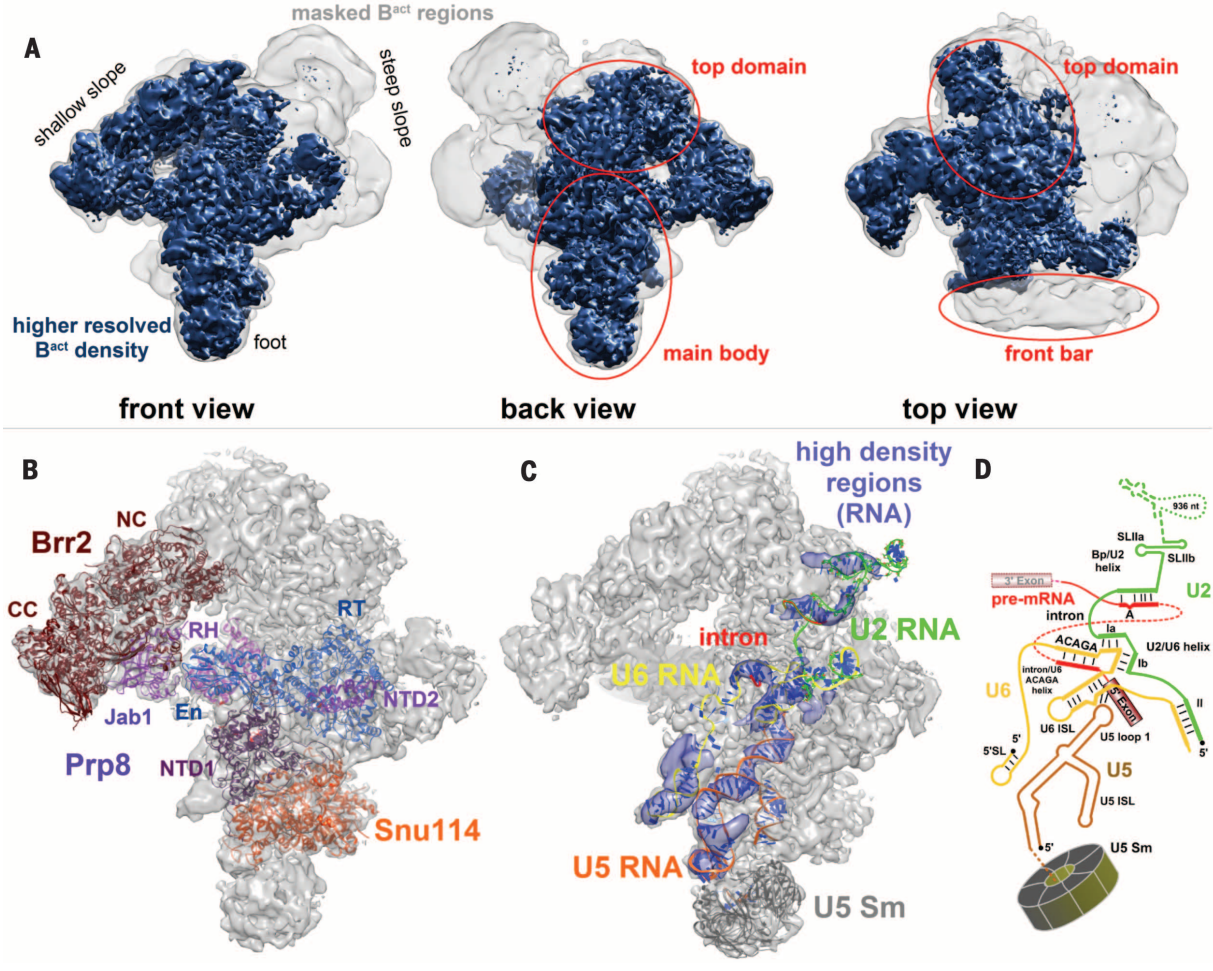

Fig. 1. 3D cryo-EM structure of the yeast B^{act} complex and location of the U5 snRNP proteins and U5, U6, and U2 snRNAs. (**A**) Different views of the B^{act} EM density map with the better resolved density in blue and the masked B^{act} regions in gray. The B^{act} spliceosome exhibits a mushroom-like shape, with a main body connected to a foot and a steep and a shallow slope. Details about the "front bar" domain are provided in fig. S13. (**B**) Position of the U5 proteins Brr2 (NC/CC, N-terminal/C-terminal helicase cassettes), Prp8 (NTD1, NTD2; N-terminal domains 1 and 2; RT, reverse-transcriptase–like; En, endonuclease-like; RH, RNase H–like; Jab1, Jab1/MPN-like), and Snu114 (domains D1 to D5 homologous to EF-G/EF-2). (**C**) RNA helical high-density regions (filtered to a resolution of 10 Å), representing U5, U6, and U2 RNA and the pre-mRNA intron. The position of the U5 Sm is also shown. (**D**) A schematic diagram of U5 and the U2/U6/pre-mRNA network and the heptameric Sm ring of U5.

Downloaded from http://science.sciencemag.org/ on September 30, 2016

RNA elements is also consistent with the existence of the catalytic triplex, as observed in the *S. pombe* ILS (*25*). There is, however, no density for the base pair between U6-G63 and U6-C84 at the base of the ISL (Fig. 3, A and D). Connectivity between both helices is nevertheless provided by a continuous stack between the U6 bases C61, and A62 to U65. This single-strand stack follows the kink of the U6 ISL near nucleotides (nt) U6-A62 and U6-U64 (Fig. 3D) (*23*, *26*). As shown in Fig. 3C, the topology of the phosphate groups of U6 nucleotides U80, G78, G60, and A59, which have been shown to coordinate Mg^{2+} ions in the spliceosome (*24*), is consistent with the possibility that the two catalytic Mg^{2+} ions are coordinated by the phosphate groups at the 4 Å distance that is optimal for RNA catalysis (fig. S7) (*24*, *26*). Although at our level of resolution we cannot discern whether catalytic Mg^{2+} ions are in place, we can conclude that no major rearrangement of the catalytic U2/U6 RNA network is subsequently required for catalysis of step 1 of splicing.

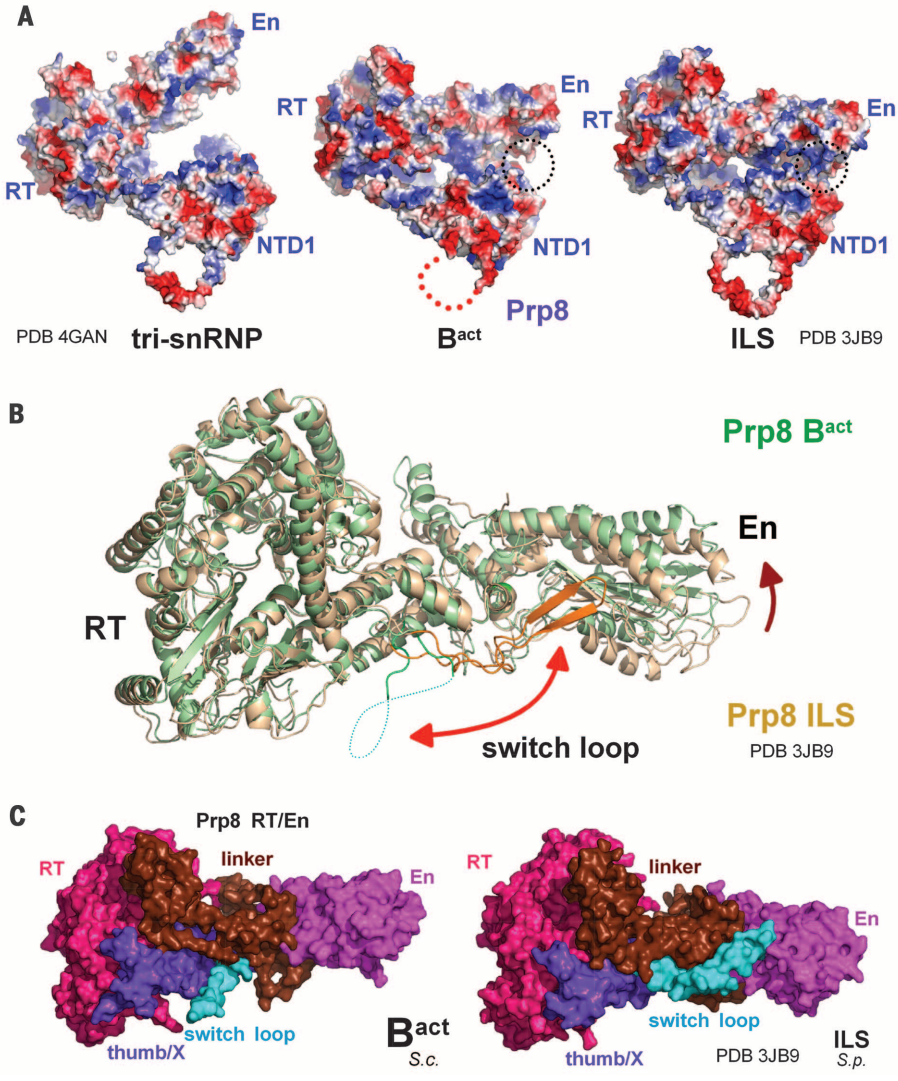

Fig. 2. Structural differences in Prp8's RT/En domains in the B^{act} complex versus *S. pombe* ILS. (**A**) Open conformation of Prp8 in the yeast tri-snRNP and closed conformation in the B^{act} and ILS structures, respectively. The surface charge of Prp8 is shown (blue represents positively charged and red negatively charged residues). The stippled red semicircle at the lower end of Prp8 (middle) indicates the location of the lasso-like region of the NTD1 domain, whose density can only be partly discerned in the B^{act} structure. The stippled black circles (middle and right) indicate the differential interactions of Prp8's En and NTD1 domains in the B^{act} and ILS complexes, respectively. (**B**) The Prp8 switch loop (comprising amino acids H1404 to L1436 in *S. cerevisiae*) that runs along the long axis of the RT/En domain in the *S. pombe* ILS is rearranged in B^{act} and protrudes from the interface between Prp8's thumb/X and linker domains (indicated by the red arrow). (Single-letter abbreviations for the amino acid residues are as follows: A, Ala; C, Cys; D, Asp; E, Glu; F, Phe; G, Gly; H, His; I, Ile; K, Lys; L, Leu; M, Met; N, Asn; P, Pro; Q, Gln; R, Arg; S, Ser; T, Thr; V, Val; W, Trp; and Y, Tyr.) The movement of the En domain in the *S. pombe* ILS ~12 Å upward to its position in the *S. cerevisiae* B^{act} complex is indicated by a dark red arrow. (**C**) The position of the switch loop in the B^{act} and ILS complexes is shown in blue in a space-filling model. The switch loop has the same conformation in the yeast and human tri-snRNPs as in the *S. pombe* ILS.

The 5′ss is shielded by protein and spatially separated from the catalytic center by 6 to 7 Å

As expected, an RNA helical element comprising the U6-ACAGA box base-paired to the 5′ end of the intron is located adjacent to the catalytic center (Fig. 3, A and E, and fig. S6). Continuing along the intron sequence (toward the 5′ss), a density element is observed that makes a U-turn close to the U6/U2 catalytic center (Fig. 3E). This density accommodates well a kinked 5′ss RNA stretch from the precatalytic group II intron structure (GUUAU/gu) (*27*, *28*), with the scissile bond of the pre-mRNA 5′ss oriented toward the catalytic center (Fig. 3E). The scissile phosphate group is, however, located 6 to 7 Å away from the catalytic site where the Mg^{2+} ions are expected to be positioned (Fig. 3C and fig. S7). Moreover, the GU dinucleotides at the intron's 5′ end are in close contact with a short protein density element (Fig. 4A). As described in fig. S8, this protein density element might represent part of the N-terminal region of the NTC protein Cef1. However, we cannot exclude that it is composed of a different protein. Irrespective of its nature, this protein element spatially separates the 5′ss from the catalytic center and at the same time hinders access of the BS adenosine—the step 1 nucleophile—to the 5′ss. Thus, during catalytic activation this protein, which contacts also the HEAT domain of the U2 Hsh155 protein (Fig. 4A), must be rearranged to liberate the 5′ss for its final docking into the catalytic center.

A 5′ exon-binding channel is located between Prp8's RT and NTD1 domain, close to Cwc22

The first 4 nucleotides (nt) of the 5′ exon upstream of the 5′ss are located close to U5 snRNA loop 1, and the EM density indicates that nucleotides 2 and 3 are base-paired with loop 1 nucleotides U96 and U97, respectively, which is consistent with earlier biochemical studies (*29*, *30*). We can trace an additional 16 nt of the exon RNA, which thread through a narrow channel between Prp8's RT and NTD1 domains and then runs next to Prp8's rearranged switch loop and then Cwc22's MA3 domain (Fig. 4C). Beyond the MA3 domain, the exon-binding region may extend along a path between Snu114's D4 and D5 domains that is carpeted with positively charged amino acids (Fig. 4C and fig. S9B). Guided by protein cross-links, we can locate the MIF4G and MA3 domains of Cwc22 on both sides of the exon channel (Fig. 4, fig. S10, and table S2) (*31*, *32*). In the human spliceosome, the evolutionarily conserved Cwc22 protein aids in the deposition of the exon junction complex (EJC) upstream of the spliced exon junction by binding the eIF4AIII helicase of the EJC through its MIF4G domain (*31*, *33*), which is

Downloaded from http://science.sciencemag.org/ on September 30, 2016

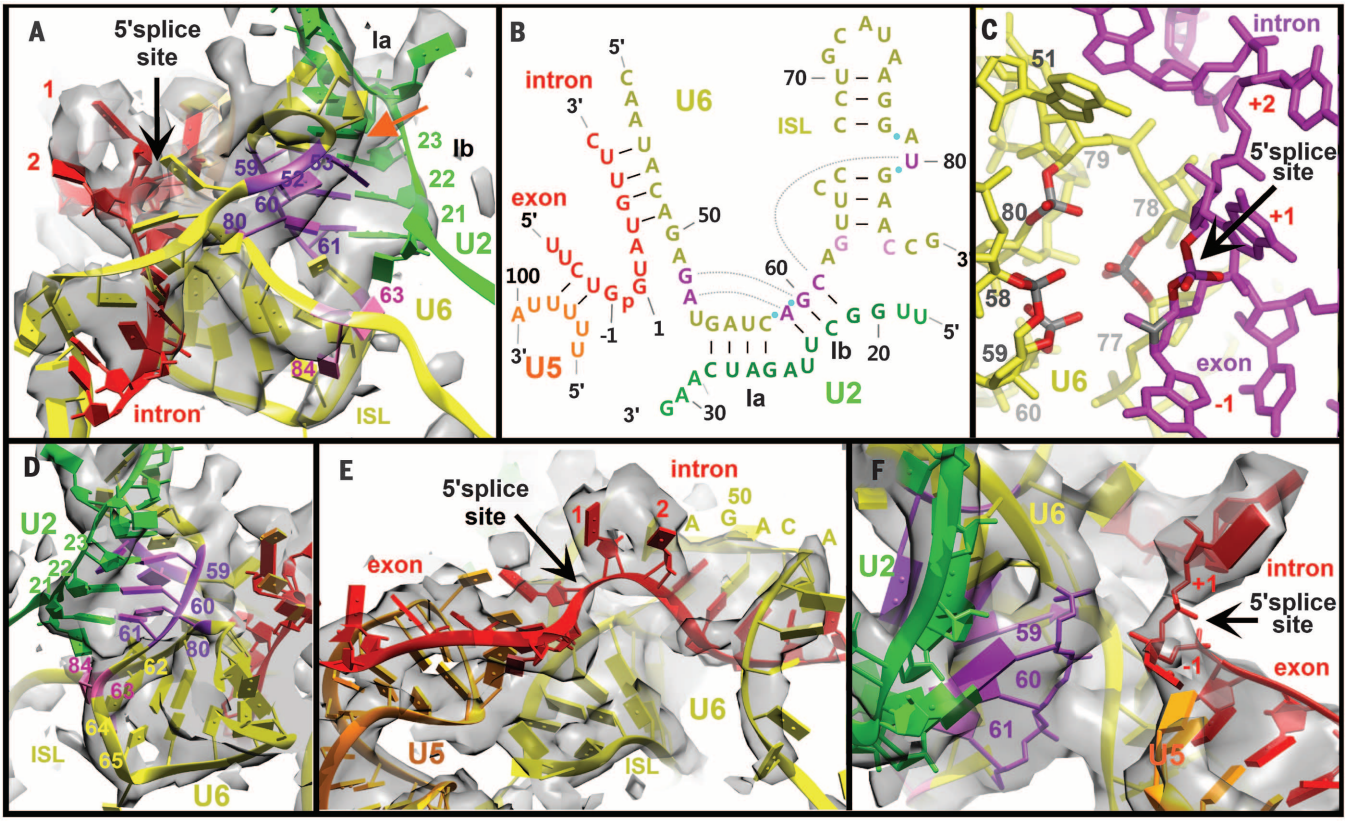

Fig. 3. Position of the 5′ss relative to RNA components of the catalytic center of the B^{act} complex. (**A**) EM density map of the catalytic core RNA elements. U6 snRNA nucleotides of the catalytic triplex are shown in purple, with unpaired nucleotides 63 and 84 in pink. U5 snRNA (not visible) lies at the back. The orange arrow denotes the sharp U6 snRNA turn between the U6 ACAGA box and U2/U6 helix Ia. (**B**) Secondary-structure interactions in the RNA core of the spliceosome. The proposed tertiary interactions (*7*) are shown as stippled lines. Nucleotides coordinating metals (*24*) are labeled with a blue dot. (**C**) Positions of the metal-coordinating phosphate groups of U6 nucleotides U80, G78, G60, and A59 [(B) and fig. S7A] relative to each other are similar to the situation in the precatalytic group II intron (*27*). Exon and intron nucleotides are purple. Phosphates and their oxygens crucial for metal coordination are highlighted gray and red, respectively. (**D**) The helical stack of U6 bases C61 to U65. (**E**) Path of the pre-mRNA in the vicinity of the 5′ss. (**F**) Close-up of the position of the 5′ss phosphate in the EM density.

consistent with the location of Cwc22 close to the exon channel (fig. S10). Last, the N-terminal region of Cwc24 is also located close to the exon channel, as evidenced by multiple cross-links to Prp8's NTD1, RH, and Jab1 domains (fig. S9D). However, in the EM map we cannot discern a clear density for this region of Cwc24, indicating that it is flexible in the B^{act} complex.

Organization of the NTC proteins

In the *S. pombe* ILS, several proteins of the Prp19 (NTC) complex—including Clf1 (Cwf4) (also named Syf3 in *S. cerevisiae*), Prp46, Prp45, and Cef1 (Cdc5)—are close to the catalytic RNA network, in addition to Prp8 (*10*). Except for the N-terminal regions of Cef1 (Cdc5) (fig. S8), the structural organization of these proteins is essentially the same in B^{act} and the ILS. Like in the *S. pombe* ILS (*10*), the tetratricopeptide repeat (TPR) proteins Syf1 (Cwf3) and Clf1 (Cwf4) form long, curved α-helical solenoids that cross one another and together form a basket-like structural element in the B^{act} complex, as seen in the low-resolution B^{act} model, which is consistent with protein cross-linking results (figs. S11 and S12, B and C). The 5′ SL of U6 and U2/U6 helix II, as well as the U6 snRNA-binding protein Cwc2 and the neighboring Ecm2 and Bud31 proteins, are also in similar positions in B^{act} and the ILS complexes (fig. S11). According to the density map of the unmasked low-resolution B^{act} model and protein cross-links, the WD40 domain of Prp17 (*34*), which was not mapped in the ILS, was localized above Ecm2 (fig. S12, A and B). The α-helical elements of the four copies of Prp19 (Cwf8), together with those of the NTC proteins Snt309 (Cwf7) and the C-terminal region of Cef1 (Cdc5), form a helical bundle (HB) that runs, as a self-contained arm II domain, parallel to the main body of the ILS and is only bound to it by thin structural elements (*10*). In the B^{act} complex, this entire Prp19 helical bundle density is repositioned considerably, adopting an orthogonal orientation relative to the central part of the main body (fig. S13).

The SF3b protein complex acts as a major scaffolding unit, bridging Prp8 and Brr2

In B^{act}, the U2 snRNP SF3a/b proteins contact the pre-mRNA intron at or near the BS (*35*, *36*) and stabilize the U2 snRNA-BS helix, suggesting that they may help to shield the BS/U2 RNA helix and thus prevent premature step 1 catalysis. Many U2 components, including the SF3a proteins and the U2 Sm core, are either not discernable or not located in the structurally well-defined region of the yeast B^{act} complex, presumably because of their structural dynamics. Thus, only their general location in B^{act} (at the top right in the front view) can be surmised in the low-resolution B^{act} EM map (fig. S12D). In contrast, using the recent crystal structure of a protease-resistant human SF3b core complex (fig. S14A) (*37*), we could precisely localize a major portion of SF3b. This includes the C-terminal 20 HEAT repeats of Hsh155 (SF3b155 in human), as well as the Rse1 (SF3b130) three-propeller (WD40) cluster and Ysf3 (SF3b10) and Rds3 (SF3b14b), all of which interact with Hsh155's C-terminal HEAT repeats and are organized in a similar manner in yeast B^{act} and the isolated human SF3b complex (Fig. 5 and fig. S14B). However, although the structures of the individual hSF3b155 and yHsh155 HEAT repeats are essentially identical, the conformation of the right-handed superhelix formed by the HEAT domain

Downloaded from http://science.sciencemag.org/ on September 30, 2016

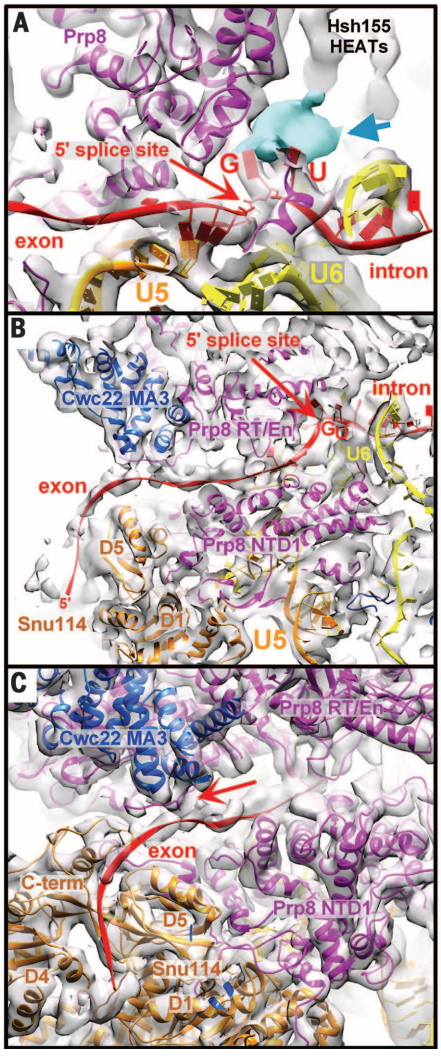

Fig. 4. A protein density element close to the 5′ss and path of the 5′ exon channel in B^{act}. (**A**) The GU dinucleotide at the intron's 5′ end is in close contact with a protein density element (blue). (**B**) A slice through the spliceosomal cryo-EM density, depicting the path of the 5′ exon leading to the catalytic center of the spliceosome. The 5′ exon is shown in red, and the proteins comprising the channel are indicated. (**C**) Path of the exon-binding region between Snu114's D4 and D5 domains. The rearranged switch loop region of Prp8 (indicated with a red arrow) is positioned close to the pre-mRNA.

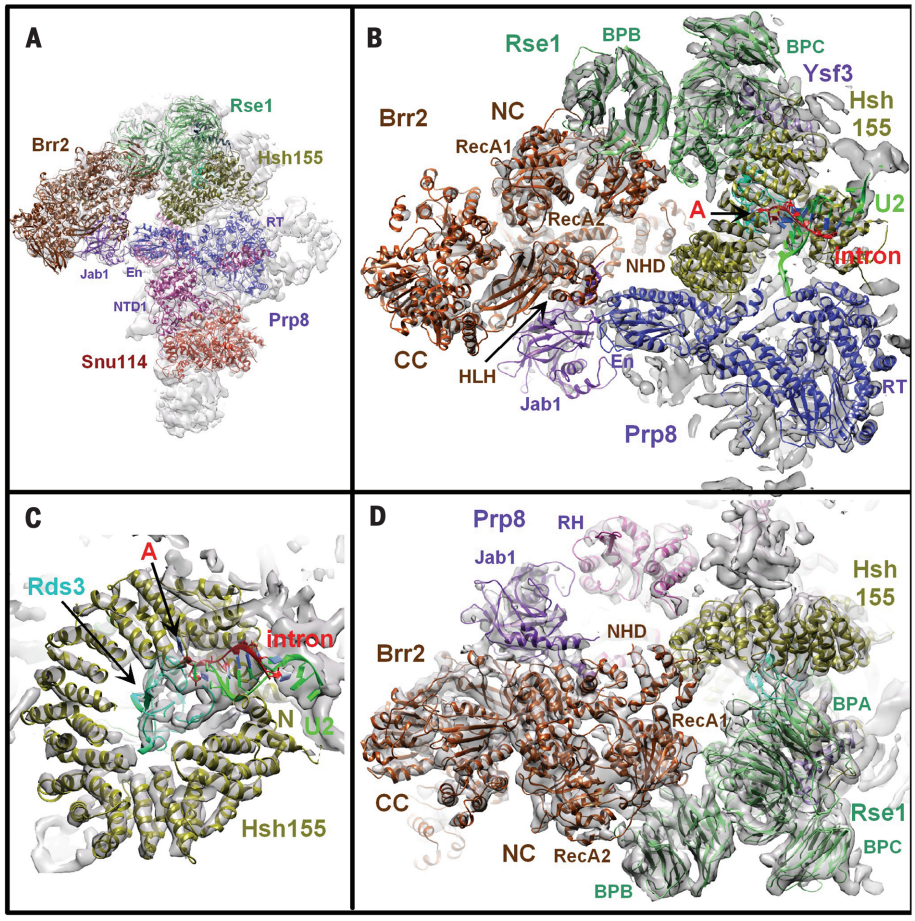

Fig. 5. Localization of the SF3b complex proteins in the B^{act} structure. (**A**) Front view of the B^{act} complex and fit of the SF3b proteins Rse1, Ysf3, Rds3, and Hsh155 at the top of the B^{act} model. (**B**) Slice of the upper region of the B^{act} complex highlighting the arrangement of SF3b proteins, position of U2/BS, and neighboring Brr2 and Prp8 proteins. Red "A" marks the BS adenosine. (**C**) Location of the U2/BS helix between the N- and C-terminal HEAT repeats of Hsh155 near Rds3. All 20 HEAT repeats of Hsh155 form one turn of a solenoid, located above the Prp8 RT/En domain. (**D**) Interface of Rse1's β-propeller BPB with both RecA domains of Brr2's NC cassette [see also (A) and (B)]. The Prp8 RH domain also contacts Hsh155's HEAT domain.

appears much more condensed in the yeast B^{act} complex (Fig. 5C, fig. S14, and movie S1). In the B^{act} structure, the HEAT domain of Hsh155 is located above the Prp8 RT/En domain (Fig. 5, A and B). The intertwined β-propellers BPA and BPC of Rse1 are located at the top of the B^{act} model and are aligned with the long axis of the main body (Fig. 5, A and B). The bottom part of BPB shares a major interface with the RecA domains of Brr2's NC cassette (Fig. 5D). Last, Brr2 also contacts Hsh155 HEAT repeats H9 to H11 via its N-terminal NHD domain (Fig. 5D). Thus, Hsh155's HEAT and Rse1's WD40 β-propeller domains bridge Prp8 and Brr2 in the B^{act} complex.

The BS/U2 RNA helix is sequestered by Hsh155's HEAT repeats and the BS-A is ~50 Å away from the 5′ss

The U2/BS helix is located between the terminal HEAT repeats of Hsh155 (Figs. 5C and 6A). The BS RNA faces the C-terminal HEAT repeats, and the BS-A is located in a protein pocket built by the β-helices of HEAT repeats H15 to H17 and capped by Rds3 (Fig. 5C). On the other side of the BS/U2 helix, the β helices of HEAT repeats 1 and 2 pack against the U2 snRNA. The orientation of the BS/U2 helix places the 5′-terminal nucleotide of U2 ~27 Å above the 3′-terminal U2 nucleotide of U2/U6 helix Ia (Fig. 1C and fig. S15), and both helices are connected by the 4-nt-long U2 linker (fig. S6). The 2′ hydroxyl of the bulged BS adenosine is spatially separated from the scissile bond of the 5′ss by 50 Å (fig. S15). Given the very high conservation of most SF3b proteins, it is very likely that the BS/U2 helix will be recognized in the human B^{act} complex in a similar way. However, *S. cerevisiae* lacks the SF3b protein p14, which could be ultraviolet (UV) cross-linked in human spliceosomes to the bulged BS-A (*38*, *39*); it will thus be interesting to see where p14 is located in the human B^{act} cryo-EM map. Our results reveal that the BS/U2 RNA helix not only is held at a remote distance from the catalytic RNA center, but also that the BS-A is occluded in an SF3b protein pocket, ensuring that the first catalytic step of splicing does not occur prematurely. This in turn explains why catalytic activation proceeds through two distinct stages (B^{act} and subsequently B*). Prp2 facilitates the final catalytic activation, including release of the BS adenosine and 5′ss, only after the extensive

Downloaded from http://science.sciencemag.org/ on September 30, 2016

rearrangements accompanying B^{act} formation have occurred.

Prp2 and RES bind to the convex side of Hsh155's HEAT domain opposite the BS/U2 helix

In the B^{act} 3D model, Prp2 is located on the convex side of the HEAT domain opposite the BS/U2 helix, where it is attached via its C-terminal OB fold domain to the upper part of HEAT repeats H7 to H9 of Hsh155 (Fig. 6A and fig. S16, A and B). This is consistent with this domain playing an essential role in mediating Prp2's interaction with the spliceosome (*40*). We were able to fit the core structure of the RES complex, including the RRM protein Snu17 (table S1), close to Prp2 and below Hsh155's HEAT repeats H6 to H8 (Fig. 6A). Additional parts of RES proteins, including Pml1's FHA domain, were mapped adjacent to Prp8's RT domain (fig. S16, C and D), indicating that the RES complex helps to bridge the Hsh155 HEAT and Prp8 RT domains. Our protein cross-linking results indicate an extensive protein-protein interaction network between Prp2, Spp2, and the RES proteins (fig. S17A), which is consistent with the latter proteins potentially playing a role in the efficiency and/or accuracy of the Prp2-facilitated remodeling of B^{act} (*41*). This protein network comprises the U2 SF3b proteins, the C-terminal region of Prp45, and the extended MA3 domain of Cwc22 that plays an important role in coupling the adenosine triphosphatase (ATPase) activity of Prp2 to catalytic activation of the spliceosome (*32*). Last, in the low-resolution model of the B^{act} complex there is additional density between Prp2 and the RES core complex, where Spp2 and unstructured regions of the RES proteins likely will be located (fig. S17B).

The path of the intron's 3′ region across the HEAT domain

The cryo-EM map of the B^{act} complex contains density for most of the first 20 nt of the intron downstream of the BS, allowing us to trace the path of this RNA region. It passes along the concave side of the N-terminal HEAT repeats, exiting the HEAT domain at the bottom of repeats H4 to H6, where it passes Snu17 and is eventually bound by Prp2, which is consistent with positively charged protein patches along the proposed RNA path (Fig. 6A and fig. S18). The distance from the 3′ end of the BS sequence to Prp2's RNA-binding channel would require 25 to 30 nt for a single-strand RNA. This path of the intron's 3′ end (BS-3′ss RNA) agrees with UV cross-linking studies that revealed cross-links of Snu17 and Prp2 to intron nucleotides 15 to 20 and 25 to 35 downstream of the BS, respectively (*3*, *35*, *42*), whereas Hsh155 cross-linked throughout the intron's 3′ end (*35*, *36*).

Cancer-related mutations in SF3b155's HEAT domain are close to RES, Prp2, and the 3′ end of the intron

Cancer-related mutations occur frequently in SF3b155's HEAT domain close to or within the intrarepeat loops of HEAT repeats H4 to H7 (*43*–*45*), and they have been proposed to change the curvature of the HEAT solenoid (*43*). These mutations lead, via an unknown mechanism, to alternative BS selection and ultimately to aberrantly spliced mRNAs (*43*, *44*). Assuming that the spatial organization of components near the SF3b155 HEAT domain is similar in human and yeast B^{act}, cancer-related hot spot mutations would be located close to the intron's 3′ end and also the binding sites for the RES complex and Prp2 in the human B^{act} complex (Fig. 6B). Thus, structural changes in the HEAT domain resulting from cancer-related mutations could potentially affect not only its interaction with the BS/U2 helix but also with the 3′

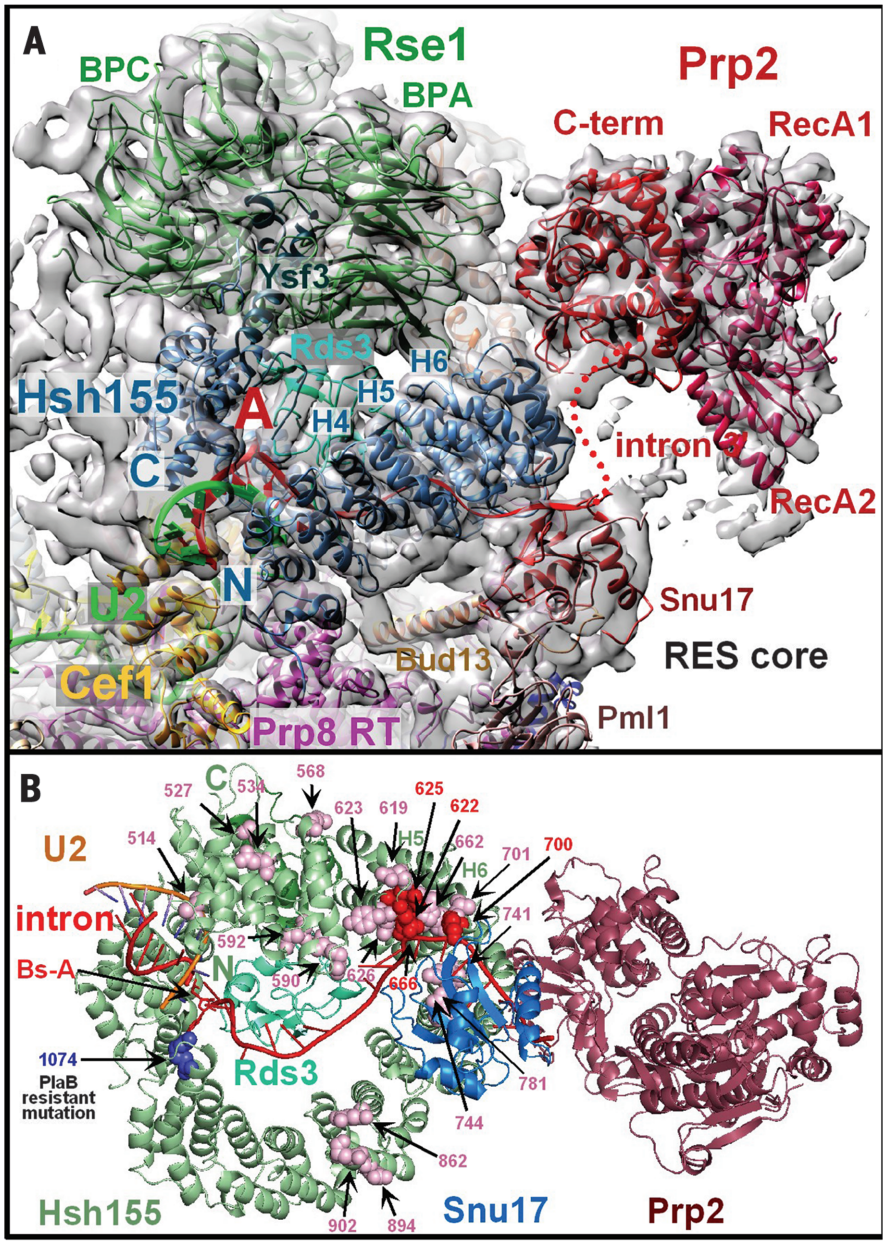

Fig. 6. Path of the intron's 3′ region across the HEAT domain of Hsh155 and location of the RNA helicase Prp2 and RES proteins. (**A**) Density fit of Prp2 and the RES core complex on the convex side of Hsh155's HEAT domain and placement of the U2/BS helix and the branch site adenosine. The intron's 3′ end region is shown as a solid or dotted red line. The Hsh155 HEAT domain also contacts the top of the Prp8 RT domain. Additional close-up views of the location of Prp2 and RES proteins are available in fig. S16. (**B**) Cancer-related mutations in the human SF3b155 (the human Hsh155 homolog) mapped on the yeast Hsh155 HEAT domain in the B^{act} complex (viewed from the bottom). The mutated amino acids are shown as pink space-filling models. The amino acids shown in red correspond to hot spot mutations that map close to the exit site of the BS-3′ss RNA from the HEAT domain and to the binding sites of RES and Prp2. The amino acid shown in blue indicates the position of R1074 in hSF3b's HEAT domain, close to the BS adenosine, whose mutation to histidine confers resistance to the tumor drug pladienolide B (*51*).

Downloaded from http://science.sciencemag.org/ on September 30, 2016

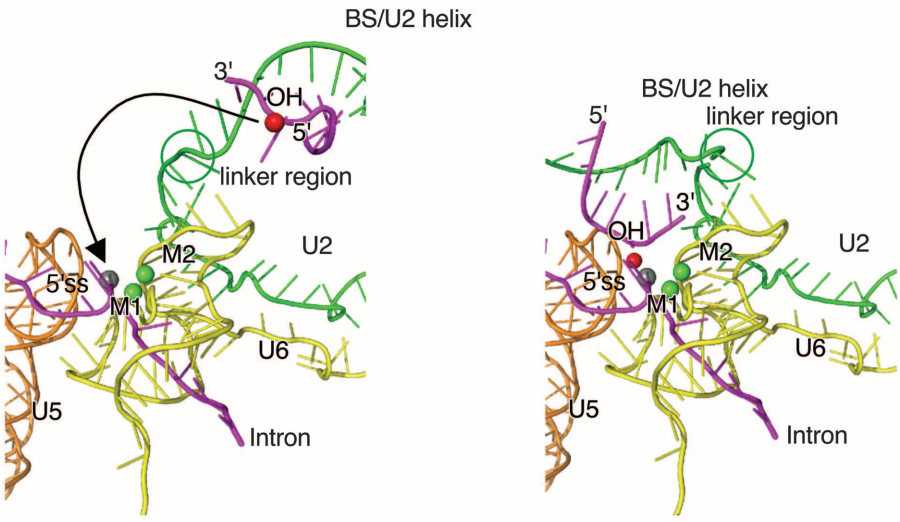

Fig. 7. Model of Prp2-mediated catalytic activation of the spliceosome. Schematic of the catalytic RNA network, showing the proposed rotation of the BS/U2 helix about the 4-nt-long U2 snRNA linker that would juxtapose the OH group (red sphere) of the BS adenosine with the 5′ splice site (gray sphere), after liberation of the catalytic step 1 reactant during Prp2-mediated B* formation. Green spheres indicate catalytic magnesium ions. Movement of the BS/U2 RNA helix into the catalytic center is likely supported and coordinated by proteins such as the nearby Prp8 α-finger, which was UV–cross-linked to the BS+2 nucleotide within spliceosomes (*13*), or Yju2, which can be cross-linked to the U2 snRNA close to the BS/U2 helix (*52*) and whose interaction is stabilized during B* formation (*4*).

end of the intron and indirectly influence BS choice. Alternatively, or in addition, mutation-dependent changes in the curvature of Hsh155's HEAT domain could affect its interactions with RES or other proteins and thereby alter the kinetics of alternative splicing and thus the levels of certain mRNAs.

A model for the mechanism of spliceosome catalytic activation

During catalytic activation, the BS/U2 snRNA helix must be released from its Hsh155- and Rds3-binding pocket, so that the BS adenosine can carry out a nucleophilic attack at the 5′ss. This remodeling is achieved through Prp2-mediated adenosine 5′-triphosphate (ATP) hydrolysis, during which Prp2 is thought to move in a 3′-to-5′ direction along the BS-3′ss RNA, leading to displacement of U2 proteins from the BS region (*42*). However, Prp2 is bound to the convex side of the Hsh155 HEAT domain, ~60 Å away from the BS/U2 helix, and thus does not have direct access to the region of the BS-3′ss RNA close to the BS/U2 helix, which is consistent with the observation that pre-mRNAs with a short piece of RNA downstream of the BS allow B^{act} complex formation but not catalytic activation by Prp2 (*2*, *42*, *46*). Thus, Prp2/Spp2–mediated remodeling of the BS has to occur from a distance. We thus propose instead that ATP hydrolysis by Prp2 mediates a change in the curvature of Hsh155's HEAT domain, destabilizing its interaction with the BS/U2 helix. Indeed, HEAT domains can generally adopt diverse conformations (*47*). In addition, the conformations of the HEAT domains of importins and exportins, for example, are regulated by the Ran GTPase (*48*, *49*). A change in the HEAT domain could be caused by a Prp2-mediated alteration in the interaction between the BS-3′ss RNA and the HEAT domain and/or be induced via changes in protein-protein interactions between Prp2/Spp2 and the HEAT domain. Whether this involves initial translocation of Prp2 along the BS-3′ss RNA remains an open question. Changes in the curvature of Hsh155's HEAT domain could also destabilize the interaction of Prp2 and the RES proteins, which is consistent with these proteins leaving after B* complex formation (*4*, *17*, *42*). Proteins that occlude the 5′ss GU dinucleotide would also have to be rearranged to "liberate" the 5′ss (Fig. 4A) and to allow its repositioning closer to the catalytic center, paving the way for the nucleophilic attack by the BS-A. In B^{act}, the BS-A is oriented so that a rotation of the BS/U2 helix about the 4-nt-long U2 snRNA linker could potentially juxtapose the two step 1 reactants (Fig. 7). Recently, the cryo-EM structure of an endogeneous *S. cerevisiae* spliceosome whose structure closely resembles our in vitro assembled B^{act} complex was reported (*50*). It will therefore be interesting to perform a detailed comparison of the structure of both complexes to ascertain whether they are stalled at an identical stage during activation. Future cryo-EM studies of the catalytically activated B* complex will be needed to reveal the structural changes that accompany the transformation of the B^{act} to B* complex.

REFERENCES AND NOTES

1. M. C. Wahl, C. L. Will, R. Lührmann, *Cell* **136**, 701–718 (2009).
2. P. Fabrizio *et al.*, *Mol. Cell* **36**, 593–608 (2009).
3. Z. Warkocki *et al.*, *Genes Dev.* **29**, 94–107 (2015).
4. T. Ohrt *et al.*, *RNA* **18**, 1244–1256 (2012).
5. S. H. Kim, R. J. Lin, *Mol. Cell. Biol.* **16**, 6810–6819 (1996).
6. R. M. Lardelli, J. X. Thompson, J. R. Yates 3rd, S. W. Stevens, *RNA* **16**, 516–528 (2010).
7. S. M. Fica, M. A. Mefford, J. A. Piccirilli, J. P. Staley, *Nat. Struct. Mol. Biol.* **21**, 464–471 (2014).
8. H. D. Madhani, C. Guthrie, *Cell* **71**, 803–817 (1992).
9. J. P. Staley, C. Guthrie, *Cell* **92**, 315–326 (1998).
10. C. Yan *et al.*, *Science* **349**, 1182–1191 (2015).
11. W. P. Galej, C. Oubridge, A. J. Newman, K. Nagai, *Nature* **493**, 638–643 (2013).
12. R. J. Grainger, J. D. Beggs, *RNA* **11**, 533–557 (2005).
13. T. H. Nguyen *et al.*, *Nature* **530**, 298–302 (2016).
14. T. H. Nguyen *et al.*, *Nature* **523**, 47–52 (2015).
15. R. Wan *et al.*, *Science* **351**, 466–475 (2016).
16. D. E. Agafonov *et al.*, *Science* **351**, 1416–1420 (2016).
17. Z. Warkocki *et al.*, *Nat. Struct. Mol. Biol.* **16**, 1237–1243 (2009).
18. B. Sander *et al.*, *Mol. Cell* **24**, 267–278 (2006).
19. E. Absmeier *et al.*, *Genes Dev.* **29**, 2576–2587 (2015).
20. T. H. Nguyen *et al.*, *Structure* **21**, 910–919 (2013).
21. S. Bessonov *et al.*, *RNA* **16**, 2384–2403 (2010).
22. K. S. Keating, N. Toor, P. S. Perlman, A. M. Pyle, *RNA* **16**, 1–9 (2010).
23. N. Toor, K. S. Keating, S. D. Taylor, A. M. Pyle, *Science* **320**, 77–82 (2008).
24. S. M. Fica *et al.*, *Nature* **503**, 229–234 (2013).
25. J. Hang, R. Wan, C. Yan, Y. Shi, *Science* **349**, 1191–1198 (2015).
26. T. A. Steitz, J. A. Steitz, *Proc. Natl. Acad. Sci. U.S.A.* **90**, 6498–6502 (1993).
27. R. T. Chan, A. R. Robart, K. R. Rajashankar, A. M. Pyle, N. Toor, *Nat. Struct. Mol. Biol.* **19**, 555–557 (2012).
28. M. Marcia, A. M. Pyle, *Cell* **151**, 497–507 (2012).
29. E. J. Sontheimer, J. A. Steitz, *Science* **262**, 1989–1996 (1993).
30. A. J. Newman, C. Norman, *Cell* **68**, 743–754 (1992).
31. A. L. Steckelberg, V. Boehm, A. M. Gromadzka, N. H. Gehring, *Cell Reports* **2**, 454–461 (2012).
32. T. C. Yeh *et al.*, *Mol. Cell. Biol.* **31**, 43–53 (2011).
33. G. Buchwald, S. Schüssler, C. Basquin, H. Le Hir, E. Conti, *Proc. Natl. Acad. Sci. U.S.A.* **110**, E4611–E4618 (2013).
34. L. A. Lindsey-Boltz, G. Chawla, N. Srinivasan, M. A. Garcia-Blanco, *RNA* **6**, 1289–1305 (2000).
35. C. Schneider *et al.*, *PLOS Genet.* **11**, e1005539 (2015).
36. D. S. McPheeters, P. Muhlenkamp, *Mol. Cell. Biol.* **23**, 4174–4186 (2003).
37. C. Cretu *et al.*, *Mol. Cell* 10.1016/j.molcel.2016.08.036 (2016).
38. C. L. Will *et al.*, *EMBO J.* **20**, 4536–4546 (2001).
39. C. C. Query, S. A. Strobel, P. A. Sharp, *EMBO J.* **15**, 1392–1402 (1996).
40. G. Edwalds-Gilbert, D. H. Kim, E. Silverman, R. J. Lin, *RNA* **10**, 210–220 (2004).
41. A. M. Wlodaver, J. P. Staley, *RNA* **20**, 282–294 (2014).
42. H. L. Liu, S. C. Cheng, *Mol. Cell. Biol.* **32**, 5056–5066 (2012).
43. R. B. Darman *et al.*, *Cell Reports* **13**, 1033–1045 (2015).
44. S. Alsafadi *et al.*, *Nat. Commun.* **7**, 10615 (2016).
45. S. Bonnal, L. Vigevani, J. Valcárcel, *Nat. Rev. Drug Discov.* **11**, 847–859 (2012).
46. B. C. Rymond, M. Rosbash, *Nature* **317**, 735–737 (1985).
47. C. Kappel, U. Zachariae, N. Dölker, H. Grubmüller, *Biophys. J.* **99**, 1596–1603 (2010).
48. E. Conti, C. W. Müller, M. Stewart, *Curr. Opin. Struct. Biol.* **16**, 237–244 (2006).
49. A. G. Cook, E. Conti, *Curr. Opin. Struct. Biol.* **20**, 247–252 (2010).
50. C. Yan, R. Wan, R. Bai, G. Huang, Y. Shi, *Science* **353**, 904–911 (2016).
51. A. Yokoi *et al.*, *FEBS J.* **278**, 4870–4880 (2011).
52. T. W. Chiang, S. C. Cheng, *Mol. Cell. Biol.* **33**, 1746–1755 (2013).

ACKNOWLEDGMENTS

We thank T. Conrad for yeast production in a bioreactor and M. Raabe and U. Pleßmann for excellent technical assistance. We are very grateful to N. Rigo and C. L. Will for advice and many helpful discussions and to J. Schmitzová for the gift of the dominant-negative Prp2 mutant. The EM map has been deposited in the Electron Microscopy Data Bank with the accession code EMD-4099. The atomic coordinates have been deposited in the Protein Data Bank with the accession code 5LQW. This work was supported by grants from the Deutsche Forschungsgemeinschaft (SFB 860) to R.L., H.S., and H.U.

SUPPLEMENTARY MATERIALS

www.sciencemag.org/content/353/6306/1399/suppl/DC1
Materials and Methods
Figs. S1 to S19
Tables S1 to S3
References (*53*–*74*)
Movies S1 and S2

20 May 2016; accepted 18 August 2016
Published online 25 August 2016
10.1126/science.aag1906

Downloaded from http://science.sciencemag.org/ on September 30, 2016

REPORTS

GEOPHYSICS

Tomography reveals buoyant asthenosphere accumulating beneath the Juan de Fuca plate

William B. Hawley,[1,2]* Richard M. Allen,[1,2] Mark A. Richards[1]

The boundary between Earth's strong lithospheric plates and the underlying mantle asthenosphere corresponds to an abrupt seismic velocity decrease and electrical conductivity increase with depth, perhaps indicating a thin, weak layer that may strongly influence plate motion dynamics. The behavior of such a layer at subduction zones remains unexplored. We present a tomographic model, derived from on- and offshore seismic experiments, that reveals a strong low-velocity feature beneath the subducting Juan de Fuca slab along the entire Cascadia subduction zone. Through simple geodynamic arguments, we propose that this low-velocity feature is the accumulation of material from a thin, weak, buoyant layer present beneath the entire oceanic lithosphere. The presence of this feature could have major implications for our understanding of the asthenosphere and subduction zone dynamics.

The physical causes of the lithosphere-asthenosphere boundary (LAB), possibly representing a zone that mechanically decouples tectonic plates from the asthenospheric mantle beneath (*1*, *2*), remain poorly understood (*3*). The LAB beneath continents appears deep and somewhat obfuscated by other discontinuities (*4*, *5*), so distinguishing the LAB has been hindered by the complicated nature of deep continental structures. Oceans are tectonically simpler than continents, so both the observation and description of the LAB should be simpler there. However, because oceans are poorly instrumented, serious difficulties remain in resolving the LAB beneath oceanic lithosphere (*6*). Of particular interest is this lithosphere-asthenosphere interaction at convergent margins. The geometry of an oceanic plate changes as it dips into the mantle at a subduction zone, and the response of the uppermost mantle remains debated (*7*–*9*). New constraints on processes beneath a dipping plate may provide insights into subduction zone dynamics as well as large-scale asthenospheric flow and its role in the evolution of tectonic plates.

First arrivals of *P* waves from distant earthquakes recorded on large seismic arrays can be used to illuminate large parts of the mantle. One such array, the Cascadia Initiative (*10*), was a 4-year (2011–2015) amphibious seismic deployment that covered the Juan de Fuca plate and the Cascadia subduction zone (Fig. 1). Using 61,559 *P*-wave arrivals observed on the Cascadia Initiative, the Transportable Array, and other regional seismic networks, we generated a *P*-wave velocity model of the region through finite-frequency tomographic inversion following the method of Obrebski *et al.* (*11*). Our application of finite-frequency sensitivity kernels means that our inversion takes into account the frequency-dependent volume that is sampled by a *P* wave traveling from the source to the seismometer and obviates the need to smooth the final model. The noise characteristics of the ocean bottom seismometers (OBSs) require that we use long-period (9.1- to 12.5-s) arrivals.

Our model (CASC16-P) shows an expected north-striking, east-dipping, high-velocity (+3% *P*-wave velocity change, dV_P/V_P) Juan de Fuca slab, seen at 150 km depth as a continuous north-south structure at about 122°W between 40°N and the northern edge of our model at 50°N (Fig. 2A and fig. S14). Vertical cross sections at 47°N (Fig. 2B) and 41°N (Fig. 2C) indicate that the slab is continuous down to the transition zone at ~410 km, or deeper, consistent with previous land-based studies in the region (*11*–*14*). A previously unidentified strong low-velocity anomaly (–2 to –3% dV_P/V_P) is seen at 150 km depth with similar strike as the Juan de Fuca slab, just to the west. Vertical cross sections through the models and synthetic tests (see figs. S6 and S7 and Materials and methods) indicate that this feature is restricted to the top 300 km of the model directly beneath the Juan de Fuca slab, meaning that it does not follow the slab all the way down to the transition zone. Further tests with various station correction terms (fig. S5) indicate that this feature is not a shallow structure being incorrectly mapped to depth. This truncated feature appears to take the shape of a horizontal cylinder, slightly elongated vertically in cross section beneath the high-velocity slab. The addition of data from the Cascadia Initiative has provided the offshore resolution needed to confidently identify the full extent of this feature, though evidence exists for the feature in previous land-based tomographic models of the region (*11*–*14*).

We propose that this low dV_P feature is related to previously reported observations of a layer of partial melt beneath the oceanic lithosphere. A range of techniques—including receiver functions from borehole OBSs on the Pacific and Philippine Sea plates (*15*), precursors to teleseismic SS-phase arrivals spanning the Pacific ocean (*16*), magnetotelluric inversion on the Nazca plate (*17*), and explosion-generated reflected *P* waves offshore of New Zealand (*18*)—resolve a narrow (10 to 25 km) region, immediately below the oceanic lithosphere, characterized by low seismic wave velocities (–6 to –10% dV_S/V_S and dV_P/V_P) and high conductivity (4 to 6 ohm·m). The interpretation for each of these studies is slightly different, but they all indicate that partial melt fractions of ~1 to 4% in the uppermost asthenosphere are consistent with their findings, with variations arising due to different geometries of melt layers, composition of the melt, and the crystal structure of the materials in the layer. The slow seismic feature we observe in CASC16-P similarly coincides with a region of high conductivity. This thin layer is not resolvable in tomographic studies that use relative travel times from teleseismic events (*11*–*13*) because such variations affect each ray path in the same way (*19*). At a subduction zone, however, this layer might become observable where it changes geometry with the slab as it descends, thus becoming detectable via teleseismic body-wave tomography.

Predicting a priori how this layer might behave beneath a subduction zone requires knowledge of its physical properties. Because we cannot resolve the layer to the west of the subduction zone, CASC16-P does not provide a direct observation of the source of the material in this layer. Previous reports (*15*–*18*) attribute the layer to volatiles and/or hydrated mantle increasing partial melt fraction in the uppermost asthenosphere, decreasing density and viscosity, separating into lenses (*20*) or channels (*15*, *21*), and ponding beneath the rigid, impermeable lithospheric lid (*22*). Our observations, as well as the land-based observation of a high-conductivity region that roughly coincides with our low velocities (*23*), could be explained by the accumulation of material from this horizontal layer due to its own buoyancy and low viscosity.

Here we use two straightforward fluid-mechanical scaling calculations to demonstrate the plausibility of the accumulation hypothesis: First, for a thin, buoyant, low-viscosity layer to accumulate beneath the downgoing slab the ratio of the upward mass flux due to the layer buoyancy (Poiseuille flow) must exceed the downward flux due to drag from the downgoing slab (Couette flow) (*24*). Referring to the notation in Fig. 3, this means that

$$\frac{\Delta\rho g \sin(\theta) h^2}{6 v_0 \mu_l} \gtrsim 1 \qquad (1)$$

Here, $\Delta\rho$ is the difference in density, g is gravitational acceleration, θ is the dip angle, h is the

[1]Department of Earth and Planetary Science, University of California, Berkeley, Berkeley, CA 94720, USA. [2]Berkeley Seismological Laboratory, 215 McCone Hall, University of California, Berkeley, Berkeley, CA 94720, USA.
*Corresponding author. Email: whawley@seismo.berkeley.edu

Downloaded from http://science.sciencemag.org/ on September 30, 2016

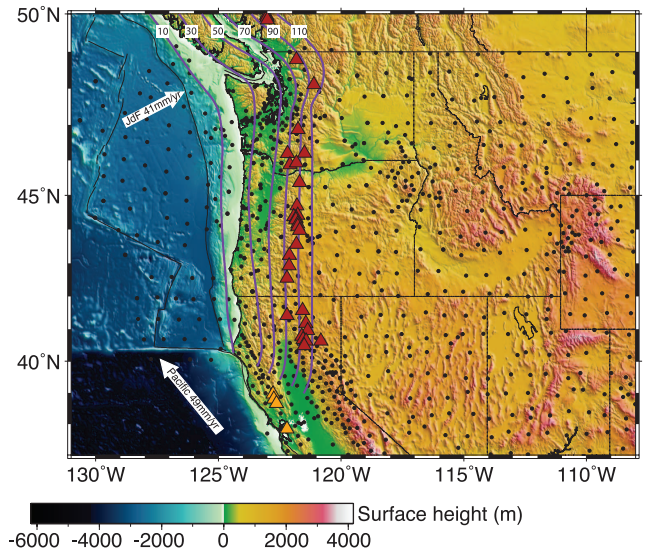

Fig. 1. Stations used in our inversion (black dots) overlain on topography. Cascade volcanoes are denoted by red triangles, and northward age-progressive volcanism of the California Coast Ranges is shown by orange triangles. White arrows indicate plate motions relative to North America. The estimated depth of the top of the subducting slab is shown by the purple contours labeled in kilometers (*36*).

layer thickness, v_0 is the plate velocity, and μ_l is the thin-layer viscosity. The second condition is that the horizontal gravitational spreading velocity of the accumulated low-velocity volume due to its own buoyancy cannot exceed the horizontal advection velocity due to plate motion (*25*), otherwise the accumulating low-viscosity body would spread out instead of accumulating to the observed thickness of $H \approx 50$ to 100 km, as inferred from our tomographic images. This means that

$$\frac{\Delta\rho g H^2}{v_0 \mu_m} \lesssim 1 \qquad (2)$$

Here, H is the thickness of the accumulated material, and $\{\mu_m\}$ is the viscosity of the underlying mantle. In obtaining Eqs. 1 and 2, we assumed that the thin-layer viscosity controlling return flow is much smaller than the underlying mantle viscosity governing gravitational spreading—that is, $\mu_l \ll \mu_m$ (see supplementary materials for details).

Assuming that $\Delta\rho \approx 5$ to 20 kg/m^3 [1 to 4% partial melt, with 500 kg/m^3 density contrast between melt and solid (*26*)], $g = 9.8$ m/s^2, $\theta = 40°$,

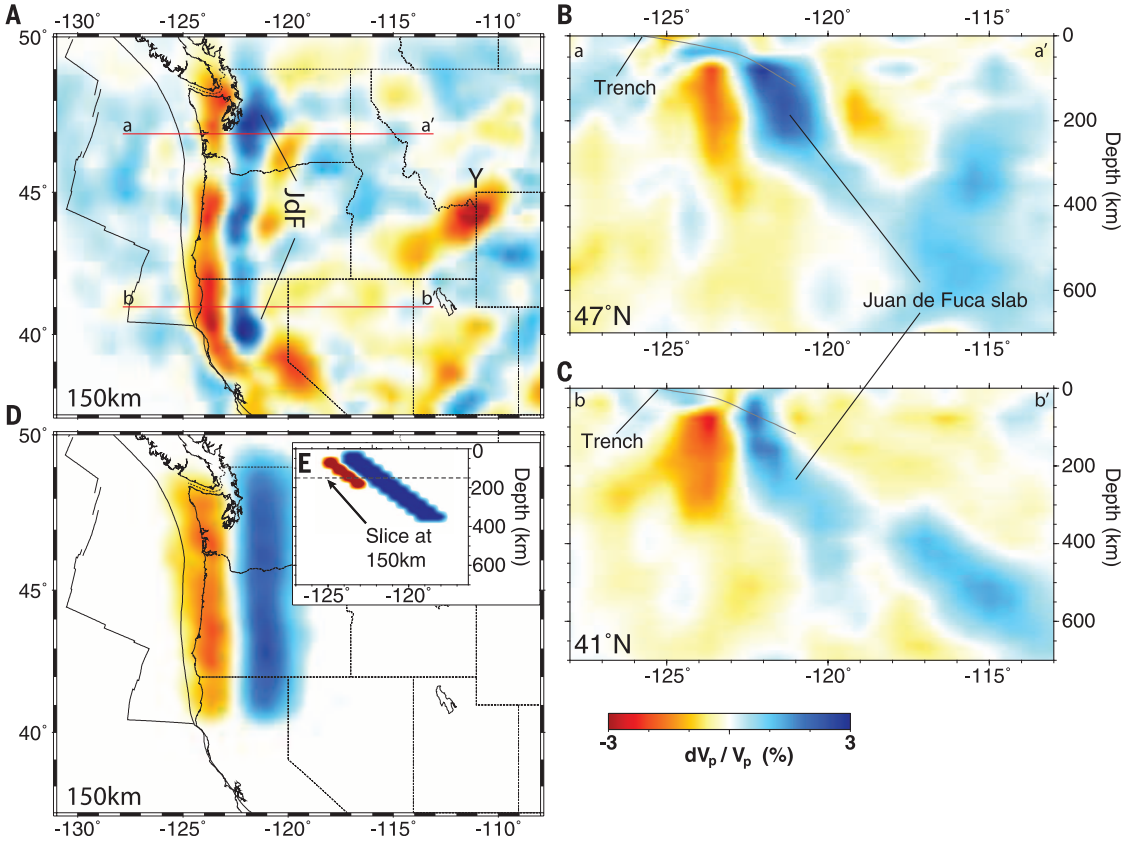

Fig. 2. Slices through CASC16-P. (**A**) A slice at 150 km depth. The slow Yellowstone (Y) and fast Juan de Fuca (JdF) slab anomalies are indicated. A strong low-velocity anomaly is seen west of the Juan de Fuca slab. Lines a-a′ and b-b′ mark the locations of vertical slices through CASC16-P at 47°N (**B**) and 41°N (**C**). These slices show the slab extending through the transition zone, whereas the low-velocity anomaly is confined to shallower depths (<~300 km). The top of the slab (*36*) is shown with a gray line that begins at the trench. There is no vertical exaggeration in the vertical slices. (**D**) A slice at 150 km depth shows the recovery of a synthetic test with a 120-km-thick +4% slab anomaly underlain by a 40-km-thick –10% layer anomaly. The input synthetic velocity model is shown in (**E**). The recovery of synthetic features (D) is similar to that observed (A).

Downloaded from http://science.sciencemag.org/ on September 30, 2016

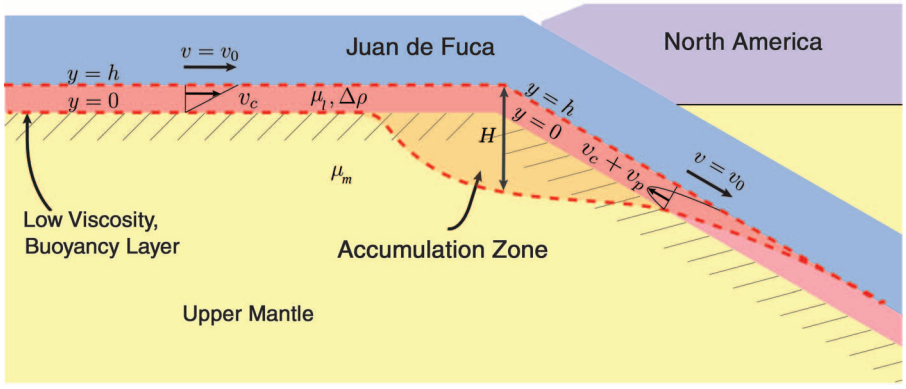

Fig. 3. Geodynamical model setup. The low-velocity layer in red (of thickness h) lies between the Juan de Fuca plate in blue and the asthenosphere in yellow. Comparison of the Couette and Poiseuille velocity terms (v_c and v_p, each as a function of y, the distance from the top of the upper mantle) yields an estimate for the viscosity of this layer (μ_l). In reality, this structure may take the shape outlined by the red dashed lines and tinted orange: thicker beneath the trench and thinning out with depth. The extent of this feature depends on the density difference ($\Delta\rho$) and the upper mantle viscosity (μ_m). The features in this model are not to scale.

v_0 = 40 mm/year, and $h \approx 10$ to 25 km, Eq. 1 implies that the viscosity of the thin, weak layer falls in the range $\mu_l \approx 0.04$ to 1.0×10^{19} Pa·s, which is reasonable for partially molten uppermost mantle (*27*). Similarly, with a low-velocity feature thickness of $H \approx 50$ to 100 km, Eq. 2 yields an underlying mantle viscosity that falls in the range $\mu_m \gtrsim 0.1$ to 1.5×10^{21} Pa·s, which is also reasonable (*27*, *28*). Furthermore, a convergence rate of ~40 mm/year indicates that about 100 to 400 km of continuous subducted lithosphere would be required to form the observed feature from accumulation of a thin buoyant, sublithospheric layer, a condition consistent with the ~400 km of continuous slab observed in our tomographic model.

A more sophisticated treatment of this interesting mantle flow problem is beyond the scope of this paper, requiring a full numerical solution to understand the balance of Couette- and Poiseuille-type flow within the asthenosphere (*29*), as well as consideration of other complicating factors, such as trench-parallel extrusion of buoyant material toward the slab edges (see below), relaxing the assumption that $\mu_l \ll \mu_m$, etc. However, satisfaction of the two necessary conditions above for accumulation and maintenance of the low-velocity feature demonstrates that our hypothesis is plausible. More precise knowledge of the geometry of the feature will help constrain critical physical parameters, but CASC16-P provides a maximum extent of the feature. The grid we used in the inversion and the smoothing due to finite-frequency sensitivity kernels make a strong, thin velocity anomaly appear thicker and weaker (Fig. 2, D and E). Further studies with higher resolution will enable more detailed geodynamical models.

The material we observe could be important for "petit spot" volcanism in the forearc bulge east of the Japan trench. Samples from these young (~5-million-year-old), alkalic volcanoes in the 120-million- to 150-million-year-old Pacific plate (notably much older than any part of the Juan de Fuca plate) are highly vesicular, suggesting the presence of CO_2, and isotopically similar to basalts found at mid-ocean ridges. One explanation for the presence of these volcanoes in such an unusual region of the ocean floor is that the volcanism is due to partial melt rising through flexure-induced fractures in the lithosphere and that it lends credence to the idea that the asthenosphere is a zone of partial melt (*30*). Other studies (*26*, *31*) argue that the entire asthenosphere need not be a zone of partial melt. The proposed low-viscosity layer could provide a source for enigmatic volcanism without requiring any assumptions of partial melt throughout the asthenosphere. Additionally, the chemistry of such basalts may help contextualize the composition of the low-viscosity layer.

This potentially somewhat molten feature may also explain the anomalous heat flow and volcanism of the Coast Ranges of California (orange triangles in Fig. 1). Lachenbruch and Sass (*32*) proposed that as the southern edge of the Juan de Fuca slab migrates northward with the Mendocino Triple Junction, the "window" that opens beneath the margin of North America is filled with asthenosphere that undergoes decompression melting, thus leading to high heat flow and volcanism. Seismic observations (*33*, *34*) reveal a high-velocity layer at the base of the North American crust beneath the California Coast Ranges. The thickness of this inferred mafic structure requires more melt than predicted by standard asthenospheric upwelling models. Both the lack of high-grade metamorphism inferred from the same seismic studies and the heat flow observations of Lachenbruch and Sass (*32*) indicate less heat than predicted from the same asthenospheric upwelling models (*33*). A mechanism to generate more melt at lower temperatures has been elusive, but the accumulated low-velocity, partially molten, and/or high volatile content material that we have imaged may provide that mechanism—that is, decompression of the accumulated, already partially molten feature as it emerges toward the south through the slab window would provide more melt at lower temperatures.

REFERENCES AND NOTES

1. M. A. Richards, W.-S. Yang, J. R. Baumgardner, H.-P. Bunge, *Geochem. Geophys. Geosyst.* **2**, 1026 (2001).
2. C. H. Craig, D. McKenzie, *Earth Planet. Sci. Lett.* **78**, 420–426 (1986).
3. K. M. Fischer, H. A. Ford, D. L. Abt, C. A. Rychert, *Annu. Rev. Earth Planet. Sci.* **38**, 551–575 (2010).
4. C. A. Rychert, P. M. Shearer, *Science* **324**, 495–498 (2009).
5. H. Yuan, B. Romanowicz, K. M. Fischer, D. Abt, *Geophys. J. Int.* **184**, 1237–1260 (2011).
6. H. Kawakatsu, *Science* **335**, 1448–1449 (2012).
7. T.-R. A. Song, H. Kawakatsu, *Geophys. Res. Lett.* **39**, L17301 (2012).
8. M. D. Long, P. G. Silver, *Science* **319**, 315–318 (2008).
9. M. D. Long, P. G. Silver, *Surv. Geophys.* **30**, 407–461 (2009).
10. D. Toomey *et al.*, *Oceanography* **27**, 138–150 (2014).
11. M. Obrebski, R. M. Allen, M. Xue, S.-H. Hung, *Geophys. Res. Lett.* **37**, L14305 (2010).
12. B. Schmandt, E. Humphreys, *Earth Planet. Sci. Lett.* **297**, 435–445 (2010).
13. Y. Tian, D. Zhao, *Phys. Earth Planet. Inter.* **200–201**, 72–84 (2012).
14. R. W. Porritt, R. M. Allen, F. F. Pollitz, *Earth Planet. Sci. Lett.* **402**, 16–25 (2014).
15. H. Kawakatsu *et al.*, *Science* **324**, 499–502 (2009).
16. N. Schmerr, *Science* **335**, 1480–1483 (2012).
17. S. Naif, K. Key, S. Constable, R. L. Evans, *Nature* **495**, 356–359 (2013).
18. T. A. Stern *et al.*, *Nature* **518**, 85–88 (2015).
19. I. D. Bastow, *Geophys. J. Int.* **190**, 1271–1278 (2012).
20. M. M. Hirschmann, *Phys. Earth Planet. Inter.* **179**, 60–71 (2010).
21. W. Zhu, G. A. Gaetani, F. Fusseis, L. G. J. Montési, F. De Carlo, *Science* **332**, 88–91 (2011).
22. G. Hirth, D. L. Kohlstedt, *Earth Planet. Sci. Lett.* **144**, 93–108 (1996).
23. R. L. Evans, P. E. Wannamaker, R. S. McGary, J. Elsenbeck, *Earth Planet. Sci. Lett.* **402**, 265–274 (2014).
24. D. L. Turcotte, G. Schubert, *Geodynamics* (Cambridge Univ. Press, 2002).
25. M. A. Feighner, M. A. Richards, *Earth Planet. Sci. Lett.* **129**, 171–182 (1995).
26. S. Karato, H. Jung, *Earth Planet. Sci. Lett.* **157**, 193–207 (1998).
27. C. Doglioni, A. Ismail-Zadeh, G. Panza, F. Riguzzi, *Phys. Earth Planet. Inter.* **189**, 1–8 (2011).
28. A. Paulson, M. A. Richards, *Geophys. J. Int.* **179**, 1516–1526 (2009).
29. T. Höink, A. Lenardic, *Geophys. J. Int.* **180**, 23–33 (2010).
30. N. Hirano *et al.*, *Science* **313**, 1426–1428 (2006).
31. U. Faul, I. Jackson, *Earth Planet. Sci. Lett.* **234**, 119–134(2005).
32. A. H. Lachenbruch, J. H. Sass, *J. Geophys. Res.* **85**, 6185–6222 (1980).
33. J. A. Hole, B. C. Beaudoin, T. J. Henstock, *Tectonics* **17**, 802–818 (1998).
34. K. P. Furlong, S. Y. Schwartz, *Annu. Rev. Earth Planet. Sci.* **32**, 403–433 (2004).
35. P. Wessel, W. H. F. Smith, R. Scharroo, J. Luis, F. Wobbe, *Eos* **94**, 409–410 (2013).
36. P. A. McCrory, J. L. Blair, F. Waldhauser, D. H. Oppenheimer, *J. Geophys. Res.* **117**, B09306 (2012).

ACKNOWLEDGMENTS

Support for this work was provided by the NSF under the Graduate Research Fellowship Program (grant DGE-1106400 to W.B.H.) and grant OCE-1139701 (to W.B.H. and R.M.A.). The seismic data used in this study are archived by the Incorporated Research Institutions for Seismology Data Management Center (http://ds.iris.edu/ds/nodes/dmc/) and the Northern California Earthquake Data Center (www.ncedc.org; doi:10.7932/NCEDC). Data are provided by many networks (see the supplementary materials), but of particular note are the Cascadia Initiative ocean bottom data collected by the Ocean Bottom Seismograph Instrument Pool (www.obsip.org/) and funded by the NSF (grant OCE-1112722). The Generic Mapping Tools software (*35*) was used to create the figures.

SUPPLEMENTARY MATERIALS

www.sciencemag.org/content/353/6306/1406/suppl/DC1
Materials and Methods
Figs. S1 to S14
References (*37*–*42*)

9 November 2015; accepted 24 August 2016
10.1126/science.aad8104

Downloaded from http://science.sciencemag.org/ on September 30, 2016

SOLAR CELLS

Screening in crystalline liquids protects energetic carriers in hybrid perovskites

Haiming Zhu,[1]* Kiyoshi Miyata,[1]* Yongping Fu,[2] Jue Wang,[1] Prakriti P. Joshi,[1] Daniel Niesner,[1] Kristopher W. Williams,[1] Song Jin,[2] X.-Y. Zhu[1]†

Hybrid lead halide perovskites exhibit carrier properties that resemble those of pristine nonpolar semiconductors despite static and dynamic disorder, but how carriers are protected from efficient scattering with charged defects and optical phonons is unknown. Here, we reveal the carrier protection mechanism by comparing three single-crystal lead bromide perovskites: $CH_3NH_3PbBr_3$, $CH(NH_2)_2PbBr_3$, and $CsPbBr_3$. We observed hot fluorescence emission from energetic carriers with ~10^2-picosecond lifetimes in $CH_3NH_3PbBr_3$ or $CH(NH_2)_2PbBr_3$, but not in $CsPbBr_3$. The hot fluorescence is correlated with liquid-like molecular reorientational motions, suggesting that dynamic screening protects energetic carriers via solvation or large polaron formation on time scales competitive with that of ultrafast cooling. Similar protections likely exist for band-edge carriers. The long-lived energetic carriers may enable hot-carrier solar cells with efficiencies exceeding the Shockley-Queisser limit.

Hybrid organic-inorganic lead halide perovskites (HOIPs) with the general formula $APbX_3$ (X = I, Br, or Cl), where A^+ is an organic cation such as methylammonium (MA), $CH_3NH_3^+$, or formamidinium (FA), $CH(NH_2)_2^+$ (*1*–*4*), are usually processed from solutions at room temperature for solar device fabrication. A high defect density is unavoidable (*5*), yet these defective semiconductors exhibit carrier properties expected of defect-free and nonpolar inorganic semiconductors. These properties include (i) inverse temperature dependence of charge carrier mobility (μ) with a power law, $\mu \propto T^{-3/2}$ (*6*–*8*), predicted for coherent transport hindered by acoustic phonon scattering (*9*); (ii) long carrier diffusion length (up to 10^2 μm) and carrier lifetime (≥1 μs), which are unexpected for a semiconductor with modest charge carrier mobility (μ ~ 1 to 100 $cm^2 V^{-1} s^{-1}$) (*2*–*4*, *10*); and (iii) low electron-hole recombination rate constant (10^{-10} $cm^3 s^{-1}$) that rivals those of the purest crystalline semiconductors (e.g., GaAs) (*6*, *11*, *12*). All of these properties suggest that charge carriers in HOIPs are protected from scattering with charged defects, optical phonons, and each other. Based on the presence of extensive dynamic disorder on multiple time scales (*13*–*16*), Zhu and Podzorov proposed that formation of large polarons (*17*) may explain the protection of charge carriers in HOIPs (*18*).

To understand the charge carrier protection mechanism in HOIPs, we have compared carrier and structural dynamics in single-crystal lead bromide perovskites with three different cations: methylammonium ($MAPbBr_3$), formamidinium ($FAPbBr_3$), and cesium ($CsPbBr_3$) using time-resolved photoluminescence (TR-PL) and time-resolved optical Kerr effect (TR-OKE) (*19*) spectroscopies. These bulk-sensitive measurements on pristine single crystals provide insights into intrinsic carrier and structural properties. Using TR-PL, we show long-lived energetic carriers (electronic temperature ≥1000 K) that cool down with markedly long time constants of ~10^2 ps in $MAPbBr_3$ or $FaPbBr_3$, but not in $CsPbBr_3$. In TR-OKE measurements, we observed liquid-like reorientation motions on subpicosecond to picosecond time scales in $MAPbBr_3$ or

[1]Department of Chemistry, Columbia University, New York, NY 10027, USA. [2]Department of Chemistry, University of Wisconsin-Madison, Madison, WI 53706, USA.
*These authors contributed equally to this work. †Corresponding author. Email: xyzhu@columbia.edu

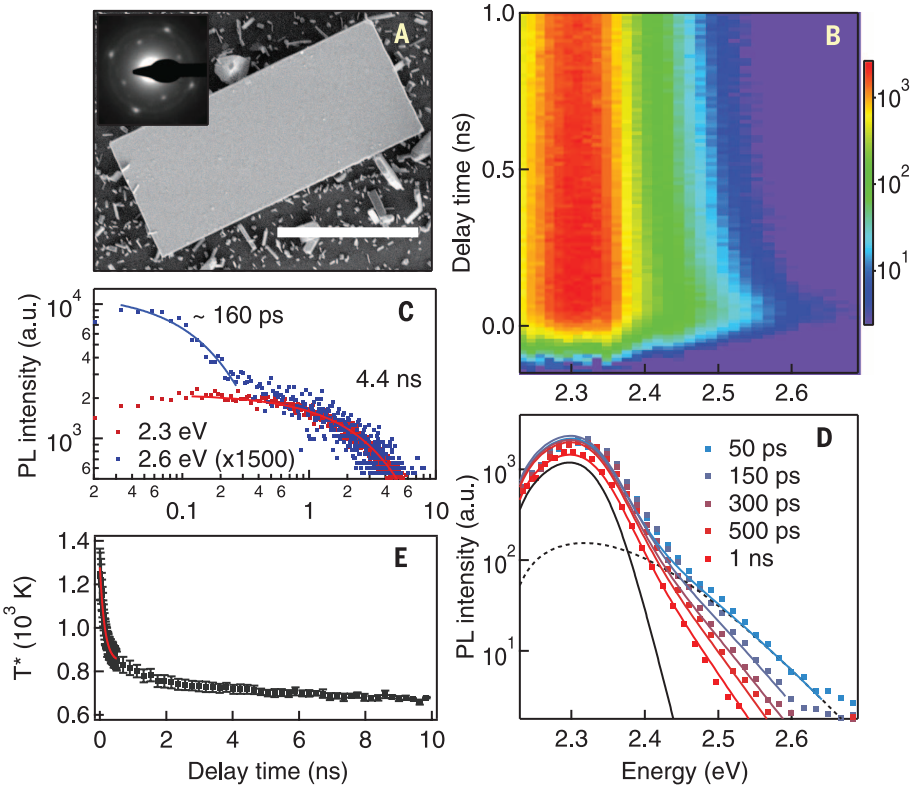

Fig. 1. Time-dependent PL spectra revealing long-lived hot carriers. (**A**) SEM image and selected area electron diffraction pattern (inset) of a single-crystal $MAPbBr_3$ microplate. Scale bar: 10 μm. (**B**) Pseudo-color (intensity) plot of TR-PL spectra from a single-crystal $MAPbBr_3$ microplate at room temperature under 3.08-eV excitation and an excitation density of 1.7 μJ cm^{-2}. (**C**) PL intensity decay kinetics at 2.3 eV (red) and 2.6 eV (blue) and single exponential fits (solid). The PL intensity at 2.6 eV has been multiplied by a factor of 1500. (**D**) PL spectra (squares) at indicated delay times and fits (colored curves) to the two-temperature model. The black solid and dashed curves show components in the fit to the spectrum at 50 ps. (**E**) Extracted electronic temperature from the hot-carrier distribution as a function of delay time. The data points are average values from three independent microplate samples. The red curve is a single exponential fit to the first 0.5 ns, which gives a hot-carrier relaxation time constant of 150 ± 30 ps.

Downloaded from http://science.sciencemag.org/ on September 30, 2016

$FAPbBr_3$, but not in $CsPbBr_3$. The correlation between TR-PL and TR-OKE measurements suggests that the liquid-like reorientational motions of organic cations provides protection for energetic charge carriers in HOIPs via solvation and screening on sufficiently fast time scales to compete with carrier cooling by optical phonon scattering. Further corroborating this, we observed the absence of hot fluorescence emission in the low-temperature orthorhombic phase of $MAPbBr_3$, where the liquid-like motions of MA ions are frozen. Thus, an HOIP possesses both crystalline solid and liquid-like behaviors and belongs to the family of solids called plastic crystals (*20*, *21*). Such an efficient screening process, which is similar to large polaron formation in physics (*17*) or solvation in chemistry, likely also exists for band-edge carriers whose long lifetime (up to microseconds) ensures coupling to the slower dynamics (>1 ps) of the soft PbX_3^- sublattice.

We synthesized optically flat, single-crystal $APbBr_3$ (A = MA, FA, or Cs) samples in the form of either macroscopic (~1 mm in lateral dimensions and ~hundreds of micrometers in thickness) (*10*, *22*) or microscopic plates (~tens of micrometers in lateral dimensions and ~hundreds of nanometers in thickness) (*23*–*25*), as detailed in the supplementary materials (*26*). The optical and scanning electron microscope (SEM) images of the single crystals are shown in figs. S1 and S2 (*26*). The corresponding powder and single-crystal x-ray diffraction (figs. S1 and S2) data confirmed cubic phases for $MAPbBr_3$ and $FAPbBr_3$ and the orthorhombic phase for $CsPbBr_3$ at room temperature. SEM imaging and diffraction analysis of a typical $MAPbBr_3$ microplate (Fig. 1A) confirmed single crystallinity. All samples were stored in a nitrogen glove-box after growth and transferred to vacuum cryostats for spectroscopic measurements at a base pressure $\leq 10^{-6}$ torr. We conducted TR-PL measurements using a home-built inverted microscope and time-correlated single photon counting (TCSPC). The TR-PL results from microplates are shown below and, along with those from macrocrystals, in the supplementary materials (*26*). Optically thin crystals in the former minimized the effects of carrier diffusion into the bulk and to reabsorption of PL emission (*27*, *28*). The TR-OKE measurements were carried out on macrocrystals with both pump and probe photon energies below the band gap.

A pseudocolor plot of TR-PL spectra from a single $MAPbBr_3$ microplate excited at 3.08 eV and at a temperature T = 293 K shows the presence of hot PL emission on the 10^2-ps time scale (Fig. 1B); see fig. S5 for results from additional $MAPbBr_3$ crystals (*26*). At this temperature, $MAPbBr_3$ is in the cubic phase, where the MA cation can freely rotate in the cuboctahedron $PbBr_3^-$ cage (*13*–*16*). Photoexcitation in $MAPbBr_3$ at room temperature and at the exciton densities used (~7×10^{16}/cm^3) gives primarily uncorrelated charge carriers instead of excitons (*29*), as verified by the quadratic dependence of PL intensity on laser pulse energy (fig. S3). The PL spectra feature strong band-edge emission at 2.31 eV and, at short times (<1 ns), a broad high-energy tail extending more than 300 meV above the band edge, which is attributed to radiative recombination of hot carriers. As shown by a comparison of PL decay kinetics at low (2.3 eV) and high (2.6 eV) energies in Fig. 1C, within 1 ns, the band-edge emission remains almost constant, but hot-carrier luminescence decays with a time constant of τ = 160 ± 10 ps. For t > 500 ps, the two kinetic curves merge and show identical PL decay kinetics with a time constant of τ = 4.4 ± 0.1 ns.

To analyze the hot PL emission, we assumed that the PL spectrum at each delay time is a sum of radiative recombination from thermalized carriers, T_1 = 293 K, and that from a hot distribution characterized by an effective carrier temperature of $T_2(t)$. The functional form for each distribution is given by the product of the combined density of state (DOS) distribution in the parabolic band approximation for the conduction and valence bands and the Fermi-Dirac function (*26*). We carried out the fitting globally using PL spectra at all delay times, and Fig. 1D shows fits (solid colored curves) along with data (squares) at selected delay times; also shown are the cold (black solid) and hot (black dashed) components of the fit to the PL spectrum at 50 ps. In the supplementary materials (*26*), we show a complete set of global fitting results (fig. S4).

The relative amplitude of PL from hot carriers, γ = 33 ± 5%, remained constant, but the effective temperature (T_2) decreased with time, consistent with the cooling of hot carriers. As shown in Fig. 1E, the hot-carrier temperature started at T^* = 1250 ± 200 K and cooled down with a cooling time constant of τ_C = 150 ± 30 ps. Beyond ~0.5 ns, cooling became very slow and T^* approached the asymptotic value of T_{as} = 670 ± 100 K. Note that T_{as} was higher than the equilibrium sample temperature of 293 K. This phenomenological T_{as} resulted from PL spectral broadening, which has been assigned to the phonon dressing effect for band-edge emission (*30*). Thus, the actual range of cooling is ΔT^* ~ 550 K within ~1 ns. The above analysis should be viewed as a qualitative estimate because of the complexity of cooling dynamics, the spectral broadening, and the simplicity of the two-temperature model. The model might underestimate the hot-carrier distribution because (i) radiative recombination rates from energetic carriers are lower than that from band-edge carriers (*31*) and (ii) hot fluorescence emission is reduced as compared to band-edge emission, owing to preferential reabsorption of the former (*27*, *28*).

We compare carrier cooling dynamics in $MAPbBr_3$ with those in hybrid $FAPbBr_3$ and the all-inorganic $CsPbBr_3$ at room temperature. Similar to $MAPbBr_3$, photoexcitation of $FAPbBr_3$ or $CsPbBr_3$ at room temperature also gave uncorrelated charge carriers at an excitation density of ~7×10^{16}/cm^3 (fig. S3). The $FAPbBr_3$ crystal contained freely rotating molecular cations (FA^+) in the room-temperature cubic phase, albeit with a dipole moment less than that of MA^+ (*32*). In contrast, such reorientational motion was absent in $CsPbBr_3$, which is in the orthorhombic phase at room temperature. The pseudocolor plot of TR-PL spectra in the first 500 ps and selected PL spectra at indicated delay times are shown in Fig. 2, A and C, for $FAPbBr_3$ and in Fig. 2, B and D, for $CsPbBr_3$ microplates. TR-PL spectra for additional $FAPbBr_3$ and $CsPbBr_3$

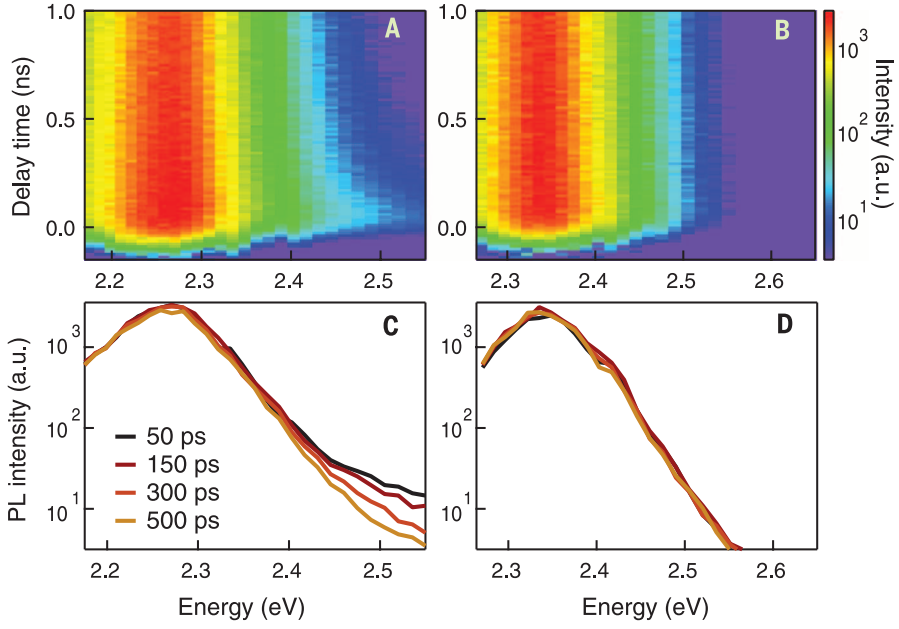

Fig. 2. Time-dependent PL spectra from $FAPbBr_3$ and $CsPbBr_3$ showing hot PL emission only from the former. (**A** and **B**) Pseudocolor plot of TR-PL spectra for a single-crystal $FAPbBr_3$ microplate (A) and a single-crystal $CsPbBr_3$ microplate (B). The excitation photon energy is 3.08 eV, and the excitation density is 1.7 μJ cm^{-2}. (**C** and **D**) PL spectra at indicated delay times for $FAPbBr_3$ microplate (C) and $CsPbBr_3$ microplate (D). The experimental conditions are identical to those for $MAPbBr_3$ in Fig. 1.

Downloaded from http://science.sciencemag.org/ on September 30, 2016

single-crystal microplates are shown in figs. S6 and S7, respectively. Similar to $MAPbBr_3$, we observed long-lived energetic carriers in $FAPbBr_3$ (Fig. 2, A and C). Analysis with the two-temperature model gave a relative hot PL population of $\gamma = 23 \pm 3\%$ (fig. S8). The effective hot-carrier temperature was ~1400 K at 50 ps and cooled down with a time constant of 190 ± 20 ps within ~0.5 ns. The cooling slowed drastically at $t \geq 0.5$ ns and, at 10 ns, reached a value of ~680 K that we attributed to PL spectral broadening. In contrast to $FAPbBr_3$ or $MAPbBr_3$, we observed no spectral shape evolution with time for $CsPbBr_3$ (Fig. 2, B and D), indicating that all excited carriers had relaxed to the band edge within our time resolution (~20 ps). We also confirmed the presence of long-lived hot carriers in $MAPbBr_3$ and $FAPbBr_3$, but not in $CsPbBr_3$, using millimeter-sized single crystals (fig. S9).

A key difference between the HOIPs ($MAPbBr_3$ and $FAPbBr_3$) and the all-inorganic $CsPbBr_3$ is the presence of reorientational motion of dipolar molecular cations at room temperature in the former, but not in the latter. To quantify the liquid-like reorientational motion directly, we applied TR-OKE spectroscopy (*19*, *33*). In this approach, a polarized optical field (pump pulse) induces anisotropy in the refractive index and, thus, transient birefringence in the sample. After a controlled time delay, a second optical field probes the decay of transient birefringence based on polarization rotation (supplementary materials). This technique has been used to probe reorientational motions in liquids (*19*), in solid-liquid phase transitions (*33*), and in the plastic crystal succinonitrile (*34*). There are generally four types of responses in molecular liquids: (i) an instantaneous electronic response; (ii) an ultrafast response (<200 fs) caused by inertial reorientation (also called libration or frustrated rotation) when there is polarization anisotropy; (iii) an intermediate response (~400 to 600 fs) caused by local-interaction–induced anisotropy associated with the molecular reorientational motion; and (iv) a slow response (>1 ps) from the diffusive reorientation of a molecule with permanent polarizability anisotropy (*19*).

Figure 3 compares TR-OKE responses from $CsPbBr_3$, $MAPbBr_3$, and $FAPbBr_3$. The signal from $CsPbBr_3$ (Fig. 3A) was characterized by an instantaneous electronic response (i), which was identical to the pump-probe cross correlation (gray, 70-fs full width at half-maximum), and an ultrafast response with a lifetime of $\tau = 140 \pm 10$ fs, which we attributed to inertial reorientation when there is polarization anisotropy (*19*). For $CsPbBr_3$, the polarization anisotropy came from local distortion of the unit cell and the inertial reorientation from libration of the distorted unit cell near a local potential minimum.

In contrast to $CsPbBr_3$, the TR-OKE transients of either $MAPbBr_3$ (Fig. 3B) or $FAPbBr_3$ (Fig. 3C) were characterized by, in addition to the instantaneous (i) and ultrafast (ii) responses, prominent, long time responses covering a broad time window, from ~10^2 fs to ~2 ps. Indeed, both HOIP spectra are similar to typical TR-OKE responses from anisotropic molecular liquids (*19*, *33*). As in liquids, we could assign the subpicosecond region (iii) and the ~1- to 2-ps region (iv) to rotational motions associated with local-interaction–induced anisotropy and to diffusive rotation of the molecular cations, respectively. The time scales of the corresponding motions are in good agreement with results from molecular dynamics simulations (*13*, *35*), two-dimensional infrared spectroscopy (*36*), neutron scattering (*13*, *14*), and nuclear magnetic resonance spectroscopy (*16*).

The TR-OKE transients in Fig. 3 reveal that molecular cations in $MAPbBr_3$ and $FAPbBr_3$ at room temperature behaved like anisotropic molecular liquids, as in plastic crystals (*33*, *34*). The liquid-like behavior in HOIPs is also supported by previous measurements on the real part of the dielectric permittivity, whose temperature dependence in the cubic and tetragonal perovskite phases is well described by the Kirkwood-Frohlich equation for polar liquids (*15*). The liquid-like behavior in $MAPbBr_3$ or $FAPbBr_3$, but not in $CsPbBr_3$, correlates well with the presence of long-lived hot carriers in the former and suggests the role of molecular dipole motion in energetic carrier protection.

To further verify the critical role of liquid-like motion, we performed TR-PL measurements on $MAPbBr_3$ single crystals at two lower temperatures, 180 and 77 K, corresponding to the tetragonal and orthorhombic phases, respectively (*15*, *16*). Compared to the free rotation in the high-temperature cubic phase, the rotational motion of the MA cation is partially hindered in an anisotropic potential in the tetragonal phase (at 180 K) and completely frozen in the orthorhombic phase (at 77 K). The TR-PL spectra for $MAPbBr_3$ crystals at 180 K are shown in Fig. 4, A and C, and revealed long-lived hot-carrier population in the tetragonal phase. Fitting to the two-temperature model yields a relative hot-carrier population of γ ~ 24%; the hot-carrier temperature started at ~1000 K and cooled down with a time constant of 150 ps (fig. S10), similar to results at 293 K in Fig. 1. In contrast, there was no hot luminescence at 77 K (Fig. 4, B and D), as shown by the absence of a high-energy tail or spectral shape evolution with time. Thus, energetic carriers must have relaxed to the band edge within our time resolution (≤20 ps) in the orthorhombic phase. In conventional semiconductors, the opposite trend is observed: The hot electron lifetime increases with decreasing temperature (*37*).

The results presented here for $MAPbBr_3$ and $FAPbBr_3$ single crystals establish the presence of long-lived hot carriers with electronic temperature ≥1000 K and with ~10^2-ps lifetimes in HOIPs. Such long-lived energetic carriers are unexpected for polar semiconductor materials, where efficient scattering of carriers (electrons and holes) with longitudinal optical (LO) phonons resulted in lifetimes on the order of 10^2 fs for energetic carriers with ~10^2 meV excess energy (*37*). In a conventional model, long-lived energetic carriers become possible only (i) when the excess electronic energy is below that of the LO phonons and the much slower acoustic-phonon scattering becomes the dominant channel for electronic energy loss (*37*); or (ii) at high excitation densities, where hot phonons are not cooled fast enough and can reheat the electronic degrees of freedom (*38*, *39*). The former is important for excess electronic energy less than tens of milli–electron volts in most semiconductors. The latter is the well-known hot "phonon bottleneck," and

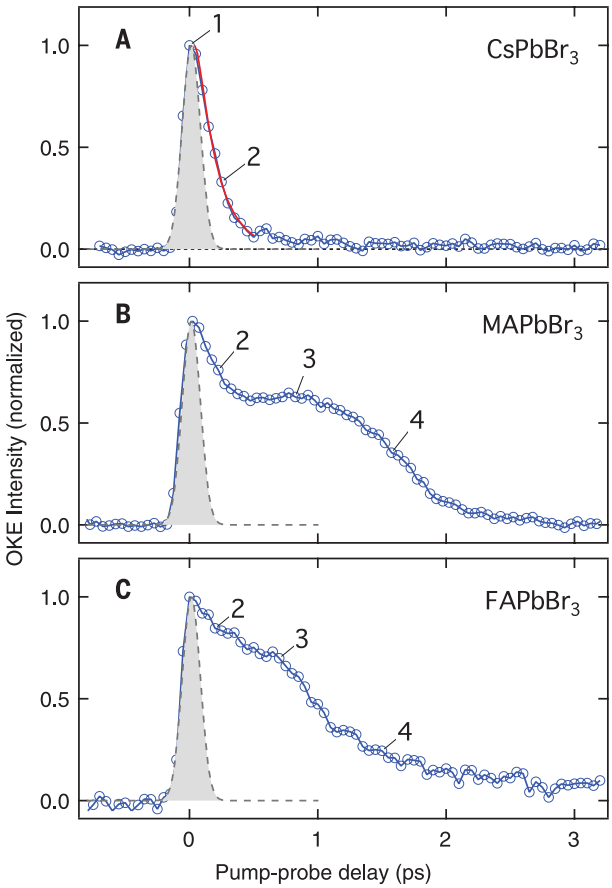

Fig. 3. Time-resolved optical Kerr effect (TR-OKE) transients. (**A** to **C**) The transients reveal liquid-like reorientational dynamics in (B) $MAPbBr_3$ or (C) $FAPbBr_3$, but not in (A) $CsPbBr_3$. The pump-probe cross correlation (CC) is depicted with gray (70 fs full width at half maximum). The red curve in (A) is an exponential fit (convoluted with the pump-probe CC), which gives a decay time constant of 140 ± 10 fs. The labels of different components (1 to 4) are detailed in the text.

Downloaded from http://science.sciencemag.org/ on September 30, 2016

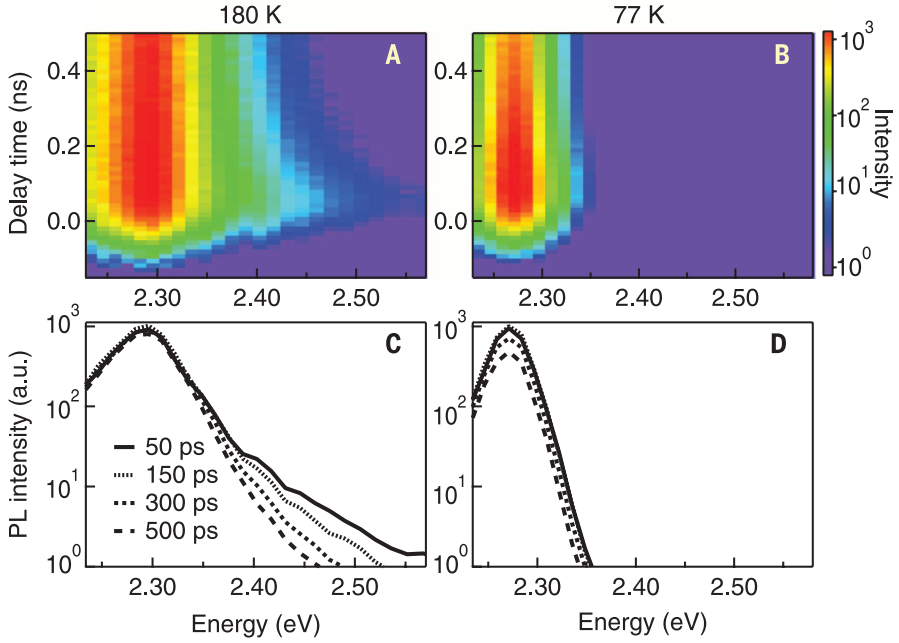

Fig. 4. Time-dependent PL spectra from $MAPbBr_3$ at two temperatures, showing hot PL emission at 180 K but not at 77 K. (**A** and **B**) Pseudocolor plot of TR-PL spectra for a single $MAPbBr_3$ microplate at 180 K (A) and at 77 K (B) under 3.08-eV excitation at an excitation density of 1.7 μJ cm^{-2}. (**C** and **D**) PL spectra at indicated delay times for $MAPbBr_3$ microplate at 180K (C) and at 77 K (D). See Fig. 1 for spectra from the same sample at 293 K.

the hot-carrier lifetime increases with excitation density, as was also observed recently for $MAPbI_3$ thin films at high excitation densities (≥10^{18}/cm^3) (*31*, *40*, *41*). However, we observed energetic carriers ($T^* \geq 1000$ K) with ~10^2-ps lifetimes for single-crystal HOIPs at excitation densities as low as 10^{16} cm^{-3} and, in contrast to the phonon bottleneck, the long-lived excess electronic energy actually decreased with increasing excitation density (fig. S11), as explained below in the large polaron model.

The correlation of the liquid-like motion with the presence of long-lived hot fluorescence in HOIPs implies that the protection of energetic carriers comes from the molecular dipoles that screen their scattering with LO phonons. We argue that the ultrafast dynamics (tens of femtoseconds to 2 ps) of this screening process protects the energetic carriers and is responsible for the slower cooling (hundreds of picoseconds) later on. Within the theoretical framework of polaron physics (*17*) since the seminal work of Landau (*42*), a large polaron (a charge carrier dressed by long-range lattice deformation) must form from an electron or hole in the highly polarizable environment in a HOIP. However, unlike the conventional picture of a large polaron resulting from the Coulomb potential between an electron or hole and the ionic lattice, a charge carrier residing in the inorganic PbX_3^- sublattice can additionally be screened by liquid-like molecular dipoles with reorientational freedom. Thus, large polaron formation in a HOIP bears a resemblance to solvation dynamics in solutions.

We can identify two possible scenarios from this liquid-like polarization environment: (i) Although a large polaron may form from the carrier-induced deformation of the lattice in either a HOIP or its all-inorganic counterpart, dynamic simulations suggest faster deformation dynamics in the former because of the coupling of the liquid-like motion of organic cations with the deformation of the PbX_3^- framework (*43*). The faster dynamics in $MAPbX_3$ or $FAPbX_3$, compared to that in $CsPbX_3$, makes the former kinetically competitive with ultrafast cooling via electron–LO phonon scattering. Although the TR-OKE transients in Fig. 3, B and C, show time scales for molecular reorientational motion on the order of ~10^2 fs to ~picoseconds, the collective motion responsible for initial large polaron formation in the presence of an extra carrier could occur at shorter time scales, as is well known in solvation dynamics of the hydrated electron (*44*). The presence of photoexcited carriers in a HOIP can also weaken the hydrogen bond interaction between an organic cation and the PbX_3^- cage, leading to faster deformation dynamics (*45*). (ii) The dynamic organization of liquid-like molecular dipoles is expected to result in preformed local ferroelectric domains on nanometer scales (*46*, *47*). A photogenerated charge carrier can move to a preformed domain or domain boundary on the order of femtoseconds (*32*), as determined by the inverse of the inter–unit-cell electronic coupling.

Although we do not know which of the two mechanisms above is more important, once a large polaron protection shield is formed around an electron or hole, the Coulomb interaction responsible for its scattering with LO phonons is screened, leading to a drastically reduced rate of hot-carrier cooling by orders of magnitude. Indeed, a recent four-wave mixing experiment comparing carrier dephasing time in $MAPbI_3$ and GaAs reported much reduced the many-body Coulomb interaction in the former (*48*). The large polaron model also explains the inverse dependence of long-lived excess electronic energy on excitation density (fig. S11). This observation is the opposite of what is expected from the conventional phonon bottleneck. Because of the competition for nuclear polarization, there is an effective interpolaron repulsive interaction that destabilizes the large polaron at high excitation densities (*17*). As a result of this destabilization of the large polaron protection shield, the cooling rate of an energetic carrier by LO-phonon scattering increases with excitation density, until the onset of a hot-phonon bottleneck at even higher densities (>10^{18} cm^{-3}) when the effective temperature of the more free-electron/hole-like carriers increases again with excitation density (*31*, *40*, *41*).

Because the long-lived excess electronic energy of the large polaron increases as excitation density decreases, this process may be relevant to the carrier density range under solar radiation and may lead to the realization of the elusive hot-carrier solar cell concept with a theoretical power conversion efficiency as high as 66% (*49*). In a conventional solar cell, excess energy from energetic carriers is lost to phonons before they can be harvested, and this loss is partially responsible for the Shockley-Queisser limit of ~31% in power conversion efficiency. The exceptionally long lifetimes (~10^2 ps) of energetic carriers in HOIPs may make hot-carrier harvesting possible.

REFERENCES AND NOTES

1. M. M. Lee, J. Teuscher, T. Miyasaka, T. N. Murakami, H. J. Snaith, *Science* **338**, 643–647 (2012).
2. S. D. Stranks *et al.*, *Science* **342**, 341–344 (2013).
3. G. Xing *et al.*, *Science* **342**, 344–347 (2013).
4. T. M. Brenner, D. Egger, L. Kronik, G. Hodes, D. Cahen, *Nat. Rev. Mater.* **1**, 15007 (2016).
5. K. Miyano, N. Tripathi, M. Yanagida, Y. Shirai, *Acc. Chem. Res.* **49**, 303–310 (2016).
6. T. J. Savenije *et al.*, *J. Phys. Chem. Lett.* **5**, 2189–2194 (2014).
7. H. T. Yi, X. Wu, X. Zhu, V. Podzorov, *Adv. Mater.* **28**, 6509–6514 (2016).
8. M. Karakus *et al.*, *J. Phys. Chem. Lett.* **6**, 4991–4996 (2015).
9. J. Bardeen, W. Shockley, *Phys. Rev.* **80**, 72–80 (1950).
10. Q. Dong *et al.*, *Science* **347**, 967–970 (2015).
11. H. Oga, A. Saeki, Y. Ogomi, S. Hayase, S. Seki, *J. Am. Chem. Soc.* **136**, 13818–13825 (2014).
12. C. Wehrenfennig, M. Liu, H. J. Snaith, M. B. Johnston, L. M. Herz, *Energy Environ. Sci.* **7**, 2269 (2014).
13. A. M. Leguy *et al.*, *Nat. Commun.* **6**, 7124 (2015).
14. I. P. Swainson *et al.*, *Phys. Rev. B* **92**, 100303 (2015).
15. N. Onoda-Yamamuro, T. Matsuo, H. Suga, *J. Phys. Chem. Solids* **53**, 935–939 (1992).
16. R. E. Wasylishen, O. Knop, J. B. Macdonald, *Solid State Commun.* **56**, 581–582 (1985).
17. D. Emin, *Polarons* (Cambridge Univ. Press, Cambridge, 2013).
18. X.-Y. Zhu, V. Podzorov, *J. Phys. Chem. Lett.* **6**, 4758–4761 (2015).
19. D. McMorrow, W. T. Lotshaw, G. Kenney-Wallace, *IEEE J. Quantum Electron.* **24**, 443–454 (1988).
20. J. Timmermans, *J. Chim. Phys.* **35**, 331–344 (1938).
21. J. Even, M. Carignano, C. Katan, *Nanoscale* **8**, 6222–6236 (2016).
22. D. Shi *et al.*, *Science* **347**, 519–522 (2015).
23. H. Zhu *et al.*, *Nat. Mater.* **14**, 636–642 (2015).
24. Y. Fu *et al.*, *Nano Lett.* **16**, 1000–1008 (2016).
25. Y. Fu *et al.*, *ACS Nano* **10**, 7963–7972 (2016).
26. Supplementary materials are available on *Science* Online.
27. Y. Yamada *et al.*, *J. Am. Chem. Soc.* **137**, 10456–10459 (2015).

Downloaded from http://science.sciencemag.org/ on September 30, 2016

28. L. M. Pazos-Outón *et al.*, *Science* **351**, 1430–1433 (2016).
29. M. Saba *et al.*, *Nat. Commun.* **5**, 5049 (2014).
30. C. Wehrenfennig, M. Liu, H. J. Snaith, M. B. Johnston, L. M. Herz, *J. Phys. Chem. Lett.* **5**, 1300–1306 (2014).
31. K. Chen, A. J. Barker, F. L. C. Morgan, J. E. Halpert, J. M. Hodgkiss, *J. Phys. Chem. Lett.* **6**, 153–158 (2015).
32. J. M. Frost, A. Walsh, *Acc. Chem. Res.* **49**, 528–535 (2016).
33. R. Righini, *Science* **262**, 1386–1390 (1993).
34. P. Foggi, R. Righini, R. Torre, L. Angeloni, S. Califano, *J. Chem. Phys.* **96**, 110–115 (1992).
35. M. T. Weller, O. J. Weber, J. M. Frost, A. Walsh, *Phys. Chem. Lett.* **6**, 3209–3212 (2015).
36. A. A. Bakulin *et al.*, *J. Phys. Chem. Lett.* **6**, 3663–3669 (2015).
37. N. Balkan, *Hot Electrons in Semiconductors* (Oxford Univ. Press, 1998).
38. A. J. Nozik, *Annu. Rev. Phys. Chem.* **52**, 193–231 (2001).
39. U. Bockelmann, G. Bastard, *Phys. Rev. B Condens. Matter* **42**, 8947–8951 (1990).
40. Y. Yang *et al.*, *Nat. Photonics* **10**, 53–59 (2016).
41. M. B. Price *et al.*, *Nat. Commun.* **6**, 8420 (2015).
42. L. Landau, *Phys. Z. Sowjetunion* **3**, 664 (1933).
43. G. R. Berdiyorov *et al.*, *J. Phys. Chem. C* **120**, 16259–16270 (2016).
44. Y. J. Chang, E. W. Castner, *J. Chem. Phys.* **99**, 7289–7299 (1993).
45. Y. Zhou *et al.*, *Nat. Commun.* **7**, 11193 (2016).
46. A. Pecchia, D. Gentilini, D. Rossi, M. Auf der Maur, A. Di Carlo, *Nano Lett.* **16**, 988–992 (2016).
47. C. Quarti, E. Mosconi, F. De Angelis, *Phys. Chem. Chem. Phys.* **17**, 9394–9409 (2015).
48. S. A. March *et al.*, https://arxiv.org/abs/1602.05186 (2016).
49. R. T. Ross, A. J. Nozik, *J. Appl. Phys.* **53**, 3813–3818 (1982).

ACKNOWLEDGMENTS

The growth of macroscopic single-crystal samples and TR-OKE measurements were supported by the U.S. Department of Energy, Office of Science–Basic Energy Sciences, grant ER46980. The PL experiments were supported by the National Science Foundation, grant DMR 1420634 (Materials Research Science and Engineering Center). S.J. acknowledges support by the Department of Energy, Office of Basic Energy Sciences, Division of Materials Sciences and Engineering, under Award DE-FG02-09ER46664, for the growth of microplate samples. We thank D. Paley for help with x-ray diffraction experiment carried out in Columbia University's Shared Materials Characterization Laboratory.

SUPPLEMENTARY MATERIALS

www.sciencemag.org/content/353/6306/1409/suppl/DC1
Materials and Methods
Table S1
Figs. S1 to S12
References (*50*, *51*)

25 April 2016; accepted 4 August 2016
10.1126/science.aaf9570

NANOMATERIALS

High-quality graphene via microwave reduction of solution-exfoliated graphene oxide

Damien Voiry,[1]*† Jieun Yang,[1]† Jacob Kupferberg,[1] Raymond Fullon,[1] Calvin Lee,[1] Hu Young Jeong,[2] Hyeon Suk Shin,[3] Manish Chhowalla[1]‡

Efficient exfoliation of graphite in solutions to obtain high-quality graphene flakes is desirable for printable electronics, catalysis, energy storage, and composites. Graphite oxide with large lateral dimensions has an exfoliation yield of ~100%, but it has not been possible to completely remove the oxygen functional groups so that the reduced form of graphene oxide (GO; reduced form: rGO) remains a highly disordered material. Here we report a simple, rapid method to reduce GO into pristine graphene using 1- to 2-second pulses of microwaves. The desirable structural properties are translated into mobility values of >1000 square centimeters per volt per second in field-effect transistors with microwave-reduced GO (MW-rGO) as the channel material and into particularly high activity for MW-rGO catalyst support toward oxygen evolution reactions.

Low yields of single-layered graphene, submicrometer lateral dimensions, and poor electronic properties remain as major challenges for solution-exfoliated graphene flakes (*1*–*4*). Oxidation of graphite and its subsequent exfoliation into monolayered graphene oxide (GO) with large lateral dimensions (*5*–*7*) produce an exfoliation yield of ~100%; however, despite numerous efforts, it has not been possible to completely remove the oxygen functional groups (*1*, *2*, *8*, *9*) so that the reduced form of GO (rGO) remains a highly disordered material with properties that are generally far inferior to graphene grown by chemical vapor deposition (CVD graphene) (*5*). Although rGO has been widely demonstrated to be a potentially useful material for catalysis (*10*–*13*) and energy storage (*14*–*18*), even in its disordered form, efficient reduction of GO into high-quality graphene should lead to substantial enhancement in performance. Here we report a simple and rapid method to reduce GO into pristine graphene by using 1- to 2-s-long microwave pulses. The microwave-reduced GO (MW-rGO) exhibits pristine CVD graphene–like features in the Raman spectrum with sharp G and 2D peaks and a nearly absent D peak. X-ray photoelectron spectroscopy (XPS) and high-resolution transmission electron microscopy (HR-TEM) suggest a highly ordered structure in which oxygen functional groups are almost entirely removed. The desirable structural properties are translated into mobility values of >1000 $cm^2 V^{-1} s^{-1}$ in field-effect transistors (FETs) with MW-rGO as the channel material and into exceptionally low Tafel slope values of ~38 mV per decade for MW-rGO catalyst support for oxygen evolution reaction (OER). These results suggest that reduction of GO using microwaves is highly efficient and realizes the goal of achieving high-quality graphene with desirable properties by solution exfoliation.

We used the modified Hummers' method to oxidize graphite and solubilize it into monolayered GO flakes in water (*19*). The stable suspension of GO sheets in water allows them be reconstituted in several different forms such as thin films (*20*), bucky paper (*21*), or fibers (*22*, *23*). GO synthesized in this manner is electrically insulating because of the presence of oxygen functional groups that are covalently bonded with the carbon atoms (*2*). Substantial effort has been devoted to recover the conducting π states of sp^2-bonded carbon atoms by removing oxygen functional groups via chemical (*1*, *24*, *25*) or thermal (*26*) reduction [even heating over 3000 K (*23*)]. By carefully tuning the reduction procedure, it is possible to realize noteworthy optical (*20*, *27*, *28*) and electronic properties (*27*) of rGO that are substantially different from those of pristine graphene because the evolution of the oxygen functional groups during reduction is accompanied by the formation of defects in the graphene basal plane (*29*). Specifically, nanoscopic holes occur through loss of carbon as CO or CO_2 (*30*), and rearrangement of the carbon atoms in the graphene basal plane leads to formation of Stone-Wales types of defects (*31*). In addition, oxygen functional groups form highly stable ether and carbonyl groups (*32*) that are difficult to remove so that rGO contains a residual oxygen concentration of 15 to 25 atomic % (at %) (*32*). These factors render rGO a highly defective material, with several studies reporting electronic mobility values on the order of 1 $cm^2 V^{-1} s^{-1}$ (*33*–*35*).

Flakes of GO with lateral dimensions as high as tens of micrometers are shown in Fig. 1A. We used microwaves from a conventional microwave oven operated at 1000 W for 1- to 2-s pulses to reduce GO [see the "Preparation of microwave-reduced graphene oxide (MW-rGO)" section in the supplementary materials] (*36*). Irradiation of GO with microwaves has been reported previously (*37*–*39*), but the reduction efficiency has been low and the rGO remains highly disordered, as indicated by the presence of an intense and broad disorder D band and the absence of the 2D band in the Raman spectra. We irradiated GO

[1]Materials Science and Engineering, Rutgers University, 607 Taylor Road, Piscataway, NJ 08854, USA. [2]Central Research Facilities and School of Materials Science and Engineering, Ulsan National Institute of Science and Technology (UNIST), Ulsan 689-798, Republic of Korea. [3]Department of Chemistry and Department of Energy Engineering, Low Dimensional Carbon Materials, UNIST, Ulsan 689-798, Republic of Korea. *Present address: Institut Européen des Membranes, University of Montpellier, Place Eugène Bataillon, 34095 Montpellier, France. †These authors contributed equally to this work. **‡Corresponding author. Email: manish1@rci.rutgers.edu**

Downloaded from http://science.sciencemag.org/ on September 30, 2016

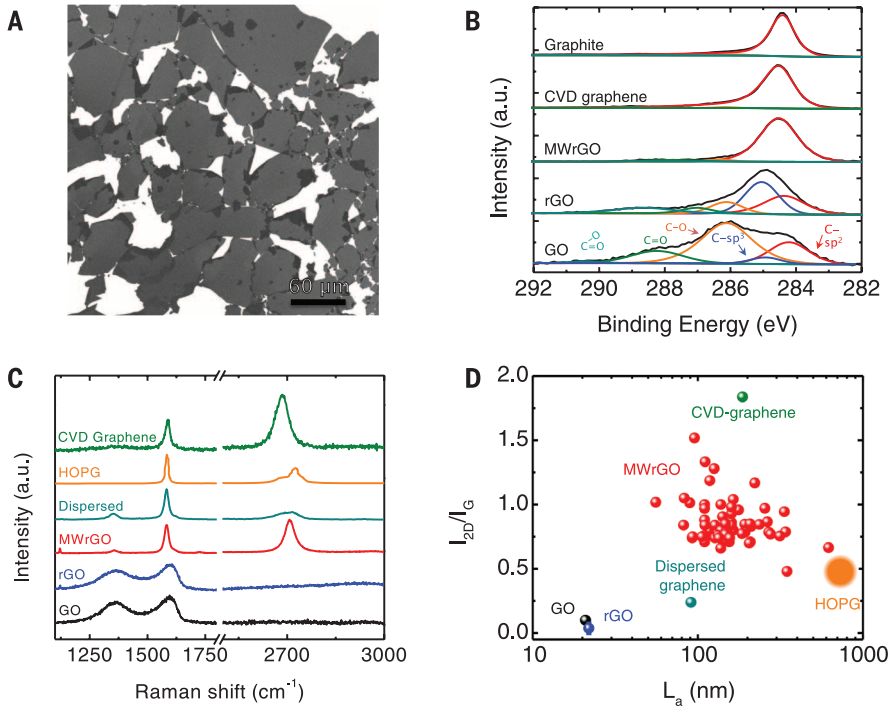

Fig. 1. Physical characterization of MW-rGO compared with pristine GO, rGO, and graphene grown by CVD. (**A**) Scanning electron microscopy of the single-layer GO flakes deposited on a silicon wafer. GO nanosheets typically have a lateral dimension of ~50 μm. (**B**) High-resolution x-ray photoelectron spectra from the C1s regions for microwaved reduced graphene oxide (MW-rGO) compared with pristine graphene oxide (GO), reduced graphene oxide (rGO), graphene grown by chemical vapor deposition (CVD graphene), and graphite. Each spectrum can be deconvoluted with components from the carbon-carbon bonds (sp^3: C–C and sp^2: C=C) as well as oxygen functional groups (C–O, C=O, and C–O=O), allowing quantification of the oxygen content. a.u., arbitrary units. (**C**) Raman spectra of MW-rGO and other graphene-based samples. The spectrum obtained for MW-rGO is similar to the spectrum of CVD graphene, with the presence of a high and symmetrical 2D band together with a minimal D band. Sharp Raman peaks indicate high crystallinity of MW-rGO and demonstrate the quality of microwave reduction. (**D**) Evolution of the I_{2D}/I_G ratio versus the crystal size (L_a) for MW-rGO, GO, rGO, highly ordered pyrolytic graphite (HOPG), dispersed graphene, and graphene from (*3*) (i.e., CVD graphene). We report 62 measurements on about five different MW-rGO samples. I_{2D}/I_G ratios and L_a values for MW-rGO are approaching those of graphene and are substantially higher than the values for rGO and dispersed graphene.

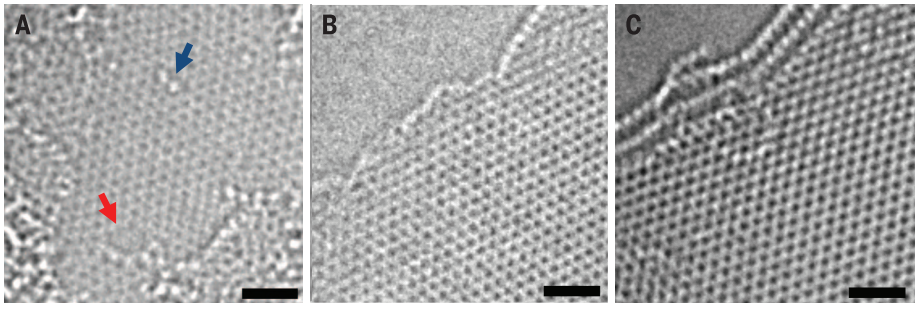

Fig. 2. High-resolution transmission electron microscopy (HR-TEM) of MW-rGO nanosheets. (**A**) HR-TEM of single-layer rGO presenting high density of defects. The red arrow denotes a hole; the blue arrow indicates an oxygen functional group. Bilayer (**B**) and trilayer (**C**) HR-TEM of MW-rGO showing highly ordered structure. Scale bars, 1 nm.

after deposition to achieve high-quality rGO. We started by slightly reducing GO by thermal annealing before exposure to microwaves, which resulted in conductive GO that could absorb microwaves. We infer that absorption of microwaves led to rapid heating of the GO (fig. S1) (*36*), causing desorption of oxygen functional groups and reordering of the graphene basal plane.

The XPS results (Fig. 1B) indicate that MW-rGO was substantially reduced with an in-plane oxygen concentration of ~4 at %, which is much lower than that theoretically predicted for rGO after annealing to 1500 K (*32*). Approximately 3 at % of noncovalently bonded adsorbed oxygen was also found in MW-rGO, CVD graphene, and graphite powder, as indicated by the fits in Fig. 1B. The full width at half maximum of the XPS peak is slightly higher in the case MW-rGO than for CVD graphene and bulk graphite, suggesting that a small amount of disorder is still present. The Raman spectra of MW-rGO, thermally reduced GO, CVD graphene, liquid-exfoliated graphene, and highly ordered pyrolytic graphite (HOPG) (for comparison) are shown in Fig. 1C. MW-rGO exhibited highly ordered graphene–like Raman features with sharp and symmetrical 2D and G peaks and a nearly absent D peak (fig. S2) (*36*). The Raman spectrum for MW-rGO (Fig. 1C) more closely resembled that of CVD graphene than the broad and highly disordered spectrum of thermally reduced rGO or that of solution-exfoliated graphene films where the 2D peak is weak and the disorder-induced D peak is also visible. The Raman spectra of MW-rGO are also different from those of electrochemically exfoliated graphene, chemically reduced GO, and microwave-exfoliated GO, all of which exhibit a high D band and a moderate or no 2D band (*25*, *37*, *40*–*42*). We have also extracted the I_{2D}/I_G Raman peak ratios (I_{2D}, intensity of the 2D peak; I_G, intensity of the G peak) as a function of the graphene domain sizes (see the "Raman spectroscopy of graphene oxide and microwaved-reduced graphene oxide" section in supplementary materials) (*36*). We found that MW-rGO exhibits substantially higher I_{2D}/I_G ratios and larger graphene domain sizes as compared with rGO and solution-exfoliated flakes (Fig. 1D).

Raman spectroscopy provides structural information averaged over regions of a few micrometers in diameter. We used aberration corrected HR-TEM to investigate local atomic structure (Fig. 2). Thermally reduced GO exhibited the well-known disordered structure with holes and oxygen functional groups on the surface (Fig. 2A). The MW-rGO exhibited highly ordered structure at the atomic scale (Fig. 2, B and C), which suggests that there is some reorganization of the carbon bonding during microwave reduction, along with removal of oxygen facilitated by achieving exceptionally high temperatures.

To investigate whether the highly ordered structure of MW-rGO can be translated into useful properties, we implemented it as the channel in FETs and as a catalyst support for the OER. The mobility values in graphene have been used as a parameter for assessing the quality of the material (*43*). To this end, several studies have reported high mobility values for rGO (100 to 1000 $cm^2 V^{-1} s^{-1}$) (*40*, *42*) to demonstrate efficacy of various reduction treatments or synthesis procedures. However, mobility values alone cannot provide information about the structural integrity of the material. Previous reports on high-mobility rGO are accompanied by Raman spectra containing large D bands and weak 2D bands, along with oxygen concentrations of 5 to 8%,

Downloaded from http://science.sciencemag.org/ on September 30, 2016

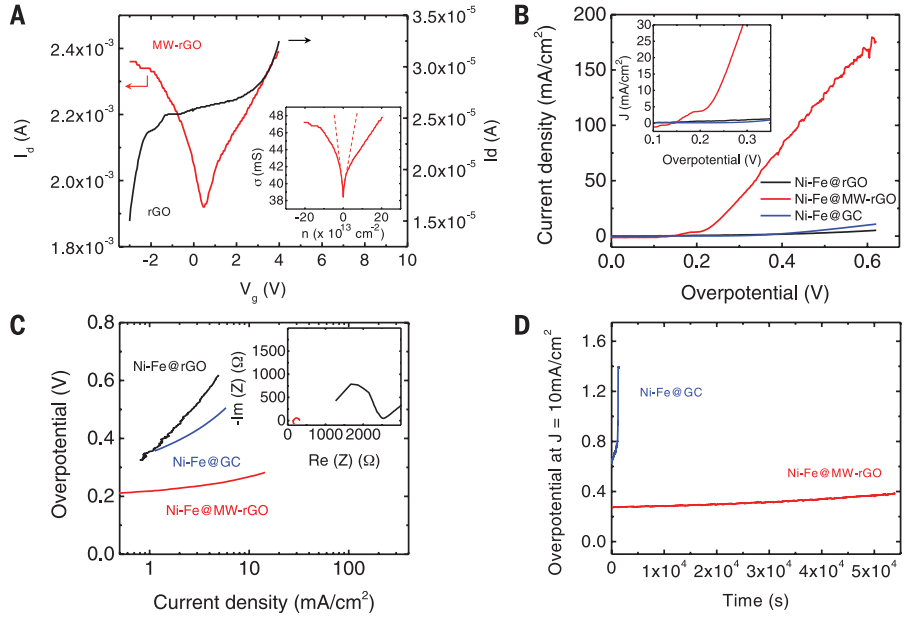

Fig. 3. Characterization of the electronic and electrocatalytic properties of MW-rGO. (**A**) Transfer characteristics of MW-rGO and rGO measured at drain voltage (V_{ds}) = 50 mV. MW-rGO displays ambipolar behavior with a Dirac cone at gate voltage (V_g) ~ 0.5 V. I_d, drain current. (Inset) Evolution of the MW-rGO conductivity with the carrier density. n, carrier concentration; σ, conductivity. (**B**) Polarization curves obtained from Ni-Fe layered double hydroxide (LDH) deposited on MW-rGO (Ni-Fe@MW-rGO), rGO (Ni-Fe@rGO), and glassy carbon (Ni-Fe@GC). (Inset) Magnification of the onset potential. J, current density. (**C**) Tafel plot of Ni-Fe LDH deposited on MW-rGO compared with GC and rGO. (Inset) Nyquist plots of the different samples obtained by electrochemical impedance spectroscopy at η = 200 mV. Ni-Fe@MW-rGO clearly shows a reduced internal resistance and minimal charge transfer resistance that can be attributed to the high conductivity of the MW-rGO nanosheets. Re (Z), real part of the impedance; -Im (Z), imaginary part of the impedance. (**D**) Galvanostatic measurements showing the electrocatalytic stability of Ni-Fe LDH deposited on glassy carbon and MW-rGO when driving a 10 mA/cm^2 current density over 15 hours. The MW-rGO support shows the best stability with minimal change of the overpotential. Contrastingly, the activity from the Ni-Fe LDH on glassy carbon decreases rapidly.

suggesting substantial disorder. Thus, mobility values >~1 cm^2 V^{-1} s^{-1} have not been widely reproducible in rGO. Transfer characteristics of FETs from MW-rGO on SiO_2 [see Materials and methods section for device-fabrication procedure (*36*)] are shown in Fig. 3A. Drain currents can be measured in the milliamp range. The electrical properties of thermally reduced GO FETs are also shown for comparison (Fig. 3A); these FETs exhibit substantially lower current values. In the case of rGO, the absence of a Dirac point is attributed to the poorly reduced and highly disordered structure of the nanosheets. Additionally, the presence of adsorbates and oxygen impurities is known to dramatically shift the position of the Dirac point and to modify the FET characteristics. The mobility values extracted from FET measurements were >1000 cm^2 V^{-1} s^{-1} for holes and electrons in MW-rGO (Fig. 3A, inset, and fig. S4) (*36*). FETs measured here consist of large channel dimensions so that the transport of carriers occurs over numerous flakes. Despite this, exceptionally high mobility values were obtained in MW-rGO, suggesting that individual flakes have very good transport properties. Although we obtain exceptional mobilities, they should be interpreted with caution as the actual values can be strongly influenced by extrinsic factors such as contact resistance and scattering by charged impurities (*44*).

Highly conducting carbon-based electrodes that are electrochemically stable are important for applications in catalysis and energy storage. Catalysts are typically loaded on highly conducting substrates (working electrodes) such as carbon cloth, glassy carbon, or nickel foam. We investigated the properties of MW-rGO as a catalyst support in OER by depositing Fe and Ni layered double hydroxide (LDH) on MW-rGO [see Materials and methods section (*36*)]. The OER properties of Fe-Ni LDH catalysts on MW-rGO, rGO, and glassy carbon electrodes (Fig. 3B) [see Materials and methods section for the electrochemical measurements (*36*)] show that the overpotential at which the reaction starts decreased to <200 mV and the current density rapidly increased when MW-rGO was used as the catalyst support. To obtain insight into surface chemistry mechanisms, we have extracted the Tafel slopes from measurements on different supports (Fig. 3C). The MW-rGO catalyst supports exhibit very low Tafel slopes of 38 mV per decade, which may indicate that the reaction $MO + OH^- = MOOH + e^-$ (where M represents an active site on the catalyst surface and e^- represents an electron) is the rate-determining step (*45*). The much higher Tafel slopes for glassy carbon and rGO electrodes of 170 mV per decade and 360 mV per decade, respectively, suggest that limiting reactions are caused by adsorption of hydroxide ions ($M + OH^- = MOH + e^-$) because of the poor electrical coupling between the catalyst and the support (*45*). The limited electrical coupling is highlighted by the inset in Fig. 3C, which shows that the impedance of the electrochemical circuit is substantially lowered when using MW-rGO, which allows the OER to proceed efficiently. Electrochemical stability of the catalysts and their supports is an important parameter in catalysis. The stability of MW-rGO supports (Fig. 3D) was maintained for more than 15 hours, in contrast with glassy carbon supports that degraded almost immediately after the reaction started. We have made similar measurements for the hydrogen evolution reaction and obtained desirable performance for MW-rGO catalyst supports, as well as very high stability for more than 100 hours [see the "Hydrogen evolution reaction (HER)" section in supplementary materials] (*36*).

REFERENCES AND NOTES

1. S. Park, R. S. Ruoff, *Nat. Nanotechnol.* **4**, 217–224 (2009).
2. K. P. Loh, Q. Bao, P. K. Ang, J. Yang, *J. Mater. Chem.* **20**, 2277–2289 (2010).
3. K. R. Paton *et al.*, *Nat. Mater.* **13**, 624–630 (2014).
4. K. P. Loh, Q. Bao, G. Eda, M. Chhowalla, *Nat. Chem.* **2**, 1015–1024 (2010).
5. C.-Y. Su *et al.*, *Chem. Mater.* **21**, 5674–5680 (2009).
6. J. Zhao, S. Pei, W. Ren, L. Gao, H.-M. Cheng, *ACS Nano* **4**, 5245–5252 (2010).
7. Q. Zheng *et al.*, *ACS Nano* **5**, 6039–6051 (2011).
8. I. Jung, D. A. Dikin, R. D. Piner, R. S. Ruoff, *Nano Lett.* **8**, 4283–4287 (2008).
9. K. Erickson *et al.*, *Adv. Mater.* **22**, 4467–4472 (2010).
10. E. Yoo *et al.*, *Nano Lett.* **9**, 2255–2259 (2009).
11. Y. Liang *et al.*, *Nat. Mater.* **10**, 780–786 (2011).
12. Y. Li *et al.*, *J. Am. Chem. Soc.* **133**, 7296–7299 (2011).
13. J. Yang *et al.*, *Angew. Chem. Int. Ed.* **52**, 13751–13754 (2013).
14. M. D. Stoller, S. Park, Y. Zhu, J. An, R. S. Ruoff, *Nano Lett.* **8**, 3498–3502 (2008).
15. J. G. Radich, P. V. Kamat, *ACS Catal.* **2**, 807–816 (2012).
16. H. Wang *et al.*, *J. Am. Chem. Soc.* **132**, 13978–13980 (2010).
17. H. Wang *et al.*, *Nano Lett.* **11**, 2644–2647 (2011).
18. G. Yu *et al.*, *Nano Lett.* **11**, 2905–2911 (2011).
19. W. S. Hummers Jr., R. E. Offeman, *J. Am. Chem. Soc.* **80**, 1339 (1958).
20. G. Eda, G. Fanchini, M. Chhowalla, *Nat. Nanotechnol.* **3**, 270–274 (2008).
21. D. A. Dikin *et al.*, *Nature* **448**, 457–460 (2007).
22. R. Cruz-Silva *et al.*, *ACS Nano* **8**, 5959–5967 (2014).
23. G. Xin *et al.*, *Science* **349**, 1083–1087 (2015).
24. S. Park *et al.*, *Nat. Commun.* **3**, 638 (2012).
25. I. K. Moon, J. Lee, R. S. Ruoff, H. Lee, *Nat. Commun.* **1**, 73 (2010).
26. X. Li *et al.*, *Nat. Nanotechnol.* **3**, 538–542 (2008).
27. G. Eda *et al.*, *Adv. Mater.* **22**, 505–509 (2010).
28. Z. Luo, P. M. Vora, E. J. Mele, A. T. C. Johnson, J. M. Kikkawa, *Appl. Phys. Lett.* **94**, 111909 (2009).
29. D. R. Dreyer, S. Park, C. W. Bielawski, R. S. Ruoff, *Chem. Soc. Rev.* **39**, 228–240 (2010).
30. R. Larciprete *et al.*, *J. Am. Chem. Soc.* **133**, 17315–17321 (2011).
31. J. Kotakoski, A. V. Krasheninnikov, K. Nordlund, *Phys. Rev. B* **74**, 245420 (2006).
32. A. Bagri *et al.*, *Nat. Chem.* **2**, 581–587 (2010).
33. Z. Luo, Y. Lu, L. A. Somers, A. T. C. Johnson, *J. Am. Chem. Soc.* **131**, 898–899 (2009).
34. H. A. Becerril *et al.*, *ACS Nano* **2**, 463–470 (2008).
35. S. Wang *et al.*, *Nano Lett.* **10**, 92–98 (2010).
36. See supplementary materials on *Science* Online.

Downloaded from http://science.sciencemag.org/ on September 30, 2016

37. Y. Zhu *et al.*, *Carbon* **48**, 2118–2122 (2010).
38. W. Chen, L. Yan, P. R. Bangal, *Carbon* **48**, 1146–1152 (2010).
39. H. Hu, Z. Zhao, Q. Zhou, Y. Gogotsi, J. Qiu, *Carbon* **50**, 3267–3273 (2012).
40. H. Feng, R. Cheng, X. Zhao, X. Duan, J. Li, *Nat. Commun.* **4**, 1539 (2013).
41. K. Parvez *et al.*, *J. Am. Chem. Soc.* **136**, 6083–6091 (2014).
42. S. Eigler *et al.*, *Adv. Mater.* **25**, 3583–3587 (2013).
43. N. Petrone *et al.*, *Nano Lett.* **12**, 2751–2756 (2012).
44. I. McCulloch, A. Salleo, M. Chabinyc, *Science* **352**, 1521–1522 (2016).
45. T. Shinagawa, A. T. Garcia-Esparza, K. Takanabe, *Sci. Rep.* **5**, 13801 (2015).

ACKNOWLEDGMENTS

M.C. and D.V. acknowledge financial support from NSF Division of Graduate Education (grant 0903661) and Electrical, Communications and Cyber Systems (grant 1128335). J.Y., J.K., and M.C. acknowledge financial support from the Rutgers Energy Institute. R.F. acknowledges financial support from the U.S. Department of Education Graduate Assistance in Areas of National Need program (grant P200A120142). C.L. and J.K. acknowledge support from the Rutgers ARESTY Research Assistant program. H.S.S. acknowledges support from the National Research Foundation (NRF) (grant NRF 2014R1A2A2A01007136) and from the Center for Advanced Soft Electronics (grant code 2011-0031630) under the Global Frontier Research Program through the NRF funded by the Ministry of Science, ICT and Future Planning, Korea. All data are in the main paper and the supplementary materials.

SUPPLEMENTARY MATERIALS

www.sciencemag.org/content/353/6306/1413/suppl/DC1
Materials and Methods
Supplementary Text
Figs. S1 to S6
Table S1
References (*46*–*57*)

12 June 2016; accepted 23 August 2016
Published online 1 September 2016
10.1126/science.aah3398

GEOPHYSICS

Surface uplift and time-dependent seismic hazard due to fluid injection in eastern Texas

Manoochehr Shirzaei,[1]* William L. Ellsworth,[2] Kristy F. Tiampo,[3]† Pablo J. González,[4]‡ Michael Manga[5]

Observations that unequivocally link seismicity and wastewater injection are scarce. Here we show that wastewater injection in eastern Texas causes uplift, detectable in radar interferometric data up to >8 kilometers from the wells. Using measurements of uplift, reported injection data, and a poroelastic model, we computed the crustal strain and pore pressure. We infer that an increase of >1 megapascal in pore pressure in rocks with low compressibility triggers earthquakes, including the 4.8–moment magnitude event that occurred on 17 May 2012, the largest earthquake recorded in eastern Texas. Seismic activity increased even while injection rates declined, owing to diffusion of pore pressure from earlier periods with higher injection rates. Induced seismicity potential is suppressed where tight confining formations prevent pore pressure from propagating into crystalline basement rocks.

In recent years, the eastern and central United States have experienced a sharp increase in the number of earthquakes, with more than 1570 events with moment magnitudes (M_w) ≥ 3 between 2009 and 2015 (*1*–*3*). Many of these events occurred near injection disposal wells and were preceded by a high rate of fluid injection over a period of months to years, suggesting a link between seismicity and injection operations (*1*, *3*–*8*). In general, earthquake hazard is proportional to the seismic rate; thus, the current increase in the seismic rate implies an elevated hazard in the central and eastern United States (*9*).

On 17 May 2012, the city of Timpson, Texas, experienced a M_w 4.8 earthquake, the largest recorded event in the region (Fig. 1A). This event was preceded and followed by several earthquakes located on an inferred northwest-southeast–trending basement fault, including three with M_w ≥ 4.0 over the following 16 months. Focal depths were shallow, ranging from 1.6 to 5.0 km, with the majority of the strain released between 3.5 and 5 km (*5*). Four high-volume class II disposal wells are located within ~10 km, and two lie directly above the site of the earthquakes (table S1). They dispose coproduced saline formation water from oil and gas production operations in the area by injecting into Lower Cretaceous limestones within the Sabine Uplift of eastern Texas (*10*). There are other injection wells in the vicinity, but none is closer than 7 km to the four studied wells (table S8 and fig. S8) or is a high-volume injector. The immediate area near the disposal wells and the earthquakes has limited oil and gas production. The four disposal wells began injection between 2005 and 2007 at a net average rate of 890,000 m^3/year until mid-2012, when injection dropped to 720,000 m^3/year (*5*).

The proximity of the earthquake clusters to the injection wells suggests a link between them (*5*, *11*). As wastewater is injected into the disposal formation, it increases pore pressure within the connected hydrogeologic system. Over time, the pressure perturbation can spread to distances of many kilometers (*12*, *13*). The increase in pore pressure caused by the injection of fluids decreases the effective normal stress on faults, bringing them closer to failure (*14*–*16*), as well as locally changing differential stress within the reservoir and surrounding rocks (*17*–*19*). Moreover, increased pore pressure can cause surface deformation (*19*), measurable using geodetic tools (*20*), which provides the possibility of documenting subsurface evolution from the surface. Among geodetic tools, interferometric synthetic aperture radar (InSAR) and the Global Positioning System (GPS) have been widely used to monitor surface deformation resulting from natural and anthropogenic processes.

We applied a multitemporal InSAR approach (*21*) to three overlapping sets of L-band SAR images (tables S2 and S3) acquired by the Advanced Land Observing Satellite (ALOS) over the Timpson area between 6 May 2007 and 14 November 2010 (Fig. 1A). High-quality interferograms were generated from these L-band data (fig. S1). We improved the signal-to-noise ratio of the measurements by estimating the linear velocity from time series obtained by inverting a large number of interferograms (*22*). Using velocity maps for each individual data set and the combined map (*22*), we found a line-of-sight (LOS) uplift rate of up to 3 mm/year over the area between the injection wells (Fig. 1B). We estimated that the rate of volume increase under the LOS velocity surface is 800,000 to 1,000,000 m^3/year, assuming an elastic material with a Poisson's ratio of 0.25 to 0.33 estimated from seismic velocities profiles, which is consistent with the net injected volume rate at the injection wells. To validate ALOS observations and evaluate the current state of ground deformation, we also applied the same processing scheme to eight C-band images acquired by the RADARSAT-2 satellite between 6 March and 21 August 2014 (fig. S2 and tables S4 and S5). Although the location of the zone of maximum deformation is consistent with the velocity map obtained from the L-band data, its spatial extent is broader, with a maximum uplift of ~5 mm over a ~6-month interval.

The two western wells (W1 and W2) inject (Fig. 1C) at a depth of 1800 m into Trinity Group

[1]School of Earth and Space Exploration, Arizona State University, Tempe, AZ 85287, USA. [2]Department of Geophysics, Stanford University, Stanford, CA 94305, USA. [3]Department of Earth Sciences, University of Western Ontario, London, Ontario, Canada. [4]Centre for the Observation and Modelling of Earthquakes, Volcanoes and Tectonics (COMET) and Institute of Geophysics and Tectonics, School of Earth and Environment, University of Leeds, Leeds LS2 9JT, UK. [5]Department of Earth and Planetary Science, University of California, Berkeley, CA 94709, USA.
***Corresponding author. Email: shirzaei@asu.edu** †Present address: Cooperative Institute for Research in Environmental Sciences and Department of Geological Sciences, UCB 216, University of Colorado, Boulder, CO 80309, USA. ‡Present address: COMET and Liverpool Earth Observatory, Department of Earth, Ocean and Ecological Sciences, University of Liverpool, Liverpool L69 3GP, UK.

Downloaded from http://science.sciencemag.org/ on September 30, 2016

formations (fig. S6), which are porous and permeable limestones overlain by the regionally extensive and much less permeable Ferry Lake Anhydrite (*10*). The east wells (E1 and E2) inject (Fig. 1C) into carbonate formations of the Washita Group at a depth of 900 m (fig. S6), which is stratigraphically above the Ferry Lake Anhydrite (*10*). We applied an inverse modeling scheme (*23*) to characterize the rate of volume strain. We discretized the volume beneath the half-space into rectangular prisms, 3 by 3 km in area and 0.2 km high, between the surface and a depth of 5 km.

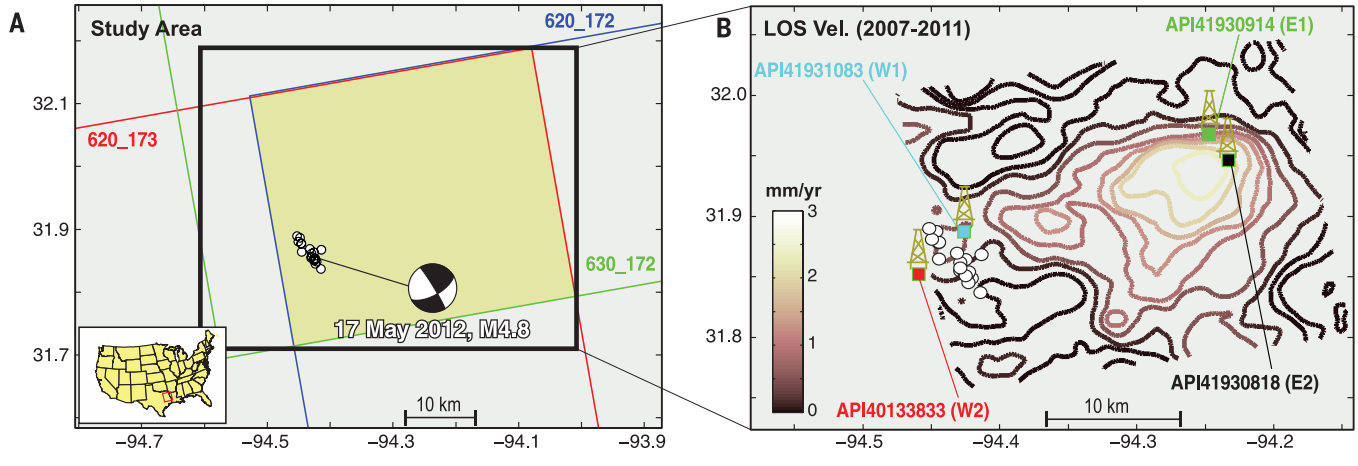

Fig. 1. Study area and data sets. (**A**) Three overlapping frames from ALOS in ascending orbit (heading = 350°, incidence = 34.5°). Locations of the seismicity and focal mechanism of the Timpson sequence are shown (white dots). Latitude and longitude are shown on the *y* and *x* axes, respectively. (**B**) Contours of the LOS deformation velocity field obtained from multitemporal processing of the overlapped ALOS SAR data set (yr, year). The west wells (W1 and W2) and the east wells (E1 and E2) are indicated. (**C**) Time series of the volume of injected fluid for each of the wells shown in (B) (Mo, month).

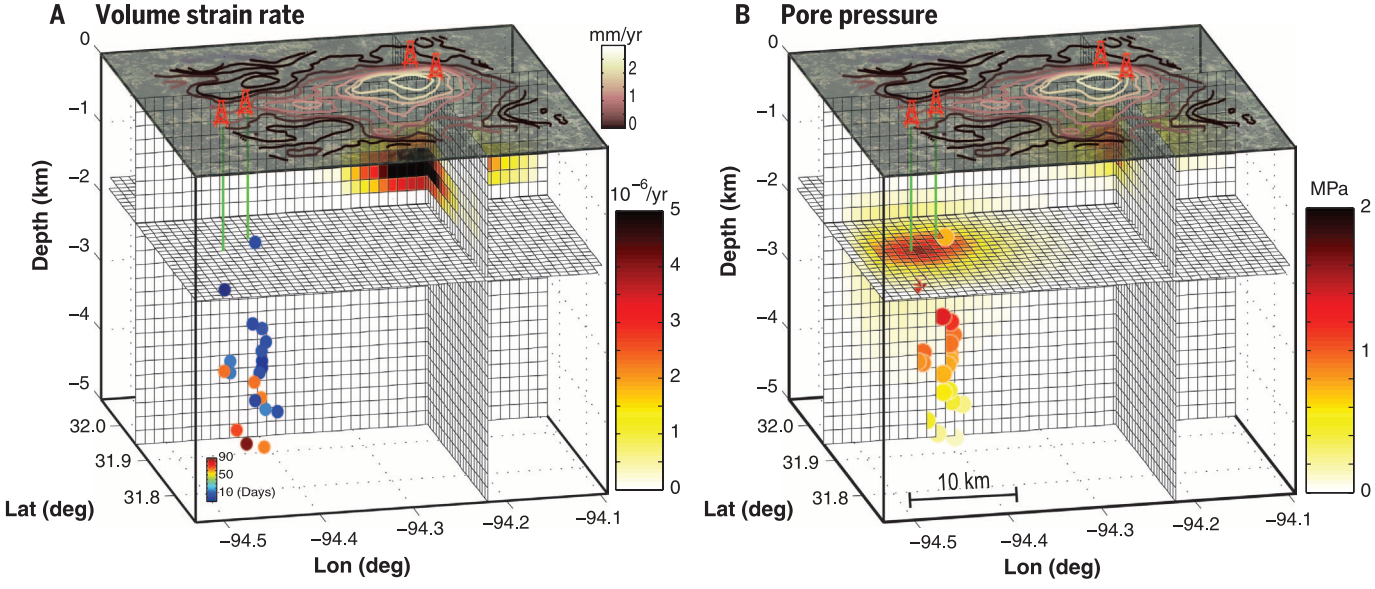

Fig. 2. Volumetric strain and pore pressure. (**A**) Distribution of the estimated volume strain rate (shaded grid cells). Colored circles show the timing of earthquakes with respect to the first event (day 0). The injection wells are shown by green bars. Contour lines show the surface deformation rate between 6 May 2007 and 14 November 2010. (**B**) Distribution of the cumulative pore pressure (shaded grid cells) between 2006 and 2013. Colored circles show the pore pressure increase at the location of the earthquakes.

Downloaded from http://science.sciencemag.org/ on September 30, 2016

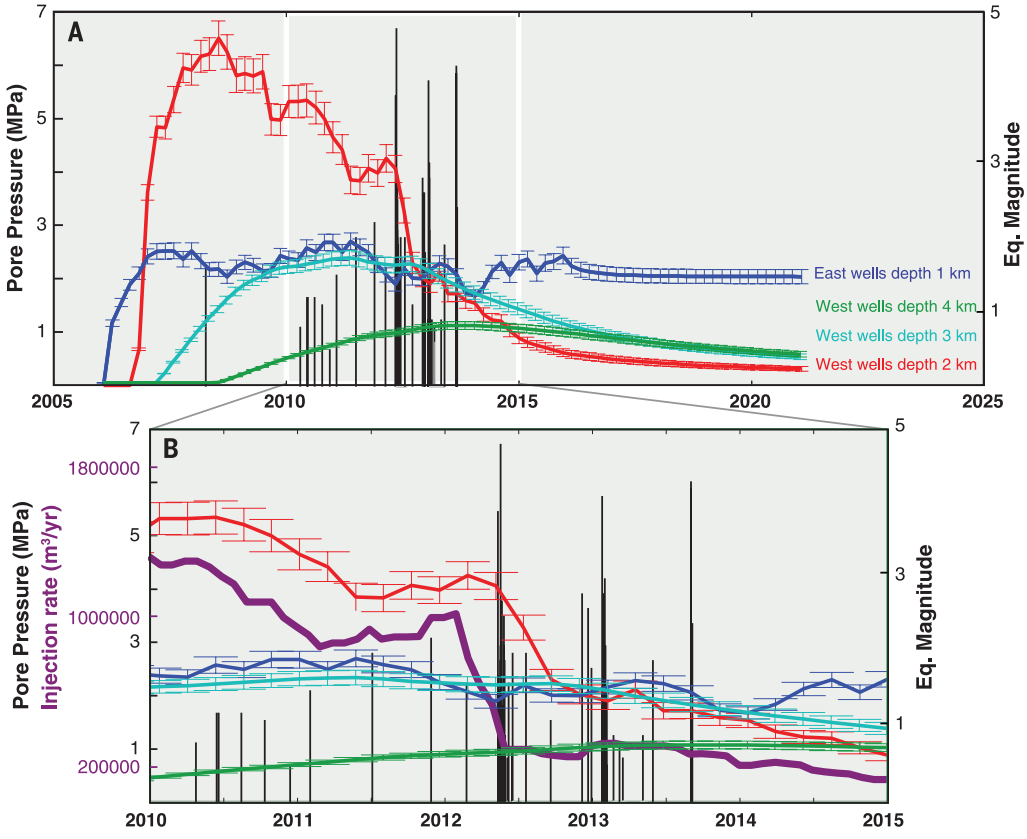

Fig. 3. Pore pressure time series. (**A**) Colored lines show time series of pore pressure at various depths. The error bars show 1-standard-deviation uncertainties and were obtained through bootstrapping. Vertical black lines show the time and magnitude of earthquakes (Eq.) in the Timpson sequence (table S7). (**B**) Close-up view of the period 2010–2015 from (A). The time series of the rate of injected fluid at the west wells is superimposed in purple.

We assumed constant volume strain within each prism (*22*). Our optimum strain model accurately reproduced the observed deformation data (fig. S3) and calculated a total volume change of 700,000 ± 1600 m^3/year, slightly lower than the injection rate. This discrepancy is likely due to diffusion of injected fluids into the surrounding rocks without generating any measurable deformation. We also found a maximum volume strain rate of ~5 × 10^{-6} yr^{-1}, located at a depth of 0.8 to 1.1 km adjacent to wells E1 and E2 (Fig. 2A).

The availability of geological profiles (fig. S6) and the distribution of hydraulic conductivity and Poisson's ratios allowed us to characterize parameters of a poroelastic layered Earth model (table S6). Using this Earth model and the time series of injected fluid volume, we solved for the evolution of the pore pressure in the crust (*22*) (Fig. 2B). We identified two zones of maximum pore pressure at depths of ~0.85 and ~1.85 km near the east and west wells, respectively. The shallower zone of elevated pore pressure coincides with the zone of maximum volume strain. Higher pressures occur around the two west wells, where uplift has been negligible. The contribution from other injection wells to the south (figs. S9 and S10) is small and of second-order importance. The pore pressure associated with wells to the north is unlikely to influence the seismicity because these wells lie on the downthrown block of the Mount Enterprise fault system (*10*), which probably acts as a barrier to southward migration of the fluids.

To investigate the relationship between the pore pressure distribution associated with injection and the observed seismicity, we estimated the increase in pore pressure at the location of the 2012 earthquake sequence, in which the main events nucleated between 3.5 and 4.5 km depth (*5*). Overall, fluid injection caused a pore pressure increase of 0.5 to 1.5 MPa at the hypocentral depth. Pressure changes of this magnitude are known to trigger earthquakes elsewhere (*24*). In the context of Mohr circle stress analysis, a localized increase in pore pressure shifts the circle to the left (i.e., reduces the effective normal stress) and changes its radius because of poroelastic strain (i.e., increases the differential stress), whereas a spatially uniform pore pressure increase only shifts the circle to the left until it touches the failure envelope (*25*). Given the historical lack of large earthquakes in the region and the 5-year delay between the initiation of injection and the first large event, we suggest that a decrease in effective normal stress (due to a homogeneous increase in pore pressure) triggered seismicity. The initiating seismicity and associated stress change may have transiently enhanced the permeability (*26*–*29*), increasing the pore pressure at the location of the deeper events, which in turn promoted additional earthquakes.

We investigated injection from two pairs of wells that began injecting at about the same time, disposing approximately the same volumes of wastewater. The main differences between them are the depth of injection and the presence of an impermeable barrier below the shallower east wells that blocks fluid and pressure from reaching deeper formations. The deeper west wells are associated with the 2012 Timpson earthquake sequence, whereas no detected seismicity occurred near the east wells. This observation highlights the importance of hydrogeology for the consequences of fluid injection.

The extent to which induced pore pressure change occurs is an important parameter for accurately estimating seismic hazard. From a regulatory perspective, however, constraining this parameter is not trivial, given its complex relationship with local hydrogeology (*30*). Using deformation data, we can put a lower bound on the extent of the rock volume change caused by a pore pressure increase. Measurable uplift more than 8 km from the east wells demonstrates the long reach of pressure perturbations, which has been inferred in other studies (*12*, *13*, *15*).

Studies of potentially induced earthquakes suggest that the majority of seismicity occurs within basement rocks, even though most of the injection is done in more shallow sedimentary layers (*2*–*5*, *7*, *31*, *32*). Although pore pressure has increased adjacent to both the east and west wells, little surface deformation was detected in the vicinity of the west wells, where the seismicity occurred (Fig. 2). This is likely due to lower rock compressibility near the west wells compared with near the east wells, a feature we did not account for in solving for the pore pressure evolution, in addition to the greater injection depth. Moreover, injection in the east wells is done in a shallow layer, typically characterized by velocity-strengthening frictional properties (*33*); thus, pore pressure changes are less likely to initiate seismic rupture at this location. The uplift signal also has an asymmetric pattern, which we cannot explain with standard models of radial pore pressure diffusion in a homogeneous medium. Our model shows that pore pressure propagates downward below the west wells with a delay and that the period of elevated seismicity between 2010 and 2014 coincides with the period of the maximum pore pressure change of 1 to 2.5 MPa at the average depth of 3 km (Fig. 3A). Though all events coincide with the period of pore pressure increase in the focal zone, the onset of the main sequence in May 2012 corresponds to

Downloaded from http://science.sciencemag.org/ on September 30, 2016

pressures of about 1 MPa reaching the focal zone (Fig. 3B).

The frequency and magnitude of seismic events reached a climax between May 2012 and September 2013, when more than 80% of events occurred, including four $M_w \geq 4$ earthquakes. This period of elevated seismic activity followed a rapid decline in injection at the west wells (Fig. 3B). Thus, the timing of seismicity may be determined by pore pressure diffusion to the depths of the earthquakes. Additional contributions to the stresses may also promote seismicity, such as from the poroelastic stresses near the well that accompany the decrease in injection. For an optimally oriented strike-slip fault with the fault-normal direction radial to the injection site, a sudden decline in injection rate relaxes the compressive stress (*34*). All of the seismic events discussed here occurred on a fault with the fault-normal direction oriented at N60°E, radial to the west injection wells.

Our coupled flow and poroelastic model allows us to predict the future pore pressure distribution after injection ends (Fig. 3A). As injection ends in the west wells by about 2016, the model shows the pressure decreasing approximately exponentially. However, the decay rate is fastest in the most permeable formations and at the depths where injection occurs. At the east wells, 10 years after shut-off, the pore pressure remains close to its maximum level. For the west wells, only 5 years after a hypothesized shut-off, pore pressure drops to less than 10% of its maximum value. This observation has direct implications for future injection operations and seismic hazard estimations. Changes in the seismicity rate are a function of changes in Coulomb stress and background stress (*35*). Our study shows that the background stress is characterized by a relaxation time that depends on both the injection history and hydrogeological properties. Therefore, injection history at a given site may modify future estimates of the seismic hazard.

Better quantification of the evolution of the stress and pore pressure in the crust is vital to forecasting fault reactivation (*9*, *36*). Despite improvements in seismic monitoring capacity and the resulting decrease in the magnitude detection threshold (*37*, *38*), observations of the in situ pore pressure and stress field remain elusive because of the scarcity of deformation observations and limited integration of those observations with physical models. This work highlights the value of monitoring surface deformation, in particular by using advanced remote sensing techniques, to understand the evolution of pore pressure and stress at depth. The ability to measure crustal stress evolution affords a proactive approach to managing the hazard associated with fluid injection. Observation of the time-dependent stress field permits the construction of temporally variable statistical frameworks (*34*), which are useful for earthquake operational forecasting (*39*). The key to successful operational earthquake hazard assessment is being able to continuously update information about the probability of a future earthquake, which can be achieved by using data and models such as those presented in this study. Geodetic monitoring and modeling schemes are valuable components of efforts to mitigate induced seismic hazard.

REFERENCES AND NOTES

1. J. L. Rubinstein, A. B. Mahani, *Seismol. Res. Lett.* **86**, 1060–1067 (2015).
2. M. Weingarten, S. Ge, J. W. Godt, B. A. Bekins, J. L. Rubinstein, *Science* **348**, 1336–1340 (2015).
3. M. J. Hornbach *et al.*, *Nat. Commun.* **6**, 6728 (2015).
4. K. M. Keranen, H. M. Savage, G. A. Abers, E. S. Cochran, *Geology* **41**, 699–702 (2013).
5. C. Frohlich *et al.*, *J. Geophys. Res. Solid Earth* **119**, 581–593 (2014).
6. C. Frohlich, E. Potter, C. Hayward, B. Stump, *Leading Edge* **29**, 270–275 (2010).
7. S. Horton, *Seismol. Res. Lett.* **83**, 250–260 (2012).
8. F. R. Walsh 3rd, M. D. Zoback, *Sci. Adv.* **1**, e1500195 (2015).
9. W. L. Ellsworth, *Science* **341**, 1225942 (2013).
10. W. H. Granata, *Cretaceous Stratigraphy and Structural Development of the Sabine Uplift Area, Texas and Louisiana* (Shreveport Geological Society, 1963).
11. Z. Fan, P. Eichhubl, J. F. Gale, *J. Geophys. Res. Solid Earth* **121**, 2798–2812 (2016).
12. P. A. Hsieh, J. D. Bredehoeft, *J. Geophys. Res.* **86**, 903–920 (1981).
13. K. M. Keranen, M. Weingarten, G. A. Abers, B. A. Bekins, S. Ge, *Science* **345**, 448–451 (2014).
14. C. B. Raleigh, J. H. Healy, J. D. Bredehoeft, *Science* **191**, 1230 (1976).
15. Y. Zhang *et al.*, *Ground Water* **51**, 525–538 (2013).
16. Y. Guglielmi, F. Cappa, J.-P. Avouac, P. Henry, D. Elsworth, *Science* **348**, 1224–1226 (2015).
17. P. Segall, *J. Geophys. Res. Solid Earth* **90**, 6801 (1985).
18. J. Du, J. E. Olson, *J. Petrol. Sci. Eng.* **30**, 181–197 (2001).
19. Z. R. Chen, *J. Petrol. Sci. Eng.* **80**, 41–52 (2011).
20. D. W. Vasco *et al.*, *Geophys. Res. Lett.* **37**, L03303 (2010).
21. M. Shirzaei, *IEEE Geosci. Remote Sens. Lett.* **10**, 456–460 (2013).
22. Materials and methods are available as supplementary materials on *Science* Online.
23. A. Mossop, P. Segall, *J. Geophys. Res. Solid Earth* **104**, 29113–29131 (1999).
24. E. A. Roeloffs, in *Advances in Geophysics*, R. Dmowska, Ed. (Academic Press, 1996).
25. A. Y. Rozhko, Y. Y. Podladchikov, F. Renard, *Geophys. Res. Lett.* **34**, L22304 (2007).
26. S. Rojstaczer, S. Wolf, *Calif. Geol.* **20**, 211 (1992).
27. Y. Kitagawa, K. Fujimori, N. Koizumi, *Geophys. Res. Lett.* **29**, 121-1–121-4 (2002).
28. E. A. Roeloffs, *Pure Appl. Geophys.* **126**, 177–209 (1988).
29. E. E. Brodsky, E. Roeloffs, D. Woodcock, I. Gall, M. Manga, *J. Geophys. Res.* **108**, 2390 (2003).
30. S. A. Shapiro, P. Audigane, J.-J. Royer, *Geophys. J. Int.* **137**, 207–213 (1999).
31. L. Seeber, J. G. Armbruster, W.-Y. Kim, *Bull. Seismol. Soc. Am.* **94**, 76–87 (2004).
32. C. Nicholson, E. Roeloffs, R. L. Wesson, *Bull. Seismol. Soc. Am.* **78**, 188 (1988).
33. C. H. Scholz, *The Mechanics of Earthquakes and Faulting* (Cambridge Univ. Press, ed. 2, 2002).
34. P. Segall, S. Lu, *J. Geophys. Res. Solid Earth* **120**, 5082–5103 (2015).
35. J. H. Dieterich, *J. Geophys. Res.* **99**, 2601–2618 (1994).
36. M. W. McClure, R. N. Horne, *GRC Trans.* **35**, 1487 (2011).
37. N. Deichmann, D. Giardini, *Seismol. Res. Lett.* **80**, 784–798 (2009).
38. W.-Y. Kim, *J. Geophys. Res. Solid Earth* **118**, 3506–3518 (2013).
39. T. H. Jordan *et al.*, *Ann. Geophys.* **54**, 315 (2011).

ACKNOWLEDGMENTS

RADARSAT-2 images were acquired under SOAR-E (Science and Operational Applications Research–Education) project 5226 of the Canadian Space Agency (www.asc-csa.gc.ca/eng/). ALOS data were obtained through Alaska Satellite Facilities (www.asf.alaska.edu/). M.S.'s contribution was supported by U.S. Geological Survey grant G13AP00040. K.F.T. was supported by a Discovery Grant from the Natural Sciences and Engineering Research Council of Canada. W.L.E. was supported by the Stanford Center for Induced and Triggered Seismicity. M.M. was supported by U.S. NSF grant EAR-1344424. P.J.G. was supported by the UK Natural Environment Research Council projects COMET and NE/K011006/1. A copy of the interferograms, LOS deformation maps, model results, and codes for InSAR processing, strain inversion, and pore pressure modeling can be obtained through the website of the Radar Remote Sensing and Tectonic Geodesy Lab (ratlab.asu.edu) or by correspondence with M.S.

SUPPLEMENTARY MATERIALS

www.sciencemag.org/content/353/6306/1416/suppl/DC1
Materials and Methods
Figs. S1 to S10
Tables S1 to S8
References (*40*–*57*)

2 May 2016; accepted 26 August 2016
10.1126/science.aag0262

CARBON CYCLE

Radiocarbon constraints imply reduced carbon uptake by soils during the 21st century

Yujie He,[1]* Susan E. Trumbore,[2] Margaret S. Torn,[3] Jennifer W. Harden,[4,5] Lydia J. S. Vaughn,[3] Steven D. Allison,[1,6] James T. Randerson[1]

Soil is the largest terrestrial carbon reservoir and may influence the sign and magnitude of carbon cycle–climate feedbacks. Many Earth system models (ESMs) estimate a significant soil carbon sink by 2100, yet the underlying carbon dynamics determining this response have not been systematically tested against observations. We used ^{14}C data from 157 globally distributed soil profiles sampled to 1-meter depth to show that ESMs underestimated the mean age of soil carbon by a factor of more than six (430 ± 50 years versus 3100 ± 1800 years). Consequently, ESMs overestimated the carbon sequestration potential of soils by a factor of nearly two (40 ± 27%). These inconsistencies suggest that ESMs must better represent carbon stabilization processes and the turnover time of slow and passive reservoirs when simulating future atmospheric carbon dioxide dynamics.

Soil carbon is a dynamic reservoir that may increase substantially in size during the 21st century, as predicted by Earth system models (ESMs), thereby influencing the sign and magnitude of carbon cycle feedbacks under climate change (*1*–*4*). Under a high radiative forcing scenario (representative concentration pathway 8.5), changes in soil carbon estimated by different models vary from a loss of 20 Pg C to a gain of more than 360 Pg C

Downloaded from http://science.sciencemag.org/ on September 30, 2016

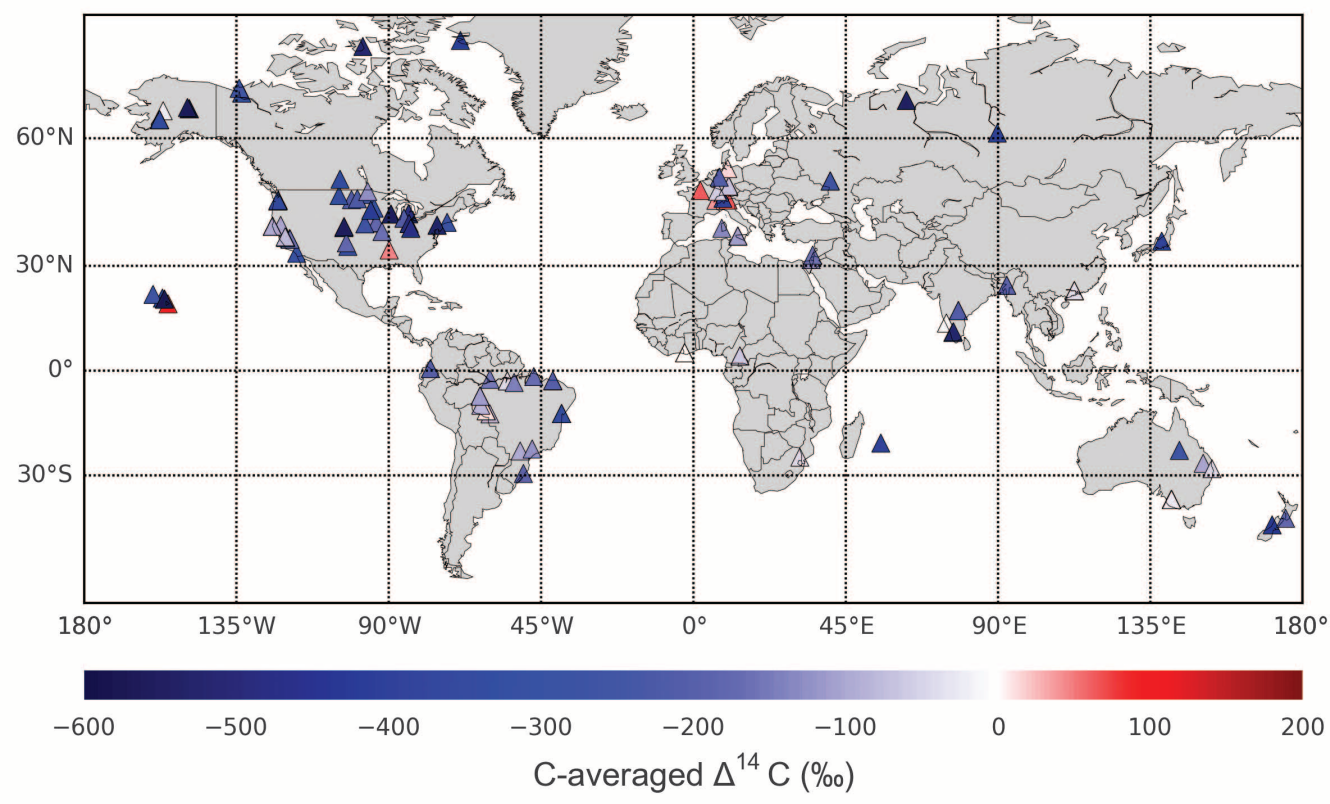

Fig. 1. Locations of radiocarbon soil profiles used to constrain ESM soil carbon mean ages and turnover times (*N* = 157). The carbon-weighted $\Delta^{14}C$ to a depth of 1 m is denoted with the color shade of each symbol. A summary of the location, sample year, and reference for each site is provided in table S2.

(*5*). These models suggest that the global carbon inventory in mineral soils may increase by 30% or more over a time span of about two centuries. The multimodel mean soil carbon accumulation of 109 Pg C (*5*) represents about one decade of global fossil fuel emissions at current rates and 5% of cumulative fossil emissions by 2100 for this scenario (*6*). This soil carbon sink represents a negative feedback on CO_2 emissions and, if robust, would slow the rate of climate change.

Still, there are substantial uncertainties in the soil carbon sink projected by ESMs (*5*). Rapid rates of carbon sequestration in ESMs contrast with findings from CO_2 and warming experiments (*7*, *8*), as well as multiple theoretical and observational constraints indicating slow (millennial) rates of soil organic carbon (SOC) accrual and turnover (*9*–*14*). Model uncertainty—as measured by intermodel spread—is high for soil carbon turnover time (τ) and exceeds the uncertainty estimated for carbon uptake through gross primary production (GPP) (*15*, *16*).

[1]Department of Earth System Science, University of California, Irvine, CA, USA. [2]Department of Biogeochemical Processes, Max-Planck-Institute for Biogeochemistry, Jena, Germany. [3]Earth Sciences Division, Lawrence Berkeley National Laboratory, Berkeley, CA, USA. [4]U.S. Geological Survey, Menlo Park, CA, USA. [5]Stanford University, Stanford, CA, USA. [6]Department of Ecology and Evolutionary Biology, University of California Irvine, Irvine, CA, USA.
***Corresponding author. Email: yujie.he@uci.edu**

In coupled model simulations, the relative sink strength (i.e., percentage change in soil carbon) depends on the responses of net primary production (NPP) and soil carbon dynamics to increasing atmospheric CO_2 concentrations and, to a lesser extent, climate change (*5*). Elevated CO_2 increases photosynthesis and NPP, which results in greater carbon inputs to soil pools with decadal or longer residence times. Carbon sequestration in soils reduces the buildup of CO_2 in the atmosphere (the carbon-concentration feedback). On the other hand, elevated CO_2 also warms the climate, which tends to accelerate soil carbon turnover and reduce carbon storage (the carbon-climate feedback) (*17*, *18*). Although these feedbacks oppose one another, the carbon-concentration feedback is more than four times as high, on average, as the carbon-climate feedback in current ESMs at the global scale (*3*). Differences in the representation of elevated CO_2 versus climate effects on ecosystem processes result in substantial variation in soil carbon sequestration estimates (*19*) (table S1).

Without a strong carbon-concentration feedback, ESMs would likely project smaller gains or larger losses of soil carbon over the 21st century. Our aim was to constrain the magnitude of the soil carbon–concentration feedback with soil radiocarbon observations. Radiocarbon content provides information about soil carbon turnover over centuries to millennia based on radioactive decay and over decades, based on inputs of ^{14}C from atmospheric weapons testing ("bomb carbon"). Accurate carbon turnover times are important for ESM projections because pools with short turnover times rapidly adjust to increasing NPP, whereas pools with long turnover times (and, by inference, low rates of inputs) change only slowly, possibly beyond the time horizon of effective climate mitigation efforts. Therefore, inaccuracies in the representation of carbon turnover times will have consequences for the rate and magnitude of the carbon-concentration feedback simulated by ESMs. Here, we used $\Delta^{14}C$ measurements at 157 sites across multiple biomes (Fig. 1 and table S2) along with carbon inventory data to constrain soil carbon dynamics in five biogeochemically coupled ESM simulations (esmFixClim1) from the Coupled Model Intercomparison Project Phase 5 (CMIP5) (*20*). In these idealized simulations, the atmospheric CO_2 mole fraction starts at a preindustrial value of 285 parts per million (ppm) and rises at a rate of 1% $year^{-1}$, thus quadrupling over 140 years. The biogeochemical components of each model experience the increasing trajectory of atmospheric CO_2, whereas the atmospheric radiation submodels do not, limiting impacts solely to the direct effects of CO_2 on plant physiology and thus enabling diagnosis of carbon-sink sensitivity to increasing CO_2.

Total initial soil carbon in the ESMs was not significantly different from the total amount in the top meter of the Harmonized World Soil Database (HWSD) (Fig. 2, A and B) for four of the five models [$P > 0.05$, except for the Community

Downloaded from http://science.sciencemag.org/ on September 30, 2016

Table 1. Global soil carbon stocks and carbon uptake for CMIP5 models that experienced a quadrupling of atmospheric CO_2 from a preindustrial value of 285 ppm over a period of 140 years.

ESM	Initial SOC (Pg C)	% change in SOC	% change in SOC after ^{14}C constraint	^{14}C-imposed sink reduction (%)	τ_{slow} (year)*	$\tau_{passive}$ (year)	r_f	r_s	^{14}C-imposed correction factors† τ_{slow}	$\tau_{passive}$	r_f	r_s
CESM1 (BGC)	571	6.3	5.1	19	56 ± 16	1310 ± 241	0.06 ± 0.05	0.33 ± 0.05	–	3.7 ± 1.5	–	0.34 ± 0.75
GFDL-ESM2M	1344	26	3.3	87	231 ± 196	–	0.17 ± 0.07	–	16 ± 18	–	0.06 ± 0.14	–
HadGE M2-ES	1028	63	33	46	208 ± 84	–	0.12 ± 0.07	–	17 ± 12	–	0.07 ± 0.32	–
IPSL-CM5A-LR	1340	27	25	5.9	218 ± 82	1181 ± 347	0.06 ± 0.03	0.29 ± 0.07	–	14 ± 8.3	–	0.07 ± 0.14
MRI-ESM1‡	1403	36	22	40	347 ± 117	1065 ± 257	0.17 ± 0.09	0.10 ± 0.06	–	13 ± 7.2	0.46 ± 0.79	0.34 ± 0.74
Mean§	1137 ± 312	32 ± 18	18 ± 12	40 ± 27	212 ± 104	1185 ± 123	0.12 ± 0.06	0.24 ± 0.12	16.5 ± 0.5	10.2 ± 4.6	–	–

*τ_{slow}, $\tau_{passive}$ denote the turnover time, and r_f, r_s denote the transfer coefficient from the fast to the slow pool and from the slow to the passive pool, respectively. Reported values were estimated as an area-weighted mean and standard deviation of all model grid cells. †The mean and standard deviation of the ^{14}C-imposed correction factors were derived from using the ^{14}C observations at each site in a single optimization and then averaging these scalar adjustments across the set of 157 optimizations. ‡The ^{14}C-constrained sink reduction and correction factor for MRI were based on an inverse analysis that changed the pool size of both slow and passive pools. The reported percentage change in SOC and sink reduction were derived from transient simulations starting at steady state with the reduced complexity model. See methods in the supporting materials. §The multimodel mean and standard deviation were estimated using the mean value from each of the five ESMs.

ESM (CESM), $P = 0.03$]. Therefore, we compared ESM-derived $\Delta^{14}C$ to observations derived from soil profiles to a 1-m depth. The carbon and ^{14}C patterns of the soil profiles we used were similar to those reported in a recent synthesis paper (*21*), and we used some of the same profiles in our analysis.

Comparing ESM outputs with ^{14}C observations requires a model analysis approach because most ESMs do not yet explicitly simulate $\Delta^{14}C$ in soils, and no ESMs had reported turnover times for soil carbon pools. Therefore, we used a reduced complexity (RC) model to approximate soil carbon dynamics in each ESM. This approach allowed us to estimate the turnover times and $\Delta^{14}C$ associated with the carbon pools in different ESMs (table S3). Where possible, we used a three-pool RC model (with fast, slow, and passive pools) to simulate carbon and ^{14}C dynamics. A multipool structure is essential because radiocarbon observations show that soil carbon fluxes (NPP inputs and heterotrophic respiration) exchange mainly with short-lived pools, whereas carbon stocks are dominated by long-lived pools (*12*, *18*, *22*, *23*). The three-pool RC model had five parameters representing turnover times of fast, slow, and passive pools (τ_{fast}, τ_{slow}, and $\tau_{passive}$) and transfer coefficients

Table 2. Summary of sensitivity experiments.

Experiment	% change in SOC after ^{14}C constraint*	^{14}C-imposed sink reduction (%)*	Correction factor for turnover time*	Correction factor for transfer coefficient*
Biome-specific inversions	17 ± 11	43 ± 24	–	–
Match SOC with HWSD at sites†	18 ± 12	31 ± 40	13 ± 4.5	0.19 ± 0.23
Match SOC with 1.5*HWSD at sites†	21 ± 12	19 ± 42	11 ± 4.5	0.38 ± 0.39
–1 SD of intersite variation	14 ± 9.9	52 ± 23	–	–
+1 SD of intersite variation	23 ± 16	25 ± 25	–	–

*The mean and standard deviation were estimated from the global mean change of each of the five individual ESMs. The correction factors for the turnover time and transfer coefficients are reported for the slowest carbon pool. †The correction factors were obtained at each site, and then the mean scalar across all sites was applied to the global forward simulation.

Downloaded from http://science.sciencemag.org/ on September 30, 2016

(r_f and r_s) that regulated carbon flow from the fast to slow, and slow to passive pools (fig. S1). We used a two-pool RC model for Geophysical Fluid Dynamics Laboratory model ESM2M (GFDL-ESM2M) because it represents soil carbon with two pools (*24*) and for Hadley Global Environment Model 2-ES (HadGEM2-ES) because it reported carbon for two pools (table S4). The two-pool RC model had three parameters, representing τ_{fast}, τ_{slow}, and r_f (fig. S1). After verifying that the RC model was a good approximation of each ESM based on minimization of root-mean-square error, we used the RC models to simulate $\Delta^{14}C$ values at each grid cell, with observed atmospheric $\Delta^{14}C$ for the past 50,000 years as a boundary condition and accounting for radioactive decay (see supplementary materials).

We used an inverse analysis to determine the RC model parameters that were most consistent with our $\Delta^{14}C$ data set. In the inversion, we adjusted the parameters described above to match both the total carbon and radiocarbon constraints. With these constraints, turnover time and carbon input rate for each pool were coupled such that an increase in turnover time required a compensatory decline in inputs (fig. S2). RC parameters derived from the inversion were subsequently used to assess consequences of ^{14}C constraints for the carbon-concentration feedback.

All ESMs projected an increase in soil carbon over 140 years with a multimodel mean of 32% (Table 1). This increase was primarily driven by increasing carbon inputs to soil under the quadrupling of CO_2 (table S3), as temperature increased by only a small amount (mean ± 1 SD was 0.52° ± 0.68°C) for this set of biogeochemically coupled simulations. CESM showed the smallest soil carbon increase (6.3%), primarily because of low litter inputs relative to other ESMs (table S3). For this time period and set of model runs, storage in soil carbon accounted for 42 ± 17% of the total accumulation of carbon in the terrestrial biosphere.

Both two- and three-pool RC models reproduced the global carbon dynamics of the original ESMs (fig. S3 to S5 and table S5). The τ_{fast} across all RC models was less than 20 years, whereas τ_{slow} varied from 40 to 600 years (fig. S6) with a multimodel mean of 212 ± 104 years. The mean $\tau_{passive}$ for the three-pool RC models from CESM, Institut Pierre Simon Laplace model (IPSL), and the Meteorological Research Institute model (MRI) was 1185 ± 123 years (Table 1 and fig. S7). Using the RC model parameters estimated at each grid cell within an ESM, we calculated the expected $\Delta^{14}C$. The resulting global average $\Delta^{14}C$ for 1995 (median sample year of site profiles) from the RC models was significantly higher than the mean of the observations [−6.4 ± 64 per mil (‰) versus −211 ± 156‰] (Fig. 2, C and D ($P < 0.001$). $\Delta^{14}C$ values from RC models approximating ESMs with passive pools were more negative (−53 ± 35‰) but still significantly higher than the observations ($P < 0.001$). Converting these $\Delta^{14}C$ observations into mean age for the soil profile yielded an estimate of 3100 ± 1800 years for the observed soil carbon integrated to 1 m and 430 ± 50 years for the ESMs (Fig. 2, E and F). These results indicated that the ESMs did not have enough old carbon that had experienced substantial levels of radioactive decay; concurrently, the models assimilated too much bomb ^{14}C.

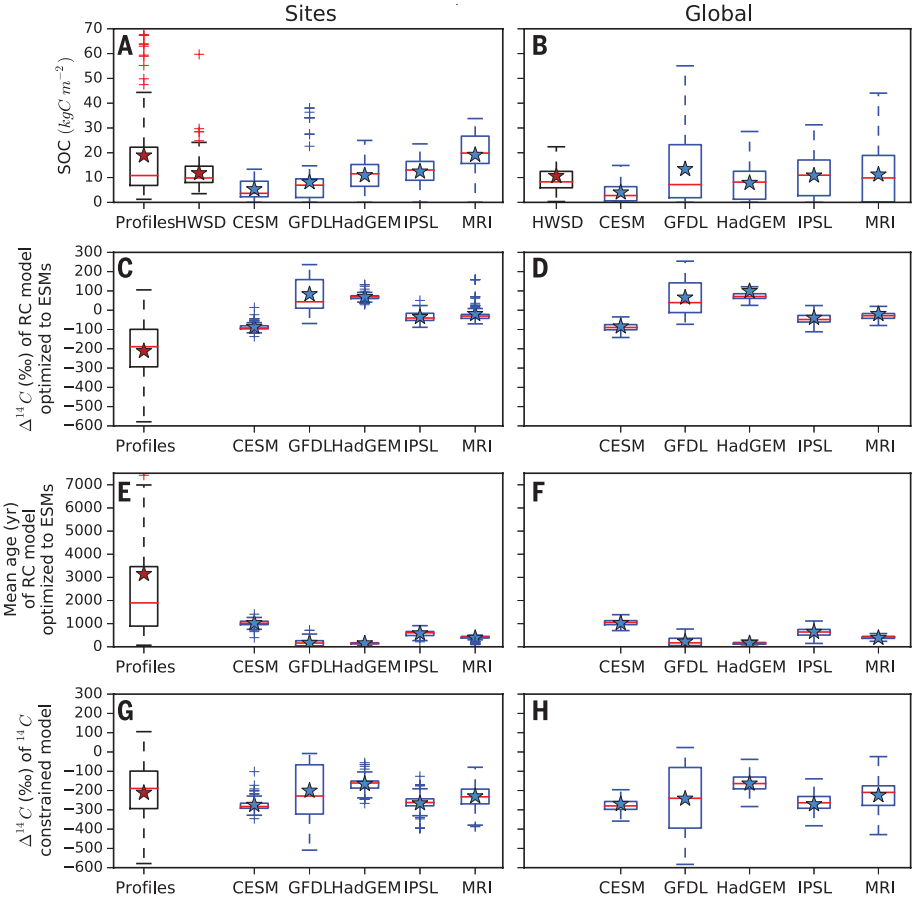

Fig. 2. Site and global values of soil carbon inventory, $\Delta^{14}C$, and mean age from observations and reduced complexity models. (**A** and **B**) SOC content of the original ESMs. (**C** and **D**) The $\Delta^{14}C$ of the reduced complexity model optimized to the original ESMs. (**E** and **F**) Corresponding mean age (**G** and **H**) The $\Delta^{14}C$ of the ^{14}C-constrained reduced complexity models. The left column shows the values of the models sampled at the locations of the individual soil profiles; the right column shows the global model distribution. Data from profile sites and the HWSD represent carbon content in the top 1 m of soil; data from ESMs are the total carbon stock. The star denotes the mean; the + symbol denotes outliers beyond the 25th and 75th percentiles.

The ^{14}C-derived mean ages indicate that organic carbon soil is often thousands of years old (*12–14*, *21*), which is an order of magnitude older than suggested by ESM turnover parameters. This discrepancy is likely a consequence of incomplete representation of key biogeochemical processes and difficulties in developing accurate parameterizations for soil carbon at a global scale. Most ESMs do not account for stabilization mechanisms whereby mineral interactions and aggregate formation protect soil organic matter from decomposition over centuries to millennia (*13*, *25–28*). Moreover, first-order decay, as represented in ESMs, may not capture the response of mineral-stabilized carbon to changes in soil moisture, temperature, and other conditions (*29–31*). In addition, some ESM turnover parameters are based on laboratory incubation studies, which are often biased fast compared with in situ decomposition rates (*32*). Finally, this set of ESMs did not explicitly resolve vertical differences in soil organic matter dynamics, which may cause underestimation of turnover times in deep soils with large carbon stocks (*21*, *25*, *33*, *34*).

Because the turnover times derived from ESMs were inconsistent with ^{14}C observations, we optimized the turnover parameters by fitting our RC models to the observations. We could then run the optimized RC models to reevaluate soil carbon storage for the transient 1% $year^{-1}$ simulations. For this inverse approach, we optimized RC model parameters in each grid cell containing an observation site (Fig. 2, G and H, and figs. S8 and S9). We optimized the τ of the slowest pool and the corresponding transfer coefficient into this pool based on the ^{14}C observations while holding soil inputs and τ for the faster pools at their ESM-derived values. The size of the slowest carbon pool was constrained by optimizing the turnover time and the transfer coefficient together using both ^{14}C and total carbon. Consequently, the optimized RC model had about the same total carbon stock as the original ESM, thereby maintaining consistency with carbon inventory data.

Downloaded from http://science.sciencemag.org/ on September 30, 2016

This optimization approach yielded τ_{slow} values of 3700 ± 2800 years for GFDL and 3500 ± 1300 years for HadGEM (using two-pool RC models), which were 16 to 17 times as long as the turnover times derived from the original ESMs.

For ESMs that included a passive pool, the optimization process yielded three distinct outcomes. For CESM, which has the largest passive pool (73% of soil carbon), the optimized $\tau_{passive}$ was 4500 years, which was 3.7 ± 1.5 times as long as $\tau_{passive}$ derived from the original model (Table 1). IPSL has a smaller fraction of passive carbon (46%) and therefore required a greater $\tau_{passive}$ (16,500 years) to obtain agreement with the observed $\Delta^{14}C$. For MRI, the passive pool size was too small (only 13% of soil carbon) to bring $\Delta^{14}C$ into alignment with the profile observations even after parameter optimization (fig. S10 and table S5). To adjust for MRI's potential bias in the passive pool size, we optimized r_f together with $\tau_{passive}$ and r_s to allow for simultaneous changes in slow and passive pool sizes. The resulting RC model for MRI was able to match observations (Fig. 2, G and H) with a passive pool fraction of 48% (see Methods and table S5). These results indicated that increasing the size and turnover time of the passive pool in ESMs would improve agreement with ^{14}C-based mean age estimates.

Bringing turnover time and carbon transfer parameters into agreement with ^{14}C observations had considerable consequences for the magnitude of the carbon-concentration feedback. Using the ^{14}C-based parameters, we conducted global transient simulations with each of the five RC models. These simulations showed that the soil as a whole (specifically the slow and passive pools) stored much less carbon in response to increasing levels of atmospheric CO_2, primarily as a consequence of reduced flow into the slow or passive pool. The soil carbon sink decreased from 32 ± 18% to 18 ± 12% (Table 1), corresponding to an absolute sink reduction of 170 ± 127 Pg C (Fig. 3). The magnitude of the soil sink reduction varied widely across the different models; those with larger and older passive fractions at the onset of the transient simulation (Table 1) generally had smaller sink reductions.

To assess the robustness of these sink reductions, we conducted a series of sensitivity experiments (see supplementary materials). We found that the sink reduction imposed by constraining the models with ^{14}C observations was robust to (i) turnover times optimized specifically for different biomes, (ii) spatial variation and magnitude of soil carbon stocks, and (iii) variations in $\Delta^{14}C$ across measurement sites (Table 2 and table S6). Sink reductions declined by a factor of 2 when the models were fit to an inventory that was 50% larger than the HWSD data set, suggesting that if soil carbon pools were larger in ESMs, ^{14}C-imposed sink reductions would be lower (*35*). Last, we used our RC model approach to analyze four fully coupled ESM runs (1pctCO_2) to address potential interactions between the carbon-climate and the carbon-concentration feedback. Constraints imposed by ^{14}C still reduced the sink by at least 40% on average (fig. S11 and table S7) in the fully coupled simulations (see supplementary materials).

We conclude that CMIP5 ESMs underestimated the mean age of soil carbon, especially for slow-cycling pools. By adjusting the turnover times of slow and passive pools to bring the models into alignment with ^{14}C observations, the potential for future soil carbon sequestration declined by 40 ± 27%. Although long-lived soil carbon pools consistent with old ^{14}C ages imply a similar potential for carbon storage at steady state, the time scale required to reach equilibrium is too long to mitigate the potentially damaging climate effects of rising CO_2 concentrations during the 21st century (fig. S2). These findings emphasize the need to incorporate ^{14}C and other diagnostics into ESM development and evaluation. In addition, models require better representation of long-term mechanisms of soil carbon stabilization such as organic matter-mineral interactions. Considered together with potential nutrient limitation of NPP inputs to soil (*36*), our analysis suggests that the carbon-concentration feedback may be weaker in the 21st century than currently expected from ESMs. Therefore, a greater fraction of CO_2 emissions than previously thought could remain in the atmosphere and contribute to global warming.

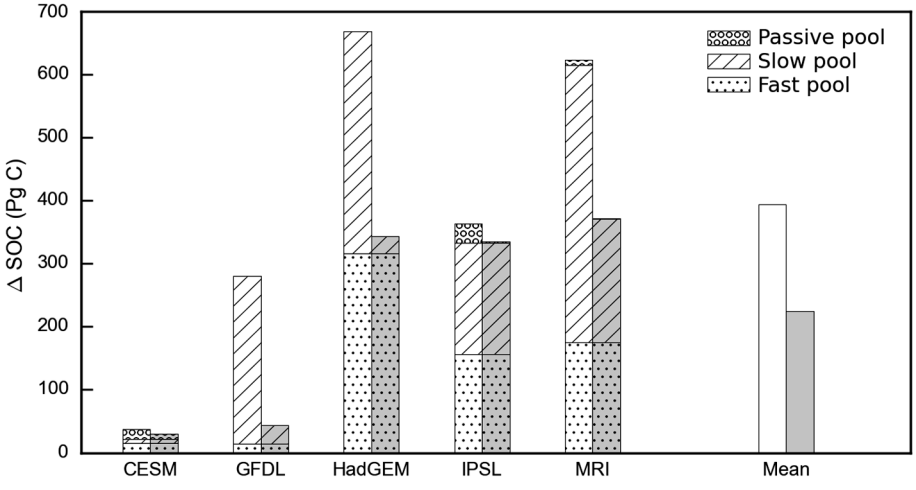

Fig. 3. Absolute change in SOC content from the reduced complexity model fit to the original ESM (bars with white background) and the estimate obtained by applying the ^{14}C constraint to the reduced complexity model (bars with gray background). The estimates on the right side show the total carbon content (sum of fast, slow, and passive) averaged across all the models, before and after applying the radiocarbon constraint.

REFERENCES AND NOTES

1. P. Friedlingstein *et al.*, *J. Clim.* **27**, 511–526 (2014).
2. IPCC, Summary for Policymakers. In *Climate Change 2013: The Physical Science Basis. Contribution of Working Group I to the Fifth Assessment Report of the Intergovernmental Panel on Climate Change*. T. F. Stocker *et al.*, Eds. (IPCC, Cambridge and New York, 2013).
3. V. K. Arora *et al.*, *J. Clim.* **26**, 5289–5314 (2013).
4. C. D. Jones, P. M. Cox, C. Huntingford, *Tellus B Chem. Phys. Meterol.* **58**, 603–613 (2006).
5. K. E. O. Todd-Brown *et al.*, *Biogeosciences* **11**, 2341–2356 (2014).
6. D. P. van Vuuren *et al.*, *Clim. Change* **109**, 5–31 (2011).
7. J. Lichter *et al.*, *Glob. Change Biol.* **14**, 2910–2922 (2008).
8. W. H. Schlesinger, J. Lichter, *Nature* **411**, 466–469 (2001).
9. J. W. Harden, R. K. Mark, E. T. Sundquist, R. F. Stallard, *Science* **258**, 1921–1924 (1992).
10. W. H. Schlesinger, *Nature* **348**, 232–234 (1990).
11. B. O'Brien, J. Stout, *Soil Biol. Biochem.* **10**, 309–317 (1978).
12. J. B. Gaudinski, S. E. Trumbore, E. A. Davidson, S. H. Zheng, *Biogeochemistry* **51**, 33–69 (2000).
13. M. S. Torn, S. E. Trumbore, O. A. Chadwick, P. M. Vitousek, D. M. Hendricks, *Nature* **389**, 170–173 (1997).
14. S. E. Trumbore, J. W. Harden, *J. Geophys. Res.* **102**, 28817–28830 (1997).
15. N. Carvalhais *et al.*, *Nature* **514**, 213–217 (2014).
16. A. D. Friend *et al.*, *Proc. Natl. Acad. Sci. U.S.A.* **111**, 3280–3285 (2014).
17. X. Wang *et al.*, *Glob. Change Biol.* **20**, 3229–3237 (2014).
18. W. Knorr, I. C. Prentice, J. I. House, E. A. Holland, *Nature* **433**, 298–301 (2005).
19. C. D. Koven *et al.*, *Biogeosciences* **12**, 5211–5228 (2015).
20. K. E. Taylor, R. J. Stouffer, G. A. Meehl, *Bull. Am. Meteorol. Soc.* **93**, 485–498 (2012).
21. J. A. Mathieu, C. Hatté, J. Balesdent, É. Parent, *Glob. Change Biol.* **21**, 4278–4292 (2015).
22. S. Trumbore, *Ecol. Appl.* **10**, 399–411 (2000).
23. W. Feng *et al.*, *Soil Biol. Biochem.* **100**, 118–124 (2016).
24. E. Shevliakova *et al.*, *Global Biogeochem. Cycles* **23**, GB2022 (2009).
25. M. W. Schmidt *et al.*, *Nature* **478**, 49–56 (2011).
26. M. Lützow *et al.*, *Eur. J. Soil Sci.* **57**, 426–445 (2006).
27. J. A. Dungait, D. W. Hopkins, A. S. Gregory, A. P. Whitmore, *Glob. Change Biol.* **18**, 1781–1796 (2012).
28. M. Kleber, R. Mikutta, M. S. Torn, R. Jahn, *Eur. J. Soil Sci.* **56**, 717–725 (2005).
29. J. S. Clemente, A. J. Simpson, M. J. Simpson, *Org. Geochem.* **42**, 1169–1180 (2011).
30. C. Koven *et al.*, *Biogeosciences* **10**, 7109–7131 (2013).
31. B. Ahrens, M. C. Braakhekke, G. Guggenberger, M. Schrumpf, M. Reichstein, *Soil Biol. Biochem.* **88**, 390–402 (2015).
32. G. B. Bonan, M. D. Hartman, W. J. Parton, W. R. Wieder, *Glob. Change Biol.* **19**, 957–974 (2013).
33. C. R. Lawrence, J. W. Harden, X. Xu, M. S. Schulz, S. E. Trumbore, *Geoderma* **247–248**, 73–87 (2015).
34. C. Rumpel, I. Kögel-Knabner, *Plant Soil* **338**, 143–158 (2011).

Downloaded from http://science.sciencemag.org/ on September 30, 2016

35. Y. Luo *et al.*, *Global Biogeochem. Cycles* **30**, 40–56 (2016).
36. W. R. Wieder, C. C. Cleveland, W. K. Smith, K. Todd-Brown, *Nat. Geosci.* **8**, 441–444 (2015).

ACKNOWLEDGMENTS

We thank C. Hatté for sharing her compilation of published ^{14}C profiles. We received funding support from the Climate and Environmental Sciences Division of Biological and Environmental Research (BER) in the U.S. Department of Energy Office of Science. This included support from the Regional and Global Climate Modeling Program to the Biogeochemical Cycles Feedbacks Science Focus Area and several grants from the Terrestrial Ecosystem Science Program (DESC0014374 and DE-AC02-05CH11231). J.W.H. serves as chair of the science steering group for International Soil Carbon Network (http://iscn.fluxdata.org); however, the work of this publication reflects efforts on behalf of the U.S. Geological Survey Scientist Emeritus Program, which provided IT and infrastructure support. The model simulations analyzed in this study were obtained from the Earth System Grid Federation CMIP5 online portal hosted by the Program for Climate Model Diagnosis and Intercomparison at Lawrence Livermore National Laboratory (https://pcmdi.llnl.gov/projects/esgf-llnl/).

SUPPLEMENTARY MATERIALS

www.sciencemag.org/content/353/6306/1419/suppl/DC1
Materials and Methods
Sensitivity Analysis Results
Fully Coupled Simulation Analysis
Figs. S1 to S11
Tables S1 to S7
References (*37*–*102*)

27 September 2015; accepted 29 August 2016
10.1126/science.aad4273

ATMOSPHERIC SCIENCE

An unexpected disruption of the atmospheric quasi-biennial oscillation

Scott M. Osprey,[1]* Neal Butchart,[2] Jeff R. Knight,[2] Adam A. Scaife,[2,3] Kevin Hamilton,[4] James A. Anstey,[5] Verena Schenzinger,[1] Chunxi Zhang[4]

One of the most repeatable phenomena seen in the atmosphere, the quasi-biennial oscillation (QBO) between prevailing eastward and westward wind jets in the equatorial stratosphere (approximately 16 to 50 kilometers altitude), was unexpectedly disrupted in February 2016. An unprecedented westward jet formed within the eastward phase in the lower stratosphere and cannot be accounted for by the standard QBO paradigm based on vertical momentum transport. Instead, the primary cause was waves transporting momentum from the Northern Hemisphere. Seasonal forecasts did not predict the disruption, but analogous QBO disruptions are seen very occasionally in some climate simulations. A return to more typical QBO behavior within the next year is forecast, although the possibility of more frequent occurrences of similar disruptions is projected for a warming climate.

Aside from those variations governed by the changing seasons or diurnal cycle, the quasi-biennial oscillation (QBO) is arguably the most repeatable mode of natural variability seen anywhere in the atmosphere. It was first discovered in the late 1950s (*1*, *2*) and features alternating eastward and westward wind jets descending through the equatorial stratosphere at roughly 1 km per month (*3*), from ~50 km (~1 hPa) down to ~16 km (~100 hPa), with the quasi-biennial periodicity being most evident in the ~20- to 40-km layer. Since the 1950s, the period of the oscillation has varied between 22 to 36 months. The oscillation is nearly zonally uniform and so is seen in both local observations and in longitudinally averaged data with roughly the same amplitude, at least for monthly means, and is confined to equatorial latitudes (*4*, *5*). On the other hand, its influence is felt throughout the atmosphere. For example, the fate of ash and sulfur from large volcanic eruptions in the tropics is affected by the QBO (*6*), and there are known surface weather and climate impacts resulting from the QBO's extratropical teleconnections (*7*–*9*); such teleconnections may provide an important source of predictability that can be exploited with seasonal and decadal prediction systems (*10*) owing to the regularity of the QBO. Disruption to the regular QBO behavior is therefore expected to have potentially far-reaching consequences.

In November 2015, the QBO winds were westward above 30 km (~15 hPa) and eastward beneath. During November and December 2015, the westward phase propagated downward as is typical (Fig. 1A), but by January 2016, its descent had stalled. Although by itself this was not unusual (Fig. 1A, during early 2009, just above 20 hPa), the stalling was followed by the unexpected formation of a second westward layer interrupting the lower stratospheric eastward phase (near 40 hPa). Subsequently, the descending westward phase in the upper stratosphere began to recede, while the anomalous westward jet below strengthened and began to descend. Here, we quantify the extent to which this behavior is anomalous compared with the previous six decades of observations containing 27 QBO cycles.

The state of the QBO is often characterized by using an updated time series of monthly mean balloon observations of near-equatorial zonal winds (*11*). This record spans essentially the entire era of operational tropical stratospheric wind soundings from January 1956 to present day and provides 724 monthly profiles of the equatorial zonal wind. For each of these profiles, we identified a "best match" month having the smallest root mean square (RMS) difference over seven levels spanning 70 to 10 hPa (Fig. 1B). For the vast majority of months, there is a close match with another month in the record, and RMS differences are typically 2 to 3 ms^{-1}. Before 2016, the month with the largest RMS difference with its best historical match was December 1988 (4.8 ms^{-1}). The unprecedented behavior in 2016 is apparent because February, March, and April 2016 have RMS differences of 6.7, 10.1, and 6.8 ms^{-1}, respectively.

Canonical theory describes the QBO as driven by the interaction of the zonal mean flow, with a spectrum of vertically propagating waves forced in the lower atmosphere and dissipated within the stratosphere (*12*, *13*). Mean-flow driving is proportional to local vertical wind shear so that where there is westward vertical shear, the mean flow is accelerated westward, and vice versa for eastward vertical shear. This leads to the downward phase propagation of the alternating QBO wind regimes seen throughout the observed record (Fig. 1A). The selective filtering of upward propagating waves by low-level jets then leads to opposite-sign acceleration at higher levels in a "shadowing effect." Climatological large-scale upwelling in the equatorial stratosphere (*14*) opposes the downward phase propagation (*15*) and can contribute to the descent stalling, whereas the forcing of the westward phase can be supplemented by horizontally propagating quasi-stationary planetary waves from the extratropics, particularly in boreal winter (*16*–*19*).

Because the strong westward accelerations near 30 to 50 hPa in late 2015 and early 2016 occur in a region of eastward mean flow shear, they cannot be accounted for by the canonical theory. On the other hand, fluxes of wave activity (Fig. 2A, arrows) averaged for February 2016 suggest that waves propagating from the Northern Hemisphere might be the most likely cause of the westward acceleration (planetary scale Rossby waves propagating from the extratropics can only transport westward momentum). Typically, during winter months upward wave activity fluxes enter the stratosphere at mid- to high latitudes then refract equatorward. In February 2016, the anomalously strong high-latitude eastward jet was unusually flanked by subtropical

[1]National Centre for Atmospheric Science (NCAS)–Climate, University of Oxford, Atmospheric, Oceanic and Planetary Physics, Clarendon Laboratory, Parks Road, Oxford, OX1 3PU, UK. [2]Met Office Hadley Centre, FitzRoy Road, Exeter, Devon, EX1 3PB, UK. [3]Department of Mathematics and Computer Science, University of Exeter, Exeter, UK. [4]International Pacific Research Center, University of Hawai`i, Honolulu, USA. [5]Canadian Centre for Climate Modelling and Analysis, University of Victoria, Victoria, British Columbia, Canada.
*Corresponding author. Email: scott.osprey@physics.ox.ac.uk

Downloaded from http://science.sciencemag.org/ on September 30, 2016

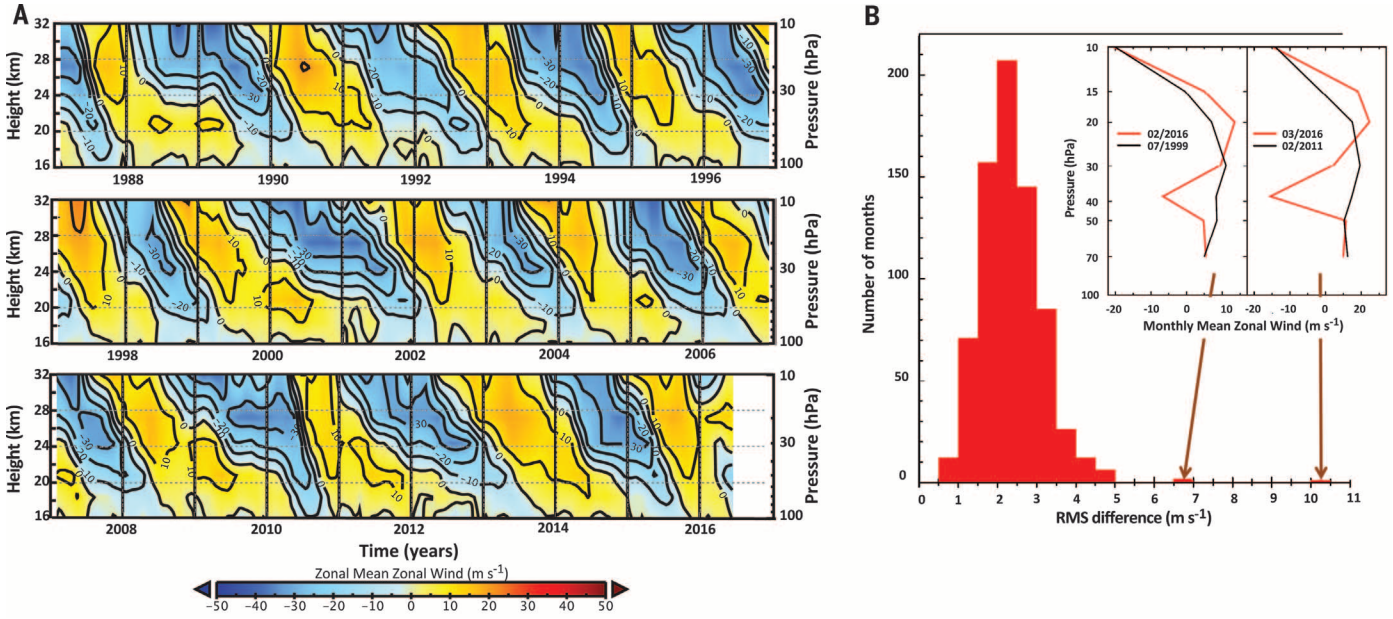

Fig. 1. Evolution of the QBO showing regular repeating wind structures and anomalous westward winds in 2016. (**A**) Vertical profile time series of monthly mean zonal mean eastward wind averaged over 5°S–5°N, showing descending eastward (yellow) and westward (blue) wind regimes (*25*) for the past 13 observed QBO cycles. (**B**) Histogram of RMS differences in monthly mean eastward wind averaged over the 70, 50, 40, 30, 20, 15, and 10 hPa levels between each of the 724 monthly profiles from all 27 observed QBO cycles and its closest match in the record (*11*). Only matches between profiles separated by more than 6 months were evaluated in order to ensure only matches from earlier or later QBO cycles were considered. (Insets) Monthly mean profiles together with their best matches for February and March 2016.

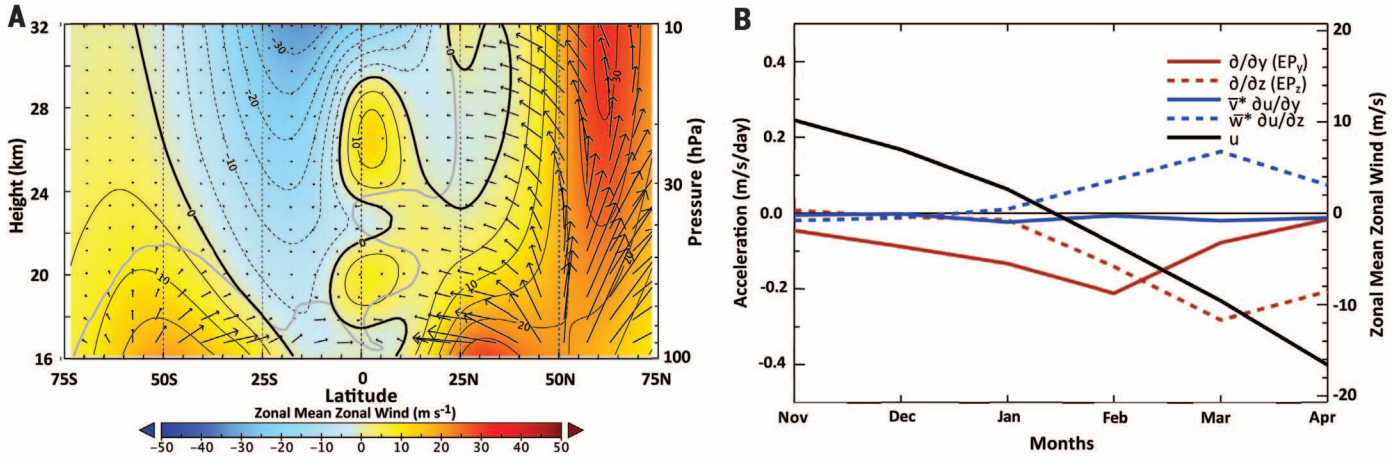

Fig. 2. Wave-driven circulation changes associated with the formation of 40-hPa westward *u* (where *u* is the zonal velocity field). (**A**) Latitude-log-pressure plot showing February 2016 mean zonal mean wind (solid and black contours), Eliassen-Palm (EP) flux (*26*) (black arrows), and their extent (gray contour). EP flux is indicative of wave propagation direction and shows wave activity leaving the troposphere near 50°N and entering the tropics near 40 hPa. (**B**) Monthly mean time series of horizontal (solid lines) and vertical (dotted lines) contributions of EP flux divergence (red) and *u*-advection (blue), averaged over 5°S–5°N. $\overline{v}^*$ and $\overline{w}^*$ are the northward and upward residual mean winds, respectively (*26*). Westward acceleration evident near 40 hPa started in November 2015 and continued during January–February 2016. Monthly mean *u* time series (solid black lines) indicates development of easterly anomaly. Diagnostics derived from 6-hourly global operational analysis data (*25*, *27*).

westward winds above ~30 hPa (Fig. 2A). Because these westward winds do not favor Rossby wave propagation (*21*), the wave flux is confined to the region below, turning horizontal and equatorward (Fig. 2A). The QBO so happened to be in its eastward phase at this level, which allows the waves to propagate all the way to the equator near 40 hPa. Summertime westward winds prevent further propagation across the equator into the Southern Hemisphere. The resultant wave dissipation causes a westward acceleration at the equator.

Confirmation of the above analysis is provided by the monthly mean momentum budget at 40 hPa for late 2015 and early 2016 (Fig. 2B). Dominating the westward acceleration of the equatorial winds at this level up to February 2016 is the contribution from the horizontally propagating waves. This contribution declines once the winds at this level become westward (negative) in February, leaving a balance between the driving from the vertically propagating waves and the opposing upwelling and a return to the standard QBO paradigm. As this westward jet develops near 40 hPa, eastward acceleration appears near 20 to 30 hPa in the familiar "shadowing" pattern predicted by the canonical theory.

Downloaded from http://science.sciencemag.org/ on September 30, 2016

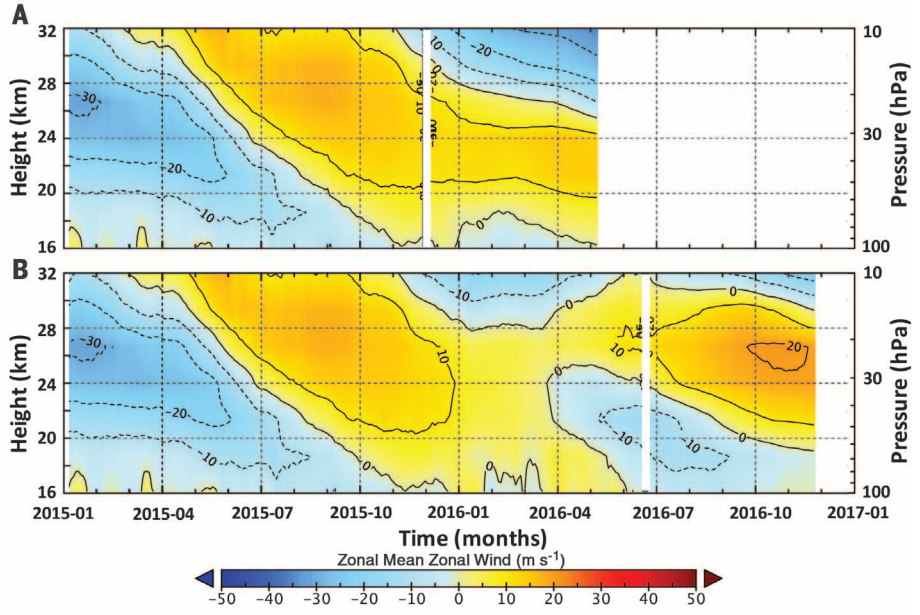

Fig. 3. Long-range forecasts of the QBO from before and during the 2016 disruption. (**A**) Forecasts from 1 December show the usual phase progression of descending eastward wind in the lower stratosphere. (**B**) Forecasts from June show growth, descent, and decay of the anomalies in westward wind near 50 hPa and a second period of eastward QBO winds in late 2016.

The QBO's long period and great regularity make it the most predictable long-term atmospheric variation after the annual cycle. Tests over many past cycles of the QBO confirm that this normally allows skilful predictions out to a few years ahead (*10*), yet the recent disruption of the oscillation shows very different characteristics. A seasonal climate prediction made in December 2015 and initialized with the atmospheric and oceanic state at the time (*20*) showed over the subsequent months a clear continuation and descent of the eastward phase of the QBO into the lower stratosphere, with no sign of the spontaneous appearance of westward flow in the lower stratosphere as occurred in observations (Fig. 3A). This is in sharp contrast to the usual skillful predictions of the QBO out to years ahead (*10*), and therefore the recent disruption of the QBO cycle was not predicted, even just 1 month in advance.

This low predictability is consistent with the origin of the QBO's disruption being found in the extratropical atmosphere, where variability is inherently less predictable. The occurrence of a disruption to the eastward phase of the oscillation is also consistent with an extratropical origin from the winter hemisphere because transient Rossby waves occurring in the winter stratosphere can only propagate into eastward flow and

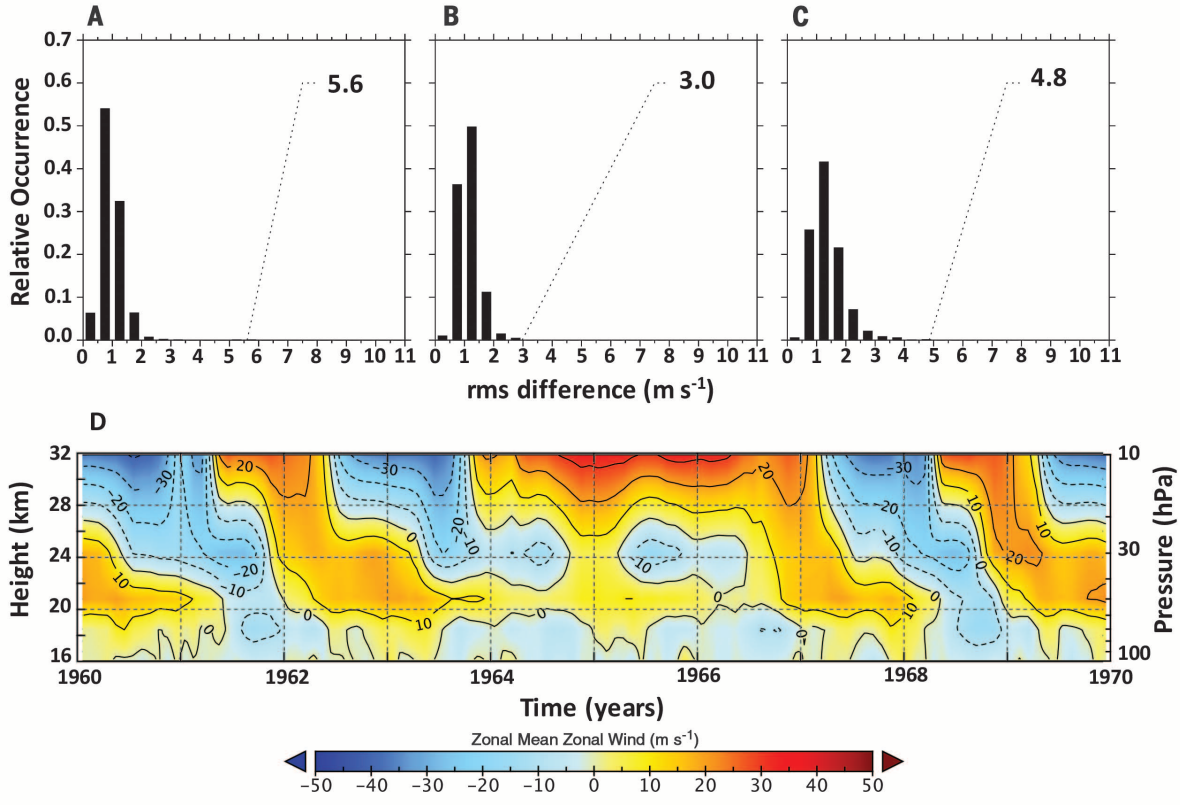

Fig. 4. Extreme QBO activity diagnosed in contributions to the Coupled Model Intercomparison Project Phase 5 (CMIP5). (**A** to **C**) Best-match RMS differences for (A) HadGEM2-CCS, (B) MIROC-ESM-CHEM, and (C) MPI-ESM-MR (*28*). Although outliers occur in the three model simulations, only one model produced analogous westward jet formation seen in observations. (**D**) The formation of westward *u* within a descending eastward jet is seen during 1964 in run r1i1p1 of MPI-ESM-MR. Anomalous westward *u* is seen near 100 hPa, and strengthened 10 hPa eastward *u* last until 1967. Only one event occurred during the 145-year run.

Downloaded from http://science.sciencemag.org/ on September 30, 2016

deliver westward acceleration to the mean flow. Furthermore, the stronger tropical upwelling during Boreal winter slows down the QBO's descent, allowing more time for the extratropical waves to impact during this particular phase.

Of course, it is also possible that our current numerical models can not properly represent the processes disrupting the QBO. To investigate this, the foregoing RMS analysis that was applied to the observational record was applied to historical global climate model runs so as to identify possible analogous events (Fig. 4, A to C). Among the available models that produce a QBO internally, only one rarely produced behavior similar to the observed disruption, with an example shown in Fig. 4D. The extreme profiles resemble those observed during 2016 with a thin layer of westward wind appearing within an otherwise eastward QBO phase.

What will happen next? The recent disruption of the QBO is a rare event that occurs in the northern winter. The forecast initialized after the disruption (Fig. 3B) suggests that the QBO will return to more regular phase progression over the coming year. The westward jet that suddenly appeared in the lower stratosphere is predicted to amplify in the summer of 2016 and progress downward with time. Eastward flow then descends from the 20-hPa level and dominates the lower stratospheric flow toward the end of 2016, returning the QBO to its typical behavior. We then expect regular and predictable QBO cycling to continue from 2017, as occurs in the available climate models (Fig. 4D). Nonetheless, as the climate warms in the future, climate models that simulate these events suggest that similar disruptions will occur up to three times every 100 years for the more extreme of the standard climate change scenarios. This is consistent with a projected strengthening of the Brewer-Dobson circulation due to increasing stratospheric wave activity (*14*) and the recently observed weakening of the QBO amplitude in the lower stratosphere (*21*) under climate change. However, robustly modeling how the QBO and its underlying processes and external influences will change in the future remains elusive.

There is a further outcome of the 2016 disruption of the QBO. After an eastward QBO at the onset of the 2015–2016 winter, the QBO at the onset of the coming winter of 2016–2017 was expected to be westward. The disruption of early 2016 means that an eastward QBO phase is now again expected in the lower stratosphere. Because of the expected QBO influence on the Atlantic jet stream, this increases the risk of a strong jet, winter storms, and heavy rainfall over northern Europe in the coming winter (*22*, *23*).

Note added in proof: A similar finding was published by Newman *et al.* (*24*) during the final revision period of the present study.

REFERENCES AND NOTES

1. R. A. Ebdon, *Q. J. R. Meteorol. Soc.* **86**, 540–542 (1960).
2. R. J. Reed, W. J. Campbell, L. A. Rasmussen, D. G. Rogers, *J. Geophys. Res.* **66**, 813–818 (1961).
3. M. P. Baldwin *et al.*, *Rev. Geophys.* **39**, 179–229 (2001).
4. J. M. Wallace, *Rev. Geophys.* **11**, 191 (1973).
5. P. H. Haynes, *Q. J. R. Meteorol. Soc.* **124**, 2645–2670 (1998).
6. U. Niemeier *et al.*, *Atmos. Chem. Phys.* **9**, 9043–9057 (2009).
7. J. R. Holton, H.-C. Tan, *J. Atmos. Sci.* **37**, 2200–2208 (1980).
8. J. A. Anstey, T. G. Shepherd, *Q. J. R. Meteorol. Soc.* **140**, 1–21 (2014).
9. J. Kidston *et al.*, *Nat. Geosci.* **8**, 433–440 (2015).
10. A. A. Scaife *et al.*, *Geophys. Res. Lett.* **41**, 1752–1758 (2014).
11. B. Naujokat, *J. Atmos. Sci.* **43**, 1873–1877 (1986).
12. R. S. Lindzen, J. R. Holton, *J. Atmos. Sci.* **25**, 1095–1107 (1968).
13. J. R. Holton, R. S. Lindzen, *J. Atmos. Sci.* **29**, 1076–1080(1972).
14. N. Butchart, *Rev. Geophys.* **52**, 157–184 (2014).
15. A. R. Plumb, R. C. Bell, *Q. J. R. Meteorol. Soc.* **108**, 335–352 (1982).
16. R. E. Dickinson, *J. Atmos. Sci.* **25**, 984–1002 (1968).
17. T. J. Dunkerton, *Atmos.-Ocean* **21**, 55–68 (1983).
18. K. Hamilton, A. Hertzog, F. Vial, G. Stenchikov, *J. Atmos. Sci.* **61**, 383–402 (2004).
19. J. S. Kinnersley, S. Pawson, *J. Atmos. Sci.* **53**, 1937–1949 (1996).
20. C. MacLachlan *et al.*, *Q. J. R. Meteorol. Soc.* **141**, 1072–1084 (2015).
21. Y. Kawatani, K. Hamilton, *Nature* **497**, 478–481 (2013).
22. R. A. Ebdon, *Aust. Meteorol. Mag.* **104**, 282–285 (1975).
23. C. Huntingford *et al.*, *Nat. Clim. Change* **4**, 769–777 (2014).
24. P. A. Newman, L. Coy, S. Pawson, L. R. Lait, *Geophys. Res. Lett.* 10.1002/2016GL070373 (2016).
25. D. P. Dee *et al.*, *Q. J. R. Meteorol. Soc.* **137**, 553–597 (2011).
26. D. G. Andrews, M. E. McIntyre, *J. Atmos. Sci.* **33**, 2031–2048 (1976).
27. NCAS British Atmospheric Data Centre, European Centre for Medium-Range Weather Forecasts: ECMWF operational analysis: Assimilated Data (2006); http://catalogue.ceda.ac.uk/uuid/c46248046f6ce34fc7660a36d9b10a71.
28. E. P. Gerber *et al.*, *Bull. Am. Meteorol. Soc.* **93**, 845–859 (2012).

ACKNOWLEDGMENTS

We thank the European Centre for Medium-Range Weather Forecasts for providing ERA-Interim and Operational Analysis data (www.ecmwf.int/en/forecasts) and the Freie Universität Berlin for providing radiosonde data (www.geo.fu-berlin.de/en/met/ag/strat/produkte/qbo). The CMIP5 data was obtained from the British Atmospheric Data Centre (browse.ceda.ac.uk/browse/badc/cmip5). A summary of data used in the study is listed in table S1. S.M.O. was supported by UK Natural Environment Research Council grants NE/M005828/1 and NE/P006779/1. A.A.S., J.R.K., and N.B. were supported by the Joint UK Business, Energy and Industrial Strategy/Defra Met Office Hadley Centre Climate Programme (GA01101). A.A.S. and J.R.K. were additionally supported by the EU Seventh Framework Programme SPECS (Seasonal-to-decadal climate Prediction for the improvement of European Climate Services) project. We acknowledge the scientific guidance of the World Climate Research Programme for helping motivate this work, coordinated under the framework of the Stratosphere-troposphere Processes and their Role in Climate (SPARC) QBOi activity led by S.M.O., J.A.A., N.B., and K.H. The analysis of observations and reanalyses was performed by K.H., C.Z., S.M.O., J.A.A., and N.B. J.R.K. and A.A.S. provided the analysis of the seasonal forecasts, and V.S. identified analogous events in global climate model output. A.A.S. first alerted us to the disruption of the QBO in observational data. All authors were equally involved in the interpretation of the results and preparation of the manuscript.

SUPPLEMENTARY MATERIALS

www.sciencemag.org/content/353/6306/1424/suppl/DC1
Table S1

2 July 2016; accepted 29 August 2016
10.1126/science.aah4156

ATMOSPHERIC OXYGEN

A Pleistocene ice core record of atmospheric O_2 concentrations

D. A. Stolper,[1]* M. L. Bender,[1,2] G. B. Dreyfus,[1,3]† Y. Yan,[1] J. A. Higgins[1]

The history of atmospheric O_2 partial pressures (P_{O_2}) is inextricably linked to the coevolution of life and Earth's biogeochemical cycles. Reconstructions of past P_{O_2} rely on models and proxies but often markedly disagree. We present a record of P_{O_2} reconstructed using O_2/N_2 ratios from ancient air trapped in ice. This record indicates that P_{O_2} declined by 7 per mil (0.7%) over the past 800,000 years, requiring that O_2 sinks were ~2% larger than sources. This decline is consistent with changes in burial and weathering fluxes of organic carbon and pyrite driven by either Neogene cooling or increasing Pleistocene erosion rates. The 800,000-year record of steady average carbon dioxide partial pressures (P_{CO_2}) but declining P_{O_2} provides distinctive evidence that a silicate weathering feedback stabilizes P_{CO_2} on million-year time scales.

The importance of O_2 to biological and geochemical processes has led to a long-standing interest in reconstructing past atmospheric O_2 partial pressures (P_{O_2}, reported at standard temperature and pressure) (*1*–*12*). However, there is no consensus on the history of Phanerozoic P_{O_2}, with reconstructions disagreeing by as much as 0.2 atm, the present-day pressure of O_2 in the atmosphere (e.g., *7*, *10*). Even over the past million years, it is not known whether atmospheric O_2 concentrations varied or whether the O_2 cycle was in steady state (Fig. 1A). Knowledge of P_{O_2} over the past million years could provide new insights into the O_2 cycle on geologic time scales and serve as a test for models and proxies of past P_{O_2}. Here we present a primary record of P_{O_2} over the past 800,000 years, reconstructed using measured O_2/N_2 ratios of ancient air trapped in polar ice.

O_2/N_2 ratios of this kind have been extensively used to date ice cores on the basis of the correlation between O_2/N_2 and local summertime

[1]Department of Geosciences, Princeton University, Princeton, NJ 08544, USA. [2]Institute of Oceanology, Shanghai Jiao Tong University, Shanghai 200240, China. [3]Laboratoire des Sciences du Climat et de l'Environnement, Gif-sur-Yvettte, France.
***Corresponding author. Email: dstolper@princeton.edu**
†Present address: U.S. Department of Energy, Washington, DC 20585, USA.

Downloaded from http://science.sciencemag.org/ on September 30, 2016

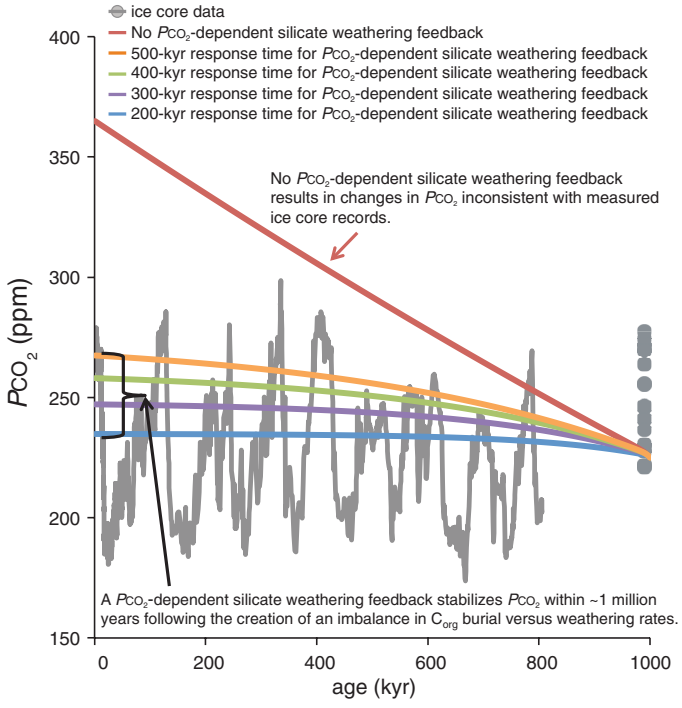

Fig. 3. Comparison of calculated and measured P_{CO_2} values due to declining P_{O_2} with and without a P_{CO_2}-dependent silicate weathering feedback. Inclusion of a silicate weathering feedback with geologically reasonable response times [200,000 to 500,000 years (*41*)] stabilizes P_{CO_2} within ~1 million years. Thus, increased silicate weathering rates could have compensated for enhanced CO_2 fluxes from increased net C_{org} oxidation more than 800,000 years ago. The P_{CO_2} records are continuous only from 800,000 years to the present. The model used to calculate P_{CO_2} values is described in (*19*); the measured P_{CO_2} values are from (*38*) and (*39*). ppm, parts per million.

the past 800,000 years (*37*–*39*) (Fig. 3). To understand how changes in P_{O_2} influence P_{CO_2}, we developed a simple model of the carbon cycle that allows for changes in weathering and burial rates of carbonates, C_{org}, and silicates (*19*). In the absence of any P_{CO_2}-dependent feedbacks, a constant decline in $\delta O_2/N_2$ of 8.4‰ over the past million years from a net imbalance in C_{org} fluxes causes P_{CO_2} to rise by ~140 parts per million over the same time frame. Such a rise is inconsistent with the P_{CO_2} record (Fig. 3). A P_{CO_2}-dependent silicate weathering feedback (*40*) can account for the higher CO_2 flux if silicate weathering is enhanced by ~6% relative to volcanic outgassing. For example, response times for silicate weathering of 200,000 to 500,000 years (*41*) stabilize P_{CO_2} levels within ~1 million years (Fig. 3).

Changes in Cenozoic climate began millions of years before the start of our ice core–based $\delta O_2/N_2$ record 800,000 years ago (e.g., *2*, *30*, *34*, *35*). Thus, we suggest that modest enhancements in silicate weathering would already have stabilized the portion of the P_{CO_2} ice core record that is controlled by differences in C_{org} and pyrite burial and oxidation. Thus, the combination of changing P_{O_2} and constant average P_{CO_2} provides distinctive evidence for feedbacks that regulate P_{CO_2} on geologic time scales (*37*). Lastly, a 2% imbalance in O_2 fluxes results in only a ~0.1‰ shift in the $^{13}C/^{12}C$ ratio of buried carbon (*19*).

Our results provide a primary record of declining P_{O_2} over the past 800,000 years sustained by a ~2% imbalance between O_2 sources and sinks. Critically, this decline is consistent with previously proposed and relatively simple models that invoke either the effects of increased Pleistocene erosion rates or decreased ocean temperature to explain feedbacks in the global cycles of carbon, sulfur, and O_2—and the effects of both could have contributed to the observed decline in P_{O_2}. Regardless, creating primary records of past P_{O_2} is the necessary first step in identifying the fundamental processes that regulate P_{O_2} on geological time scales. Given evidence that both global erosion rates and temperature have changed markedly over the Cenozoic (*42*), the ideas presented here may have implications for the history of P_{O_2} beyond the Pleistocene.

REFERENCES AND NOTES

1. L. R. Kump, R. M. Garrels, *Am. J. Sci.* **286**, 337–360 (1986).
2. N. Shackleton, *Geol. Soc. Lond. Spec. Publ.* **26**, 423–434 (1987).
3. R. A. Berner, D. E. Canfield, *Am. J. Sci.* **289**, 333–361 (1989).
4. L. A. Derry, C. France-Lanord, *Paleoceanography* **11**, 267–275 (1996).
5. K. W. Hansen, K. Wallmann, *Am. J. Sci.* **303**, 94–148 (2003).
6. N. M. Bergman, T. M. Lenton, A. J. Watson, *Am. J. Sci.* **304**, 397–437 (2004).
7. P. G. Falkowski *et al.*, *Science* **309**, 2202–2204 (2005).
8. R. S. Arvidson, F. T. Mackenzie, M. Guidry, *Am. J. Sci.* **306**, 135–190 (2006).
9. R. A. Berner, *Geochim. Cosmochim. Acta* **70**, 5653–5664 (2006).
10. R. A. Berner, *Am. J. Sci.* **309**, 603–606 (2009).
11. I. J. Glasspool, A. C. Scott, *Nat. Geosci.* **3**, 627–630 (2010).
12. R. Tappert *et al.*, *Geochim. Cosmochim. Acta* **121**, 240–262 (2013).
13. M. L. Bender, *Earth Planet. Sci. Lett.* **204**, 275–289 (2002).
14. K. Kawamura *et al.*, *Nature* **448**, 912–916 (2007).
15. M Suwa, M. L. Bender, *Quat. Sci. Rev.* **27**, 1093–1106 (2008).
16. A. Landais *et al.*, *Clim. Past* **8**, 191–203 (2012).
17. L. Bazin *et al.*, *Clim. Past* **12**, 729–748 (2016).
18. M. E. Smith, thesis, Princeton University, Princeton, NJ (1998).
19. Materials and methods are available as supplementary materials on *Science* Online.
20. M. Battle *et al.*, *Nature* **383**, 231 (1996).
21. M. Bender, T. Sowers, V. Lipenkov, *J. Geophys. Res. Atmos.* **100**, 18651–18660 (1995).
22. T. Kobashi *et al.*, *Atmos. Chem. Phys.* **15**, 13895–13914 (2015).
23. J. P. Severinghaus, R. Beaudette, M. A. Headly, K. Taylor, E. J. Brook, *Science* **324**, 1431–1434 (2009).
24. H. Craig, Y. Horibe, T. Sowers, *Science* **242**, 1675–1678 (1988).
25. R. A. Berner, *Geology* **34**, 413–415 (2006).
26. H. D. Holland, *Geochim. Cosmochim. Acta* **66**, 3811–3826 (2002).
27. The imbalance is calculated as follows: The total imbalance (moles per million years) for O_2 is $0.0084 \times n_{O_2}$, where n_{O_2} is the total number of moles of O_2 in the atmosphere. The O_2 flux is n_{O_2} divided by its residence time. The residence time of O_2 is about 2 million years. The percent imbalance is the total imbalance divided by the total flux, or $0.0084 n_{O_2}/(n_{O_2}/2) = 0.017$ (1.7%).
28. F. Herman *et al.*, *Nature* **504**, 423–426 (2013).
29. J. K. Willenbring, F. von Blanckenburg, *Nature* **465**, 211–214 (2010).
30. M. A. Torres, A. J. West, G. Li, *Nature* **507**, 346–349 (2014).
31. A. S. Colman, F. T. Mackenzie, H. D. Holland, *Science* **275**, 406–407 (1997).
32. P. Van Cappellen, E. D. Ingall, *Science* **271**, 493–496 (1996).
33. J. I. Hedges, R. G. Keil, *Mar. Chem.* **49**, 81–115 (1995).
34. C. H. Lear, H. Elderfield, P. A. Wilson, *Science* **287**, 269–272 (2000).
35. B. Cramer, K. Miller, P. Barrett, J. Wright, *J. Geophys. Res. Oceans* **116**, C12023 (2011).
36. H. E. Garcia, L. I. Gordon, *Limnol. Oceanogr.* **37**, 1307–1312 (1992).
37. R. E. Zeebe, K. Caldeira, *Nat. Geosci.* **1**, 312–315 (2008).
38. B. Bereiter *et al.*, *Geophys. Res. Lett.* **42**, 542–549 (2015).
39. J. A. Higgins *et al.*, *Proc. Natl. Acad. Sci. U.S.A.* **112**, 6887–6891 (2015).
40. J. C. Walker, P. Hays, J. Kasting, *J. Geophys. Res.* **86**, 9776–9782 (1981).
41. D. Archer, *J. Geophys. Res. Oceans* **110**, C09S05 (2005).
42. M. Raymo, W. F. Ruddiman, *Nature* **359**, 117–122 (1992).

ACKNOWLEDGMENTS

D.A.S. acknowledges funding from a National Oceanic and Atmospheric Administration Climate & Global Change postdoctoral fellowship. J.A.H. and M.L.B. acknowledge support from National Science Foundation grant ANT-1443263. All data presented are available in the supplementary materials. We thank W. Fischer, I. Halevy, N. Planavsky, J. Severinghaus, and D. Sigman for helpful discussions and three anonymous reviewers for helpful comments on the manuscript. D.A.S., J.A.H., and M.L.B. conceived the study and wrote the manuscript. D.A.S., J.A.H., M.L.B., and Y.Y. analyzed the data. G.B.D. measured the Dome C $\delta Ar/N_2$ data. The views expressed in this article are those of the authors and do not necessarily represent the views of the Department of Energy or the U.S. Government.

SUPPLEMENTARY MATERIALS

www.sciencemag.org/content/353/6306/1427/suppl/DC1
Materials and Methods
Figs. S1 to S6
Tables S1 to S3
References (*43*–*78*)

25 February 2016; accepted 2 August 2016
10.1126/science.aaf5445

Downloaded from http://science.sciencemag.org/ on September 30, 2016

CONVERGENT EVOLUTION

Convergent local adaptation to climate in distantly related conifers

Sam Yeaman,[1,2]* Kathryn A. Hodgins,[3]* Katie E. Lotterhos,[4] Haktan Suren,[5] Simon Nadeau,[2] Jon C. Degner,[2] Kristin A. Nurkowski,[3] Pia Smets,[2] Tongli Wang,[2] Laura K. Gray,[6] Katharina J. Liepe,[6] Andreas Hamann,[6] Jason A. Holliday,[5] Michael C. Whitlock,[7] Loren H. Rieseberg,[8] Sally N. Aitken[2]†

When confronted with an adaptive challenge, such as extreme temperature, closely related species frequently evolve similar phenotypes using the same genes. Although such repeated evolution is thought to be less likely in highly polygenic traits and distantly related species, this has not been tested at the genome scale. We performed a population genomic study of convergent local adaptation among two distantly related species, lodgepole pine and interior spruce. We identified a suite of 47 genes, enriched for duplicated genes, with variants associated with spatial variation in temperature or cold hardiness in both species, providing evidence of convergent local adaptation despite 140 million years of separate evolution. These results show that adaptation to climate can be genetically constrained, with certain key genes playing nonredundant roles.

Evolutionary convergence has provided a window into the constraints that shape adaptation (*1*, *2*). Studies of convergent local adaptation among closely related lineages commonly find evidence of many shared genetic changes (*3*), but such evidence may be a result of shared standing variation, rather than shared constraints in how genotypes give rise to phenotypes (*4*–*6*). Across time scales where shared standing variation is precluded, adaptation sometimes arises by mutations in the same genes, such as melanism via *Mc1r* and *agouti* (*7*). However, such examples of adaptation via large-effect loci may not be representative of the true spectrum of phenotypes (*8*). Highly polygenic traits may have greater genetic redundancy than traits governed by a single molecular pathway, and might therefore exhibit less repeatable signatures of adaptation (*9*). Relatively little is known about the genome-wide repeatability of local adaptation in more highly polygenic traits in distantly related species, where shared standing variation is precluded.

We compared signatures of local adaptation in lodgepole pine (*Pinus contorta*) and interior spruce (*Picea glauca*, *Picea engelmannii*, and their hybrids), which inhabit similar environmental gradients across montane and boreal regions of western North America, and last shared a common ancestor more than 140 million years ago (*10*). Like many conifers, these species show patterns of local adaptation to climate that reflect a tradeoff between competition for light resources and acquisition of freezing tolerance (*11*, *12*). Although some candidate genes have been identified that may drive these phenotypic responses (*13*, *14*), we still know little about the genomic basis of adaptation. Comparative gene expression studies indicate that plastic responses to temperature and moisture are highly conserved in spruce and pine, with ~70% of differentially expressed orthologs showing parallel responses in both species (*15*) and lower rates of protein evolution (*16*). Plastic responses to climate appear to be relatively conserved and highly polygenic, but the extent to which local adaptation involves similar responses at the genomic level is unknown.

To characterize the basis of adaptation in these large genomes (~20 Gb), we sampled individuals from >250 populations across their geographic ranges and identified more than 1 million single-nucleotide polymorphisms (SNPs) in ~23,000 genes (*17*). We searched for correlations between individual SNPs and (i) 17 phenotypes measured in growth chambers [genotype-phenotype association (GPA)] and (ii) 22 environmental variables [genotype-environment association (GEA)]. We identified top-candidate genes as those with an exceptional proportion of their total SNPs being GPA or GEA outliers (99th percentile) (*17*) (Fig. 1A).

The strongest phenotypic signatures of local adaptation to climate were for correlations between fall and winter cold injury traits and low-temperature stress–related environmental factors, including latitude (*12*) (Fig. 1B). The strength of these correlations was similar in pine and spruce, providing evidence of convergent phenotypic local adaptation. These two phenotypic traits and five environmental factors (hereafter the "main variables") also showed the strongest signatures of selection, with the largest number of top-candidate genes in both species (Fig. 1, C and D) and greatest mean strength of association (ρ^2) across all SNPs (fig. S1). Although these results suggest that adaptation to climate is highly polygenic, not all variables had similar genomic signatures in both species. Many top GEA candidates were found for longitude in pine but not spruce, whereas the converse was true for precipitation falling as snow (Fig. 1D), indicating that these species are divergent in some aspects of adaptation (*17*).

To study the repeatability of local adaptation on a gene-by-gene basis, for each gene identified as a top candidate for at least one of the seven main variables in one species, we examined the strength of associations in orthologous gene(s) in the other species (Fig. 2). To quantify similarity in signatures of association underlying convergent adaptation (hereafter "signatures of convergence"), we compared the strength of association (ρ^2) for all SNPs within each of these top-candidate orthologs to a null distribution constructed from all non–top-candidate orthologs [which we term the "null-*W* method" (*17*)]. For the one-to-one orthologs, 22.3 to 27.5% of tested orthologs (spruce) and 5.7 to 11.6% of tested orthologs (pine) were in the 5% tail of the null distribution, and for most variables tested, the observed proportion was significantly higher than expected by chance (Fig. 3; see also fig. S2).

If the observed overlap of gene involvement in local adaptation occurs because of fundamental constraints in how genotype gives rise to phenotype, then duplication and neofunctionalization may increase flexibility in the genetic program (*18*). Consistent with this prediction, genes

Table 1. Number of genes with signatures of convergence. Columns report the number of cases where a gene from one species that was orthologous to a top candidate in the other species was significantly associated to at least one of the seven main variables by the null-*W* test after adjusting for false discovery rate.

False discovery rate	One-to-one orthologs	One-to-many: Both duplicates convergent	One-to-many: One duplicate convergent	Total number of genes with strong signatures of convergence
0.01	6	0	0	6
0.05	40	0	7	47
0.10	71	2	8	83

[1]Department of Biological Sciences, University of Calgary, Calgary, Canada. [2]Department of Forest and Conservation Sciences, University of British Columbia, Vancouver, Canada. [3]School of Biological Sciences, Monash University, Melbourne, Australia. [4]Department of Marine and Environmental Science, Northeastern University, Nahant, MA, USA. [5]Department of Forest Resources and Environmental Conservation, Virginia Polytechnic Institute and State University, Blacksburg, VA, USA. [6]Department of Renewable Resources, University of Alberta, Edmonton, Canada. [7]Department of Zoology, University of British Columbia, Vancouver, Canada. [8]Department of Botany, University of British Columbia, Vancouver, Canada.
*These authors contributed equally to this work. †Corresponding author. Email: sally.aitken@ubc.ca

Downloaded from http://science.sciencemag.org/ on September 30, 2016

duplicated in either species were also more likely to have strong signatures of convergence. Across all comparisons, signatures of convergence were 65% more common in cases where one ortholog was duplicated than in one-to-one orthologs (Fig. 3 shows results on a copy-for-copy basis, mean ratio 1.65, range 0.67 to 4.0; fig. S5 shows results on a per-orthogroup basis, mean ratio 1.98, range 0.67 to 4.3). Independent of convergence signatures, duplicated genes also had a higher probability of being top candidates, although the effect was nonsignificant in most cases (fig. S3). Linkage disequilibrium (LD) between tandem duplicates may be responsible for these patterns, as LD is high among paralogs with at least one member that is a top candidate (fig. S4). However, LD and tandem duplication cannot explain the enrichment of association signatures in the single-copy orthologs to duplicated top candidates (Fig. 3 and fig. S2, orange bars), nor the duplicated orthologs, because binning duplicates before repeating the analysis yielded similar results (fig. S5). Thus, convergent local adaptation and gene duplication are associated in these conifers, possibly as a means to increase genetic flexibility. Alternatively, duplications of genes involved in local adaptation may have been favored under migration-selection balance, due to changes in linkage relationships (*19*) or dominance-associated masking of migration load (*20*).

Overall, 47 genes exhibit signatures of convergence at a false discovery rate (FDR) of 5% (or 83 at FDR = 10%), out of 260 and 450 top candidates with identified orthology relationships in pine and spruce, respectively (Table 1; see fig. S6 for phylogenies). This suggests that ~10 to 18% of locally adapted genes are evolving convergently, a lower rate than typically found for candidate genes or quantitative trait loci (*3*); however, the true proportion may be much higher. Many of the top candidates identified within either species (Fig. 1, C and D) are likely false positives due to the lack of control for population structure (*21*) or because they are physically linked to a causal locally adapted gene but are not themselves locally adapted. The former artifact is not expected to affect the convergence candidates significantly above the rate represented by our null hypothesis (horizontal gray line, Fig. 3), as drift is unlikely to give rise to the same false positive in both species (*17*). Although we found evidence of considerable LD among some top candidates (fig. S4), the convergence candidates were not usually in strong LD with each other; hence, this latter artifact is also not causing many false positives (figs. S7 and S8). Because these artifacts are likely to inflate the number of top candidates identified within species but not to significantly affect signatures of convergence, the true proportion of genes adapting convergently may be higher than 10 to 18%.

Data on gene expression in response to climate stress [from (*18*)] revealed that 61 convergence candidates with expression data had conserved patterns of differential expression in both species, while 17 had divergent patterns (a factor of ~3.5 difference). This is approximately twice the ratio of conserved:divergent expression observed in non-convergently adapted genes (P = 0.014, Fisher's exact test; table S6). Genes with signatures of convergence were also enriched for transcription factors and genes involved in biological regulation and RNA metabolism (enrichment significant in spruce convergence candidates but not pine; tables S8 and S9). Thus, although genes involved in convergent local adaptation are disproportionately conserved in their expression, they are also more likely to affect the expression of other genes. Evidence from *Arabidopsis* suggests that the protein products of several of these convergent genes could be relevant to seasonal transitions and abiotic stress (table S9). For example, PSEUDO-RESPONSE REGULATOR 5 (PRR5) directly regulates the circadian clock and associated developmental transitions (*22*); FY regulates processing of *FCA* mRNA, which in turn regulates accumulation of *FLOWERING LOCUS C* (*FLC*) mRNA (*23*); and REGULATORY COMPONENT OF ABA RECEPTOR 1 (RCAR1) functions as a sensor of abscisic acid, a key abiotic stress–related phytohormone (*24*).

Taken together, our results indicate that local adaptation is more repeatable at the genomic level than might be expected, given the highly polygenic basis of these traits (*8*, *9*) and the potential for considerable genetic redundancy. Furthermore, gene duplication appears to contribute importantly to convergence, although the reason for this is unknown. Whether gene duplication is a common facilitator of convergent genotypic evolution across the domains of life remains to be seen.

Our results suggest that long-diverged conifers share a suite of genes that play an important role in adaptation to temperature, and should enable functional annotation and tools for candidate-augmented genomic selection. However, they also show that adaptation is highly polygenic and involves heterogeneous, nonconvergent responses

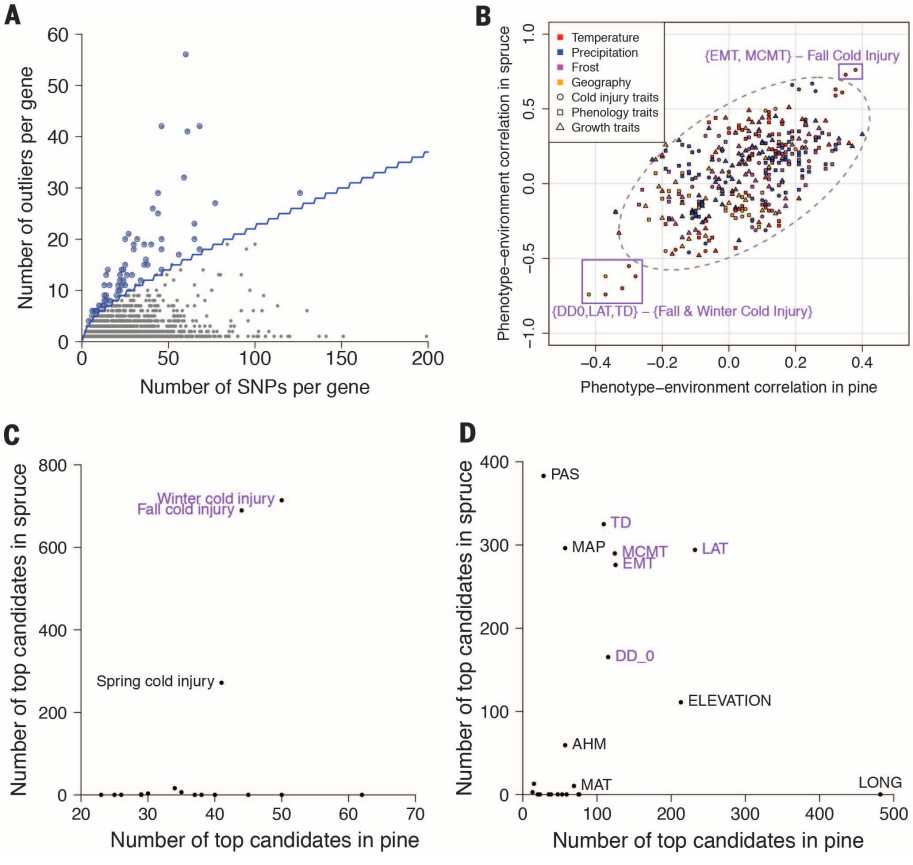

Fig. 1. Signatures of convergent adaptation at the phenotypic and genomic level. Spearman correlations were calculated between each SNP and the 22 environmental and 17 phenotypic variables. (**A**) Top-candidate genes for each of the 39 tests were identified as those with an extreme number of outlier SNPs relative to a binomial expectation, shown in blue (mean annual temperature in pine). (**B**) Cold injury response phenotypes were strongly correlated to temperature variables in both lodgepole pine and interior spruce, with the most strongly correlated cases shown in purple ("main variables"). (**C** and **D**) The seven main variables with strong phenotype-environment correlations also had the largest number of top-candidate genes for phenotypes (C) and environments (D); labels are omitted for data points near the axes for clarity. EMT, extreme minimum temperature; MCMT, mean coldest-month temperature; DD_0, degree-days below 0°C; LAT, latitude; TD, temperature difference; MAT, mean annual temperature; PAS, precipitation as snow; MAP, mean annual precipitation; AHM, annual heat-moisture index; LONG, longitude (see tables S1 and S2).

Downloaded from http://science.sciencemag.org/ on September 30, 2016

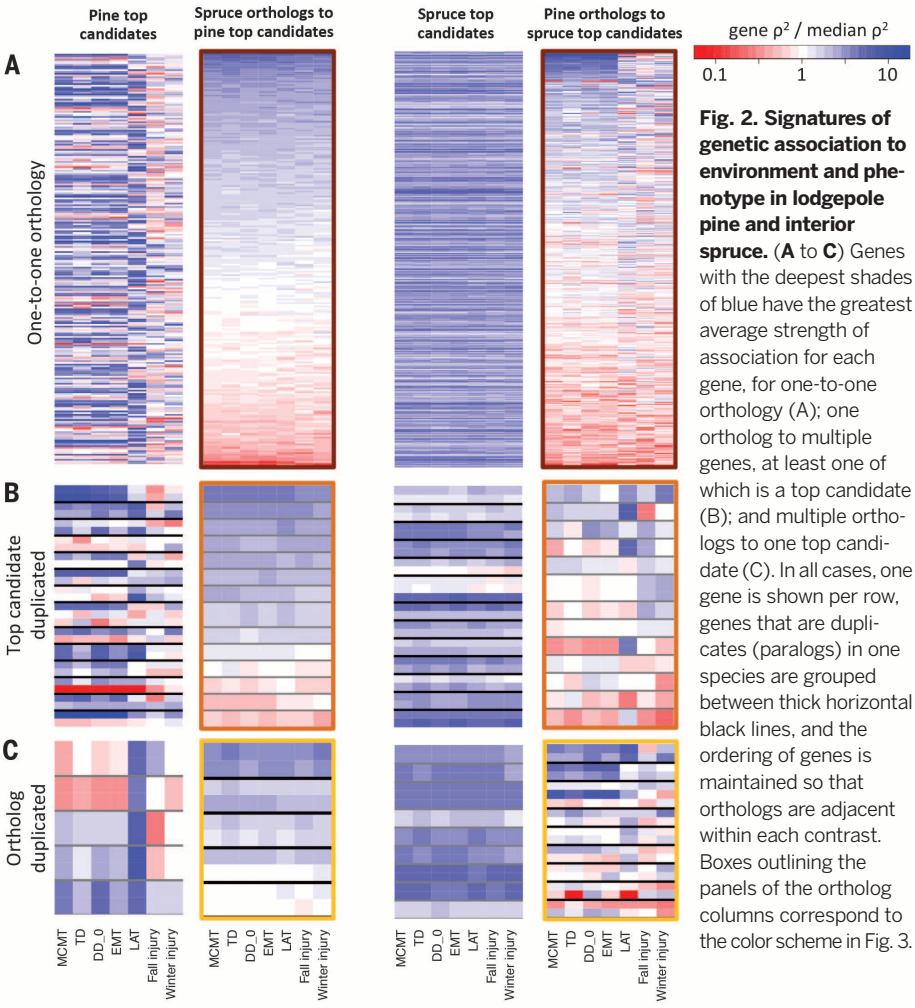

Fig. 2. Signatures of genetic association to environment and phenotype in lodgepole pine and interior spruce. (**A** to **C**) Genes with the deepest shades of blue have the greatest average strength of association for each gene, for one-to-one orthology (A); one ortholog to multiple genes, at least one of which is a top candidate (B); and multiple orthologs to one top candidate (C). In all cases, one gene is shown per row, genes that are duplicates (paralogs) in one species are grouped between thick horizontal black lines, and the ordering of genes is maintained so that orthologs are adjacent within each contrast. Boxes outlining the panels of the ortholog columns correspond to the color scheme in Fig. 3.

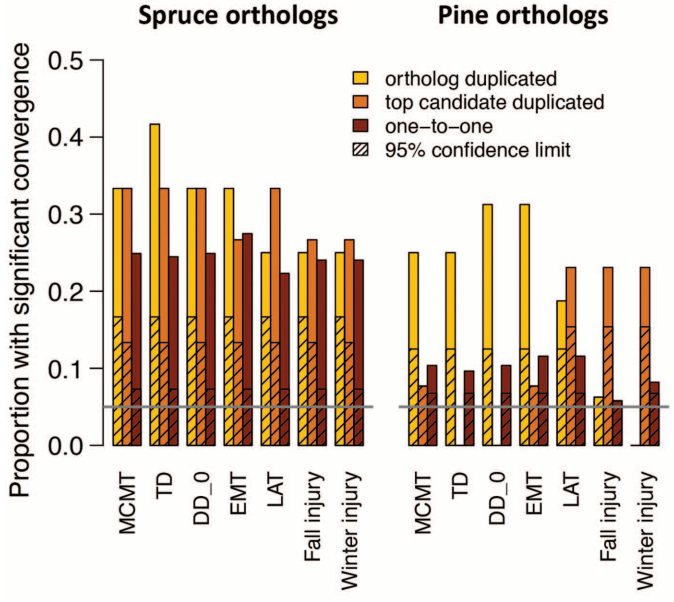

Fig. 3. Proportion of top-candidate orthologs with significant signatures of convergent local adaptation. All orthologs from Fig. 2 were tested with the null-*W* test with $\alpha = 0.05$; colors correspond to the outlines in the respective panels. The horizontal gray line at 0.05 indicates the expected number of significant results under the null hypothesis of pure drift. Hatching indicates the upper 95% confidence limit for this null hypothesis (based on a binomial test with $P = 0.05$).

at many other genes. The success of climate change mitigation strategies such as assisted migration and breeding for new climates will depend on a thorough understanding of adaptation to climate (*25*), and exploration of the genomic basis of adaptation will inform these activities.

REFERENCES AND NOTES

1. D. L. Stern, *Nat. Rev. Genet.* **14**, 751–764 (2013).
2. A. Martin, V. Orgogozo, *Evolution* **67**, 1235–1250 (2013).
3. G. L. Conte, M. E. Arnegard, C. L. Peichel, D. Schluter, *Proc. R. Soc. B* **279**, 5039–5047 (2012).
4. P. F. Colosimo *et al.*, *Science* **307**, 1928–1933 (2005).
5. V. Soria-Carrasco *et al.*, *Science* **344**, 738–742 (2014).
6. J. A. Holliday, L. Zhou, R. Bawa, M. Zhang, R. W. Oubida, *New Phytol.* **209**, 1240–1251 (2016).
7. M. Manceau, V. S. Domingues, C. R. Linnen, E. B. Rosenblum, H. E. Hoekstra, *Philos. Trans. R. Soc. B* **365**, 2439–2450 (2010).
8. M. V. Rockman, *Evolution* **66**, 1–17 (2012).
9. S. Yeaman, *Am. Nat.* **186** (suppl. 1), S74–S89 (2015).
10. X. Q. Wang, D. C. Tank, T. Sang, *Mol. Biol. Evol.* **17**, 773–781 (2000).
11. O. Savolainen, T. Pyhäjärvi, T. Knürr, *Annu. Rev. Ecol. Evol. Syst.* **38**, 595–619 (2007).
12. K. J. Liepe, A. Hamann, P. Smets, C. R. Fitzpatrick, S. N. Aitken, *Evol. Appl.* **9**, 409–419 (2016).
13. T. L. Parchman *et al.*, *Mol. Ecol.* **21**, 2991–3005 (2012).
14. B. Hornoy, N. Pavy, S. Gérardi, J. Beaulieu, J. Bousquet, *Genome Biol. Evol.* **7**, 3269–3285 (2015).
15. S. Yeaman *et al.*, *New Phytol.* **203**, 578–591 (2014).
16. K. A. Hodgins, S. Yeaman, K. A. Nurkowski, L. H. Rieseberg, S. N. Aitken, *Mol. Biol. Evol.* **33**, 1502–1516 (2016).
17. See supplementary materials on *Science* Online.
18. S. Ohno, *Evolution by Gene Duplication* (Springer-Verlag, 1970).
19. S. Yeaman, *Proc. Natl. Acad. Sci. U.S.A.* **110**, E1743–E1751 (2013).
20. A. Yanchukov, S. Proulx, *Evolution* **66**, 1543–1555 (2012).
21. K. E. Lotterhos, M. C. Whitlock, *Mol. Ecol.* **24**, 1031–1046 (2015).
22. N. Nakamichi *et al.*, *Proc. Natl. Acad. Sci. U.S.A.* **109**, 17123–17128 (2012).
23. G. G. Simpson, P. P. Dijkwel, V. Quesada, I. Henderson, C. Dean, *Cell* **113**, 777–787 (2003).
24. Y. Ma *et al.*, *Science* **324**, 1064–1068 (2009).
25. S. N. Aitken, M. C. Whitlock, *Annu. Rev. Ecol. Evol. Syst.* **44**, 367–388 (2013).

ACKNOWLEDGMENTS

We thank D. Bachelet, E. Buckler, G. Howe, O. Savolainen, P. Ingvarsson, J. Mee, T. Parchman, R. Barrett, and D. Schluter for comments, and R. Baranowski for support on Westgrid. Seeds were kindly provided by 63 forest companies and agencies in British Columbia and Alberta (listed at adaptree.sites.olt.ubc.ca/seed contributors), facilitated by the BC Tree Seed Centre and the Alberta Tree Improvement and Seed Centre. D. Neale and J. Bohlmann generously provided access to loblolly pine and white spruce draft genomes prior to their release. This research was part of the AdapTree Project (S.N.A. and A.H., co–project leaders) funded by Genome Canada, Genome BC, Genome Alberta, Alberta Innovates BioSolutions, the Forest Genetics Council of British Columbia, Virginia Tech, the University of British Columbia, NSF Plant Genome Research Program grant IOS:1054444 (J.A.H.), USDA National Institute of Food and Agriculture, McIntire Stennis Project grant 10005394 (J.A.H.), and the British Columbia Ministry of Forests, Lands and Natural Resource Operations. Sequence data are deposited in the Short Read Archive (SRP071805; PRJNA251573) and data and analysis scripts are deposited in Dryad (doi:10.5061/dryad.0t407). The authors declare no conflicts of interest.

SUPPLEMENTARY MATERIALS

www.sciencemag.org/content/353/6306/1431/suppl/DC1
Materials and Methods
Supplementary Text
Figs. S1 to S24
Tables S1 to S10
References (*26*–*61*)

31 March 2016; accepted 11 August 2016
10.1126/science.aaf7812

Downloaded from http://science.sciencemag.org/ on September 30, 2016

HOST TOLERANCE

A secreted bacterial peptidoglycan hydrolase enhances tolerance to enteric pathogens

Kavita J. Rangan,[1]* Virginia A. Pedicord,[1,2] Yen-Chih Wang,[1] Byungchul Kim,[1] Yun Lu,[3] Shai Shaham,[3] Daniel Mucida,[2] Howard C. Hang[1]*

The intestinal microbiome modulates host susceptibility to enteric pathogens, but the specific protective factors and mechanisms of individual bacterial species are not fully characterized. We show that secreted antigen A (SagA) from *Enterococcus faecium* is sufficient to protect *Caenorhabditis elegans* against *Salmonella* pathogenesis by promoting pathogen tolerance. The NlpC/p60 peptidoglycan hydrolase activity of SagA is required and generates muramyl-peptide fragments that are sufficient to protect *C. elegans* against *Salmonella* pathogenesis in a *tol-1*–dependent manner. SagA can also be heterologously expressed and secreted to improve the protective activity of probiotics against *Salmonella* pathogenesis in *C. elegans* and mice. Our study highlights how protective intestinal bacteria can modify microbial-associated molecular patterns to enhance pathogen tolerance.

Dysbiosis of the gut microbiota is associated with metabolic disorders, inflammatory bowel disease, and increased pathogen susceptibility (*1*). Nonetheless, individual bacterial species and factors involved in host protection have been difficult to characterize (*2*). *Enterococci* are lactic acid bacteria associated with the intestinal microbiome of diverse species ranging from humans to flies and can attenuate host susceptibility to enteric pathogens, including *Salmonella* (*3*, *4*). Nonpathogenic strains of *Enterococcus faecium* have been used as probiotics, but their protection mechanisms are unclear (*5*). Because *E. faecium* can colonize the *Caenorhabditis elegans* intestine without causing apparent disease (*6*), we used *C. elegans* as a model organism (*7*) to elucidate the protective mechanism (or mechanisms) underlying *E. faecium* probiotic activity. To investigate whether *E. faecium* can attenuate enteric bacterial pathogenesis in *C. elegans*, we developed a treatment-infection assay with *Salmonella enterica* serovar Typhimurium (fig. S1A), which causes persistent intestinal infection and death in *C. elegans* (*8*–*10*). In our assay, *E. faecium*–treated animals appeared less fragile and more motile than did control *Escherichia coli* OP50–treated animals after *S.* Typhimurium infection (fig. S1B). *C. elegans* survival was increased in animals fed *E. faecium* before infection as compared with animals fed *E. coli* OP50 or *Bacillus subtilis* 168 (Fig. 1A and fig. S1C). Multiple strains of *E. faecium*, including a pathogenic strain, were able to inhibit *S.* Typhimurium pathogenesis (fig. S1, D and E). *E. faecium*–treated animals were also more resistant to the intrinsic pathogenesis of *E. coli* OP50 (fig. S1F) as well as pathogenesis caused by *Enterococcus faecalis* V583 (fig. S1G) (*6*). These results suggest that the mechanism of protection is conserved among *E. faecium* strains and is active against diverse enteric pathogens.

We next analyzed the effect of *E. faecium* on *S.* Typhimurium colonization and persistence. Fluorescence imaging of mCherry–*S.* Typhimurium 3 days after infection showed comparable *S.* Typhimurium colonization with or without *E. faecium* treatment (Fig. 1B and fig. S1H). Viable *S.* Typhimurium [colony-forming units (CFU)] recovered from lysed worms revealed a ~2 log decrease in *S.* Typhimurium colonization 1 day after infection in *E. faecium*–treated *S.* Typhimurium–infected animals (Fig. 1C). However, by 3 days after infection, *S.* Typhimurium titer was similar in OP50- and *E. faecium*–treated *S.* Typhimurium–infected animals (Fig. 1C). To determine whether this transient decrease in *S.* Typhimurium colonization represented niche competition early in our assay, we monitored *E. faecium* CFU throughout the infection assay (fig. S1I). Whereas *E. faecium* initially colonized worms to ~10^5 CFU/worm, *E. faecium* numbers decreased to ~10 to 10^2 CFU/worm 1 day after infection, demonstrating that the transient decrease in *S.* Typhimurium colonization was not concomitant with an increase in *E. faecium* load. Electron microscopy of worm transverse sections 4 days after infection revealed substantial degradation of the intestinal microvilli in OP50-treated *S.* Typhimurium–infected animals as compared with uninfected or *E. faecium*–treated animals (Fig. 1D). In OP50-treated *S.* Typhimurium–infected animals, bacteria had escaped the intestinal lumen and caused extensive tissue damage (Fig. 1D, middle). In contrast, *E. faecium*–treated *S.* Typhimurium–infected animals contained a similar bacterial load to the intestinal lumen and showed no apparent tissue damage (Fig. 1D, right), suggesting improved epithelial barrier integrity. These results demonstrate that *E. faecium* does not prevent *S.* Typhimurium colonization or replication but may enhance host tolerance to pathogens.

We next explored whether specific factors produced by *E. faecium* were sufficient for protection against *S.* Typhimurium pathogenesis. *E. faecium* culture supernatant was as effective as live bacterial cultures in inhibiting *S.* Typhimurium pathogenesis (Fig. 2A). Activity of the supernatant was sensitive to proteinase-K treatment, trichloroacetic acid precipitation, and 10-kDa size exclusion (fig. S2, A to C), leading us to analyze the protein composition of *E. faecium* culture supernatant by means of mass spectrometry (fig. S2, D and E, and table S1). This revealed a number of secreted proteins and an enrichment of peptidoglycan remodeling factors (Fig. 2B). We focused on secreted antigen A (SagA), the most abundant protein identified in the supernatant (Fig. 2B), which encodes a putative secreted NlpC/p60 peptidoglycan hydrolase that is essential for *E. faecium* viability (*11*). Imaging of animals treated with *E. faecium*–expressing mCherry under the *sagA* promoter (*psagA:mcherry*) showed that *E. faecium* expresses SagA in vivo (Fig. 2C). Treatment of animals with recombinant SagA-His_6 purified from either *E. coli* BL21-RIL(DE3) or *E. faecium* Com15 was sufficient to inhibit *S.* Typhimurium pathogenesis (Fig. 2, D and E; fig. S3; and table S2). All sequenced *E. faecium* strains encode a *sagA* ortholog in their genomes, whereas sequenced *E. faecalis* strains do not. We inserted *sagA-his*$_6$ into the *E. faecalis* OG1RF chromosome to generate *E. faecalis–sagA* (figs. S4 and S5). Treatment of *C. elegans* with *E. faecalis–sagA* attenuated *S.* Typhimurium pathogenesis comparably with *E. faecium*, whereas treatment with wild-type *E. faecalis* was not protective (Fig. 2F and fig. S6A). *S.* Typhimurium load was similar across all infected conditions, demonstrating that *E. faecalis–sagA* does not inhibit *S.* Typhimurium colonization in vivo but rather improves pathogen tolerance (fig. S6B). SagA expression also counteracted the intrinsic pathogenesis of *E. faecalis* OG1RF (fig. S6C) (*6*). These results demonstrate that SagA is sufficient to enhance host tolerance against bacterial pathogens.

The protective activity of *E. faecium* against multiple enteric pathogens suggested that SagA may engage host pathways to limit pathogenesis. A survey of *C. elegans* immunity-associated mutants indicated no major role for the p38 MAPK/Pmk-1 pathway (*12*, *13*), the transforming growth factor–β (TGF-β)–like/Dbl-1 pathway (*14*), the insulin-like receptor/Daf-2 pathway (*15*), or the Npr-1–mediated pathogen avoidance pathway (fig. S7) (*16*, *17*). *C. elegans* encodes one homolog of Toll-like receptor (TLR), *tol-1* (*18*). *C. elegans* lacking the *tol-1* TIR signaling domain [*tol-1(nr2033)*] exhibit defective pathogen avoidance to *S. marsescens* (*19*) and increased susceptibility to *S.* Typhimurium infection (*20*). We assessed SagA-mediated protection in *tol-1(nr2033)* animals and found that neither *E. faecium* nor *E. faecalis–sagA* were protective against *S.* Typhimurium infection in this mutant background, which suggests that SagA

[1]Laboratory of Chemical Biology and Microbial Pathogenesis, The Rockefeller University, New York, NY 10065, USA. [2]Laboratory of Mucosal Immunology, The Rockefeller University, New York, NY 10065, USA. [3]Laboratory of Developmental Genetics, The Rockefeller University, New York, NY 10065, USA. *Corresponding author. Email: krangan@rockefeller.edu (K.J.R.); hhang@rockefeller.edu (H.C.H.)

Downloaded from http://science.sciencemag.org/ on September 30, 2016

enhances pathogen tolerance through *tol-1* signaling (Fig. 2G).

To evaluate the mechanism of SagA protection (*21*), we generated an active site mutant as well as a C-terminal domain truncation of the NlpC/p60 hydrolase domain (Fig. 3A and fig. S8A). Neither mutant was able to inhibit *S.* Typhimurium pathogenesis, indicating that the NlpC/p60 hydrolase activity is required for SagA-mediated protection (Fig. 3B). SagA did not affect *S.* Typhimurium colonization of *C. elegans* or directly attenuate *S.* Typhimurium growth or virulence mechanisms

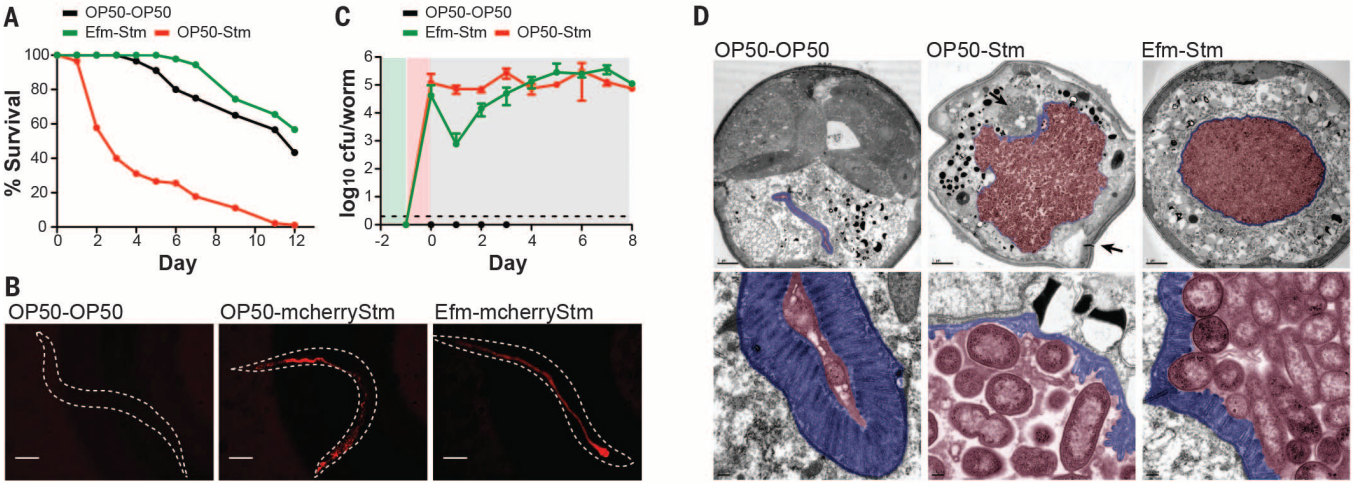

Fig. 1. *E. faecium* induces host tolerance to *S.* Typhimurium. (**A**) Survival curve showing *E. faecium* (Efm, Com15)–mediated inhibition of *S.* Typhimurium (Stm, 14028) pathogenesis ($P < 10^{-10}$). The legend indicates treatment-infection. Control worms were fed *E. coli* OP50 for both the treatment and infection stages of the assay. For *C. elegans* survival curves in all figures, significance was calculated by means of log-rank test with Bonferroni correction for multiple comparisons. Data points represent mean survival from 90 worms from a representative experiment independently replicated at least twice. (**B**) Fluorescence images of *C. elegans* infected with Stm-expressing plasmid-encoded mcherry (mcherryStm) at 3 days after infection. The dashed lines indicate an outline of the worm body. Scale bars, 100 μm. (**C**) Stm CFU measured in *C. elegans* throughout the infection assay. Data points represent average CFU from five worms ± SD of two independent experiments. The dashed line indicates detection limit. The background shading represents stage of the treatment-infection assay. Green indicates treatment, red indicates infection, and gray indicates *E. coli* (OP50) feeding. (**D**) Electron microscopy of transverse sections of *C. elegans* (top) and magnification of intestinal region (bottom) at 4 days after infection. The intestinal microvilli are highlighted blue; the intestinal lumen is highlighted red. (Top middle) The top arrow indicates bacteria that have breached the epithelial barrier, and the bottom arrow indicates loss of overall turgidity. Scale bars, 5 μm (top row) and 200 nm (bottom row).

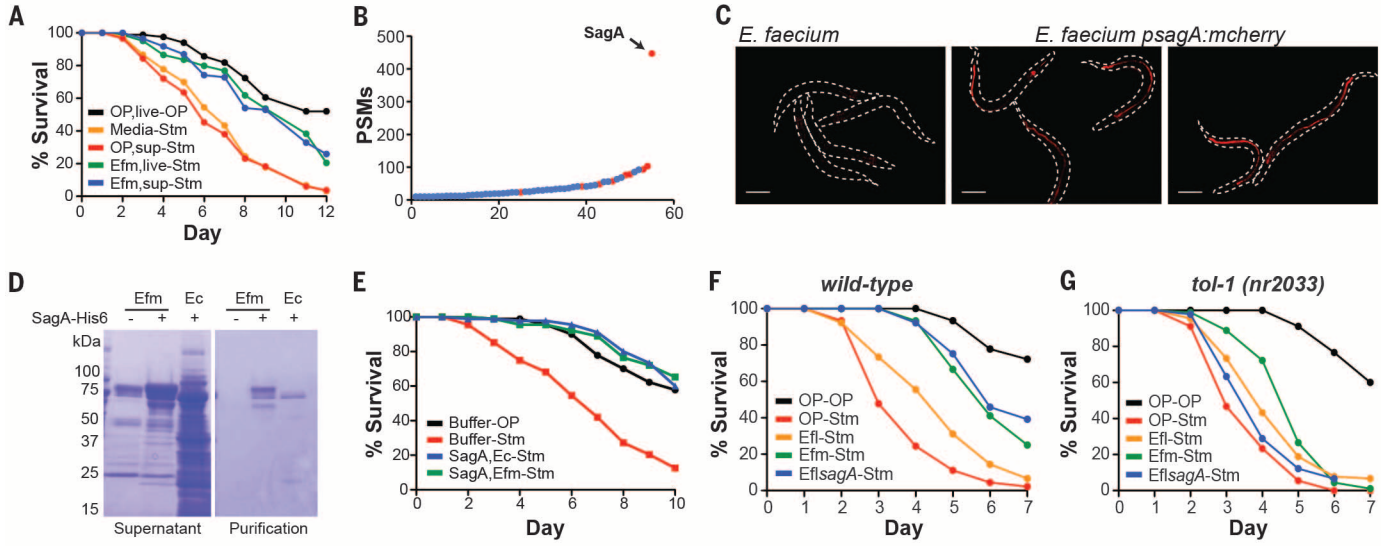

Fig. 2. SagA is sufficient for inducing pathogen tolerance in a *tol-1*–dependent manner. (**A**) Survival curve showing that both *E. faecium* culture supernatant (Efm, sup) ($P < 10^{-6}$) and live *E. faecium* culture (Efm, live) ($P < 10^{-7}$) inhibit *S.* Typhimurium (Stm)–induced death. OP50 culture supernatant (OP, sup) is not protective ($P = 1$). (**B**) Summary of proteins identified in Efm culture supernatant by means of mass spectrometry with at least 10 peptide spectrum matches (PSMs). Proteins involved in peptidoglycan remodeling are in red (table S1). The *x* axis represents arbitrary protein number. (**C**) Fluorescence images of *C. elegans* treated for 1 day with wild-type Efm or Efm-expressing mcherry under the sagA promoter (psagA:mcherry). The dashed lines indicate an outline of the worm body. Scale bars, 200 μm. (**D**) Coomassie stained SDS–polyacrylamide gel electrophoresis of culture supernatants and SagA-His_6 purifications from *E. faecium* Com15 (Efm) and *E. coli* BL21-RIL(DE3) (Ec). (**E**) Survival curve showing that SagA-His_6 purified from either *E. coli* BL21-RIL(DE3) (SagA, Ec) ($P < 10^{-10}$) or *E. faecium* Com15 (SagA, Efm) ($P < 10^{-10}$) inhibits Stm pathogenesis. (**F**) Survival curve from a continuous infection assay (fig. S6A) showing that *E. faecalis* (Efl, OG1RF)–sagA inhibits Stm pathogenesis ($P < 10^{-10}$) similarly to Efm (Com15) ($P = 1$) as compared with *E. faecalis* (Efl, OG1RF) and OP50. (**G**) Survival curve from a continuous infection assay showing that Efl-*sagA* ($P = 0.053$) does not inhibit Stm pathogenesis in *tol-1(nr2033) C. elegans*.

Downloaded from http://science.sciencemag.org/ on September 30, 2016

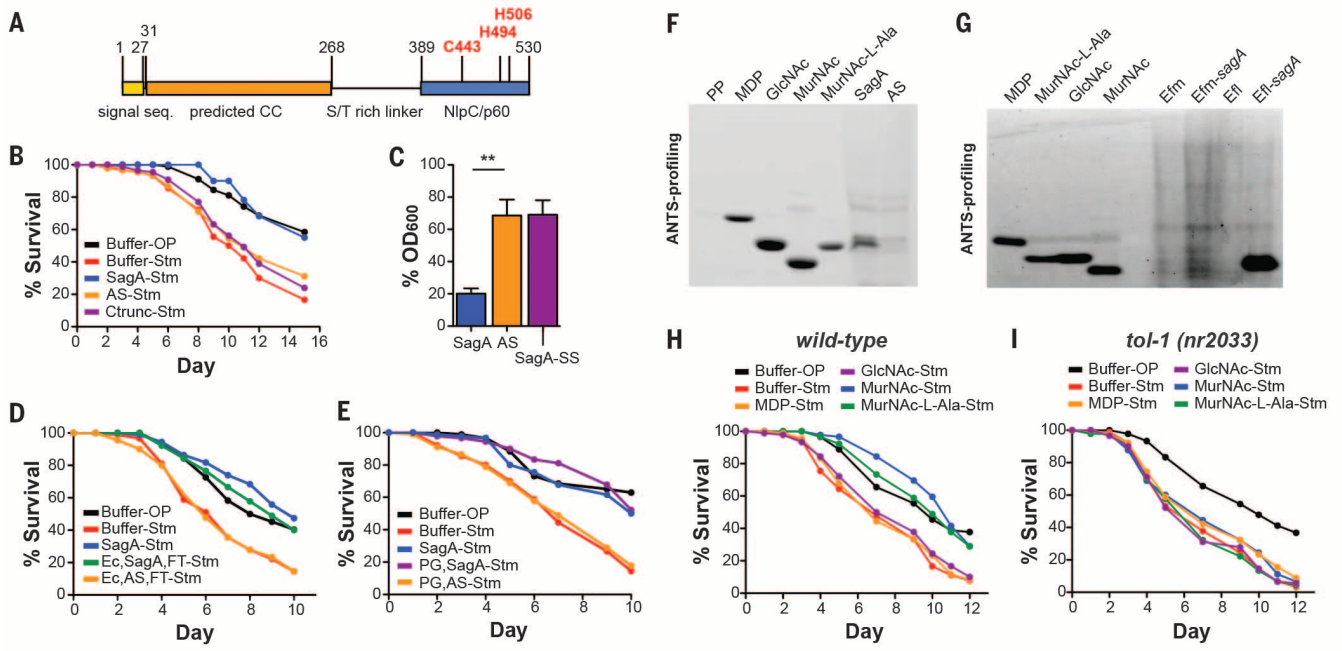

Fig. 3. Enzymatic activity of SagA is required for enhancing pathogen tolerance. (**A**) Schematic of SagA domain organization. The signal sequence is yellow, a predicted coiled-coil (CC) domain is orange, and the NlpC/p60-type hydrolase domain is blue. Active site residues are in red type. (**B**) Survival curve showing that SagA inhibits *S.* Typhimurium (Stm) pathogenesis ($P < 10^{-10}$), whereas an active site mutant (AS) and C-terminal truncation mutant (Ctrunc) do not ($P = 0.42$ and 0.98, respectively). (**C**) OD_{600} of *E. coli* BL21-RIL(DE3) expressing SagA, the active site mutant, or cytoplasmically localized SagA (SagA-SS) 1 hour after induction. Bars represent mean ± SEM from three independent experiments. Significance was calculated by means of unpaired *t* test. $^{**}P < 0.01$. (**D**) Survival curve showing that 5-kDa-MWCO column-filtered *E. coli* culture supernatants expressing SagA-His_6 (Ec, sagA-FT) inhibit Stm pathogenesis ($P < 10^{-4}$), whereas filtered *E. coli* culture supernatants expressing the active site mutant (Ec, AS-FT) do not ($P = 1$). (**E**) Survival curve showing that purified *E. coli* peptidoglycan treated with SagA (PG, SagA) can inhibit Stm pathogenesis ($P < 10^{-10}$), whereas *E. coli* peptidoglycan treated with the active site mutant (PG, AS) cannot ($P = 1$). (**F**) ANTS visualization of *E. coli* culture supernatants expressing SagA-His_6 or the active site mutant. A sugarless pentapeptide (PP) shows ultraviolet signal specificity. (**G**) ANTS visualization of peptidoglycan fragments in Efm, Efm-*sagA*, Efl, and Efl-*sagA* culture supernatants. (**H**) Survival curve showing that treatment with MurNAc ($P < 10^{-5}$) or MurNAc-L-Ala ($P < 10^{-10}$) can inhibit Stm pathogenesis, whereas MDP ($P = 1$) and GlcNAc ($P = 1$) are not protective. (**I**) Survival curve showing that MurNAc ($P = 1$) and MurNAc-L-Ala ($P = 0.61$) do not inhibit pathogenesis in *tol-1(nr2033) C. elegans*.

(fig. S8, B to E). In culture, recombinant SagA had no effect on *E. coli* growth rate (fig. S9A), but induction of SagA expression caused a decrease in culture optical density (OD) (Fig. 3C and fig. S9, B and C), indicating cell lysis. In contrast, expression of the active site mutant or cytoplasmically localized SagA did not induce *E. coli* cell lysis (Fig. 3C and fig. S9, B and C). These data suggest that although exogenous addition of SagA is not bacteriolytic, SagA is a functional hydrolase that can cleave peptidoglycan when targeted to the periplasm.

We hypothesized that SagA generates peptidoglycan fragments responsible for enhancing pathogen tolerance. Consistent with this hypothesis, we found that the flow-through from 5-kDa molecular weight cut-off (MWCO) column-filtered culture supernatants of *E. coli* expressing SagA, but not the active site mutant, protected *C. elegans* from *S.* Typhimurium pathogenesis (Fig. 3D and fig. S10A), which suggests that lower-molecular-weight products of SagA enzymatic activity are sufficient for protection. To test whether SagA-generated *E. coli* peptidoglycan fragments can protect *C. elegans* from *S.* Typhimurium, we digested purified *E. coli* peptidoglycan with lysozyme and either SagA or the active site mutant then filtered the digests to exclude protein. *C. elegans* treated with the SagA peptidoglycan digests survived similarly to SagA-treated animals, whereas active site mutant digests failed to attenuate pathogenesis (Fig. 3E). These results suggest that SagA-generated peptidoglycan fragments, and not SagA itself, are responsible for enhancing pathogen tolerance.

To identify the peptidoglycan fragment (or fragments) generated by SagA, we analyzed filtered bacterial culture supernatants by means of 8-aminonaphthalene-1,3,6-trisulfonic acid (ANTS) labeling and gel-based profiling (*22*, *23*). From *E. coli* expressing SagA, we detected a SagA-specific product that migrated similarly to the synthetic peptidoglycan fragments MurNAc-L-Ala and GlcNAc, but not to MurNAc-L-Ala-D-Glu (MDP) or MurNAc (Fig. 3F). ANTS analysis of *E. faecium*, *E. faecalis*, and *E. faecalis–sagA* peptidoglycan extracts revealed that SagA expression alters the muropeptide profile (fig. S11). From *E. faecalis–sagA* culture supernatant, we detected an ANTS-labeled product that comigrates with MurNAc (Fig. 3G), which suggests that heterologous SagA expression induces muropeptide shedding in both *E. coli* and *E. faecalis*. In contrast, 10-kDa-MWCO–filtered *E. faecium* culture supernatant did not yield detectable levels of MurNAc-L-Ala or MurNAc (Fig. 3G) and was not protective when administered to *C. elegans* (fig. S2C). *E. faecium* that expresses SagA endogenously is likely resistant to SagA-induced peptidoglycan shedding. Because SagA is abundantly secreted by *E. faecium* (fig. S4 and tables S1 and S4) and is protective after purification (Fig. 2, D and E), soluble SagA may hydrolyze extracellular peptidoglycan fragments derived from digested bacteria in vivo. Indeed, incubation of purified *E. coli* peptidoglycan with lysozyme and recombinant SagA, but not the active site mutant, yielded a peptidoglycan cleavage product with similar mobility to that of MurNAc-L-Ala (fig. S10B). These data suggest that heterologous expression of SagA in bacteria can remodel bacterial peptidoglycan (fig. S11), induce shedding of small muropeptide fragments (Fig. 3, F and G), and cleave extracellular peptidoglycan when secreted (fig. S10B). We next assessed the protective activity of SagA-generated peptidoglycan fragments, MurNAc and MurNAc-L-Ala, as well as GlcNAc and MDP. Treatment of *C. elegans* with either MurNAc or MurNAc-L-Ala was sufficient to inhibit *S.* Typhimurium pathogenesis, whereas treatment with MDP or GlcNAc was not (Fig. 3H). MurNAc and MurNAc-L-Ala were not protective in *tol-1(nr2033)* animals (Fig. 3I), which suggests that *tol-1* is required for mediating host protection in response to these peptidoglycan fragments. These data are consistent with the activity of muropeptides in mammals (*24*, *25*) but show that MurNAc-L-Ala and MurNAc are the minimal peptidoglycan components that enhance pathogen tolerance in *C. elegans*.

Downloaded from http://science.sciencemag.org/ on September 30, 2016

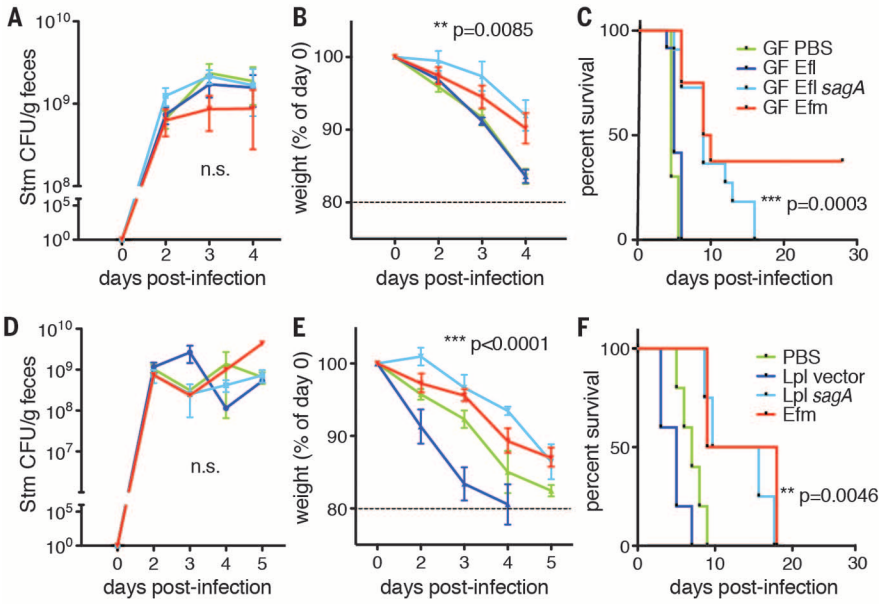

Fig. 4. *E. faecium* and SagA enhance pathogen tolerance in mice. (**A** to **C**) Germ-free (GF) C57BL/6 mice were orally gavaged with 10^8 CFU *E. faecalis* (Efl), Efl-expressing *sagA* (Efl-*sagA*), or *E. faecium* (Efm) 7 days before oral infection with 10^2 CFU *S.* Typhimurium (Stm). (A) Stm CFU in feces, (B) weight loss, and (C) survival are shown. Pooled data are from four independent experiments, $n = 10$ to 14 mice per group. (**D** to **F**) Mice were given an ampicillin, metronidazole, neomycin, and vancomycin (AMNV) antibiotic cocktail for 14 days and colonized with 10^8 CFU *L. plantarum* (Lpl) harboring an empty plasmid vector (Lpl-vector) or a *sagA* plasmid (Lpl-*sagA*) or 10^8 CFU Efm before oral infection with 10^6 CFU Stm. (D) Stm CFU in feces, (E) weight loss, and (F) survival are shown. Pooled data are from two independent experiments, $n = 2$ to 5 mice per group. [(A), (B), (D), and (E)] Mean ± SEM, 2-way analysis of variance, *P* value shown comparing *sagA*-expressing Efl or Lpl to wild type (WT) or vector controls, respectively. n.s., not significant. [(C) and (F)] Log-rank analysis, *P* value shown comparing Efm, *sagA*-expressing Efl, or Lpl to WT or vector controls, respectively. $^{**}P \leq 0.01$, $^{***}P \leq 0.001$ for all analyses. Comparisons with no asterisk had $P > 0.05$ and were not considered significant.

We next evaluated SagA-mediated protection against *Salmonella* pathogenesis in mice. Germ-free mice were monocolonized with *E. faecium*, *E. faecalis*, or *E. faecalis–sagA* 7 days before infection with *S.* Typhimurium. *Enterococcus* and *Salmonella* load were measured in the feces, and mouse survival was tracked. All *Enterococcus* strains were similarly recovered from the feces after gavage, indicating efficient intestinal colonization (fig. S12). Consistent with our results in *C. elegans*, *S.* Typhimurium CFU in the feces were similar across all conditions throughout infection (Fig. 4A), which suggests that *E. faecium* does not inhibit *Salmonella* colonization. Remarkably, mice gavaged with *E. faecium* or *E. faecalis–sagA* before infection exhibited reduced weight loss and prolonged survival, with a median survival of 9 days, as compared with that of *E. faecalis*–treated mice (Fig. 4, B and C). Although *Enterococci* are used as probiotics in livestock, their pathogenic potential makes them problematic for use in humans (*26*). We thus introduced *sagA* into a nonpathogenic probiotic, *Lactobacillus plantarum* (*27*), and confirmed its expression and secretion (fig. S13). *sagA*-expressing *L. plantarum* significantly prevented weight loss and improved survival in an antibiotic-induced *S.* Typhimurium infection model compared with *L. plantarum* (Fig. 4, D to F, and fig. S14). These results indicate that SagA is sufficient to attenuate *Salmonella* pathogenesis in mammals and is protective even when expressed by other probiotic bacteria.

We demonstrate that *C. elegans* is an effective model with which to explore the protective mechanisms of intestinal bacteria and show that SagA from *E. faecium* is sufficient to protect *C. elegans* and mice from enteric pathogens. Our results suggest that the NlpC/p60 hydrolase activity of SagA generates distinct peptidoglycan fragments that may activate host immune pathways to enhance epithelial barrier integrity and confine pathogens to the intestinal lumen, ultimately promoting tolerance to infection (fig. S15). Our analysis of *E. faecium* and engineered SagA-expressing bacterial strains in mice suggests that SagA also improves intestinal epithelial barrier integrity to limit bacterial pathogenesis in mammals (*28*). The protective activity of *E. faecium* and SagA in mice requires the TLR signaling adaptor MyD88, the peptidoglycan pattern recognition receptor NOD2, and the C-type lectin RegIIIγ (*28*). These results together suggest that *E. faecium* and SagA may function through evolutionarily conserved pathways to enhance epithelial barrier integrity and protect animals from enteric pathogens. Last, this study suggests that bacterial NlpC/p60-type peptidoglycan hydrolases (*29*–*32*) can enhance host tolerance to pathogens and that these enzymes could be used to improve the activity of existing probiotics.

REFERENCES AND NOTES

1. K. Honda, D. R. Littman, *Annu. Rev. Immunol.* **30**, 759–795 (2012).
2. C. G. Buffie, E. G. Pamer, *Nat. Rev. Immunol.* **13**, 790–801 (2013).
3. F. Lebreton, R. J. L. Willems, M. S. Gilmore, in *Enterococci: From Commensals to Leading Causes of Drug Resistant Infection*, M. S. Gilmore, D. B. Clewell, Y. Ike, N. Shankar, Eds. (Boston Massachusetts Eye and Ear Infirmary, 2014).
4. C. Staley, G. M. Dunny, M. J. Sadowsky, *Adv. Appl. Microbiol.* **87**, 147–186 (2014).
5. C. M. Franz, M. Huch, H. Abriouel, W. Holzapfel, A. Gálvez, *Int. J. Food Microbiol.* **151**, 125–140 (2011).
6. D. A. Garsin *et al.*, *Proc. Natl. Acad. Sci. U.S.A.* **98**, 10892–10897 (2001).
7. J. E. Irazoqui, J. M. Urbach, F. M. Ausubel, *Nat. Rev. Immunol.* **10**, 47–58 (2010).
8. A. Haraga, M. B. Ohlson, S. I. Miller, *Nat. Rev. Microbiol.* **6**, 53–66 (2008).
9. A. Aballay, P. Yorgey, F. M. Ausubel, *Curr. Biol.* **10**, 1539–1542 (2000).
10. A. Labrousse, S. Chauvet, C. Couillault, C. L. Kurz, J. J. Ewbank, *Curr. Biol.* **10**, 1543–1545 (2000).
11. F. Teng, M. Kawalec, G. M. Weinstock, W. Hryniewicz, B. E. Murray, *Infect. Immun.* **71**, 5033–5041 (2003).
12. D. H. Kim *et al.*, *Science* **297**, 623–626 (2002).
13. R. P. Shivers, T. Kooistra, S. W. Chu, D. J. Pagano, D. H. Kim, *Cell Host Microbe* **6**, 321–330 (2009).
14. G. V. Mallo *et al.*, *Curr. Biol.* **12**, 1209–1214 (2002).
15. D. A. Garsin *et al.*, *Science* **300**, 1921 (2003).
16. E. Z. Macosko *et al.*, *Nature* **458**, 1171–1175 (2009).
17. K. L. Styer *et al.*, *Science* **322**, 460–464 (2008).
18. N. Pujol *et al.*, *Curr. Biol.* **11**, 809–821 (2001).
19. E. Pradel *et al.*, *Proc. Natl. Acad. Sci. U.S.A.* **104**, 2295–2300 (2007).
20. J. L. Tenor, A. Aballay, *EMBO Rep.* **9**, 103–109 (2008).
21. M. Firczuk, M. Bochtler, *FEMS Microbiol. Rev.* **31**, 676–691 (2007).
22. S. Y. Li, J. V. Höltje, K. D. Young, *Anal. Biochem.* **326**, 1–12 (2004).
23. K. D. Young, *J. Bacteriol.* **178**, 3962–3966 (1996).
24. D. J. Philpott, M. T. Sorbara, S. J. Robertson, K. Croitoru, S. E. Girardin, *Nat. Rev. Immunol.* **14**, 9–23 (2014).
25. J. Royet, R. Dziarski, *Nat. Rev. Microbiol.* **5**, 264–277 (2007).
26. B. Lund, C. Edlund, *Clin. Infect. Dis.* **32**, 1384–1385 (2001).
27. L. M. Dicks, M. Botes, *Benef. Microbes* **1**, 11–29 (2010).
28. V. A. Pedicord *et al.*, *Sci. Immunol.* 10.1126/sciimmunol.aai7732 (2016).
29. W. Vollmer, B. Joris, P. Charlier, S. Foster, *FEMS Microbiol. Rev.* **32**, 259–286 (2008).
30. F. Yan *et al.*, *J. Clin. Invest.* **121**, 2242–2253 (2011).
31. F. Yan *et al.*, *Gastroenterology* **132**, 562–575 (2007).
32. F. Yan *et al.*, *J. Biol. Chem.* **288**, 30742–30751 (2013).

ACKNOWLEDGMENTS

We thank M. Tesic for liquid chromatography–mass spectrometry (LC-MS)/MS analyses, S. T. Chen for cloning pET21a-SagA-SS, A. Rogoz and T. Rendon for assistance with germ-free mouse care, and the Bargmann laboratory for reagents and helpful discussions. We also thank M. S. Gilmore, B. E. Murray, J. T. Singer, A. J. Bäumler, and B. Sartor for reagents. The data presented in this manuscript are tabulated in the main paper and in the supplementary materials. All *C. elegans* strains were provided by the Caenorhabditis Genetics Center, which is funded by the NIH Office of Research Infrastructure Programs (P40 OD010440). K.J.R. received support from the David Rockefeller Graduate Program and a Helmsley Graduate Fellowship. V.A.P. thanks the Center for Basic and Translational Research on Disorders of the Digestive System Pilot Award through the generosity of the Leona M. and Harry B. Helmsley Charitable Trust. Y.-C.W. is a Cancer Research Institute Irvington Fellow supported by the Cancer Research Institute. This work was supported by the NIH–National Institute of General Medical Sciences grant R01GM103593 and Robertson Therapeutic Development Fund to H.C.H. and D.M. H.C.H also thanks the Lerner Trust for support. The authors declare no competing financial interests. K.J.R, V.A.P., D.M., and H.C.H. are inventors on patent PCT/US2016/028836, submitted by The Rockefeller University, which covers modified microorganisms expressing SagA as anti-infective agents, probiotics, and food components.

SUPPLEMENTARY MATERIALS

www.sciencemag.org/content/353/6306/1434/suppl/DC1
Materials and Methods
Figs. S1 to S15
Tables S1 to S4
References (*33*–*50*)

28 January 2016; accepted 26 August 2016
10.1126/science.aaf3552

Downloaded from http://science.sciencemag.org/ on September 30, 2016

Gordon Research Conferences

Frontiers of Science

Applications can be submitted now at **www.grc.org** *for GRC meetings being held January - May 2017. Preliminary programs appear below, and detailed information about programs, fees, and conference locations is available online. Join us and see why our conferees rate their GRC as the top meeting in their field. Apply today!*

Gordon Research Seminars (GRS) are 2-day meetings designed for graduate students, post-docs, and other young scientists to present and exchange cutting-edge ideas, and to grow their professional networks. GRSs are held prior to the start of their associated GRCs. Seed funding for new GRSs is provided by the Kenan Institute for Engineering, Technology & Science at North Carolina State University, and by Merck & Co, Inc.

Discussion leaders are noted in bold italics.

NEW! Alcohol-Induced End Organ Diseases

Metabolic Reprogramming and Molecular Mechanisms of Tissue Injury by Alcohol

MARCH 26 – 31, 2017

FOUR POINTS SHERATON / HOLIDAY INN EXPRESS, VENTURA, CA

CHAIRS: Bin Gao & Andras Orosz

VICE CHAIR: Laura E. Nagy

- **Keynote Session: Novel Mechanisms of Multiple-Organ and Tissue Injury** ***Jan Hoek,*** Bernd Schnabl, Gyongyi Szabo
- **Proteostasis (Protein Homeostasis) in Alcohol-Induced Organ Injury** ***Stephen Pandol,*** Neil Kaplowitz, Pranoti Mandrekar, Wen-Xing Ding, Srinivasan Dasarathy
- **Alcohol, Stem Cells, and Cancer** ***Helmut Seitz,*** Lorraine Gudas, Vasilis Vasiliou, Keigo Machida
- **Immunologic Mechanisms** ***Gavin Arteel,*** Elizabeth Kovacs, Cynthia Ju, Patricia Molina, Ilhem Messaoudi
- **Non-Coding RNA and Extracellular Vesicles** ***David Brigstock,*** Li Wang, Won-IL Jeong, Vijay Shah
- **Alcohol, Gut Microbiota, Intestinal Barrier Function, and Fat Metabolism** ***Carol Casey,*** Hidekazu Tsukamoto, Craig McClain, Min You, Ali Keshavarzian, Flavia Souza-Smith
- **Mitochondria in Alcohol-Induced Organ Damage** ***John Lemasters,*** Gyorgy Hajnoczky, Shannon Bailey, Narayan Avadhani
- **Preclinical/Translational Approaches and Treatment in Alcohol-Associated Diseases** ***Mack Mitchell,*** George Kunos, Ramon Bataller, Philippe Mathurin, Shelly Lu, Urszula Iwaniec
- **Post-Metabolic Signaling and Stress Pathways** ***Charles Lang,*** Pal Pacher, Daria Mochly-Rosen, Jason Gardner

Antimicrobial Peptides

How Animals and Plants Use Antimicrobial Peptides, How They Work, and How to Design Interesting New Molecules

FEBRUARY 26 – MARCH 3, 2017

FOUR POINTS SHERATON / HOLIDAY INN EXPRESS, VENTURA, CA

CHAIRS: Wuyuan Lu & Michael A. Zasloff

VICE CHAIRS: Donald J. Davidson & Henk P. Haagsman

- **Keynote Session: AMPs at the Interface of Chemistry and Biology** ***Pieter Hiemstra, Julia Dorin,*** William Degrado, David Schneider
- **Evolution of AMPs Within Invertebrates** ***Jens Rolff, Delphine Destoumieux-Garzon,*** Roland Regoes, Abdelaziz Heddi, Nichole Broderick, Robert Unckless, Tonatiuh Melgarejo
- **AMPs as Components of Plant Immune Defense** ***Karin Thevissen, Octavio Franco,*** David Craik, Marilyn Anderson, Barbara De Coninck, Attila Kereszt
- **AMPs in Human Health and Disease** ***Charles Bevins, Nita Salzman,*** Robert Moir, Michael Selsted, Richard Gallo, Brice Sperandio
- **AMPs from the Pathogen's Perspective** ***Victor Nizet, Jason Smith,*** Rupert Kaul, Molly Hughes, Andrew Koh, Jennifer Bomberger
- **How Do AMPs Interact with Their Targets?** ***Karl Lohner, Burkhard Bechinger,*** Gerard Wong, James Mason, Lorenzo Stella
- **Critical Design Features and Novel Synthesis of AMPs** ***Stephen Kent, David Craik,*** John Vederas, Sonia Henriques
- **AMPs in Cancer** ***Joost Oppenheim, Aaron Weinberg,*** Marco Bianchi, Ge Jin, De Yang
- **Latest Developments with AMPs / Late-Breaking Topics** ***Robert Lehrer, Andre Ouellette,*** Dominik Filipp, Manuela Raffatellu, Elizabeth Nolan, Dmitri Kudryashov

GRS Antimicrobial Peptides

Innovative Strategies in the Research and Development of Antimicrobial Peptides to Increase Therapeutic Potential

FEBRUARY 25 – 26, 2017

CHAIR: Anne M. Van Der Does

Cancer Genetics & Epigenetics

Cancer Epigenetics: Mutations, Functions, and Therapies

APRIL 23 – 28, 2017

RENAISSANCE TUSCANY IL CIOCCO, LUCCA (BARGA), ITALY

CHAIR: X. Shirley Liu

VICE CHAIR: Jonathan D. Licht

- **Keynote Session: From Epigenetic Mechanism to Epigenetic Therapy** ***Jonathan Licht,*** Scott Armstrong, Shelley Berger, Peter Jones
- **Genetic and Epigenetic Changes in Hematological Malignancies** ***Ross Levine,*** Omar I. Abdel-Wahab, Peggy Goodell, Pier Giuseppe Pelicci
- **Mutations of Chromatin Regulators in Cancer** ***Kristian Helin,*** Cigall Kadoch, Ross Levine, Chi Wai Eric So
- **Chromatin Altered Function in Cancer** ***Sharon Dent,*** Emily Bernstein, Luciano Di Croce, Kristian Helin
- **Animal Models for Cancer Epigenetics** ***Mathieu Lupien,*** Iannis Aifantis, Sharon Dent, Johannes Zuber
- **Regulatory Genomics and Epigenomics of Cancer** ***Saverio Minucci,*** Lauri Aaltonen, Howard Chang, Mathieu Lupien, Amos Tanay
- **Functional Genomics, Epigenomics and Proteomics of Cancer** ***Ricky Johnstone,*** Tiziana Bonaldi, Benjamin Ebert, Christopher Vakoc, Ting Wang
- **Cancer Epigenetic Therapies** ***Jacques Neefjes,*** Mark Dawson, Ricky Johnstone, Ari Melnick
- **Interplay Between Cancer Epigenetics and Cancer Immunity** ***X. Shirley Liu,*** Stephen Baylin, Ben Lehner, Jacques Neefjes, Weiping Zou

THE GRC POWER HOUR

The GRC Power Hour is an informal gathering for all meeting participants. It is designed to help address the challenges women face in science and support the professional growth of women in our communities by providing an open forum for discussion and mentoring.

Look for Power Hours and the names of their respective organizers throughout these program listings.

Cardiac Arrhythmia Mechanisms

Model Systems, Emerging Technologies and Precision Medicine in Arrhythmia Research and Therapeutic Development

FEBRUARY 5 – 10, 2017

VENTURA BEACH MARRIOTT, VENTURA, CA

CHAIR: Gail A. Robertson

VICE CHAIR: Al George

- **The Future of Arrhythmia Therapeutic Development** ***Lori Isom,*** Joseph Wu, Igor Efimov, Emilia Entcheva
- **Specificity and Variability in Predictive Modeling** ***James Weiss,*** Blanca Rodriguez, David Christini, Najah Abi Gerges, Jamie Vandenberg
- **Arrhythmia Triggers** ***Penelope Boyden,*** Beth Habecker, Peter Ruben, Glenn Fishman
- **Atrial Fibrillation** ***Jose Jalife,*** Stanley Nattel, Barbara Casadei, Patrick Boyle, Karen Ocorr
- **Allostery, Pro-Arrhythmia and New Therapeutic Strategies** ***Robert Kass,*** Riccardo Olcese, Peter Larsson, Jonathan Silva
- **New Targets and Macromolecular Complexes in Cardiac Excitability** ***Mario Delmar,*** Nipavan Chiamvimonvat, Elise Balse, Calum Macrae, Timothy Kamp
- **Mechano-Electrical Signaling in Arrhythmia** ***Natalia Trayanova,*** Peter Kohl, Shelly Tzlil
- **Transcriptional and Translational Mechanisms in Arrhythmia** ***Connie Bezzina,*** Barry London, Jeanne Nerbonne, Ivan Moskowitz
- **Keynote Session: Old Targets, New Diseases and Mendelian Mysteries** ***Al George,*** Mohamed Chahine, Lee Eckhardt, Dan Roden

GRS Cardiac Arrhythmia Mechanisms

Model Systems, Emerging Technologies and Precision Medicine in Arrhythmia Research and Therapeutic Development

FEBRUARY 4 – 5, 2017

CHAIRS: Emily L. Ongstad & Nicole M. De Jesus

Downloaded from http://science.sciencemag.org/ on September 30, 2016

Cartilage Biology & Pathology

Understanding Biology to Achieve Better Cartilage Health

APRIL 2–7, 2017

RENAISSANCE TUSCANY IL CIOCCO, LUCCA (BARGA), ITALY

CHAIRS: Frank Beier & Elazar Zelzer

VICE CHAIRS: Yingzi Yang & John F. Bateman

- **Joint Development** *Veronique Lefebvre,* Amitabha Bandyopadhyay, Terence Capellini, Gage Crump
- **Cartilage Development and Growth Plate** *Ernestina Schipani,* Kathryn Song Eng Cheah, Christine Hartmann, Carmine Settembre, Natalie Sims
- **Evolution of the Skeletal System** *Bjorn Olsen,* Maria Barna, Ronen Schweitzer
- **Articular Cartilage and Osteoarthritis** *Rosa Serra,* Virginia Kraus, Anne-Marie Malfait, Qing-Jun Meng, Tonia Vincent
- **Cartilage in the Context of the Musculoskeletal System** *Cheryle Seguin,* Gabrielle Kardon, Chisa Shukunami
- **Extracellular Matrix** *Danny Chan,* Suneel Apte, Attila Aszodi, Karl Kadler, Johanna Myllyharju
- **Mechanobiology of Cartilage** *Andrew Pitsillides,* Farshid Guilak, Marjolein Van Der Meulen
- **Genetics and Epigenetics** *Matthew Warman,* John Loughlin, Ingrid Meulenbelt, Stefan Mundlos, Eileen Shore
- **Metabolism** *Andrea Vortkamp,* Aris Economides, Fanxin Long

Cartilage Biology & Pathology
Comprehending Cartilage Formation, Function, and Failure for Improving Joint Health
APRIL 1–2, 2017
CHAIRS: Matthew R. McCann & Blandine Poulet

Cell Biology of Megakaryocytes & Platelets

Fundamental Biology and Disorders of the Megakaryocyte Lineage: From Hematopoietic Stem Cell to Hemostasis

FEBRUARY 26–MARCH 3, 2017

RENAISSANCE TUSCANY IL CIOCCO, LUCCA (BARGA), ITALY

CHAIR: Benjamin T. Kile

VICE CHAIR: Wolfgang Bergmeier

- **Keynote Session: From Fundamental Biology to Novel Therapies** *Jack Levin,* Andrew Weyrich, Martine Jandrot-Perrus
- **Platelet Signaling: Lipids, Granules, and Membranes** *Elizabeth Gardiner,* Junling Liu, Lawrence Brass, Alastair Poole, Justin Hamilton
- **Embryonic and Ontological Development of Megakaryocytes and Platelets** *James Palis,* Samir Taoudi, Martha Sola-Visner, Ana Cvejic
- **Achilles' Heels: Identifying the Causes of Congenital Platelet Disorders** *Kathleen Freson,* Hana Raslova, Jorge Di Paola, Patrizia Noris, Neil Morgan
- **Backbone of the Lineage: TPO and c-Mpl Signaling in Health and Disease** *Nichola Cooper,* Warren Alexander, Ian Hitchcock, James Bussel
- **Myeloproliferative Neoplasms and Acute Megakaryoblastic Leukemia** *Thomas Mercher,* Tanja Gruber, Stefan Constantinescu, Norio Komatsu, John Crispino
- **Form and Function: Cytoskeletal Regulation in Megakaryocytes and Platelets** *Antonija Begonja,* Markus Bender, Catherine Leon, Steve Thomas
- **Platelets, Inflammation, and Innate Immunity** *Craig Jenne,* Jane Freedman, Eric Boilard, Marieke Essers, Adam Cunningham
- **Tumour Cells and Platelets: Une Affaire Compliquée** *Emma Josefsson,* Myriam Labelle, Anil Sood, Elisabeth Battinelli
- **Power Hour** *Elizabeth Gardiner, Kellie Machlus*

Cell Biology of Megakaryocytes & Platelets
The Extraordinary Journey from Stem Cell to Platelet: Roles in Hemostasis and Beyond
FEBRUARY 25–26, 2017
CHAIRS: Natalie S. Poulter & Sarah J. Fletcher

Chemical & Biological Terrorism Defense

Innovation and Advancement: Fundamental Science Resulting in Next-Gen Solutions for Chemical and Biological Threats

MARCH 5–10, 2017

VENTURA BEACH MARRIOTT, VENTURA, CA

Chair: Steven R. Blanke

Vice Chairs: Catharine M. Bosio & Patrick M. McNutt

- **Keynote Session: Chemical and Biological Threats: Emerging Challenges Requiring Innovative Solutions** *Patrick McNutt,* Arik Eisenkraft
- **Neural Dysfunction Due to Biological and Chemical Threat Agents: Mechanisms, Detection, and Countermeasures** *John McDonough,* Pamela Lein, Douglas Cerasoli, Andrew Pickett
- **Mechanisms and Consequences of Host Immune Interactions with Emerging and Existing Threat Agents** *Manuela Raffatellu,* Carolyn Coyne
- **Host Barrier Function and Dysfunction** *Catharine Bosio,* Debra Laskin, Wyndham Lathem
- **Targeting Metabolism** *Molly Hughes,* Jean Challacombe, Michael Lagunoff
- **Extended and Emerging Threats to Human Health and Security** *Jacqueline Fletcher,* Owain Edwards, Townsend Peterson, William Schneider
- **Late-Breaking Topics** *Thomas Blake*
- **Smart Approaches for Detection, Prevention, and Intervention** *Molly Stevens,* Charles Thompson, Esther Chang
- **Working at the Periphery: Bioengineering-Inspired Solutions for Counteracting Biological and Chemical Threats** *Patrick Stayton,* Harald Ott, Nicole Steinmetz

Chemical & Biological Terrorism Defense
Basic and Translational Research Advances in the Field of Chemical Defense and Biological Defense of Humans, Animals, and Plants
MARCH 4–5, 2017
CHAIR: Katie M. Hoffman

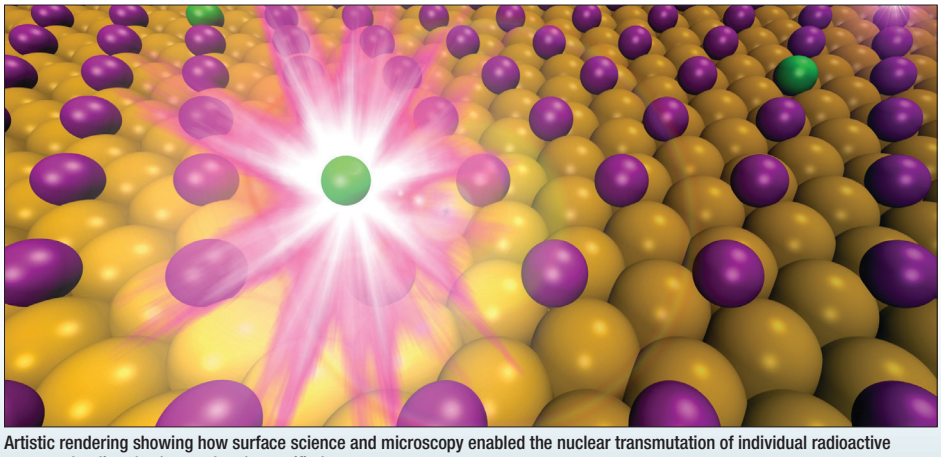

Artistic rendering showing how surface science and microscopy enabled the nuclear transmutation of individual radioactive atoms to be directly observed and quantified. COURTESY OF THE SYKES (TUFTS) AND MICHAELIDES (UCL) GROUPS. IMAGE CREATED BY PHILIPP PEDE. SUBMITTED BY THE 2017 CHEMICAL REACTIONS AT SURFACES GRC CHAIR.

> ***"Without the Gordon Conferences, scientists would be less willing to share unpublished results and would lose opportunities for forging valuable collaborations."***
>
> R. TOM BAKER, UNIVERSITY OF OTTAWA

Chemical Reactions at Surfaces

Defining the Next Generation Challenges in Surface Chemistry and Surface Science

FEBRUARY 5–10, 2017

RENAISSANCE TUSCANY IL CIOCCO, LUCCA (BARGA), ITALY

CHAIR: Andrew J. Gellman

VICE CHAIR: Christof Woell

- **Chirality and Enantioselectivity** *Kalle Ernst,* Ron Naaman, Francisco Zaera
- **Surface Chemistry— Mechanisms** *John Kitchin,* Giorgio Contini, Enrique Ortega, Jose Rodriguez
- **Electron- and Photon-Induced Surface Chemistry** *Swetlana Schauermann,* John Polanyi, Cynthia Friend
- **Liquids and Electrochemistry** *Junfa Zhu,* Joerg Libuda, Heon Kang, Hans-Peter Steinrueck
- **Theory— Advances and Limits** *Gianfranco Pacchioni,* Felix Studt, Alexander Tkatchenko
- **Structure and Dynamics** *Charles Campbell,* Katharina Franke, Hajo Freund, Angelika Khunle
- **Water and Environmental Surfaces** *Franz Geiger,* Heather Allen, Bruce Kay
- **Nanoparticle Surface Chemistry** *Judy Yang,* Michael Filler, Gabor Somorjai, Kijung Yong
- **Theory— Applications** *Manos Mavrikakis,* Stephen Jenkins, Philippe Sautet
- **Power Hour** *Judy Yang*

Chemical Reactions at Surfaces
Understanding Complexity in Surface Reactivity Through Multidisciplinarity
FEBRUARY 4–5, 2017
CHAIRS: Albert Bruix & Irem Sen

Chloroplast Biotechnology

Breaking Ground Toward Plant Synthetic Biology

JANUARY 8–13, 2017

VENTURA BEACH MARRIOTT, VENTURA, CA

CHAIR: Ralph Bock

VICE CHAIR: Maureen R. Hanson

- **Organelles, Genomes, and Genome Interactions** *Ralph Bock,* Katherine Osteryoung, Jesse Woodson, Stephan Greiner
- **Engineering Organellar Genes, Genomes, and Transcripts: Technical Advances** *Phil Dix,* Pal Maliga, Keiji Numata, Anil Day, Ian Small, Alice Barkan, Takahiro Nakamura
- **Transcription and RNA Metabolism in Plastids** *Christian Schmitz-Linneweber,* David Stern, Sabeeha Merchant, Stephane Bentolila
- **Recombinant Protein Expression** *Pal Maliga,* Jihong Liu Clarke, Fernando Bravo-Almonacid, Henry Daniell, Rima Menassa
- **Translation, Protein Stability, Protein Folding and Assembly** *Alice Barkan,* Francis-Andre Wollman, Michael Schroda
- **Engineering Photosynthesis** *Jean-David Rochaix,* Spencer Whitney, Christine Raines, Martin Jonikas, Justin McGrath, Steven Kelly
- **Engineering of Plastids and Their Metabolism in Algae** *Stephen Mayfield,* Joseph Ostrand, Silvia Ramundo, Saul Purton, Geoffrey McFadden
- **Synthetic Biology: From Cyanobacteria to Chloroplasts** *Maureen Hanson,* Daniel Ducat, Cheryl Kerfeld, Martin A.J. Parry, Alison Smith, Benjamin Rubin
- **Synthetic Biology: Redesigning Chloroplasts and Their Metabolism** *Alison Smith,* Kevin Redding, Poul Erik Jensen
- **Power Hour** *Maureen Hanson, Katherine Osteryoung*

Visit the Frontiers of Science at a Gordon Conference! www.grc.org
Downloaded from http://science.sciencemag.org/ on September 30, 2016

These groups of cells helped RIPE researchers refine the transformation process to insert genes that will increase yields of staple food crops. PHOTOGRAPHER: HALEY AHLERS. PICTURE CREDIT: THE RIPE PROJECT AT THE CARL R. WOESE INSTITUTE FOR GENOMIC BIOLOGY (UNIVERSITY OF ILLINOIS). SUBMITTED BY THE 2017 CO2 ASSIMILATION IN PLANTS FROM GENOME TO BIOME GRC CHAIRS

Cilia, Mucus & Mucociliary Interactions

Advancements in Molecular Understanding and Therapeutic Targeting of Mucociliary Disorders

FEBRUARY 12–17, 2017

HOTEL GALVEZ, GALVESTON, TX

CHAIRS: Elizabeth Smith & Heymut Omran
VICE CHAIRS: Chris Evans & Hannah M. Mitchison

- **Keynote Session: Cilia, Mucus, and Mucociliary Diseases** *Martina Brueckner, David Thornton,* Burton Dickey, Marcus Mall, Daniela Nicastro
- **Differentiation, Assembly, and Regulation of Mucociliary Components** *Maimoona Zariwala,* Monica Bettencourt-Dias, Stephen King, Ivana Yang
- **Technical Advancements to Study Mucociliary Biology** *Maureen Wirschell,* Susan Birket, Katharina Ribbeck
- **Mucociliary Dysfunction: Balancing Homeostasis and Pathophysiology** *Burton Dickey,* Steven Brody, Cecilia Lo, Johanna Raidt
- **Protein Assembly and Glycosylation** *Martin Blum,* Thomas Gerken, Chris Kintner, Mary Porter
- **Mucociliary Defense and Immunity** *Ivana Yang,* Bruce Bochner, Sumaira Hasnain, Rodney Newberry, Yogesh Saini
- **Cellular and Developmental Aspects of Cilia and Mucus Biology** *Benedicte Durand, Michael McGuckin,* Jeffrey Axelrod, Hiroshi Hamada, Lin He, Kelly Ten Hagen
- **Molecular Understanding of Muco- and Ciliopathies** *Mehmet Kesimer,* Brian Button, Pleasantine Mill, David Schwartz, Masahide Kikkawa
- **Novel Therapeutic Targets and Strategies for Disorders of Mucus and Cilia** *Chris Evans,* Richard Boucher, Amy Firth, Jung Soo Suk

GRS Cilia, Mucus & Mucociliary Interactions

Interdisciplinary Approaches to Investigate Cilia, Mucus, and Mucociliary Interactions Throughout the Body

FEBRUARY 11–12, 2017

CHAIRS: Adrianne L. Stefanski & Tabea Menchen

CO_2 Assimilation in Plants from Genome to Biome

Adapting Photosynthesis to Insure Against an Uncertain Future

APRIL 30–MAY 5, 2017

RENAISSANCE TUSCANY IL CIOCCO, LUCCA (BARGA), ITALY

CHAIRS: Stephen P. Long & Martha Ludwig
VICE CHAIRS: Joy K. Ward & Martin A.J. Parry

- **Engineering Increased Photosynthesis for Food Security and Bioenergy** *Steve Long,* Tsuyoshi Furumoto, Martin Jonikas, Patricia Lopez-Calcagno, Ron Milo, Mark Stitt
- **Advancing Quantification and Engineering of the Global Sinks for CO_2** *Carl Bernacchi,* Joseph Berry, Beverly Law, Jonathan Lloyd, Dan Yakir
- **Rubiscos and Photorespiration** *Robert Sharwood,* Oula Ghannoum, Martin Hagemann, Donald Ort, Grant Pearce
- **Stomata— How Do They Link to Mesophyll CO_2 Assimilation?** *Tracy Lawson,* Margaret Barbour, John Evans, Diana Santelia, Julian Schroeder
- **Inorganic C Transporters and Increasing Mesophyll Conductance** *Susanne Von Caemmerer,* Wagner Araujo, David Hanson, Maureen Hanson, Danny Tholen
- **Evo-Devo of the CO_2 Assimilation Apparatus** *Urte Schlueter,* David Heckmann, Jane Langdale, Tammy Sage, Thomas Slewinski
- **Intra- and Inter-Compartmental Fluxes** *Yuhang Wang,* Douglas Allen, Lee Sweetlove, Michael Hodges
- **CO_2 Concentrating Mechanisms** *Martin A.J. Parry,* Sarah Davis, Christopher Dupont, Sascha Offermann, J. Eduardo Zabaleta
- **Adapting to Global Atmospheric Change** *Elizabeth Ainsworth,* Jill Anderson, Sotirios Archontoulis, Katie Becklin, James Ehleringer, Howard Griffiths

GRS CO_2 Assimilation in Plants from Genome to Biome

Expanding the Relevance of Photosynthesis Research for the Next Generation of Plant Scientists

APRIL 29–30, 2017

CHAIRS: Berkley J. Walker & Yu Wang

NEW! Complex Active & Adaptive Material Systems

Designing Biomimetic, Dissipative Material Systems

JANUARY 29–FEBRUARY 3, 2017

FOUR POINTS SHERATON / HOLIDAY INN EXPRESS, VENTURA, CA

CHAIR: Anna C. Balazs
VICE CHAIR: Julia Yeomans

- **Learning from Nature** *Jeff Brinker,* Zvonimir Dogic, Juan de Pablo
- **Enabling Approaches to Creating Dissipative Systems for Biomimetic Functionality** *Ximin He,* Maria Santore, Krzysztof Matyjaszewski, Monica Olvera de la Cruz
- **Designing the Basic Active and Adaptive Units: Artificial Cells and Smart Colloids** *Neha Kamat,* Daniel Hammer, Paul Chaikin
- **Biomimetic-Directed Motion** *Neils Holten-Anderson,* Ayusman Sen, Olga Kuksenok, Andrew Turberfield
- **Dynamically Responsive Soft Materials** *Todd Emrick,* Richard Vaia, Randall Kamien
- **Biomimetic Energy Utilization** *Mary Galvin,* Samuel Stupp, Ralph Nuzzo, Oliver Steinbock
- **Autonomous Machines** *Arthi Jayaraman,* Igor Aronson, Sharon Glotzer
- **Synchronization in Complex Biological Networks and Chemical Computers** *Atul Parikh,* Rebecca Schulman, Nader Engheta, Irving Epstein
- **New Robotic Systems** *Elizabeth Smela,* George Whitesides, Joseph Wang
- **Power Hour** *Sambeeta Das*

Dendrites: Molecules, Structure & Function

The Roles of Dendrites in Neurons, Circuits, Systems, and Behaviors

MARCH 26–31, 2017

RENAISSANCE TUSCANY IL CIOCCO, LUCCA (BARGA), ITALY

CHAIRS: Randy Bruno & Ryohei Yasuda
VICE CHAIRS: Karen Zito & Jackie Schiller

- **Dendritic Development and Remodeling** *Wesley Grueber,* Holly Cline, Julie Lefebvre, Michisuke Yuzaki
- **New Techniques for Imaging Dendrites** *Matthew Larkum,* Alessio Attardo, Moritz Helmstaedter, Na Ji
- **Dendritic Excitability** *Attila Losonczy,* Veronica Egger, Lucy Palmer, Alon Polsky
- **Molecular and Biochemical Signaling in Dendrites** *Rachel Wong,* Haruhiko Bito, Michael Ehlers, Yasunori Hayashi, Erin Schuman
- **Dendritic Integration and Plasticity** *Steven Siegelbaum,* Anthony Holtmaat, Greg Stuart
- **Clustering on Dendrites** *Michael Hausser,* David Digregorio, David Fitzpatrick, Christian Lohmann, Judit Makara
- **Dendrites in Skill Learning** *Masanori Murayama,* Jun Ding, Wenbiao Gan, Akiko Hayashi-Takagi
- **Inhibitory Signaling on Dendrites** *Bartlett Mel,* Jeffrey Magee, Idan Segev, Nelson Spruston
- **Dendrites in Memory Engrams** *Elly Nedivi,* Todd Sacktor, Johannes Letzkus

GRS Dendrites: Molecules, Structure & Function

Dendrites in Health and Disease

MARCH 25–26, 2017

CHAIRS: Christine Grienberger & Trace Henry

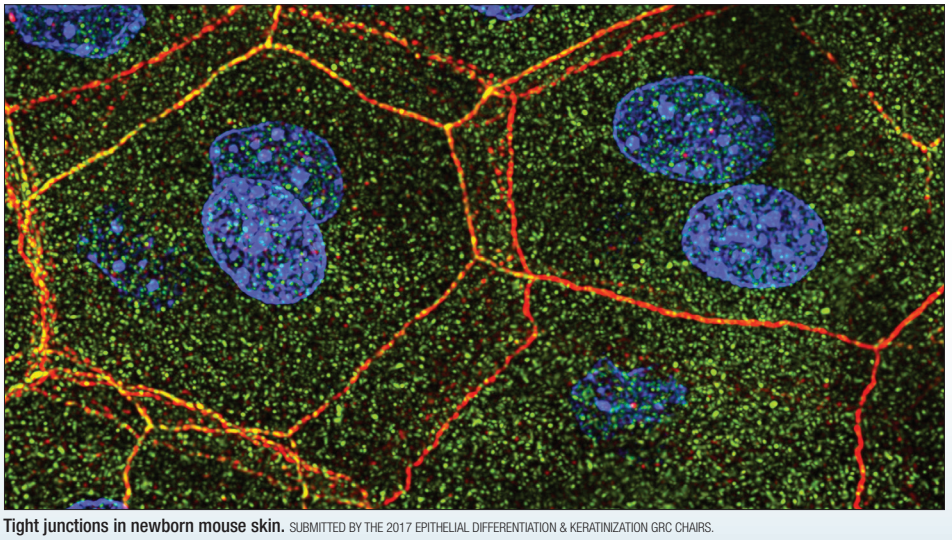

Tight junctions in newborn mouse skin. SUBMITTED BY THE 2017 EPITHELIAL DIFFERENTIATION & KERATINIZATION GRC CHAIRS.

Downloaded from http://science.sciencemag.org/ on September 30, 2016

Directed Cell Migration

Mechanisms of Collective and Single Cell Motility in Development, Homeostasis, and Disease

JANUARY 22–27, 2017

HOTEL GALVEZ, GALVESTON, TX

CHAIR: Denise Montell

VICE CHAIR: Orion D. Weiner

- **Keynote Session: 25 Years of Rac and Rho** *Clare Waterman,* Anne Ridley, Sandrine Etienne-Manneville
- **Directed Cell Migration in Development** *Andrew Ewald,* Roberto Mayor, Sally Horne-Badovinac, Brian Stramer, Eduardo Moreno
- **Chemotaxis Signaling** *Milka Sarris,* Carole Parent, Robert Insall, Peter Devreotes
- **Directed Cell Migration in Wound Repair** *Ronald Germain,* Anna Huttenlocher, Tobias Meyer, Will Wood
- **Cell Migration in Cancer** *Celeste Nelson,* Andrew Ewald, Erik Sahai, Cynthia Reinhart-King
- **Immune Cell Migration** *Anna Huttenlocher,* Ronald Germain, Milka Sarris, Orion Weiner
- **Mechanics of Cell Migration** *Tobias Meyer,* Nir Gov, Clare Waterman, Celeste Nelson
- **Migration and Metastasis** *Erik Sahai,* Peter Friedl, Raghu Kalluri, Adam Marcus
- **Cytoskeleton Dynamics in Migrating Cells** *Sandrine Etienne-Manneville,* James Bear, Margaret Gardel, Michael Sixt

Directed Cell Migration
Cell Migration in Focus: From Live Imaging to Mechanics
JANUARY 21–22, 2017
CHAIRS: Joseph P. Campanale & Brian R. Graziano

Epithelial Differentiation & Keratinization

Epithelial Interactions in Development, Homeostasis, Disease, and Therapy

MAY 7–12, 2017

RENAISSANCE TUSCANY IL CIOCCO, LUCCA (BARGA), ITALY

CHAIR: Carien M. Niessen

VICE CHAIR: Valentina Greco

- **Visualizing Interactions in Epithelial Homeostasis and Disease** *Kathleen Green,* Ronald Germain, Angela Christiano
- **Homeostatic Growth and Regeneration of Epithelia: Novel Concepts in Cell Death and Renewal** *Valerie Horsley,* Jayaraj Rajagopal, Philip Jones, Kim Jensen, Eugenia Piddini, Valentina Greco
- **Evolution and Morphogenesis of Skin and Its Appendages** *Carien Niessen,* Christiane Nuesslein-Volhard, Sarah Millar, Cheng-Ming Chuong, Anthony Oro
- **Cancerous Growth, Migration, and Invasion of Epithelia** *G. Paolo Dotto,* Peter Friedl, Allan Balmain, Cedric Blanpain, Elaine Fuchs, Andrzej Dlugosz
- **Genetic and Epigenetic Determinants of Epithelial Cell Fate** *Vladimir Botchkarev,* Howard Chang, Paul Khavari, Tudorita Doina Tumbar
- **Regulators of Cell and Tissue Architecture** *Birgit Lane,* Roberto Mayor, Terry Lechler, Sara Wickstrom, Pierre Coulombe
- **Cellular Stress Responses in Homeostasis and Degeneration** *Salvador Aznar Benitah,* David Sabatini, Michaela Frye
- **Epithelia Micro-Environment in Homeostasis and Disease** *Michael Rendl,* Manolis Pasparakis, Fiona Watt, Ellen Lumpkin, George Cotsarelis
- **Novel Translational Concepts in Epithelial Based Disease** *Dennis Roop,* Julie Segre, Akiharu Kubo, Graziella Pellegrini

Epithelial Differentiation & Keratinization
Multicellular Interactions Underlying Adhesion, Polarity, Growth, and Disease
MAY 6–7, 2017
CHAIR: Aaron F. Mertz

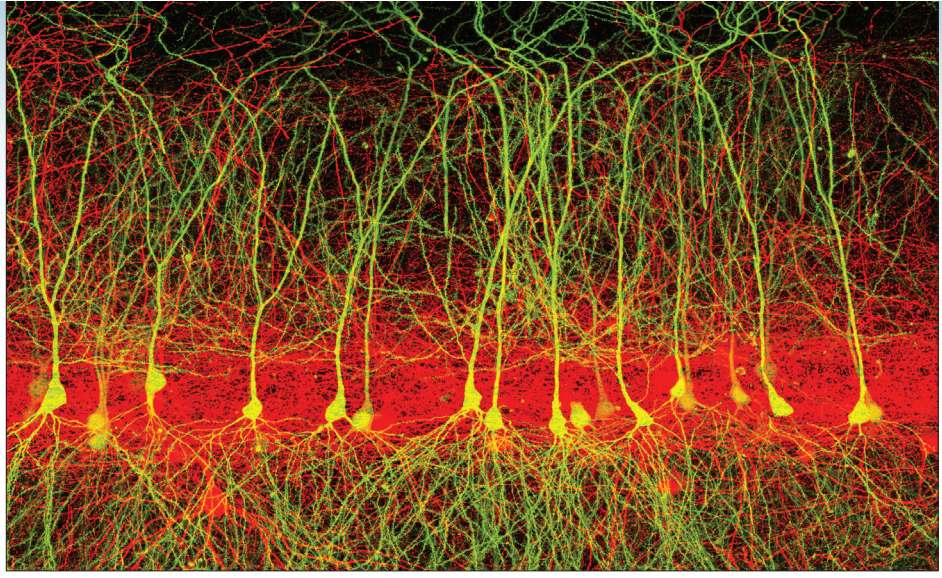

High-resolution array tomography enables the detailed structure of synaptic connectivity to be mapped across the entire dendritic arbor of fluorescently labeled neurons. This image shows the tight laminar structure of synaptic connections between parvalbumin-expressing interneurons (red) and pyramidal neurons (green) within the mouse hippocampal CA1 microcircuit.

IMAGE BY ERIK BLOSS (SPRUSTON LAB, JANELIA RESEARCH CAMPUS). SUBMITTED BY THE 2017 DENDRITES: MOLECULES, STRUCTURE & FUNCTION GRS CHAIRS.

Fibronectin, Integrins & Related Molecules

The Regulation of Cell Behaviour by Cell-Extracellular Matrix Interactions

JANUARY 29–FEBRUARY 3, 2017

VENTURA BEACH MARRIOTT, VENTURA, CA

CHAIR: Charles H. Streuli

VICE CHAIRS: Roy Zent & Johanna Ivaska

- **Keynote Session: The Dawn of the Extracellular Matrix in Tissue Function** *Charles Streuli,* Billy Hudson
- **How Signals from the Matrix Control Cell Fate** *Ambra Pozzi,* Alfred Nordheim, Qing-Jun Meng, Florian Bentzinger, Peter Friedl
- **Matrix Architecture and Cell Function** *Christine-Maria Horejs,* Michael Sherratt, Christopher Chen
- **Mechanotransduction** *Janine Erler,* Joachim Spatz, Jing Yang, Andres Garcia, Patricia Keely
- **The Extracellular Matrix and Stem Cells** *Florian Bentzinger,* Charles ffrench-Constant, Jennifer Elisseeff
- **Cell Adhesion in Cancer** *Patricia Keely,* Valerie Weaver, Clare Isacke, Janine Erler, John Marshall
- **Cell Migration** *Tobias Zech,* Laura Machesky, Nils Gauthier
- **Integrin Trafficking** *Johanna Ivaska,* Ludger Johannes, Ralph Boettcher, David Lyden, Jim Norman
- **Keynote Session: How the Adhesome Works** *Roy Zent,* Mark Ginsberg

Fibronectin, Integrins & Related Molecules
Extracellular Matrix Dynamics and Cell Fate
JANUARY 28–29, 2017
CHAIRS: Christine-Maria Horejs & Guanqing Ou

Gaseous Ions: Structures, Energetics & Reactions

Gas-Phase Ion Chemistry: From Fundamentals to Applications

FEBRUARY 12–17, 2017

VENTURA BEACH MARRIOTT, VENTURA, CA

CHAIR: Julia Laskin

VICE CHAIR: Gert von Helden

- **Ions in Real World** *Gereon Niedner-Schatteburg,* Scott Anderson, Michal Farnik
- **Ions in Droplets: Solvation, Reactivity, and Evaporation** *Abraham Badu-Tawiah,* Styliani Constas, Graham Cooks, Chris Hogan, Paul Scheier
- **Chemistry of Radical Ions** *Ivan Chu,* Ryan Julian, Yu Xia
- **Ion Spectroscopy** *Jana Roithova,* Andre Fielicke, Marie-Pierre Gaigeot, Rebecca Jockusch, Mark Johnson
- **Reactivity of Gaseous Ions** *J. Katherine Lee,* Shaun Ard, Christoph Schalley
- **Ion Structures and Energetics** *Xuebin Wang,* Michael Bowers, Mary Rodgers, Balint Sztaray, Einar Uggerud
- **Ion-Surface Collisions: Fundamentals and Applications** *William Hase,* Grant Johnson, Vicki Wysocki
- **New Techniques for Studying Gaseous Ions** *Evan Williams,* Matthew Bush, Manfred Kappes, Adam Trevitt, Roland Wester
- **Keynote Session: Ion Chemistry: From the Gas Phase to Air–Water and Water–Organic Interfaces** *Peter Armentrout,* Jack Beauchamp
- **Power Hour** *Yu Xia*

Gaseous Ions: Structures, Energetics & Reactions
Gaseous Ions: From Catalysis to Biology
FEBRUARY 11–12, 2017
CHAIRS: Sarah E. Waller & Christian Van Der Linde

Glial Biology: Functional Interactions Among Glia & Neurons

Neuron–Glia Interactions in Health and Disease

MARCH 5–10, 2017

FOUR POINTS SHERATON / HOLIDAY INN EXPRESS, VENTURA, CA

CHAIR: Beth A. Stevens

VICE CHAIR: Dwight Bergles

- **Contribution of Glia to Brain Wiring** *Cagla Eroglu,* David Lyons, Etienne Audinat, Staci Bilbo, Dorothy Schafer
- **Glial Contributions to Synaptic Plasticity and Neuromodulation** *Vladimir Parpura,* Nicola Allen, Jaideep Bains, Marc Freeman, Sergey Kasparov, Brian MacVicar, Stephane Oliet
- **Glia as Mediators of Circuit Dysfunction** *Philip Haydon,* Susan Campbell, Cagla Eroglu, Eric Huang, Michael Salter
- **Metabolic Control by Glia** *Bruce Ransom,* Klaus-Armin Nave, Michael Robinson, Stefanie Schirmeier, Mark Verheijen, Bruno Weber
- **Glial Contributions to Neurovascular Coupling** *David Attwell,* Serge Charpak, Grant Gordon, Elizabeth Hillman, Eric Newman
- **Structural and Functional Heterogeneity Among Glia** *Helmut Kettenmann,* Mario Capecchi, Patrizia Cassacia, Frank Kirchhoff, Anna Molofsky, Ye Zhang, Keith Murai
- **Glial Cell Development** *Kelly Monk,* Sonia Garel, Magdalena Gotz, Freda Miller
- **New Technologies for Understanding Glial Cell Function** *Maiken Nedergaard,* Baljit Khakh, Steve McCarroll, Axel Nimmerjahn, Anne Schaefer, Ko Matsui
- **Gliogenesis in Health and Disease** *Michael Sofroniew,* Alison Lloyd, Michelle Monje, Harald Sontheimer, Hui Zhong

Glial Biology: Functional Interactions Among Glia & Neurons
Neuron-Glia Interactions in Health and Disease
MARCH 4–5, 2017
CHAIRS: Lasse Dissing-Olesen & Sarah D. Ackerman

Visit the Frontiers of Science at a Gordon Conference! www.grc.org
Downloaded from http://sciencemag.org/ on September 30, 2016

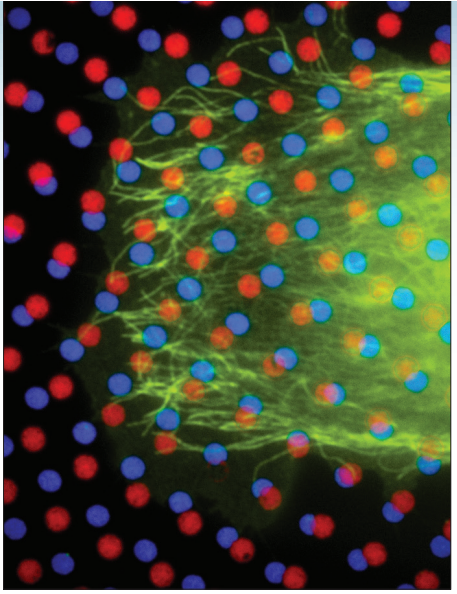

A human foreskin fibroblast spread on micropatterns (2 um in diameter) with alternating patches of stimulatory (red) and inhibitory (blue) anti-b1 integrin monoclonal antibodies was stained for a-tubulin (green). CREDIT: GUILLAUME JACQUEMET (UNIVERSITY OF TURKU). SUBMITTED BY THE 2017 FIBRONECTIN, INTEGRINS & RELATED MOLECULES GRC CHAIR.

Glycobiology

Glycan Function and Structure from Nucleus to Niche

MARCH 19–24, 2017

VENTURA BEACH MARRIOTT, VENTURA, CA

CHAIR: Michael Tiemeyer

VICE CHAIR: Rita Gerardy-Schahn

- **Keynote Session: Interdisciplinary Glycobiology** *Kelly Ten Hagen,* Pamela Stanley, Jeffrey Esko, Markus Aebi
- **Glycans in Niche Communities and Innate Immunity** *Anne Imberty, Fikri Avci,* Hiutung Chu, Alisdair Boraston, Ronald Schnaar
- **Glycosylation and Signaling** *John Hanover,* Gerald Hart, Kay Grobe, William Sessa
- **Omics, Informatics, Evolutionary, and Developmental Glycobiology** *Nicolle Packer, Robert Haltiwanger,* Anne Dell, Michael Snyder, Pascal Gagneux, Hamed Jafar-Nejad
- **Leveraging Glycoscience for Developing Therapeutics** *Michael Pierce,* James Paulson, Stephen Withers, Thomas Clausen
- **Cellular and Molecular Pathways for Glycoprotein Trafficking and the Glycobiology of Microbes and Parasites** *Richard Steet, Richard Cummings,* Tadashi Suzuki, Hans Wandall, Michael A. Ferguson, Christine Szymanski
- **Structural Biology of Glycogene Products** *Karen Colley,* Jochen Zimmer, Kelley Moremen
- **Glycobiology of the HIV Virus and the Pathobiochemistry of Glycosylation Diseases** *Thierry Hennet, Linda Baum,* Max Crispin, Gaiit Alter, Lance Wells, Nancy Dahms
- **Glycobiology of Neural Function and Disease** *Rita Gerardy-Schahn,* Maria Lehtinen, Vlad Panin

Glycobiology
Glycan Function and Structure in Development, Disease, and Host-Pathogen/Symbiont Interactions
MARCH 18–19, 2017
CHAIR: Melody (Mindy) Porterfield

IGF & Insulin System in Physiology & Disease

IGF/Insulin Signaling: New Discoveries in Metabolism and Growth, Stem Cells and Epigenetics, Aging, Cancer, and Neurological Disease

MARCH 12–17, 2017

VENTURA BEACH MARRIOTT, VENTURA, CA

CHAIR: Cunming Duan

VICE CHAIRS: Claire M. Perks & Shin-Ichiro Takahashi

- **Keynote Session: Regulation of IGF and Insulin Expression and Secretion** *Cunming Duan, Claire Perks,* Thomas Sudhof
- **mTOR in IGF/Insulin Signaling and Nutrient Sensing** *Derek Leroith,* Michael Hall, Kun-Liang Guan, David Sabatini, Pan Zheng
- **IGF/Insulin Signaling in Aging** *Cheryl Conover,* Diana Van Heemst, Luigi Fontana, Pinchas Cohen
- **IGF/Insulin Signaling in Cancer** *Rosemary O'Connor,* Carlos Lopez-Otin, Emily Gallagher, Jeff Holly, Thomas Bogenrieder
- **IGF Binding Proteins** *Robert Baxter,* Yihong Wan, Wendie Cohick, Lester Lau
- **Neural Stem Cells, Neurological Diseases/Regeneration** *John Pintar,* Terri Wood, Tzumin Lee, Inna Slutsky, Zhigang He
- **IGF/Insulin Signaling in Metabolism, Growth, and Disease** *Peter Rotwein,* Thomas Clemens, Hongxia Ren, Francois Leulier
- **Epigenetics and Stem Cells/Cell Differentiation** *Briony Forbes, Linheng Li,* Marisa Bartolomei, Joseph Avruch, Marie-Liesse Asselin-Labat, David Clemmons
- **Keynote Session: New Lessons from Model Organisms** *Andrzej Bartke, Shin-Ichiro Takahashi,* Gary Ruvkun
- **Power Hour** *Briony Forbes, Cheryl Conover*

Immunology of Fungal Infections

Fundamental Insights and Therapeutic Potential: Advances in Understanding the Host–Fungus Interaction

JANUARY 15–20, 2017

HOTEL GALVEZ, GALVESTON, TX

CHAIRS: George Deepe & Mihai Netea

VICE CHAIRS: Sarah L. Gaffen & Neil Gow

- **Cutting Edge in Fungal Immunology** *Gordon Brown,* Jean-Paul Latge, Julian Naglik, Arturo Zychlinsky
- **Recognition of Fungi by Innate Cells** *Salome Leibundgut-Landmann,* Michael Lorenz, Betty Wu-Hsieh, Gordon Brown, Amariliz Rivera, Beth Garvy
- **Immune–Metabolic Interactions in Fungal Immunity** *Georgios Chamilos,* Robert Cramer, Leo Joosten, Peter Murray, Constantin Urban
- **Humoral and Cellular Effectors in Fungal Immunity** *Amariliz Rivera,* Scott Filler, Nancy Keller, Bruce Klein, Mari Shinohara, Chad Steele
- **Maladaptive Immunity** *Frank Van De Veerdonk,* Vera Calich, Georgios Chamilos, Kirsten Nielsen, Teresa Zelante
- **Immunogenetics and Pathophysiology of Fungal Immunity** *Kirsten Nielsen,* Frank Van De Veerdonk, Vinod Kumar, Desa Lilic, Xin Lin, Caitlin Pepperall, Anne Puel
- **Mycobiome and Host Defense Mechanisms** *Floyd Wormley,* Yvonne Huang, Andrew Koh, David Underhill, Salome Leibundgut-Landmann
- **Innate and Adaptive Memory in Fungal Infection** *Vera Calich,* Floyd Wormley, Ashraf Ibrahim, Jessica Quintin, Sing Sing Way, Christina Zielinski
- **Host-Directed Therapy: From Vaccines to Immunotherapy** *Jatin Vyas,* Stuart Levitz, Adilia Warris, Peter Williamson, Jack Edwards

Immunology of Fungal Infections
Exploring the Hosts' Weaknesses: New Insights from Basic Mechanisms to Complex Host–Pathogen Interactions to Combat Fungal Infections
JANUARY 14–15, 2017
CHAIRS: Jessica Quintin & Jeanette Wagener

Inorganic Reaction Mechanisms

Metal-Based Reactions that Enable Scientific Advances in Energy, Biology, Materials, and Catalysis

MARCH 5–10, 2017

HOTEL GALVEZ, GALVESTON, TX

CHAIR: Patrick Holland

VICE CHAIR: Timothy Warren

- **Mechanisms in Catalysis with Inexpensive Metals** *Alison Fout,* Paul Chirik, Rebecca Ruck
- **Mechanisms of Polymerization Catalysis** *Crisita Carmen Atienza,* Brad Bailey, Eugene Chen, Jian Yang, Larry Sita
- **Mechanisms of Electrocatalysis** *Morris Bullock,* Jillian Dempsey, Yogesh Surendranath
- **Mechanisms of Organometallic Catalysis for Organic Synthesis** *Daniel Weix,* Jennifer Schomaker, Eric Simmons, Michael Neidig, Carl Busacca
- **Mechanisms at the Edge of the Periodic Table** *Eric Schelter,* Suzanne Bart, Gary Schrobilgen
- **Mechanisms of Multimetallic Compounds** *John Berry,* Theodore Betley, Zhaomin Hou, Christine Thomas, Franc Meyer
- **Mechanisms on Metallic Surfaces** *Susannah Scott,* Randy Yeates, Alessandra Quadrelli
- **Mechanisms in Bioinorganic Chemistry** *Anne Jones,* Thomas Rauchfuss, Stephen Ragsdale, Julie Kovacs, Lance Seefeldt
- **Mechanistic Techniques in Organometallic Chemistry** *Daniel Mindiola,* Robert Bergman
- **Power Hour** *Rebecca Ruck*

Inorganic Reaction Mechanisms
Catalysis, Mechanisms, and New Methodologies for Interdisciplinary Problems in Inorganic Chemistry
MARCH 4–5, 2017
CHAIRS: Christopher Caputo & Emily J. Thompson

Lysosomal Diseases

Understanding Lysosomal Biology and Disease Mechanisms to Develop New Therapies for Lysosomal Diseases

MARCH 5–10, 2017

RENAISSANCE TUSCANY IL CIOCCO, LUCCA (BARGA), ITALY

CHAIR: Andrea Ballabio

VICE CHAIR: Beverly Davidson

- **Keynote Session: New Frontiers in Intracellular Trafficking** *Beverly Davidson, Andrea Ballabio,* Scott Emr, Tom Kirchhausen
- **Lysosomal Positioning and Movement** *J. Paul Luzio, William Sly,* Juan Bonifacino, Ana-Maria Lennon-Dumenil, Harald Stenmark, Gillian Griffiths
- **Lysosomal Membrane Proteins and Human Diseases** *Bruno Gasnier, Volkmar Gieselmann,* Paul Saftig, Thomas Jentsch, Emyr Lloyd-Evans
- **Mechanisms of LSDs** *Alessandra D'Azzo, Steven Walkley,* Elina Ikonen, Thomas Braulke, Frances Platt, Jeffery Kelly
- **Lysosomal Dysfunction in Diseases Other than LSDs** *Tony Futerman, Maurizio Scarpa,* Ralph Nixon, Seung-Jae Lee, Judith Klumperman
- **Innovative Therapies** *Albert Seymour, James Wilson,* Timothy Cox, Silvia Muro, Charles Vite, Kim Hemsley
- **Diagnostics and Biomarkers for LSDs** *Joe Clarke, John Hopwood,* Hans Aerts, Olaf Bodamer
- **Ongoing and Upcoming Clinical Trials** *Brian Bigger, Daniel Ory,* Gregory Pastores, Angela Schulz, Fatima Bosch, Roberto Giugliani
- **Late-Breaking Topics / Selected Presentations from the GRS** *Nicola Brunetti-Pierri, Thomas Braulke*

Lysosomal Diseases
Decoding Lysosomal Signals to Understand Disease Mechanisms and Define New Therapeutic Strategies for Lysosomal Storage Disorders
MARCH 4–5, 2017
CHAIRS: Chiara Di Malta & Ian M. Williams

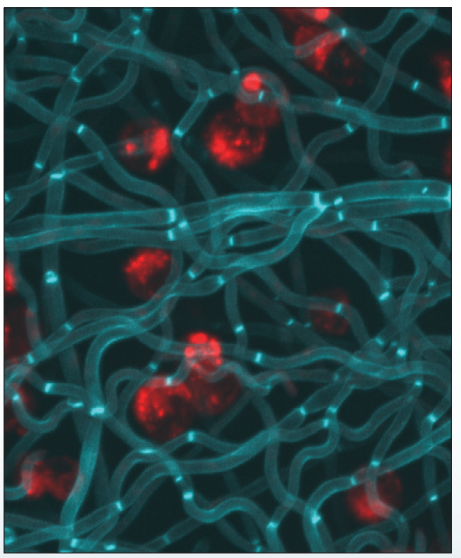

Candida albicans (stained blue with Calcofluor White) and murine macrophages (stained with Lysotracker Red). IMAGE BY JUDITH BAIN (ABERDEEN FUNGAL GROUP, UNIVERSITY OF ABERDEEN). SUBMITTED BY THE 2017 IMMUNOLOGY OF FUNGAL INFECTIONS GRC CHAIRS.

Downloaded from http://science.sciencemag.org/ on September 30, 2016

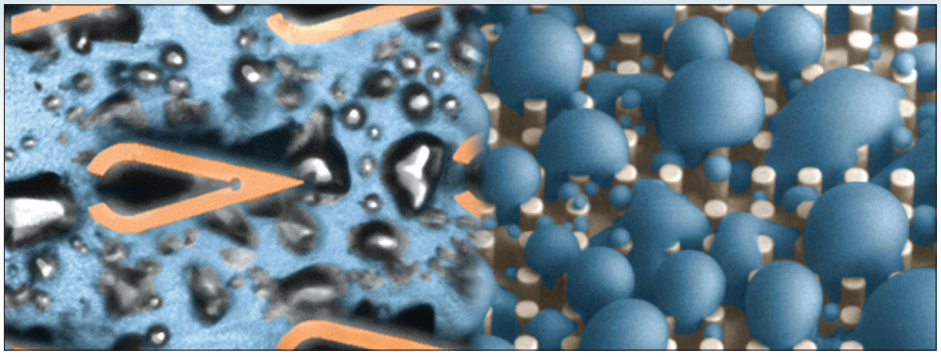

Phase change heat transfer, both liquid-to-vapor and vapor-to-liquid, can be enhanced with micro- and nanoscale surface design. Microfabricated piranha pin fins are shown at left in a flow boiling setup, where flowing liquid boils and the vapor is then collected by outlets as it flows into the "mouths" of downstream fins. In contrast, condensation occurs on a micropillar array at right, where nucleation and growth within the pillars will result in highly-pinned droplets and impede heat transfer, demonstrating the need for optimal surface design in phase change applications. SUBMITTED BY THE 2017 MICRO & NANOSCALE PHASE CHANGE HEAT TRANSFER GRC CHAIR.

Mammalian DNA Repair

Frontiers of Mammalian Genomic Stability in Human Health

FEBRUARY 19–24, 2017

FOUR POINTS SHERATON / HOLIDAY INN EXPRESS, VENTURA, CA

CHAIR: Wei Yang

VICE CHAIR: David Cortez

- **Keynote Session: The Leading Edge in Mammalian DNA Repair** *Wei Yang,* Bik Tye, Daniel Durocher
- **DNA Damage and Repair: Longevity and Quality of Life** *Samuel Wilson,* Caroline Kisker, Jurgen Marteijn, Priscilla Cooper, Orlando Scharer, Nicolas Thoma
- **From Basic Mechanism to Lethal Weapons** *Caroline Kisker,* Samuel Wilson, Judith Campbell, Thomas Helleday
- **Replication Fork Progression and Mutation Avoidance** *David Cortez,* Anthony Carr, Guo-Min Li, Grant Stewart, Agata Smorgorzewska, Alessandro Vindigni
- **Selected Poster Presentations: The Frontiers of Mammalian DNA Repair in 2017** *Karlene Cimprich*
- **DNA Damage Signaling and Repair Coordination** *Tanya Paull,* Roger Greenberg, Karlene Cimprich, Simon Boulton, Zhenkun Lou, Shan Zha
- **Mechanisms for DNA Double-Strand Break Repair** *Roger Greenberg,* Tanya Paull, Ilya Finkelstein, Andre Nussenzweig, Eric Greene
- **Chromatin Structures and Genome Stability** *Alan D'Andrea,* Patricia Opresko, Kyle Miller, Jessica Downs, Agnel Sfeir, Karen Usdin
- **Crosslinks and Cross Talk** *Patricia Opresko,* Alan D'Andrea, Michael Seidman, Scott Williams

GRS Mammalian DNA Repair

Frontiers of Mammalian Genomic Stability in Human Health

FEBRUARY 18–19, 2017

CHAIRS: Abigail Lubin & Molly Hardebeck

Metals in Biology

Biological Metals: Regulation, Catalysis, Medicine, the Environment, and Chemical Evolution

JANUARY 22–27, 2017

FOUR POINTS SHERATON / HOLIDAY INN EXPRESS, VENTURA, CA

CHAIR: R. David Britt

VICE CHAIR: Yi Lu

- **Metals and Biological Signalling** *Emily Weinert,* Michael Marletta, Thomas O'Halloran, Daniella Goldfarb
- **Metal Ion Homostasis, Proteins, and Nucleic Acids** *Sheila David,* Victoria DeRose, Lauren Waters, Walter Chazin, David Giedroc
- **Metal Ion Regulation and Human Health** *Celia Goulding,* Ashley Bush, Guenter Schwarz, Dianne Newman
- **Global Chemical Cycles: Nitrogen** *Yilin Hu,* Jonas Peters, Serena Debeer, Leslie Murray, Lance Seefeldt
- **Global Chemical Cycles: Energy** *Anne Jones,* Fraser Armstrong, Michael Rose, Leslie Dutton
- **Metalloenzymes: Mechanisms and Models** *Michael Green,* Steve Yu, Joseph Martin Bollinger, Judith Klinman, John Peters

> *"The GRS allows for significant interaction between early career investigators, and is an experience that is not easily duplicated elsewhere."*
>
> HEATHER FORD, CHAIR,
> 2015 INTERIOR OF THE EARTH GRS

- **Metals and the Environment, from the Deep Past to Today** *William Casey,* Alison Butler, Dan Rothman, Thomas Spiro
- **Water Oxidation/Oxygen Evolution** *Richard Debus,* Woodward Fischer, Victor Batista, Nicholas Cox, Petra Fromme
- **Oxygen, Life in the Balance** *Kara Bren,* Harry Gray
- **Power Hour** *Victoria DeRose, Lauren Rajakovich*

GRS Bioinorganic Chemistry

Biological Roles of Metals and Harnessing Their Chemical Power

JANUARY 26–29, 2017

CHAIR: Lauren J. Rajakovich

Micro & Nanoscale Phase Change Heat Transfer

Fundamental Mechanisms to Applications of Phase Change Heat Transfer

JANUARY 8–13, 2017

HOTEL GALVEZ, GALVESTON, TX

CHAIR: Evelyn N. Wang

VICE CHAIRS: Joel Plawsky & Jungho Kim

- **Interfacial Thermodynamics and Transport** *David Quere, Hadi Ghasemi,* Signe Kjelstrup, Kathleen Stebe
- **Role of Contact Line Heat Transfer in Phase Change Systems** *Vladimir Ajaev, Andrea Prosperetti,* Peter Stephan, Shalabh Maroo, Sunando DasGupta
- ***A Priori* Prediction of Nucleation Site Density** *Andrea Luke,* James Klausner, Detlef Lohse
- **Applications of Phase Change Heat Transfer** *Mark Spector,* John Lienhard, Amy Fleischer, Jianjun Wang
- **Enhancing Heat Transfer for Refrigerants and Other Low Surface Tension Fluids** *Srinivas Garimella,* Doris Vollmer, Andrei Fedorov
- **Mechanistic Understanding of Critical Heat Flux** *Satish Kandlikar,* In-Cheol Chu, Matthew McCarthy, Ho-Young Kim
- **Designing Structured Surfaces for Maximum Heat Transfer** *Amy Betz,* Paul Nealey, Anish Tuteja
- **Numerical Methods for Phase Change Heat Transfer** *Pawel Keblinski, Miad Yazdani,* Ying Sun, Gretar Tryggvason, Sebastien Tanguy
- **Enhancing Heat Transfer Using Fluid Mixtures** *Yasuyuki Takata, Xuehua Zhang,* Van Carey, Yoav Peles

Molecular Pharmacology

GPCRs: From Single Molecules to New Forms of Treatment

MARCH 12–17, 2017

RENAISSANCE TUSCANY IL CIOCCO, LUCCA (BARGA), ITALY

CHAIRS: Martin J. Lohse & Jurgen Wess

VICE CHAIRS: Roger K. Sunahara & Laura M. Bohn

- **Structural Basis of GPCR Function** *Roger Sunahara,* Tracy Handel, Brian Kobilka
- **Novel Approaches to Study GPCR/Membrane Protein Structure** *Gebhard Schertler,* Sebastien Granier, Fiona Marshall
- **GPCRs: Single Molecule Studies** *Jean-Philippe Pin,* Benjamin Kaupp, Akihiro Kusumi
- **Novel Tools and Technologies for GPCR Research** *JoAnn Trejo,* Anne Andrews, Meritxell Canals, Bryan Roth
- **GPCRs: Signal Compartmentation** *Alan Smrcka,* Jean-Pierre Vilardaga, Manuela Zaccolo, Jin Zhang
- **Diversity of GPCR Ligands: Clinical Implications** *Marc Caron,* Arthur Christopoulos, Jeff Conn, Thue Schwartz
- **Central GPCRs as Drug Targets** *Laura Bohn,* Michael Bruchas, Kathryn Cunningham, Gregory Scherrer, Jeffrey Witkin
- **GPCRs: Regulation of Body Weight, Glucose Homeostasis, and Other Metabolic Functions** *Graeme Milligan,* Lora Heisler, Michael Krashes, Stefan Offermanns, Alexander Pfeifer
- **GPCR Activation and Signaling** *Paul Insel,* Robert Lefkowitz, Torsten Schoeneberg

GRS Molecular Pharmacology

Understanding GPCR Function from Structural Biology to In Vivo Models

MARCH 11–12, 2017

CHAIRS: Daniel J. Shiwarski & Kelsie Eichel

NEW! Movement Ecology of Animals

The Development of an Animal Movement Paradigm

MARCH 19–24, 2017

FOUR POINTS SHERATON / HOLIDAY INN EXPRESS, VENTURA, CA

CHAIR: Anders Hedenstrom

VICE CHAIR: Ran Nathan

- **Integrating Animal Movement Ecology Research** *Ran Nathan,* Simon Levin, Jean Clobert
- **Large Animals and Small Creatures: Do They Move Differently?** *Lars-Anders Hansson,* Geoff Spedding, Alan Wilson
- **Animals on the Move in Their Environment** *Emily Shepard,* Peter Marra, Henri Weimerskirch
- **Modeling Movement** *Judy Shamoun-Baranes,* Iain Couzin, Kami Safi
- **The Neurophysiology of Navigating the World** *Susanne Akesson,* Michael Dickinson
- **What Is the Adaptive Benefit of Migration?** *Anders Hedenstrom,* Alice Boyle
- **Global Environmental Changes and Movement** *Gil Bohrer,* Christian Both, Justin Travis
- **Pathogens on the Move** *Helena Westerdahl,* Wayne Getz, Karen McCoy
- **Observing Movements: How to Track Organisms Across Multiple Scales** *David Winkler,* Martin Wikelski, Jason Chapman

Multi-Drug Efflux Systems

Integrated Approaches to Understanding the Role of Multi-Drug Efflux Systems in Health and Disease

MARCH 26–31, 2017

HOTEL GALVEZ, GALVESTON, TX

CHAIRS: Suresh V. Ambudkar & Melissa H. Brown

VICE CHAIRS: Deanna L. Kroetz & Miguel Viveiros

- **Keynote Session: Regulation and Function of Multidrug Efflux Systems** *Michael Gottesman, Olga Lomovskaya,* Susan Cole, William Shafer
- **Structural Basis of the Mechanism of MDR Pumps** *Guillermo Altenberg, Rajeev Misra,* Vassilis Koronakis, Di Xia, Ina Urbatsch, Edward Yu, Xuejun Zhang, Suneet Shukla
- **Influx and Efflux Systems: Similarities and Differences** *Lei Zhang,* Bert Poolman, Navjot Pabla, Mathias Winterhalter
- **Omics and Meta Systemic Approaches** *Miguel Viveiros, Eitan Bibi,* Caroline Lee, Karl Hassan, D. Branch Moody, Koen van de Wetering, Per Artursson

Visit the Frontiers of Science at a Gordon Conference! www.grc.org
Downloaded from http://science.sciencemag.org/ on September 30, 2016

"Gordon Conferences are different from other scientific conferences because of their intensity of science, new ideas, discussion, and fun."

CLIFF KUBIAK, UCSD

- **Molecular Basis of Polyspecificity of the Multidrug Transporters** *John Golin,* Karl Kuchler, Megan O'Mara, Raymond Turner, Min Lu
- **Strategies for Development of New Antibacterials and Modulators** *Rajendra Prasad, George Tegos,* Gerhard Ecker, Matthew Cooper, Thomas Efferth, Glenn Kaatz
- **Microbiome in Health and Diseases** *Hendrik van Veen,* Terence Crofts, Julia Oh
- **Preclinical and Clinical Studies** *Deanna Kroetz, Victor Ling,* Shashank Gupta, Erin Schuetz, Orit Lavi, Toshihisa Ishikawa
- **New Technologies / Late-Breaking Topics** *Jessica Blair,* Zhe-Sheng (Jason) Chen
- **Power Hour** *Susan Bates, Helen Zgurskaya*

GFS **Multi-Drug Efflux Systems**
Linking Molecular Mechanisms to Biological Functions of Transporters Through Innovation and Multidisciplinary Approaches
MARCH 25–26, 2017
CHAIRS: Yu Toyoda & Karl A. Hassan

Nanomaterials for Applications in Energy Technology

Energy Conversion, Storage, and Transport at Nanoscale
FEBRUARY 26–MARCH 3, 2017
VENTURA BEACH MARRIOTT, VENTURA, CA
CHAIR: Yi Cui
VICE CHAIR: Vanessa C. Wood

- **Keynote Session: Nano and Energy Science** *Yi Cui,* Paul Alivisatos, Juan Bisquert
- **Photon Energy Conversion** *Shanhui Fan,* Dirk Weiss, Harry Atwater, Xiaoyang Zhu
- **Thermal Energy Conversion** *Jia Zhu,* Shanhui Fan, Jeff Snyder
- **Energy Storage: Materials Design** *Vanessa Wood,* Gerbrand Ceder, Hyuk Chang, Liwei Chen
- **Energy Storage: Characterization** *William Chueh,* Bilge Yildiz, Robert Kostecki
- **Energy Efficiency** *Kang Wang,* Eli Yablonovitch, Shoucheng Zhang
- **Advanced Nanomaterials Synthesis for Energy** *Delia Milliron,* Yury Gogotsi, Uwe Kortshagen
- **Catalysis and Chemical Fuels: Mechanism** *Haotian Wang,* Vojislav Stamenkovic, Kyoung-Shin Choi, Peng Chen
- **Catalysis and Chemical Fuels: Materials Design** *Shannon Boettcher,* Peidong Yang, Emily Carter

GFS **Nanomaterials for Applications in Energy Technology**
Tailoring Chemical and Physical Processes for Next-Generation Energy Nanomaterials
FEBRUARY 25–26, 2017
CHAIRS: Kannatassen Appavoo & Mimi N. Hang

Neural Crest & Cranial Placodes

Insights into Gene Networks, Disease Models, and Evolutionary Mechanisms of Neural Crest and Cranial Placode Development
FEBRUARY 5–10, 2017
FOUR POINTS SHERATON / HOLIDAY INN EXPRESS, VENTURA, CA
CHAIR: Sally A. Moody
VICE CHAIR: Clare V. H. Baker

- **Keynote Session: Gene Regulatory Networks** *Tatjana Sauka-Spengler,* Marianne Bronner, Andrea Streit
- **Evolutionary Origins** *Gerhard Schlosser,* Bernd Fritzsch, Lucia Manni, Kai Sky Yu

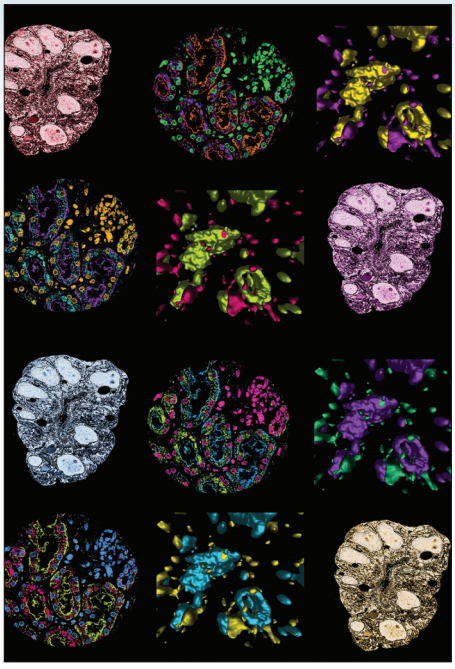

Different color patterning of Lowe zebrafish proephro, biopsies of Lowe syndrome patients, and 3d reconstruction of autophagosome-lysosome interaction. COURTESY OF ANTONELLA DE MATTEIS AND LEOPOLDO STAIANO (TELETHON INSTITUTE OF GENETICS AND MEDICINE, ITALY). SUBMITTED BY THE 2017 LYSOSOMAL DISEASES GRC CHAIR.

- **The Border Zone and Regional Patterning** *Andrew Groves,* Jean-Pierre Saint Jeannet, Marcos Simoes-Costa
- **EMT, Delamination, and Migration** *Elisa Marti,* Dominique Alfandari, Anna Cariboni, Pablo Strobl-Mazzulla
- **Morphogenesis and Tissue Interactions** *Chaya Kalcheim,* Sophie Creuzet, Michelle Southard-Smith
- **Differentiation, Potential and Mechanisms** *Bruce Riley,* Marthe Howard, Peter Lwigale
- **Birth Defects** *Karen Liu,* Thomas Maynard
- **Stem Cells and Regeneration** *Paolo Forni,* Carole LaBonne, Shannon Davis, Jean-Francois Cloutier
- **Diseases of Neural Crest and Cranial Placodes** *Martin Garcia-Castro,* Salil Lachke, Constantine Stratakis

GFS **Neural Crest & Cranial Placodes**
Insights into Embryogenesis, Stemness, and Translational Applications of Neural Crest and Cranial Placodes
FEBRUARY 4–5, 2017
CHAIRS: Shachi Bhatt & Betsy N. Schock

NEW! Neuroimmune Communication in Health & Disease

Neuro-Immune Interactions During Homeostasis and Neurological Disorders
JANUARY 15–20, 2017
VENTURA BEACH MARRIOTT, VENTURA, CA
CHAIRS: Dorian McGavern & Zsuzsanna Fabry
VICE CHAIR: Jonathan Kipnis

- **Keynote Session: Lessons Learned from Multiple Sclerosis** *Hartmut Wekerle,* Vanja Lazarevic, Claudia Lucchinetti, Lawrence Steinman
- **Microglia Functions During Homeostasis and Neurological Diseases** *Ari Waisman,* Marco Colonna, Florent Ginhoux, Marco Prinz, Beth Stevens
- **Immune Signaling in the CNS** *Lisa Boulanger,* Dongsheng Cai, Alexandre Prat, Francisco Quintana, Carla Shatz
- **Immune Effects on Brain Function** *Zsuzsanna Fabry,* Robin Franklin, Michal Schwartz, Judy Van de Water, Rita Balice-Gordon
- **Immunity and Neurodegeneration** *Costantino Idaecola,* Dritan Agalliu, Tika Benveniste, Li Gan, Frank Heppner
- **DAMPs, PAMPs, and Alarmins that Regulate Immunity in the CNS** *Monica Carson,* Katerina Akassoglou, Melissa Brown, Kodi S. Ravichandran, Jenny Ting
- **Microbiome–Brain Communication** *Emeran Mayer,* Josef Anrather, Rachel Caspi, Elaine Hsiao, Sven Pettersson
- **Impact of Infectious Immunity on CNS Function** *Charles Howe,* Christopher Hunter, Robyn Klein, Karin Peterson, Matyas Sandor
- **PNS–Immune Interactions** *Nader Ghasemlou,* Issac Chiu, Asya Rolls, Paul Sawchenko, Kevin Tracey

Nitric Oxide

Reactive Nitrogen Signaling: Mechanism to Medicine
FEBRUARY 19–24, 2017
VENTURA BEACH MARRIOTT, VENTURA, CA
CHAIR: Sruti Shiva
VICE CHAIR: Neil Hogg

- **Keynote Session: Physiological NO Signaling** *Harry Ischiropoulos,* Joseph Loscalzo
- **Canonical and Non-Canonical Signaling Through sGC** *Dennis Stuehr,* Emmanuel Buys, Annie Bueve, Greg Thatcher, Adam Straub
- **NO, Mitochondria, and Metabolic Syndrome** *Victor Darley-Usmar,* Brad Hillgartner, Jon Lundberg, Jane Reusch
- **NO Signaling via Post-Translational Modifications** *Andrew Gow, Rakesh Patel,* Paschalis-Thomas Doulias, Joshua Hare, Lisa Palmer, Jennifer Van Eyk
- **Taking the NO Pathway to the Clinic: Current Clinical Trials** *Eddie Weitzberg, Serpil Erzurum,* Mark Gladwin, Diane Jorkasky, Todd Milne
- **NO Production and Crosstalk with Other Gasotransmitters** *Martin Feelisch,* John Calvert, Jon Fukuto, Bindu Paul, Hiroshi Takagi, Megan Frost
- **NO Modulation of Cancer Progression** *Katrina Miranda, David Wink,* Debashree Basudhar, Jenny Chang, Sharon Glynn, Douglas Thomas
- **Novel Paradigms of NO-Dependent Cardiovascular Signaling** *Amrita Ahluwalia,* Ye Chen-Izu, Annarita Di Lorenzo, John Pernow, Thomas Van 't Erve
- **Keynote Session: Biochemical NO Signaling Mechanisms** *Neil Hogg,* Rafael Radi

GFS **Nitric Oxide**
Nitric Oxide Biochemistry in Mammalian, Plant, and Microbial Systems
FEBRUARY 18–19, 2017
CHAIRS: Courtney E. Sparacino Watkins & Filip Larsen

Oxidative Stress & Disease

Redox Biology in Disease and Translational Medicine
MARCH 19–24, 2017
RENAISSANCE TUSCANY IL CIOCCO, LUCCA (BARGA), ITALY
CHAIRS: La Dora V. Thompson & Giuseppe Poli
VICE CHAIRS: Dean P. Jones & Helen R. Griffiths

- **Keynote Session: The Redox Language in Medical Research** *Helmut Sies,* Rafael Radi, Harald Schmidt
- **Proteostasis and Longevity** *Kelvin Davies,* Richard Morimoto, Ana Maria Cuervo
- **Revisiting: The Cross-Talk Between ROS Signaling and Cell Homeostasis** *Deborah Ferrington,* Gerald Shadel
- **ROS/RNS in Vascular Aging** *Giovanni Mann,* Anne Negre-Salvayre, Anna Csiszar
- **Mitochondrial Quality and Control in the Diseased Brain** *Enrique Cadenas,* Marzia Perluigi, Grazia Isaya
- **Emerging Challenges: Inflammation and Diseases of the Gut, Lung, and Pancreas** *Juan Sastre,* Patricia Oteiza, Suzanne Cloonan
- **Examining the Impacts of Oxidative Stress on Infectious Diseases** *Carroll Cross,* David Lembo, Regina Medvedev
- **Cellular Mechanisms Underlying Oxidative Stress and Exercise** *Jose Vina,* Carmen Gomez-Cabrera, Nathalie Sumien, Malcolm Jackson
- **Redox-Orientated Biotechnology and Medicine** *Cesar Fraga,* Tilman Grune, Gaetano Serviddio

GFS **Oxidative Stress & Disease**
Oxidative Stress Biomarkers for Diseases — Prospects and Challenges
MARCH 18–19, 2017
CHAIRS: Devi Annamalai & Laura E. Corrales-Diaz Pomatto

Downloaded from http://science.sciencemag.org/ on September 30, 2016

NEW! Physical Science of Cancer

Cancer Forces, Structures, and Mathematical Predictions

FEBRUARY 5–10, 2017

HOTEL GALVEZ, GALVESTON, TX

CHAIR: Dennis E. Discher

VICE CHAIR: Franziska Michor

- **Keynote Session: Migration–Invasion Physics of Single Cancer Cells and Populations** *Robert Gatenby,* Valerie Weaver, Xavier Trepat
- **Tumor Matrix Stiffening and Cytoskeletal Stress Under Flow and Pressure** *Paul Janmey,* Josef Kaes, Maria Plodinec
- **Cancer Physics in Adhesive Signals and Cell Fates** *Claudia Fischbach,* Michael Sheetz, Herbert Levine
- **Nuclear Physics in Cancer** *John Marko,* Katarina Wolf, G.V. Shivashankar
- **Chromatin Physics** *G.V. Shivashankar,* Roger Greenberg, Bo Huang
- **Cancer Genome Principles and Computations** *Herbert Levine,* Orly Alter, Rong Li
- **Cancer Dynamics Theory and Computation** *Rong Li,* Jean-Francois Joanny, Niko Beerenwinkel
- **Multiscale Physics Modeling Mathematics** *Jean-Francois Joanny,* Lisa Manning, Alexander Anderson, Vittorio Cristini
- **Mathematical and Physics-Based Modeling for Novel Clinical Trials** *Mithat Gonen,* Robert Gatenby, Lance Munn

Physical Virology

Structure–Function Relations in Viruses and Virus-Like Materials

JANUARY 29–FEBRUARY 3, 2017

RENAISSANCE TUSCANY IL CIOCCO, LUCCA (BARGA), ITALY

CHAIRS: Brian Bothner & Jeroen J.L.M. Cornelissen

VICE CHAIRS: Wouter H. Roos & Tuli Mukhopadhyay

- **Keynote Session: Virus Assembly: Theory and Practice** *Brian Bothner,* Adam Zlotnick
- **Biomedical Applications** *M.G. Finn,* Aravind Asokan, Maya Shmulevitz, Kah Peng
- **Materials and Devices** *Mauri Kostiainen,* Trevor Douglas, Matthew Francis, Nicole Steinmetz, Xian-En Zhang
- **Structural Studies of Viruses** *Mavis Agbandje-McKenna,* Pepe Caston, Kay Grunewald, Hong Zhou
- **Virus Structure-Function** *Rebecca Dutch,* Mei Hong, Kristin Parent
- **Assembly and Biomechanics of Viruses** *Charles Knobler,* Alex Evilevitch, William Gelbart, Roya Zandi
- **Viruses with Membranes** *Felix Rey,* Susan Daniel, Kelly Lee, Mark Sansom
- **Protein Cages by Design** *Adam Zlotnick,* Donald Hilvert, Roman Jerala, Junghae Suh
- **Keynote Session: Enabled Studies of Viruses** *Jeroen Cornelissen,* Michael Rossmann

GRS Physical Virology

Nanoscale Exploration of Viral Structure and Function for Applications in Medicine and Materials Research

JANUARY 28–29, 2017

CHAIRS: Anna Czapar & Raphael Frey

Plant Lipids: Structure, Metabolism & Function

Plant Lipid Signaling and Cellular Homeostasis

JANUARY 29–FEBRUARY 3, 2017

HOTEL GALVEZ, GALVESTON, TX

CHAIRS: Katayoon Dehesh & Anthony J. Kinney

VICE CHAIRS: Susanne Hoffmann-Benning & Ingo Heilmann

- **Keynote Session: Role of Plant Lipids in Human and Animal Nutrition** *Anthony Kinney,* Peter Gillies, Johnathan Napier, Susan Knowlton, Joe Hibbeln
- **Role of Lipids in Biotic and Abiotic Stress Responses** *Edgar Cahoon,* Marina Gavilanes-Ruiz, Jean Greenberg, Alisa Huffaker, Jonathan Markham, Nick Roberts
- **Lipid Signaling and Cellular Homeostasis** *Susanne Hoffmann-Benning,* Ingo Heilmann, Edgar Cahoon, Glenda Gillaspy, Teun Munnik

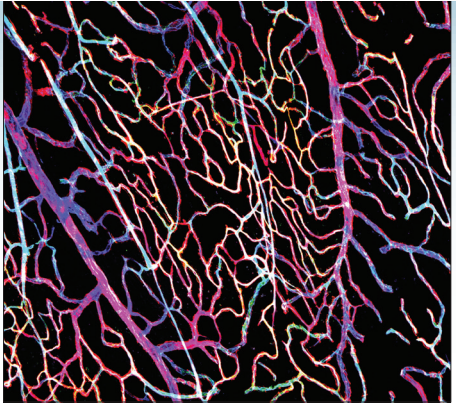

Confocal whole-mount image of meningeal vasculature 14 days after mild traumatic brain injury positive for CD31 (blue), tomato lectin (green) and laminin (red). The highly branched, new blood vessels in the center of the image were formed after the original vasculature was damaged. IMAGE GENERATED BY MATTHEW RUSSO (DORIAN MCGAVERN LAB, NINDS/NIH). SUBMITTED BY THE 2017 NEUROIMMUNE COMMUNICATION IN HEALTH & DISEASE GRC CHAIRS.

- **Role of Lipids in Cellular Structure and Function** *Jean Greenberg,* Peter Dormann, Timothy Durrett, Ivo Feussner, Patrick Horn, Rebecca Roston
- **Lipids and Cellular Trafficking** *Glenda Gillaspy,* Christoph Benning, Maryse Block, Lawrence Griffing, Katrin Philippar
- **Genome Modification Approaches to Metabolic Engineering of Lipid Biosynthesis** *John Dyer,* Clint Chapple, Navdeep Mutti, John Shanklin, Daniel Voytas
- **Lipids, Energy and Bio-Renewables** *Kent Chapman,* Allen Green, Robert Mullen, Hardy Rolletschek, Chengchang Xu
- **"Omic" Platforms for Lipid Analyses** *Ruth Welti,* Doug Allan, David Gang, Aruna Kilaru, Sam Wang, Eve Wurtele
- **Lipid Imaging, Spectroscopy, and Functional Analyses** *Sam Wang,* Ljudmilla Borisjuk, Kent Chapman, Jedrzej Szymanski, Ruth Welti

GRS Plant Lipids: Structure, Metabolism & Function

Plant Lipid-Mediated Post-Translational Modification

JANUARY 28–29, 2017

CHAIRS: Anastasiya Lavell & Yingqi Cai

Plant-Herbivore Interaction

Novel Approaches and Technologies for Understanding How Plants and Herbivores Interact at Multiple Scales

FEBRUARY 12–17, 2017

FOUR POINTS SHERATON / HOLIDAY INN EXPRESS, VENTURA, CA

CHAIR: Nicole M. Van Dam

VICE CHAIR: Spencer T. Behmer

- **Keynote Session: Plant–Herbivore Interactions: Bridging Multiple Dimensions** *Nicole Van Dam,* Fred Gould
- **Ecology of Plant–Herbivore Interactions** *Elizabeth Pringle,* Vojtech Novotny, Kailen Mooney, Alistair Poore, Karen Abbott
- **Large Herbivores** *Spencer Behmer,* Jessica Rothman, Fred Provenza
- **Plant–Herbivore Interactions in Times of -Omics** *Jacqueline Bede,* Heiko Vogel, Jonathan Eisen, Linda Walling, Kirsten Leiss
- **Induced Responses by Intimate Enemies** *David Giron,* Sybille Unsicker, Godelieve Gheysen
- **Priming and Induced Responses in Plants** *Anke Steppuhn,* Nina Fatouros, Ainhoa Martinez Medina, Jennifer Thaler, Carlos Ballare
- **Plant–Herbivore Interactions: An Evolutionary Perspective** *Katja Poveda,* Patrick Abbot, Dena Smith
- **Herbivores Overcoming the Challenges of Feeding on Plants** *Shai Morin,* Christelle Robert, Greg Sword, Takema Fukatsu, Kevin Kohl
- **Effects of Global Change on Plant–Herbivore Interactions** *Mary Jamieson,* Kwang Pum Lee, Christer Bjorkman
- **Power Hour** *Dena Smith, Linda Walling*

GRS Plant–Herbivore Interaction

Investigating How Plants and Herbivores Interact on Multiple Scales

FEBRUARY 11–12, 2017

CHAIRS: Paul A. Lenhart & Meredith Schuman

Polar Marine Science

Understanding Polar Ecosystem Change Through Time Series Observations, Technological Advances, and Biophysical Coupled Modeling

MARCH 26–31, 2017

VENTURA BEACH MARRIOTT, VENTURA, CA

CHAIR: Jacqueline M. Grebmeier

VICE CHAIR: Jean-Eric Tremblay

- **Keynote Session: Marine Ecosystem Status and Change in the Antarctic and Arctic** *Jody Deming,* Michael Meredith, Thomas Soltwedel
- **Physical Drivers in Polar Marine Systems** *Anna Whalin,* Julienne Stroeve, Keiichiro Ohshima, Andrey Proshutinsky
- **Paleoceanographic Time Series Studies in Polar Regions** *Beth Caissie,* Heidemarie Kassens, Amy Leventer
- **Biogeochemical Interactions in Polar Marine Ecosystems** *Lee Cooper,* Francois Fripiat, Naomi Harada, Sanghoon Lee
- **Lower Trophic Level Marine Time Series Studies** *Monika Kedra,* Jorgen Berge, Irene Schloss
- **Upper Trophic Level Marine Time Series Studies** *Sue Moore,* George Watters
- **Biophysical Coupled Modeling Using Time Series Data in Polar Regions** *Wieslaw Maslowski,* Nadja Steiner, Martin Vancoppenolle
- **Technological Advances and Issues of Scaling for Time Series Data Collections** *Jessica Cross,* Finlo Cottier, Seth Danielson, Ari Friedlaender
- **Connecting Marine Observing Systems at the Poles: Regionally and Globally** *Eddy Carmack,* Mary-Louise Timmermans, Andrew Constable

GRS Polar Marine Science

Advancing the Physical-Biological Understanding of Polar Marine Ecosystems Through Innovative Technology

MARCH 25–26, 2017

CHAIRS: Ingrid Wiedmann & Nicole Couto

Quantitative Genetics & Genomics

Exploiting Context and Increasing Predictive Value in Complex Trait Genetics

FEBRUARY 26–MARCH 3, 2017

HOTEL GALVEZ, GALVESTON, TX

CHAIR: Ann E. Stapleton

VICE CHAIR: Mike Goddard

- **Statistical Predictions and Models: Causality, Scale and Experimental Connections** *Chris-Carolin Schoen,* Silvia Richardson, Eric Green
- **Genetics of Risk and Prediction: Applications** *Rebecca Doerge,* Natalia De Leon, Iona MacLeod, David Heckerman

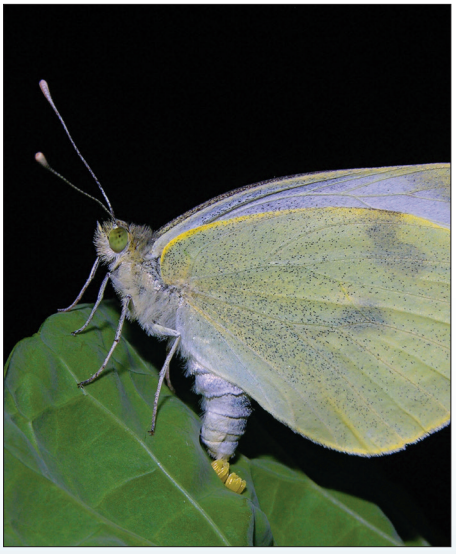

A Large White butterfly (Pieris brassicae) ovipositing her eggs on a cabbage leaf. Eggs deposition may prime plants to strengthen their induced defense response against herbivores. IMAGE BY HANS SMID (WAGENINGEN UNIVERSITY). SUBMITTED BY THE 2017 PLANT-HERBIVORE INTERACTION GRC CHAIR.

Visit the Frontiers of Science at a Gordon Conference! www.grc.org
Downloaded from http://science.sciencemag.org/ on September 30, 2016

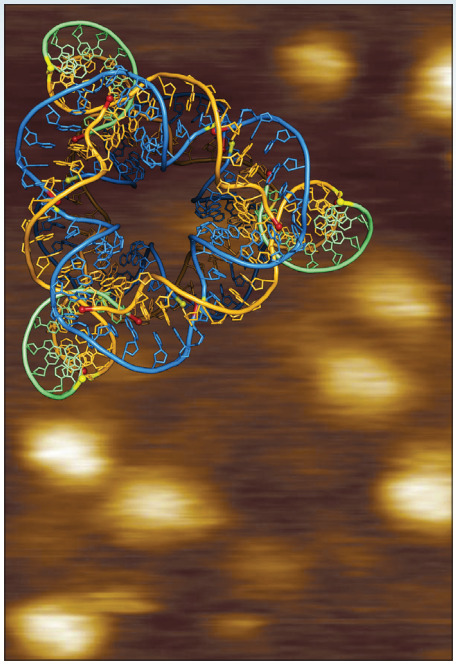

Atomic force microscopy (AFM) image of a triangular RNA nano-prism obtained from programmed self-assembly of 15 oligonucleotides. The insert shows a top-down view of the RNA nano-prism structure. IMAGE CREATED BY THOMAS HERMANN. SUBMITTED BY THE 2017 RNA NANOTECHNOLOGY GRC CHAIRS.

- Evolutionary Contexts for Prediction and Selection *Josephine Pemberton,* John Novembre, Nicholas Barton
- Genetic Context: Making Sense of Multivariate Phenotypes *Lauren McIntyre,* Barbara Engelhart, Eleazar Eskin, Bin Yu
- Modeling of Context: Interaction Terms and Beyond *Bruce Walsh,* Ian Ehrenreich, Paul Magwene
- Late-Breaking Topics *Peter Visscher,* Christine Queitsch, Matthew Webster, Alexis Battle
- Context: Drugs, Weather and the Systems to Integrate Genotypes and Environments *Ed Buckler,* Mark Cooper, Sally Aitken
- Quantitative Perspectives on Gene Editing: Why to Edit What *Ann Stapleton,* Kevin Esvelt, Mattheos Koffas
- Next Generation Quantitative Genetics and Genomics *Mike Goddard,* Gustavo Stolovitsky, Jeff Leek

Quantitative Genetics & Genomics
Interpreting Genetic Variation in Context
FEBRUARY 25–26, 2017
CHAIRS: Amelie Baud & Gregor Gorjanc

RNA Editing

Biology and Mechanisms of RNA and DNA Modification
MARCH 12–17, 2017
FOUR POINTS SHERATON / HOLIDAY INN EXPRESS, VENTURA, CA
CHAIRS: Reuben S. Harris & Heather A. Hundley
VICE CHAIRS: Valerie A. De Crecy-Lagard & Jin Billy Li

- New Frontiers in Editing *Reuben Harris,* Eric Greer, Jane Jackman, Eli Eisenberg, Erez Levanon
- Physiological Functions for Editing and Modification *Kazuko Nishikura,* Chuan He, Carl Walkley, Valerie De Crecy-Lagard, Hilde Nilsen, Jody Puglisi, Joshua Rosenthal, Brenda Bass
- Regulation of RNA Editing and Modification *Linda Chelico,* Juan Alfonzo, Gideon Rechavi, Kazuko Nishikura, Eric Phizicky
- Editing in Immunity *Silvestro Conticello,* Daniel Stetson, Charles Samuel, Nina Papavasiliou, Mary O'Connell, Javier Di Noia, Michael Jantsch
- Epitranscriptomics *Erez Levanon,* Samie Jaffrey, Bora Baysal, Mark Helm, Jin Billy Li, Yi-Tao Yu
- Molecular Mechanisms of Editing Machines *Juan Alfonzo,* Peter Beal, Linda Chelico, Harold Smith, Brandt Eichman, Ruslan Aphasizhev, Jonatha Gott, Maureen Hanson
- Genome and Transcriptome Engineering Technologies *Joshua Rosenthal,* Martin Jinek, Rebecca Terns, Laurie Read, Stewart Shuman, Peter Dedon
- RNA and DNA Modifications in Cancer *Nina Papavasiliou,* Tomas Lindahl, David Schatz, Anjana Rao, Nicholas Davidson, Silvestro Conticello, Polly Chen, Sohail Tavazoie
- Neuro-Editing *Heather Hundley,* Michaela Frye, Marie Ohman, Robert Reenan, William Joiner
- Power Hour *Jonatha Gott*

RNA Editing
Mechanisms of RNA and DNA Modification and Health Impacts
MARCH 11–12, 2017
CHAIR: Amy M. Molan

RNA Nanotechnology

Discovering and Assembling RNA Architectures for Materials, Therapeutics and Diagnostics
JANUARY 22–27, 2017
VENTURA BEACH MARRIOTT, VENTURA, CA
CHAIR: Neocles B. Leontis
VICE CHAIRS: Tushar Patel & Thomas Hermann

- RNA Computation and Modeling *Anne Condon,* Eckart Bindewald, Rhiju Das, Craig Zirbel
- RNA Folding and 3D Structure *Sarah Woodson,* Juli Feigon, Jeffrey Kieft, Nils Walter
- Basic Cellular Biology of Extracellular Vesicles *Tushar Patel,* Alissa Weaver, David Katzmann, Xandra Breakefield
- RNA Synthetic Biology *Robert Batey,* Lydia Contreras, Ming Hammond, Julius Lucks
- Pharmacology and Immunology of RNA Nanotechnologies *Muthiah Manoharan,* Art Krieg, Punit Seth, Kazunori Kataoka
- RNA Nanoparticles for Sensor and Therapeutics Development *Peixuan Guo,* Arkadiusz Chworos, Chengde Mao, Yoshiya Ikawa, Varathara Thiviyanathan
- Extracellular RNA for Therapeutic Development *Samir El Andaloussi,* Giovanni Camussi, Janusz Rak, Anastasia Khvorova
- Extracellular RNA for Biomarker Development *Jan Loetvall,* Saumya Das, Louise Laurent, Kendall Van Keuren-Jensen
- Cross-Fertilization by DNA Nanotechnology *William Shih,* Mark Bathe, Rebecca Schulman, Georg Seelig

RNA Nanotechnology
RNA Nanotechnology and Extracellular RNA
JANUARY 21–22, 2017
CHAIRS: Sayantan Maji & Ely Porter

Salivary Glands & Exocrine Biology

Understanding Development, Function, and Regeneration of Secretory Tissues: Novel Signaling Pathways and Approaches to Treat Exocrine Disorders
FEBRUARY 19–24, 2017
HOTEL GALVEZ, GALVESTON, TX
CHAIRS: Gary A. Weisman & Catherine E. Ovitt
VICE CHAIRS: Sarah M. Knox & Stefan Ruhl

- Keynote Session: Frontiers in Tissue Engineering *Gary Weisman, Catherine Ovitt,* David Mooney, Linda Griffith
- Exocrine Gland Development *Deborah Andrew, Matthew Hoffman,* Helen Makarenkova, Lisa Sandell, Abigail Tucker, Kenneth Yamada
- Emerging Concepts in Regenerative Medicine *Darlene Dartt, Simon Tran,* Quynh-Thu Le, Driss Zoukhri, Danielle Benoit, Melinda Larsen
- Functional Relevance of Mucins and Salivary Proteins *Mary Reyland, David Wong,* Gordon Proctor, Paul Breslin, Eva Helmerhorst, Walter Siquiera
- Membrane Functions in Exocrine Glands *Indu Ambudkar, Brij Singh,* Roberto Weigert, Sarah Hamm-Alvarez, David Yule, Shmuel Muallem
- Understanding the Etiology of Autoimmune Disease: From Mice to Humans *Ammon Peck, Julian Ambrus,* Markus Hardt, Rachel Ettinger, Umesh Deshmukh, Jay Chiorini
- Targeting Inflammation to Retard Disease Pathogenesis *Maria Kukuruzinska, David Ann,* Marco Colonna, Yuka Kanno, Haralampos Moutsopoulos, Kirsten Limesand

> *"GRCs are different from other scientific conferences because they provide the best opportunity to talk to other scientists on a one-to-one basis, and to gain exposure to cutting-edge research across the whole of my multidisciplinary field."*
> 2014 GRC ATTENDEE

- Mechanisms of Exocrine Gland Repair and Regeneration *Isabelle Lombaert, Rob Coppes,* Matthias Hebrok, Stephen Konieczny, Jason Mills, Jonathan Axelrod
- Keynote Session: Clinical Trials for Sjögren's Syndrome *Sarah Knox, Stefan Ruhl,* Robert Fox

Salivary Glands & Exocrine Biology
Exocrine Gland Biology, Organogenesis, and Regeneration
FEBRUARY 18–19, 2017
CHAIRS: Mahmoud Khalafalla & Elaine P. Emmerson

Speciation

Progress, Synthesis, and Integration at the Frontiers of Speciation Research
FEBRUARY 19–24, 2017
RENAISSANCE TUSCANY IL CIOCCO, LUCCA (BARGA), ITALY
CHAIR: Ake Brannstrom
VICE CHAIR: Rebecca Safran

- Challenges and Opportunities *Ulf Dieckmann,* Axel Meyer, Kerry Shaw
- Behaviour, Sexual Selection, and Speciation *Tamra Mendelson,* Brian Langerhans, Mike Ritchie, Maria Servedio
- Mechanisms of Reproductive Isolation *Daniel Matute,* Florence Debarre, Robin Hopkins
- Introgression and Hybrid Speciation *Sean Mullen,* Erik Dopman, Carole Smadja, Scott Taylor
- Experimental Demonstrations of Speciation *Daniel Ortiz-Barrientos,* Rowan Barrett, Daven Presgraves
- Sources of Divergent Selection *Martine Maan,* Pim Edelaar, Tatiana Giraud, Sander van Doorn
- Explaining Patterns of Species Richness *Michael Alfaro,* Helene Morlon, Dan Rabosky
- Advances in Speciation Genomics *Patrik Nosil,* Philine Feulner, Zach Gompert, Cheng-Ruei Lee
- Integrative Perspectives *Ole Seehausen,* Trevor Price, Dolph Schluter
- Power Hour *Rebecca Safran*

Speciation
Progress, Synthesis and Integration at the Frontiers of Speciation Research
FEBRUARY 18–19, 2017
CHAIRS: Amanda K. Hund & Laurel Symes

Stem Cells & Cancer

Mechanisms of Stem Cell Aging, Cancer Initiation, and Progression
FEBRUARY 12–17, 2017
RENAISSANCE TUSCANY IL CIOCCO, LUCCA (BARGA), ITALY
CHAIR: Lenhard Rudolph
VICE CHAIR: Amy J. Wagers

- Keynote Session: Cancer Initiation *Andreas Trumpp,* Ronald Depinho, Hans Clevers
- Stem Cell Biology *Sean Morrison,* Irving Weissman, David Traver, Leanne Jones, Leonard Zon
- Genome Integrity *Emmanuelle Passegue,* Andre Nussenzweig, Allison Bardin, Ross Levine
- Epigenome *Leonard Zon,* Maarten Van Lohuizen, Anne Brunet, Henri Jasper, Thomas Rando

Downloaded from http://science.sciencemag.org/ on September 30, 2016

- **Stem Cell Niche and Environment** *Leanne Jones,* Valentina Greco, Sean Morrison, Amy Wagers
- **Clonal Selection** *Ross Levine,* Cedric Blanpain, Douglas Winton, Hans-Reimer Rodewald, Catriona Jamieson
- **Stem Cell Metabolism and Signaling** *Anne Brunet,* Emmanuelle Passegue, David Sabatini, Andreas Trumpp
- **Plasticity and Heterogeneity** *Maarten Van Lohuizen,* Fred De Sauvage, David Langenau, Tannishtha Reya, Christopher Heeschen
- **Keynote Session: Developmental Pathways** *Cedric Blanpain,* Manuel Serrano, Elaine Fuchs, Margaret Goodell

Stem Cells & Cancer
Signals Driving Proliferation, Differentiation, and Self-Renewal in Normal Tissues, Aging, and Cancer
FEBRUARY 11–12, 2017
CHAIRS: Jeevisha Bajaj & Seerat Bajwa

Stochastic Physics in Biology

Landscapes, Stochastic Dynamics, and Heterogeneity in Biology
JANUARY 8–13, 2017
FOUR POINTS SHERATON / HOLIDAY INN EXPRESS, VENTURA, CA
CHAIR: Jin Wang
VICE CHAIR: Wallace F. Marshall

- **Keynote Session: Stochastic Physics in Molecular and Systems Biology** *Jin Wang,* Klaus Schulten, Jose Onuchic, Mans Ehrenberg
- **Biomolecular Stochastic Dynamics** *Klaus Schulten,* William Eaton, Masaki Sasai, Margaret Cheung, Benjamin Schuler
- **Cell Fate Decision Making** *Jose Onuchic,* James Ferrell, Xiaona Fang, Jie Liang
- **Cell Differentiation and Development** *Sunney Xie,* Chao Tang, Dave Thirumalai, Qi Ouyang, Nihal Altan-Bonnet
- **Cancer Mechanisms** *Zan Schulten,* Sunney Xie, Wei Wang
- **Cell Structure and Dynamics** *Wallace Marshall,* Jean-Francois Joanny, David Weitz, Frank Julicher, Ned Wingreen
- **Whole Cells** *Chao Tang,* Ken Dill, Zan Schulten, Chenghang Zong
- **Evolution and Ecology** *Mans Ehrenberg,* Nigel Goldenfeld, Jeff Gore, Curtis Callan, Ting Lu
- **Cell Dynamics and Functions** *Ken Dill,* Zhongcan Ouyang, Steve Presse, Ao Ma, Stephen Hagen, Jian Liu

Translation Machinery in Health & Disease

Decoding Translation for Homeostasis
MARCH 19–24, 2017
HOTEL GALVEZ, GALVESTON, TX
CHAIR: Sunghoon Kim
VICE CHAIR: Susan L. Ackerman

- **Keynote Session: Opening the New World of Translation** *Sunghoon Kim,* Nahum Sonenberg, C. Thomas Caskey
- **Post-Transcriptional Regulation in Cancer** *Robert Schneider,* Katherine Borden, Raul Mendez, Davide Ruggero, Estela Jacinto, Jung Min Han, Maria Barna
- **Metabolic Diseases** *Andrew Weyrich,* John Blenis, Vadim Gladyshev, Scot Kimball, Paul Fox
- **Infectious and Inflammatory Diseases** *Michael Ibba,* Nancy Woychik, Mirim Jin, Jeffrey Kieft, Karin Musier-Forsyth, Andrew Mouland
- **Translational Control of Cancer Cells** *Davide Ruggero,* Jerry Pelletier, Robert Schneider, Stephane Pyronnet, Ivan Topisiroivc
- **Neurological Disorders** *Tao Pan,* Susan Ackerman, Samie Jaffrey, Joel Richter, Paul Taylor, Xiang-Lei Yang
- **Translational Responses to Stress** *Xiang-Lei Yang,* Nilabh Shastri, Tao Pan, Shu-Bing Qian, Michael Ibba
- **Innovative Technologies for Translation Research** *Robert Singer,* Hiroaki Suga, Bin Wu, Jeffrey Chao, Nicholas Ingolia
- **Vascular and Hematologic Disorders** *Paul Fox,* Andrew Weyrich, Myung Hee Kim, Jie Jia

Translation Machinery in Health & Disease
Unveiling Mechanisms to Understand Pathogenesis
MARCH 18–19, 2017
CHAIRS: Eva Maria Novoa & Adrian G. Torres

Tropical Infectious Diseases

Advances in Basic and Translational Research in Tropical Infectious Diseases
MARCH 12–17, 2017
HOTEL GALVEZ, GALVESTON, TX
CHAIR: Jesus Valenzuela
VICE CHAIR: Carolina Barillas Mury

- **Keynote Session: Vector–Host and Vector–Pathogen Interactions** *Jesus Valenzuela,* Jose Ribeiro, Serap Aksoy
- **Helminth Research and Control** *Maria Elena Bottazzi,* Meera G. Nair, Conor Caffrey, Pauline Mwinzi, Alex Loukas
- **Chagas Disease, Genomics, Pathogenesis, and Immunity** *Eric Dumonteil,* Santuza Teixeira, Nisha Garg, Igor Almeida, Walderez Dutra
- **Emergent Arboviruses: Zika, Dengue and Chikungunya** *Nikos Vasilakis,* Scott Weaver, Albert Ko, Dorothee Misse, Eva Harris, Shee Mei Lok, Stephen Whitehead
- **Microbiomes of Tropical Disease Vectors** *Serap Aksoy,* Mary Wilson, George Dimopoulos, Shaden Kamhawi
- **Advances in Vector Biology Research** *Jose Ribeiro,* Joao Pedra, Alvaro Molina-Cruz, Pamela Pennington, Abdoulaye Diabate, Leslie Vosshall
- **Basic and Field Work Advances in Malaria** *Rick Fairhurst,* Xin-Zhuan Su, Kirk Deitsch, Peter Crompton, Peter Billingsley
- **Translational Strategies to Prevent Tropical Diseases** *Peter Hotez,* Afzal Siddiqui, Steven Reed, Hira Nakhasi, Maria Elena Bottazzi, Luciano Moreira, Anandasankar Ray
- **Keynote Session: Host-Parasite Interactions and Innate Immunity** *Carolina Barillas Mury,* Ricardo Gazzinelli, Marcelo Jacobs-Lorena
- **Power Hour** *Carolina Barillas Mury, Serap Aksoy*

Tropical Infectious Diseases
Advances in Basic and Translational Research in Tropical Infectious Diseases
MARCH 11–12, 2017
CHAIR: Chanaki Amaratunga

Vascular Cell Biology

Emerging Mechanisms of Vascular Biology, Disease and Treatment
JANUARY 15–20, 2017
FOUR POINTS SHERATON / HOLIDAY INN EXPRESS, VENTURA, CA
CHAIR: Mark Kahn
VICE CHAIR: Tatiana V. Byzova

- **Keynote Session: Paracrine Vascular Signaling** *Mark Kahn,* Timothy Hla, Christer Betsholtz, Brant Isakson
- **Vascular Development** *Christer Betsholtz,* Ralf Adams, Anne Eichmann, Natasza Kurpios, Kristy Red-Horse, Brant Weinstein
- **Mechanotransduction in Vascular Development and Disease** *Tatiana Byzova,* Mary Dickinson, Tatiana Petrova, Nathan Lawson, Julien Vermot, Martin Schwartz
- **Vascular Immunology and Inflammation** *Timothy Hla,* Mark Ginsberg, Luisa Iruela-Arispe, Gwendalyn Randolph
- **Specialized Vascular Beds** *Luisa Iruela-Arispe,* Kathleen Caron, Chenghua Gu, Calvin Kuo, Richard Lang, Susan Quaggin
- **The Vascular Niche in Regeneration** *Richard Lang,* Paul Frenette, Eli Keshet, Shanin Rafii, Nancy Speck
- **Translation to Vascular Therapies** *Martine Clozel,* Morris Birnbaum, Shaun Coughlin, Anthony Muslin
- **Vascular Metabolism** *Courtney Griffin,* Kari Alitalo, Zoltan Arany, Michael Potente, Stephen Young, Michael Simons
- **Epigenetic Regulation of Vascular Biology and Disease** *Zoltan Arany,* Jason Fish, Paul Fox, Courtney Griffin

Vascular Cell Biology
Future Directions in Vascular Biology: Old Friends and New Players in Vessel Development and Disease
JANUARY 14–15, 2017
CHAIRS: Natalie M. Kofler & Alexandre Dubrac

Viruses & Cells

Biology, Pathogenesis, and Treatment of Viral Infections
MAY 14–19, 2017
RENAISSANCE TUSCANY IL CIOCCO, LUCCA (BARGA), ITALY
CHAIR: Blossom Damania
VICE CHAIR: Julie Pfeiffer

- **Virus Structure and Entry** *Erica Ollmann Saphire,* Sean Whelan, Richard Longnecker, Felix Rey, Ari Helenius
- **The Immune Response to Viral Infection** *Ralph Baric, Carolina Lopez,* Herbert Virgin, Zhijian James Chen, Kate Fitzgerald, Charles Rice
- **Viral Replication and Persistence** *Andrew Pekosz,* Ronald Desrosiers, Carolyn Coyne, Rolf Renne, Stacey Schultz-Cherry
- **Viral Pathogenesis** *Lynn Enquist, Matt Evans,* Lisa Ng, Mya Breitbart, Christiane Wobus, Julie Overbaugh
- **Virus–Host Interactions** *Micah Luftig, Chris Sullivan,* Rozanne Sandri-Goldin, Kanta Subbarao, Nels Elde
- **Viral Evasion of Host Immunity** *Melanie Brinkmann, Stacy Horner,* Soren Paludan, Ana Fernandez-Sesma, Mark Heise, Joanna Shisler
- **Modulation of Cellular Pathways by Viruses** *Britt Glaunsinger,* Joan Steitz, Carla Saleh, Felicia Goodrum
- **Viruses and Cancer** *Robert Yarchoan,* Yuan Chang, Lou Laimins, Erle Robertson, Ethel Cesarman
- **Viral Therapeutics** *Terence Dermody, Sankar Swaminathan,* Michael Gale, Matthais Gromeier, Matthew Frieman

Viruses & Cells
The Interplay Between Viruses and Their Hosts Through Molecular Recognition, Establishment of Infection and Cellular Response
MAY 13–14, 2017
CHAIRS: Sayantan Bose & Victoria Meliopoulos

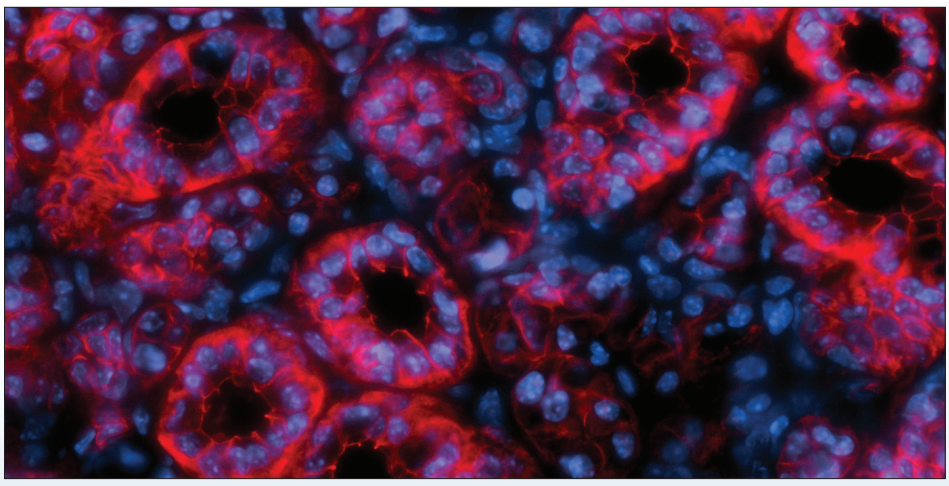

Fibrosis is a major contributor to tissue damage in many human diseases and the mouse salivary gland duct ligation model recapitulates many aspects of tissue fibrosis in humans. Expression of E-cadherin (red; cell nuclei in blue) is increased in salivary epithelium during duct ligation-induced salivary gland fibrosis, perhaps as a protective response. IMAGE TAKEN BY LUCAS WOODS (WEISMAN LAB, UNIVERSITY OF MISSOURI). SUBMITTED BY THE 2017 SALIVARY GLANDS & EXOCRINE BIOLOGY GRC CHAIRS.

Visit the Frontiers of Science at a Gordon Conference! www.grc.org
Downloaded from http://science.sciencemag.org/ on September 30, 2016

Human Genomic Reference Samples

iPLEX reference standards are now available for performance verification of oncology assays used on the MassARRAY System. The standards contain somatic variants in key oncogenic genes implicated in colon, lung, and skin cancers. Made from genetically engineered cell lines, these standards will be provided at fixed and known allelic frequencies, thereby mimicking real patient tumors. The MassARRAY System enables rapid assay development for targeted and highly sensitive mutation analysis. Tens to hundreds of actionable genetic variants are easily tested. The system is used globally in diverse research fields such as cancer profiling for solid tumor and liquid biopsies, inherited genetic disease testing, pharmacogenetics, agricultural genomics, and clinical research. However, robust assay performance requires up-front analytical verification and validation. These standards will be a valuable resource for laboratories to speed analytical validation and will serve as ongoing positive controls, complementing laboratories' evaluation of clinical research specimens.

Agena Bioscience
For info: 312-506-5202
www.agenabioscience.com

Immunoassays

Matched recombinant, monoclonal antibody pair kits provide assays with reproducible, sensitive, and high-throughput detection. Matched antibody pairs are central to enzyme-linked immunoabsorbent assays (ELISAs), which are widely used to study secreted biomarkers and are fundamental to research in areas such as immunology and cancer. Using patented recombinant monoclonal antibody technology such as RabMab, the pairs avert the reproducibility and scalability challenges previously faced by researchers, which cause variability in results. The pairs are screened for sensitive performance and rigorously tested in a variety of complex sample types including plasma, serum, and cell lysates. These optimized pairs are already part of Abcam's SimpleStep ELISA kits, and will now be available as stand-alone matched antibody pair kits. The new stand-alone, high-volume format provides greater flexibility to researchers and facilitates cost-effective drug discovery by enabling scale-up from small pilot studies to large-scale, high-throughput assay platforms.

Abcam
For info: 888-77-22226
www.abcam.com

Bead Mill

A new, compact, and robust horizontal bead mill system provides versatility for a wide range of laboratory dispersion tasks. Dispermat SL-B is for fine-grinding batch sizes from 150 mL to 750 mL. It features an integrated mill-base circulation system and a speed control that adjusts from 0 rpm to 6,000 rpm. The mill base is pressed out to ensure that the dispersed product can be almost completely regained with minimal wastage. Product samples are conveyed through the horizontal milling chamber by a spiral conveyor, while the separation of the mill base is made by a dynamic gap. Dispermat SL-B features a wear-resistant, stainless-steel milling chamber and a milling rotor made of hardened nitride steel. Shaft sealing is provided by a mechanical seal with integrated pressure system and cooling. The speed and timer controls are contained in separate stainless-steel housing with an easy-to-read digital display. An explosion-proof ATEX-approved version is also available.

Fullbrook Systems
For info: +44-(0)-1442-876777
www.fullbrooksystems.co.uk

Arc Process Sensors

ArcAir enables reliable, economical Bluetooth 4.0 wireless connectivity in all environments. The new Bluetooth capability allows users to view or control Hamilton Arc sensors from numerous devices, including smartphones and tablets. ArcAir apps are available for both Android and iOS platforms in three versions: ArcAir Lite (free), ArcAir Basic, and ArcAir Advanced. Arc sensor technology has a built-in microprocessor that provides direct digital and analog communication and eliminates the need for separate transmitters. Arc sensors have improved process measurement accuracy and speed while reducing installation and maintenance costs. The ArcAir mobile application for pH, dissolved oxygen, and conductivity measurements can communicate wirelessly with up to 30 individual sensors at the same time. Hamilton also offers a Bluetooth version of its GMP Compliance Package software, which works with ArcAir Advanced and provides centralized management of users and validation reports for calibration, verification, configuration, and communication.

Hamilton Company
For info: 800-648-5950
www.hamiltoncompany.com

Pathology Image Analysis Software

Established as the industry's fastest and most user-friendly analysis platform for digital pathology images, HALO 2.0 adds new capabilities and support for file formats. HALO 2.0 sports a more modern look and feel, including interchangeable skins to ease eyestrain when working with darkfield and brightfield images. It also adds a new tuning interface to facilitate analysis; the ability to create spatial plots, heat maps, and histograms from any HALO analysis result; and tools for data import/export, sharing, archiving, and report generation. For immuno-oncology and angiogenesis researchers, the spatial analysis module is a suite of tools for analyzing proximity and relative spatial distribution of objects, cells, and/or features across single tissues or serial sections. The high-plex FL module can simultaneously analyze up to eight markers and can be used with most fluorescent whole-slide image formats, including multispectral floating-point .qptiff images and whole-slide images produced from the Perkin-Elmer Vectra 3 platform.

Indica Labs
For info: 505-492-0979
http://indicalab.com

Electronically submit your new product description or product literature information! Go to www.sciencemag.org/about/new-products-section for more information.

Newly offered instrumentation, apparatus, and laboratory materials of interest to researchers in all disciplines in academic, industrial, and governmental organizations are featured in this space. Emphasis is given to purpose, chief characteristics, and availability of products and materials. Endorsement by *Science* or AAAS of any products or materials mentioned is not implied. Additional information may be obtained from the manufacturer or supplier.

Downloaded from http://science.sciencemag.org/ on September 30, 2016

DEPArray™ NxT

choose 100% purity

BREAKING THE BARRIER OF TUMOR HETEROGENEITY

Get conclusive data by selecting, sorting and collecting pure tumor and stromal cells to clearly assign genetic variant frequency. Achieving the unlimitate level of purity is a necessary step to unambiguously resolve sample heterogeneity.

NEW FEATURES

High-resolution Imaging • 96 Recoveries • High-level Automation • Benchtop Instrument

D 2.23 ft x W 2.62 ft x H 2.02 ft

www.siliconbiosystems.com

MENARINI silicon biosystems

AMERICAN ASSOCIATION FOR THE ADVANCEMENT OF SCIENCE

BE THE CORE MIND SPIRIT FACE HEART REACH CENTER VOICE OF SCIENCE.

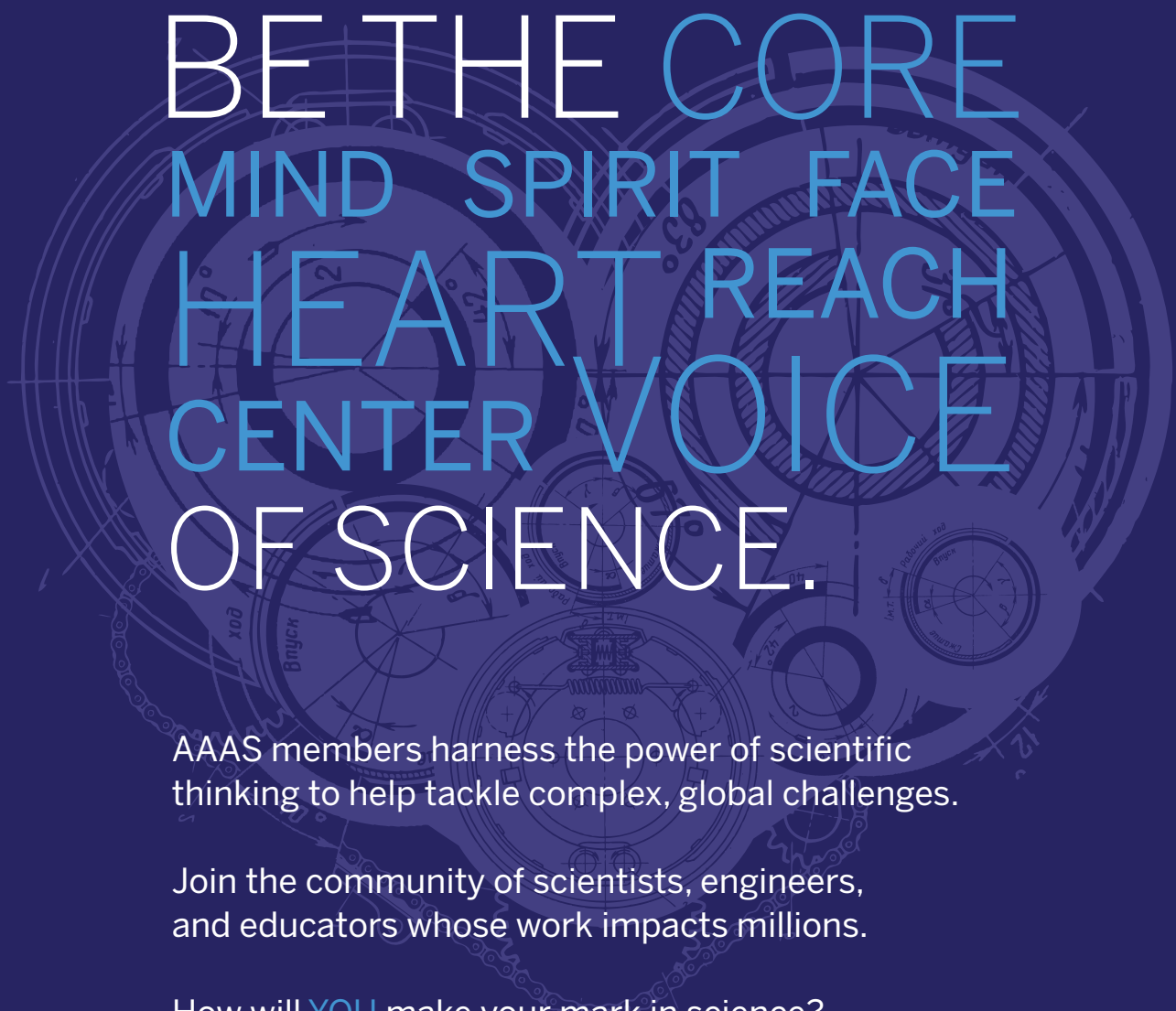

AAAS members harness the power of scientific thinking to help tackle complex, global challenges.

Join the community of scientists, engineers, and educators whose work impacts millions.

How will YOU make your mark in science?

Join AAAS today.
www.aaas.org/join

AAAS

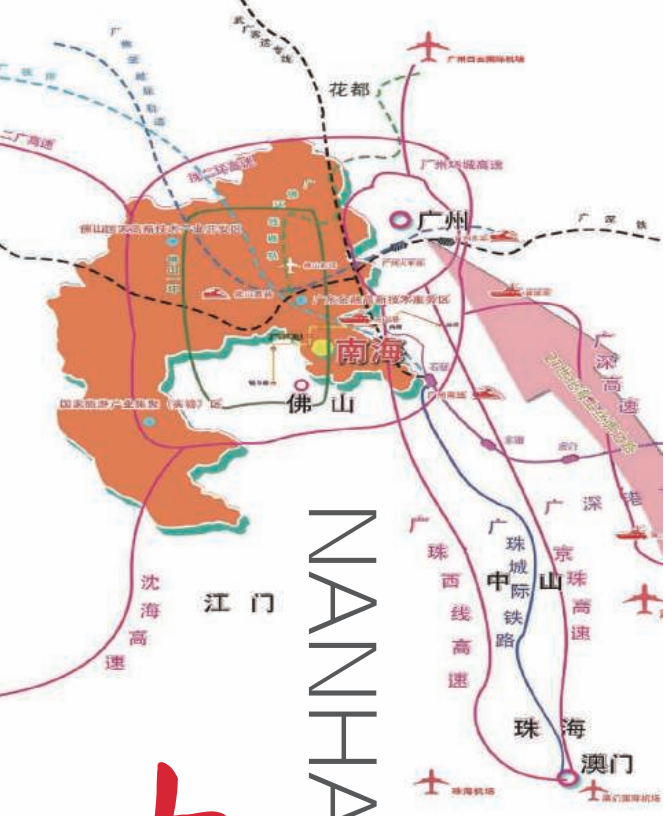

NANHAI

南海

Located in the hinterland of the Pearl River Delta, Nanhai District of Foshan is bordered by Guangzhou to the east and by Hong Kong and Macau to the south. Nanhai has its unique geometric advantages and advanced traffic networks since it is a part of the Guangdong-Hong Kong-Macau economic cooperation zone as well as the incorporated geographic center of Pearl River Delta, and in the core zone of Guangzhou-Foshan metropolitan Area. As one of the "Four Kwong Tung Tigers", Nanhai has been repeatedly ranked in the top 3 positions in the "Top 100 Counties of China". It is also the pioneer city in Guangdong to carry out the reform and opening up policy.

The reginal GDP of Nanhai was 222.7 billion RMB in 2015, ranked No. 2 for its comprehensive strength among cities in the same tier.

Area under administration	1073.8 Km2
Permanent resident population	2.65 million
Various market subjects	180430 household
Number of foreign investment enterprises	1945
"Fortune 500" projects	38

ADVERTISEMENT

Industries in Nanhai

Nanhai has a prominent advantage of manufacturing. Its total industrial output value has reached 579.5 billion RMB and its products are famous in China, such as its mechanical equipment, aluminum profile, textile and garment. The service industry is growing rapidly in Nanhai. The Guangdong High Tech Service Zone for Finance Industries was established in Nanhai and has become an important financial center and financial supporting service center in Southern China.

Livable Nanhai

Nanhai is a highly civilized city worth visiting. It is also considered as the national sanitary city, one of the pilot cities for promoting information technology, national demonstration zone of technological innovation, and one of the highly-educated cities in Guangdong. With the beautiful environment, enlightened culture, prosperous economy and well-constructed recreational infrastructures, Nanhai is a desirable place for living as well as working.

Transportation in Nanhai

From Nanhai, it only takes about 20 minutes to Guangzhou South Railway Station by taking the subway and it takes about 40 minutes to Guangzhou Baiyun International Airport and 2 hours to Hong Kong and Macau. Nanhai is equipped with 5 freight terminals like Sanshan Harbor International Freight Terminal, which is able to reach Hong Kong Port directly. Moreover, it is close to Huangpu and Nansha Deepwater Port.

ADVERTISEMENT

DOES YOUR LAB SEEK TO UNDERSTAND MECHANISMS OF DRUG RESISTANCE OR DISEASE PATHOLOGY?

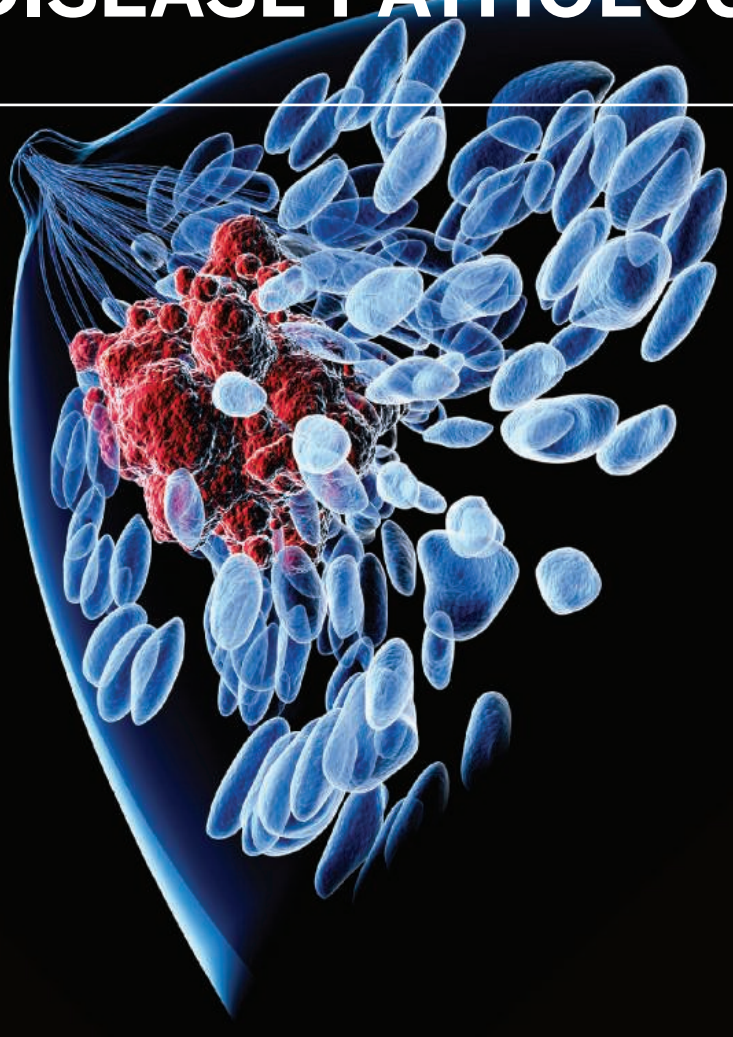

Leslie K. Ferrarelli, "Focus Issue: Refining the War on Cancer", *Sci. Signal.* 7, 318eg2 (2014). Image: Raycat/iStockphoto

Science Signaling | AAAS

CELL SIGNALING IN PHYSIOLOGY AND DISEASE

Find out more about the scope of the journal and submit your research today!
ScienceSignaling.org

eppendorf

New: 4 liter capacity!

More Capacity

Centrifuge 5920 R

The new Centrifuge 5920 R delivers extraordinary high capacity in a very compact and ergonomic product design. Its state-of-the-art refrigeration system provides excellent cooling performance and keeps your temperature sensitive samples safe.

> Max. capacity: 4 × 1000 mL or 52 × 50 mL conical
> Outstanding rotor versatility
> Space-saving design
> Advanced temperature management
> NEW: Eppendorf Conical Tubes, 15 mL and 50 mL

www.eppendorf.com/centrifugation

Eppendorf® and the Eppendorf logo are registered trademarks of Eppendorf AG, Germany. U.S. Design Patents are listed on www.eppendorf.com/ip
All rights reserved, including graphics and images. Copyright © 2016 by Eppendorf AG.

Watch video!

See the Total Solar Eclipse August 21, 2017

Sun Valley Idaho Eclipse

Tetons & Yellowstone • August 18-26, 2017

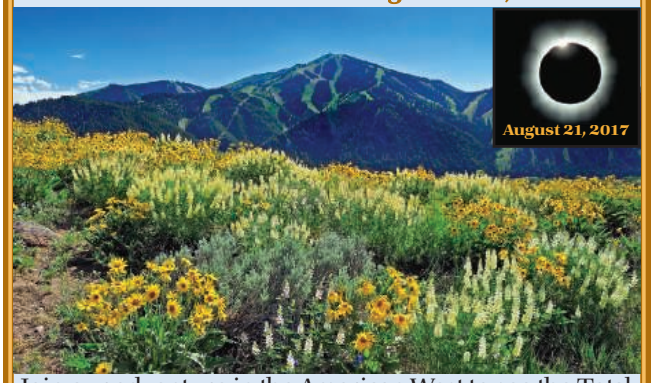

Join our adventure in the American West to see the Total Solar Eclipse overlooking Sun Valley, Idaho! Discover prehistoric sites from Boise to the Tetons. Follow the Snake River to an important fossil site. Ride in cable cars with an incredible 360-degree view of Jackson Hole, the Tetons, and Yellowstone National Park. Trip fee: $4,595 + air.

AAAS *Travels*

For a detailed brochure, call (800) 252-4910
All prices are per person twin share + air

BETCHART EXPEDITIONS Inc.
17050 Montebello Rd, Cupertino, CA 95014
Email: AAASInfo@betchartexpeditions.com
www.betchartexpeditions.com

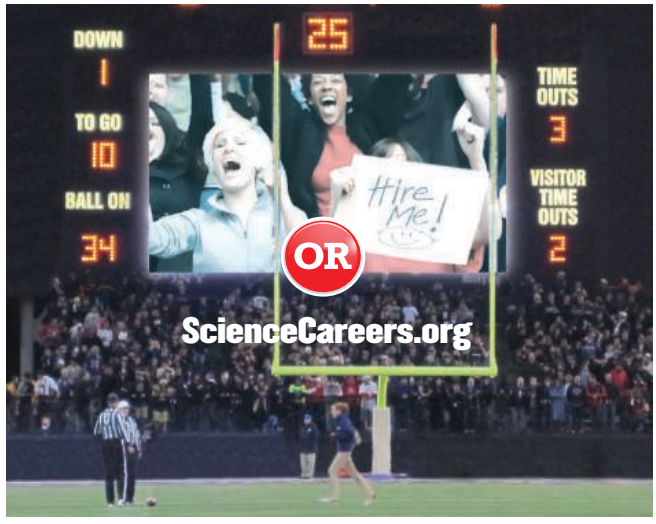

Keep your job search out of the cheap seats.

- Search thousands of job postings
- Create job alerts based on your criteria
- Get career advice from our Career Forum experts
- Download career advice articles and webinars
- Complete an individual development plan at "myIDP"

Target your job search using relevant resources on **ScienceCareers.org**.

Science Careers
FROM THE JOURNAL SCIENCE AAAS

CALL FOR PAPERS!
WILL YOUR RESEARCH LEAD TO BETTER LIVES FOR PATIENTS?

Gopinath Sutendra and Evangelos D. Michelakis, "Pulmonary Arterial Hypertension: Challenges in Translational Research and a Vision for Change", *Sci. Transl. Med.* 5, 208sr5 (2013) Credit: *Science* Source

Challenge your thinking with the leading online journal of high-impact, peer-reviewed translational research that matters most for human health.

Part of the *Science* family of journals, *Science Translational Medicine* publishes weekly and showcases findings on interdisciplinary topics driving preclinical and clinical applications, including immunology, cancer, infectious disease, drug discovery, genomic medicine, and bioengineering.

Learn more and submit your research today.
ScienceTranslationalMedicine.org

Science Translational Medicine
AAAS

Be Among the First to Publish in *Science Robotics*

Image: jim/AdobeStock

NOW ACCEPTING MANUSCRIPTS

ScienceRobotics.org

Science Robotics is a unique journal created to help advance the research and development of robotics for all environments. *Science Robotics* will provide a much-needed central forum to share the latest technological discoveries and to discuss the field's critical issues.

Join in the excitement for the Fall 2016 debut!

Science Robotics

AAAS

want new technologies?

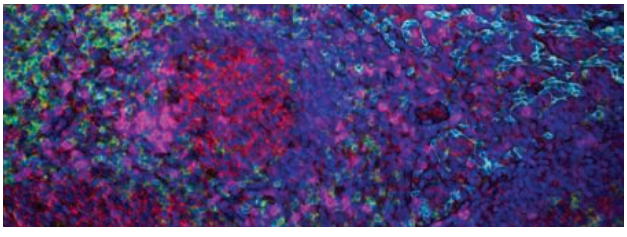

antibodies
apoptosis
biomarkers
cancer
cytometry
data
diseases
DNA
epigenetics
genomics
immunotherapies
medicine
microbiomics
microfluidics
microscopy
neuroscience
proteomics
sequencing
toxicology
transcriptomics

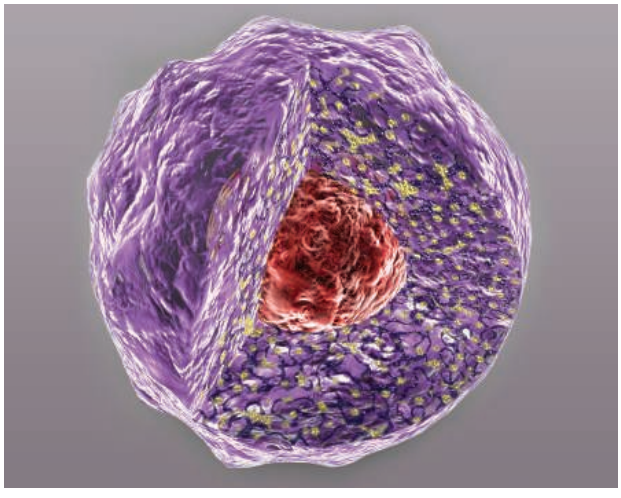

watch our webinars

Learn about the latest breakthroughs, new technologies, and ground-breaking research in a variety of fields. Our expert speakers explain their quality research to you and answer questions submitted by live viewers.

VIEW NOW!
webinar.sciencemag.org

Science
AAAS

Brought to you by the *Science*/AAAS Custom Publishing Office

@SciMagWebinars

applied biosystems

For when every move needs to be precise

Applied Biosystems™ thermal cyclers enable consistent, precise results no matter the challenge

- Engineered with your highest standards in mind
- Designed to consistently deliver the highest performance
- Accuracy you need to advance your research

Request an in-lab demo at **thermofisher.com/consistent**

ThermoFisher SCIENTIFIC

For Research Use Only. Not for use in diagnostic procedures. © 2015 Thermo Fisher Scientific Inc. All rights reserved.
All trademarks are the property of Thermo Fisher Scientific and its subsidiaries unless otherwise specified. **COL02311 0816**

Science Careers Advertising

For full advertising details, go to ScienceCareers.org and click For Employers, or call one of our representatives.

Tracy Holmes
Worldwide Associate Director
Science Careers
Phone: +44 (0) 1223 326525

THE AMERICAS

E-mail: advertise@sciencecareers.org
Fax: +1 (202) 289 6742

Tina Burks
Phone: +1 (202) 326 6577

Nancy Toema
Phone: +1 (202) 326 6578

Online Job Posting Questions
Phone: +1 (202) 312 6375

EUROPE / INDIA / AUSTRALIA / NEW ZEALAND / REST OF WORLD

E-mail: ads@science-int.co.uk
Fax: +44 (0) 1223 326532

Sarah Lelarge
Phone: +44 (0) 1223 326527

Kelly Grace
Phone: +44 (0) 1223 326528

Online Job Posting Questions
Phone: +44 (0) 1223 326528

JAPAN

Katsuyoshi Fukamizu (Tokyo)
E-mail: kfukamizu@aaas.org
Phone: +81 3 3219 5777

Hiroyuki Mashiki (Kyoto)
E-mail: hmashiki@aaas.org
Phone: +81 75 823 1109

CHINA / KOREA / SINGAPORE / TAIWAN / THAILAND

Danny Zhao
E-mail: dzhao@aaas.org
Phone: +86 131 4114 0012

All ads submitted for publication must comply with applicable U.S. and non-U.S. laws. *Science* reserves the right to refuse any advertisement at its sole discretion for any reason, including without limitation for offensive language or inappropriate content, and all advertising is subject to publisher approval. *Science* encourages our readers to alert us to any ads that they feel may be discriminatory or offensive.

ScienceCareers
FROM THE JOURNAL SCIENCE AAAS

ScienceCcareers.org

POSITIONS OPEN

RESEARCH ASSOCIATE IN NEUROSCIENCE

Position available at **POSTDOCTORAL** or **ASSOCIATE RESEARCH SCIENTIST** level at Yale Medical School, for Ph.D. or M.D. with prior experience in axonal biology or neurodegeneration, to join a multidisciplinary team studying mechanisms of injury in peripheral neuropathy and central axonopathies including EAE (see *Persson et al*, Trends in Molecular Med., **22**:377-390, 2016; *Estacion et al*, J Neurophysiol., **114(3)**:1554-64, 2015). Prior publications in neuroscience, and expertise with tissue culture, immunocytochemistry, and morphometrics are essential. Experience with *in vitro* and/or *in vivo* models of nerve injury, neurodegeneration, neuroglial interactions, or bioenergetics are desired. This is a superb opportunity for a well-trained neuroscientist to work within a highly productive, highly collaborative group at Yale Medical School. Send CV, statement of interest and three letters of reference to: **Stephen G. Waxman, MD, PhD, Center for Neuroscience and Regeneration Research, Yale University, email: stephen.waxman@yale.edu.** *Equal Opportunity/Affirmative Action Employer.*

POSITIONS OPEN

MEDICAL COLLEGE OF WISCONSIN

POSTDOCTORAL RESEARCHER in CANCER LAB OF DR. MING YOU

Postdoctoral researcher positions are open in the laboratory of Dr. Ming You at Medical College of Wisconsin (Milwaukee, WI). Successful candidate will work on one of the following projects: (1) immunoprevention of cancer using peptide vaccines; (2) chemoprevention of cancer with mitochondria-targeted agents; and (3) identification of predictive biomarkers of cancer using next-generation sequencing technology. Ideal candidates will have a strong background in cancer immunology, synthesis and characterization of mitochondria-targeted agents, or computational biology (NGS including single cell sequencing, mRNA/miRNA sequencing, and exosome-related miRNA sequencing). Individuals should be able to work independently and have strong English communication and writing skills. Interested applicants should send curriculum vitae, statement of research interests and contact information for three references to Michele Ward at e-mail: **mward@mcw.edu.** Application Deadline is **October 31, 2016**.

For recruitment in science, there's only one *Science*.

Job Focus:
Neuro-science
Issue date: Nov 4
Book ad by Oct 18 to guarantee space*

Why choose this job focus for your advertisement?

- Relevant ads lead off the career section with special neuroscience banner
- Bonus distribution to Society for Neuroscience, Nov 12–16, San Diego, CA.

*Ads accepted until Oct 28 if space allows.
Produced by the *Science*/AAAS Custom Publishing Office.

SCIENCECAREERS.ORG

Science Careers AAAS

To book your ad: **advertise@sciencecareers.org**

The Americas
202 326 6582

Europe/RoW
+44 (0) 1223 326500

Japan
+81 3 3219 5777

China/Korea/Singapore/Taiwan
+86 186 0082 9345

Post your jobs Fast and Easy
Science Careers
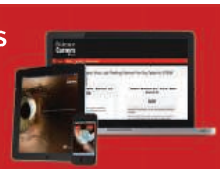
employers.sciencecareers.org

GAIN THE STRENGTH OF A MARKET LEADER — AND THE ENERGY OF A START-UP.

Are you a leader in proteostasis?

AbbVie has made a commitment to finding new therapies for Alzheimer's Disease and other neurodegenerative diseases by opening the Foundational Neuroscience Center (FNC) in Cambridge, Boston.

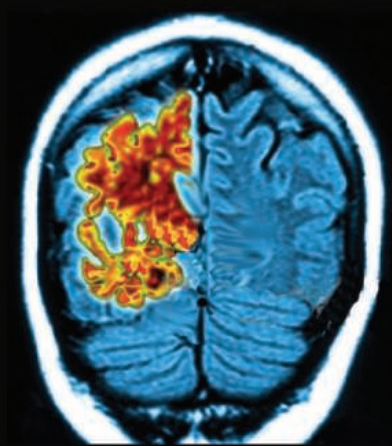

We seek a proteostasis expert to lead a team of 10 scientists. As a member of the FNC leadership team, the ideal candidate will have a strong publication record with a vibrant international network. Prior experience in biotech is advantageous – a desire to see novel discoveries translate into patient benefit is essential.

We seek scientists at all levels for research groups investigating neuroinflammation and tau pathobiology.

Visit abbviecareers.com and reference job ID 1600000118

PEOPLE. PASSION.
POSSIBILITIES.

abbvie

AMERICAN ASSOCIATION FOR THE ADVANCEMENT OF SCIENCE

Career Development Center

Career Development Center

Meet career challenges head-on with online courses designed for scientists

- Public engagement
- R&D funding analysis
- Effective communication
- Proposal writing
- Career development
- Science policy and advocacy

REGISTER TODAY
CareerDevelopment.aaas.org

AAAS

Young Investigators Awards and Postdoc opportunities in Brazil

The São Paulo Research Foundation (FAPESP), one of the leading Brazilian agencies dedicated to the support of research, offers funding schemes to bring researchers from abroad to excellence centers in São Paulo (Brazilian citizenship is not a requirement):

- **Young Investigators Awards (YIA)**: this program is open to scientists who have had a few years of post-doctoral experience and demonstrated research leadership capabilities to lead the creation of new research group in the state of São Paulo, Brazil. The selected candidates will start and lead their own research groups working in internationally competitive themes. The research project will have a duration of 4 years (extendable for another year) and the funding request can include: research equipment, consumables, travel, laboratory infrastructure, a fellowship for the Principal Investigator (to be paid for three years of until the PI obtains a permanent contract at the university or research institute hosting the project), and scholarships for MSc and DrSc students to be supervised by the PI. From 2013 to 2015 FAPESP awarded 198 Young Investigator Awards. Interested candidates can contact FAPESP at **yia@fapesp.br**. A sample of recently approved proposals can be seen at **www.bv.fapesp.br/en/2/young-investigators-grants-jp-4-year-grants**

- **FAPESP Post-Doctoral Fellowships**: program is open to researchers with a recent doctorate degree and a successful research track record. There are two entry points:
(1) open positions are announced at **www.fapesp.br/oportunidades**;
(2) candidates can also contact directly a prospective supervisor in higher education and research institutions in São Paulo and discuss the preparation of a proposal which can be submitted to FAPESP on a rolling date basis. Fellowships include a stipend, travel costs to and from São Paulo, Brazil, support for relocation expenses, plus 15% of the yearly stipend paid to be used in small research expenses. Awardees of FAPESP post-doctoral fellowships can request an additional fellowship to spend up to one year working in a high profile international research group. Norms for the Post-doctoral Fellowships Program are at **www.fapesp.br/en/postdoc**. From 2013 to 2015 FAPESP awarded 2,513 Post-doctoral Fellowships. A sample of recently approved proposals is at **www.bv.fapesp.br/37960**

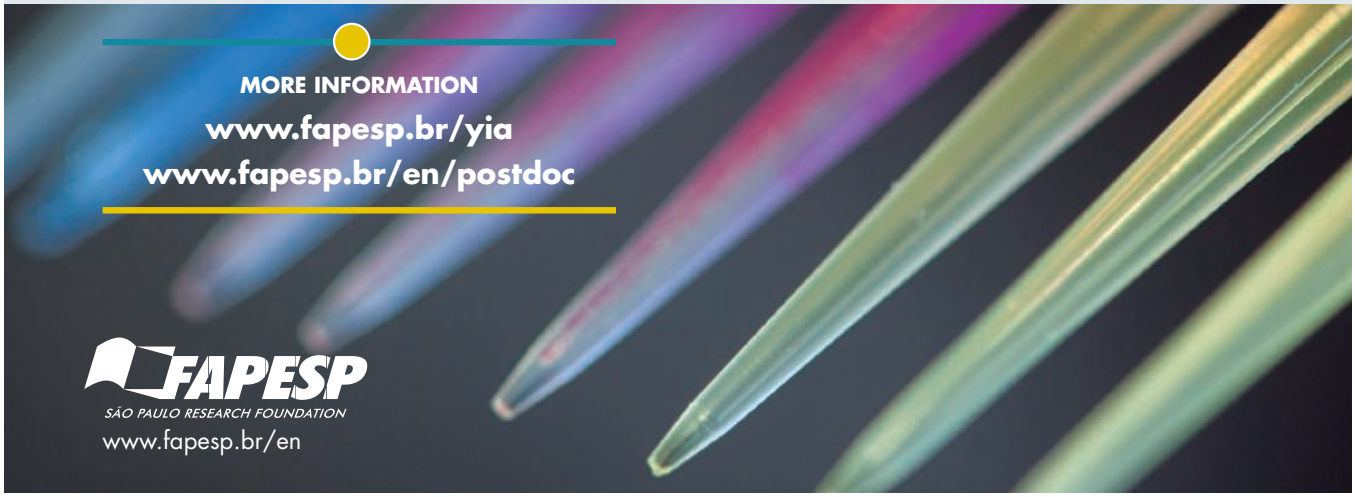

FEATURED EMPLOYER
ScienceCareers online @sciencecareers.org

ScienceCareers online @sciencecareers.org

Faculty Careers

Issue date: October 7

Ads accepted until Oct 3 if space allows

For recruitment in science, there's only one *Science*.

Hiring Faculty? The October 7 feature covers business principles for researchers. Reach *Science* readers and share opportunities at your university.

What makes *Science* the best choice for recruiting?

- Read and respected by 400,000 readers around the globe
- 62% of our weekly readers work in academia and 65% are Ph.D.s. *Science* connects you with more scientists in academia
- Your ad dollars support AAAS and its programs, which strengthens the global scientific community.

Why choose this Faculty Feature for your advertisement?

- Relevant ads lead off this career section with a special Faculty banner
- October 7 issue will be distributed at the American Society of Human Genetics meeting, 18 –22 October, Vancouver.

Expand your exposure by posting your print ad online:

- Link on the job board homepage directly to Faculty jobs
- Dedicated landing page for faculty positions.

Produced by the *Science*/AAAS Custom Publishing Office.

Deliver your message to a global audience of targeted, qualified scientists.

129,574
subscribers in print every week

352,966
monthly unique browsers on ScienceCareers.org

65%
of our weekly readers are Ph.D.s

SCIENCECAREERS.ORG

ScienceCareers
FROM THE JOURNAL SCIENCE AAAS

To book your ad: **advertise@sciencecareers.org**

The Americas
+202 326 6582

Japan
+81 3 3219 5777

Europe/RoW
+44(0)1223 326500

China/Korea/Singapore/Taiwan
+86 186 0082 9345

HOWARD HUGHES MEDICAL INSTITUTE

2017 Hanna H. Gray Fellows Program

The Howard Hughes Medical Institute (HHMI) is pleased to announce the new Hanna H. Gray Fellows Program. This program seeks to increase diversity in the biomedical research community by recruitment and retention of individuals from groups underrepresented in the life sciences. Through their successful careers as academic scientists, Hanna H. Gray Fellows will move science forward and inspire the next generation of scientists from America's diverse talent pool.

Fellows will receive funding for their postdoctoral training and, if eligible, in their early career years as independent faculty. The program includes opportunities for career development, including mentoring and active involvement in the HHMI scientific community. The Institute will select up to 15 Fellows in this first competition, which will open in Fall 2016.

Eligibility:

- The program is open to individuals who are from gender, racial, ethnic, and other groups underrepresented in the life sciences at the career stages targeted by this program, including those from disadvantaged backgrounds.
- Applicants must have a PhD and/or MD (or equivalent) by the start of the grant term and have no more than 12 months of postdoctoral research experience at the time of the application due date.
- The competition is open to applicants of any citizenship or nationality who have been accepted to join a laboratory as a postdoctoral fellow at a research institution located in the U.S. (including Puerto Rico).
- The program is open to basic science researchers and physician-scientists in all biomedical and life science disciplines.

Awards may start as early as November 15, 2017 but no later than January 15, 2018.

Fellows will receive a non-renewable grant of $80,000 annually for up to four years of postdoctoral training support followed by a non-renewable grant of $270,000 annually for up to four years of the faculty phase, if program criteria are met.

Applications are due on February 15, 2017. Mentor and reference letters must be received by February 23, 2017.

Additional information:

www.hhmi.org/HannaHGrayFellows2017

For questions contact program staff at fellows@hhmi.org

hhmi Howard Hughes Medical Institute

UNIVERSITY OF MICHIGAN FACULTY POSITIONS IN MATHEMATICAL/COMPUTATIONAL BIOLOGY

The Department of Mathematics and the Department of Molecular, Cellular, and Developmental Biology (MCDB) in the College of Literature, Science and the Arts at the University of Michigan solicit applications for faculty positions in mathematical/computational biology at the assistant professor level, but appointment at a more senior level is possible for applicants with suitable experience. We encourage applications from scientists with a strong background in the life sciences who use mathematical modeling, or apply computational approaches to large datasets to understand basic cellular, genetic, developmental and/or physiological processes. We are most interested in candidates who not only use, but also develop cutting edge models and tools from applied, computational and/or interdisciplinary mathematics to solve real world problems in the biological sciences. The faculty position will be tenure track or tenured with a university year appointment starting September 1, 2017 or January 1, 2018. Successful candidates will be expected to establish a vigorous, extramurally funded research program and to be involved with instruction of both undergraduate and graduate students. For further information about research areas in Mathematics please visit https://lsa.umich.edu/math, and for MCDB http://lsa.umich.edu/mcdb.

All applications must be submitted on-line at **http://www.mathjobs.org**. You will be asked to upload the following materials: A cover letter, a *curriculum vitae*, a brief summary of recent research accomplishments and statement of future research plans, a statement of teaching philosophy and experience, and evidence of teaching excellence for those who have teaching experience. Candidates for appointment at the assistant professor level should provide names and contact information for at least three references, as instructed in the **on-line application form**. To ensure full consideration, all materials should be received by **October 14, 2016**.

Women and underrepresented minorities are encouraged to apply. The University of Michigan is supportive of the needs of dual career couples and is an Equal Opportunity/Affirmative Action Employer.

Penn
University of Pennsylvania

Tenure-Track Position in Animal Behavior

The Department of Biology at University of Pennsylvania invites applicants for a tenure-track position in Animal Behavior at the level of Assistant Professor. We are especially interested in integrative research that explores animal behavior in a natural context. We will consider all types of behaviors and animal models, but we have a particular interest in behaviors that include a social, interactive component. The anticipated start date for this position is July 2018.

Penn's Department of Biology has a long-standing tradition of maintaining an integrated research and educational program across all basic biological sciences, including Molecular and Cellular Biology, Microbiology, Neuroscience, Animal Behavior, Genomics, Ecology and Evolution, and Plant Sciences. The Department values interdisciplinary research, collaboration, and collegiality, with a vision that emphasizes "Life in its Natural Context".

Candidates are expected to have demonstrated excellence and productivity in research and to participate in undergraduate and graduate teaching. Interested candidates should submit materials through **http://facultysearches.provost.upenn.edu/postings/957** and include a curriculum vitae, concise statements of research and teaching interests, a short annotated description of up to five publications, and the name and contact information of at least three referees. Recommenders will be contacted by the University with instructions on how to submit a letter to the website. Review of applicants will begin **November 7, 2016** and continue until the position is filled.

The Department of Biology is strongly committed to Penn's Action Plan for Faculty Diversity and Excellence and to creating a more diverse faculty (for more information see: http://www.upenn.edu/almanac/volumes/v58/n02/diversityplan.html). The University of Pennsylvania is an Equal Opportunity Employer. Minorities/Women/Individuals with Disabilities/Protected Veterans are encouraged to apply.

10 ways that *Science* Careers can help advance your career

1. Register for a free online account on **ScienceCareers.org**.
2. Search thousands of job postings and find your perfect job.
3. Sign up to receive e-mail alerts about job postings that match your criteria.
4. Upload your resume into our database and connect with employers.
5. Watch one of our many webinars on different career topics such as job searching, networking, and more.
6. Download our career booklets, including Career Basics, Careers Beyond the Bench, and Developing Your Skills.
7. Complete an interactive, personalized career plan at "my IDP."
8. Visit our Career Forum and get advice from career experts and your peers.
9. Research graduate program information and find a program right for you.
10. Read relevant career advice articles from our library of thousands.

Visit **ScienceCareers.org** today — all resources are free

ScienceCareers

FROM THE JOURNAL SCIENCE AAAS

SCIENCECAREERS.ORG

2016 Annual
Top Employers in Biotech & Pharma

Special Career Feature:
October 28, 2016

Reserve your ad by October 11 to guarantee space.

Ads accepted until October 21 if space is still available.

For recruitment in science, there's only one **Science**

WHO IS NO. 1 THIS YEAR?

Science publishes the results of its 15th annual Top Employers Survey on October 28. *Science* has a long history of providing a forum for scientists to express their opinions about the biotech and pharma industry.

Recruit or brand your organization and reach both ACTIVE and PASSIVE job seekers.

Start building your pipeline today with *Science*.

SCIENCECAREERS.ORG

ScienceCareers
FROM THE JOURNAL SCIENCE AAAS

To book your ad:
advertise@sciencecareers.org

The Americas
202-326-6582

Japan
+81-3-3219-5777

Europe/RoW
+44 (0) 1223-326500

China/Korea/Singapore/Taiwan
+86-186-0082-9345

PURDUE UNIVERSITY

MULTIPLE FACULTY POSITIONS
Department of Medicinal Chemistry and Molecular Pharmacology

The Department of Medicinal Chemistry and Molecular Pharmacology (http://www.mcmp.purdue.edu) invites applications for MULTIPLE TENURE-TRACK FACULTY POSITIONS at all ranks. Preference will be given to qualified candidates with strong programs in neuroscience that complement or strengthen the existing departmental focus areas, although outstanding candidates in cancer biology, immunology/infectious diseases, and/or medicinal chemistry will also be seriously considered.

The Department offers a unique multidisciplinary and collaborative environment with synergistic strengths in both chemistry and biology, spanning a wide range of topics including signal transduction, epigenetics, macromolecule structure and function, structural and computation biology, molecular pharmacology, systems biology, chemical biology, medicinal chemistry and drug discovery. The Department also contributes significantly to the NCI-designated Purdue University Center for Cancer Research (https://www.cancerresearch.purdue.edu/), Purdue Institute for Integrative Neuroscience (http://www.purdue.edu/discoverypark/pillars/integrative-neuroscience-center/index.php), Purdue Institute for Inflammation, Immunology and Infectious Disease (http://www.purdue.edu/discoverypark/pillars/pi4d/index.php), and Purdue Institute for Drug Discovery (http://www.purdue.edu/discoverypark/drug-discovery/).

Purdue University is investing more than $250 million in the life sciences over the next five years and offers state-of-the-art facilities for transgenic animals, imaging, genomics, bioinformatics, proteomic and metabolomics, NMR, X-ray crystallography, CryoEM, and chemical genomics. Faculty have the opportunity to train graduate students in the departmental and university-wide interdisciplinary programs. Highly competitive salary, start-up funds and laboratory space will be provided.

Candidates must have a Ph. D. degree or equivalent in a relevant scientific discipline and relevant post-doctoral experience. The successful candidate will be expected to establish and/or maintain a strong extramurally-funded research program and will participate in undergraduate, professional, and graduate education/teaching. Applications should consist of (1) a cover letter including the names and contact information of three references, (2) a curriculum vitae, (3) a statement of teaching philosophy and experience, and (4) a summary of planned and/or ongoing research. These materials should be submitted electronically to **http://purdue.taleo.net/careersection/wlfac/jobdetail.ftl?job=1602100&lang=en&sns_id=mailto#.V-A4yleS-rU**. Please contact Barb Mullenberg at **davidsba@purdue.edu** if you have questions about uploading documents or the search. Review of applications will begin on **October 15, 2016** and will continue until the positions are filled. Applications will be held in confidence until the interview phase of the process, and the applicants' permission to contact references prior to that time will be obtained. A background check will be required for employment in this position.

Purdue University is an EOE/AA Employer. All individuals, including minorities, women, individuals with disabilities, and veterans are encouraged to apply.

Stanford | ENGINEERING

Materials and Processes for Water Quality Engineering

The School of Engineering at Stanford University invites applications for a tenure-track faculty appointment at the junior level (Assistant or untenured Associate Professor) in the broadly defined field of materials and processes for water quality engineering. Priority will be given to the overall originality and promise of the candidate's work over any particular specialization area or department affiliation. Applicants should have an earned Ph.D., evidence of the ability to pursue an independent program of research, a strong commitment to both graduate and undergraduate teaching, and the ability to initiate and conduct research across disciplines. We seek applicants with expertise in materials and chemical or physical processes for water and environmental applications with research that focuses on development and application of new materials and improved processes for water treatment and/or sustainable approaches for managing the world's critical water, energy, and food needs. This may include novel membranes, mass and heat transport studies, improved catalysts, new sensors, and integration of new materials with biotechnology to produce novel hybrid systems. An ideal candidate would be capable of achieving breakthrough results relevant to new technologies at the water-energy-food nexus, while assisting in the translation of these technologies to environmental practice.

The appointment of the successful candidate is envisioned to be in one or two of the departments of Civil and Environmental Engineering, Chemical Engineering, and Materials Science and Engineering, although a joint appointment with another department will also be considered.

Applications should include a research and teaching plan (not to exceed five pages), a detailed resume including a publications list, and the names and addresses of five references.

Candidates should apply online at **http://cee.stanford.edu/about/academic-openings**. Applications will be accepted through **December 1, 2016**. Questions may be directed to search administration at **ceesearch@lists.stanford.edu**, or Search Committee Chair, Richard G. Luthy, **luthy@stanford.edu**.

Stanford University is an Equal Opportunity Employer and is committed to increasing the diversity of its faculty. We welcome nominations of and applications from women, members of minority groups, protected veterans and individuals with disabilities, as well as from others who would bring additional dimensions to the university's research, teaching and clinical missions.

By **Shane M. Hanlon**

Managing my fear of missing out

"You have a lot of jobs." That's something that I hear all the time when I talk to folks about how I've included science in my life. At the moment I technically have three jobs—a full-time science communication and policy role, a science storytelling gig with shows every few months, and a monthlong teaching position each summer—and I recently picked up an adjunct position, so make that four. Why do I have all these jobs? Well, I have science FOMO. Short for "fear of missing out," FOMO describes the feelings of someone who just can't say "no" to anything, even when they're already overextended. In social contexts, I'm OK with missing out. But when it comes to science, I feel the need to seize every opportunity.

I don't think that I'm the only former academic in this predicament. My attitude is likely a carryover of a mentality ingrained in graduate students: Do everything you can and expect little in return. As a student, in addition to my academic responsibilities, I represented my department in student government, was an outreach liaison to a conservation organization, and regularly talked about my research at outreach events. At the time, I believed that I was doing all of these things to add to my CV. Looking back, though, I realize that I was also driven by a nagging concern that I was never doing enough. I took on as much as I could in part to alleviate those doubts. It wouldn't be the last time.

"I was ... driven by a nagging concern that I was never doing enough."

FOMO kicked in again when I decided to leave academia after getting my Ph.D. I worried that being away from research would make me forget my academic training and that I would lose contact with my former colleagues. I even thought that I would get dumber if I wasn't actively planning research projects. So, during my John A. Knauss Marine Policy Fellowship at the U.S. Fish and Wildlife Service, I used my vacation time—and oftentimes cobbled together my own funds—to continue attending conferences, keeping up on current research, and writing manuscripts related to conservation biology. It was tough to manage at times—I essentially had two jobs, even though one didn't pay—but the reward of feeding my scientific interests kept me at it.

After the fellowship, I bounced around between short-term and temporary positions, trying to find the right combination of activities to satisfy my FOMO. I was a science policy and communications fellow at the National Academy of Sciences, where I told a story for the science storytelling organization The Story Collider. I wrote questions for a science quiz bowl organization. I started teaching an annual, monthlong field course in disease ecology. I was feeding my FOMO, but as time passed, I struggled with the lack of professional and financial security. I didn't just want a job; I wanted a career. And, I reasoned, I could still do all of these "extra" activities in addition to a full-time job.

I eventually found my place at the American Geophysical Union, where I help fellow scientists communicate their research to broad audiences. I dabble in communications, policy, teaching, and academia, which should satisfy my FOMO. And it does—but not entirely. So I still teach the field course every year. I started cohosting and producing Story Collider shows. I've also recently picked up an adjunct teaching position in an environmental management department. And I imagine that I'll be involved with more activities in the future, both because I enjoy the opportunities to do new things and to quell the internal voice that still sometimes tells me that I'm not doing enough.

FOMO has given me the drive to explore many different ways of working in science. But I have also realized that sometimes it can be too much, so I need to make sure that it doesn't rule me. In addition to being a scientist, I'm also a partner, a son, a friend, an uncle. I'm not going to let my science FOMO cause me to miss out on life. ■

Shane M. Hanlon is a specialist with the Sharing Science program at the American Geophysical Union and Washington, D.C., producer for The Story Collider. Send your career story to SciCareerEditor@aaas.org.

ILLUSTRATION: ROBERT NEUBECKER

Downloaded from http://science.sciencemag.org/ on September 30, 2016

Published by AAAS